APPLIED COMPUTATIONAL ELECTROMAGNETICS SOCIETY JOURNAL

May 2019
Vol. 34 No. 5
ISSN 1054-4887

The ACES Journal is abstracted in INSPEC, in Engineering Index, DTIC, Science Citation Index Expanded, the Research Alert, and to Current Contents/Engineering, Computing & Technology.

The illustrations on the front cover have been obtained from the research groups at the Department of Electrical Engineering, The University of Mississippi.

MAY 2019 REVIEWERS: REGULAR PAPERS

Amsaveni A.
Sajjad Abazari Aghdam
Ahmed Abdelrahman
Mohammad Alibakhshikenari
Manuel Arrebola
Rezaul Azim
Mehmet Belen
Muhammad Bilal
Subhradeep Chakraborty
Kent Chamberlin
Raghvendra Chaudhary
Pasquale Dottorato
Alistair Duffy
Abdelnasser Eldek
Chonghua Fang
Ian Flintoft
Idayachandran Govindanarayanan
Chi-Fang Huang
Mousa Hussein
Mourad Ibrahim
Amir Jafargholi
Irum Jafri
Saughar Jarchi
Tianqi Jiao
Michael Johnson
Yasushi Kanai
Mithilesh Kumar
Bing Li
Wen-Jiao Liao
Chia-Hsien Lin
Haiwen Liu
Shengyuan Luo
Kourosh Mahdjoubi
Peyman Mahouti
Riyadh Mansoor
Amir Mirbeik-Sabzevari
Zia Ur Mohammad
Sathiyamoorthy Murugan
Dhirgham Naji
Javad Nourinia
Xiao-Min Pan
Ikmo Park
Andrew Peterson
K. C. Raju
Abhishek Rawat
C.J. Reddy
Sobhan Roshani
Avisankar Roy
Thennarasan Sabapathy
Albert Sabban
Reza Safian
Ping Jack Soh
Yuvaraja T.
Yogesh Thakare
Anjini Tiwary
Fikret Tokan
Kagan Topalli
Roberto Vincenti Gatti
Ana Vukovic
Wei-Chung Weng
Julia Wolff
Zhihong Ye
Wenhua Yu
Yujuan Zhao

MAY 2019 REVIEWERS: EXPRESS PAPERS

Yang Bao
Fangyuan Chen
Amin Gorji
Samir Gupta
Changrong Liu
Jian Liu
Quang Nguyen
C.J. Reddy
Alain Reineix
Christopher Trueman

THE APPLIED COMPUTATIONAL ELECTROMAGNETICS SOCIETY JOURNAL

Vol. 34 No. 5 May 2019

TABLE OF CONTENTS – REGULAR PAPERS

TABLE OF CONTENTS – EXPRESS PAPERS

Miniaturized Cross-Lines Rectangular Ring-Shaped Flexible Multiband Antenna

Aqsa Javed [1], Asma Ejaz [1], Sumrin Mehak [1], Yasar Amin [1,2], Jonathan Loo [3], and Hannu Tenhunen [2,4]

[1] ACTSENA Research Group, Department of Telecommunication Engineering
University of Engineering and Technology, Taxila, Punjab 47050, Pakistan

[2] iPack Vinn Excellence Center, Department of Electronic Systems, Royal Institute of Technology (KTH)
Isafjordsgatn 39, Stockholm SE-16440, Sweden

[3] Department of Computer Science, School of Engineering and Information Sciences
Middlesex University, London, United Kingdom

[4] Department of Information Technology, TUCS, University of Turku, Turku 20520, Finland

Abstract ─ A compact, flexible antenna for wireless applications, i.e., WLAN/WiMAX/Wi-Fi, UMTS2100, C-Band, and DSRC is presented. The quad-band antenna is designed and analyzed in terms of efficiency, gain, radiation pattern, return loss, and VSWR. The optimized design consists of a CPW fed rectangular ring patch with the semi-circular ground. The cross-lines and the semi-circular ground is investigated to ascertain the multi-band effect. A concept of inset feed mechanism is also interpolated to enhance impedance matching. The framed antenna is examined under the bent condition as well. The reported work is an apt candidate for the proposed applications because of its high efficiency of 95% with a peak gain of 3.22 dBi along with VSWR less than 2. With stable radiation pattern and bandwidth, there is a justified concurrence between simulated and measured results.

Index Terms ─ Compact, CPW, cross-lines, flexible, inset feed, multi-band, rectangular ring.

I. INTRODUCTION

Emerging wireless communication technologies are fostering the ways for the multiband antennas that are conveniently mergeable with the anticipated systems. The communication systems are operable at different frequencies, and it leads to the coverage of diversified applications. Consequently, multi-band antennas are essential units for these multifunctional packages. The name of microstrip patch antennas has been marked in the list of most demanding antenna type due to the additional perks of mini-sized, lightweight and low-cost. Therefore, antenna designers are eagerly working on multiband microstrip patch antennas. Many techniques can be applied to make an antenna multiband in nature such as, substrate-integrated suspended-line technique [1], slotted patch [2, 3], adding stubs [4], defected ground structures [5], proximity coupled technique [6], cutting edges [7] and many more.

Traditionally, the antennas were designed by using the rigid substrates like FR4 as reported in [8-10]. The development in the flexible electronics market sparked the idea of scaled-down flexible antennas. The diminutive size of the antenna permits its easy integration into advanced electronic packages. The conformal devices are unable to assimilate rigid substrates and demand moldable antennas. The persistent advancement stimulates the researchers to work for the latest communication systems by designing miniaturized antennas under the flexible substrates for utilization in diverse applications. The advantages of low cost, easy fabrication, and light-weight of flexible substrates rate their value high in the market. In the near past, a lot of work focus has been directed towards multiband antennas on the conformal substrates, for example, kapton [11], liquid crystal polymer (LCP) [12], Rogers RT/duroid [13], cotton layer [14], polyethylene terephthalate (PET) film [15] and paper [16]. These recent research findings give a boost to the implementation of the conformal antennas as bending causes minimal effect on the performance of the antenna.

A novel CPW fed rectangular ring patch antenna is investigated in this paper. The presented work is unique in the category of multiband antennas for its compactness and flexibility. The metallic cross-lines are added to the rectangular ring and optimized along with circular ground for achieving multi-band effect of the antenna. The inset feed mechanism is used to improve impedance

Submitted On: December 20, 2018
Accepted On: January 26, 2019

matching. The presented work is suitable for UMTS (1900–2200 MHz), WiMAX (3.2–3.8, 5.1–5.8 GHz) bands WLAN/Wi-Fi (5.1-5.8 GHz), C-band (4-8 GHz) and dedicated short-range communication (DSRC 5.9 GHz) operations.

II. DESIGN PROCESS

A flexible CPW fed patch antenna is put forward in this paper. The antenna operates in multiple bands having the compact dimensions of $0.2176\lambda_0 \times 0.203\lambda_0$ and $0.59\lambda_0 \times 0.55\lambda_0$ with respect to lowest and highest resonant frequency, respectively. The simulations are performed in a commercially available simulation tool, i.e., CST Microwave Studio Suite®. The design is implemented on a flexible dielectric substrate Rogers® RT/duroid 5880 whose ε_r=2.2 and the tanδ=0.0009 with the thickness of 0.127 mm. The design process is executed by primarily designing a rectangular patch antenna. The design procedure went through four steps which will be discussed in the coming sections.

A rectangular ring patch antenna with embedded metallic cross-lines is shown in Fig. 1 (a). The semi-circular ground and the inserted cross-lines inside the rectangular ring are responsible for making the design operable in multiple frequency bands. The final antenna design resonates at four frequencies. The frequency bands achieved by the proposed antenna are 2.097-2.264 GHz for UMTS2100, 3.218-3.353 GHz for 3.5 GHz WiMAX, 4.28-4.81 GHz for C-band, and 5.7-6.2 GHz for 5/5.5/5.8 GHz WLAN/WiMAX/Wi-Fi, and DSRC.

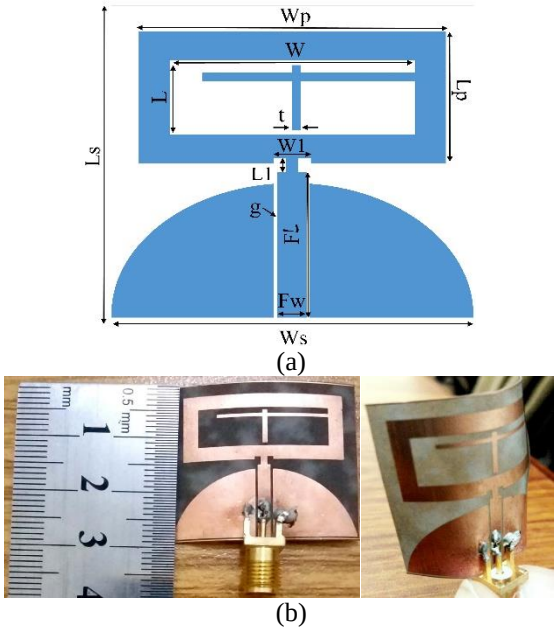

(a)

(b)

Fig. 1. (a) Proposed antenna parameters with *Ls*=28mm, *Ws*=30mm, *Lp*=12mm, *Wp*=26mm, *L*=7mm, *W*=21mm, *L1*=1.5mm, *W1*=3mm, *Fw*=2mm, *Fl*=13mm, *t*=0.8mm, *g*=0.2mm, and (b) fabricated prototype.

A. Design approach

Initially, a CPW fed rectangular ring-shaped patch antenna is designed. Equation (1) and (2) provide a close estimation to predict the dimensions [17]:

$$W = \frac{c}{2f_r}\sqrt{\frac{2}{\varepsilon_r+1}}, \quad (1)$$

$$L = \frac{c}{2f_r\sqrt{\varepsilon_{reff}}} - 2\Delta L, \quad (2)$$

where W and L is the width and length of the patch, respectively, c is the speed of light, f_r stands for the resonant frequency, ε_r is the relative permittivity, ε_{reff} is the effective permittivity, and ΔL is the effective length. The dimensions of the design are finalized after running through a series of investigations and modifications. The performed simulation analyses authenticate that the addition of metal strips creates a way for the surface currents and paves a way to reach the four resonant frequencies.

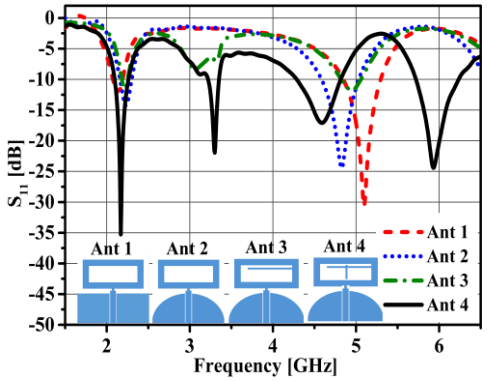

Fig. 2. The S-parameters of the four antennas.

Figure 2 illustrates the effects of a series of design modifications. The results of the optimized rectangular ring show that the antenna resonates at a frequency of 5.09 GHz (Ant 1). The ground structure is modified to semi-circular shape for an increased number of bands and improved impedance matching. Thus, the antenna starts resonating at two distinct bands, i.e., 2.24 GHz and 4.84 GHz (Ant 2). A horizontal metallic line is introduced inside the rectangular ring (Ant 3) which results in three different resonating frequency bands, i.e., 2.22 GHz, 3.09 GHz, and 4.96 GHz. At this stage, the frequency bands do not match accurately. A straight vertical metallic line is introduced onto the already embedded horizontal-line (Ant 4), and it tends to add another band. Thus, we get four frequency bands at 2.17 GHz, 3.3 GHz, 4.59 GHz, and 5.93 GHz by antenna type 4, whereas only three frequency bands are achieved in [18]. The concept of inset feed is introduced with stepped feed design to improve the impedance matching. Ant 4 is characterized as the final proposed antenna. The -10dB impedance bandwidth of all the four accomplished bands is greater than 100 MHz. The achieved peak gain is 3.22 dBi. The highest efficiency

among the resonating bands is 95%.

III. RESULTS AND DISCUSSION

The fabricated prototype of the antenna is tested, and juxtaposition of the simulated and the measured results is reported. There is decent cooperation between the simulated and measured results. The slight mismatch in the results is owing to the fabrication errors, SMA connector soldering and, measurement limitations during the prototype formation. The design is simulated and analyzed under the bent condition as well. The proposed antenna is curved to a radial value of 30 mm. There is a slight change observed in the outcomes of the flat and curved antenna, but the curved antenna nicely covers the targeted bands.

A. Return loss

The return loss of the proposed antenna-under-test is co-plotted in Fig. 3. The results are displayed using a different colour scheme for a better pictorial representation. The antenna resonates at four distinct frequency bands with return loss values of 34.97 dB, 21.928 dB, 17.06 dB, and 24.41 dB at the resonant frequencies of 2.17 GHz, 3.3 GHz, 4.59 GHz, and 5.93 GHz, respectively. The bandwidths achieved are 167 MHz (2.097-2.264 GHz), 135 MHz (3.218-3.353 GHz), 530 MHz (4.28-4.81 GHz), and 500 MHz (5.7-6.2 GHz) at each resonant frequency, with reference to -10 dB line [19]. The return loss of the flat and the curved antenna is analysed, and no great deprivation in the results is spotted. A slight frequency shift occurs towards the right side at the 2nd resonant frequency. Whereas, the other resonating bands remain at the same position with some impact on S_{11} value.

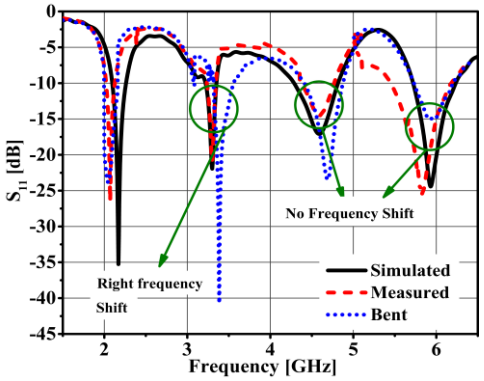

Fig. 3. Return loss of the proposed antenna.

B. Radiation patterns

The radiation characteristics of the presented antenna have also been studied. Figures 4 (a)-(h) depict the simulated and measured radiation patterns for the E ($\varphi=0^0$, y-z) and H ($\varphi=90^0$, x-z) plane at each central frequency. The E-plane characteristics depict the pattern like the number "Eight" which is a sound explanation for the antenna radiating bi-directional in E-plane. Whereas, the H-Plane radiation patterns illustrate that the antenna radiations are partially omni-directional and bi-directional at different resonant dips.

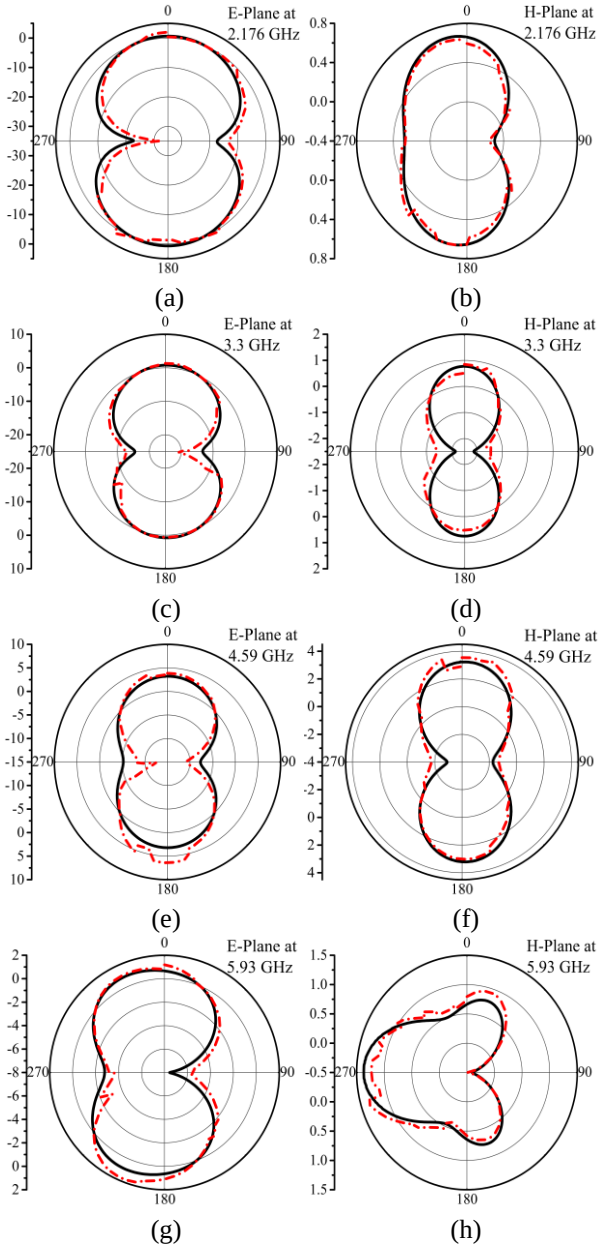

Fig. 4. Measured (dash line) and simulated (solid line) radiation pattern at each resonant frequency.

C. Current distributions

Figures 5 (a)-(d) offer the surface current distributions of the proposed antenna. They give satisfactory details about the effective area which tend to make suggested

antenna resonate at the specific frequencies. Figure 5 (a) provides a visible indication of the antenna structure responsible for producing the lowest dip at 2.176 GHz. This figure depicts that the maximum density of current is at the edges of the ground and the main rectangular ring patch. Figure 5 (b) explains the appearance of another dip at 3.3 GHz. The figure gives a well-summarized description that the current density is along the horizontal line. Moreover, the current concentration is high at the upper and lower part of the rectangular ring. The current density around vertical line is highest at 4.93 GHz and is presented in Fig. 5 (c). This figure explains the reason for the third band as the position and size of the vertical line in the antenna causes the third frequency band to resonate. The current density at 5.93 GHz is depicted by Fig. 5 (d) which shows that the distribution of current is highest at the patch.

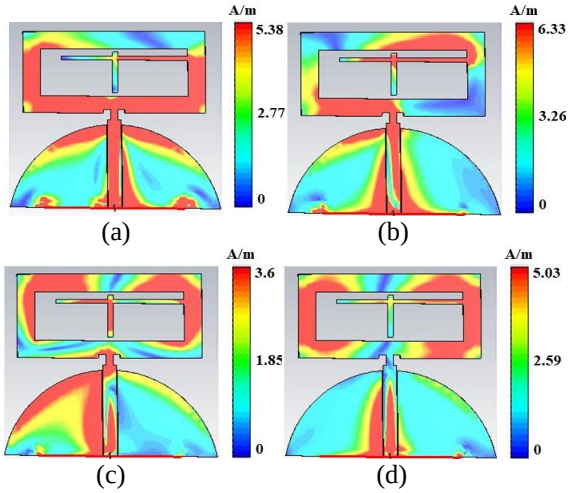

Fig. 5. Current distributions at each resonant frequency: 2.176 GHz, 3.3 GHz, 4.59 GHz, and 5.93 GHz.

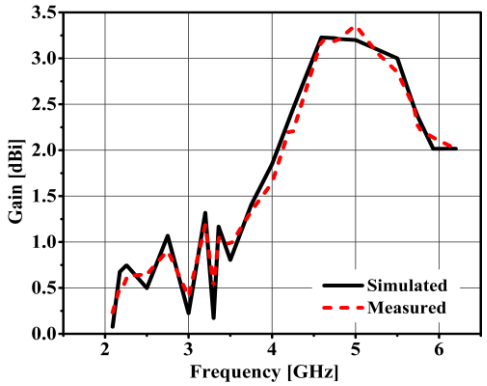

Fig. 6. Measured and simulated gain.

C. VSWR, gain and efficiency

The ascertained gain at operating frequency of each band is rational enough for a simple patch antenna. The attained peak gain is 3.22 dBi. Figure 6 depicts the gain at each resonating band.

The presented antenna is investigated for radiation efficiency. An admirable value of 95% efficiency is achieved highest among all the four bands. The VSWR values at each resonant frequency are below 2 which completely satisfies the required criteria [20].

Table 1 highlights the proposed antenna performance parameters such as gain, efficiency, bandwidth, return loss and VSWR for both states, i.e., bent and flat, which are fairly analogous and in good agreement.

Table 1: Comparison of antenna parameters before and after bending

Parameters	Before Bending				After Bending			
Freq. (GHz)	2.176	3.3	4.59	5.93	2.176	3.3	4.59	5.93
Return Loss (dB)	34.9	21.9	17.0	24.4	23.8	40.7	23.4	15.0
Bandwidth (MHz)	167	135	530	500	160	180	460	470
VSWR	1.06	1.18	1.32	1.12	1.27	1.09	1.29	1.43
Gain (dBi)	0.67	0.17	3.22	2.01	0.5	0.48	3.14	1.95
Efficiency (%)	72.9	54.8	87.8	95	71	70	80.9	97.1

The proposed work is kept under the comparative analysis with other related published work. The evaluated assessment is reported in Table 2. This table is an indication for the presented work to be a better choice for the desired applications.

Table 2: Comparison of proposed and previously reported antenna performance parameters

References	[2]	[10]	[13]	[16]	Proposed Antenna
Area (mm^2)	40 × 40	40 × 38	90 × 60	35 × 40	30×28
No. of operating bands	4	3	4	3	4
Gain (dBi)	1.43-3.06	1.03, 1.33, 1.84	5.47, 5.88, 1.97, 3.56	~0.3, ~0.35, ~2.9	0.67, 0.17, 3.22, 2.015
Bandwidth (MHz)	25, 25, 39, 41	109.5, 86.8, 283.9	260, 200, 160, 360	1320, 290, 990	165.7, 131.78, 529.8, 513.6
Efficiency (%)	42-74	79.7, 76.9, 76.7	------	45-58	72.9, 54.8, 87.8, 95
Flexibility	No	No	Yes	Yes	Yes

IV. CONCLUSION

A miniaturized flexible multi-frequency band antenna for quad-band operations is presented. The postulated design is appropriate for applications of WiMAX/WLAN/Wi-Fi, C-band, and DSRC. Cross-lines

along with circular ground structure caused the antenna to interpret itself as multi-band in nature. An inset feed mechanism is applied to achieve the impedance matching followed by stepped feed structure. The prototype is kept under the bending analysis. There is a defensible correlation between simulated and measured results. The proposed antenna is analyzed and investigated concerning different performance parameters including return loss, gain, efficiency, and radiation pattern. The stable radiation characteristics are reported with an appropriate gain along with a very good antenna efficiency. The proposed work is an upright selection for the recommended wireless applications.

ACKNOWLEDGMENT

The authors would like to thank Higher Education Commission of Pakistan for Technology Development Fund (HEC-TDF) and Vinnova (The Swedish Government Agency for Innovation Systems) for financial assistance of this work.

REFERENCES

[1] Y. He, K. Ma, N. Yan, and H. Zhang, "Dual-band monopole antenna using substrate-integrated suspended line technology for WLAN application," *IEEE Antennas and Wireless Propagation Letters*, vol. 16, pp. 2776-2779, 2017.

[2] A. Boukarkar, X. Q. Lin, Y. Jiang, and Y. Q. Yu, "Miniaturized single-feed multiband patch antennas," *IEEE Transactions on Antennas and Propagation*, vol. 65, no. 2, pp. 850-854, Feb. 2017.

[3] A. Araghi, "A compact planar ultra wideband antenna with triple-notched bands using capacitive coupled and parallel LC elements," *Applied Computational Electromagnetics Society Journal*, vol. 31, no. 12, pp. 1416-1420, 2016.

[4] Y. F. Cao, S. W. Cheung, and T. I. Yuk, "A multiband slot antenna for GPS/WiMAX/WLAN aystems," *IEEE Transactions on Antennas and Propagation*, vol. 63, no. 3, pp. 952-958, Mar. 2015.

[5] N. Gad and M. Vidmar, "Design of a microstrip-fed printed-slot antenna using defected ground structures for multiband applications," *Applied Computational Electromagnetics Society Journal*, vol. 33, pp. 854-860, 2018.

[6] N. Majidi, M. R. Sobhani, B. Kılıç, M. Imeci, O. S. Güngör, and Ş. T. Imeci, "Design and comparison of 4 types of dual resonance proximity coupled microstrip patch antennas," *Applied Computational Electromagnetics Society Journal*, vol. 33, no. 10, pp. 1135-1139, 2018.

[7] C. Hsu and S. Chung, "Compact multiband antenna for handsets with a conducting edge," *IEEE Transactions on Antennas and Propagation*, vol. 63, no. 11, pp. 5102-5107, Nov. 2015.

[8] M. Wu and M. Chuang, "Multibroadband clotted bow-tie monopole antenna," *IEEE Antennas and Wireless Propagation Letters*, vol. 14, pp. 887-890, 2015.

[9] A. S. Supriya and J. Rajendran, "A low-cost tri-band microstrip patch antenna for GPS application," *2017 Progress in Electromagnetics Research Symposium - Fall (PIERS - FALL)*, Singapore, pp. 60-65, 2017.

[10] A. Ahmad, F. Arshad, S. I. Naqvi, Y. Amin, and H. Tenhunen, "Design, fabrication, and measurements of extended L-shaped multiband antenna for wireless applications," *Applied Computational Electromagnetics Society Journal*, vol. 33, no. 4, pp. 388-393, 2018.

[11] S. Ahmed, F. A. Tahir, A. Shamim, and H. M. Cheema, "A compact Kapton-based inkjet-printed multiband antenna for flexible wireless devices," *IEEE Antennas and Wireless Propagation Letters*, vol. 14, pp. 1802-1805, 2015.

[12] E. Haque, S. Mahmuda, and F. Ahmed, "A capsule-like flexible multiband antenna for WBAN applications," *TENCON 2017 - 2017 IEEE Region 10 Conference*, Penang, pp. 1614-1619, 2017.

[13] H. Liu, P. Wen, S. Zhu, B. Ren, X. Guan, and H. Yu, "Quad-band CPW-fed monopole antenna based on flexible pentangle-loop radiator," in *IEEE Antennas and Wireless Propagation Letters*, vol. 14, pp. 1373-1376, 2015.

[14] S. M. H. Varkiani and M. Afsahi, "Grounded CPW multi-band wearable antenna for MBAN and WLAN applications," *Microwave and Optical Technology Letters*, vol. 60, no. 3, pp. 561-568, 2018.

[15] A. T. Castro and S. K. Sharma, "Inkjet-printed wideband circularly polarized microstrip patch array antenna on a PET film flexible substrate material," *IEEE Antennas and Wireless Propagation Letters*, vol. 17, no. 1, pp. 176-179, Jan. 2018.

[16] H. F. Abutarboush, M. F. Farooqui, and A. Shamim, "Inkjet-printed wideband antenna on resin-coated paper substrate for curved wireless devices," in *IEEE Antennas and Wireless Propagation Letters*, vol. 15, pp. 20-23, 2016.

[17] C. A. Balanis, *Antenna Theory, Analysis and Design*. 2nd ed., New York: J. Wiley & Sons, 1997.

[18] P. S. Bakariya, S. Dwari, M. Sarkar, and M. K. Mandal, "Proximity-coupled microstrip antenna for bluetooth, WiMAX, and WLAN applications," *IEEE Antennas and Wireless Propagation Letters*, vol. 14, pp. 755-758, 2015.

[19] Mehr-e-Munir and U. Farooq, "Multiband microstrip patch antenna using DGS for L-band, S-band, C-band & mobile applications," *2016 13th Inter-*

national Conference on Modern Problems of Radio Engineering, Telecommunications and Computer Science (TCSET), Lviv, pp. 198-201, 2016.

[20] V. Singh, B. Mishra, P. N. Tripathi, and R. Singh, "A compact quad-band microstrip antenna for S and C-band applications," *Microwave and Optical Technology Letters*, vol. 58, no. 6, pp. 1365-1369, 2016.

Aqsa Javed received her bachelor's degree in B.Sc. Telecommunication Engineering in 2017 from University of Engineering and Technology, Taxila, Pakistan. In 2017, she has joined ACTSENA research group as a Research Scholar plus started to pursue her master's degree focused on antennas from UET, Taxila, Pakistan.

Asma Ejaz received her B.Sc. and M.Sc. degree in Telecommunication Engineering from University of Engineering and Technology Taxila, Pakistan in 2013 and 2015, respectively. At present, she is an Instructor and a Ph.D. Research Scholar in the same institute. She is working under ACTSENA Research Group focused on passive chipless RFID tags and advancements in antenna design. She is also a student member of IEEE and Applied Computational Electromagnetics Society (ACES).

Sumrin Mehak Kabir received her B.E. degree from National University of Modern Languages, Islamabad, Pakistan, in 2013. She completed her M.S. in Electrical Engineering from National University of Sciences and Technology, Pakistan. Her research interest includes communication systems, signal processing, information coding, and antennas and wave propagation. Until now she has 8 publications in different journals and international conferences. Currently, she is doing her Ph.D. at the University of Engineering and Technology Taxila.

Yasar Amin is Chairman and Associate Professor of Telecommunication Engineering Department University of Engineering and Technology, Taxila, Pakistan. He is the Gounder of ACTSENA Research Group at UET Taxila, Pakistan. He did his B.Sc. in Electrical Engineering in 2001 and M.Sc. in Electrical Engineering in 2003 from Royal Institute of Technology (KTH), Sweden with specialization in System-on-chip design. His Ph.D. is in Electronic and Computer Systems from Royal Institute of Technology (KTH), Sweden, with his research focus printable green RFID antennas for embedded sensors. He is presently serving as leading Guest Editor at two International Journals and active Reviewer of more than a dozen well reputed international journals. He has contributed to over 40 journal papers, over 30 reviewed international conference papers.

Jonathan Loo a.k.a. Kok-Keong-Loo received his M.Sc. degree in Electronics from the University of Hertfordshire, UK in 1998 and his Ph.D. degree in Electronics and Communications from the same university in 2003. He leads a research team of 8 Ph.D. students in the area of communication and networking. His research interest includes network architecture, communication protocols, network security, embedded systems, video coding and transmission, wireless communications, digital signal processing, and optical networks. He has successfully graduated 13 Ph.D.'s as Principle Supervisor and contributed over 150 publications in the aforementionedspecialist areas.

Hannu Tenhunen is Chair Professor of Electronic Systems at Royal Institute of Technology (KTH), Stockholm, Sweden. Tenhunen has held Professor position as Full Professor, Invited Professor or Visiting Honorary Professor in Finland (TUT, UTU), Sweden (KTH), USA (Cornel U), France (INPG), China (Fudan and Beijing Jiaotong Universities) and Hong Kong (Chinese University of Hong Kong) and has an Honorary Doctorate from Tallinn Technical University. He has been Director of national large-scale research programs. He has actively contributed to VLSI and SoC in Finland and Sweden via creating new educational programs and research directions.

Frequency Adjustable Dual-Band Microstrip Gap-Ring-Slot Antenna Design Using the Cylindrical TLM Method

Tijana Z. Dimitrijevic, Jugoslav J. Jokovic, and Nebojsa S. Doncov

Faculty of Electronic Engineering
University of Niš, Niš, 18000, Serbia
tijana.dimitrijevic@elfak.ni.ac.rs, jugoslav.jokovic@elfak.ni.ac.rs, nebojsa.doncov@elfak.ni.ac.rs

Abstract ─ This paper introduces a design of a frequency adjustable dual-band circular patch antenna with a gap-ring-slot accompanied by a study of a cylindrical TLM method effectiveness and capabilities. The antenna is fabricated on Rogers 4003 substrate and measured results have been used to validate the used approach. Through comparison with corresponding rectangular TLM mesh results, the cylindrical TLM method has been found not only as more efficient requesting much smaller number of cells to be applied but also more capable to accurately describe narrow ring slots and small angular features. The designed antenna resonates at two frequencies, 2.77 GHz and 3.72 GHz, with the possibility of additional frequency tuning. A frequency adjustments study has been carried out and, accordingly, design corrections have been proposed either to independently tune the frequency or to simultaneously adjust both frequencies.

Index Terms ─ Cylindrical meshing, dual-band patch antennas, frequency tuning, gap ring slot, transmission line-matrix method.

I. INTRODUCTION

Nowadays rapid development of wireless communication systems puts a high demand on the design of devices for various services requesting miniaturized multipurpose antennas to be used that are preferably to support multi-frequency operation with desired radiation characteristics. Accordingly, practising the most versatile, the most feasible and the most accurate design methodology for low-profile and compact antennas is inevitable, yielding enhancement of established numerical techniques as well as the generation of hybrid or some novel techniques in conjunction with the development of commercial or in-house solvers [1-4].

Available approximate techniques, such as the cavity model or the transmission line modelling, are applicable only in simplified cases of the microstrip patch antennas [1,2]. Therefore, a usage of a relevant full-wave method that allows modelling of a complex geometry while taking into account inhomogeneous materials, wire elements and boundaries, emerges as a good starting point in the antenna design. There are many full-wave methods that are widely used in the area of electromagnetic field propagation modelling, such as Method of Moments (MoM) [5], Finite-Difference Time-Domain (FD-TD) [6], Finite Element Method (FEM) [7], Transmission-Line Matrix (TLM) method [3] etc. No solution is perfectly accurate and it is the designer's decision to choose which one is to be used while fulfilling specific requirements in terms of the geometry or purpose.

Among various designs of microstrip patch antennas, annular-ring patch antennas and annular-slot antennas have attracted a significant interest because of their appealing features such as a miniaturized configuration, light weight, ease of fabrication and compatibility with small portable units for wireless communication. A circular patch-ring antenna with a wide bandwidth, designed by TLM, was presented in [8]. A multi-frequency operation of microstrip-fed slot-ring antennas on thin substrates with a low-dielectric permittivity was investigated using the Integral Equation MoM simulator [9]. FEM was used to design strip-loaded annular-ring microstrip patch antennas [10], while an asymmetric feedline was used to excite multiple modes on an annular-ring slot antenna in [11]. A dual-band annular slot antenna for radio base stations and bidirectional radiated circularly polarized annular-ring slot antenna for a portable RFID reader were also designed using FEM [12,13].

In addition to antenna compactness, multi-functionality plays an important role in modern wireless communications as well. Hence, design of multiband antennas and frequency reconfigurable antennas has gained a full attention among researchers. As inferred from published literature, different techniques have been applied to achieve a multiband operation for antennas. By embedding narrow open rectangular ring slot close to the boundary of a rectangular patch of single layer and single feed, dual frequency operation was obtained in antenna designed using FEM in [14]. By using inverted-L- and T-shaped parasitic elements a multiband antenna

Submitted On: October 5, 2018
Accepted On: December 27, 2018

was developed [15], whereas a substrate-integrated waveguide (SIW) cavity-backed annular ring slot antenna was designed by FEM in [16].

Notwithstanding their flexibility and efficiency, the numerical computational methods face many problems and limitations when modelling of structures containing curvilinear surfaces is concerned. Therefore, conformity of the mesh is an important issue that has to be pointed out in a microstrip antenna design since it affects the modelling solution in two manners: one is a demand to accurately describe curvilinear boundaries and material surfaces, and the other is consumption of available computational resources in the most effective way, both in terms of simulation time and memory. The TLM method [3] is a well-established method and used by commercial software packages, such as the CST Microwave Studio [4], enabling modelling and analyses of complex microwave structures and devices. It is originally developed in the rectangular coordinate system with a basic cubic cell [3]. Although it is proved to be efficient in versatile cases, there are cases, however, where usage of staircase approximation for describing curvilinear surfaces leads to increased simulation run-time, greater memory requirements and sometimes numerical errors [17, 18]. Recently developed UTLM (Unstructured TLM), based on unstructured meshes (triangular, tetrahedral) provides better conformity of the mesh, but it may also be computationally more demanding [19, 20]. Therefore, the authors of this paper are of the opinion that some specific structures can be more conveniently and more efficiently described using the mesh in the corresponding grid, such as, for instance, the orthogonal polar mesh applied to the circular patch antenna, [21]. A development of an in-house solver that uses the TLM method in the orthogonal polar mesh (3DTLMcyl_cw) with efficiently embedded wire model was presented in [22]. Even though its possibilities are limited to structures containing cylindrical/circular surfaces, in these cases, however, results can be reached in the most efficient manner. This advantage is especially emphasized in specific cases where narrow slots are to be described, because of the perfect adjustments of the mesh to the considered structure as explored in [8,18].

This paper is focused on the coaxially fed slotted circular patch antenna, designed using the cylindrical TLM solver, where the dual-band operation is accomplished by loading a ring slot with a small gap. Similar approach has already been used in [14], but on an example of a rectangular patch antenna. An open rectangular slot embedded near the rectangular patch boundary provides reactive loading around the resonance frequency. As a consequence, a dual frequency operation can be obtained. The proposed design here, in addition to the dual frequency operation, contains specific geometrical surfaces (circular/cylindrical), of which are especially interesting narrow radial and angular features, making it suitable to further explore possibilities and meshing/ modelling advantages of the applied method. As it will be shown in this paper, the cylindrical TLM approach has been used to design the circular antenna with dual-band operation while the approach itself has been investigated from the point of view of the modelling accuracy and efficiency. A novel, specific challenge in modelling of the structures considered in this paper can be contributed to the presence of the narrow ring slot and the small annular gap. What is more, the cylindrical TLM solver has been used to conduct a parametric study of the designed antenna allowing for additional frequency adjustments of the excited modes. Accordingly, design techniques have been proposed to achieve independent adjustment of the lower resonant mode in the frequency range of interest and tuning of both modes simultaneously.

The paper is organized through several sections. After the Introduction, Section II is devoted to a brief theory of the TLM method in a cylindrical coordinate system including the numerical procedure and modelling issues. The antenna design is presented in Section III, the frequency adjustments study is given in Section IV, whilst the cylindrical meshing capabilities together with the efficiency are explored in Section V. Verification of the approach through comparing the simulated and measured results are presented in Sections VI, after which the major conclusions are drawn.

II. CYLINDRICAL TLM APPROACH

The TLM method is a numerical method that is based on the physical model of a system, therefore, it is suitable for numerical modelling rather than just numerical analysis. As a differential method, the TLM is convenient for solving problems in inhomogeneous mediums, for considering of nonlinear characteristics and for solving problems in the time-domain. It is based on the network of transmission lines where voltages and currents are equivalently connected to electromagnetic field components defined by Maxwell's equations. A space of electromagnetic field propagation is described by the network of cells comprised of transmission lines interconnection. The basic cell is Symmetrical Condensed Node (SCN) [3], but to allow for a construction of a non-uniform mesh and to define different material properties as well as to speed up a simulation process, the hybrid symmetrical condensed nodes (HSCN) [23] can be used instead.

An in-house solver, 3DTLMcyl_cw, used in this paper for the antenna design and analysis, is developed in the cylindrical coordinate system and uses the HSCN adapted to the cylindrical grid [22]. The code has been enhanced by the implementation of the compact wire model adjusted to the cylindrical grid. The model uses a wire network consisted of link and stub lines to account for the increase of the capacitance and inductance of the medium caused by the wire and it is interposed over the

existing network of nodes [24]. The TLM wire node belonging to the straight wire segment running in z-direction is presented in Fig. 1 (a).

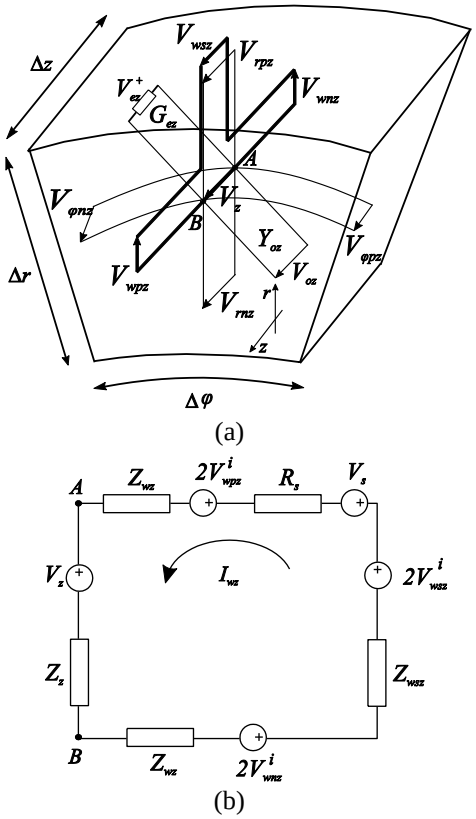

Fig. 1. (a) TLM wire node for a wire running in z-direction, and (b) Thevenin circuit for the wire segment in z-direction.

Within a scattering procedure in a wire network for a segment running in z-direction, reflected voltage pulses are calculated in specific wire nodes as follows:

$$\begin{aligned} V^r_{wnz} &= V^i_{wnz} - I_{wz} Z_{wz} \\ V^r_{wpz} &= V^i_{wpz} + I_{wz} Z_{wz} \\ V^r_{wsz} &= V^i_{wsz} - I_{wz} Z_{wsz} \end{aligned}, \tag{1}$$

and a current propagating through the wire placed along *z*-direction is determined as:

$$I_{wz} = \frac{2V^i_{wnz} + 2V^i_{wsz} - 2V^i_{wpz} - V_z - V_S}{2Z_{wz} + Z_{wsz} + Z_z + R_S}, \tag{2}$$

where V^i_{wnz}, V^i_{wpz}, and V^i_{wsz} are incident voltage pulses, V^r_{wnz}, V^r_{wpz}, and V^r_{wsz} reflected voltage pulse, V_S and R_S are the voltage and the impedance of the source connected to the wire, respectively. Z_z and V_z are calculated when regular node ports are determined using the Thevenin circuit between A and B (Fig. 1 (b)).

Boundaries in the cylindrical TLM solver can be modelled as internal or external ones, representing circular or cylindrical surfaces. An analogy between the electric field and the voltages at TLM nodes enables defining the boundaries through introducing corresponding reflection coefficients. In case of a patch antenna modeling, a perfect electric conductor (PEC) is used to describe metallic layers: a radiated patch and a ground plane. It is also possible to model conductance losses by introducing finite characteristic impedance and calculating relevant reflection coefficient which would be greater than -1. By using the reflection coefficient equal to 1, a metallic wall can be described at the center of the orthogonal polar TLM mesh with a circle of an infinitesimal circumference. Finally, the TLM network of transmission lines can be loaded with theirs characteristic impedance (i.e., ρ=0), defining an absorbing boundary, which find its purpose in modeling of open boundary structures such as the microstrip patch antennas. Namely, the boundaries of the patch antenna modeling space have to be extended beyond the realistic antenna dimensions and described as absorbing with properly calculated reflection coefficients of the link lines.

Adapting the compact wire model to the orthogonal polar mesh has enabled describing the wire elements. From the computational point of view, an implementation of the compact wire model into the cylindrical TLM algorithm resulted in additional subroutine involving calculation and exchange of link-line impedances of the nodes along which the wire passes due to different cross-section of the wire nodes. In case of patch antennas, this model can be used to model the inner coaxial wire connecting the radiated patch and the ground plane, while a voltage source of Vg=1V with an internal resistance Rg=50Ω is attached through the so-called wire port to the wire end. However, the wire element modeling faces limitation related to maximum wire radius, since it is determined by the cell size through which the wire passes. Therefore, a compromise should be made between the wire radius and the mesh resolution. Taking advantage of the conformity of the cylindrical mesh to the structures of circular/cylindrical geometry, the cylindrical mesh gives more possibilities [17], and the limitation might be overcome, especially in cases when wires are placed along radial direction, where the space discretization allows thicker wires to be embedded.

Since the TLM method demands a discretization of a modeling space, it is of importance to appropriately define a mesh resolution in order to provide a satisfactory accuracy. To provide satisfactory accuracy of results in a frequency range of interest, there is a general recommendation to use the space discretization between adjacent nodes smaller than λ/10, where λ is the wavelength and the relative permittivity is 1. In case of inhomogeneous media it is essential to ensure time

synchronism in the mesh. Therefore, the approximate wavelength is $\lambda_m = \lambda/\sqrt{\varepsilon_r}$, hence the condition $\Delta l < \lambda_m/10$ should be accomplished, where Δl represents the cell size. However, when the considered structure contains fine features, thin layers or narrow parts, the mesh of higher resolution should be applied. According to defined electromagnetic characteristics of a medium and defined space discretization, TLM algorithm calculates the time-step.

An in-house solver which is based on the TLM numerical procedure handles of all the above modeling issues. It starts with the model description through defining the problem dimensions, mesh resolution adjustments, defining media properties, setting up an impulse or a voltage source excitation and defining the wanted output result. These parameters are imported by the user within the input text file. When it runs, the solver checks imported values and handles possible errors in terms of maximum number of iterations, maximum computational area in all corresponding directions, maximum number of boundaries, metallic layers, wire elements and excitations, as well as maximum number of regions which are used to reduce computations within the same medium. After that follows imposing initial conditions and determination of link and stub lines impedances for each HSCN as well as determination of wire nodes impedances. Then, the algorithm goes through iterative stages: calculation of equivalent voltages and currents for each node (EM field components can be calculated at this stage as well), scattering procedure for regular and wire nodes, connection procedure for regular and wire nodes, modification of the connection procedure at boundaries, calculation of the current induced in the probe wire (output result) in the time domain, transforming data into the frequency domain, and calculation of S parameters or input impedance [22].

III. ANTENNA DESIGN

Design and fabrication of the dual-band coaxially fed antenna with a gap-ring-slot were preceded by the development of a model of a simple circular patch (CP) antenna of a radius 15 mm and a coaxial feed position ρ = 3.5 mm. As a substrate, Rogers 4003 with the relative permittivity ε_r = 3.38 and the height h = 1.524 mm, was used. Simulated results representing reflection coefficients for the CP antenna is shown in Fig. 2. According to the simulations in both rectangular and cylindrical TLM solvers with the same cell size along x- and y-axes, and along the r-axis (λ/60, λ corresponds to the maximum frequency of interest), the fundamental mode is excited at about 3.12 GHz.

The layout and the experimental model of the CP gap-ring-slot antenna are shown in Fig. 3.

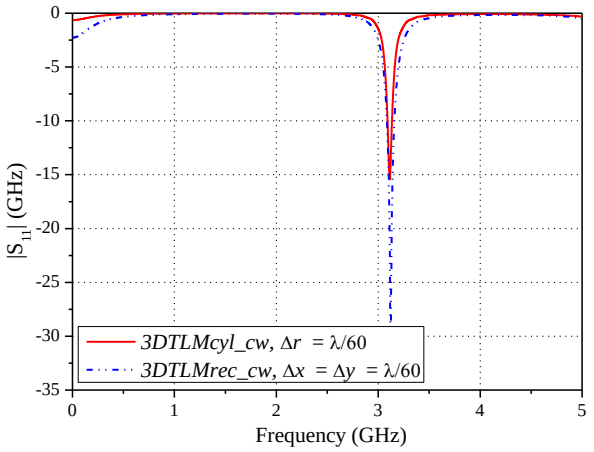

Fig. 2. Simulated reflection coefficient for the circular patch antenna of radius a = 15mm.

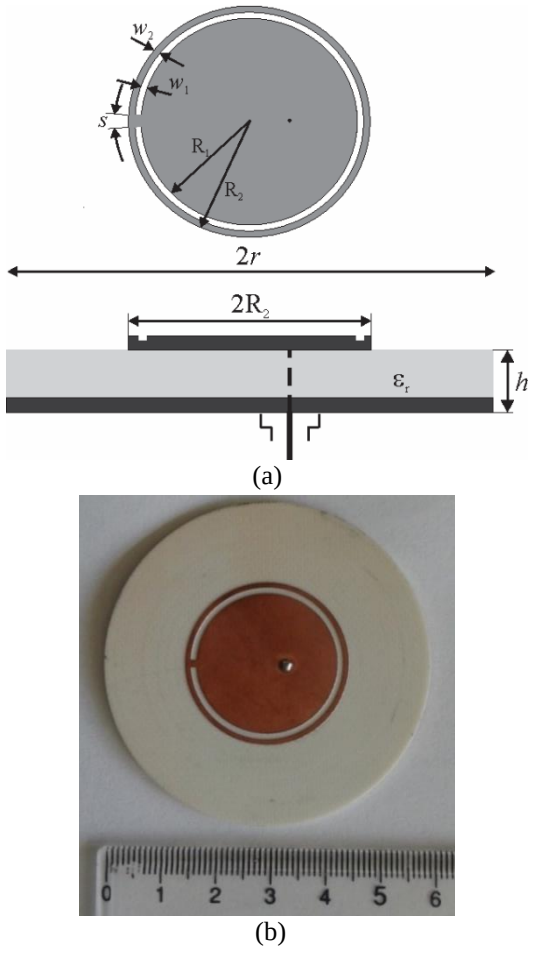

Fig. 3. Configuration of the circular patch antenna with a gap-ring-slot: (a) antenna geometry and layout, and (b) experimental model.

In order to design a low profile circular patch (CP) antenna that exhibits dual frequency operation, a narrow slot (w_1 = 1 mm) shaped like a ring with an annular gap (the gap angle s = 6˚) has been loaded into the radiated patch surface of radius R_2 = 15 mm close to the patch boundary. A distance of the slot from the patch edge is w_2 = 1 mm. In the given design, with R_1 and R_2 are marked radii of two circular patches, which contribute to the excitation of two resonant frequencies, both associated with the TM_{11} mode.

The optimal position of the coaxial feed providing an impedance matching between the feed and the antenna has been deduced according to the simulations for different feed positions with radius r_w = 0.15 mm (Fig. 4). According to the results, the optimum feed position for the fabricated antenna is set to be ρ = 3.5 mm, while relevant dimensions for the antena layout parameters have been chosen in accordance with the parametric study.

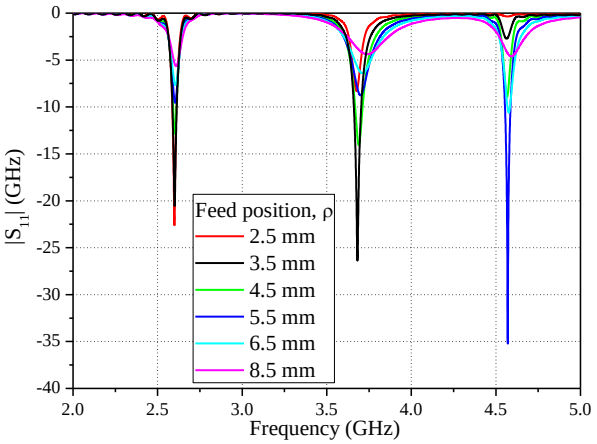

Fig. 4. Optimization of the feed position at the CP gap-ring-slot antenna.

IV. FREQUENCY ADJUSTMENT STUDY

Using the presented in-house solver based on an orthogonal polar TLM mesh, a parametric study has been carried out to explore the way in which finer design adjustments affect first two operating modes of the circular patch gap-ring-slot antenna. In this paper, we present a technique for independently tuning the lower resonant frequency of the antenna, followed by the technique for mutual adjustment of both resonant frequencies.

Figure 5 presents how a gap width s influences the resonant frequencies for the first two resonant modes (f_1 and f_2) and the frequency ratio. As shown, the angle of the gap affects more the lower resonant frequency than the higher one. By increasing the gap s, the lower mode is rising whereas the higher mode remains almost the same. In overall, by changing the gap spacing, the lower resonant frequency can be altered up to 8.4%, while the frequency ratio can be tuned in the range from 1.287 to 1.384. The corresponding dual frequency behaviour by listing the modes values with suitable bandwidth values (obtained from 10 dB return loss) is given in Table 1.

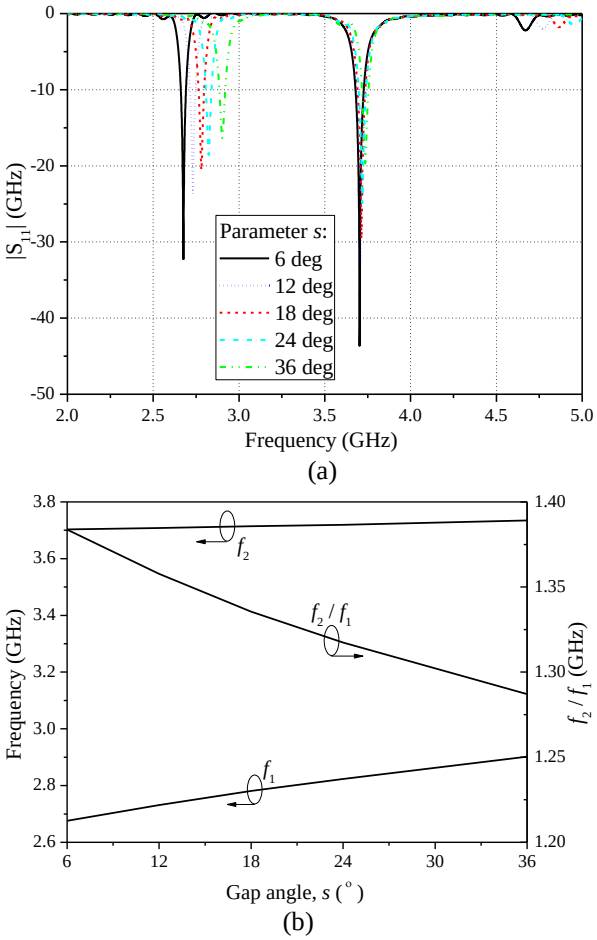

Fig. 5. Simulated results for the circular patch gap-ring-slot antenna with various gap angles s: (a) reflection coefficients, and (b) resonant frequencies and frequency ratio.

Table 1: Resonant frequencies and bandwidth of the CP gap-ring-slot antenna with various gap widths

Gap Spacing, s, (˚)	**f_1 (GHz)**	**BW (%)**	**f_2 (GHz)**	**BW (%)**	**f_2 / f_1**
6	2.676	1.15	3.703	1.29	1.384
12	2.731	1.15	3.708	1.27	1.357
18	2.781	1.17	3.714	1.21	1.335
24	2.823	1.17	3.719	1.17	1.317
36	2.902	1.16	3.735	0.99	1.287

Frequency adjustments of both operating modes of the circular patch gap-ring-slot antenna can be achieved by varying the ring-slot width w_1 or the width w_2. Influence of the widths w_1 and w_2 on resonant frequency

values is illustrated in Figs. 6. and 7, respectively. In contrast to the gap *s*, increasing the ring-slot width w_1 (while the radius R_2 remains constant), yields higher frequency to rise up to 8.5%, and the lower mode to decrease down to 3.7%. It is seen that the higher frequency is increased faster than the lower one is decreased. Also, the frequency ratio is tunable in the range from 1.325 to 1.494, as presented in Table 2.

On the other hand, the slot width w_2 (while the radius R_1 remains constant) affects more the lower mode which increase up to 6.3%, whereas the higher mode go down up to 1.65%, that is the frequency ratio is tunable in the range from 1.359 to 1.475, as presented in Table 3.

It can be concluded that the lower mode is more dependent on the radius R_2 of the circular patch, whereas the higher one mainly depends on the disk radius R_1. Therefore, due to different effects on the resonant modes, the dual-frequency operation with the tunable frequency ratio can be achieved.

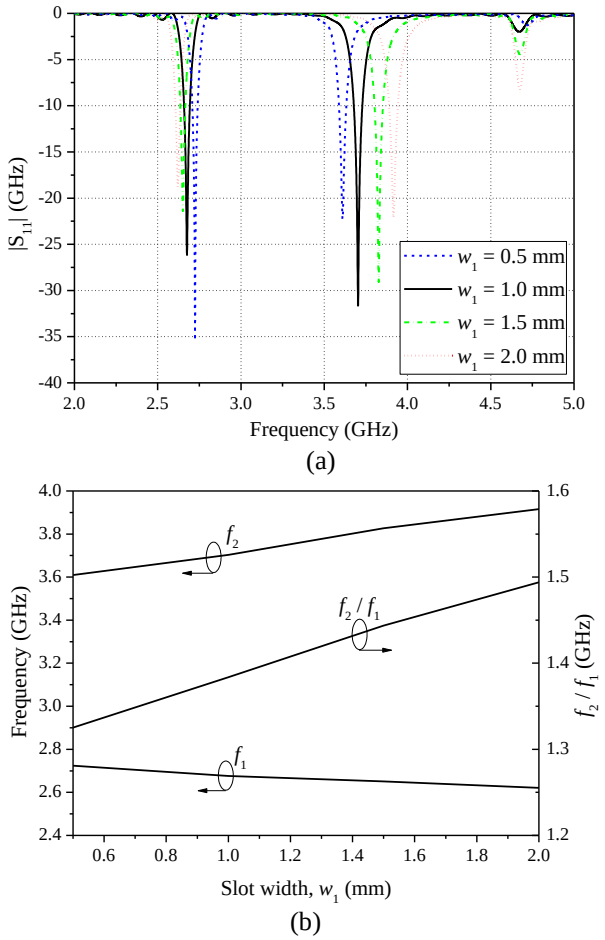

Fig. 6. Simulated results for the CP gap-ring-slot antenna with various ring slot widths w_1: (a) reflection coefficient, and (b) resonant frequencies and frequency ratio.

Table 2: Resonant frequencies and bandwidths of the CP gap-ring-slot antenna with various ring-slot widths, w_1

Ring-Slot Width, w_1, (mm)	f_1 (GHz)	BW (%)	f_2 (GHz)	BW (%)	f_2 / f_1
0.5	2.724	1.29	3.610	1.22	1.325
1.0	2.676	1.27	3.703	1.38	1.384
1.5	2.651	1.17	3.827	1.31	1.444
2.0	2.621	1.09	3.916	1.33	1.494

Table 3: Resonant frequencies and bandwidths of the CP gap-ring-slot antenna with various widths, w_2

Width, w_2, (mm)	f_1 (GHz)	BW (%)	f_2 (GHz)	BW (%)	f_2 / f_1
0.5	2.682	1.05	3.646	1.46	1.359
1.0	2.600	1.01	3.681	1.20	1.416
1.5	2.593	1.21	3.712	1.22	1.432
2.0	2.513	1.26	3.706	1.19	1.475

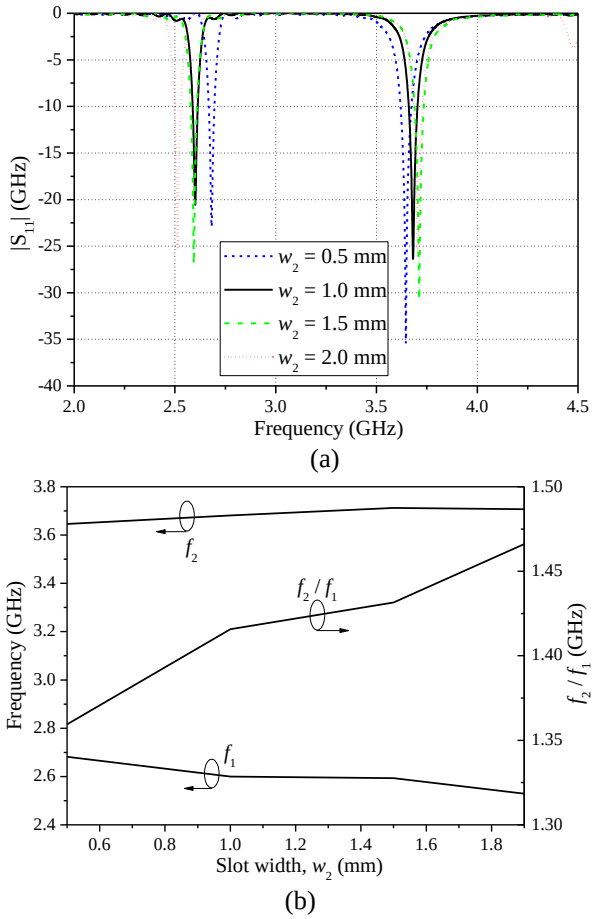

Fig. 7. Simulated results for various ring widths w_2: (a) reflection coefficient, and (b) resonant frequencies and frequency ratio.

Finally, Table 4 represents the comparison of antenna characteristics, such as frequency ratio and

bandwidth, between the fabricated proposed antenna and referenced antennas. By adjustment of the dimensional parameters of the proposed antenna, a small frequency ratio can be achieved which is an advantage in many applications.

Table 4: Comparison of frequency ratio and bandwidth

Ref.	1st BW (%)	2nd BW (%)	f_2 / f_1
[25]	1.4	1.8	2.0 ÷ 3.2
[26]	0.91 ÷ 1.17	1.04 ÷ 1.05	1.766 ÷ 1.983
[27]	6.9	0.6	1.28
[28]	0.48 ÷ 3.1	0.73 ÷ 6.1	1.58 ÷ 1.76
Here	1.05 ÷ 1.29	0.99 ÷ 1.46	1.287 ÷ 1.494

V. CYLINDRICAL MESHING CAPABILITIES

Mesh representations in the rectangular and cylindrical coordinate system for the CP gap-ring-slot antenna considered here are illustrated in Fig. 8. To ensure numerical results to be valid, it is requested to realize a TLM model which is in accordance with a physical antenna model as much as possible.

Since a radiated patch surface in the given design contains a narrow ring slot with a small angular gap, a specific attention during the modelling procedure has been put on these parameters. Opposed to a cylindrical mesh, where these features are described straightforwardly and accurately, a staircase approximation has had to be applied in a rectangular mesh. To explore benefits of the cylindrical meshing in contrast to the widespread rectangular mesh, different cell sizes have been used in both solvers and the most representative results are summarized in Fig. 9.

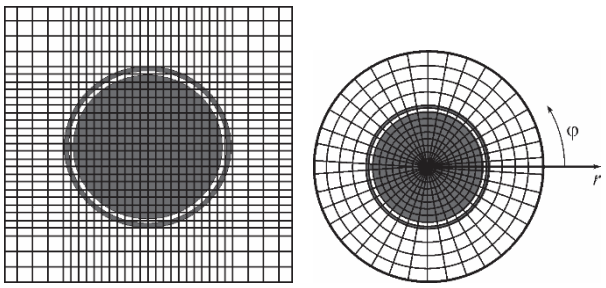

Fig. 8. Meshing in: (a) rectangular grid, (b) cylindrical grid.

As can be seen, the applied rectangular mesh ($\Delta x = \Delta y = \lambda/60$ within the substrate area, short-dash-dot line in Fig. 9.) does not provide expected results, i.e., only one resonant frequency is excited instead of two. This is definitely a consequence of not adequate meshing since the applied mesh does not allow for the relevant description of the narrow ring and the small angular gap (Fig. 8 (a)). Therefore, the rectangular mesh of higher resolution is inevitable to be used, such as for instance $\Delta x = \Delta y = \lambda/120$ within the substrate area, as shown in Fig. 9. (dash-dot line). Additionally, the cell size limits the radius of the wire feed used for excitation, which affects the resonant modes as well, and hence may lead to inaccuracies. Opposed to the rectangular mesh, the orthogonal polar mesh (Fig. 8 (b)) gives very good result even with the radial cell size $\Delta r = \lambda/60$ (short-dash-line in Fig. 9.), whereas the cell size $\Delta r = \lambda/120$ provides better results (dash-line in Fig. 9.). Note that cell size in the air-filled area along the specific axis is set up to be greater than within the substrate, due to maintaining time synchronism during simulations [3, 22].

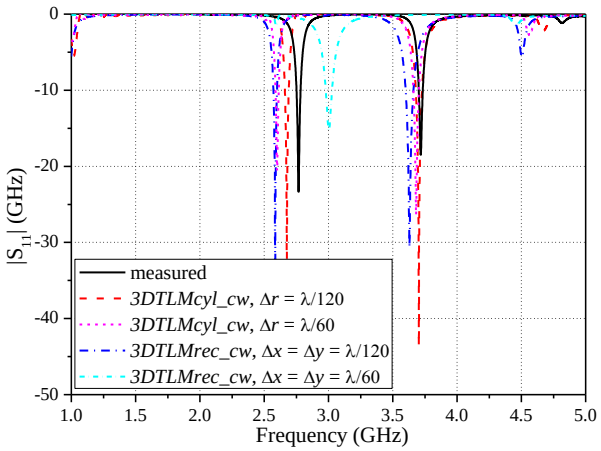

Fig. 9. Measured and simulated reflection coefficient for the circular patch antenna with a gap-ring-slot for different mesh resolutions.

In overall, limitations of the rectangular meshing heighten when applied to some specific structures that comprise narrow slots. From one hand, it is memory and time consuming due to the extremely higher number of cells used, and from the other hand, it cannot be resolved with a realistic wire radius, which instead has to be decreased so the simulation can proceed. On the other hand, advantages of the cylindrical meshing applied to the circular/cylindrical geometry are seen in accurate describing of fine annular and radial features accompanied with a less demanding computation since boundaries approximation is avoided as well as in the considerably reduced number of cells applied, leading to less memory for the storage, and more efficient scattering and connection procedures. If we assume that the number of nodes can be evaluated as Nx×Ny×Nz (Nx = Ny) in the rectangular mesh, and Nφ×Nr×Nz in the cylindrical mesh, and bearing in mind that Nr = Nx/2, while Nφ < Nx, it is easy to conclude that the cylindrical TLM demands much smaller number of cells than the rectangular TLM. To prove that, Table 5. summarizes cell dimensions and

a number of cells needed for modelling of the circular patch antennas with the gap-ring-slot in the cylindrical and rectangular TLM solvers.

Table 5: Properties of the cylindrical and rectangular TLM meshes applied to the CP gap-ring-slot antenna

Solver	Δx, Δy, Δr in Substrate (at 5GHz)	Mesh/ Number of Cells	Error (%)	
			1st Mode	2nd Mode
3DTLM rec_cw	λ/60	86×85×69/ 498.525	Invalid results	
	λ/120	184×185×69/ 2.348.760	6.5	2.4
3DTLM cyl_cw	λ/60	60×46×67/ 184.920	6.1	1.0
	λ/120	60×92×67/ 369.840	3.6	0.5

Obviously, the number of rectangular cells is considerably greater than the number of cylindrical cells making the cylindrical meshing much more efficient. According to the resonant frequency values errors relative to the experimental results, one can find that similar accuracy is achieved for λ/120 cell size in the rectangular mesh and λ/60 cell size in the cylindrical mesh, while the accuracy <5% for both simulated frequency values is achieved only for the cylindrical mesh with the cell size λ/120. Also, the rectangular mesh with λ/60 cell size cannot provide valid results due to inappropriate meshing. Note that a computational area in the cylindrical mesh for the case of λ/120 cell size is equal to 2π rad×60 mm×61.524 mm, whereas the computational area in the corresponding rectangular mesh is 120 mm×120 mm×61.524 mm.

VI. SIMULATED AND MEASURED RESULTS

The antenna characteristics have been measured on the network analyzer (VNA) and in an anechoic chamber of the Technische Universität Ilmenau, Germany.

Measured and simulated reflection coefficients for the proposed CP gap-ring-slot antenna are shown in Fig. 10. The plotted results correspond to the cell size $\Delta x = \Delta y = \lambda/120$ in the rectangular mesh and to the cell size along the *r*-axis in the cylindrical mesh that is equal to $\Delta r = \lambda/60$. The feed position in simulations has been adjusted accordingly. As can be seen from Fig. 10, two resonant frequencies (2.77 GHz and 3.72 GHz) instead of a single frequency for the conventional CP antenna are excited. Table 6 shows operating mode values obtained by measurements and simulations in both solvers. It can be found that the simulated results agree well with the measured result obtained by using the VNA. Discrepancies are the result of the fabrication procedure related to the slight deviation of slots dimension and feed positioning as well as the connectors and coaxial cable losses. A mutual agreement between simulated results obtained by rectangular and cylindrical mesh is satisfactory, but it has to be pointed out that considerably finer rectangular mesh has been applied compared to the cylindrical one, which was thoroughly investigated previously.

Table 6: Measured and simulated resonant frequency values for the CP gap-ring-slot antenna

Results	Resonant Frequency* (GHz)	
3DTLMcyl_cw	2.60	3.68
3DTLMrec_cw	2.59	3.63
Measured	2.77	3.72

*Results correspond to the cylindrical ($\Delta r = \lambda/60$) and rectangular ($\Delta x = \Delta y = \lambda/120$) TLM meshes.

The radiation pattern of the antenna is measured in the anechoic chamber, and it is illustrated in Fig. 11 (a) together with the simulated one. A good agreement is achieved. Results for two operating frequencies at 2.77 GHz and 3.72 GHz are shown in Figs. 11 (b) and 11 (c), respectively. It is seen that good broadside radiation patterns are obtained, with the maximum radiation in direction theta equal to 0 degrees. Also, similar broadside radiation characteristics can be observed for both of the operating modes, hence both resonant frequencies are associated with the TM_{11} mode. Results indicate that the peak antenna gain reaches about 6.2 dBi and 6.8 dBi, respectively for two operating modes. Therefore, the gain is slightly improved at higher resonant frequency.

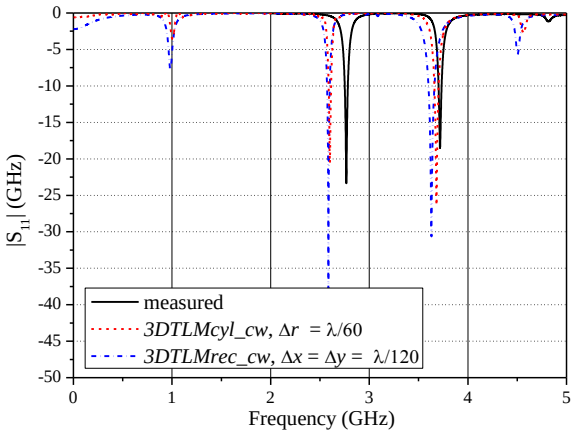

Fig. 10. Measured and simulated reflection coefficient for the circular patch antenna with a gap-ring-slot.

VII. CONCLUSION

In this paper, a dual-band coaxially fed circular patch antenna is designed by using the TLM method adapted to the orthogonal polar mesh and enhanced with the compact wire model. The antenna is realized on the Ro4003 substrate and contains a ring slot with an angular

gap, contributing to excitation of two resonant modes instead of one, thus making the antenna capable of dual frequency operation. A prototype of the designed antenna has been fabricated and measured. The measured results have been used to validate the cylindrical TLM approach. Advantages of applying the cylindrical mesh to the proposed antenna structure have been explored through comparison with the corresponding rectangular TLM mesh parameters. The cylindrical TLM has been proven as much more efficient than the rectangular TLM due to requested smaller number of applied cells, with capabilities of accurate describing of curvilinear boundaries including narrow ring slots and small angular gaps along with more possibilities related to modeling of realistic wire properties due to greater cell size.

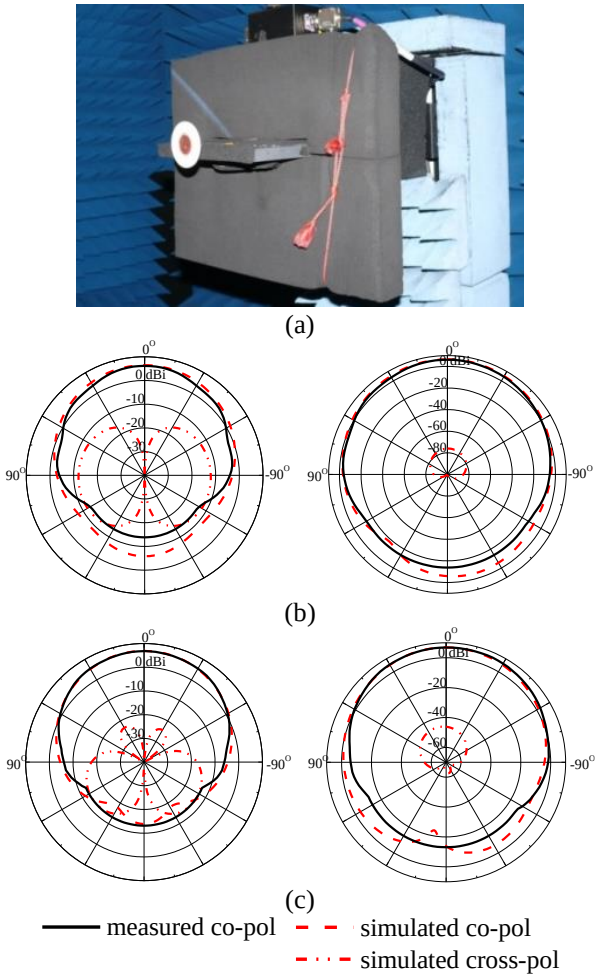

Fig. 11. Measurements in an anechoic chamber: (a) experimental setup, (b) measured and simulated E- and H-plane at 2.77 GHz, and (c) measured and simulated E- and H-plane at 3.72 GHz.

Results of a parametric study to explore frequencies adjustment capabilities of the presented antenna design have also been presented. A technique to achieve independent lower frequency adjustment has been introduced by varying the angular gap, while the mutual frequency tuning is shown to be possible by changing the ring-slot width. By adjusting the various geometric parameters, the frequency ratio and the bandwidth of each mode can be easily controlled.

Proven capabilities and efficiency of the cylindrical TLM approach will be of great help for the design of multi-band or reconfigurable circular patch antennas, containing very narrow angular or radial slots, which will be a part of the future investigation.

ACKNOWLEDGMENT

We want to thank the head of the RF and Microwave Research Laboratory of the Technische Universitaet Ilmenau Prof. M. A. Hein and Dr. Kurt Blau who helped us to realize the antenna samples and to carry out the measurements. This work was supported by the Ministry of Education, Science and Technological Development of Republic of Serbia (III44009 and TR32052).

REFERENCES

[1] C. A. Balanis, *Antenna Theory: Analysis and Design*. John Wiley & Sons, New York, 2012.

[2] R. Garg, *Microstrip Antenna Design Handbook*. Artech House, 2001.

[3] C. Christopoulos, *The Transmission-Line Modelling Method: TLM*. IEEE Press, 1995.

[4] https://www.cst.com, 2018.

[5] R. F. Harrington, *Field Computation by Moment Method*. *IEEE Press*, New York, 1993.

[6] A. Z. Elsherbeni and V. Demir, *The Finite-Difference Time-Domain Method for Electro-magnetics with MATLAB Simulations*. 2nd Edition (ACES Series on Computational Electromagnetics and Engineering). Edison, NJ: SciTech Publishing, an Imprint of the IET, 2015.

[7] J. R. Brauer, *Finite-Element Method*. Magnetic Actuators and Sensors, Wiley-IEEE Press, 2014.

[8] T. Z. Dimitrijevic, J. J. Jokovic, and N. S. Doncov, "Efficient modeling of a circular patch-ring antenna using the cylindrical TLM approach," *IEEE Antenn. Wirel. Pr.*, vol. 16, pp. 2070-2073, Apr. 2017.

[9] H. Tehrani and K. Chang, "Multifrequency operation of microstrip-fed slot-ring antennas on thin low-dielectric permittivity substrates," *IEEE Trans Antennas Propag.*, vol. 50, no. 9, pp. 1299-1308, Sep. 2002.

[10] X. L. Bao and M. J. Ammann, "Comparison of several novel annular-ring microstrip patch antennas for circular polarization," *J. Electromag. Waves Appl.*, vol. 20, no. 11, pp. 1427-1438, 2006.

[11] X. L. Bao and M. J. Ammann, "Microstrip-fed dual-frequency annular-slot antenna loaded by split-ring-slot," *IET Microwaves Antennas Propag*., vol. 3, no. 5, 757-764, July 2009.

[12] R. L. Farias, C. Lucatel, and M. V. T. Heckler, "Dual-band annular slot antenna for radio base stations," *The 8th European Conference on Antennas and Propagation (EuCAP 2014)*, The Hague, pp. 2055-2059, 2014.

[13] Y.-F. Lin, Y.-C. Kao, S.-C. Pan, and H.-M. Chen, "Bidirectional radiated circularly polarized annular-ring slot antenna for portable RFID reader," *ACES Journal*, vol. 23, no. 3, pp. 182-189, Mar. 2010.

[14] G. M. Kale, R. P. Labade, and R. S. Pawase, "Open rectangular ring slot loaded rectangular microstrip antenna for dual frequency operation," *Microw. Opt. Technol. Lett.*, vol. 57, pp. 2448-2452, July 2015.

[15] J. Kim, T. Jung, H. Ryu, J. Woo, C. Eun, and D. Lee, "Compact multiband microstrip antenna using inverted-L- and T-shaped parasitic elements," *IEEE Antennas Wirel. Propag. Lett.*, vol. 12, pp. 1299-1302, Sep. 2013.

[16] D. Guan, Z. Qian, W. Cao, L. Ji, and Y. Zhang, "Compact SIW annular ring slot antenna with multiband multimode characteristics," *IEEE Trans. Antennas Propag.*, vol. 63, no. 12, pp. 5918-5922, Dec. 2015.

[17] T. Dimitrijevic, J. Joković, and N. Doncov, "TLM modeling of an annular ring coupled to a circular patch with a shorting pin," *Proc. TELSIKS 2015*, Nis, Serbia, pp. 200-204, Oct. 2015.

[18] T. Dimitrijević, J. Joković, and N. Dončov, "Advantages of using integral cylindrical TLM method for modelling of coax-fed microstrip circular antenna," *Proc. TELSIKS 2013*, Nis, Serbia, pp. 200-204, Oct. 33-36, 2013.

[19] P. Sewell, T. M. Benson, C. Christopoulos, D. W. P. Thomas, A. Vukovic, and J. G. Wykes, "Transmission-line modeling (TLM) based upon unstructured tetrahedral meshes," *IEEE Trans. Microw. Theory Tech.*, vol. 53, no. 6, pp. 1919-1928, June 2005.

[20] X. Meng, P. Sewell, N. H. A. Rahman, A. Vukovic, and T. M. Benson, "Experimental benchmarking of unstructured transmission line modelling (UTLM) method in modelling twisted wires," *ACES Express Journal*, vol. 1, no. 3, pp. 101-104, Mar. 2016.

[21] H. Meliani, D. De Cogan, and P. B. Johns, "The use of orthogonal curvilinear meshes in TLM models," *Int. J. Numer. Model. Electron. Netw. Devices Fields*, vol. 1, no. 4, pp. 221-238, Dec. 1988.

[22] T. Dimitrijević, J. Joković, B. Milovanović, and N. Doncov, "TLM modeling of a probe-coupled cylindrical cavity based on compact wire model in the cylindrical mesh," *Int. J. RF Microw. Comput.-Aided Eng.*, vol. 22, no. 2, pp. 184-192, Mar. 2012.

[23] R. Scaramuzza and A. J. Lowery, "Hybrid symmetrical condensed node for the TLM method," *Electron Lett.*, vol. 26, no. 23, pp. 1947-1949, Nov. 1990.

[24] V. Trenkic, A. J. Wlodarczyk, and R. A. Scaramuzza, "Modeling of coupling between transient electromagnetic field and complex wire structures," *Int. J. Numer. Model. Electron. Netw. Devices Fields*, vol. 12, no. 4, pp. 257-273, July 1999.

[25] K.-L. Wong and W.-S. Chen, "Compact microstrip antenna with dual-frequency operation," *Electron. Lett.*, vol. 33, no. 8, p. 646, Apr. 1997.

[26] K.-P. Yang and K.-L. Wong, "Dual-band circularly-polarized square microstrip antenna," *IEEE Trans. Antennas Propag.*, vol. 49, no. 3, pp. 377-382, Mar. 2001.

[27] Nasimuddin, Z. N. Chen, and X. Qing, "Dual-band circularly polarized S-shaped slotted patch antenna with a small frequency-ratio," *IEEE Trans. Antennas Propag.*, vol. 58, no. 6, pp. 2112-2115, June 2010.

[28] D. Yu, S. Gong, Y. Wan, and W. Chen, "Omni-directional dual-band dual circularly polarized microstrip antenna using TM01 and TM02 modes," *IEEE Trans. Antennas Propag.*, vol. 13, pp. 1104-1107, June 2014.

Tijana Z. Dimitrijevic was born in Nis, Serbia, in 1977. She received the Dipl.-Ing., M.Sc. and Ph.D. degrees from the Faculty of Electronic Engineering, University of Nis, Serbia, in 2003, 2007, and 2015, respectively. From 2003 to 2008, she was a Researcher, and she is currently a Teaching Assistant with the Department of Telecommunications, University of Nis, Serbia. Her main research interests include computational developments and application of the numerical TLM method for the purpose of an investigation of microwave applicators and microstrip antennas. She was the 2006 recipient of the Nikola Tesla National Award in Creativity of the Young category.

Jugoslav J. Jokovic was born in Novi Pazar, Serbia, in 1974. He received the Dipl.-Ing., M.Sc., and Ph.D. degrees from the Faculty of Electronic Engineering, University of Nis, Serbia, in 2000, 2004 and 2007, respectively. In 2000, he joined the Department of Telecommunications, University of Nis, Serbia, where he is now a Research and Teaching Assistant. His current research

interests include theoretical developments and experimental verification of the numerical TLM method and its application to EMC and microwave heating.

Nebojsa S. Doncov was born in Nis, Serbia, in 1970. He received the Dipl.-Ing., M.Sc., and Ph.D. degrees from the Faculty of Electronic Engineering, University of Nis, Serbia, in 1995, 1999 and 2002, respectively. From 1995 to 2001, he was with the Department of Telecommunications, Faculty of Electronic Engineering, Serbia, as a Research Assistant. From 2001 to 2004 he was working with Flomerics Ltd, Electromagnetics Division, U.K., as a Research and Development Engineer. In 2004, he joined the Department of Telecommunications, Faculty of Electronic Engineering, Serbia, where he is now a Full Professor. His current research interests are in computational and applied electromagnetics with a particular emphasis on TLM and network methods applications in microwaves and EMC. Doncov was the recipient of the International Union of Radio Science (URSI) Young Scientist Award in 2002.

Shaped-Beam Circularly-Polarized Practical Antenna Array for Land Imaging SAR Systems

M. Abo El-Hassan [1], K. F. A. Hussein [1], A. E. Farahat [1], and K. H. Awadalla [2]

[1] Electronics Research Institute (ERI), Cairo, Egypt
mayaboelhassan@yahoo.com, Khalid_elgabaly@yahoo.com, asmaa@eri.sci.eg

[2] Faculty of Electronic Engineering, Menoufia University Egypt
kamal_awadalla@hotmail.com

Abstract — A planar array of $M \times N$ circularly polarized microstrip patch antennas is proposed for high resolution land-imaging applications using an airborne side-looking Synthetic Aperture Radar (SAR) systems. The microstrip patch is designed to produce either right-hand or left-hand circular polarization. The planar array is designed to produce a circularly polarized three-dimensional beam of cosecant-squared shape in the range direction and uniform shape in the azimuth direction. The mutual coupling between the adjacent patches in the proposed array is studied for the assessment of the final array design and is shown to have no bad effects on the resulting beam shape or the array performance. A computationally efficient Particle Swarm Optimization (PSO) algorithm is developed and applied to find the amplitude and phase distributions of the feeding voltages over the planar array elements required to produce the desired radiation patterns. This technique is achieved by developing a fast algorithm to extend the amplitudes and phases calculated for M-element and N-element linear arrays to be applied to the elements of a two-dimensional $M \times N$ planar array without the need to apply the PSO to calculate the amplitudes and phases for the entire elements of the planar array. A perfect three-dimensional pattern with the desired shapes in both azimuth and range directions is achieved. The input impedance, the axial ratio and the shapes of the radiation patterns produced by the proposed antenna array are investigated and shown to be satisfactory over the frequency band of $3.91 - 4.11$ GHz.

Index Terms — Axial ratio, beam shaping, cosecant squared, microstrip patch antenna, planar antenna arrays, PSO, synthetic aperture radar.

I. INTRODUCTION

The Synthetic Aperture Radar (SAR) system uses the time delay and Doppler information to generate a two-dimensional image with the desired range and azimuth resolutions, respectively [1]. This requires a SAR antenna with an aperture of high aspect ratio (the antenna aperture should be long in the azimuth direction and narrow in the range direction) and capable of achieving beam steering and beam shaping. A typical airborne or spaceborne side-looking SAR system uses an antenna with a beam that has a flat-top shape in the plane of the azimuth direction and a cosecant-squared shape in the plane of the range direction. This gives uniform illumination over the SAR beam footprint on the earth surface to get the incident power independent of the radar range for a constant height aircraft or spacecraft [2]. The planar arrays for both airborne and spaceborne SAR systems have many advantages including (i) its ability to achieve high aspect ratio of the antenna aperture that is long in the azimuth direction and narrow in the range direction and (ii) its ability to achieve the desired beam shapes in the two perpendicular azimuth and range directions.

Linearly polarized arrays are the most commonly used antenna type for SAR applications, especially for high-resolution land imaging. The currently used linearly polarized SAR systems are affected by Faraday's rotation during wave propagation from the satellite to the earth or random reflections from the atmospheric clutter [3]. Faraday's rotation is a result of the interaction of the propagating electromagnetic field and the earth's magnetic field. Some experimental SAR systems that use circular polarization are introduced in [4-6]. A SAR system which relies on circular polarization is proposed for a spaceborne platform [4]. An L-band circularly polarized SAR system that works at 1.275 GHz is introduced in [5] and compared to linearly polarized SAR system in a fully polarimetric experiment in an anechoic chamber. The comparison shows that circular polarization is less affected by the orientation angle of the target and could avoid the misalignment between the transmitter and receiver antenna during system operation. In [6] a complete fully polarimetric circularly polarized SAR system is developed for a microsatellite to observe land deformation on earth surface. However there is no beam shaping for the antenna array designed in [6]. The present

Submitted On: August 8, 2018
Accepted On: December 24, 2018

work aims to produce accurately formed beam.

A circularly polarized antenna can be realized using arranged antennas of linear or circular polarized elements. In [7], a 2×2 planar antenna array of linearly polarized elements is introduced where unequal feed lines are used in order to produce two orthogonal electric fields with equal amplitudes and 90° phase difference. In [8], a feed network is used to split an input signal into four signals in phase quadrature and equal magnitudes and connected to four Vivaldi antennas sequentially rotated by 90°. Nevertheless, circular polarization can be produced using a single microstrip patch antenna with a single feed. Several methods have been proposed to provide circular polarization without the complexities inherent in dual-feed devices [9-10]. The design of a circularly polarized single-element single-feed microstrip patch antenna relies on the geometry of the antenna that enables the generation of two degenerate orthogonal modes to produce circularly polarized radiation. By introducing some asymmetry into the microstrip antenna geometry, the degeneracy of the two modes is removed. Examples of this technique are the square microstrip patch with a tilted slot, the corner-fed rectangular patch, the slightly elliptical patch, the pentagon-shaped patch, and the circular disc with perturbation element [11]. A compact single-feed circularly polarized microstrip antenna is proposed in [9] to achieve circular polarization over a wide beamwidth. In [10], a single-feed slotted circular microstrip patch antenna is introduced for operation in RFID applications. In the present work, a single-feed circularly polarized microstrip patch antenna is designed to operate as an array element for a land imaging side-looking SAR operating in the strip mapping mode at 4GHz. Arrays of such a microstrip patch are suitable for beam shaping and beam steering over a wide angular zone.

The methods of beam synthesis using antenna arrays depend on finding the complex excitation voltages of the array elements or the physical layout of the array that produces the radiation pattern close to the desired one. The most effective beam synthesis methods are the optimization techniques that depend on Evolutionary Algorithms (EAs). Several global optimization algorithms such as Differential Evolution (DE) [12], Genetic Algorithm (GA) [13], Simulated Annealing (SA) [14], and Ant Colony Optimization (ACO) have been used in antenna array pattern synthesis. The Particle Swarm Optimization (PSO) is one of the evolutionary optimization algorithms that are proposed in the present work to optimize the antenna pattern on the basis of the system requirements. The main objectives are to satisfy the required shape of the antenna main lobe and the minimum side lobe level within a specified mask pattern. The proposed PSO algorithm is simple, easy to implement and requires minimum mathematical processing.

In the following sections, the design of a single-feed Right-Hand Circularly Polarized (RHCP) as well as Left-Hand Circularly Polarized (LHCP) microstrip patch antenna are presented and the antenna characteristics including the input impedance, radiation pattern, axial ratio, and bandwidth are discussed. The mutual coupling, axial ratio and radiation patterns between two adjacent elements of such a patch arranged along x-axis and$y$-axis; for magnetic and electric coupling respectively; are investigated for different values of the separation distance. The PSO algorithm is applied to a 20-element linear array of microstrip patches to synthesize a cosecant-squared radiation pattern. It is also applied to a 10-element linear array to synthesize a fan-shaped beam. Finally, a proposed computationally efficient PSO is developed and applied to optimize the distribution of the excitation voltages of a planar array to achieve a cosecant-squared radiation pattern in the plane of the range direction and a flat-top radiation in the plane of the azimuth direction.

II. FOUR-SLOT TRUNCATED-CORNERS MICROSTRIP PATCH FOR CIRCULAR POLARIZATION

An asymmetric square microstrip patch, shown in Fig. 1, with four unequal circular sectors cut at the corners of the patch and four slots cut along the horizontal and vertical axes of symmetry is proposed to produce circular polarization. Such a microstip patch is intended to be used as an element for circularly polarized SAR antenna array. This microstrip patch is similar to that introduced in [15] with modifications to work at a frequency of 4 GHz. This microstrip patch has the advantages of low profile, lightweight, and ease of manufacturing using printed circuit techniques. The dimensional design parameters of the antenna are illustrated in Fig. 1. The substrate material is FR4 with dielectric constant $\varepsilon_r = 4.4$ and the loss tangent $\delta = 0.02$.The length of the square patch and the ground plane is denoted as L_P and G, respectively. As shown in Fig. 1, a coaxial feed is positioned at $x = 0, y = F$, where the origin is at the center of the microstrip patch. The radii of the four circular sector cuts are not equal and denoted as r_1, r_2, r_3, and r_4. Each of the four slots has length of L_s and width of W_s.The unequal truncated 90° circular sectors cut at the four corners of the square patch will produce two phase quad. This is required to produce circularly polarized rarature and spatially orthogonal modes with equal magnitudesdiated field.

A. Mechanism of producing circular polarization

The mechanism of producing circular polarization from such a microstrip patch can be attributed to electric field distribution in the four slots. The path of the surface current on the patch is truncated by each of the four slots causing the electric charges to be accumulated on the slot edges producing a strong horizontal electric field in the vertical slots, and a strong vertical electric field in the horizontal slots. The magnitudes of the vertical and

horizontal electric field components are nearly equal whereas the phase shift between them is about 90°, and thus, circularly polarized radiation is produced.

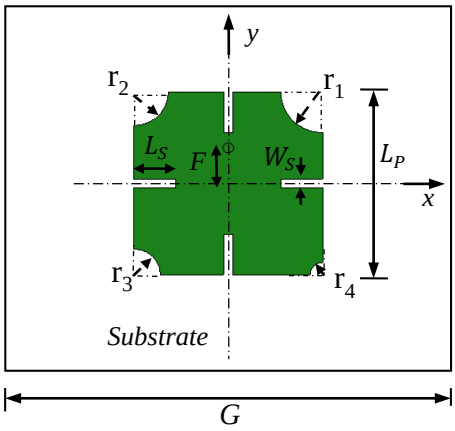

Fig. 1. Geometry of the proposed circularly polarized patch antenna.

B. Controlling the sense of polarization

By varying the sector radii of the truncated corner such that ($r1 > r2 > r3 > r4$) as shown in Fig. 2 (a), the patch antenna produces RHCP. By analogy, if the corner cuts are made such that ($r1 < r2 < r3 < r4$) as shown in Fig. 2 (b) the patch antenna produces LHCP.

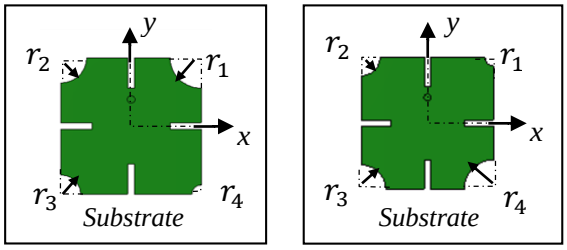

(a) Design for RHCP (b) Design for LHCP

Fig. 2. Controlling the sense of circular polarization produced by the patch antenna.

C. Mutual coupling between two adjacent patches

Consider two adjacent antennas fed by ports (1) and (2). According to the definition of the S_{21} parameter: it is the ratio of the voltage induced at port (2) to the voltage applied at port (1), which exactly expresses the mutual coupling between the two antennas. In a planar array arrangement the patch antenna will be repeated in two orthogonal directions (x- and y-directions). The effects of coupling between the elements in both directions are investigated. The distance between any two elements in the x or y-direction is denoted as d. For two elements arranged along the x-axis, the coupling coefficient is calculated for different separation distances. Also, the axial ratio and the circularly polarized radiation pattern are studied in the operating frequency range of the antenna for different separation distances between elements. The same parameters are calculated for two elements arranged along the y-axis. The two investigated configurations are shown in Fig. 3.

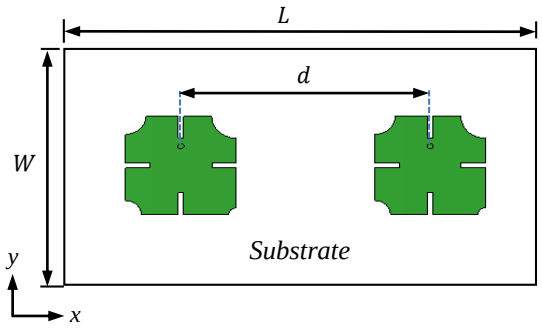

(a) Linear array arranged along x-axis

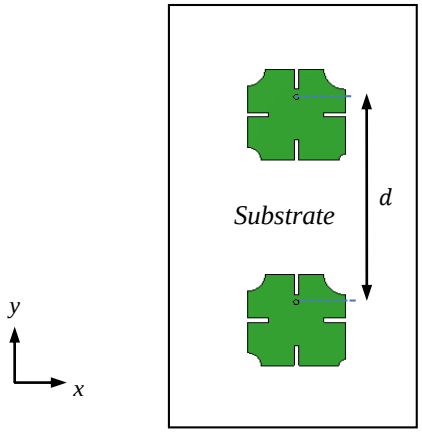

(b) Linear array arranged along y-axis

Fig. 3. Linear arrays of two patches,

III. PARTICLE SWARM OPTIMIZATION TECHNIQUE FOR LINEAR AND PLANAR ARRAYS

The Particle Swarm Optimization (PSO) is a popular optimization technique proposed for solving global numerical optimization problems. PSO technique is a robust stochastic evolutionary computation technique based on the movement and intelligence of swarms. It is simple to implement and quickly converges to good results. PSO has been used in the optimization of electromagnetic (EM) problems in the recent few decades [16]. In the present work, a computationally efficient PSO algorithm is developed to optimize the planar array radiation pattern to produce the beam shape required for land imaging SAR system. This beam is

cosecant-squared-shaped in the ground range direction and fan-shaped in azimuth direction. It aims to calculate the amplitude and phase of excitation for each element in the planar array. Such a radiation pattern can't be synthesized using one-dimensional array.

A. Conventional algorithm for PSO

The PSO algorithm is based on the analogy of movement of bird flocks or fish schools on one side, and the optimization on the other side. The PSO algorithm searches for the global minimum of the cost function, i.e., minimizes the cost function of an electromagnetic problem by simulating movement and interaction of particles (agents) in a swarm. The position of a particle corresponds to one possible solution of the EM problem, i.e., it corresponds to one point in the optimization space. The velocity and position update equations for the swarm particles are given in [17].

As the main goal of the PSO during its iterations is to reduce the cost function, the latter should be increased as the achieved radiation pattern further deviates from the ideal pattern. Thus, the cost function can be, simply, the absolute difference between the achieved and the desired (ideal) patterns of the electric field as follows:

$$F_C = \left|E(\theta) - \hat{E}(\theta)\right|. \tag{1}$$

In conclusion, the amplitudes and phases of excitation are determined by the PSO algorithm so as to satisfy the required beam shape and the remaining objectives of the antenna array design such as the axial ratio and the sidelobe level.

B. Development of computationally efficient PSO algorithm for planar arrays

Assuming that the array elements are arranged in N_x rows and N_y columns; the rows are perpendicular to the x-axis whereas the columns are perpendicular to the y-axis. The electric field radiated in the far zone can be expressed as [18]:

$$E(\theta,\phi) = \sum_{n_x=1}^{N_x}\sum_{n_y=1}^{N_y} A_{n_x,n_y} e^{j\varphi_{n_x,n_y}} \times e^{jk_o((n_x-1)D_x cos\phi + (n_y-1)D_y sin\phi)sin\theta}, \tag{2}$$

where, D_x is the separation between successive rows, D_y is the separation between successive columns and $A_{n_x,n_y}$and $\varphi_{n_x,n_y}$are the magnitude and phase of the excitation voltage, respectively, for the array element lying in the row number n_x and the column number n_y.

Thus, to get the beam produced by the planar array oriented in the direction (θ_o, ϕ_o), the phase of the excitation of each element in the planar array should be given as:

$$\varphi_{n_x,n_y} = -k_o\left[(n_x-1)D_x cos\phi_o + (n_y-1)D_y sin\phi_o\right] sin\theta_o. \tag{3}$$

On the other hand, the amplitudes of the excitation A_{n_x,n_y} are left to be determined by the PSO algorithm so as to satisfy the remaining objectives of the antenna array design

Applying the PSO algorithm on a planar array is much time-consuming. The amplitude of the excitation of each element of the planar array expressed as the product of two multiplicands; that is:

$$A_{n_x,n_y} = A_{x_{n_x}} A_{y_{n_y}}. \tag{4}$$

On the other hand, the phase of excitation of each element of the planar array expressed as the product of the sum of two angles; that is:

$$\varphi_{n_x,n_y} = \varphi_{x_{n_x}} + \varphi_{y_{n_y}}. \tag{5}$$

Equation (2) can be written as the product of two multiplicands:

$$E(\theta,\phi) = \sum_{n_x=1}^{N_x} A_{x_{n_x}} e^{j\varphi_{x_{n_x}}} e^{jk_o(n_x-1)D_x sin\theta\, cos\phi} \times \sum_{n_y=1}^{N_y} A_{y_{n_y}} e^{j\varphi_{y_{n_y}}} e^{jk_o(n_y-1)\,D_y sin\theta\, sin\phi}, \tag{6}$$

or simply,

$$E(\theta,\phi) = E^{(Lx)}(\theta,\phi) \times E^{(Ly)}(\theta,\phi), \tag{7}$$

where,

$$E^{(Lx)}(\theta,\phi) = \sum_{n_x=1}^{N_x} A_{x_{n_x}} e^{j\varphi_{x_{n_x}}} e^{jk_o(n_x-1)D_x sin\theta\, cos\phi}, \tag{8}$$

and,

$$E^{(Ly)}(\theta,\phi) = \sum_{n_y=1}^{N_y} A_{y_{n_y}} e^{j\varphi_{y_{n_y}}} e^{jk_o(n_y-1)\,D_y sin\theta\, sin\phi}. \tag{9}$$

It should be noticed that (8) gives an expression for the electric field radiated from a linear array of point sources arranged along the x-axis, whereas (9) gives an expression for the electric field radiated from a linear array of point sources arranged along the y-axis. In the special case of a beam which is symmetric about the direction of its maximum (θ_o, ϕ_o), the array elements are fed with progressive phase shifts in the x and y directions given, respectively, by the following expressions:

$$\Delta\varphi_x = -k_o D_x\, sin\theta_o\, cos\phi_o, \tag{10}$$

$$\Delta\varphi_y = -k_o D_y\, sin\theta_o\, sin\phi_o. \tag{11}$$

Consequently, the phases are given by:

$$\varphi_{x_{n_x}} = -k_o(n_x-1)\,D_x\, sin\theta_o\, cos\phi_o, \tag{12}$$

$$\varphi_{y_{n_y}} = -k_o\left(n_y-1\right)D_y\, sin\theta_o\, sin\phi_o. \tag{13}$$

In this case, the PSO algorithm can be run to optimize the shape of the radiation pattern (8) by iteratively setting the amplitudes $A_{x_{n_x}}$. In the same manner, the PSO algorithm can run to optimize the shape of the radiation pattern (9) by iteratively setting the amplitudes $A_{y_{n_y}}$.

The optimization process to obtain a symmetric beam shape from a planar array using the PSO algorithm that runs to optimize linear arrays can be described as follows.

1- Consider that planar array lies in the *x*-*y* plane and consider the required beam with its desired shape is oriented normal to the array plane (*z*-direction). This means to set $\varphi_{x_{n_x}} = 0$ and $\varphi_{y_{n_y}} = 0$ for all the array elements in both equation (8) and equation (9).
2- Give expression to describe the (ideal) beam shapes in *z*-*x* and *y*-*z* planes as $E_{opt}^{(Lx)}(\theta, 0)$ and $E_{opt}^{(Ly)}(\theta, \pi/2)$.
3- Apply PSO algorithm to optimize $E^{(Lx)}(\theta, \phi)$ given by equation (8) after setting $\varphi_{x_{n_x}} = 0$ and $\phi = 0$. This determines the optimum values of $A_{x_{n_x}}$.
4- Apply PSO algorithm to optimize $E^{(Ly)}(\theta, \phi)$ given by equation (9) after setting $\varphi_{y_{n_y}} = 0$ and $\phi = \pi/2$. This determines the optimum values of $A_{y_{n_y}}$.
5- Calculate A_{n_x,n_y} using equation (4).
6- Calculate φ_{n_x,n_y} using equation (3) to get the shaped beam oriented at (θ_o, ϕ_o).
7- Finally, calculate the total radiated electric field using the expression in equation (2).
8- Using this method, the approximate run time required for the PSO algorithm to optimize two-dimensional planar antenna array is only twice the time required to optimize the one-dimensional linear antenna array.

IV. RESULTS AND DISCUSSIONS

It may be worthwhile to mention that a circularly polarized patch antenna of the same type as that proposed in the present work, is introduced in [15] and is designed to operate for global navigation satellite systems in the frequency band (1.566–1.582GHz). In the present work, the design of the same type of patch antenna is modified to operate for land imaging SAR systems in the frequency band (3.91 to 4.11 GHz). The CST commercially available electromagnetic simulation package is used for assessment of the antenna performance. The optimal design parameters of the patch antenna to produce RHCP are $L_P = 16.4$ mm, $G = 44$ mm, $r_1 = 3.65$ mm, $r_2 = 3$ mm, $r_3 = 2.31$ mm, $r_4 = 1.1$ mm, $L_s = 3.6$ mm, $W_s = 0.8$ mm, $F = 3.2$ mm, $h = 1.5$ mm, $\varepsilon_r = 4.4$ mm, and $\delta = 0.02$. It should be noted that in the following presentation and discussions of the numerical results the patch antenna has the same design parameters listed above unless otherwise indicated.

A. The mechanism of producing circular polarization

A RHCP patch supports two orthogonal modes with equal magnitudes and 90˚ phase difference. This is realized by cutting the four unequal 90˚ circular sectors at the four corners of the microstrip patch. To demonstrate the mechanism of producing circular polarization, the surface current distributions at different phase angles of the wavelength at 4 GHz are shown in Fig. 4, namely at phases 0°, 45°, 90°, and 135° which are corresponding to the 0, 1/8, 1/4, and 3/8 of the periodic time of the microwave oscillation. At a phase of 0°, the current density on the patch surface is concentrated around the two vertical slots (along the *y*-axis), which generates *x*-directed electric field in the vertical slots. At phase of 90°, the surface currents are mainly concentrated around the horizontal slots (along the *x*-axis) producing *y*-directed electric field in the horizontal slots. At a phase of 45°, the charge concentration around the four slots is almost the same resulting in equal electric field magnitudes in both *x*- and *y*-directions, with a resultant electric field inclined 45° to the horizontal or vertical axis. Thus a circulating electric field is produced between phases 0° and 90°, i.e., the electric field vector generated in the near zone will change its direction from pure E_x component at phase 0°, to pure E_y component at phase 90°. This produces a circularly polarized electric field in the far zone rotating in the same direction.

B. Frequency band of operation of the circularly polarized patch antenna

The simulation results for the reflection coefficient of the proposed patch antenna considering a feed line of **50Ω** characteristic impedance against the frequency are shown in Fig. 5. The return loss is maintained below $-10\ dB$ in the frequency range **3.91GHz** to **4.11GHz** (**200MHz**). In the same figure, the axial ratio is plotted against the frequency where it is maintained below **3dB** through the frequency range **3.984 GHz to 4.027 GHz** (43 MHz). Thus the antenna bandwidth for acceptable performance can be considered (**3.984 − 4.027 GHz**).

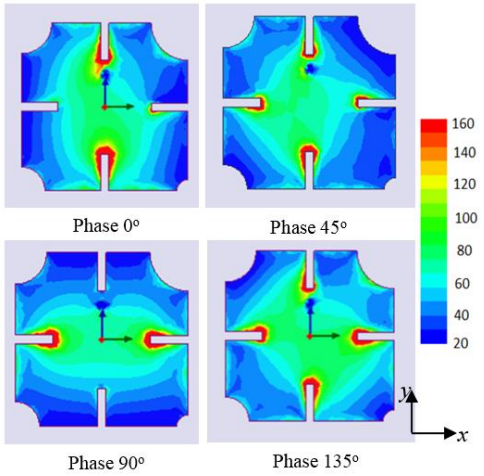

Fig. 4. Current distribution (A/m) on the surface of a microstrip patch at different phase angles.

A prototype of a single patch antenna is fabricated in the laboratory for experimental verification of the simulation results concerning the dependence of the return loss on the frequency. Top and bottom views of the fabricated antenna are presented in Fig. 6 (a), the vector network analyser of the Agilent Field Fox N9918A is used to measure $\boldsymbol{S_{11}}$ at the antenna port against the frequency. Figure 6 (b) shows the experimental setup with the fabricated prototype of the proposed antenna. A comparison between the experimental and simulation results of the return loss of the antenna shows good agreement as shown in Fig. 7.

C. Radiation patterns of circularly polarized fields

For experimental assessment of the RHCP radiation pattern, the dual circular polarized antenna model JXTXLB-OSJ-20180 is used as a reference antenna and the experimental setup is made as shown in Fig. 8.

A good agreement between the experimental and simulation results of the right-hand circularly polarized radiation patterns of the patch antenna is shown in Fig. 9. The radiation patterns are measured at 4 GHz in the two principal planes $x-z$ ($\phi = 0°$) and $y-z$ ($\phi = 90°$). It is clear in the figure that the radiation is dominated by right-hand circularly polarized electric field component.

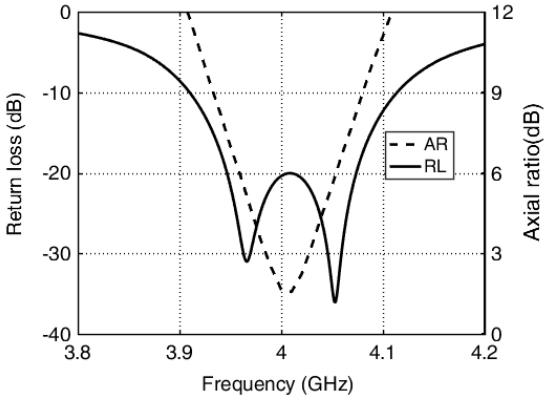

Fig. 5. Simulated return loss and axial ratio versus frequency for the circularly polarized patch antenna with the geometry presented in Fig. 1.

Top view Bottom view

(a) Top and bottom views of the fabricated prototype

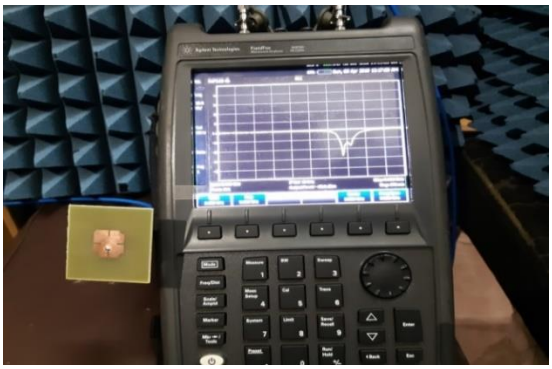

(b) Experimental setup for measuring S_{11}

Fig. 6. Experimental measurements of the circularly polarized patch antenna.

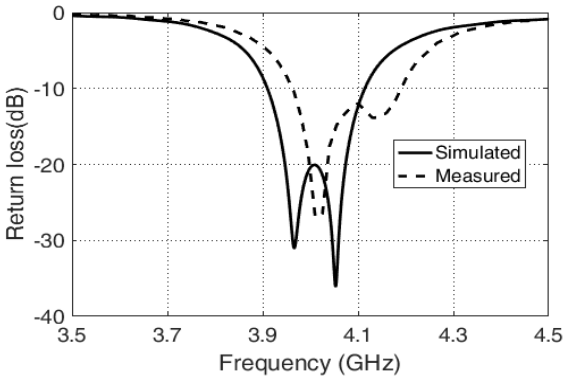

Fig. 7. Frequency dependence of the experimentally measured S_{11} for the fabricated antenna compared with the simulation results.

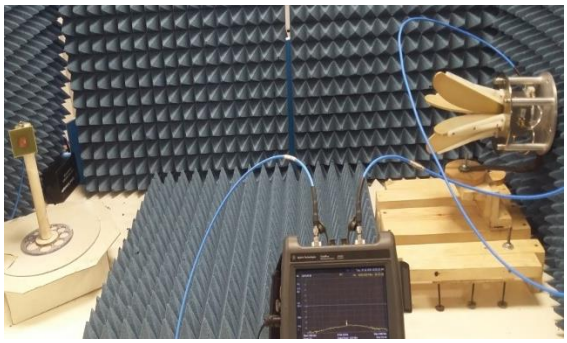

Fig. 8. Experimental setup for measurement of the antenna radiation patterns.

D. Beam width of circular polarization of a single patch antenna

The axial ratio, as a function of the angle θ, is shown in Fig. 10 for the two principle planes $\phi = 0°$ and $\phi = 90°$ at a frequency of 4 GHz. It is clear that the 3 dB axial ratio beam width is about 110° in the plane $\phi = 0°$ and about 180° in the plane $\phi = 90°$. This is considered

good radiation characteristics of a single-element to synthesize the beam shapes required for land imaging SAR applications using planar arrays of such an element.

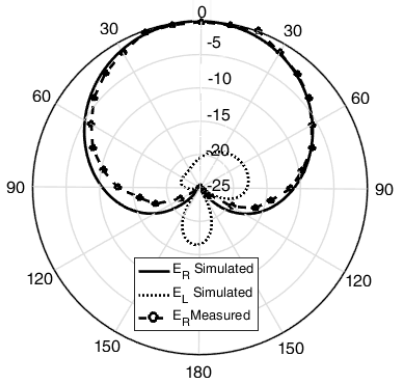

(a) Radiation patterns in the plane $\phi = 0°$

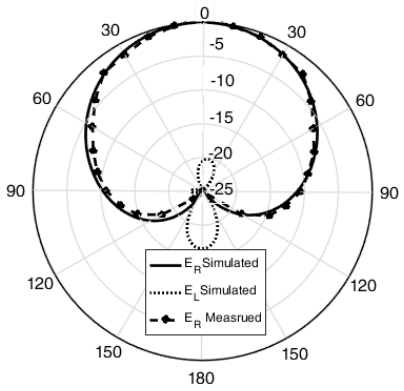

(b) Radiation patterns in the plane $\phi = 90°$

Fig. 9. Simulated and measured radiation patterns for RHCP and LHCP of the microstrip patch prototype presented in Fig. 1.

E. Coupling between two adjacent patch antennas

Mutual coupling between array elements is an important factor that may affect the performance of an antenna array, especially the coupling between adjacent elements. In printed antennas the mutual coupling mainly arises due to either the currents induced by the near field coupling from the other antennas or the surface waves on the substrate. By reducing the mutual coupling between array elements, the scan blindness effects will be reduced and the implementation of beam shaping will be much easier [18].

The coupling between two adjacent elements of the microstrip antenna is studied both computationally by simulation and experimentally using a vector network analyzer. Two elements of the proposed microstrip patch antenna are arranged in two configurations. In one of them the two elements are arranged along the x-axis and in the other configuration, the elements are arranged along the y-axis as shown in Fig. 3 (a) and Fig. 3 (b), respectively. The effect of the variation of the distance between the two elements on the coupling coefficient (S_{21}) over the frequency band $3.8 - 4.2$GHz can be explained in view of the plots of S_{11} and S_{21} presented in Fig. 11 for separation distances of 22 mm, 30 mm, and 37 mm for both arrays. It is clear from the figure that the coupling between the two elements decreases as the distance increases for both array configurations. For all the separation values, the magnitude of S_{11} and S_{21} presents weak coupling, which is a promising result for a subsequent beam shaping process using planar arrays.

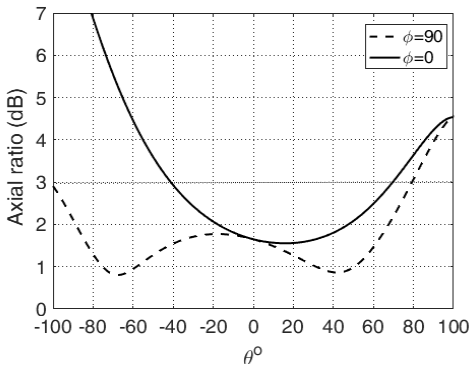

Fig. 10. Axial ratio in the elevation planes $\phi = 0°$ and $\phi = 90°$ for the patch antenna presented in Fig. 1 at 4 GHz.

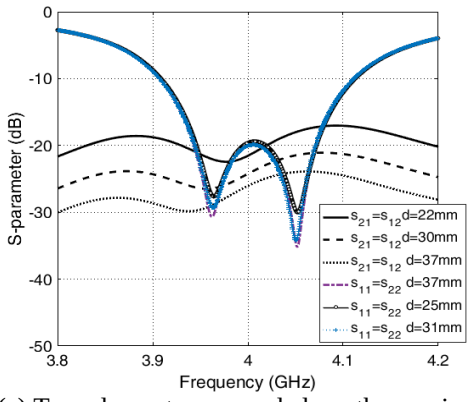

(a) Two elements arranged along the *x*-axis

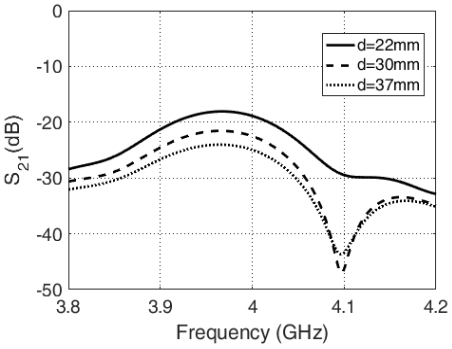

(b) Two elements arranged along the y-axis

Fig. 11. Mutual coupling between two adjacent patches for different values of the separation distance.

Two-element arrays of the circularly polarized patch antenna are laboratory fabricated to get two different configurations: one in which the elements are arranged along x-axis and the other in which the elements are arranged along y-axis. The separation between the two elements is 37 mm ($\lambda/2$) for both array configurations. Photographs for both fabricated arrays are presented in Fig. 12. The setup for measuring the radiation pattern is presented in the same figure.

The coupling coefficient between the two ports (S_{21}) is measured using a vector network analyser. Figure 13 presents comparisons between the simulation and measurement results for S_{21} for both antenna arrangements. The comparisons show good agreement.

Top view Bottom view

(a) Fabricated *x*-arranged array

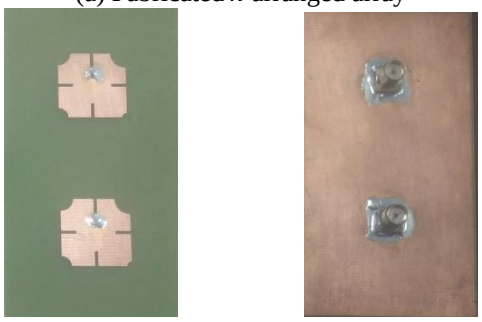

Top view Bottom view

(b) Fabricated *y*-arranged array

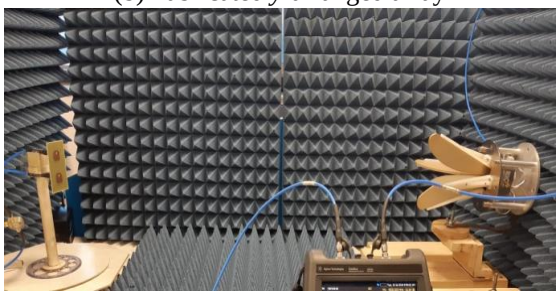

(c) Experimental setup for radiation pattern measurements

Fig. 12. Photographs for fabricated arrays of the circularly polarized antenna and the experimental setup for radiation pattern measurements.

It is also important to study the dependence of the 3dB axial ratio beam width of the two-element arrays on the separation between the elements. In Figs. 14 and 15, the axial ratio is plotted against θ at 4 GHz for separation distances of 22mm, 30 mm, and 37 mm in the planes $\phi = 0°$and $\phi = 90°$, respectively.

It is clear that the separation distance has a significant effect on the beam width over which the axial ratio is maintained below 3dB. The separation distance has a greater effect on the 3dB axial ratio beam width for the array arranged along the y-axis than that effect on the array arranged along the x-axis. For the y-arranged array the 3dB axial ratio beam width in the plane $\phi = 0°$ changes from 180° for a separation distance of 22mm to about 90° for a separation distance of 37mm. For the same array the 3dB axial ratio beam width in the plane $\phi = 90°$changes from 115° for a separation distance of 22 mm to about 60° for a separation distance of 37 mm. For the x-arranged array the 3dB axial ratio beam width in the plane $\phi = 0°$changes from 110° for a separation distance of 22mm to about 83° for a separation distance of 37mm. The 3dB axial ratio beam width of the x-arranged array in the plane $\phi = 90°$ seems to have insignificant dependence on the separation between the adjacent elements.

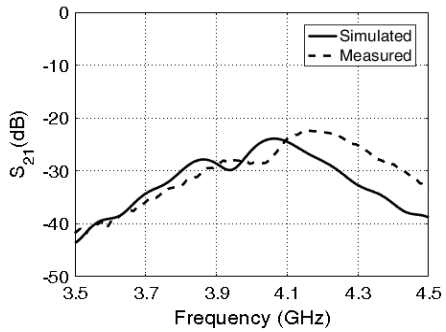

(a) Two-element array arranged along the *x*-axis

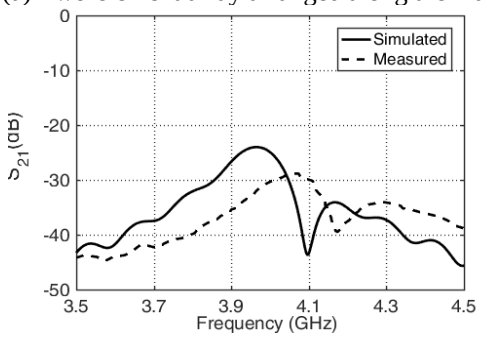

(b) Two-element array arranged along the *y*-axis

Fig. 13. Comparison between the experimental and simulation results for the frequency behavior of the coupling coefficient S_{21} for both array arrangements at separating distance of $\lambda/2$ between the array elements.

Comparisons between the experimental and simulation results for the patterns of the circularly polarized fields radiated by both the *x*-arranged and *y*-arranged array configurations are presented in Fig. 16 and Fig. 17, respectively. The radiation patterns are plotted in the plane of the array arrangement (i.e., in the plane $\phi = 0°$ for x-arranged array and in the plane

$\phi = 90°$ for the y-arranged array). The comparisons show good agreement between the computational and experimental results.

V. BEAM SHAPING USING CIRCULARLY POLARIZED PLANAR ARRAYS OF PATCH ANTENNAS

In the present section, the PSO algorithm is applied to set the proper amplitude and phase distributions of the feeding voltages over linear arrays of the proposed asymmetric circularly polarized patch antennas. Each element in the array has a separate coaxial feeder but the array is placed over a common substrate and ground plane.

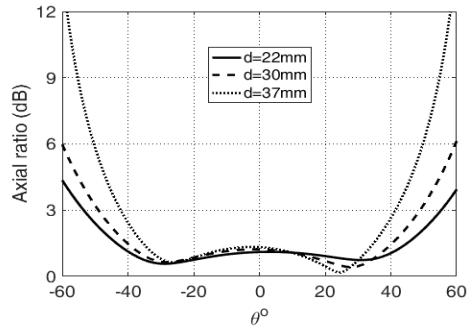

(a) $\phi = 0°$

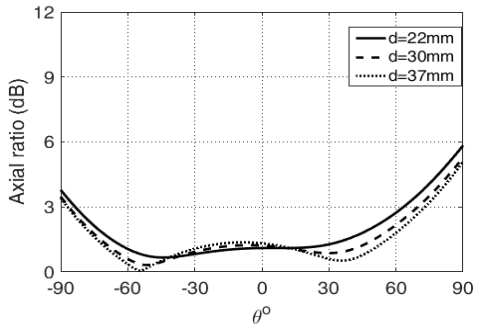

(b) $\phi = 90°$

Fig. 14. Axial ratio versus θ for two-element array arranged along x-axis for different values of the separation distance at 4 GHz.

The side-looking imaging SAR radiation pattern has cosecant-squared shape in the range direction and fan shape in the cross-range (azimuth) direction. The cosecant-squared radiation pattern provides a uniform earth illumination where the received power is independent of the range distance between the SAR and the imaged land. It is a means of achieving more uniform signal strength at the input of the receiver of the SAR system. In the azimuth direction the radiated beam should have a flat-top beam to ensure uniform distribution of the power density over the illuminated area in the azimuth direction.

The three-dimensional radiation pattern required for land imaging side looking SAR system has cosecant-squared shape in the range direction and uniform (flat-top) shape in the azimuth direction. This pattern cannot be achieved unless a planar array is used to synthesize the required beam shapes in the two orthogonal planes. In a similar way to that applied for beam shaping using linear arrays, the PSO algorithm is, first, applied to optimize the beam produced by a planar array of 20×10 point-source elements in the x-direction and y-direction respectively, through the control of the amplitudes and phases of excitation voltages to obtain cosecant-squared beam shape in the range direction ($\phi = 0°$ plane) within the angular zone $-15° < \theta < 15°$and fan-shaped beam in the azimuth direction ($\phi = 90°$ plane) within the angular zone $-20° < \theta < 20°$.

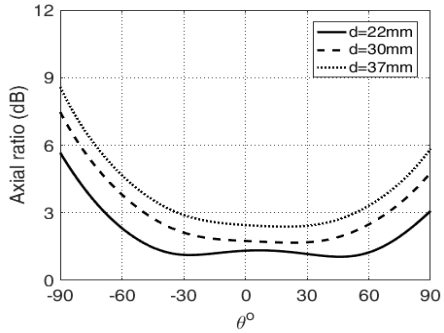

(a) $\phi = 0°$

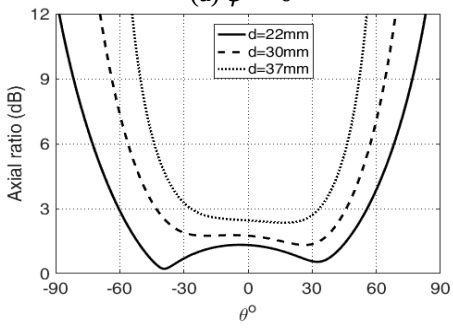

(b) $\phi = 90°$

Fig. 15. Axial ratio versus θ for two-element array arranged along y-axis for different values of the separation distance at 4 GHz.

The excitation coefficients are calculated as described in Section III.B for optimizing the radiation pattern of a planar array. The obtained excitation voltages are then applied to an array of 20×10 elements of the circularly polarized microstrip patches through electromagnetic simulation using CST© commercial package at 4.0 GHz. The array elements are placed over a comman ground plane and fed through 20×10 symmetrical 50Ω SMA coaxial feed points. The separation distance between the contiguous patches is 0.4λ in both x- and y-directions and the total array antenna size is 614mm×314 mm. The resulting RHCP radiation patterns are shown in Fig. 18 in both $\phi = 0°$and $\phi = 90°$ planes and compared to

the ideal (desired) beam shape. The axial ratio is plotted in the same figure in both planes, where it is shown to be maintained below 3dB within the angular zone of interest. The average error between the desired radiation pattern and the actually achieved radiation pattern is about 6.6 %.

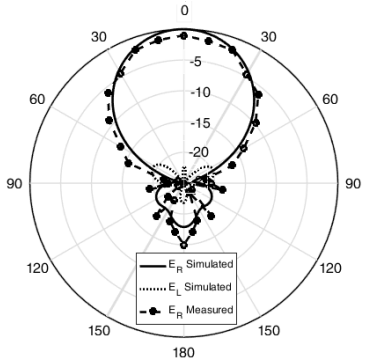

(a) $\phi = 0°$

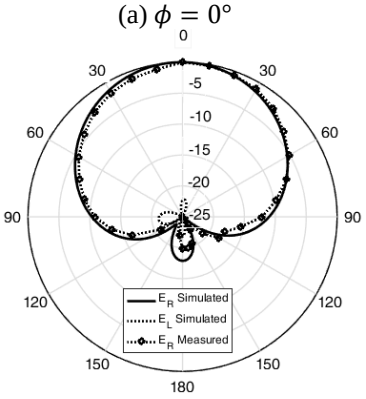

(b) $\phi = 90°$

Fig. 16. Simulated radiation patterns for RHCP and LHCP with the angle θ for two-element array arranged along x-axis compared with the experimental measurements at 4 GHz.

The three-dimensional radiation pattern produced by 20×10 elements array of circularly polarized microstrip patch antenna is presented in Fig. 19 compared to a sketch of the desired three-dimensional beam where the latter is drawn using a dashed line.

As shown in Fig. 20, the radiation efficiency for the final array is about 64% for a lossy FR4 substrate material whereas is about 93% for low-loss FR4 substrate.

It may worthwhile to mention that the antenna array designed in [5], [6], [19] and [20] produces circular polarization for synthetic aperture radar. However, this array produces pencil beam that is steerable over a specific angular range. The present paper is concerned with the design of an antenna array that produces a shaped-beam to get uniform illumination within the beam footprint on the ground surface in both the range and azimuth directions. Nevertheless, we have included discussions of the published results mentioned in Table 1.

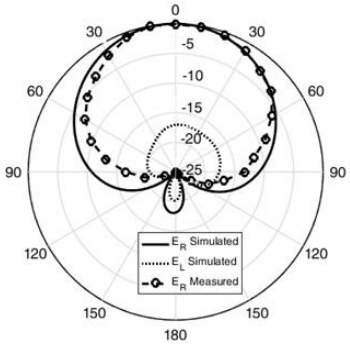

(a) $\phi = 0°$

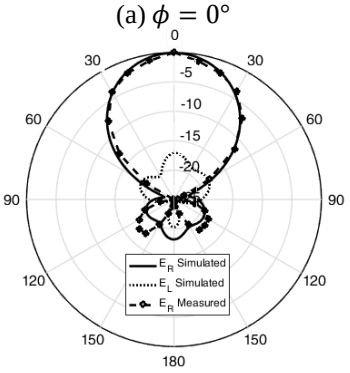

(b) $\phi = 90°$

Fig. 17. Simulated radiation patterns with θ for two-element array arranged along y-axis compared with the experimental measurements at 4 GHz.

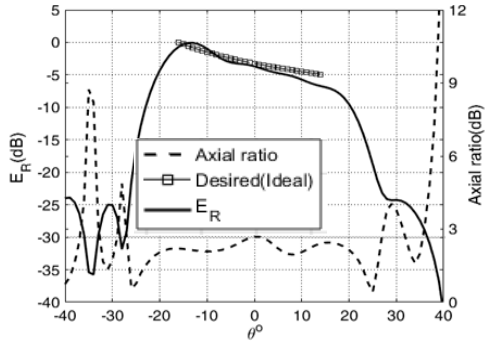

(a) Cosecant-squared beam shape in the plane $\phi = 0°$

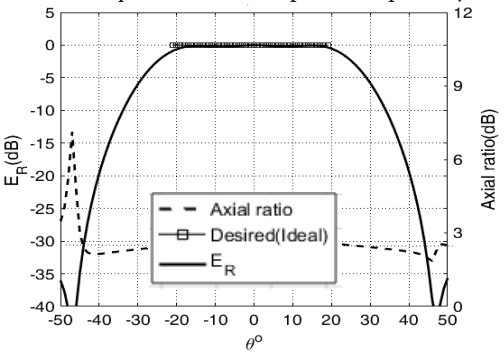

(b) Flat-top beam shape in the plane $\phi = 90°$

Fig. 18. Shaped beam and axial ratio for planar array of 20×10 elements.

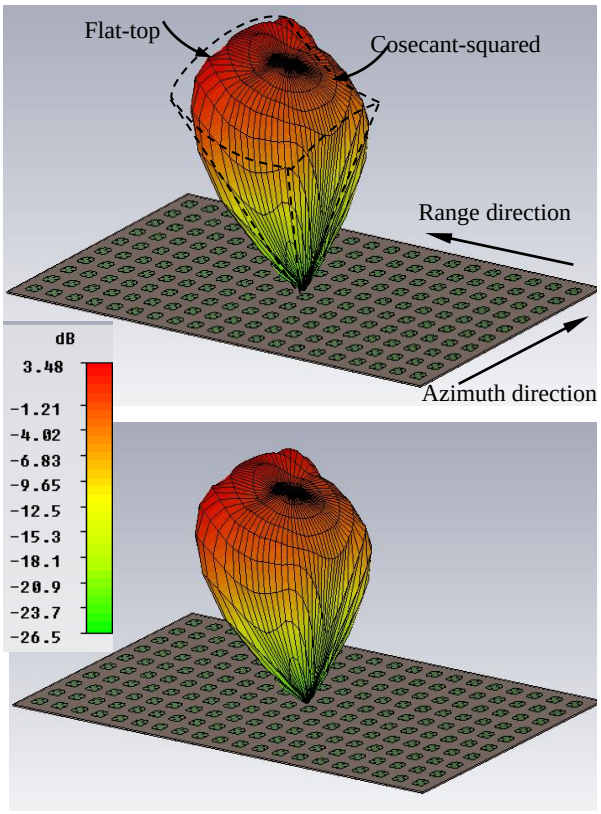

Fig. 19. 3D patterns (cosecant-squared/fan-shaped) synthesized by planar array of 20×10 elements at 4.0 GHz (top figure) and 4.05 GHz (bottom figure).

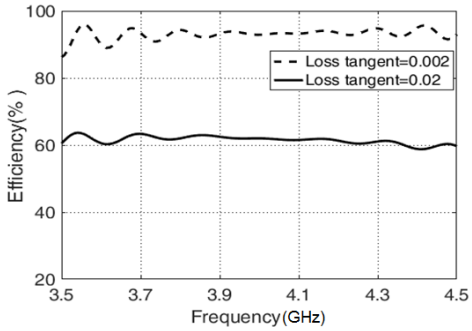

Fig. 20. Antenna efficiency against the frequency.

Table 1: Comparative performance parameters between the present work achievement and that of [19]

Parameters	Reference [19]	Present Work
Frequency	1.27 GHz	4.0 GHz
Axial ratio	≤3 dB	≤3 dB
Efficiency	80%	64%
Azimuth beamwidth	≥ 6.77°	40° (Shaped Beam)
Elevation beamwidth	3.57-31.02°	30° (Shaped Beam)
Antenna size	810×325mm	614×314mm
Polarization	RHCP + LHCP	RHCP + LHCP

VI. CONCLUSIONS

An array of microstrip patches is proposed for SAR systems which can produce either RHCP or LHCP. The effects of mutual coupling between two adjacent elements on the array performance are studied for different separation distances between the elements. The optimum separation between the contiguous elements is determined. Finally, a planar array of 20×10 elements is designed and optimized by applying the PSO algorithm to obtain the beam shape required for land imaging side-looking SAR system, which is cosecant-squared in the range direction and flat-top in the azimuth direction. When compared with the desired beam shapes, the achieved patterns show excellent agreement and the array performance regarding the impedance matching and the axial ratio are acceptable over the operating frequency band.

REFERENCES

[1] Y. Kim and R. Jordan, "Spaceborne SAR antennas for earth science," *Spaceborne Antennas for Planetary Exploration*, pp. 305-340, 2006.

[2] A. K. Behera, A. Ahmad, S. K. Mandal, G. K. Mahanti, and R. Ghatak, "Synthesis of cosecant squared pattern in linear antenna arrays using differential evolution," *In Information and Communication Technologies* (ICT), *IEEE Conference*, pp. 1025-1028, 2013.

[3] A. Freeman, et al., "Detection, estimation and correction of Faraday fotation in linearly polarized SAR backscatter signatures," 1998.

[4] P. Rizki Akbar, J. Tetuko S. S., and H. Kuze, "A novel circularly polarized synthetic aperture radar (CP-SAR) system on board a spaceborne platform," *International Journal of Remote Sensing*, vol. 31, no. 4, pp. 1053-1060, Feb. 2010.

[5] J. Tetuko S. S., V. C. Koo, T. S. Lim, T. Kawai, T. Ebinuma, Y. Izumi, M. Z. Baharuddin, and S. Gao, "Development of circularly polarized synthetic aperture radar on-board UavJX-1," *International Journal of Remote Sensing*, pp. 2745-2756, 2017.

[6] J. Tetuko, S. Sumantyo, and K. V. Chet, "Development of synthetic aperture radar on board unmanned aerial vehicle," *Geoscience and Remote Sensing Symposium (IGARSS, IEEE International)*, pp. 2301-2304, 2013.

[7] M. A. Rahman, Q. D. Hossain, and E. N. I. Toyoda "Design of an X-band microstrip array antenna for circular polarization," *8th International Conference on Electrical and Computer Engineering*, 20-22, Dec. 2014.

[8] K. K. Chan, A. Tan, and K. Rambabu, "Decade bandwidth circularly polarized antenna array," *IEEE Transactions on Antennas and Propagation*, vol. 61, no. 11, Nov. 2013.

[9] X. Ye, M. He, P. Zhou, and H. Sun, "A compact

single-feed circularly polarized microstrip antenna with symmetric and wide-beamwidth radiation pattern," *International Journal of Antennas and Propagation, Hindawi Publishing Corporation*, 2013.

[10] Nasimuddin, Z. N. Chen, and X. Qing, "Asymmetric-circular shaped slotted microstrip antennas for circular polarization and RFID applications," *IEEE Trans. Antennas Propagation*, vol. 58, no. 12, Dec. 2010.

[11] J. James, *Handbook of Microstrip Antennas*. vol. 1, IET, 1989.

[12] A. Qing, *Differential Evolution. Fundamentals and Applications in Electrical Engineering*. John Wiley & Sons (Asia) Pte Ltd., pp. 335-351, 2009.

[13] F. J. Ares Pena, J. A. Rodriguez-Gonzalez, E. Villanueva-Lopez, and S. R. Rengarajan, "Genetic algorithms in the design and optimization of antenna array patterns," *IEEE Trans. Antennas Propag.*, vol. 47, pp. 506-510, Mar. 1999.

[14] J. A. Rodriguez, L. Landesa, J. L. Rodriguez Obelleiro, F. Obelleiro, F. Ares, and A. Garcia-Pino, "Pattern synthesis of array antennas with arbitrary elements by simulated annealing and adaptive array theory," *Microw. Opt. Technol. Lett.*, vol. 20, no. 1, pp. 48-50, Jan. 1999.

[15] L. Xie, Y. Li, and Y. Zheng, "A wide axial-ratio beamwidth circularly polarized microstrip antenna," *IEEE International Conference*, 2016.

[16] J. Robinson and Y. R. Sammi, "Particle swarm optimization in electromagnetics," *IEEE Transactions on Antennas and Propagation*, vol. 52, no. 2, pp. 397-407, Feb. 2004.

[17] M. Abo El-Hassan, K. F. A. Hussein, A. E. Farahat, and K. H. Awadalla, "Wide band shaped beam array of U-slot patches for high resolution SAR and satellite communications," *34th National Radio Science Conference (NRSC 2017), Arab Academy for Science, Technology & Maritime Transport, (Abou Qir)*, Alexandria, Egypt, B14, Mar. 13-16, 2017.

[18] W. L. Stutzman and G. A. Thiele, *Antenna Theory and Design*. 3rd Edition, Wiley, New York, pp. 319, 2012.

[19] V. Wissan, "Development of circularly polarized array antenna for synthetic aperture radar sensor installed on UAV," *Progress in Electromagnetics Research*, 19, pp. 119-133, 2011.

[20] M. Baharuddin, "Study on circularly polarized synthetic aperture radar: Patch array antennas and scattering experiments in an anechoic chamber," *Ph.D. Thesis*, Chiba University, 2016.

Wideband Quasi-Yagi Antenna with Broad-Beam Dual-Polarized Radiation for Indoor Access Points

Son Xuat Ta [1], Cong Danh Bui [3], and Truong Khang Nguyen [2,3,*]

[1] School of Electronics and Telecommunications
Hanoi University of Science and Technology, Ha Noi, Viet Nam
xuat.tason@hust.edu.vn

[2] Division of Computational Physics, Institute for Computational Science
Ton Duc Thang University, Ho Chi Minh City, Vietnam

[3] Faculty of Electrical and Electronics Engineering
Ton Duc Thang University, Ho Chi Minh City, Vietnam
*nguyentruongkhang@tdtu.edu.vn

Abstract ─ This paper presents a wideband, broad beamwidth, dual-polarized antenna for the indoor access points. Its primary radiating elements are two quasi-Yagi antennas, which are arranged orthogonally. The antenna element employs two balanced directors to broaden bandwidth and avoid the structural conflict of the orthogonal installation. A microstrip-slotline transformer is used in the feeding structure for allowing the wideband operation and high port-to-port isolation. The dual-polarized quasi-Yagi antenna is incorporated with a metallic cavity in order to improve the unidirectional radiation in terms of gain, front-to-back ratio, and beamwidth. The final prototype has been fabricated and tested. The antenna yielded a wide impedance bandwidth covering a frequency range from 1.64 to 3.0 GHz (60%) for both ports with port-to-port isolation of a higher than 25 dB. In addition, at both ports, the antenna achieves stable unidirectional radiation with broad beamwidth, high front-to-back ratio, and high radiation efficiency.

Index Terms ─ Balanced directors, beamdwidth, cavity-backed reflector, dual polarization, microstrip-slotline transformer, quasi-Yagi antenna.

I. INTRODUCTION

Quasi-Yagi antenna, which was first presented by Qian et al. in 1998 [1], has been one of the most popular choices for the modern wireless communication systems owing to its features of planar structure, broadband, high directivity, high front-to-back (F-B) ratio, low cross-polarization level, high efficiency, ease of realization and low cost. The basic configuration of a quasi-Yagi antenna includes a truncated ground plane acted as a reflector, a driver, and directors [2]. In order to be easily integrated with the other circuit components (e.g., printed power dividers, phase shifters …) or the standard connector, the quasi-Yagi antennas are normally fed by an unbalanced feed-line such as microstrip line [1–3] or coplanar waveguide [4–6]. Consequently, these antennas require a transformer between the driver and the feed-line. In the past years, the main considerations in designing the quasi-Yagi antenna are broadening bandwidth, reducing the size, and improving radiation characteristics. Several double dipole quasi-Yagi antennas [7–9] have been proposed for broadening the impedance matching bandwidth and achieving a small gain variation. The double-dipoles, however, increase the antenna size considerably. In [10], [11], the compact quasi-Yagi antennas with microstrip line to slotline transition achieved bandwidth > 90%. Recently, the bandwidth of a quasi-Yagi antenna was enlarged up to 94% by using metamaterial resonators [12]. However, due to the small reflector element, the antennas [10] – [12] yielded a relatively large back radiation. Also, their beamwidths are significantly different for the E- and H-plane radiation patterns.

On the other word, in order to achieve steady services regardless of place, a large number of indoor access points for the modern wireless communication systems are needed to be installed in shaded areas, such as tunnels, inside of high buildings, subway stations, as well as other underground areas. Antennas for the indoor access points [13–18] focus not only bandwidth but also radiation characteristics. The antennas with wideband characteristic [13], [16], were proposed for use in several wireless communication systems, while the multi-band antennas [14], [15] were designed for the systems operating in different frequency bands. To achieve the desired coverage, the antennas were developed to yield appropriate radiation characteristics such as high-gain

Submitted On: August 7, 2018
Accepted On: March 3, 2019

[14], wide beamwidth [15], or omnidirectional pattern [16]. The above access point antennas are linear polarization. Recently, dual-polarized antennas [17], [18] have been presented for the indoor access points to enhance the channel capacity and mitigate the effects of multipath fading. In [17], a dual-polarized antenna with an overall size of 70 mm × 70 mm × 14 mm achieved an operational bandwidth of about 16.4% (2.4 – 2.83 GHz), isolation of > 40 dB and the peak gain of 9 dBi. This antenna, however, requires a complicated feeding network, which includes microstrip-lines, metal shorting plates, and U-shaped microstrip coupling lines. In [18], a crossed enlarged dipole antenna using parasitic elements achieved an impedance bandwidth of about 44.5%, isolation of > 31 dB and gain of > 7.0 dBi. Its radiation patterns are not very symmetric, in particular, at the high frequencies. This could be attributed to the feeding structure; i.e., the crossed dipole elements are fed coaxial-lines directly.

In this paper, a wideband dual-polarized antenna with broad-beam radiation is presented. The antenna consists of two printed quasi-Yagi antenna elements, which are orthogonal and vertically placed at the center of a cylinder metallic cavity for achieving the broad-beam radiation and mitigating the difference for beamwidths of the E- and H-plane patterns. In order to avoid the structural conflict of the orthogonal installation, the quasi-Yagi antennas employ two directors, which are arranged symmetrically. The antenna elements are fed by a microstrip-slotline transformer for allowing the wideband operation and high port-to-port isolation. The proposed design was characterized via the ANSYS High-Frequency Structure Simulator (HFSS). The optimized prototype was fabricated and measured.

II. ANTENNA DESIGN AND CHARACTERISTICS

A. Antenna geometry

The geometry of the proposed antenna is illustrated in Fig. 1. It is composed of two printed quasi-Yagi antennas, which are orthogonal and vertically placed at the center of the metallic cavity. Each antenna element consists of a feeding structure of microstrip-slotline transformer, a driver, two directors, and a truncated ground plane. The microstrip-slotline transformer is composed of a folded microstrip-line and a rectangular slot. The quasi-Yagi antennas are printed on both sides of FR4 substrates with a dielectric constant of 4.4, a loss tangent of 0.02, and a thickness of 0.8 mm. For allowing the orthogonal installation without the structure conflict, the directors are arranged symmetrically and two slots are separately embedded in the antenna elements. The cavity has a cylindrical shape with 100-mm diameter and height of H_{cav}. The center frequency was chosen as 2.2 GHz. All of the antenna-designs were numerically simulated using the HFSS (ANSYS Electronics Desktop) version 17.1.

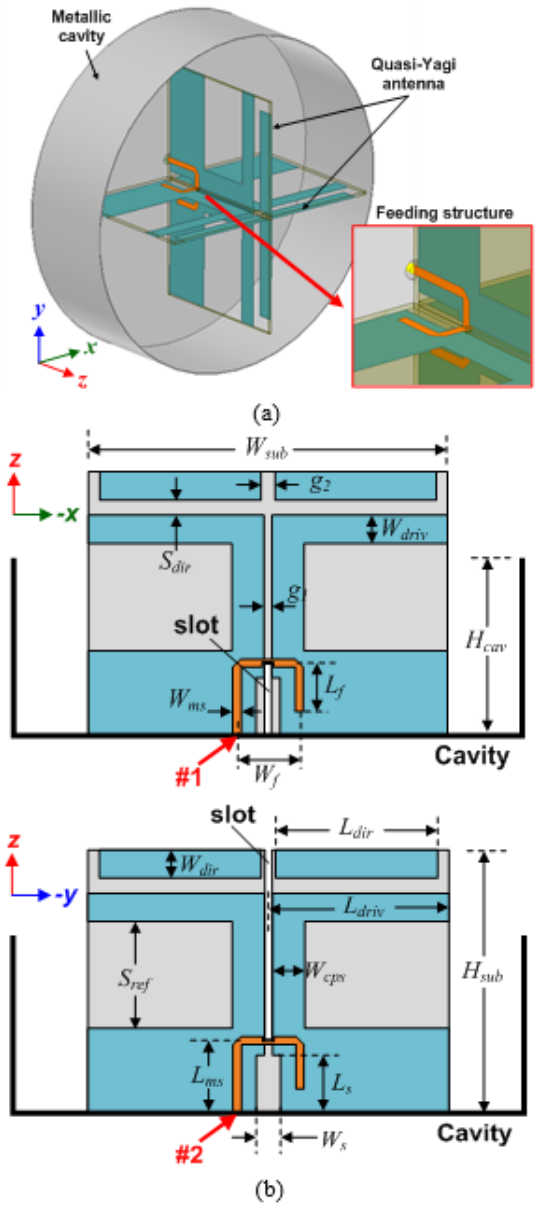

Fig. 1. Geometry of the proposed antenna: (a) perspective view and (b) cross-sectional views.

The solution type is set to a driven model. As the HFSS requirement, the radiation box walls are a quarter-wavelength (for the lowest frequency considered) away from the antenna for the desired accuracy in the calculation of the far-fields. The antenna is excited by two circular lumped ports that are renormalized to 50-Ω full port impedance at all frequencies. Two 10-mm coaxial

lines (d = 1.4 mm, D = 3.2 mm, ε_r = 1) were inserted between the lumped ports and the microstrip-lines. Real copper was used in all of the simulations, the conductivity being set to σ = 5.8 × 107 S/m, the relative permittivity being set to μ = 1, and without surface roughness. The dual-polarized antenna was optimized vias a series of the HFSS simulations to achieve a wideband operation, a high port-to-port isolation, a broad-beam radiation pattern, and a high front-to-back ratio. Its optimized design parameters are as follows: W_{sub} = 70, H_{sub} = 45, L_{gnd} = 15, S_{ref} = 17, W_{cps} = 6, L_{driv} = 35, W_{driv} = 5, S_{dir} = 3, L_{dir} = 30, W_{dir} = 5, W_s = 4, L_s = 10, W_f = 10, L_{ms} = 12, W_{ms} = 1.5, L_f = 8, g_1 = 1, g_2 = 2 and H_{cav} = 30 (Units: mm).

B. Evolution of the cavity-backed quasi-Yagi antenna element

Figure 2 shows the design evolution of the quasi-Yagi antenna, which was used as the primary radiation elements in the dual-polarized configuration. Ant. #1 is a planar quasi-Yagi antenna without a director and with a 100-mm truncated ground plane. Ant. #2 is Ant. #1 with adding two balanced directors. Ant. #3 is a quasi-Yagi antenna backed by a 100-mm diameter cavity reflector. Ants. #2 and #3 were optimized for a wideband characteristic at the 2.2 GHz center frequency. The design parameters of Ant. #3 are same as those of the proposed antenna, whereas the design parameters of Ant. #1 are same as those of the Ant. #2. Due to the planar configuration, the design parameters of Ant. #2 are slightly different from those of Ant. #3. Referring to Fig. 1 (b), the optimized parameters of Ant. #2 are as follows: W_{sub} = 100, H_{sub} = 50, L_{gnd} = 15, S_{ref} = 20, W_{cps} = 6, L_{driv} = 66, W_{driv} = 5, S_{dir} = 3, L_{dir} = 30, W_{dir} = 5, W_s = 4, L_s = 10, W_f = 10, L_{ms} = 12, L_f = 8, g_1 = 1, and g_2 = 2 (units: mm). The three configurations were characterized via the HFSS and their performances are given in Fig. 3.

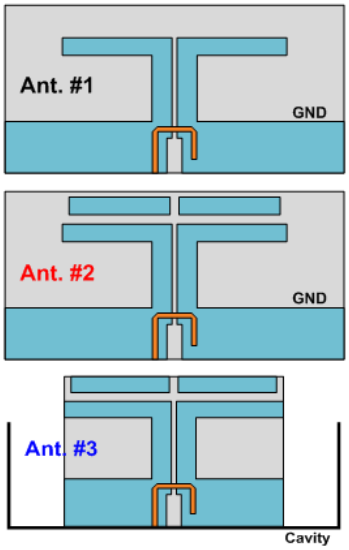

Fig. 2. Different configurations of quasi-Yagi antenna.

From Fig. 3 (a), the quasi-Yagi antenna without a director (Ant. #1) yielded two resonances of 1.7 GHz and 2.4 GHz in the examined frequency range. The presence of the directors broadened the bandwidth of the antennas; both configurations of Ant. #2 and Ant. #3 yielded three resonances and a significantly broader bandwidth as compared to Ant. #1. Also, the presence of directors improved the end-fire radiation of the planar quasi-Yagi antenna considerably. As shown in Figs. 3 (b, c), Ant. #2 had a higher gain and a higher F-B ratio over Ant. #1. Due to the natural radiation of the printed quasi-Yagi antenna, the beamwidth is significantly different for the E- and H-plane patterns. This difference was mitigated by using the cavity-backed reflector; i.e., the beamwidth of E-plane pattern was broadened, whereas the beamwidth of H-plane was narrowed. Also, the presence of the cavity produced an average increase of 2.1 dB in the gain relative to the planar antennas, as shown in Fig. 3 (b).

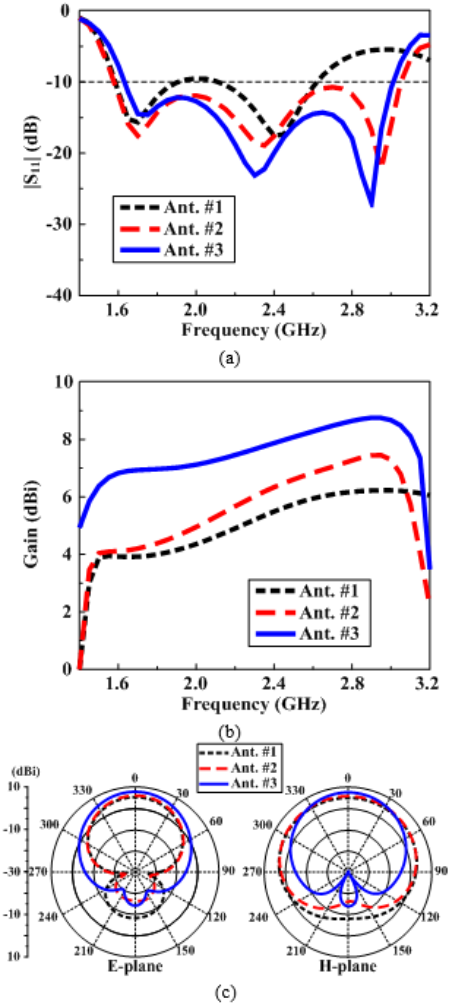

Fig. 3. Simulated (a) $|S_{11}|$, (b) gain, and (c) 2.2 GHz total-gain radiation patterns of the quasi-Yagi antenna in different configurations.

C. Cavity-backed reflector

As mentioned above, the radiation characteristics of the quasi-Yagi antenna were significantly improved by using the cavity reflector. For a better understanding of this issue, the performances of Ant. #3 were calculated for different heights of the cavity (H_{cav}) and given in Figs. 4 and 5. As H_{cav} increased, the resonances shifted toward the lower frequency [Fig. 4 (a)], whereas the radiation characteristics changed significantly; i.e., as shown in Fig. 4 (b), the gain decreased in the low-frequency region but increased in the high-frequency region. As shown in Fig. 4 (c), the F-B ratio improved with H_{cav} increasing from 0 mm to 30 mm, but degraded in almost the frequency range with the cavity height at 30-45 mm.

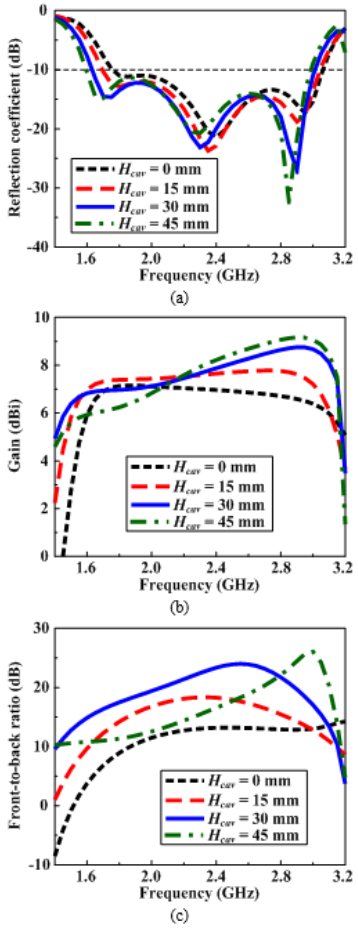

Fig. 4. Simulated (a) $|S_{11}|$, (b) gain, and (c) F-B ratio of Ant. #3 for different H_{cav}.

From Fig. 5, it is observed that with increasing H_{cav}, the beamwidth of E-plane pattern broadened, whereas the beamwidth of H-plane narrowed. With the cavity height of H_{cav} = 15 mm, the antenna offered the flattest gain (7.4 ± 0.4 dBi), an F-B ratio of > 10 dB at 1.6-3.0 GHz, and beamwidths of 71° and 91° for the E- and H-planes at 2.2 GHz, respectively. The antenna with H_{cav} = 30 mm yielded a gain of 7.7 ± 0.8 dBi, the highest F-B ratio at 1.6-3.0 GHz, and beamwidths of 76° and 80° for the E- and H-planes at 2.2 GHz, respectively. Therefore, H_{cav} = 30 mm was chosen for the final design based on a trade-off between the constant gain, the high front-to-back ratio and similar beamwidth in the *E*- and *H*-planes.

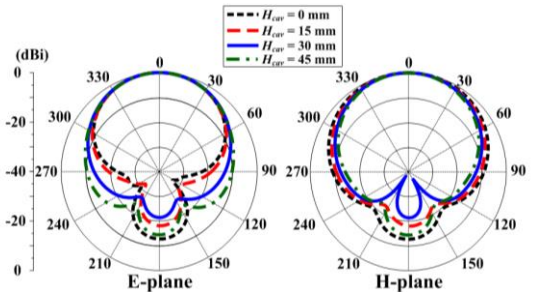

Fig. 5. Normalized 2.2 GHz total-gain radiation patterns of Ant. #3 for different H_{cav}.

III. FABRICATION AND MEASUREMENT

The dual-polarized quasi-Yagi antenna was realized and tested. A fabricated sample of the antenna is illustrated in Fig. 6. The quasi-Yagi antennas were fabricated by using printed circuit board technology, whereas the cavity was made of 0.2-mm copper sheets. The two orthogonal quasi-Yagi elements were vertically welded at the center of the cavity. Two coaxial-lines were used to feed the prototype; their inner parts passed through the cavity and connected to the microstrip-line of the transformer, whereas their outer parts were connected to the reflector. The prototype has a total volume of $\pi \times 50^2 \times 45$ mm^3.

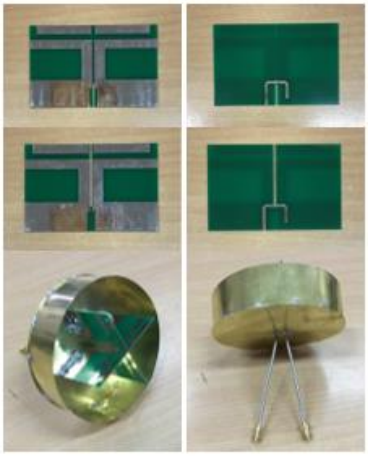

Fig. 6. Fabricated sample.

Figure 7 (a) illustrates the reflection coefficients of the fabricated antenna at two ports. The measurements

agreed rather closely with the simulations and both indicated a wideband operation. At Port #1, the measurement resulted in a reflection coefficient < -10 dB bandwidth of 1.59-2.97 GHz (60.5%), while the simulated bandwidth was 1.63-2.97 GHz (58.3%). At Port #2, the measured reflection coefficient < -10 dB was from 1.59 GHz to 3.06 GHz (63.2%), whereas the simulated value ranged from 1.64 GHz to 3.02 GHz (59.2%). The port-to-port isolation of the antenna is illustrated in Fig. 6 (b). The measurement resulted in isolation of > 25 dB relative to the simulated value of > 23 dB across the entire operating bandwidth. There was a slight difference between the measured and HFSS predicted results. This difference could be attributed the fabrication tolerances and the effects of tin-conductor (not included in the simulations), which was used to coat the copper part of the printed quasi-Yagi antennas and to weld the coaxial lines and the feeding structure.

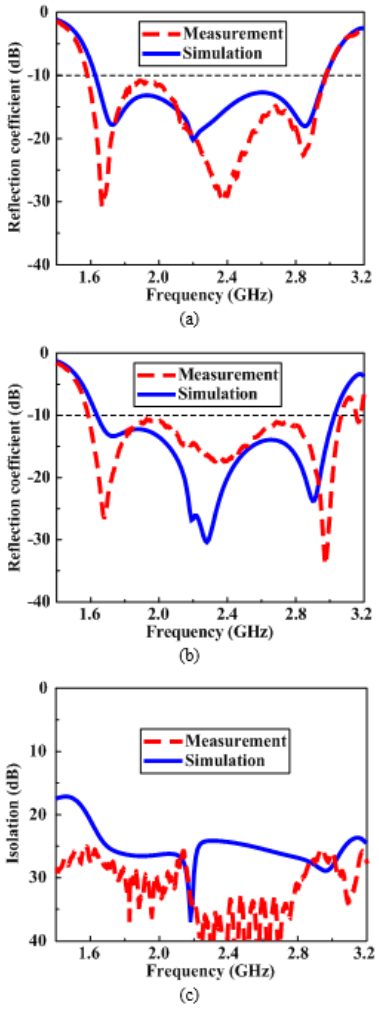

Fig. 7. Simulations and measurements of the dual-polarized quasi-Yagi antenna: reflection coefficients at: (a) Port #1, (b) Port #2, and (c) port-to-port isolation.

Figure 8 shows the radiation patterns of the prototype for Port #1 excitation. Again, there is a good agreement between measurement and simulation. It is observed that the antenna yielded good unidirectional radiation with a highly symmetric profile, high F-B ratio, and wide beamwidth. The F-B ratio is > 20 dB at all examined frequencies. As the frequency increased from 1.6 GHz to 3.0 GHz, half-power beam width (HPBW) in the E-plane is decreased from about 94° to 60°, whereas the HPBW in the H-plane is decreased from about 100° to 70°. Due to the structure symmetry, the results of the prototype for Port #2 are almost identical to those of Port #1, thus, they are not shown for brevity.

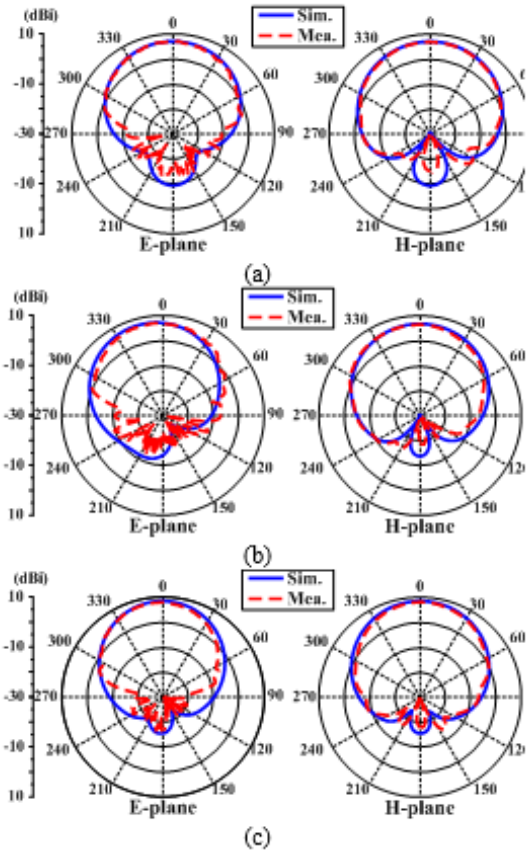

Fig. 8. Measured and simulated total-gain radiation patterns of the dual-polarized quasi-Yagi antenna at port #1: (a) 1.7 GHz, (b) 2.2 GHz, and (c) 2.7 GHz.

Figure 9 shows the measured and simulated gains of the antenna prototype. Within the operational bandwidth, the antenna yielded measured broadside gains of 6.4-7.0 dBi and 6.0-8.0 dBi for the ports #1 and #2, respectively, as compared to the simulated values of 6.9-8.5 dBi for both ports. In addition, the measurement resulted in radiation efficiency better than 75% as compared to the simulated value of > 80% when exciting from either port. The measured gain and radiation efficiency were slightly

smaller than the HFSS simulated values. This difference could be attributed to a difference in the dielectric loss used in our simulation and the real value in the measurement.

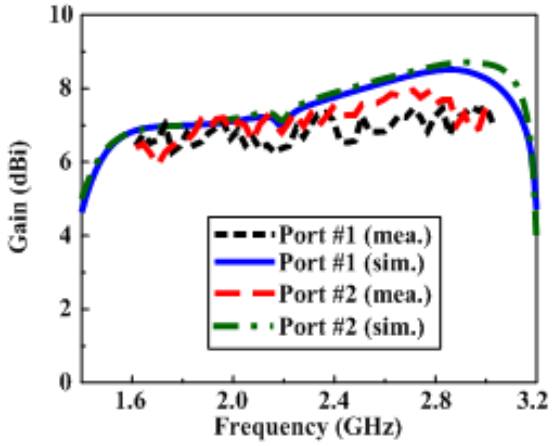

Fig. 9. Simulation and measurement gain of the dual-polarized quasi-Yagi antenna.

In order to signify how the two elements of the proposed antenna are coupled to each other, the envelope correlation coefficient (ECC) was calculated from the S-parameters using the following formula [19]:

$$\mathrm{ECC} = \frac{|S_{11}^{*}S_{12} + S_{21}^{*}S_{22}|}{(1-|S_{11}|^2-|S_{12}|^2)(1-|S_{21}|^2-|S_{22}|^2)}. \quad (1)$$

The simulated and measured ECC values of the fabricated antenna are shown in Fig. 10. Both simulation and measurement indicated that the ECC was less than 0.001 within its impedance matching bandwidth. As a result, the two elements of the proposed antenna have a very small coupling to each other.

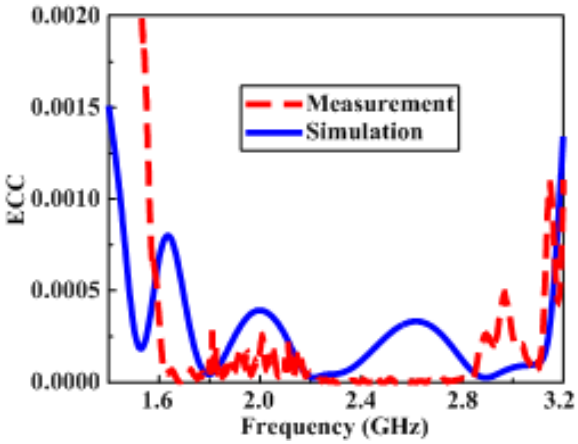

Fig. 10. simulated and measured ECCs of the dual-polarized quasi-Yagi antenna.

IV. CONCLUSION

A cavity-backed quasi-Yagi antenna with wideband and broad-beam dual-polarized radiation has been presented for use in the indoor access points. The antenna consists of two orthogonal printed quasi-Yagi antennas, which are fed by a microstrip-slotline transformer to allow the wideband operation and high port-to-port isolation. The quasi-Yagi antenna elements employed two balanced directors to not only broaden the frequency bandwidth but also avoid the structural conflict of the orthogonal installation. The cavity-backed reflector is utilized for improving the unidirectional radiation of the antenna element in terms of gain, front-to-back ratio, and beamwidth. The final prototype resulted in an impedance matching bandwidth of > 60% for both ports and isolation of > 25 dB. Its operational bandwidth completely covers DCS/PCS/UMTS/LTE 1, 2, 3, 4, 7, 9, 10, 15, 16, 23, 25/WiMAX 2.3 GHz, 2.5 GHz/WLAN 2.4-GHz bands (1710 – 2690 MHz). Moreover, at both ports, the antenna achieves stable unidirectional radiation with broad beamwidth, high front-to-back ratio, and high radiation efficiency.

ACKNOWLEDGMENT

This research is funded by Vietnam National Foundation for Science and Technology Development (NAFOSTED) under grant number 102.04-2016.02.

REFERENCES

[1] Y. Qian, W. R. Deal, N. Kaneda, and T. Itoh, "Microstrip-fed quasi-Yagi antenna with broad-band characteristics," *Electron. Lett.*, vol. 34, no. 23, pp. 2194-2196, Nov. 1998.

[2] N. Haneda, W. R. Deal, Y. Qian, R. Waterhouse, and T. Itoh, "A broad–band planar quasi–Yagi antenna," *IEEE Trans. Antenna Propagat*., vol. 50, no. 8, pp. 1158-1160, Aug. 2002.

[3] S. X. Ta, B. Kim, H. Choo, and I. Park, "Wideband quasi-Yagi antenna fed by microstrip-to-slotline transition," *Microwave Opt. Technol. Lett*., vol. 54, no. 1, pp. 150-153, July 2012.

[4] J. Sor, Y. Qian, and T. Itoh, "Coplanar waveguide fed quasi–Yagi antenna," *Electronics Letters*, vol. 36, no. 1, pp. 1-2, Jan. 2000.

[5] H. K. Kan, R. B. Waterhouse, A. M. Abbosh, and M. E. Bialkowski, "Simple broadband planar CPW-fed quasi-Yagi antenna," *IEEE Antenna Wireless Propagate. Lett*., vol. 6, pp. 18-20, 2007.

[6] Z. Du, Z. Wu, M. Wang, J. Rao, and P. Lue, "Compact quasi-Yagi antenna for handheld UHF RFID reader," *ACES Journal*, vol. 30, no. 8, pp. 860-865, Aug. 2015.

[7] A. A. Eldek, "Ultrawideband double rhombus antenna with stable radiation patterns for phased array applications," *IEEE Trans. Antenna Propag*., vol. 55, no. 1, pp. 84-91, Jan. 2007.

[8] S. X. Ta, H. Choo, and I. Park, "Wideband double-dipole Yagi-Uda antenna fed by a microstrip-slot coplanar stripline transition," *Progress in Electromagnetics Research B*, vol. 44, pp. 71-87, 2012.

[9] J. Wu, Z. Zhao, Z. Nie, and Q. Liu, "Bandwidth enhancement of a planar printed quasi-Yagi antenna with size reduction," *IEEE Trans. Antenna Propagat*., vol. 62, no. 1, pp. 463-467, Jan. 2014.

[10] J. Wu, Z. Zhao, Z. Nie, and Q. Liu, "Design of a wideband planar printed quasi-Yagi antenna using stepped connection structure," *IEEE Trans. Antenna Propagat*., vol. 62, no. 6, pp. 3431-3435, June 2014.

[11] J. Yeo and J. Lee, "Bandwidth enhancement of double dipole quasi-Yagi antenna using stepped slotline structure," *IEEE Antennas Wireless Propag. Lett*., vol. 15, pp. 694-697, 2016.

[12] M. Aeini, S. Jarchi, and S. Faraji-Dana, "Compact, wideband-printed quasi-Yagi antenna using spiral metamaterial resonators," *Electron. Lett.*, vol. 53, no. 21, pp. 1393-1394, Oct. 2017.

[13] C. R. Medeiros, E. B. Lima, J. R. Costa, and C. A. Fernandes, "Wideband slot antenna for WLAN access points," *IEEE Antennas Wireless Propag. Lett.*, vol. 9, pp. 79-82, 2010.

[14] S. W. Su, "High-gain dual-loop antennas for MIMO access points in the 2.4/5.2/5.8 GHz bands," *IEEE Trans. Antennas Propag.*, vol. 58, no. 7, pp. 2412-2419, July 2010.

[15] S. X. Ta, J. Han, H. Choo, and I. Park, "Dual-band printed dipole antenna with wide beamwidth for WLAN access points," *Microw. Opt. Technol. Lett.*, vol. 54, no. 12, pp. 2806-2811, Dec. 2012.

[16] Z. Y. Zhang, G. Fu, W. J. Wu, J. Lei, and S. X. Gong, "A wideband dual-sleeve monopole antenna for indoor base station application," *IEEE Antennas Wireless Propag. Lett.*, vol. 10, pp. 45-48, 2011.

[17] J. Lee, K. Lee, and P. Song, "The design of dual-polarized small base station antenna with high isolation having a metallic cube," *IEEE Trans. Antennas Propag*., vol. 63, no. 2, pp. 791-795, Feb. 2015.

[18] H. Lee and B. Lee, "Compact broadband dual-polarized antenna for indoor MIMO wireless communication systems," *IEEE Trans. Antennas Propag*., vol. 64, no. 2, pp. 766-770, Feb. 2016.

[19] L. Chen, J. Hong, and M. Amin, "A compact CPW-fed MIMO antenna with band-notched characteristic for UWB system," *ACES Journal*, vol. 33, no. 7, pp. 818-821, July 2018.

A Wide-Beam Antenna Based on Missile Telemetry System

Lizhong Song [1] and Xiuwen Tian [2]

[1] College of Information Science and Engineering
Harbin Institute of Technology at Weihai, Weihai, 264209, China
songlz@hit.edu.cn

[2] College of Information Science and Engineering
Harbin Institute of Technology at Weihai, Weihai, 264209, China
hittxw@163.com

Abstract ─ This paper presents an antenna system with multiple patches and multiple layer substrates for missile telemetry application. The antenna is comprised by a driven microstrip line, which is printed on the bottom layer dielectric substrate, and two parasitic patch radiators which are printed on the upper dielectric substrate. The microstrip line is excited by a coaxial probe directly, and the two parasitic patches are excited by the coupling energy. In order to broaden the beam width of the microstrip antenna, two parasitic patch radiators with different sizes are printed on the upper dielectric substrate. The width of the microstrip line is linearly varied to obtain a wide impedance-matching bandwidth. This antenna is simulated and optimized by using the full wave electromagnetic simulation technique. The simulated results show that the voltage standing wave ratio (VSWR) is less than 1.9 between 2.15GHz and 2.17GHz. At 2.16GHz, the VSWR of port is 1.29 and the 3dB beam widths of radiation patterns at E planes and H planes were more than 89.2 degrees. The proposed antenna is processed and measured. The measured results show that the proposed antenna achieves the expected radiation performance and validates the effectiveness of the antenna design. The antenna scheme studied in this paper is suitable for missile telemetry system. The research results have laid a technical foundation for its practical engineering application.

Index Terms ─ Gain, missile telemetry system, radiation pattern, telemetry antenna, wide angle coverage.

I. INTRODUCTION

Microstrip antenna has many advantages, such as easy processing, small size, light weight, simple manufacturing process, easy to realize conformal and so on. Because the microstrip antenna is easily printed on the circuit board, the microstrip antenna can be produced in large quantities. The above-mentioned advantages make them suitable for numerous applications [1-2]. Microstrip antenna arrays have been used for missile telemetry system. With the development of microwave technology, the requirements for the application of microstrip antenna arrays are becoming ever more demanding now. Due to the need for target tracking, the telemetry system needs a wider working beam. Therefore, it is of great practical significance to design an antenna unit with wide coverage range suitable for missile telemetry system. However, the inherent constraints of the microstrip antenna are the narrow bandwidth and beam width. Microstrip antennas have narrow beam width, which is typically 1–5% [3]. The wide band microstrip antenna has been a main issue of research in this field since the 1970s [4-5].

A lot of methods to broaden bandwidth in practical engineering have been proposed, and the general techniques include multi-resonators, stacked electromagnetically coupled and aperture-coupled patches, parasitic patch, ferrite substrates, et al. For example, the broadband impedance monopoles with finite ground planes have been reported in reference [6]. The reference [7] expanded the range of radiation by increasing the area of the dielectric substrate. A microstrip antenna, which is composed of a composite dielectric plate, was proposed in reference [8]. In order to broad antenna beam width, the teference [9] expanded the conductive wall around the patch antenna, and narrowed the antenna radiation aperture, and reducing antenna gain. In order to increase the beam width, Tang added three dimensions to microstrip circularly polarized antenna and the gain has decreased by 1.7dB [10]. Wu loaded the electric dipole around the circular polarized microstrip antenna to broaden the radiation beam of the antenna [11]. Shi used a single arm tapered gradient spiral antenna and 8 vertical electric dipole sub columns to widen the beam [12]. Pan proposed a method to broaden the beam width by loading the metal ring above the circular polarized microstrip antenna [13]. Luk used complementary characteristics of magnetic electric dipole radiation

Submitted On: July 27, 2018
Accepted On: December 25, 2018

pattern to design a wide beam circularly polarized antenna which works in 1.6-2.47GHz [14]. Park used cross electric dipole and magnetic electric dipole to design a circularly polarized antenna which wideband is 1.39-1.82GHz [15]. In literature [16], a cross dipole circular polarized antenna with a reflective cavity in 1.1-1.6GHz was designed, which was mainly used in GPS. In literature [17], a circular polarized patch antenna, which can realize the axis ratio wide beam, was designed by using two pairs of parallel dipoles.

In this paper, the research and development of the printed antenna for the missile telemetry system application is presented. A specific antenna scheme with wide space coverage based on missile telemetry system was designed. The antenna solved the application problem in the practical engineering and met the practical engineering requirements.

II. ANTENNA STRUCTURE

The model of the wide beam microstrip antenna is shown in Fig. 1.

The antenna comprises a driven microstrip line radiator with two parasitic patch radiators. The antenna structure consists of two dielectric substrates which have the same relative dielectric constant; the microstrip line printed on the bottom substrate, and two parasitic patch radiators printed on the upper dielectric substrates.

The wide beam microstrip antenna of removing the substrate of the wide beam microstrip antenna is presented in Fig. 2 (a). The microstrip line is excited by a coaxial probe directly, and the two parasitic patches are excited by the coupling energy. Figure 2 (b) is the top view of the upper substrate. Two dielectric substrates with different sizes can be used to broaden the antenna beam width. Figure 2 (c) shows the top view of the bottom substrate. The width of the microstrip line is linear variety to obtain a wide impedance-matching bandwidth. Two dielectric substrates are a common FR4 material. The thickness of the two dielectric substrates are 1mm. The thickness of microstrip line and two parasitic patches are 0.036mm.

This paper uses the full wave electromagnetic simulation software (CST) to build the antenna. The radiation performance of the antenna is calculated and optimized by the full wave electromagnetic simulation software.

(a) The overhead view of the antenna

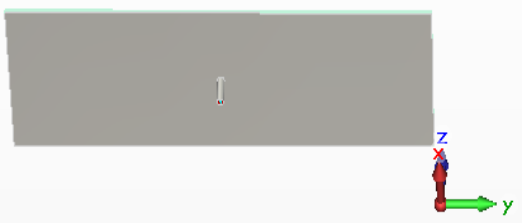

(b) The invert view of the antenna

Fig. 1. The model of the antenna.

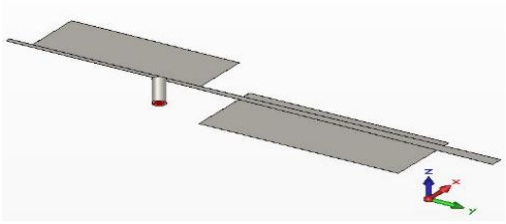

(a) The antenna of removing the substrate

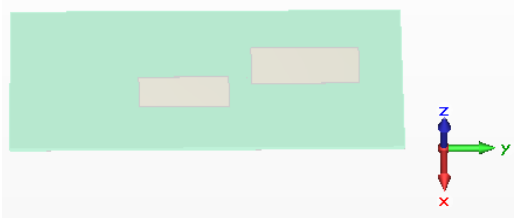

(b) Top view of the upper substrate

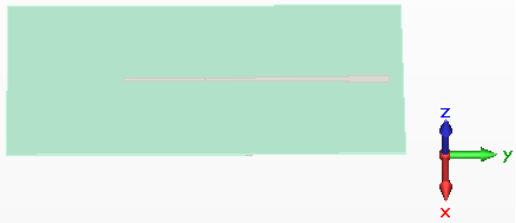

(c) Top view of the bottom substrate

Fig. 2. Configuration of the proposed wide beam microstrip antenna.

The sizes of the proposed antenna structure on both sides of dielectric substrate are presented in Figs. 3 (a), (b) respectively.

The sizes of the parasitic patch radiators can be approximated by the formula:

$$W\_Patch = \frac{c}{2f}\left(\frac{\varepsilon_r + 1}{2}\right)^{\frac{-1}{2}}, \tag{1}$$

$$L\_Patch = \frac{c}{2f\sqrt{\varepsilon_e}} - 2\Delta l, \tag{2}$$

$$\Delta l = 0.412h\frac{(\varepsilon_e + 0.3)(a/h + 0.264)}{(\varepsilon_e + 0.258)(a/h + 0.8)}. \tag{3}$$

In formula (1) and (2), W_P is the width of the parasitic patch radiators, L_P is the length of the

parasitic patch radiators.

We can calculate the sizes of the microstrip line from the formula:

$$Z_0 = \frac{120\pi}{2\sqrt{2\pi}\sqrt{\varepsilon_r+1}} \ln\left\{1+\frac{4h}{w'}\left[\frac{14+8/\varepsilon_r}{11}\frac{4h}{w'}\sqrt{\left(\frac{14+8/\varepsilon_r}{11}\right)^2\left(\frac{4h}{w'}\right)^2+\frac{1+1/\varepsilon_r}{2}\pi^2}\right]\right\}, \quad (4)$$

Where:

$$w' = w + \Delta w', \quad (5)$$

$$\Delta w' = \Delta w\left(\frac{1+1/\varepsilon_r}{2}\right), \quad (6)$$

$$\frac{\Delta w}{L} = \frac{1}{\pi}\ln\left[\frac{4e}{(t/h)^2+\left(\frac{1/\pi}{w/t+1.1}\right)^2}\right]. \quad (7)$$

In formula (7), Z_0 is the impedance of the microstrip line, t is the thickness of the microstrip line, w is the width of the microstrip line, L is the length of the microstrip line.

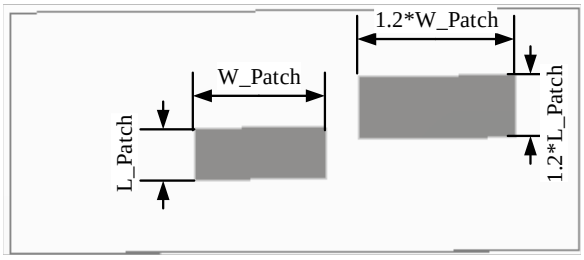

(a) The size of two rectangular patches

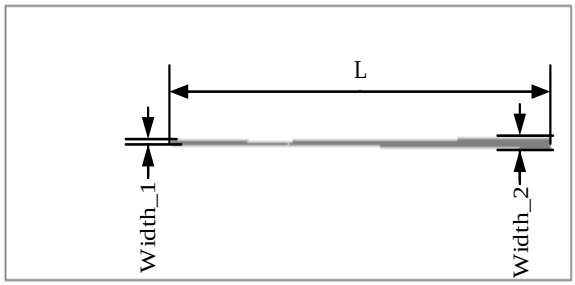

(b) The length and width of the microstrip line

Fig. 3. The engineering drawing of wide beam antenna.

According to the formula (1), (2), (3), (4), (5), (6), (7), we can get the initial value of the parasitic patch radiators and the microstrip line. Then, the final sizes can be obtained through the full wave electromagnetic simulation and optimization. The dimensions of the designed antenna are showed at Table 1.

Table 1: The dimensions of the designed antenna

Parameters	Sizes	Units
L_patch	26	mm
W_patch	66.5	mm
L	195	mm
Wdith_1	5	mm
Wdith_2	2	mm

III. SIMULATIONAND ANALYSIS

This paper uses the full wave electromagnetic simulation software (CST) to build the antenna. All the simulated results are obtained from CST. The voltage standing wave ratio (VSWR) of the port1 is shown in Fig. 4. As illustrated in Fig. 4, at 2.15GHz, 2.16GHz, and 2.17GHz, the VSWR of the port1 is about 1.68, 1.29, and 1.64, respectively. The VSWR is less than 1.7 within the range of 2.15GHz~2.17GHz. The impedance-matching bandwidth of port1 is not wide. Adjusting the sizes of those parameters, including microstrip line and two parasitic patch, can obtain a wide impedance-matching bandwidth. The simulated VSWR of port1 is suitable for practical application.

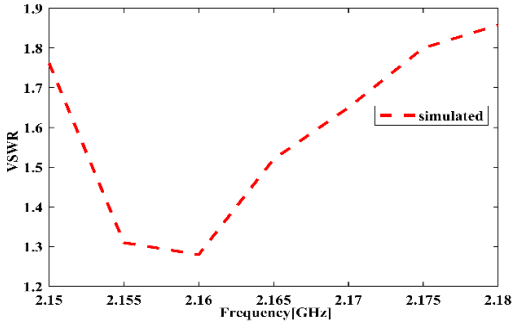

Fig. 4. Simulated VSWR of port1.

Figure 5 shows the electric energy density of the proposed antenna at 2.15 GHz, 2.16GHz and 2.17 GHz. Electric Energy distribution and current transmission path are presented clearly in Fig. 5.

Figure 5 shows that the electric energy density is higher on the microstrip line, two parasitic patches and coaxial probe. The current, through coaxial probe, flow into the microstrip line. The microstrip line radiates energy to space. The two parasitic patches are excited by the coupling energy. Hence, the two parasitic patches have higher electric energy density, and radiate energy into space.

The simulated radiation patterns of the wide beam antenna at 2.15GHz, 2.16GHz and 2.17GHz are shown in Fig. 6, Fig. 7 and Fig. 8 respectively. At each frequency point, the radiation pattern of the port1 on the xoz plan and the yoz plan is given respectively.

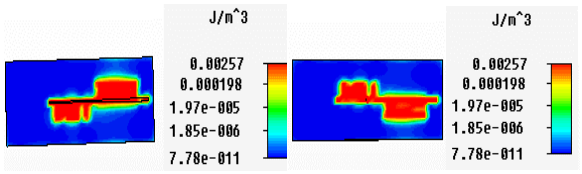

(a) The positive structure at 2.15 GHz

(b) The reverse structure at 2.15 GHz

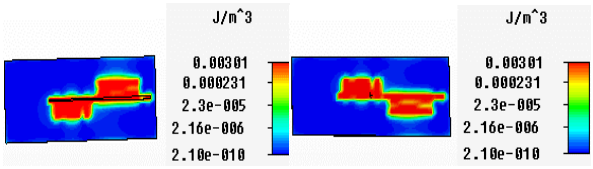

(c) The positive structure at 2.16GHz

(d) The reverse structure at 2.16GHz

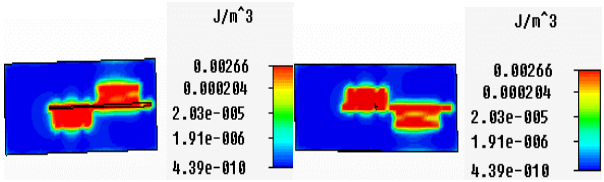

(e) The positive structure at 2.17GHz

(f) The reverse structure at 2.17GHz

Fig. 5. Simulated electric energy density of port1.

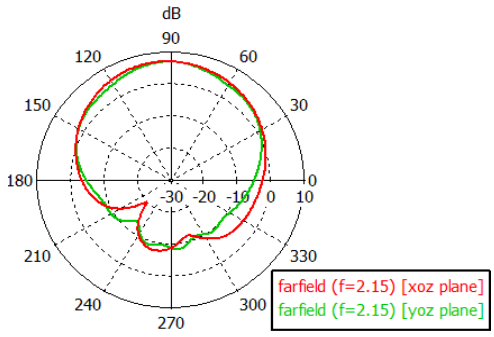

Fig. 6. The radiation pattern at 2.15GHz.

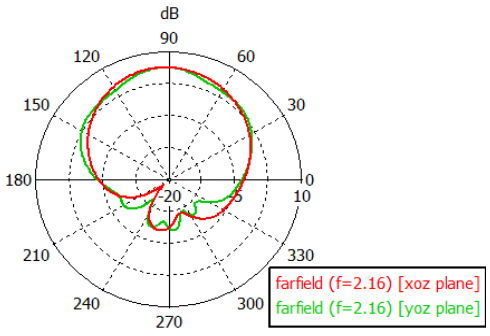

Fig. 7. The radiation pattern at 2.16GHz.

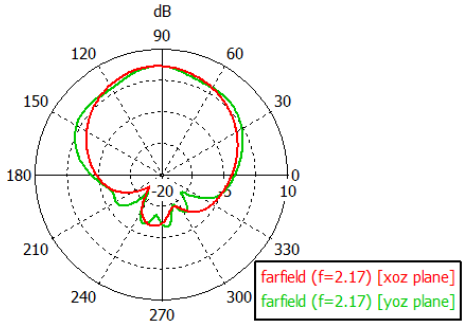

Fig. 8. The radiation pattern at 2.17GHz.

According to the simulated radiation patterns, it can be observed that the radiation pattern of the antenna port1 is more regular at xoz plane and yoz plane. The radiation gain of the antenna port1 is greater than 4.8dB. The 3dB beam width is more than 78.9°. At 2.15GHz, the 3dB beam width of the xoz plane and the yoz plane is 87.8° and 78.9° respectively. At 2.16GHz, the 3dB beam width of the xoz plane and the yoz plane is 89.2° and 127.4° respectively. At 2.17GHz, the 3dB beam width of the xoz plane and the yoz plane is 84.1° and 140° respectively.

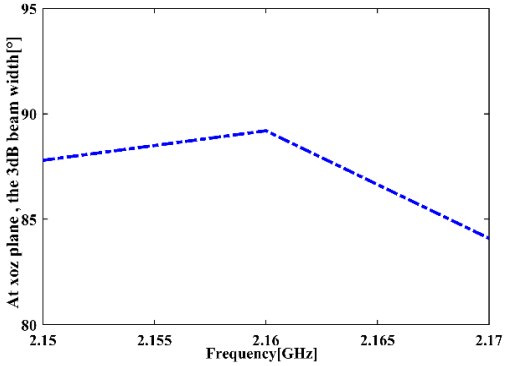

(a) At xoz plane

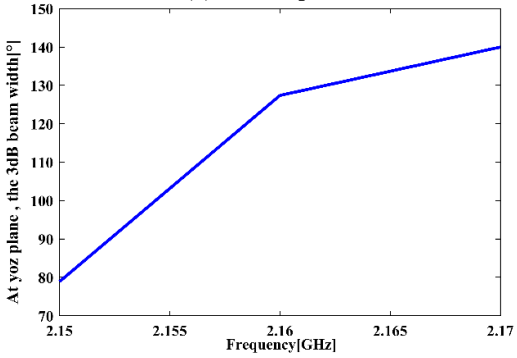

(b) At yoz plane

Fig. 9. The curve of antenna beam width with frequency.

The curve of antenna beam width with frequency variation at xoz plane and at yoz plane are shown in Fig. 9. The simulated results present that the 3dB beam width of the proposed antenna is between 84.1°and 89.2° at the xoz plane. The 3dB beam width of the proposed antenna is linear increasing with frequency at 2.15~2.16GHz and linear decreasing with frequency at 2.16~2.17GHz. At yoz plane, the 3dB beam width is between 78.9°and 140°. At 2.16~2.17GHz, Fig. 8 shows that the 3dB beam width at yoz plane is better than the 3dB beam width at xoz plane. The 3dB beam width is more than 78.9° at 2.15~2.17GHz. The simulated results indicate that the proposed antenna, at 2.17GHz, can obtain 140° at yoz plane and 84.1° at xoz plane. Therefore, the proposed antenna has a wider beam width performance. The designed antenna can obtain a wider beam width by adjusting the sizes of two parasitic patch.

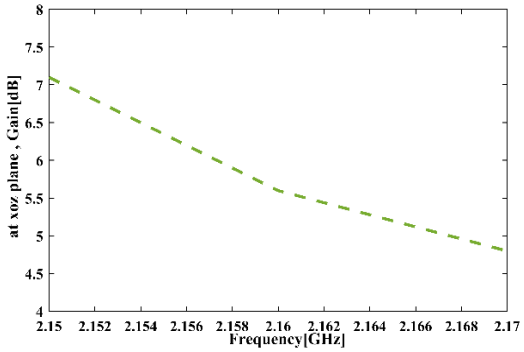

(a) At xoz plane

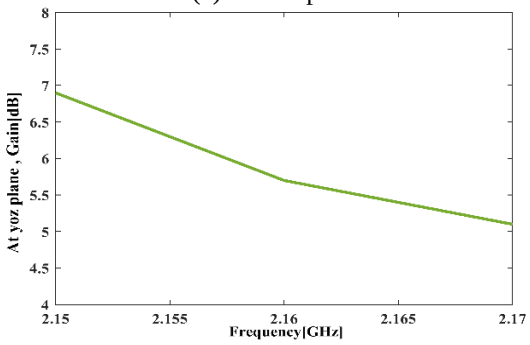

(b) At yoz plane

Fig. 10. The curve of antenna gain with frequency.

Figure 10 (a) shows that the gain, at 2.15~2.17GHz, is between 4.8dB and 7.1dB and decreasing with frequency at xoz plane. Figure 10 (b) reveals that the gain, at 2.15~2.17GHz, is between 5.1dB and 6.9dB and is linear decreasing at yoz plane. At yoz plane, the gain is decreasing with 3dB beam width increasing. Figure 9 presents that the gain, both xoz plane and yoz plane, is maximum at 2.15GHz.

In this section, the influence of several key parameters on the performance of the antenna circuit are discussed. Figure 11 reveals that the size of rectangular patch has large influence on the resonant frequency.

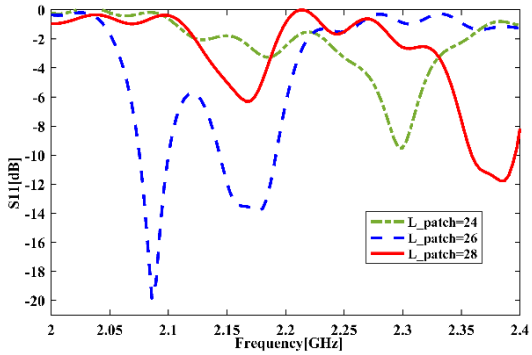

(a) The influence of L_patch

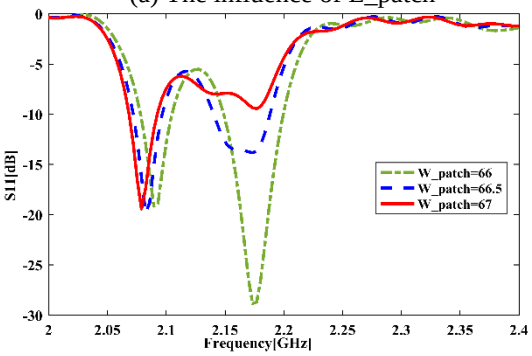

(b) The influence of W_patch

Fig. 11. The influence of the size of the parasitic patch radiation reflection coefficients.

As shown in Fig. 11 (a), with the increase of the length of the rectangular patch(L_patch), the resonant frequency moves toward the low frequency, and the return wave loss (S11) is gradually decreasing. When the L_patch is more than 26mm, the return wave loss (S11) increases, and the waveform becomes worse. In Fig. 11 (b), with the increase of the width of the rectangular patch(W_patch), the resonant frequency slightly moves toward the low frequency, and the return wave loss (S11) gradually decrease. When the L_patch is 66mm, the return wave loss (S11) has a better performance. But, when the L_patch is 66.5mm, S11 becomes worse. The simulated results present that a wide impedance-matching bandwidth can obtain by altering the size of two parasitic patches radiator.

IV. FABRICATION AND MEASUREDRESULTS

According to the proposed antenna structure and size, the wide beam antenna was fabricated and its prototype photo is shown in Fig. 12.

The measured results are given in Fig. 13. The VSWR is less than 1.9 at 2.15~2.18GHz. The measured VSWR meet the design requirement, and are closed to

the simulated VSWR.

Fig. 12. Fabricated wide beam antenna.

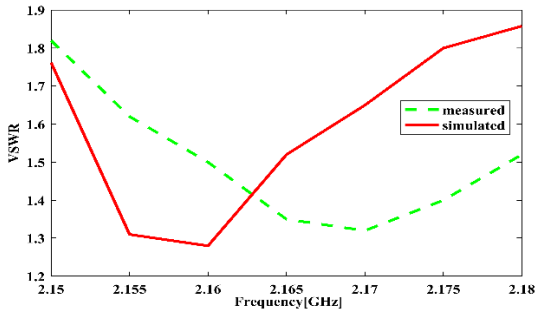

Fig. 13. The measured VSWR of the fabricated wide beam antenna.

The measured and simulated patterns of the co-polarisation and cross-polarisation 3dB beamwidths, at E-plane and H-plane, are presented in Figs. 14, 15 and 16, respectively.

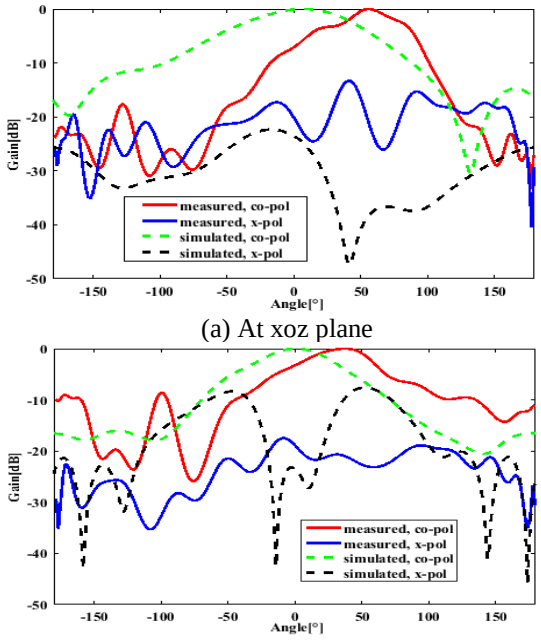

(a) At xoz plane

(b) At yoz plane

Fig. 14. The radiation pattern at 2.15GHz.

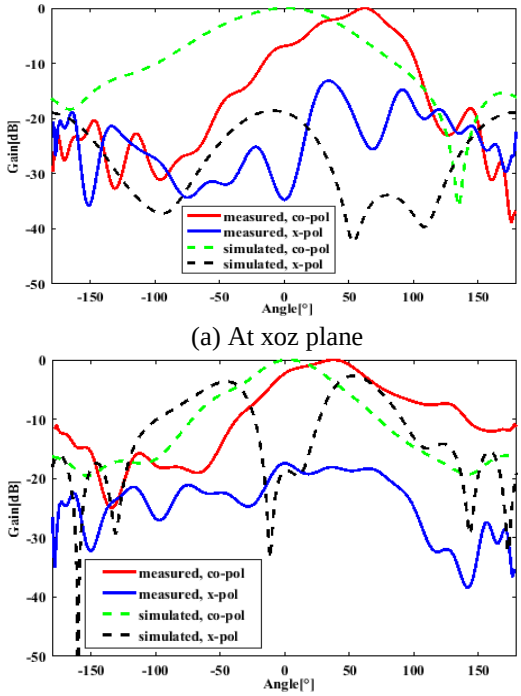

(a) At xoz plane

(b) At yoz plane

Fig. 15. The radiation pattern at 2.16GHz.

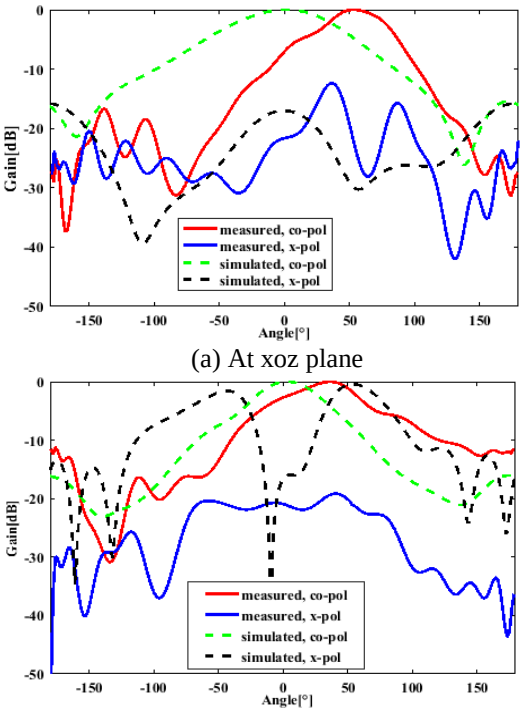

(a) At xoz plane

(b) At yoz plane

Fig. 16. The radiation pattern at 2.17GHz.

The antenna measured patterns are not as smooth as the simulations. The other environmental noise may influence the patterns. At 2.15GHz, the measured co-

polarisation 3 dB beamwidths of xoz plane and yoz plane are 52°and 75°, while the simulated results are 61.9° and 87.7°, respectively. At 2.16GHz, the measured co-polarisation 3dB beamwidths of E-plane and H-plane are 67° and 56°, while the simulated results are 127.4° and 89.7° respectively. At 2.17GHz, the measured co-polarisation 3dB beamwidths of E-plane and H-plane are 67° and 56°, while the simulated results are 75° and 50.9°, respectively. Thus, the proposed antenna has a good wider beam radiation performance, which is high enough to be applied to missile telemetry system. In order to meet the needs of the missile telemetry system, the antenna with wide beam and big efficiency was designed. Both the measurement and simulation results meet the requirements of the missile telemetry system.

V. CONCLUSION

As the requirement for information acquisition is increasing, the missile telemetry system requires a wider beam coverage range. Therefore, it is of practical significance to develop a wide beam antenna element which is suitable for practical engineering applications. A new way to achieve wider bandwidth and broad beam width of microstrip antennas based on the two parasitic patch radiators with different sizes and microstrip line radiator is proposed. The structure of the proposed antenna is based on a two-layer dielectric substrates. The microstrip line is excited by a coaxial probe directly, and the two parasitic patches are excited by the coupling energy. The width of the microstrip line is linearly varied to obtain a wide impedance-matching bandwidth. The sizes of the parasitic patches can be adjusted to increase the beam width of the proposed antenna. The proposed antenna in this paper is suitable for the missile telemetry system, and is very convenient to be applied to practical engineering. In this paper, the stricture of the proposed antenna and the simulated and measured results are discussed in detail. The measured results show that the proposed antenna meets the requirements of missile telemetry system in VSWR, the co-polarisation and cross-polarisation 3 dB beam widths and gain. Thus, the proposed antenna has a good wider beam radiation performance, which is high enough to be applied to missile telemetry system. For some specific engineering project, this paper designed a missile antenna system. In order to meet the requirements of the missile telemetry system, the printed antenna with wide beam was designed. Both the measurement and simulation results meet the requirements of the missile telemetry system.

ACKNOWLEDGMENT

This work is sponsored by the National Natural Science Foundation of China (Grant No. 61571154), the Science Foundation of Aeronautics of China (Grant No. 20160177005).

REFERENCES

[1] K. R. Carver and J. W. Mink, "Microstrip antenna technology" *IEEE Transactions on Antennas & Propagation* [J], AP-29, pp. 2-24, 1981.

[2] R. J. Mailloux, et al, "Microstrip array technology," *IEEE Transactions on Antennas & Propagation*, AP-29, pp. 25-37, 1981.

[3] G. Kumar and K. P. Ray, *Broadband Microstrip Antennas*. Artech House, Boston, MA and London, pp. 18-23, 2003.

[4] A. G. Derneryd, "Microstrip disc antenna covers multiple frequency," *Microware Technology [J]*, pp. 77-79, 1978.

[5] K. P. Ray, "Broadband, dual-frequency and compact microstrip antennas," *Ph.D. Thesis*, Indian Institute of Technology, Bombay, India, 1999.

[6] Z. N. Chen, et al., "Planar antennas," *IEEE Antennas and Propagation Magazine*, vol. 7, no. 6, pp. 63-73, 2006.

[7] H. D. He, "A novel wide beam circular polarization antenna microstrip-dielectric antenna," *Telecomunication Engineering [J]*, pp. 381-384, 2003.

[8] S. Chattopadhyay, J. Y. Siddiqui, and D. Guha, "Rectangular microstrip patch on a composite dielectric substrate for high-gain wide-beam radiation patterns," *IEEE Transactions on Antennas & Propagation [J]*, vol. 57, no. 10, pp. 3325-3328, 2009.

[9] C. W. Su, S. K. Huang, and C. H. Lee, "CP microstrip antenna with wide beam width for GPS band application," *Electronics Letters [J]*, vol. 43, no. 20, pp. 1062-1063, 2007.

[10] C. L. Tang, J. Y. Chiou, and K. L. Wong, "Beamwidth enhancement of a circularly polarized microstrip antenna mounted on a three-dimensional ground structure," *Microwave & Optical Technology Letters [J]*, vol. 32, no. 32, pp. 149-153, 2002.

[11] C. Wu, L. Han, F. Yang, et al., "Broad beam width circular polarization antenna: Microstrip monopole antenna," *Electronics Letters [J]*, vol. 48, no. 19, pp. 1162-1163, 2012.

[12] L. Shi and J. Li, "A compact broadband circularly polarized composite antenna with wide beam width," *Microwave & Optical Technology Letters [J]*, vol. 50, no. 11, pp. 2973-2975, 2008.

[13] Z. K. Pan, W. X. Lin, and Q. X. Chu, "Compact wide-beam circularly-polarized microstrip antenna with a parasitic ring for CNSS application," *IEEE Transactions on Antennas and Propagation [J]*, vol. 62, no. 5, pp. 2847-2850, 2014.

[14] M. J. Li and K. M. Luk, "Wideband magneto-electric dipole antennas with dual polarization and circular polarization," *IEEE Antennas and Propagation Magazine [J]*, vol. 57, no. 1, pp. 110-119, 2015.

[15] S. X. Ta and I. Park, "Crossed dipole loaded with

magneto-electric dipole for wideband and wide-beam circularly polarized radiation," *IEEE Antennas and Wireless Propagation Letters [J]*, vol. 14, pp. 358-361, 2015.

[16] Y. F. Wei, B. H. Sun, C. Shi, et al., "Method for broadening the beamwidths of crossed dipole for wideband marine GPS applications," *Progress in Electromagnetics Research Letters [J]*, vol. 12, pp. 31-40, 2009.

[17] Y. Luo, Q. X. Chu, and L. Zhu, "A low-profile wide-beam-width circularly-polarized antenna via two Pairs of parallel dipoles in a square contour," *IEEE Transactions on Antennas & Propagation [J]*, vol. 63, no. 3, pp. 931-936, 2015.

Lizhong Song was born in 1975. He received master degree and Ph.D. degree from Harbin Institute of Technology in 2001 and 2005, respectively. He is a Professor and Doctoral Supervisor of Harbin Institute of Technology. He focuses his academic interests on antenna design, wireless electromagnetic wave propagation, microwave technology and radar signal processing.

Xiuwen Tian received the B.E. degree in Electronic and Information Engineering from Harbin University of Science and Technology, China, in 2017. Currently, he is a master student in the College of Information Science and Engineering at Harbin Institute of Technology, China. His research interests include antenna design and microwave technology.

Ku-Band Phase-Gradient Metasurface for Broadband High-Gain Circularly Polarized Lens Antenna

Jianxun Su [1], Zhi Li [1], Zengrui Li [1], Qingxin Guo [1], and Yaoqing (Lamar) Yang [2]

[1] School of Information Engineering
Communication University of China, Beijing, 100024, China
zrli@cuc.edu.cn

[2] Department of Electrical and Computer Engineering
University of Nebraska-Lincoln, Nebraska, 68182, USA

Abstract ─ In this paper, a novel broadband high-gain, circularly polarized planar lens antenna is presented. We used the rotation elements to design a transmission-type polarization conversion planar phase-gradient metasurface (PPGM). By adjusting the rotational angles of the metal patch on the element, we obtained the desired transmission phase shift for PPGM. We used a patch antenna as a feed source, which formed a lens antenna system integrated with the PPGM. The simulation results showed that the PPGM can achieve a high-efficiency, cross-polarization conversion for vertical incidence of a right-handed circularly polarized plane wave. Our numerical and experimental results agreed well with each other, indicating that the antenna system had a peak gain of 18.8 dB, a good axial ratio better than 2 dB at 13 GHz, with an aperture efficiency of 50.56% and a focal length/diameter (F/D) ratio of 0.307. In addition, its -10 dB impedance and 3dB axial ratio bandwidth reached up to 940 MHz. The lens antenna performed well and can be applied in many communication systems.

Index Terms─ Circular polarization, lens antenna, planar phase-gradient metasurface (PPGM), plane wave.

I. INTRODUCTION

In recent years, metasurfaces have been attracting more research due to their remarkable ability to manipulate the reflections or transmissions of incoming waves in communication systems. A metasurface (MS) is the two-dimensional plane of metamaterials. Their extraordinary flexibility enables the amplitude, phase, and polarization of electromagnetic waves to be tailored. Metasurfaces have been widely used in stealth technology, high performance antennas, polarization modulation, and other applications [1].

As a pioneer in MS research, the Capasso group has realized a planar phase-gradient metasurface (PPGM) in the optical band through the "V" structure [2] for the first time and has verified the singular refraction which satisfies the generalized Snell's law of refraction. The PPGM has a greater degree of freedom in the direction of propagation of the wave emitted, which can change the beam propagation direction by the phase accumulation of propagation paths. The PPGM's subwavelength thickness structure can contribute greatly to the miniaturization of optical components. So far, there are usually three ways of implementing phase regulation. The first approach is to change the size of the structure. For example, Li et al. [3], who has designed the reflective focusing metasurface to achieve phase changes by varying the size of the H-shaped element. The second approach is to load active components. For example, Zhu et al. [4], uses the loading of active components to design an adjustable impedance metasurface to achieve a reflection wave which has a phase shift of 360 degrees. The third approach is to implement phase control of a circularly polarized wave by using a rotating unit and the Pancharatnam-Berry phase principle. For example, Yu et al. [5], designed a circularly polarized reflectarray antenna that uses a rotating, single-layer, fractured square ring. Motivated by such achievements, we designed a single-layer rotating element to build a focusing MS and a high-gain broadband, circularly polarized lens antenna.

At present, the most used method of transmission of a PPGM changes the unit structure size and multilayer structure to achieve an efficient goal [6]. Those methods have inherent challenges, such as complex processing, high cost, and difficult integration. This paper presented a single-layer, high-efficiency transmission PPGM designed using the element rotation technique, which effectively overcomes these shortcomings. First, we designed a single-layer, double E-shaped metasurface element, as shown in Fig. 1 (a). When the circularly polarized wave is vertically incident in the 12-14 GHz band, the transmitted wave is efficiently converted into a cross-polarized wave resulting in singular refraction.

Then, we took advantage of the principle that the rotation unit can control the phase of the circularly

Submitted On: May 22, 2018
Accepted On: December 29, 2018

polarized wave and designed a broadband, two-dimensional, transmission-type polarization conversion focusing planar phase-gradient metasurface [7,8]. Furthermore, a circularly polarized patch antenna was placed at the focal point as the feed source, and the near-plane wave was transmitted to the focusing PPGM, which greatly improves the gain of the feed. Thus, a low-profile broadband, circularly polarized, high-gain planar lens antenna can be realized in the Ku-band.

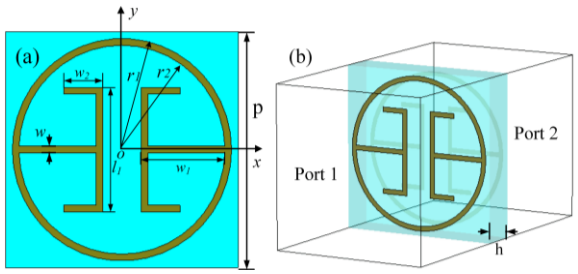

Fig. 1. Configuration of the proposed metasurface unit cell and the simulated setup: (a) top view and (b) perspective view.

II. ANALYSIS AND DESIGN

A. Design of the PPGM unit cell

To convert the circularly polarized spherical wave emitted from a feed source into a cross-polarized plane wave, we first utilized the element rotation method [9] to compensate for the phase deviation of a circularly polarized wave. Then we designed a unit cell to realize polarization conversion of a circularly polarized wave. According to the Pancharatnam-Berry phase principle, when the x-polarized wave and the y-polarized wave illuminate the unit, respectively, it must satisfy two critical requirements: first, the transmissive phase difference of the x-polarized (ϕ_x) and y-polarized (ϕ_y) wave should meet with $|\phi_x - \phi_y| = \pi$ to ensure a pure circularly polarized transmission wave, and second, the amplitudes of the transmission coefficient of the x-polarized (T_x) and y-polarized (T_y) wave should be equal and as close to 1 as possible to improve the transmission efficiency.

The transmission process of circularly polarized waves is deduced as follows. Assume that a right-handed circularly polarized (RHCP) wave is vertically incident onto a unit cell along the +z direction, as shown in Fig. 1 (a). The E field of the incident RHCP wave can be expressed as:

$$\boldsymbol{E}_i = (\hat{\boldsymbol{x}} - j\hat{\boldsymbol{y}})e^{-jkz}, \tag{1}$$

and the transmitted wave is:

$$\boldsymbol{E}_t = (\hat{\boldsymbol{x}}T_x e^{j\phi_x} - j\hat{\boldsymbol{y}}T_y e^{j\phi_y})e^{-jkz}, \tag{2}$$

where T_x and T_y are the amplitudes of the transmission coefficient of the x-polarized and y-polarized wave components, and ϕ_x and ϕ_y are the phase shifts of the x-polarized and y-polarized components of the incident wave. When the metallic unit structure is rotated by θ, as shown in Fig. 2 (a), the rotated coordinate can be written as:

$$\begin{cases} \hat{\boldsymbol{x}} = \hat{\boldsymbol{x}}'\cos\theta - \hat{\boldsymbol{y}}'\sin\theta, \\ \hat{\boldsymbol{y}} = \hat{\boldsymbol{x}}'\sin\theta + \hat{\boldsymbol{y}}'\cos\theta, \end{cases} \tag{3}$$

and the incident wave in the rotated coordinate is expressed as:

$$\begin{aligned} \boldsymbol{E}_i &= [(\hat{\boldsymbol{x}}'\cos\theta - \hat{\boldsymbol{y}}'\sin\theta) - j(\hat{\boldsymbol{x}}'\sin\theta + \hat{\boldsymbol{y}}'\cos\theta)]e^{-jkz} \\ &= (\hat{\boldsymbol{x}}' - j\hat{\boldsymbol{y}}')e^{-jkz}e^{-j\theta}. \end{aligned} \tag{4}$$

Then, the transmitted wave is:

$$\boldsymbol{E}_t = (\hat{\boldsymbol{x}}'T_x'e^{j\phi_x'} - j\hat{\boldsymbol{y}}'T_y'e^{j\phi_y'})e^{-jkz}e^{-j\theta}. \tag{5}$$

In the xyz coordinate, as $\phi_x = \phi_x'$ and $\phi_y = \phi_y'$, $T_x = T_x'$, and $T_y = T_y'$, the transmitted wave can be written as:

$$\begin{aligned} \boldsymbol{E}_t &= [(\hat{\boldsymbol{x}}\cos\theta + \hat{\boldsymbol{y}}\sin\theta)T_x e^{j\phi_x} - j(-\hat{\boldsymbol{x}}\sin\theta + \hat{\boldsymbol{y}}\cos\theta)T_y e^{j\phi_y}]e^{-jkz}e^{-j\theta} \\ &= \frac{1}{2}(\hat{\boldsymbol{x}} + j\hat{\boldsymbol{y}})(T_x e^{j\phi_x} - T_y e^{j\phi_y})e^{-jkz}e^{-j2\theta} \\ &\quad + \frac{1}{2}(\hat{\boldsymbol{x}} - j\hat{\boldsymbol{y}})(T_x e^{j\phi_x} + T_y e^{j\phi_y})e^{-jkz} \end{aligned}. \tag{6}$$

From (6), the transmitted wave consists of two parts: the left-hand rotation $\boldsymbol{E}_{t(\mathrm{LHCP})}$ and right-hand rotation $\boldsymbol{E}_{t(\mathrm{RHCP})}$ components. When $T_x = T_y = T$ and $|\phi_x - \phi_y| = \pi$, the following result can be obtained using equation (6):

$$\begin{aligned} \boldsymbol{E}_{t(LHCP)} &= \frac{T}{2}(\hat{\boldsymbol{x}} + j\hat{\boldsymbol{y}})(1 - e^{j(\pm\pi)})e^{j\phi_x}e^{-jkz}e^{-j2\theta} \\ &= T(\hat{\boldsymbol{x}} + j\hat{\boldsymbol{y}})e^{j\phi_x}e^{-jkz}e^{-j2\theta} \end{aligned}, \tag{7}$$

$$\begin{aligned} \boldsymbol{E}_{t(RHCP)} &= \frac{T}{2}(\hat{\boldsymbol{x}} - j\hat{\boldsymbol{y}})(1 + e^{j(\pm\pi)})e^{j\phi_x}e^{-jkz} \\ &= 0 \end{aligned}. \tag{8}$$

From (7) and (8), we can see that after the right-handed circularly polarized wave is transmitted through the unit cell, it is converted into a left-handed circularly polarized wave [10]. The transmission phase of the transmitted wave, with respect to the incident wave, is doubled.

The unit cell of the PPGM designed is shown in Fig. 2 (b). It is composed of two metallic layers and one intermediate dielectric layer with thickness of 1.5 mm, relative permittivity of 2.65 and loss tangent of 0.0026. The detailed parameters of the structure depicted in Fig. 1 are p=7mm, r_1=3.3mm, r_2=3.1mm, l_1=3.5mm, w=0.2 mm, w_1 = 2.218 mm, w_2 = 1.06 mm, and h = 1.5 mm. The unit cell was simulated with CST Microwave Studio® by using periodic boundary.

Figure 3 shows the phase and amplitude curves of the transmitted wave under x-polarized and y-polarized waves, respectively. It is shown that the amplitude T_x= T_y=0.94 and the phase $|\phi_x - \phi_y| = \pi$ at 13 GHz. Therefore, this unit cell can be used for efficient cross-polarization transmission under the condition of a circularly polarized incident wave. A RHCP plane wave illuminates on the unit cell vertically along the +z direction.

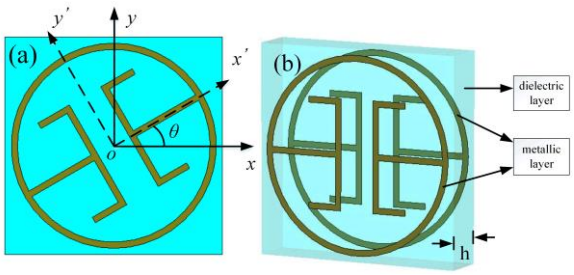

Fig. 2. (a) The rotation angle of the metallic unit, and (b) the composition of the metal unit.

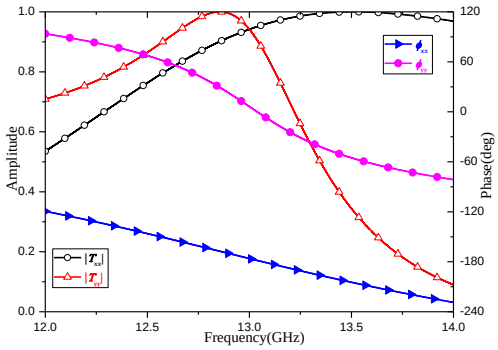

Fig. 3. Amplitude and phase of transmitted wave under x-polarized and y-polarized plane wave illumination.

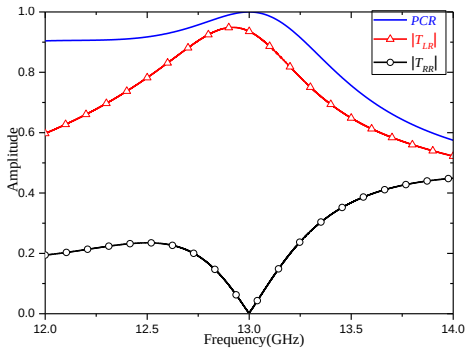

Fig. 4. The transmission amplitude and PCR under RHCP wave incidence.

Figure 4 shows that the cross-polarization transmission amplitude $|T_{LR}|$ reaches 0.94 at about 13 GHz. We used the polarization conversion ratio (PCR) to characterize the proportion of the cross-polarized component in the transmitted wave, and the PCR is defined as:

$$PCR = T_{LR}^2 / \left(T_{LR}^2 + T_{RR}^2\right), \tag{9}$$

where T_{LR} is the cross-polarization transmission coefficient and T_{RR} is the co-polarized transmission coefficient. From the PCR curve calculated by equation (9), we can see that the cross polarization conversion rate is greater than 90% in 12 ~13.3 GHz, which indicates that the RHCP plane wave is efficiently converted into a LHCP plane wave after transmitting the unit.

To verify the phase and polarization conversion characteristics of the rotating unit, we used the RHCP plane wave to illuminate the rotated elements respectively along the +z direction. In Fig. 5, the element is rotated with a step of 30°, and then we get the transmitted waves (LHCP) which achieves an accurate phase shift of 2θ. Meanwhile, these transmission amplitudes are almost equal and maintained up to 0.94. The above results demonstrate the high transmission and cross-polarization conversion characteristics of the unit cell, which meets the design requirements.

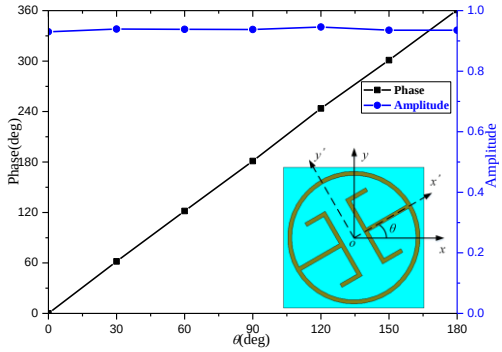

Fig. 5. The phase and amplitude of transmitted waves under RHCP plane wave illumination at 13 GHz.

B. Design of planar lens antenna based on PPGM

The unit can achieve efficient cross-polarization conversion over a wide frequency band and compensate for any phase offset in the range of [0, 2π] by the rotation unit. In order to enable the vertical incidence circularly polarized plane waves to converge to one point after transmitting the PPGM, the phase distribution of the elements in the xoy plane should be satisfied by the following parabolic equation:

$$\phi(x,y) = \frac{2\pi}{\lambda_0}\left(\frac{x^2+y^2}{4f}\right) + \phi_0 . \tag{10}$$

Where $\phi(x,y)$ is the required phase compensation at the point (x,y), ϕ_0 is the center point phase of the lens, λ_0 is the free space wavelength at the design frequency, and f is the physical focal distance from the center point of the feed source to the center point of the PPGM.

Due to the reversibility of the electromagnetic wave transmission [11], we placed a patch antenna on the focal point of the PPGM along the –z direction at xoy-plane that can radiate a right-handed circularly polarized wave at 13 GHz. The PPGM contained 11 × 11 structural units, and the optimal size of the overall PPGM was 79.2 × 79.2 mm^2. The focal length-to-diameter ratio (F/D) was 0.307. According to equation (10), the compensation phase of each unit can be calculated, and then the angle of rotation of each unit is obtained. The physical structure

diagram of the overall lens antenna system integrated with the PPGM is shown in Fig. 6.

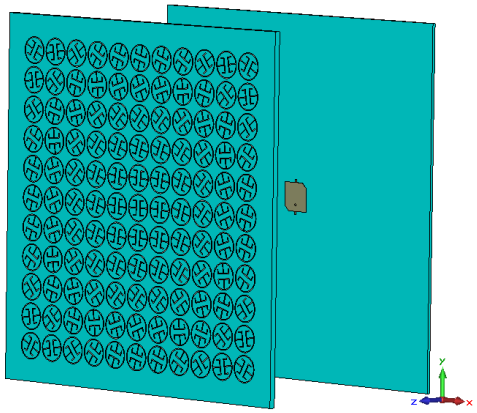

Fig. 6. The physical structure diagram of the overall lens antenna system integrated with the PPGM.

III. MEASUREMENT AND DISCUSSION

In Section II, we demonstrated our design of the overall PPGM lens antenna system at the Ku-band. Section III verified the radiation characteristics of the lens antenna by using CST software simulation with a transient solver. By fine-tuning the focal distance during simulation, we can obtained the optimal length of the focal distance (f = 28.5mm). Thus, we placed a feeding patch antenna 28.5 *mm* away from the PPGM along the −z-direction at xoy-plane. The E_x distributions of the patch antenna with and without the PPGM are shown in Fig. 7. As shown in Fig. 7, the PPGM lens transformed the quasi-sphere wave emitted from the patch antenna into a plane wave, as per the theoretical prediction. Due to the high directivity of the plane wave, the beam width of the patch antenna decreased greatly and the gain was remarkably enhanced.

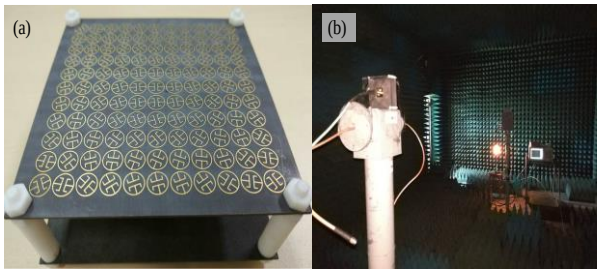

Fig. 7. Simulated electric field distributions (Ex) at 13 GHz. (a) xoz-plane for the patch antenna; (b) xoz-plane for the PPGM; (c) yoz-plane for the patch antenna; (d) yoz-plane for the PPGM.

Figure 8 depicts a three-dimensional (3D) simulation of the far-field radiation patterns of the patch antenna and the PPGM lens antenna at 13 GHz. It shows that the gain of the patch antenna was 7.68 dB, and the gain of the PPGM lens antenna was 18.8 dB. So we conclude that the PPGM lens can remarkably enhance the gain of the patch antenna at 13 GHz and that the peak gain of the patch antenna improved by 11.12 dB.

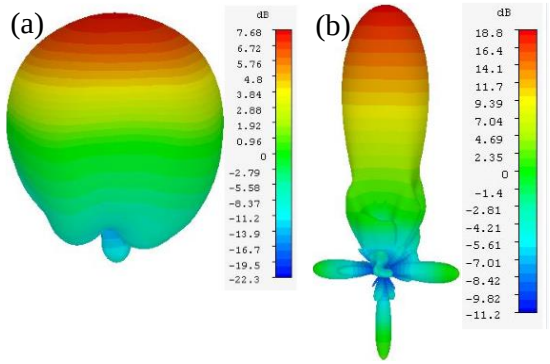

Fig. 8. The simulated 3D far-field radiation patterns at 13 GHz. (a) the patch antenna and (b) the PPGM lens antenna.

To validate the simulation results, the PPGM lens and patch antenna were fabricated, as shown in the photograph in Fig. 9 (a). The far-field measurement setup shown in Fig. 9 (b), the patch antenna was connected to the PPGM by four dielectric cylinders with a length of 28.5 mm.

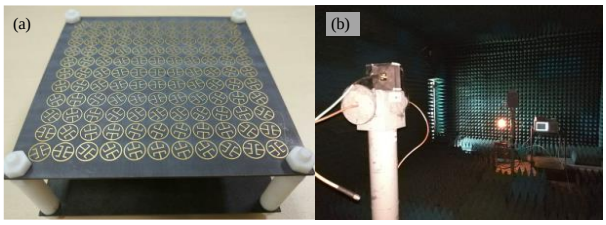

Fig. 9. Fabrication and measurement: (a) prototypes of the proposed PPGM lens antenna, and (b) measurement in anechoic chamber.

Figure 10 shows the structure of the patch antenna. It is a square metal radiation patch with a cutting angle, which is fed by a 50-Ω SMA connector on the bottom metallic layer. The substrate has a thickness of 0.787 mm, a relative permittivity of 2.2 and a loss tangent of 0.0009, and the size of the substrate was 79.2 × 79.2 mm^2. This feed patch antenna which can emit the RHCP wave, and when the wave illuminates the PPGM vertically, it will be converted into a LHCP wave. Figure 10 also shows the measured reflection coefficients of the patch antenna with and without the PPGM. It can be seen that the patch antenna with the PPGM operated at a broadband −10 dB bandwidth from 12.6 GHz to 13.54 GHz. Figure 11 shows the comparison of the simulated

and measured axial ratios of the patch antenna and the lens antenna. We found that the axial ratio was better than 2 dB around 13 GHz and operated at a broadband 3 dB axial ratio bandwidth ranging from 12.6 to 13.54 GHz. The simulated and measured radiation patterns in the xoz- and yoz-planes at 13 GHz are illustrated in Fig. 12. We observed that the PPGM lens enhanced the gain of the patch antenna considerably, and right-handed circularly polarized waves (RHCP) are well converted into left-handed circularly polarized waves (LHCP). Meanwhile, the half power beam width reduced from 81°to 16.5°. Figure 13 presents that the simulated and measured peak gains of the PPGM lens antenna versus frequency. We can see that the measured 1 dB gain bandwidth achieved by this PPGM lens antenna is 0.58 GHz (Fractional bandwidth of 4.5%). The measured gain is approximately 0.3 dB below the gain obtained in simulation. The discrepancy could be due to manufacturing tolerances or test environment tolerances. The overall measured and simulated results of the PPGM lens antenna are compared in Table 1. The measured results of the fabricated antenna were generally consistent with the simulation, which validates the proposed design methodology.

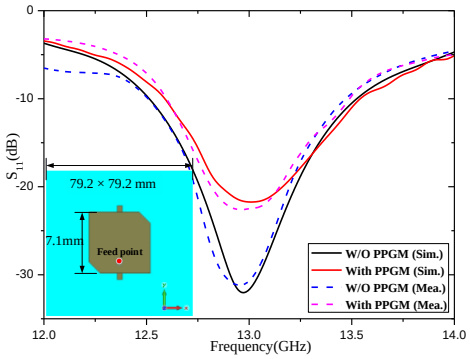

Fig. 10. Simulated and measured reflection coefficients of patch antenna with/without the PPGM.

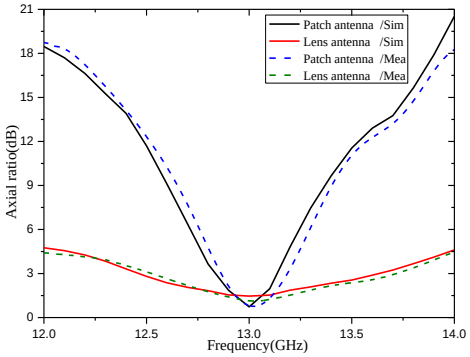

Fig. 11. Simulated and measured axial ratios of the patch antenna (RHCP) and the PPGM lens antenna (LHCP).

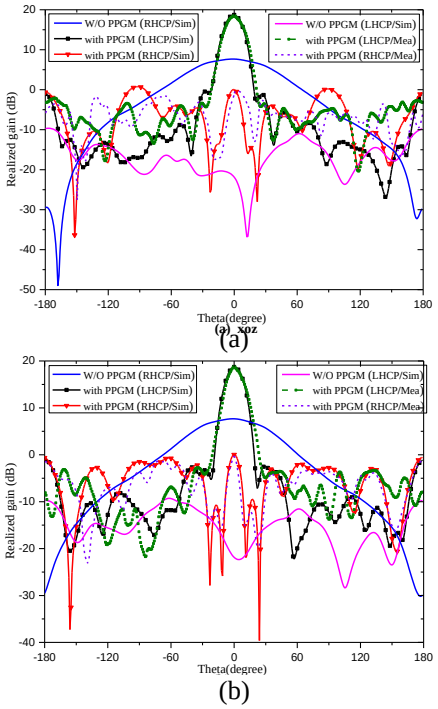

Fig. 12. Simulated and measured far-field radiation patterns of the patch antenna and the PPGM lens antenna at 13 GHz: (a) xoz-plane and (b) yoz-plane.

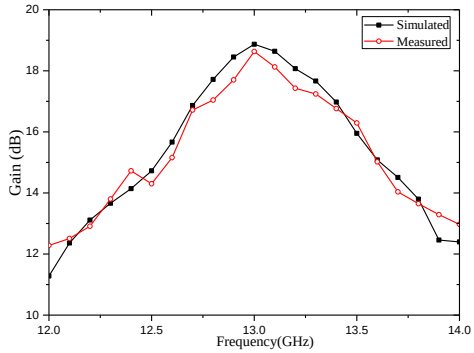

Fig. 13. Simulated and measured peak gains of the PPGM lens antenna versus frequency.

Table 1: Results comparison of measured and simulated PPGM lens antenna

Parameter	Measured Value	Simulated Value
Peak gain (dB)	18.5	18.8
1dB gain bandwidth	0.58GHz (4.5%)	0.67GHz (5.2%)
3 dB AR bandwidth	0.8GHz (6.15%)	0.94GHz (7.2%)
HPBW (degree)	16.5	17.2
Side lobe level (dB)	–18.2	-19.8

IV. CONCLUSION

In this paper, a new method of designing a high-gain broadband, circularly polarized planar lens antenna was proposed based on the element rotation method. The planar lens antenna was designed, fabricated, and measured at Ku-band. The PPGM had a thickness of 1.5 mm and dimensions of 79.2 × 79.2 mm^2 with an F/D of 0.307. High transmission and polarization conversion efficiency of the unit cell and great focusing effect of the PPGM guaranteed the good performance of the transmitting lens antenna, which achieved a peak gain of 18.8 dB, SLL of −18.2 dB, HPBW of 16.5°, F/B of 18.2 dB, axial ratio of 2 dB, and a high aperture efficiency of 50.56% at 13 GHz. This design provides a new approach for a low profile planar lens antenna with high gain, broadband, circularly polarized, high radiation efficiency. Thus, it can be widely used in long distance wireless communication and imaging sensing systems.

ACKNOWLEDGMENT

The authors are grateful to support from the National Natural Science Foundation of China under Grant No. 61331002, No. 61671415 and No. 61701448.

REFERENCES

[1] Y. F. Li, J. Q. Zhang, S. B. Qu, *et al*., "Wideband radar cross section reduction using two-dimensional phase gradient metasurfaces," *Appl. Phys. Lett.*, vol. 104, no. 22, pp. 221110-221115, June 2014.

[2] N. F. Yu, *et al*., "Light propagation with phase discontinuities: Generalized laws of reflection and refraction," *Science*, vol. 334, pp. 333-337, 2011.

[3] X. Li, S. Y. Xiao, B. G. Cai, Q. He, T. J. Cui, and L. Zhou, "Flat metasurfaces to focus electromagnetic waves in reflection geometry," *Opt. Lett.*, vol. 37, no. 23 pp. 4940-4942, Dec. 2012.

[4] P. Y. Chen, C. Argyropoulos, and A. Alù, "Broadening the cloaking bandwidth with non-foster metasurfaces," *Phys. Rev. Lett.*, vol. 111, no. 23, pp. 233001-233014, Dec. 2013.

[5] A. Yu, F. Yang, A. Z. Elsherbeni, J. Huang, and Y. Kim, "An offset-fed X-band reflectarray antenna using a modified element rotation technique," *IEEE Trans. Antennas Propag.*, vol. 60, no. 3, pp. 1619-1624, Mar. 2012.

[6] H. Li, G. Wang, H. Xu, T. Cai, and J. Liang, "X-band phase-gradient metasurface for high-gain lens antenna application," *IEEE Trans. Antennas Propag.*, vol. 63, no. 11, pp. 5144-5149, Nov. 2015.

[7] X. Wan, Y. B. Li, B. G. Cai, and T. J. Cui, "A broadband transformation optics metasurfaces lens," *Appl. Phys. Lett.*, vol. 105, p. 151604, 2014.

[8] J. B. Pendry, "Negative refraction makes a perfect lens," *Phys. Rev. Lett.*, vol. 85, no. 18, pp. 3966-3969, Oct. 2000.

[9] L. D. Palma, *et al*., "Circularly polarized transmit-array with sequential rotation in ka-band," *IEEE Trans. Antennas Propag.*, vol. 63, no. 11, pp. 5118-5124, Nov. 2015.

[10] T. Cai, *et al*., "Ultra-thin polarization beam splitter using 2-D transmissive phase gradient metasurface," *IEEE Trans. Antennas Propag.*, vol. 63, no. 12, pp. 5629-5636, Dec. 2015.

[11] X. Chen, H. F. Ma, X. Y. Zou, W. X. Jiang, and T. J. Cui, "Three dimensional broadband and high-directivity lens antenna made of metamaterials," *Appl. Phys.*, vol. 110, pp. 0449041-0449048, Aug. 2011.

Jianxun Su received the M.S. degree and the Ph.D. degree in Electromagnetic Field and Microwave Technology from the Communication University of China and Beijing Institute of Technology, Beijing, China, in 2008 and 2011, respectively.

From 2012 to 2014, he was with China Electronics Technology Group Corporation (CETC), where he engaged in phased-array system research. He is currently working as Associate Researcher at School of Information Engineering, Communication University of China and also with the Science and Technology on Electromagnetic Scattering Laboratory. His special research interests include integral equation method, computational electromagnetics, metamaterial, phased-array antenna, radar target characteristics.

Zhi Li received the B.S. degree in Henan University, Henan Province, China, in 2013. From 2015 to now, he is pursuing the M.S. degree of Electromagnetic Field and Microwave Technology at Communication University of China, Beijing, China. His research interests include metamaterials, lens antennas, reflector antennas, microstrip array antennas, etc.

Zhengrui Li received the B.S. degree in Communication and Information System from Beijing Jiaotong University, Beijing, China, in 1984; the M.S. degree in Electrical Engineering from Beijing Broadcast Institute, Beijing, China, in 1987; and the Ph.D. degree in Electrical Engineering from Beijing Jiaotong University, Beijing, China, in 2009.

He is currently a Professor with the Communication University of China, Beijing, China. He studied at Yokohama National University, Yokohama, Japan, from 2004 to 2005. His research interests include the areas of finite-difference time-domain (FDTD) methods, electromagnetic scattering, metamaterials and antennas.

Li is a Senior Member of the Chinese Institute of Electronics.

Yaoqing (Lamar) Yang received his B.S. degree from the Northern Jiaotong University, China, and his M.S. degree from the Beijing Broadcast Institute, China, both in Electrical Engineering. He received his Ph.D. degree in the area of Wireless Communications and Networks from the University of Texas (UT) at Austin. He is now an Associate Professor in the Department of Electrical and Computer Engineering, University of Nebraska-Lincoln (UNL).

His current research interests lie in wireless communications, radio propagations, and statistical signal processing. Yang is a Senior Member of IEEE.

24 GHz Graphene Patch Antenna Array

Varindra Kumar

Department of Engineering, University of Cambridge, Cambridge, CB2 1PZ, UK
Varindra@ieee.org

Abstract ─ The discovery of Graphene has created new applications for the next generation electronics due to its electrical characteristic. A compact patch antenna with graphene as conducting media has been designed for wearable, medical and consumer electronics application at 24 GHz. The patch has a dimension of 5x5 mm and is designed over 0.254 mm thick roger material. The antenna has been combined to make it an array form for increasing its gain while various antenna parameters have been obtained for its comparison with copper conductive patch. The ground patch is made of Perfect Electric Conductor (PEC) in both cases. Various parametric results show that graphene patch similar to copper patch provides a comparable return loss and VSWR although there has been observed some decrease in its gain and efficiency and an increase in its bandwidth. Thus, graphene can be a good alternative to copper conductive patch within higher GHz and THz frequency range.

Index Terms ─ 24 GHz, antenna, array, graphene, patch.

I. INTRODUCTION

The last few years has seen an increase in the arrival of small and portable electronics for its wide-ranging applications from IoT, consumer, medical and wearable electronics. In order to make these electronics smaller and robust, every component of these devices need to be small and low profile while providing similar output. Antenna being the communication component across these devices needs to be small while providing good performance. An array of the antenna can provide an increase in its parametric values with increasing gain and radiation efficiency in certain direction while suppressing these values in undesired direction [1-5]. Various researchers in the past have proposed the design of an array antenna with traditional conducting media such as copper, silver etc to increase the gain and bandwidth but very few have designed an array antenna with graphene conductive media [6-7] at low GHz frequency range. Graphene [8] is hexagonally arranged honeycombed lattice structure with high mobility (8000 cm^2/V) [8-9], thermal conductivity of 5000 W/m/K [8-9], mechanical strength [8-9] and noticeable flexibility [10]. Recently graphene as a material has become quite popular and has provided many applications in microwave to mm-wave domain [11-12]. The application in microwave and mm wave is often associated with high propagation and penetration losses. However, this paper proposes the graphene application in GHz communication with an array to increase the signal strength, gain and directivity. The low conductivity of the graphene flake at lower GHz frequency range requires a layer combination where the conductivity can be increased with an increase in number of layers although the constraint lies in the manufacturing of a thick layer of graphene flake [13-15].

II. ANTENNA DESIGN

Microstrip patch antenna has a conductive patch laid over a substrate with a metallic conductor underneath to provide a ground plane. The performance of a patch such as resonant frequency, gain, directivity, radiation and bandwidth depends on the patch dimension and size, substrate type and feed. The effective permittivity of the substrate can be defined using (1) [16] while the patch dimension can be obtained using its required resonant frequency after a calculation from (2-7) [16] with the assumption 'W' width being greater than substrate thickness 'h':

$$\varepsilon_{reff} = \frac{\varepsilon_r+1}{2} + \frac{\varepsilon_r-1}{2}\frac{1}{\sqrt{1+\frac{12h}{W}}}, \tag{1}$$

$$W = \frac{c}{2f_o\sqrt{\frac{\varepsilon_r+1}{2}}}, \tag{2}$$

$$L_{eff} = \frac{c}{2f_o\sqrt{\varepsilon_{reff}}}, \tag{3}$$

$$\Delta L = 0.412h\frac{\left(\varepsilon_{reff}+0.3\right)\left(\frac{W}{h}+0.264\right)}{\left(\varepsilon_{reff}-0.258\right)\left(\frac{W}{h}+0.8\right)}, \tag{4}$$

$$L = L_{eff} - 2\Delta L, \tag{5}$$

$$L_g = 6h + L, \tag{6}$$

Submitted On: February 22, 2018
Accepted On: December 25, 2018

$$W_g = 6h + W. \quad (7)$$

The proposed antenna is a rectangular radiation patch with a feeding patch structure of 50Ω characteristic impedance and is shown in Fig. 1. The antenna designs have been converted into an array form and are shown in Figs. 2-4, while Fig. 5 shows the stack-up of the design [17]. The conducting patch (3.4 mm x 2.38 mm) has been designed using copper and graphene media with roger material as substrate (dielectric constant ϵ_r = 6.15 and tan δ = 0.002) with dimensional size of 10 mm x 10 mm and PEC at its ground layer with dimensional size of 10 mm x 10 mm. The patch and its ground layer have a thickness of 0.01 mm while the substrate is 0.254 mm thick. The patch is excited through a feed with the dimension of 0.32 mm x 4.71 mm x 0.01 mm.

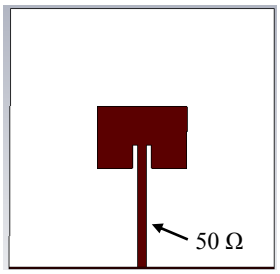

Fig. 1. Patch antenna.

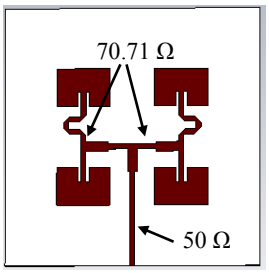

Fig. 2. 2x2 Patch antenna.

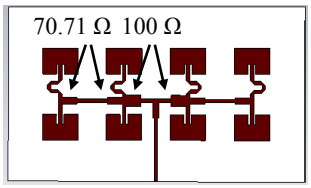

Fig. 3. 2x4 Patch antenna.

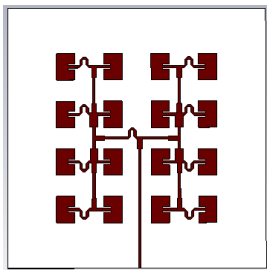

Fig. 4. 4x4 Patch antenna.

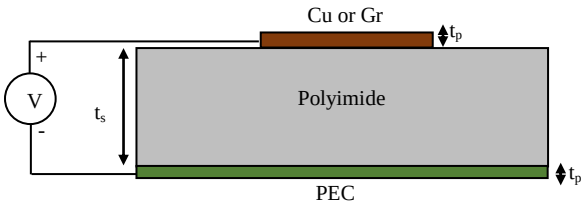

Fig. 5. Copper/graphene patch antenna (side view).

III. GRAPHENE AND ITS CONDUCTIVITY

The graphene surface conductivity arises from the Kubo formula [18-19] in the absence of an external electric and magnetic field; however is frequency dependent and is represented as a complex number. The first term of (8) represents intraband conductivity while the second term represents interband conductivity. Various parameters ω, μ_C, τ, T, e and ħ of the following equations (8-16) are defined by the operating frequency, external chemical bias to a graphene structure, carrier scattering time constant (1/τ defines carrier scattering rate), room temperature, electronic constant and reduced Planck's constant respectively. Similarly, k_B, $f_d(\epsilon)$, V_f and n_s represents the Boltzmann constant, Fermi Dirac distribution function, Fermi velocity (10^6 m/s) and electron mobility respectively:

$$\sigma(\omega,\mu_C,\tau,T) = \frac{je^2/\pi\hbar^2}{\omega - j(2/\tau)} \times \int_0^\infty \varepsilon \left[\frac{\partial f_d(\varepsilon)}{\partial \varepsilon} - \frac{\partial f_d(-\varepsilon)}{\partial \varepsilon} \right] d\varepsilon + je^2/\pi\hbar^2(\omega - j(2/\tau) \times \int_0^\infty \frac{f_d(\varepsilon) - f_d(-\varepsilon)}{(\omega - j(2/\tau))^2 - 4(\varepsilon/\hbar)^2} d\varepsilon, \quad (8)$$

$$f_d(\varepsilon) = \left[1 + e^{\frac{\varepsilon + |\mu_C|}{k_B T}} \right]^{-1}, \quad (9)$$

$$n_s = \frac{2}{\pi\hbar^2 V_f^2} \int_0^\infty \varepsilon \left[\begin{matrix} f_d(\varepsilon - \mu_C) - \\ f_d(\varepsilon + \mu_C) \end{matrix} \right] d\varepsilon, \quad (10)$$

$$\tau = \frac{\mu \mu_C}{e V_f^2}, \quad (11)$$

$$\mu_C = \sqrt{\pi\hbar^2 V_f^2 n_s}, \quad (12)$$

$$n_s = \frac{2}{\pi\hbar^2 V_f^2} (k_B T)^2 \left(e^{\frac{2\mu_C}{k_B T}} - 1 \right), \quad (13)$$

$$\sigma_{\text{int ra}}(\omega,\mu_C,\tau,T) = j \frac{8\sigma_0 k_B T/h}{\omega - j2/\tau} \times \left[\frac{\mu_C}{k_B T} + 2\ln\left(e^{-\frac{\mu_C}{k_B T}} + 1 \right) \right], \quad (14)$$

$$\sigma_{\text{int er}}(\omega,\mu_C,\tau,T) = -j \frac{\sigma_0}{\pi} \times \left[\frac{2|\mu_C| - (\omega - j2/\tau)\hbar}{2|\mu_C| + (\omega - j2/\tau)\hbar} \right], \quad (15)$$

$$\delta = \sqrt{\frac{2}{\omega\mu\sigma}}. \quad (16)$$

Fermi Dirac function and carrier mobility can be represented using (9) and (10) while scattering time constant and chemical bias are represented using (11) and (12). Solving (10) with the help of (9), the carrier mobility as defined in (13) can be obtained. Based on (14) and (15), a normalized conductivity plot with the chemical potential ranging from 0.1 eV to 1.1 eV for a graphene flake within the GHz - THz frequency range has been obtained and plotted using Matlab as shown in Fig. 6. The conductivity has been normalized here to its static conductivity $\sigma_0 = e^2/(4\hbar)$ for its plot. The graphene has a lattice structure with extremely thin layer of height (δ = 0.334 nm) and hence it can be considered as a two dimensional crystalline structure. For the electromagnetic simulation, the lattice structure's minimum thickness δ is selected such that the electromagnetic field distribution can see the thickness of the graphene and a wave propagation can occur. Hence the graphene conductivity can be

expressed as volumetric conductivity with $\sigma_v = \sigma_s/\delta$. With a layer of graphene flake to create a patch (thickness tp) in antenna design, the effective surface conductivity in its simplified form can be represented as $\sigma = tp \times \sigma_v$. Here N-layered graphene with tp/δ has been assumed to have the same relaxation time and fermi energy for its simplicity.

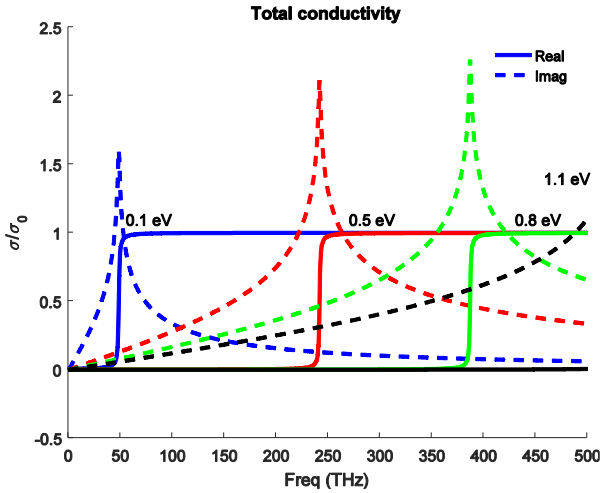

Fig. 6. Normalized total conductivity of Graphene.

IV. RESULTS AND DISCUSSION

A full field solver tool, CST Microwave studio [20] is used for the design and simulation of the antenna and Matlab is used to plot the data within the frequency band from 20 GHz to 28 GHz.

Figures 7-10 show the S11 parameter comparison for the copper and graphene patch for its configurations 1x1, 2x2, 2x4 and 4x4 while a comparison of its gain for the patch array with copper and graphene media has been shown in Figs. 11-14. As shown in these figures, the resonance frequency of the copper patch compares well with the graphene patch at around 24 GHz resonance with 0.1 eV DC bias. The gain behavior as shown in Figs. 11-14 shows that with an increase in the number of patch element forming an array increases the gain. The patch with graphene media shows slightly lesser gain while still providing enough performance for its antenna application.

Using the transmission line theory, various equations to obtain antenna parameters for a rectangular patch lying in x-y plane (perpendicular to z- axis) with length 'L' and width 'W' using simple formulas can be obtained and are defined in (17-25) [21-22]. As the reflection coefficient at its load can be defined using (17), the reflection coefficient as a function of x along its length (or y along its width) can be obtained using (18), while the Voltage Standing Wave Ratio (VSWR) can be obtained using (19).

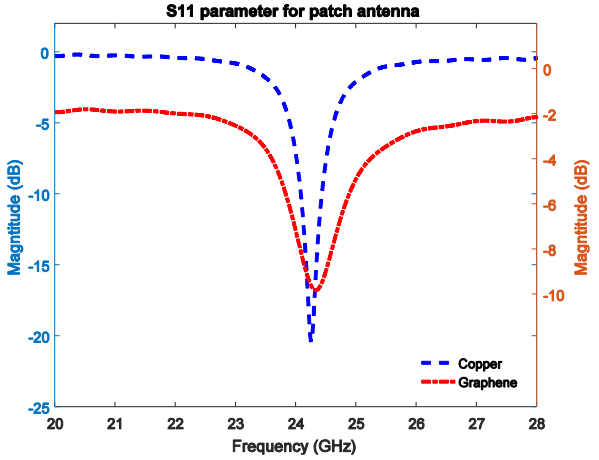

Fig. 7. S11 parameter comparison for Copper and Graphene - 1x1 patch.

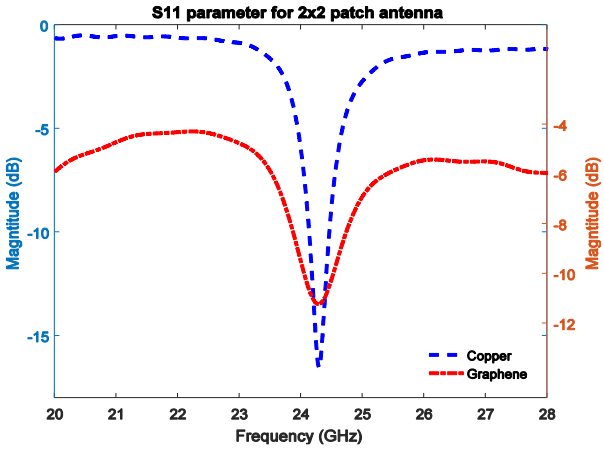

Fig. 8. S11 parameter comparison for Copper and Graphene - 2x2 patch.

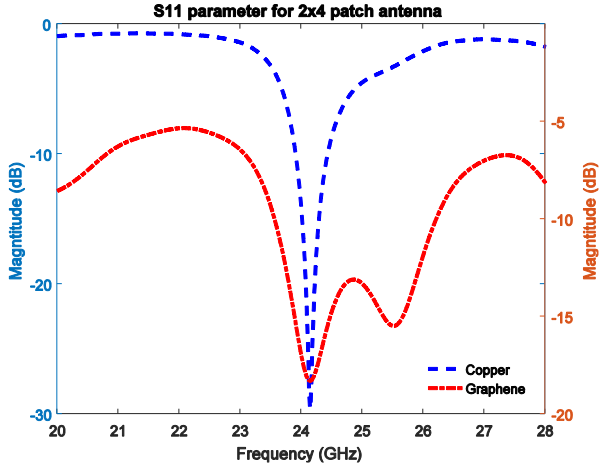

Fig. 9. S11 parameter comparison for Copper and Graphene - 2x4 patch.

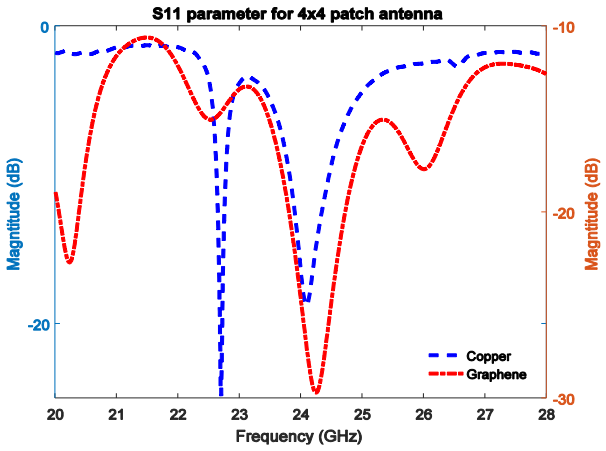

Fig. 10. S11 parameter comparison for Copper and Graphene - 4x4 patch.

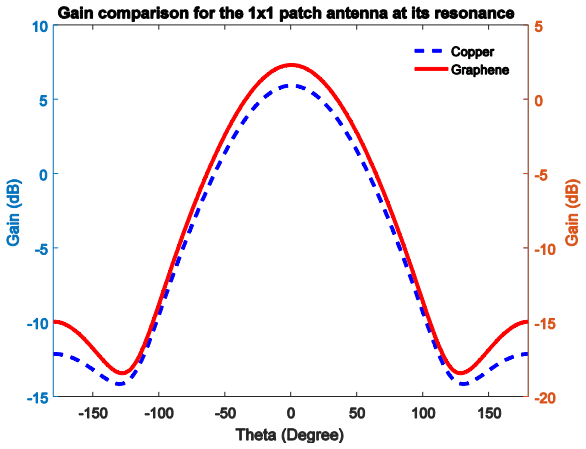

Fig. 11. Gain comparison for 1x1 patch antenna.

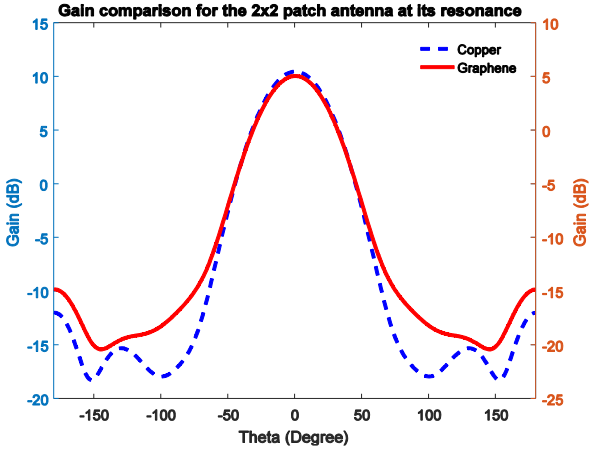

Fig. 12. Gain comparison for 2x2 patch antenna.

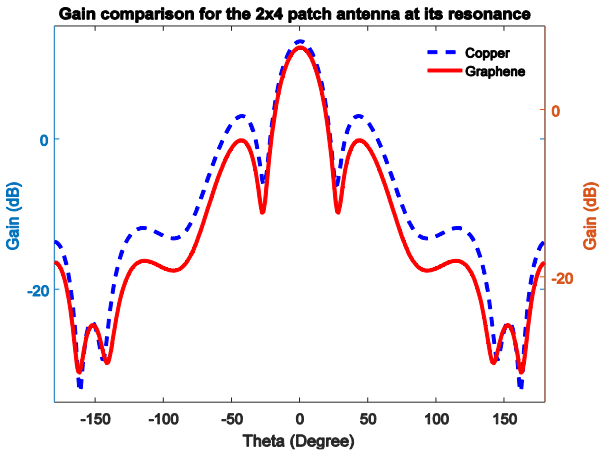

Fig. 13. Gain comparison for 2x4 patch antenna.

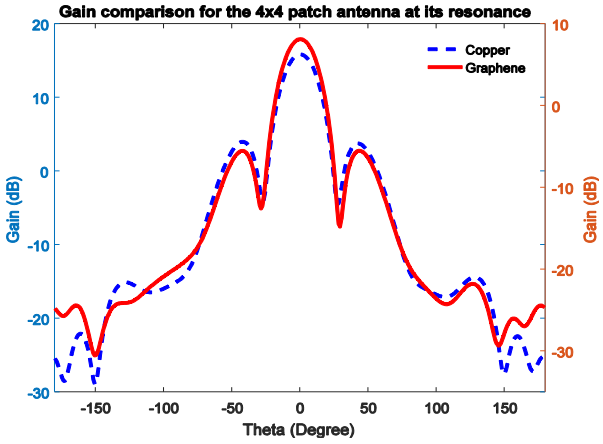

Fig. 14. Gain comparison for 4x4 patch antenna.

The resonance frequency of a rectangular patch with length 'L' and width 'W' in general is dependent on the mode of its excitation and can be defined by its TE, TM, TEM mode based on the integer values of m and n as in (20) while the bandwidth (BW) as in (21) can be obtained with its upper and lower -10dB crossing point. Similarly based on the dielectric and conductor loss of a conductive patch over a substrate can provide a relationship for gain and directivity for its radiation efficiency and can be defined using (22) while the normalized electromagnetic fields with respect to peak field at its corner can be obtained using (23), (24), and (25). Here $k_0 = 2\pi/\lambda$, where λ is the wavelength of the excited frequency of operation:

$$\Gamma_L = \frac{Z_L - Z_o}{Z_L + Z_o}, \tag{17}$$

$$\Gamma(x) = \Gamma_L e^{2j\beta x}, \tag{18}$$

$$\text{VSWR} = \frac{1+|\Gamma(x)|}{1-|\Gamma(x)|}, \tag{19}$$

$$f_O = \frac{c}{2\sqrt{\varepsilon_r}}\left[\left(\frac{m}{L}\right)^2 + \left(\frac{n}{W}\right)^2\right]^{1/2}, \tag{20}$$

$$\text{BW} = (f_H - f_L), \tag{21}$$

$$G(\theta,\varphi) = \delta_e D(\theta,\varphi), \tag{22}$$

$$E_z = \cos\left(\frac{m\pi x}{L}\right)\cos\left(\frac{n\pi y}{W}\right), \tag{23}$$

$$H_x = -\frac{j\omega\varepsilon_0}{k_0^2}\frac{n\pi}{W}\cos\left(\frac{m\pi x}{L}\right)\sin\left(\frac{n\pi y}{W}\right), \tag{24}$$

$$H_y = \frac{j\omega\varepsilon_0}{k_0^2}\frac{m\pi}{L}\sin\left(\frac{m\pi x}{L}\right)\cos\left(\frac{n\pi y}{W}\right). \tag{25}$$

The radiation field of an array at a far point as defined in (26) can be assumed as a weighted sum of the radiation due to an array of elements, with a consideration of the phase for individual element, similarly the gain can be obtained as the weighted sum of individual array element [23]. Here r_n represents the (x, y, z) distance of the calculation point from the individual element of the array:

$$R_{sum}(x_f, y_f, z_f) = \sum_{n=1}^{N} R_n(x_f, y_f, z_f) \times w_n \frac{e^{-jkr_n}}{r_n}. \tag{26}$$

A far-field radiation diagram for various patch antenna has been obtained and are shown in Figs. 15-22. As shown here, Figs. 15-18 show the radiation pattern for the copper patch for its various array structures. With an increase in array dimension, the directivity of the patch shows an increase. Similarly, Figs. 19-22 show the radiation pattern for the graphene patch for its various array structures. A comparison of the radiation pattern for copper and graphene patch shows that the directivity of the graphene closely follows the corresponding pattern of copper patch.

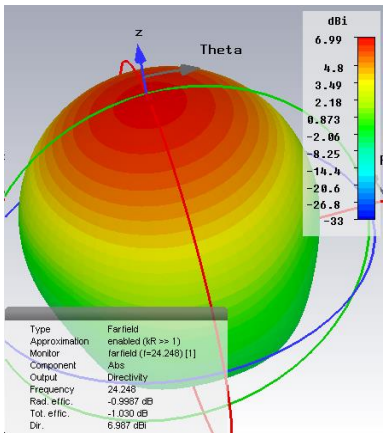

Fig. 15. Radiation diagram for 1x1 Copper patch.

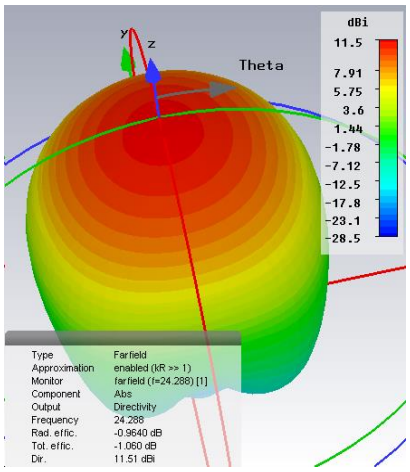

Fig. 16. Radiation diagram for 2x2 Copper patch.

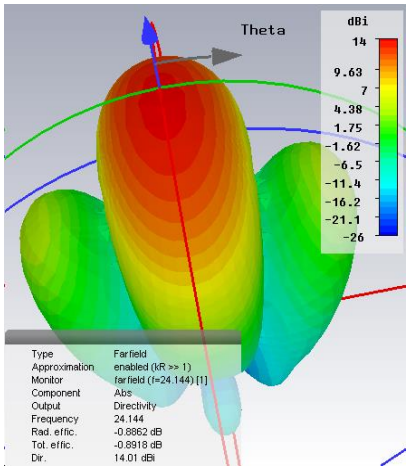

Fig. 17. Radiation diagram for 2x4 Copper patch.

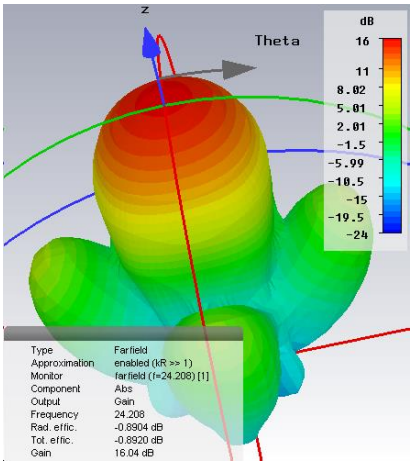

Fig. 18. Radiation diagram for 4x4 Copper patch.

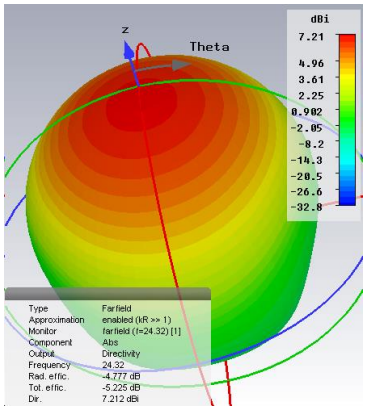

Fig. 19. Radiation diagram for 1x1 Graphene patch.

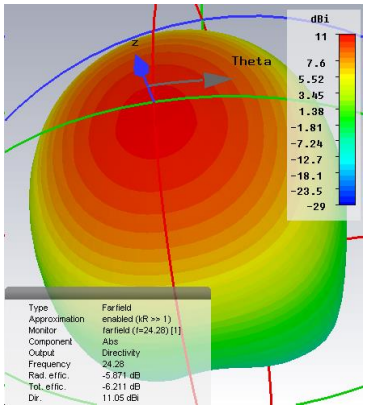

Fig. 20. Radiation diagram for 2x2 Graphene patch.

Table 1 provides a comparison of various antenna parameters for copper and graphene conductive patch in its array form such as resonant frequency, VSWR, return loss, Directivity, Gain, Directivity and radiation efficiency. Although radiation efficiency is lower for the graphene media, these patch elements can still be used for antenna application.

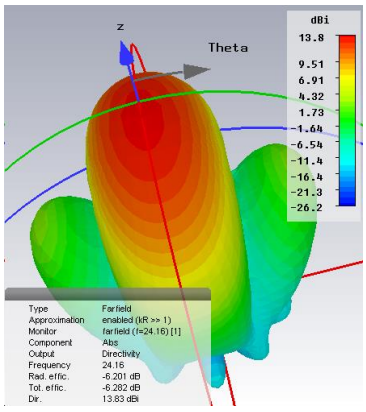

Fig. 21. Radiation diagram for 2x4 Graphene patch.

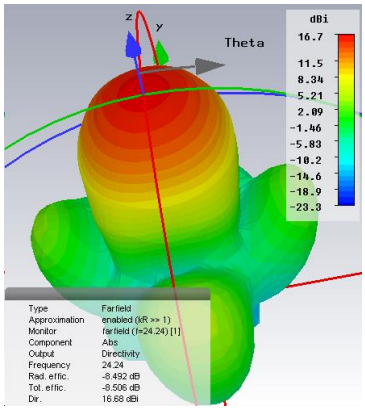

Fig. 22. Radiation diagram for 4x4 Graphene patch.

Table 1: Antenna parametric comparison for graphene and copper

	Conductor	Freq. (GHz)	Bandwidth (MHz)	S11 (dB)	VSWR
1x1	Copper	24.248	348	-20.37	1.21
	Graphene	24.32	0	-10.0	1.96
2x2	Copper	24.288	327	-16.51	1.35
	Graphene	24.28	47	-11.21	1.76
2x4	Copper	24.144	523	-29.58	1.07
	Graphene	24.16	2640	-18.29	1.28
4x4	Copper	24.208	613	-27.43	1.09
	Graphene	24.24	8000	-29.69	1.07

	Conductor	Directivity (dBi)	Angular Width (°)	Gain (dB)	Radiation Eff. (%)
1x1	Copper	6.99	36.1	5.99	79.46
	Graphene	7.21	32.7	2.43	33.29
2x2	Copper	11.51	21.9	10.55	80.09
	Graphene	11.05	22.5	5.18	25.88
2x4	Copper	14.01	22.0	13.12	81.54
	Graphene	13.83	22.7	7.63	23.98
4x4	Copper	16.93	16.6	16.04	81.46
	Graphene	16.68	15.2	8.19	14.15

V. SPICE EQUIVALENT

A Spice equivalent circuit for the 4x4 graphene patch antenna has been obtained using ADS tool and the obtained S11 parameter has been compared with the S11 parameter obtained from CST tool as shown in Figs. 24 and 25. Figure 23 shows the obtained 7 stage RLC ladder circuit with its parametric values and is shown in Table 2. A transfer function representing zeros and poles can be used to define the S11 parameter of the patch and using the transmission line theory, the complete patch can be represented using a [RLGC] matrix and after some optimization using ADS tool, its equivalence can be obtained:

$$H(S)=\sum_{i=1}^{N}\left(\frac{Z_i}{S-P_i}\right)+d. \qquad (27)$$

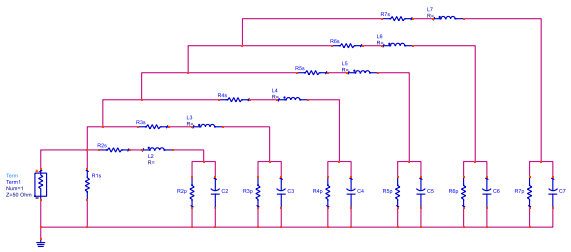

Fig. 23. S11 parameter Spice circuit for 4x4 graphene patch.

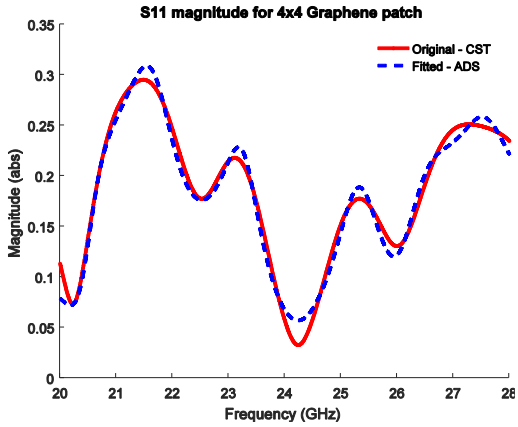

Fig. 24. S11 original and fitted magnitude for Graphene Patch.

Table 2: RLC parameters for the spice circuit

RLC Parameters	Stage 1	Stage 2
R_s(i) (Ω)	61.314446338757	-6859.00485872161
L(i) (nH)		38.1581758308437
C(i) (fF)		0.528633569251257
Rp(i) (kΩ)		10.2896757212470

RLC Parameters	Stage 3
R_s(i) (Ω)	1019.41363184957
L(i) (nH)	11.5125787550172
C(i) (fF)	2.30779927956048
Rp(i) (kΩ)	-5.16417026902054

RLC Parameters	Stage 4	Stage 5
R_s(i) (Ω)	1262.47629042827	2762.15685319658
L(i) (nH)	12.9777407332746	-20.1487936026862
C(i) (fF)	2.76783830152791	-1.20537208494751
Rp(i) (kΩ)	-3.88857348344465	-5.79145334311434

RLC Parameters	Stage 6	Stage 7
R_s(i) (Ω)	-1475.59209098543	-1977.56405676355
L(i) (nH)	12.8363609393114	-13.3267861687389
C(i) (fF)	1.90704567947197	-1.63138998131753
Rp(i) (kΩ)	4.36159370923036	4.35594530526759

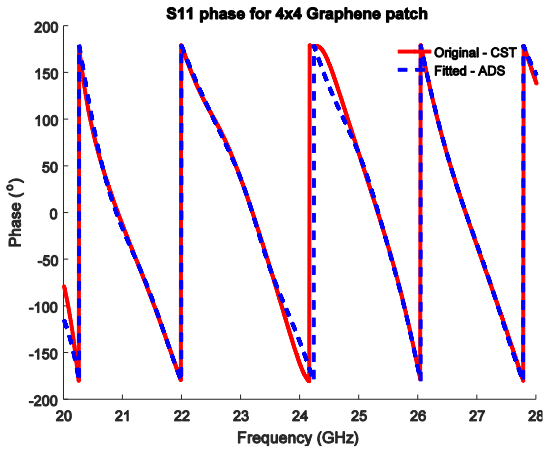

Fig. 25. S11 original and fitted phase for Graphene Patch.

VI. CONCLUSION

Here graphene-based array antenna for the medical and wearable electronics applications and operating at 24 GHz has been proposed and its result has been compared with copper conducting media. The simulation results show that the gain and radiation pattern of the graphene patch antenna compares reasonably well to a conventional copper patch antenna. This shows promising results for the graphene material in the upper GHz frequency range. A Spice equivalence with RLGC parameters of the 4x4 graphene patch for its S11 parameter has been obtained for its inclusion in a traditional spice solver tool and its result has been compared with a 3D field solver result.

ACKNOWLEDGMENT

The author would like to acknowledge the funding and support received from the Department of Engineering, University of Cambridge.

REFERENCES

[1] G. Casu, C. Moraru, and A. Kovacs, "Design and implementation of microstrip patch antenna array," *2014 10th International Conference on Communications (COMM)*, Bucharest, pp. 1-4, Doi: 10.1109/ICComm.2014.6866738, 2014.

[2] N. Ghassemi and K. Wu, "High-efficient patch antenna array for E-band gigabyte point-to-point wireless services," *IEEE Antennas and Wireless Propagation Letters*, vol. 11, pp. 1261-1264, Doi: 10.1109/LAWP.2012.2224087, 2012.

[3] Y. J. Cheng, Y. X. Guo, and Z. Q. Liu, "W-Band large-scale high-gain planar integrated antenna array," *IEEE Transactions on Antennas and Propagation*, vol. 62, pp. 3370-3373, Doi: 10.1109/TAP.2014.2310483, 2014.

[4] J. Kim II, B. M. Lee, and Y. J. Yoon, "Wideband printed dipole antenna for multiple wireless serv-

ices," *Proceedings RAWCON 2001, 2001 IEEE Radio and Wireless Conference (Cat.No.01EX514)*, Waltham, MA, pp. 153-156, Doi: 10.1109/RAWCON. 2001.947575, 2001.

[5] J. D. Kraus, R. J. Marhefka, and A. S. Khan, *Antennas for All Applications*. Tata McGraw-Hill, 3rd ed., New Delhi, ISBN-10: 0-07-060185-2, 2006.

[6] S. N. H. Sa'don, M. R. Kamarudin, F. Ahmad, M. Jusoh, and H. A. Majid, "Graphene array antenna for 5G applications," *Appl. Phys. Mater. Sci. Process*, vol. 123, pp. 1-4, Doi: 10.1007/s00339-016-0749-5, 2017.

[7] M. Donelli and G. Oliveri, "Design of tunable graphene-based antenna arrays for microwave applications," *Proc. IEEE APSURSI*, Memphis, TN, USA, pp. 6-12. Doi: 10.1109/aps.2014.6904782, 2014.

[8] A. K. Geim and K. S. Novoselov, "The rise of graphene," *Nature Mater.*, vol. 6, pp. 183-191, Doi: 10.1038/nmat1849, 2007.

[9] K. S. Novoselov, A. K. Geim, S. V. Morozov, D. Jiang, Y. Zhang, S. V. Dubonos, I. V. Grigorieva, and A. A. Firsov, "Electric field effect in atomically thin carbon films," *Science*, vol. 306, pp. 666-669, Doi: 10.1126/science.1102896, 2004.

[10] R. Song, Q. Wang, B. Mao, Z. Wang, D. Tang, B. Zhang, J. Zhang, C. Liu, D. He, Z. Wu, and S. Mu, "Flexible radio films with high conductivity for radio frequency antennas," *Carbon*, vol. 130, pp. 164-169, Doi: 10.1016/j.carbon.2018.01.019, 2018.

[11] J. H. Warner, F. Schaffel, M. Rummeli, and A. Bachmatiuk, *Graphene Fundamentals and Emergent Applications*. Elsevier, Oxford, 2013.

[12] M. Bozzi, L. Pierantoni, and S. Bellucci, "Applications of graphene at microwave frequencies," *Radioengineering*, vol. 24, pp. 661-669, Doi: 10.13164/ re.2015.0661, 2015.

[13] Q. Zheng and J.-K. Kim, *Graphene for Transparent Conductors: Synthesis, Properties and Applications*, Springer-Verlag, New York, Doi: 10.1007/978-1-4939-2769-2, 2015.

[14] Y. Wang, S. W. Tong, X. F. Xu, B. Ozyilmaz, and K. P. Loh, "Interface engineering of layer-by-layer stacked graphene anodes for high-performance organic solar cells," *Adv. Mater.*, vol. 23, pp. 1514-1518, Doi: 10.1002/adma.201003673, 2011.

[15] R. R. Nair, P. Blake, A. N. Grigorenko, K. S. Novoselov, T. J. Booth, T. Stauber, N. M. R. Peres, and A. K. Geim, "Fine structure constant defines visual transparency of graphene," *Science*, vol. 320, pp. 1308, Doi: 10.1126/science.1156965, 2008.

[16] C. A. Balanis, *Antenna Theory: Analysis and Design*. John Wiley & Sons, New Jersey, USA, 2005.

[17] T. Stauber, N. M. Peres, and A. K. Geim, "Optical conductivity of graphene in the visible region of the spectrum," *Physical Review B*, vol. 78, pp. 085432, Doi: 10.1103/PhysRevB.78.085432, 2008.

[18] S. A. Mikhailov and K. Ziegler, "New electromagnetic mode in graphene," *Physical Review Letters*, vol. 99, pp. 016803, Doi: 10.1103/ PhysRevLett.99.016803, 2007.

[19] G. W. Hanson, "Dyadic Green's functions and guided surface waves for a surface conductivity model of graphene," *J. Appl. Phys.*, vol. 103, pp. 064302, Doi: 10.1063/1.2891452, 2008.

[20] CST Microwave Studio, Computer Simulation Technology, Framingham, MA [online]. http://www.cst.com, 2019.

[21] S. Bae, H. Kim, Y. Lee, X. Xu, J. S. Park, Y. Zheng, J. Balakrishnan, T. Lei, H. R. Kim, Y. I. Song, Y. J. Kim, K. S. Kim, B. Ozyilmaz, J. H. Ahn, B. H. Hong, and S. Iijima, "Roll-to-roll production of 30-inch graphene films for transparent electrodes," *Nat. Nanotechnol.*, vol. 5, pp. 574-578, Doi: 10.1038/nnano.2010.132, 2010.

[22] Y. Huang and K. Boyle, *Antenna from Theory to Practice*. 1st ed., Wiley & Sons Ltd., New Delhi, ISBN: 978-0-470-51028-5, 2006.

[23] J. R. James, P. S. Hall, and C. Wood, *Microstrip Antenna Theory and Design*. Peter Peregrinus Ltd, London, ISBN: 0-86341-088, 1986.

[24] R. J. Mailloux, *Phased Array Antenna Handbook*. 2nd ed., Artech house, Norwood, MA, ISBN: 1-58053-689-1, 2005.

Varindra Kumar has obtained his Bachelor of Engineering in Electronics from National Institute of Technology (Formerly REC) Rourkela and Master of Technology in Electronics and Communication Engineering from Indian Institute of Technology, Varanasi (Formerly IT BHU). Subsequently after working across various electronics design companies, he joined for Ph.D. at the University of Nottingham in EMC Macromodeling. After finishing his Ph.D. in the year 2014, he is working as Postdoc Research Associate at the Department of Engineering, University of Cambridge. His research interest lies in electronics design, microprocessor architecture, sensor design, wearable electronics, electromagnetic and antenna design etc.

A Microstrip Patch Array Antenna with Metal Mesh Structure for Cross Polarization Suppression

Qingjun Zhang

China Academy of Space Technology, Beijing, 100089, China
ztzhangqj@163.com

Abstract ─ A 1×4 microstrip patch array antenna is presented for Ku-band radar systems. A metal mesh structure working as a polarizing filter (twist reflector) is employed to reduce the cross-polarization of the antenna. The metal mesh structure is simple and easy to be printed on a commercial substrate. The proposed antenna has been designed and analyzed by using commercially available software – Computer Simulation Technology Microwave Studio (CST MWS), which is based on the finite-difference-time-domain algorithm. A prototype antenna is built and tested. The return loss has been compared between measured and simulated data under the criterion of VSWR less than 2 throughout the designed 14.9 to 15.1 GHz frequency range. The cross-polarization levels in both E and H planes are better than -21 dB, with fair regular radiation patterns.

Index Terms ─ Cross polarization, metal mesh, microstrip antenna, patch array.

I. INTRODUCTION

Microstrip patch radiators are widely used due to their compact size, low-profile, low-weight, low-cost, easy integrability into arrays or with microwave integrated circuits [1, 2]. An array of these elements is commonly employed in order to meet required specific applications, such as wider bandwidth, lower sidelobes, and higher power [3–5].

In microstrip patch array design, stacked patches (including parasitic elements and low-loss substrates) and aperture coupled patches are usually considered capable of enhancing the antenna performance. However, the stacked patches will increase antenna layers. Increased layers will lead to the antenna further thickness and fabrication errors. In the aperture-coupled patch antenna, ground plane is above the feed line, a parallel plate mode between the back plate and the ground plane will be excited [6].

In this paper, a novel low-cost 1×4 microstrip patch array antenna is presented. The antenna is easy to be fabricated and the whole structure is low-profile. A simple coplanar patch array antenna is designed on a single layer substrate. The radiation and reflection characteristics of the coplanar patch array are calculated. The return loss of the coplanar patch array is low, but the cross-polarization is high. In order to discriminate the cross-polarization, a metal mesh structure which is a twist reflector is employed. The principle of twist reflector is presented in Section II. Section III describes the antenna design procedure. A detailed description of the simulation and measurement results are explained in Section IV followed by the conclusion drawn in Section V.

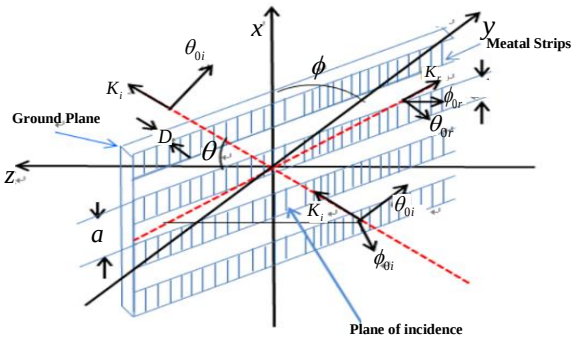

Fig. 1. Geometry of twist reflector for arbitrary plane wave incidence.

II. PRINCPLE OF TWIST REFLECTOR

The twist reflector is made up of a unidirectional periodic metallic grating approximately a quarter wavelength above a conducting ground plane [7]. The geometry of the twist reflector for arbitrary angle and plane of incidence is shown in Fig. 1. It is assumed that the grating is planar, periodic in *x* direction and uniform in the *y* direction.

The angle of incidence θ is depicted in Fig. 1 as the angle between k_i and *z*. The reflected angle is π-θ. The plane of incidence makes angle φ with *x*-axis:

$$k_z = j(k' - jk''), \tag{1}$$

where $k' = \omega\sqrt{\mu'\epsilon'}$, $k'' = \frac{1}{2}\omega\sqrt{\mu'/\epsilon'} \times \epsilon''$, $\tan\delta = \epsilon''/\epsilon'$, $\omega = 2\pi f$. f is the frequency of operation, δ is dielectric loss angle, μ', ϵ', and ϵ'' are the permeability, permitivity and loss factor of the material respectively.

The equivalent circuits applicable to both the strip grating and parallel plate twist reflectors is given in [7].

Submitted On: February 12, 2018
Accepted On: February 21, 2019

In the *E*-type mode, the circuits consists of an inductive reactance (X_L'), and in the *H*-type mode, a capacitive susceptance (B_c'') is included. Considerate the loss factor, the modal reflection coefficients of *E*-type (Γ') and *H*-type (Γ'') modes given in [7] are modified as [8]:

$$\Gamma' = \frac{jX_L' \frac{Z_\varepsilon'}{Z'} \tanh\left(k_z D\right) - \frac{Z_\varepsilon'}{Z'} \tanh\left(k_z D\right) - X_L'}{jX_L' \frac{Z_\varepsilon'}{Z'} \tanh\left(k_z D\right) + \frac{Z_\varepsilon'}{Z'} \tanh\left(k_z D\right) + X_L'}, \quad (2)$$

$$\Gamma'' = \frac{1 - j\left(B_c'' - \frac{Y_\varepsilon''}{Y} \coth\left(k_z D\right)\right)}{1 + j\left(B_c'' - \frac{Y_\varepsilon''}{Y} \coth\left(k_z D\right)\right)}. \quad (3)$$

Assumed the incident field $E_{\theta i}$=1 and $E_{\varphi i}$=0, the cross-polarization suppression ratio for 90° polarization rotation after reflection, which is defined as the ratio of field in the undesired polarization after reflection to the incident filed is given by [7]:

$$E_{\theta r} = \frac{-\Gamma' \cos^2\phi \cos^2\theta}{1 - \sin^2\phi \sin^2\theta}\left(\tan^2\phi + \frac{\Gamma''}{\Gamma'} \sec^2\theta\right), \quad (4)$$

$$E_{\phi r} = \frac{\Gamma' \sin\phi \cos\phi \cos\theta}{1 - \sin^2\phi \sin^2\theta}\left(1 - \frac{\Gamma''}{\Gamma'}\right). \quad (5)$$

If the material is lossless, the two conditions for perfect conversion of $E_{\theta r}$ into $E_{\varphi r}$ are:

$$\Gamma''/\Gamma' = 1 \quad \text{electrical}, \quad (6)$$

$$\tan\phi = \sec\theta \quad \text{geometrical}. \quad (7)$$

The important parameters in the twist reflector design are dielectric material, copper strip width, periodicity of the grating and thickness of the substrate material [8].

III. ANTENNA DESIGN PROCEDURE

A. Coplanar patch array antenna

In this section, a coplanar patch array antenna with power divider network is proposed. The geometry of the 1 × 4 array is shown in Fig. 2. The antenna array is employed to increase the antenna gain. The equal power distributed network is printed on the same plane. The antenna is fed by copper cable. Four patch elements and power divider network are printed on a 1-mm-thick Rogers RT/duroid 5880 substrate (ε_r = 2.2, tanδ = 0.0009). The parameters of the antenna dimensions are optimized according to impedance bandwidth, and radiation requirements.

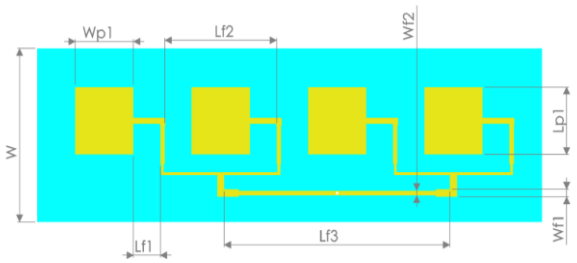

Fig. 2. Geometry of the coplanar patch array antenna.

The simulated return loss of the coplanar array antenna is shown in Fig. 3. The return loss is less than -10 dB in 14.8GHz-15.2 GHz. At 15GHz, the return loss is -23dB.

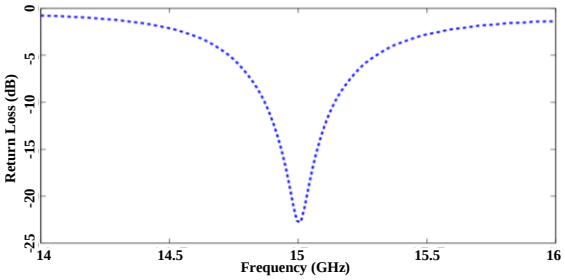

Fig. 3. Simulated return loss of the coplanar patch array antenna.

The co-polarizations lower than -10 dB from 14.9 to 15.1 GHz, the cross polarizations are higher than -8 dB, as shown in Fig. 4. To overcome this disadvantage, a metal strip structure is employed subsequently.

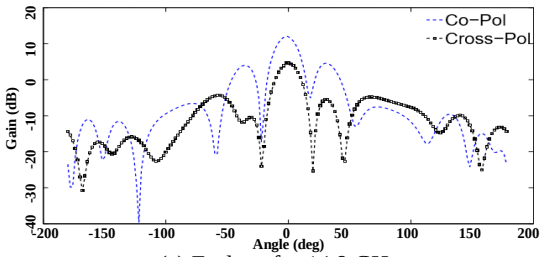

(a) E-plane for 14.9 GHz

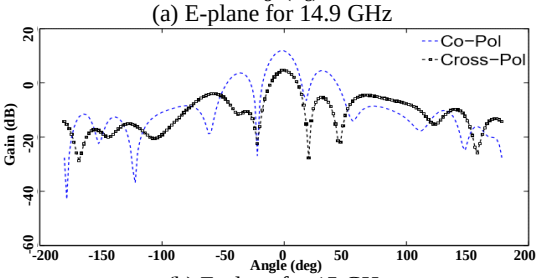

(b) E-plane for 15 GHz

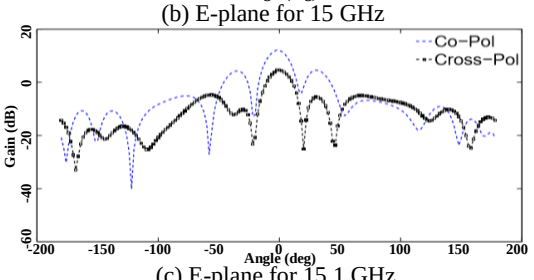

(c) E-plane for 15.1 GHz

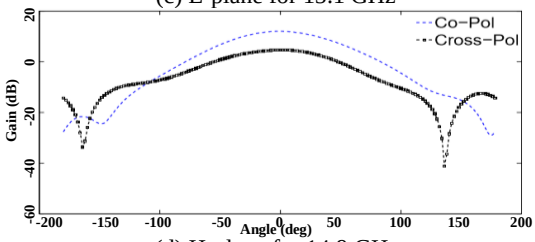

(d) H-plane for 14.9 GHz

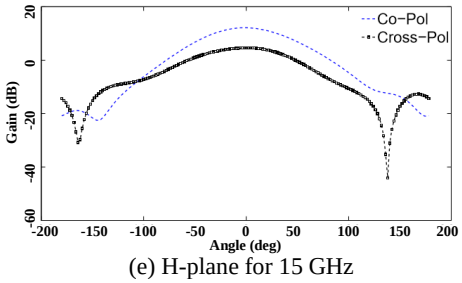

(e) H-plane for 15 GHz

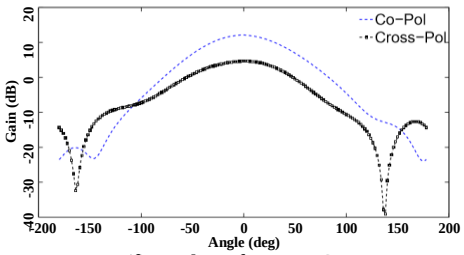

(f) H-plane for 15.1 GHz

Fig. 4. Simulated radiation patterns in the E-plane of the coplanar patch array antenna for: (a) 14.9 GHz, (b) 15 GHz, (c) 15.1 GHz, as well as in the H-plane for (d) 14.9 GHz, (e) 15 GHz, and (f) 15.1 GHz.

B. Patch array with metal mesh structure

The basic geometry of the novel array proposed is shown in Fig. 5, which introduces a metal mesh structure printed on a commercial FR4 substrate.

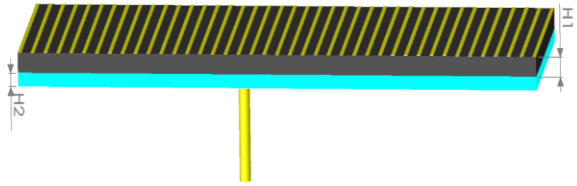

(a) Whole structure of the patch array antenna with a metal mesh

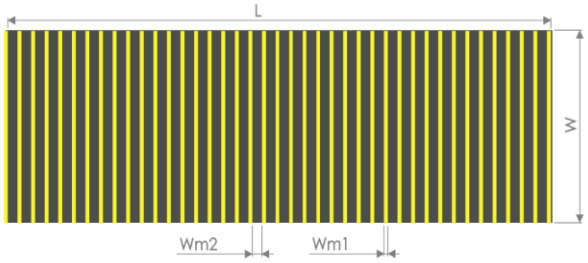

(b) Top structure of the proposed antenna

Fig. 5. Configuration of the patch array antenna with a metal mesh.

In order to simplify the antenna fabrication process, the antenna is separated into two parts: bottom part (the same as Fig. 5 (a)) and top part (as shown in Fig. 5 (b)). The same as the antenna described above, four patch elements and power divider network are printed on a 1-mm-thick Rogers RT/duroid 5880 substrate. Different from the coplanar patch array, there is a metal strip structure discriminating the cross-polarization. The metal strip is printed on a 1.5-mm-thick FR4 substrate (ε_r = 4.8, tanδ = 0.016), which is low-cost and used widely in industry or commerce.

IV. ANTENNA PERFORMANCE

The performance of the antenna is studied numerically and verified experimentally. The numerical results are obtained by using CST MWS based on the finite-difference-time-domain algorithm. The dual-polarized antenna configuration finally selected has the following dimensions: L = 56.5 mm, W = 18 mm, Wp1 = 6.5 mm, Lp1 = 7 mm, Wf1 = 0.8 mm, Wf2 =0.5 mm, Lf1 = 3 mm, Lf2 = 12.5 mm, Lf3 = 25.2 mm, Wm1 = 0.4 mm, Wm2 = 1 mm.

The antenna discussed above has been realized, and a photograph of the antenna is shown in Fig. 6. The S-parameter measurements are carried out with Agilent E8362B vector network analyzer (VNA). The simulated and measured reflection characteristics of the antenna are shown in Fig. 7. The proposed antenna offers a bandwidth from 14.9 to 15.1 GHz for 2:1 VSWR.

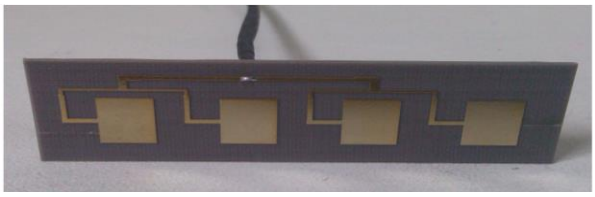

(a) Coplanar patch array antenna

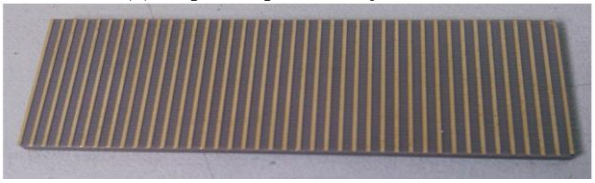

(b) Metal mesh

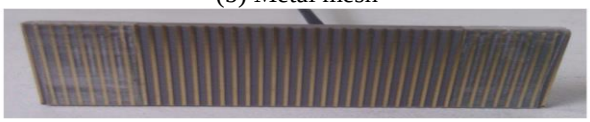

(c) Patch array with a metal mesh structure

Fig. 6. Photographs of the designed antenna.

Antenna radiation performance is measured and recorded in two orthogonal principal planes (E-plane and H-plane). The pattern is plotted in the form of rectangular coordinates. The radiation characteristics of the proposed antenna in E and H principal planes for both ports are shown in Fig. 8. Generally, agreement between the measurement and simulation results are good for both co-polar and cross-polar components. The slight

deviations may be manufacturing inaccuracies.

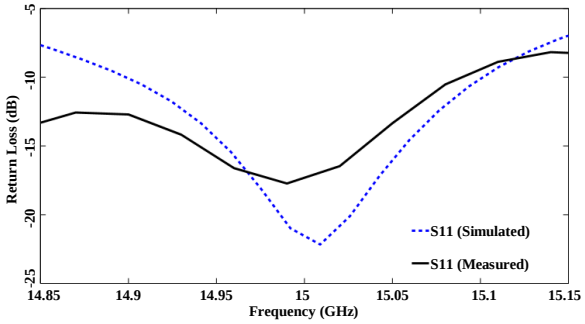

Fig. 7. Simulated and measured return loss of the patch array antenna with a metal mesh structure.

As illustrated in Fig. 8, the cross polarizations are reduced more than 13 dB. The proposed antenna exhibits cross-polar discrimination of better than -21 dB along the boresight direction.

The measured half power beam width in the E plane are wider than 20°, and those are wider than 72° in the H plane. The measured gains of the proposed antenna are higher than 5.8 dBi throughout the designed frequency.

V. CONCLUSION

A novel patch array antenna has been designed, fabricated, and tested. The cross polarizations significantly discriminated when a metal strip structure is employed. The whole structure is compact, low-profile, and can be easily arranged in larger arrays. Promising features make it a potential candidate for *Ku*-band radar systems.

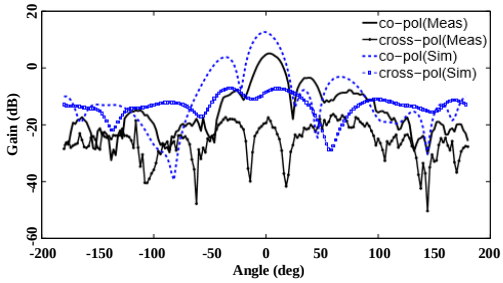

(a) E-plane at 14.9 GHz

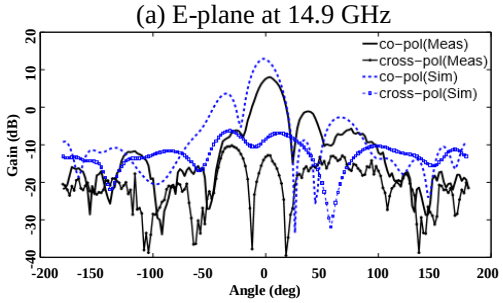

(b) E-plane at 15 GHz

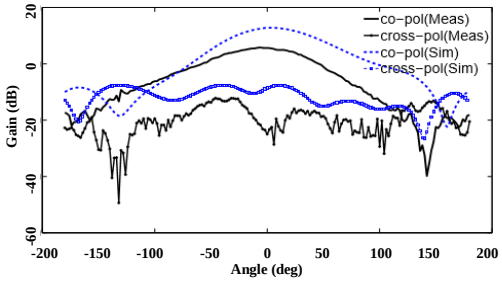

(c) E-plane at 15.1 GHz

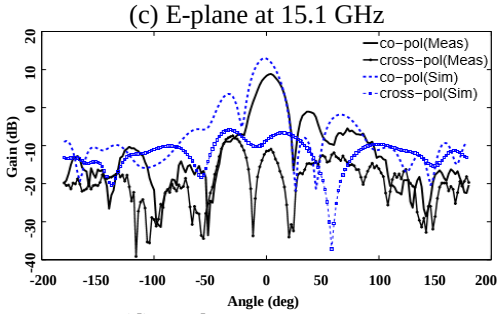

(d) H-plane at 14.9 GHz

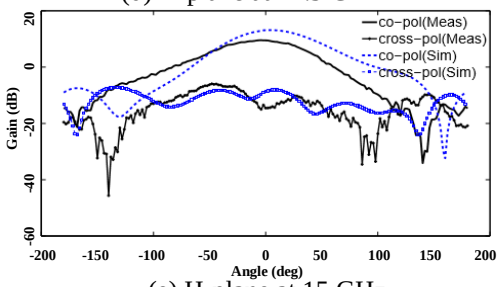

(e) H-plane at 15 GHz

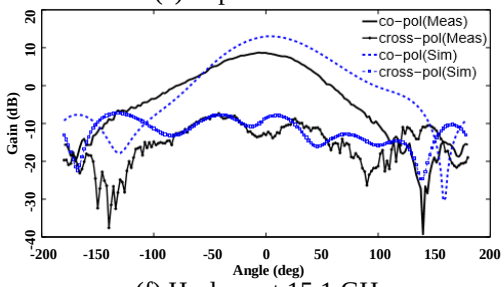

(f) H-plane at 15.1 GHz

Fig. 8. Simulated (blue dashed) and measured (black solid) radiation patterns of the patch array antenna with a metal mesh.

ACKNOWLEDGMENT

This work is supported by the Ministry of Equipment Development of the Central Military Commission of China (Grant No. 6140415010305) and the National Key R&D Program of China (2017YFB0502900).

REFERENCES

[1] K. R. Carver and J. Mink, "Microstrip antenna technology," *IEEE Transactions on Antennas and*

Propagation, vol. 29, no. 1, pp. 2-24, 1981. A. Z. Elsherbeni, *FDTD Course Notes*, Department of Electrical Engineering, The University of Mississippi, MS, Spring 2001.

[2] D. M. Pozar, "Microstrip antennas," *Proceedings of the IEEE*, vol. 80, no. 1, pp. 79-91, 1992.

[3] C. Van Coevorden, S. G. Garcia, M. F. Pantoja, A. R. Bretones, and R. G. Martin, "Microstrip-patch array design using a multiobjective ga," *IEEE Antennas Wireless Propag. Lett*., vol. 4, no. 1, pp. 100-103, 2005.

[4] R. J. Mailloux, J. F. McIlvenna, and N. P. Kernweis, "Microstrip array technology," *IEEE Transactions on Antennas and Propagation*, vol. 29, pp. 25-37, 1981.

[5] H. D. Chen, C. Y. D. Sim, J. Y. Wu, and T. W. Chiu, "Broadband high-gain microstrip array antennas for wimax base station," *IEEE Transactions on Antennas and Propagation*, vol. 60, no. 8, pp. 3977-3980, 2012.

[6] D. Sun, W. Dou, and L. You, "Application of novel cavity-backed proximity-coupled microstrip patch antenna to design broadband conformal phased array," *Antennas and Wireless Propagation Letters, IEEE*, vol. 9, pp. 1010-1013, 2010.

[7] J. D. Hanfling, G. Jerinic, and L. R. Lewis, "Twist reflector design using e-type and h-type modes," *IEEE Transactions on Antennas and Propagation*, vol. 29, no. 4, pp. 622-629, 1981.

[8] V. Borkar, V. Pandharipande, and R. Ethiraj, "Millimeter wave twist reflector design aspects," *IEEE Transactions on Antennas and Propagation*, vol. 40, no. 11, pp. 1423-1426, 1992.

Qingjun Zhang was born in 1969. He received B.E. and M.E. degrees from North China Electric Power University in 1986 and 1990, respectively. He is the Deputy Chief Designer of Manned Spacecraft, and Chief Designer and Director of Resource Series Satellite at the China Academy of Space Technology. He focuses his academic interests on remote-sensing image fusion, manned space-crafts, microwave remote sensing and spacecraft system.

Ultra-Wideband Six-port Network Constructed by 90° and In-Phase Power Dividers

Norhudah Seman [1*], Khairul Huda Yusof [2], Mohd Haizal Jamaluddin [1], and Tharek Abd Rahman [1]

[1] Wireless Communication Centre, School of Electrical Engineering
University Teknologi Malaysia, 81310 UTM Johor Bahru, Johor, Malaysia
huda@fke.utm.my, haizal@fke.utm.my, tharek@fke.utm.my

[2] Faculty of Engineering and Information Technology, MAHSA University, 42610 Jenjarom, Selangor, Malaysia
khairulhuda@mahsa.edu.my

Abstract ─ This article proposes a six-port network design with an ultra-wideband operation from 3.1 to 10.6 GHz. The proposed six-port configuration is constructed by two types of power dividers with different phase characteristics of 0° (in-phase) and 90°. The new proposed configuration eliminates one unused port of the conventional six-port. Both components forming the proposed six-port are designed utilizing the microstrip-slot technique to accomplish the designated UWB operating frequency. The six-port is designed via the use of CST Microwave Studio (CST MWS) and realised by applying Rogers TMM4 substrate. Comparable simulated and measured performances are achieved in terms of S-parameters and phase differences between each consecutive port across UWB frequency range.

Index Terms ─ Microstrip-slot, power divider, six-port, ultra-wideband.

I. INTRODUCTION

Nowadays, an intense growth in the number of mobile broadband service subscribers is noted every year. There is an increasing demand for mobile and faster Internet access, instant communication with others, immediate access to information and advanced multimedia, and latest trendy wireless mobile devices such as smartphones and tablets. Hence, the designers and engineers are facing endlessly requirement of new wireless devices and applications for mobility and high data rate. Attributable to the demand, the fifth-generation (5G) wireless system that anticipated being deployed by 2020 is extensively studied. 5G will realise network capability of providing zero-distance connectivity between people and connected machines. The architecture of new 5G technologies has a separated solution for the applications in indoor and outdoor. Particularly for applications in indoor, the architecture applies a distributed antenna system (DAS) solution, while for outdoor, massive multiple-input multiple-output (MIMO) technology is utilized [1]. Therefore, high-data-rate and high-quality services to indoor users can be offered, whilst simultaneously lessening the pressure on outdoor applications. In order to fulfill this necessity, numerous researches are conducted in the designs of front-end components such as a complementary option to the mixer. Commonly, the mixer design utilizes active devices that require a biasing circuit that causes design complexity. This mixer-based approach in the front-end communication transceiver can be replaced by using a six-port network to reduce the complexity. Similar to the mixer, six-port can operate as a modulator and demodulator [2]-[4]. This alternative architecture of the six-port network does not require any use of active devices, which eliminates the existence of intermediate frequency (IF) and the image produced by the mixer. Consequently, the high price-tag IF filter and image rejection filter are not required in the design [5]. Therefore, with the use of the six-port network in the transceiver system, the complexity of the circuit can be reduced and allows easier circuit integration with other components.

Various design techniques have been studied to realise a wideband six-port. Such as in [6], a compact six-port design is proposed, which comprises four 90° hybrid rounded couplers. This six-port has a bandwidth of 570 MHz, which operates from 1.68 to 2.25 GHz. The design is realised using Rogers 3006 substrate with a size of 65 x 65 mm^2. A smaller size of a six-port network is proposed in [7] with a 55 x 61 mm^2 that composed by one Wilkinson power divider and three miniaturized 90° hybrid couplers. In the proposed design, four transmission lines, which utilizes two high-low impedance shunt stubs have been introduced to the designed power divider and 90° hybrid coupler in order to reduce six-port size. It has

Submitted On: May 21, 2017
Accepted On: December 24, 2018

a fairly good performance across a frequency band of 2.2-2.6 GHz, which narrower than [6]. Meanwhile in [8], another design of six-port network for a reflection coefficient measurement purpose has been reported, which contains a Wilkinson power divider, four coupled-line couplers and a section of a transmission line. Its performance is experimentally verified across a frequency range of 2-3.5 GHz.

However, the six-port networks proposed in [4]-[8] have limited bandwidth, which may be inapplicable in applications that require a wider band. Thus, considering this bandwidth limitation, a wideband six-port network is proposed by Ibrahim et. al in [9] by integrating four quadrature and in-phase Wilkinson dividers. In this proposed design, the quadrature Wilkinson divider has a phase difference of 90° between its two output ports, which obtained through the implementation of a 90° phase shifter at one of the output ports. Furthermore, the configuration used in this design has eliminated one unused port that contributes to lessening error. Despite that, its performance only covers from 3 to 8 GHz. As known, the more components used, the more transmission lines are required that leads to higher losses as the signals have to go through many transmission lines. Another technique to increase bandwidth is by using the multilayer technique [2]. In [2], the proposed six-port is constructed by using three tight coupling rectangular-shaped couplers with virtual stubs and an in-phase power divider with equal power division. Multilayer microstrip-slot design technique is used in the proposed six-port to enhance the operating frequency. It has demonstrated agreeable simulated and measured across 2-6 GHz with small dimension size of 54 mm x 62 mm. The use of two substrates in this multilayer structure of six-port may lead to difficulty in fabrication, which experiencing problems of an air gap and misalignment. Even though the performances proposed in [2] and [9] are wider, but still not covering the desired UWB frequency range.

Thus, to overcome the problems in [2], [4]-[9], a new six-port network design that can operate over the UWB frequency range is essential to be proposed. Each of the components constituting the proposed six-port is designed by implementing the microstrip-slot technique. The design applies Rogers TMM4 substrate that has 4.5 relative permittivity, 0.002 loss tangent, 35 µm conductor coating and 0.508 mm substrate thickness.

II. SIX-PORT NETWORK DESIGN

The new design six-port network is having a configuration that integrates three in-phase power dividers (D), which two of them are connected to three 90° power dividers (90° D) as presented in Fig. 1. Moreover, it can be noted from Fig. 1, the input ports of the six-port network are labeled as P1 and P2, meanwhile the output ports as P3, P4, P5 and P6. This new configuration eliminates one unused port of conventional six-port configuration that requires matched termination as presented in [2], [3] and [7].

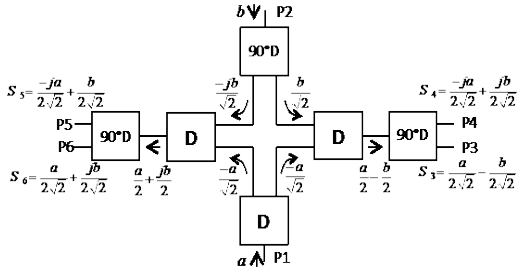

Fig. 1. The block diagram of the proposed six-port configuration.

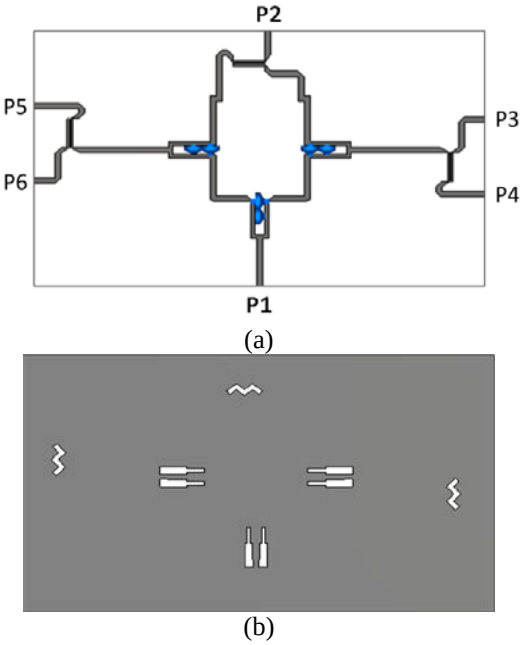

Fig. 2. The layout view of (a) top and (b) bottom layer of the proposed six-port network.

As presented by the configuration in Fig. 1, the proposed six-port has four output signals at its respective output ports of P3 to P6, which are denoted as S_i. i are referring to the output ports, which can be derived as follows:

$$S_3 = \frac{a}{2\sqrt{2}} - \frac{b}{2\sqrt{2}}, \tag{1}$$

$$S_4 = -j\frac{a}{2\sqrt{2}} + j\frac{b}{2\sqrt{2}}, \tag{2}$$

$$S_5 = -j\frac{a}{2\sqrt{2}} + \frac{b}{2\sqrt{2}}, \tag{3}$$

$$S_6 = \frac{a}{2\sqrt{2}} + j\frac{b}{2\sqrt{2}}, \tag{4}$$

where the input signals are denoted by the variable a

and *b* at the respective Port 1 (P1) and Port 2 (P2). Meanwhile, the symbol of '*j*' implies a phase shift or delay by 90° of the complex signal. The design and simulation of the UWB six-port network are concerning the centre frequency of 6.85 GHz with a designated range of 3.1-10.6 GHz, which performed by employing CST Microwave Studio (CST MWS). The CST MWS generated layout of the proposed six-port network is presented in Fig. 2.

A. In-phase power divider (D)

The layout of the power divider with equal power division and 0° phase difference (in-phase) between its output ports that used in the construction of the six-port network and its fabricated prototype are depicted in the respective Figs. 3 and 4. The design comprises of the top conductive layer, which has microstrip lines that linked to three designated ports of Ports 1 to 3 (P1 – P3). Whilst at the ground plane, there are two rectangular-shaped slots that placed symmetrically beneath microstrip lines of output arms. The transmission line of microstrip with a slot underneath is also branded by term 'microstrip-slot' [10]. These microstrip-slot lines with the characteristic impedance of Z_1 (84.09 ohm) and Z_2 (59.46 ohm) form two-section quarter-wave transformers to achieve the bandwidth specification. Two resistors, R_1 (130 ohm) and R_2 (200 ohm) are positioned at the end of each quarter-wave transformer section to ensure good isolation is achieved between output ports, and any reflected power is dissipated at wider frequency range.

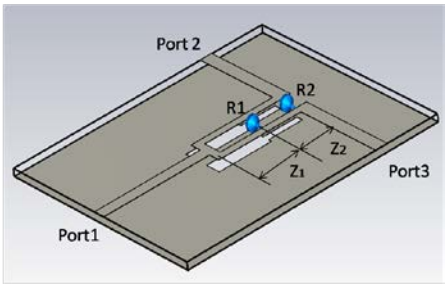

Fig. 3. The in-phase power divider layout in its perspective view.

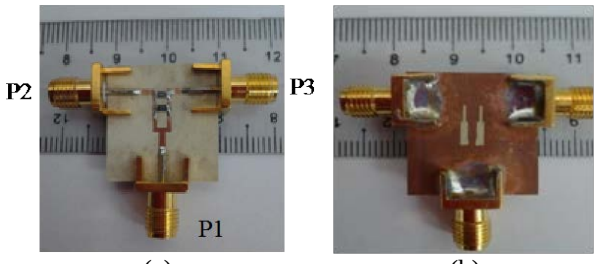

(a) (b)

Fig. 4. (a) Top and (b) bottom view of the fabricated power divider.

This two-section power divider has a UWB operation within 3.1 to 10. 6 GHz demonstrated by the presented results of simulation and measurement in Fig. 5. As demonstrated in Fig. 5 (a), it is noted that the results of S_{21} and S_{31} for simulation and measurement are showing an almost similar performance of -3.55 ± 0.15 dB and -3.8 ± 0.5 dB across 3 to 11 GHz, accordingly. Meanwhile, the simulation and measurement results of S_{11} and S_{23} are less than -10 dB. Furthermore, the simulation result for the phase characteristic is 0° ± 0.2° between Ports 2 and 3 as shown in Fig. 5 (b). While the measurement result is showing a comparable performance with a slight degradation of 0° ± 2° across 3.1 to 10.6 GHz. This observed degradation could be due to the small difference in transmission lines' lengths of the fabricated prototype compared the simulated design, which occurred normally.

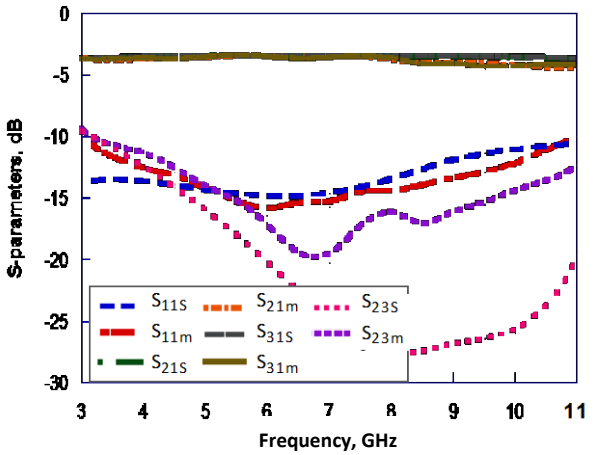

(a)

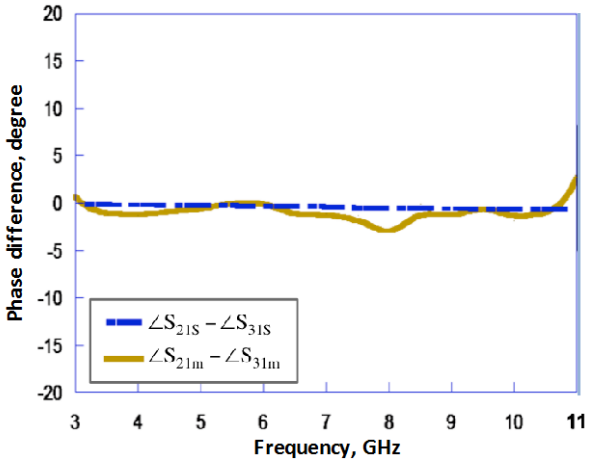

(b)

Fig. 5. The performance of (a) S-parameter characteristics and (b) phase difference between Ports 2 and 3 of the power divider (notation 's' and 'm' are referring to the respective simulation and measurement).

By implementing the rectangular-shaped slot underneath microstrip line to construct the quarter-wave transformer into the design of the power divider, the quarter-wave transformer length can be reduced to 4.153 mm, which equivalent to $\lambda_{m\text{-}s}/4$ [10]. This is due to the defection in the ground layer, which interrupts the current distribution. Subsequently, increase the effective inductance and capacitance of the microstrip line [11-12]. This contributes to reducing the size of the power divider circuit up to 23.33%. In addition to that, the bandwidth performance has been improved up to 11.9% compared to the conventional two-section power divider as described in [13]. Furthermore, it can be noted that it exhibits a good relative agreement between simulation and measurement result, which guarantee a wideband operation of the proposed six-port network.

B. 90º power divider (90º D)

Figures 6 and 7 illustrate the respective layout and prototype of the 90° power divider that used to form the proposed six-port network, that is attained via the removal of the coupled-line coupler's isolated port, which proposed in [14]. This design comprises of a microstrip coupled-line with a zig-zag-shaped slotline beneath that has an effective quarter-wavelength. Therefore, this divider has an equal power division and the phase difference of 90° between its output ports. The implementation of the zig-zag slot provides a slower phase velocity, which increases the length of the current path, that consequently reduces the total physical length of the divider [14-15].

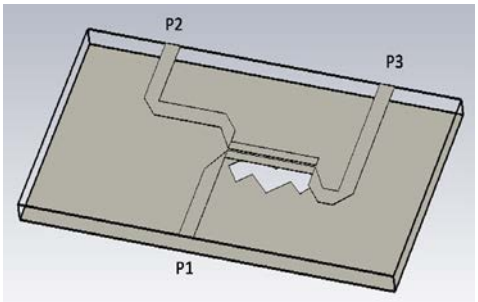

Fig. 6. The layout of the 90° power divider in its perspective view.

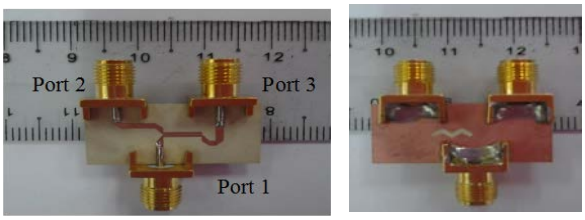

(a) (b)

Fig. 7. The fabricated 90° power divider: (a) top and (b) bottom view.

As shown in Fig. 8, the divider operates well at UWB frequency range, verified by both simulation and measurement results. The simulated and measured S_{11} and S_{41} are less than -10 dB across 3.1 to 10.6 GHz. Whilst, both transmission coefficient results of S_{21} and S_{31} are approximately at -3 dB. In addition, Fig. 8 (b) shows the phase characteristic performance of the 90° power divider, where, both simulated and measured phase differences are -90° ± 5°. Thus, a comparable simulation and measurement results can be observed. Therefore, this divider with very well UWB performance suits to be applied in the proposed six-port formation, which has the configuration as shown in Fig. 1.

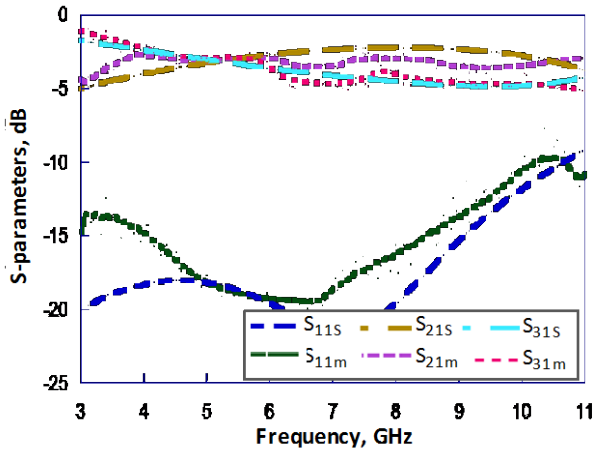

(a)

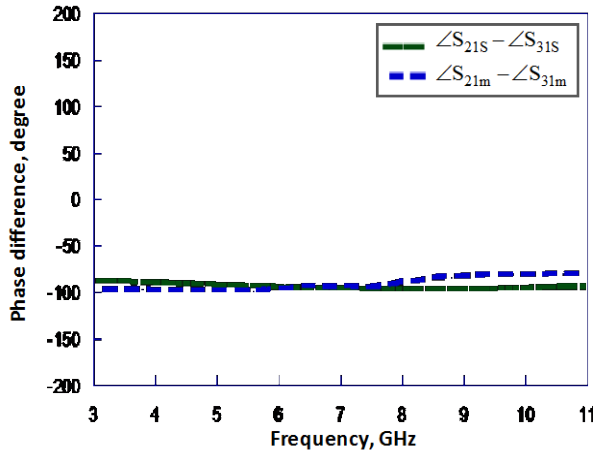

(b)

Fig. 8. The simulated and measured (a) S-parameters and (b) phase characteristic of the 90º power divider (notation 's' and 'm' are referring to the respective simulation and measurement).

III. THE FABRICATED SIX-PORT NETWORK AND ITS PERFORMANCE

The fabricated of the proposed UWB six-port network forming by in-phase power dividers and 90°

power dividers is presented in Fig. 9. The proposed six-port is fabricated onto Rogers TMM4 substrate with 4.5 mm relative permittivity, 0.002 loss tangent, 35 µm conductor coating and 0.508 mm substrate thickness. This six-port network has a dimensional size of 81.7 x 50.92 mm^2.

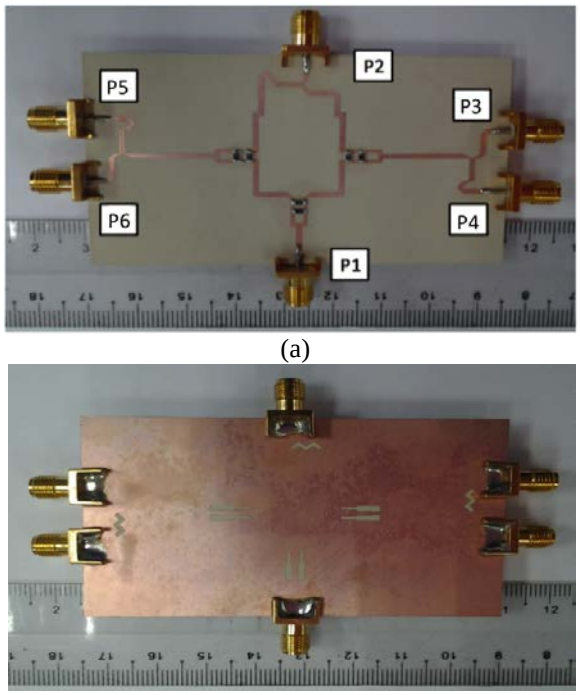

(a)

(b)

Fig. 9. The fabricated UWB six-port network: (a) top and (b) bottom view.

Figure 10 shows the simulation and measurement performance of the proposed six-port network. Both simulation and measurement performance are assessed considering S-parameters and phase differences between each consecutive port. First, the performance of transmission coefficients, S_{ij}, where i = 3, 4, 5, 6 and j = 1, 2 are evaluated. The simulated transmission coefficients of S_{i1} have the performance of -9 dB ± 3 dB within 3.1 and 10.6 GHz. While, the measured transmission coefficients of S_{i1} show a comparable performance of -9 dB ± 4 dB, except S_{41} with -13.5 dB ± 2.5 dB. Meanwhile, the simulated and transmission coefficients of S_{i2} perform the respective -11 dB ± 4 dB, and -13.5 dB ± 3 dB from 3.1 to 10.6 GHz. The shown deviation is expected to be observed from the ideal value of -9 dB ($|S_{i1}| = |S_{i2}| = \frac{1}{2\sqrt{2}}$), which contributed from the individual imperfect performance of the in-phase power divider and 90° power divider. Furthermore, the microstrip lines used to connect the components are also contributing to the losses that lead to the observed deviation.

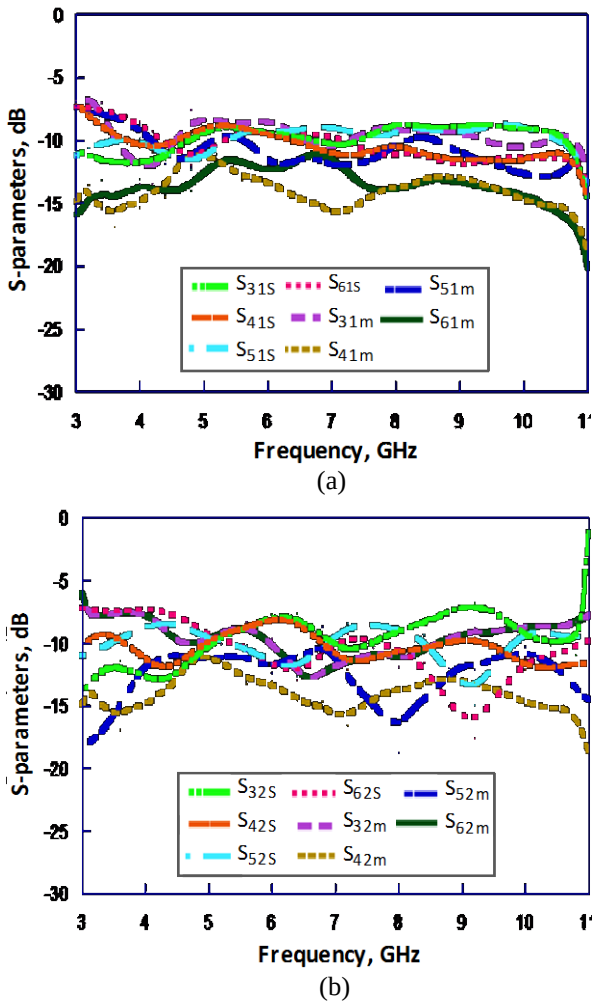

(a)

(b)

Fig. 10. The S-parameter performance of proposed six-port network: (a) transmission coefficients of S_{i1}, and (b) transmission coefficients of S_{i2} (notation 's' and 'm' are referring to the respective simulation and measurement).

Then, the next concern is to evaluate the simulated and measured the performance of return loss at Port 1 and Port 2. From the observation, both demonstrate quite similar performances that exceed 10 dB across 3.1 to 10.6 GHz, as plotted in Fig. 11. Meanwhile, the simulation and measurement performance of isolation between Ports 1 and 2 also have comparable performance, where both are greater than 10 dB across the similar frequency range of UWB.

The next assessment concerns the simulation and measurement of the six-port network's phase differences, which plotted in Fig. 12. The simulated and measured phase differences between Ports 3 and 4 are approximately at 90° ± 13° and 90° ± 17° over the designated operating frequency of 3.1–10.6 GHz, accordingly. While similar simulated and measured deviations of the respective ± 13° and ± 17° are noted from the ideal phase difference

between Port 5 and Port 6 of -90°.

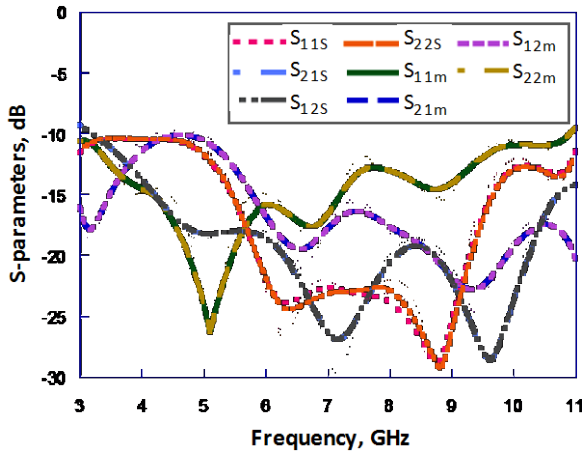

Fig. 11. The reflection coefficient and isolation performance of proposed six-port network (notation 's' and 'm' are referring to the respective simulation and measurement).

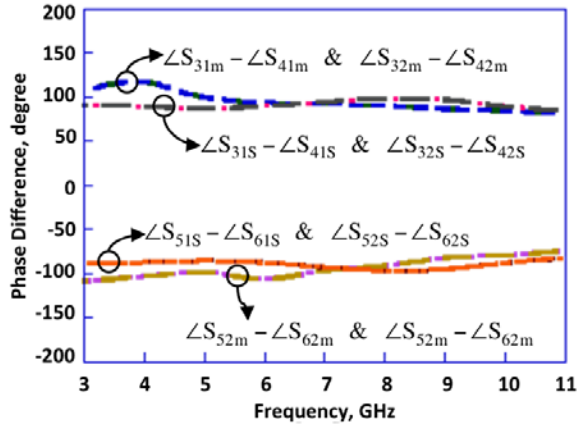

Fig. 12. The reflection coefficient and isolation performance of proposed six-port network (notation 's' and 'm' are referring to the respective simulation and measurement).

IV. CONCLUSION

This article has proposed a six-port network design with a capability of ultra-wideband (UWB) operation. The new proposed configuration of the six-port network is constructed by six 3-dB power dividers; three 90° dividers and three 0° (in-phase) dividers, which has been presented utilizing electromagnetic (EM) simulator of CST MWS. This configuration has removed one unused port in the conventional six-port configuration reported in [2] and [7]. Moreover, this six-port has accomplished a good UWB performance between simulation and measurement within operating frequency of 3.1 and 10.6 GHz with 81.7 x 50.92 mm^2 overall dimensional size. Consequently, it has the best phase characteristic with the measured phase imbalance of ± 17° compared to the designs reported in [2] and [9], which are ± 29°, and ± 25°, accordingly. The bandwidth performance of proposed six-port has been increased up to 50% and 87.5% compared to the respective design in [9] and [2]. This improvement has been achieved due to the use of microstrip-slot in the design of individual components forming the six-port, which are 90° dividers and in-phase two-section power dividers.

ACKNOWLEDGMENT

This work is carried out with the financial support from the Malaysian Ministry of Education (MOE) and Universiti Teknologi Malaysia (UTM) via GUP, Flagship, HiCoE, PRGS and FRGS Grant with the respective vote number of 05H43, 03G41, 4J212, 4L684 and 5F048.

REFERENCES

[1] C.-X. Wang, F. Haider, X. Gao, et al., "Cellular architecture and key technologies for 5G wireless communication networks," *IEEE Commun. Mag.*, vol. 52, no. 2, pp. 122-130, Feb. 2014.

[2] N. Seman and S. N. A. M. Ghazali, "Quadrature phase shift keying (QPSK) modulator design using multi-port network in multilayer microstrip-slot technology for wireless communication applications," *Radioengineering*, vol. 24, no. 2, pp. 527-534, June 2015.

[3] N. Seman and M. E. Bialkowski, "Design of a UWB microwave reflectometer with the use of a microstrip-slot technique," *Microw. Opt. Technol. Lett.*, vol. 51, no. 9, pp. 2169-2175, June 2009.

[4] S. O. Tatu, E. Moldovan, K. Wu, and R. G. Bosisio, "A new direct millimeter-wave six-port receiver," *IEEE Trans. Microw. Theory Tech.*, vol. 49 no. 12, pp. 2517-2522, May 2001.

[5] H.-S. Lim, W.-K. Kim, J.-W. Yo, H.-C. Park, W.-J. Byun, and M.-S. Song, "Compact six-port transceiver for time-division duplex system," *IEEE Microw. Wirel. Compon. Lett.*, vol. 17, no. 5, pp. 2766-2772, May 2007.

[6] R. Hussain and M. S. Sharawi, "A dual six-port with two-angle resolution and compact size for mobile terminals," *IEEE Radio and Wireless Symp.*, Long Beach, CA, pp. 226-228, Jan. 2014.

[7] X.-T. Fang, X.-C. Zhang, and C.-M. Tong, "A novel miniaturized microstrip six-port junction," *Progress In Electromagnetics Research Letters*, vol. 23, pp. 129-135, 2011.

[8] K. Staszek, S. Gruszczynski, and K. Wincza, "Design and accuracy analysis of a broadband six-port reflectometer utilizing coupled line directional couplers," *Microw. Opt. Technol. Lett.*, vol. 55, no. 7, pp. 1485-1490, July 2013.

[9] S. Z. Ibrahim, A. Abbosh, and M. Bialkowski, "Design of wideband six-port network formed by in-phase and quadrature Wilkinson dividers," *IET*

Microw. Antennas Propag., vol. 6, no. 11, pp. 1215-1220, Aug. 2012.
[10] K. H. Yusof, N. Seman, M. H. Jamaluddin, and D. N. A. Zaidel, "Characterization and formulation of microstrip-slot impedance with different thickness and relative permittivity," *Applied Mechanics and Materials*, vol. 781, pp. 53-56, 2015.
[11] A. S. Mohra, M. A. Alkanhal, and E. A. Abdullah, "Size-reduced defected ground microstrip directional coupler," *Microw. Opt. Technol. Lett.*, vol. 52, no. 9, pp. 1933-1937, Sep. 2010.
[12] L. G. Maloratsky, "Microstrip circuit with a modified ground plane," *High Frequency Electronic, Summit Technical Media*, 2009.
[13] L. G. Maloratsky, *Passive RF and Microwave Integrated Circuits*. Elsevier, 2004.
[14] K. H. Yusof, N. Seman, M. H. Jamaluddin, and D. N. A. Zaidel, "Design of ultra wideband 3 dB coupled-line coupler and 90° power divider with zig-zag-shaped slot for wireless communication applications," *Wirel. Pers. Commun.*, vol. 84, no. 4, pp. 2599-2611, Oct. 2015.
[15] M. Winebrand and R. Vladimir, "Slot spiral miniatureized antenna," *United States Patent*, US6791497 B2, pp. 1-17, 2014.

Norhudah Seman received the B.Eng. in Electrical Engineering (Telecommunications) degree from the Universiti Teknologi Malaysia, Johor, Malaysia, in 2003 and M.Eng. degree in RF/Microwave Communications from The University of Queensland, Brisbane, St. Lucia, Qld., Australia, in 2005. In 2010, she received her Ph.D. degree from The University of Queensland. Currently, she is an Associate Professor and Director (Communication Engineering) in School of Electrical Engineering and Research Fellow in HiCoE Wireless Communication Centre (WCC), Universiti Teknologi Malaysia. Her research interests concern the design of microwave/ millimeterwave devices for biomedical and industrial applications, effects of electromagnetic field radiation including specific absorption rate (SAR), and mobile communications.

Khairul Huda Yusof received the diploma in Electrical Engineering (Telecomunication) and degree of B.Eng. in Electrical Engineering (Microelectronics) from Universiti Teknologi Malaysia in 2008 and 2011, respectively. Currently, she just completed her Ph.D. study in Electrical Engineering at Universiti Teknologi Malaysia, majoring in Telecomunication and has been appointed as a Lecturer in MAHSA University.

Mohd Haizal Jamaluddin was born in Selangor, Malaysia. He received his Bachelor degree and Master degree in Electrical Engineering from Universiti Teknologi Malaysia (UTM), Malaysia in 2003 and 2006, respectively. He received the Doctoral degree in Signal Processing and Telecommunications from the University of Rennes 1, Rennes, France in 2010. He is currently an Associate Professor UTM. His main field of interest is on antenna design, especially on dielectric resonator antenna, reflect array antenna and lens antenna.

Tharek Abd Rahman is a Professor at School of Electrical Engineering, Universiti Teknologi Malaysia (UTM). He obtained his B.Sc. in Electrical & Electronic Engineering from University of Strathclyde UK in 1979, M.Sc. in Communication Engineering from UMIST Manchester UK and Ph.D. in Mobile Radio Communication Engineering from University of Bristol, UK in 1988. He is the Director of Wireless Communication Centre (WCC), UTM. His research interests are radio propagation, antenna and RF design and indoors and outdoors' wireless communication. He has also conducted various short courses related to mobile and satellite communication to the Telecommunication Industry and Government body since 1990. He has a teaching experience in the area of mobile radio, wireless communication system and satellite communication.

VHF-UHF Monocone Antenna for Ground Penetrating Radar Application

Tamer G. Abouelnaga [1] and Esmat A. Abdallah [2]

[1] Department of Microstrip Circuits
Electronics Research Institute, Giza, Egypt
Higher Institute of Engineering and Technology-Kafr Elsheikh, Egypt
tamer@eri.sci.eg

[2] Department of Microstrip Circuits
Electronics Research Institute, Giza, Egypt
esmataa2@hotmail.com

Abstract ─ This paper introduces a VHF-UHF monocone antenna for ground penetrating radar GPR application. The proposed antenna covers different bandwidths through only changing the cone geometry. Same ground plane shape and feeding system are used. Firstly, both conventional and proposed monocone antennas are designed, simulated and their simulated results are compared. One antenna cone is fabricated and measured for verification purpose. Good agreement is obtained between measured and simulated bandwidths. The measured bandwidth extends from 73 MHz to 500 MHz. Secondly, another antenna cone is designed and simulated without altering the upper or the lower cone radii. The second cone antenna bandwidth extends from 130 MHz to 1000 MHz. The receiver antenna of the commercial SIR 2000 impulse GPR is replaced by the proposed VHF-UHF first monocone antenna and the field test results are recorded and discussed.

Index Terms ─ GPR, MCA.

I. INTRODUCTION

Ground Penetrating Radar uses electromagnetic waves to locate and characterize objects beneath the ground surface. The main components of a typical GPR system are illustrated in Fig. 1. The transmitter generates an electric signal, which is radiated by the transmitting antenna. At receiver, reflections from above and below the ground are gathered, digitized, and stored for processing and interpretation. High and low frequencies are used to detect small size and deep buried objects, respectively. GPR's usually operate in the VHF-UHF electromagnetic spectrum. Frequencies as low as 20 to 50 MHz are used for locating deep caves, mine tunnels, water detection or ice thickness measurement. Frequency of 150 MHz is a typical center frequency for cart mounted radars. Frequencies as high as 300 to 500 MHz are used for shallow and high-resolution probing [1].

The performance of GPR depends on the proper design of transmitter and receiver (T/R) antennas. Many antennas were developed to cover the VHF-frequency band such as microstrip antenna [2, 3], VHF spiral antenna [4], compact multiband VHF antenna [5], monopole cone antenna [6], electrically small broadband printed monopole antenna [7], conformal VHF antenna [8], and conical monopole antenna [9]. Table 1 shows a comparison of the aforementioned antennas.

Table 1: VHF antennas

Reference	Bandwidth (MHz)	Antenna Size (cm^3)
[2-3]	127-172	116 x 116 x 26.66
[4]	90 - 300	295 x 295 x 100
[5]	37.6 - 38.1, 72.9 – 74, 150.4 - 151.9	271,6 x 207.9 x 5
[6]	53.6 - 500	120 x 120 x 150
[7]	165 - 175	39 x 31 x 0.1
[8]	95 - 241	116 x 62
[9]	70 - 220	400 x 400 x 74.4

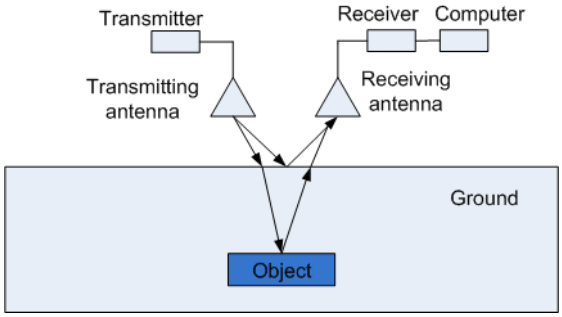

Fig. 1. Illustration of a typical GPR system.

In this paper the proposed antenna is designed to cover different bandwidths of the VHF/UHF frequency bands. The proposed compact VHF-UHF-MCA antenna

Submitted On: March 22, 2016
Accepted On: January 26, 2019

covers the bandwidths from 73 to 500 MHz and from 130 to 1000 MHz when first and second cones are used, respectively. The proposed VHF-UHF-MCA has dimensions of 70 cm by 70 cm by 90 cm. The paper explains antenna design in second section. Measuring and fabrication are introduced in section three. Finally, the conclusions section is presented in section four.

II. ANTENNA DESIGN

In wireless communication systems, conventional wire monopole is one of the most widely used antennas due to its low cost, omni-directional radiation patterns, simple structure, and ease for matching to 50 Ohm [10]. Also, it is unbalanced, thus balun is eliminated, which may have a limited bandwidth [11]. Bandwidth increases with the increase of the radius-to-length ratio, this indicates that a fatter structure will lead to a broader bandwidth because the current area, and hence the radiation resistance is increased [12]. However, when the monopole radius is too large related to the feeding line, the impedance mismatch between them will become significant and the bandwidth can't be further increased.

As stated by Victor Rumsey in the 1950s [13], that the impedance and pattern properties of an antenna will be frequency independent if the antenna shape is specified only in terms of angles. So, a conical shape can be used instead of wire structure. The main challenge in this paper is to design a conical monopole antenna operating in the VHF-UHF frequency bands and has considerable light weight for field measurement purpose.

In Section IIA, a conventional VHF-UHF Monocone antenna is designed and simulated using CST and HFSS for comparison purpose. The proposed compact VHF-UHF-MCA with modified ground plane shape is introduced. Effect of the probe tip load is studied using CST simulator. Also, the performance of the proposed antenna with its second cone is investigated.

A. Conventional VHF-UHF monocone antenna

Figure 2 (a) shows the three-dimensional view of the axially symmetric conventional VHF-monocone antenna. This antenna is designed based on [14]. It consists of a metallic cone with top radius R_t, bottom radius R_b, height h and a circular metallic ground plane with radius R_g. A probe feed method is used as feeding scheme.

The conventional VHF-MCA is simulated using both CST and HFSS simulators, Fig. 2 (b). The difference between the two solvers is related to the different boundary conditions which are used by both CST and HFSS simulators. Both CST and HFSS solvers are based on Finite Element Time Domain numerical methods. CST simulator and HFSS are used to analyze the antenna different structure throughout the whole paper.

The resonance frequency of conventional VHF-UHF-MCA is 70 MHZ and its -10 dB bandwidths extend from 54 MHz to 146 MHz, 197 to 230, 281 to 416 and all the curve points are under -8.4 dB. The antenna occupy a cone volume of $9.16 \times 10^5\ cm^3$ and ground plane area of 6842.67 cm^2 which is a major problem for any moving GPR system.

Stutzman and Kim in [15] and [16] had introduced a stable radiation pattern and a model for the monocone antenna, respectively. When increasing the ground plane size of monocone antenna, the performance will be quite similar to the biconical antenna but with an input impedance of half value of the biconical one. Theoretically, infinite length biconical antenna is capable of providing frequency-independent impedance.

The impedance is given by the following expression:

$$Z_o = 120ln\left(cot\frac{\theta}{2}\right), \quad (1)$$

where θ is the angle of the cone, as shown in Fig. 2 (a), and Z_o is the characteristic impedance of the antenna. In practice, the size is truncated which introduces reflections and limits the operating bandwidth, [17]. So, when the monocone antenna's ground plane radius reach certain value, input impedance performance will not be affected much with more increment. This can be clearly seen in Fig. 2 (c).

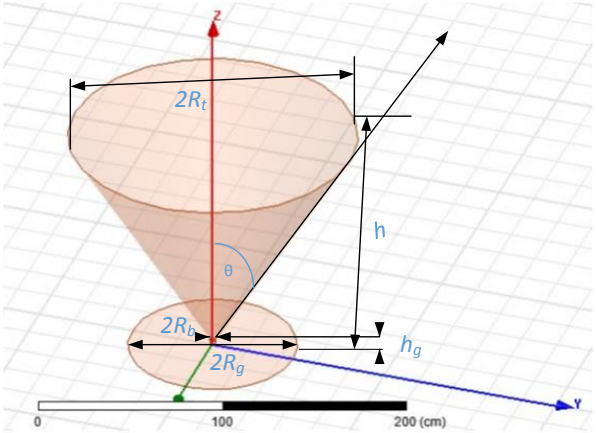

(a)

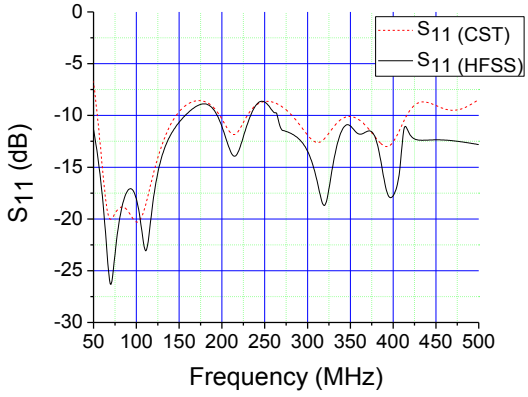

(b)

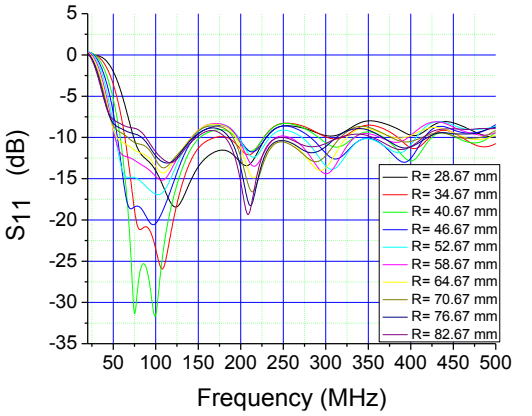

(c)

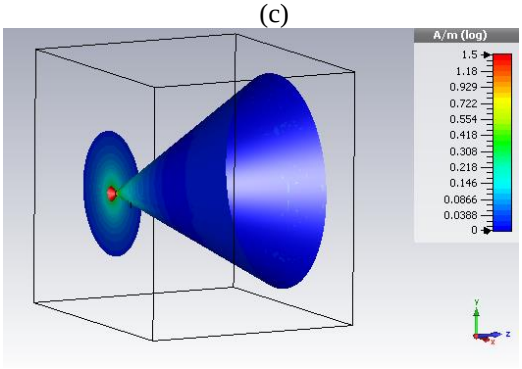

(d)

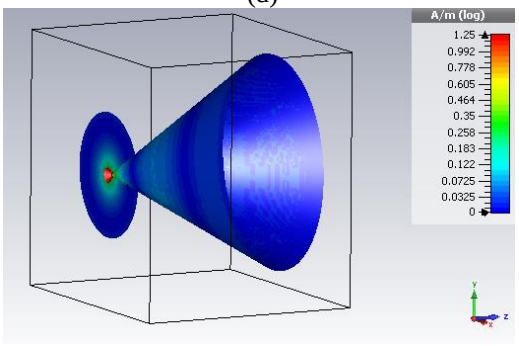

(e)

Fig. 2. (a) Conventional VHF-MCA antenna, (b) Conventional VHF-Monocone antenna reflection coefficient versus frequency, (c) Conventional VHF-Monocone antenna reflection coefficient versus frequency at different ground radii, (d) Conventional VHF-Monocone antenna surface current distribution at 100 MHz, and (e) Conventional VHF-Monocone antenna surface current distribution at 215 MHz.

Table 2 shows that, as the ground plane radius increases from 28.67 mm to 46.67 mm, the resonant frequency has shifted back from 123 MHz to 97 MHz, respectively. As ground plane radius increases from 52.67 mm to 58.67 the resonant frequency has shifted forward from 104.5 MHz to 108 MHz, respectively. As the radius increase from 64.67 mm to 82.67 mm, it can be noticed that the resonant frequency is kept at 110 MHz and the antenna reflection coefficient does not change much. So, the size of ground plane doesn't affect much the resonant frequency, but it can be used for matching enhancement process. However, if the ground plane size has been reduced, the antenna may not be frequency dependent anymore.

The surface current distribution of the conventional monocone antenna is shown in Figs. 2 (d) and (e) where the current is concentrated at the cone bottom and at the center area of the ground plane. The proposed antenna will have a bigger ground surface area through using a hollow cube instead of simply a conductor sheet. The center area where the surface current is concentrated is kept as it is. The outer area will be removed and is replaced by an outer ring. By this structure both frequency dependent performance and the surface current distribution may be kept almost the same and the proposed structure will be lighter.

Table 2: CMCA resonance frequency at different ground radii

Resonant Frequency (MHz)	S_{11} **(dB)**	**Ground Plane Radius** R_g **(mm)**
123	-18.5	28.67
107	-26	34.67
99.5	-31.5	40.67
97	-20.6	46.67
104	-17	52.67
108	-15.2	58.67
110	-14.28	64.67
110	-13.7	70.67
110	-13.04	76.67
110	-12.8	82.67

B. Proposed VHF-UHF monocone antenna

The proposed VHF-UHF monocone antenna consist of a metallic cone with radius R_t at the top, R_b at the bottom of the cone and height h. The 3D ground plane is shaped as a hollow metallic box with removed bottom face. This hollow box is welded with a metallic ring with radius R_g. Four steel strips with thickness of 3 mm and width of 4 cm are used to connect the four box sides with the ring, Fig. 3. The feeding scheme consists of probe feed loaded at its probe tip with rectangular metal of 4 cm by 4 cm.

Figure 4 (a) shows the effect of the rectangular metal load on the antenna matching. One can note that as the rectangular load size is increased the better is the matching which add an additional degree of freedom in matching adjustment process. After many trials using CST simulator, the ground plane box is found to be 50 x 50 x 20 cm^3 and the surrounded outer ring radius is 35.5 cm. The resonance frequency of the proposed compact VHF-UHF MCA is 88 MHZ and its -10 dB bandwidths extend from 78.6 MHz to 107 MHz, 176 to 300, 387 to 492, Fig. 4 (b). Figure 4 (c) shows that the proposed

antenna gain is reduced by 0.25 dB at 100 MHz and 2 dB at 350 MHz. the gain reduction is expected because of size reduction. The antenna occupy a cone volume of $1.19 \times 10^5\ cm^3$, ground plane area of 3959.19 cm^2 and weight of 23 kg.

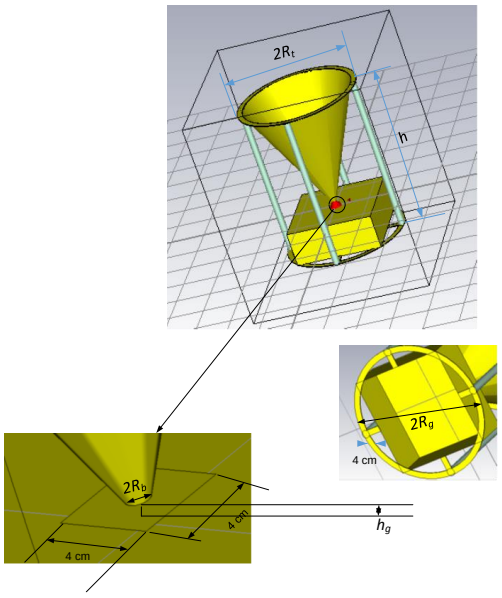

Fig. 3. Compact VHF-MCA antenna.

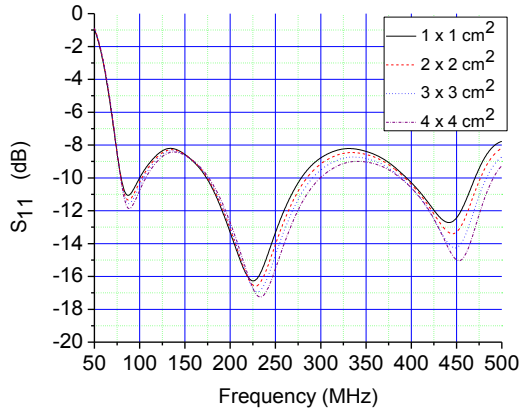

(a)

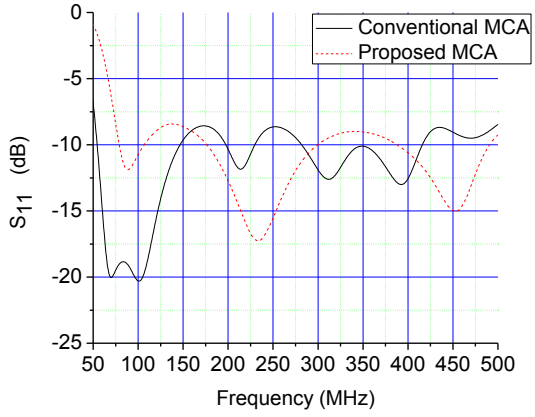

(b)

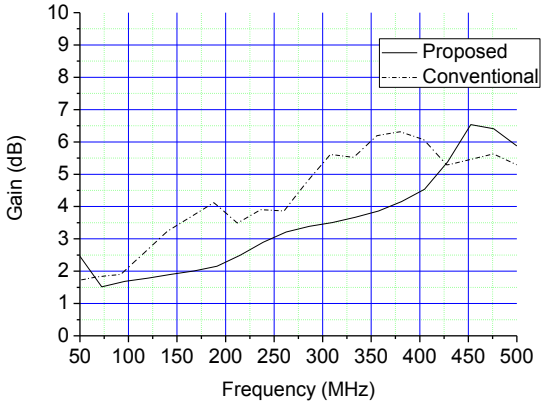

(c)

Fig. 4. (a) Metal rectangular load size effect versus frequency, (b) Conventional MCA and proposed MCA with its first cone reflection coefficients versus frequency, and (c) Conventional VHF-UHF MCA and proposed MCA with its first cone gain versus frequency.

The radiation pattern of the proposed antenna with its first cone is shown in Fig. 5. It can be noticed that the 3-dB beam width becomes narrower as the resonance frequency increases from 230 to 440 MHz, respectively. Same antenna feeding is used and the cone geometry is changed. For mechanical assembling simplicity, only the height of the cone is changed from 90 cm to 60 cm. The cone upper and lower radii are kept at the same values. The simulated bandwidth of the second cone antenna extends from 130 MHz to 1000 MHz, Fig. 6 (a). Also it can be noticed that the 3-dB beam width becomes narrower, Figs. 6 (b) and (c) as the frequency increases from 250 to 800 MHz, respectively.

Table 3 shows a comparison between the dimensions of conventional VHF-MCA, proposed VHF-UHF MCA and SATIMO commercial MCA. It can be noticed that the proposed MCA is much smaller and lighter than SATIMO commercial MCA.

Table 3: Conventional VHF-MCA (CMCA), proposed VHF-UHF MCA and SATIMO MCA

Antenna	**CMCA**	**VHF-MCA**	**SATIMO-MCA**
R_t (cm)	80	35.5	39.75
R_b (cm)	1.667	0.5	5
h (cm)	136.66	90	74.4
R_g (cm)	46.67	35.5	200
h_g (cm)	3.33	1	~1
Weight (Kg)	-	23	159

Table 4 shows a comparison between the radiation parameters of the proposed antenna when first and second cone geometries are used.

Table 4: Proposed VHF-MCA radiation parameters

Antenna	First Cone VHF-UHF MCA		Second Cone VHF-UHF MCA	
Frequency (MHz)	230	440	250	800
Main lobe direction (degree)	60	25	120	15
3 dB beamwidth (degree)	74.7	28.9	115.5	17.5

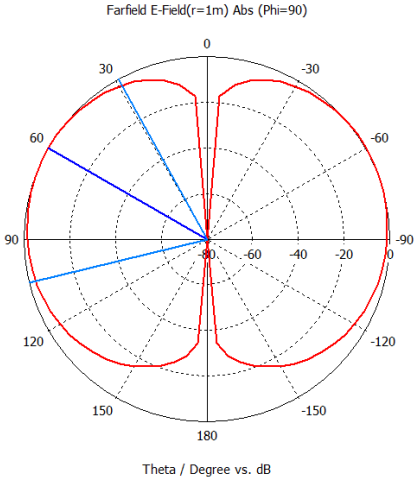

(a)

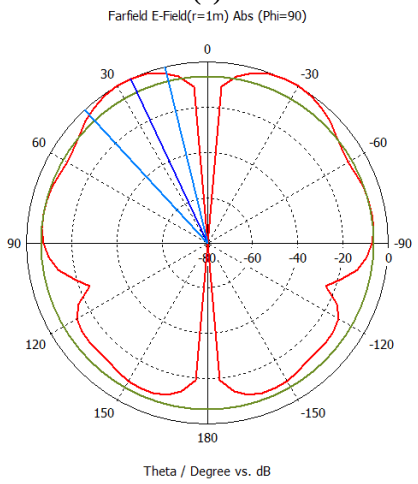

(b)

Fig. 5. (a) Proposed VHF-UHF MCA with its first cone radiation pattern at 230 MHz, and (b) proposed VHF-UHF MCA with its first cone radiation pattern at 440.

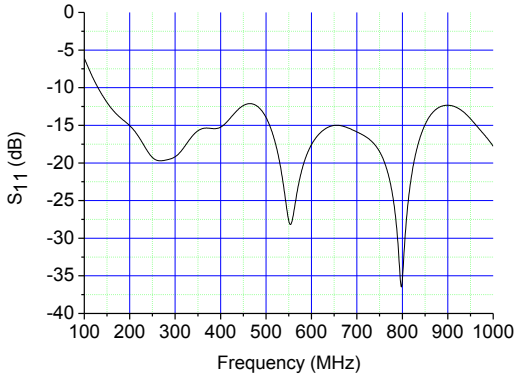

(a)

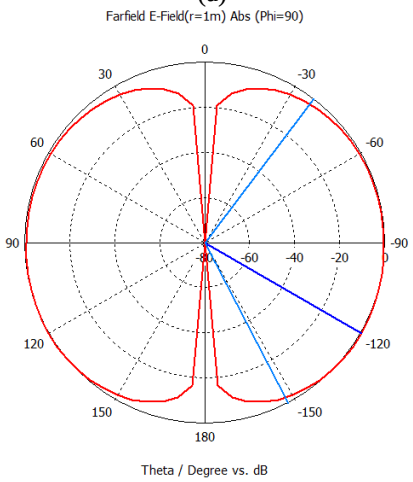

(b)

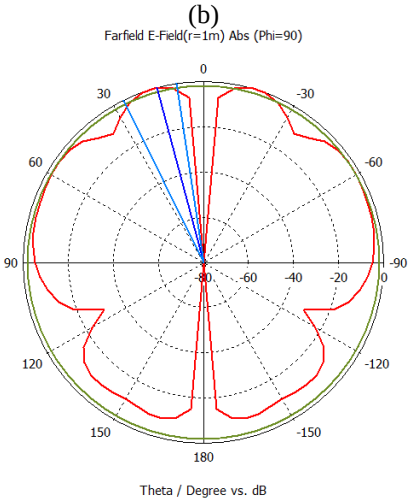

(c)

Fig. 6. (a) Proposed VHF-UHF MCA with its second cone reflection coefficients versus frequency, (b) proposed VHF-UHF MCA with its second cone radiation pattern at 250 MHz, and (c) proposed VHF-UHF MCA with its second cone radiation pattern at 800 MHz.

III. MEASUREMENT AND FABRICATION

A. Proposed VHF-UHF antenna Measurement

The proposed VHF-UHF monocone antenna is fabricated in a high precision workshop. The antenna design is aimed to make the antenna compact, lightweight and mechanically assembled and disassembled, Fig. 7. The proposed ground plane is reshaped as metallic ring which is fasten to a parallel rectangular. Teflon posts are used to connect the metallic ring with cone piece. Eight metallic nails are used to connect cone antenna piece with the ground through the four Teflon posts. The proposed first cone VHF-UHF MCA antenna is simulated and measured. One notices that the simulated -10 dB (SWR = 2) bandwidth is extended from 80.5 MHz to 103 MHz, 171 MHz to 308.5 MHz and from 383 MHz to 500 MHz. The measured frequency bandwidth is better than the simulated one and extends from 73 MHz to 500 MHz, Fig. 8. This discrepancy between measured and simulated results can be referred to that the cone position is not fixed on the tip of the N type connector so, it could be move a little bit from the cone center.

Fig. 7. Practical first cone VHF-MCA photo.

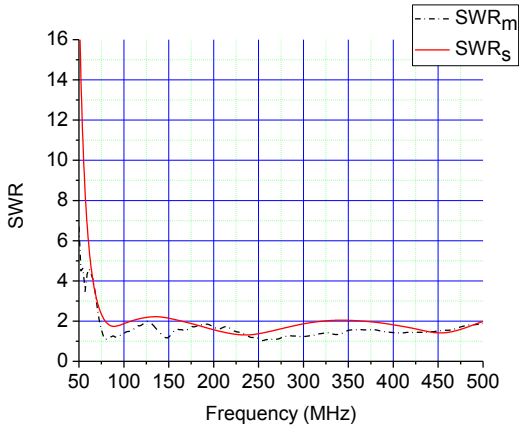

Fig. 8. First cone VHF-UHF MCA simulated and measured SWR versus frequency.

B. Proposed antenna measurement using SIR 2000 GPR system

The GPR system basically consists of transmitter, receiver and controller units. The transmitter unit includes a signal generator, power amplifiers, and transmitter antenna. The receiver unit includes a receiver antenna, a low-noise amplifier (LNA), a sample and hold detector, mixer or demodulator, and analog-to-digital converter (ADC). The controller unit includes a timer, a synchronizer of T/R units, microcontroller, and a data acquisition card. Finally, the raw data are processed to obtain clear subsurface imaging for the detection and identification of buried objects.

The GPR system scan vertically (y axis) and horizontally (x axis), i.e., the y axis presents the depth and x axis present the horizontally distance to be scanned. Designed conical antenna is tested by attaching it to the SIR 2000 GPR model instead of its commercial one at the receiver side. Commercial bowtie antenna of resonance frequency of 100 MHz is used at transmitter side.

The most typical shape found in the obtained GPR images is the hyperbola that corresponds to some targets like pipes and buried objects. These targets appear as hyperbolic shapes because they enter in the emission cone of the antenna in 3 certain space domains surrounding their actual location. The presence of these shapes in the profiles can sustain further calculation of the medium properties. Also, we had placed two metal objects to test how accuracy could our test setup reach.

Figure 9 shows the depth in cm on the vertical axis and the scanned distance in cm on horizontal axis. The horizontal part from 25 cm to 450 cm, shows useful signal with some detected objects at horizontal distance of 450 cm and vertical depth of 100 cm under the earth surface. This results agree well with the obtained results where commercial antenna is installed.

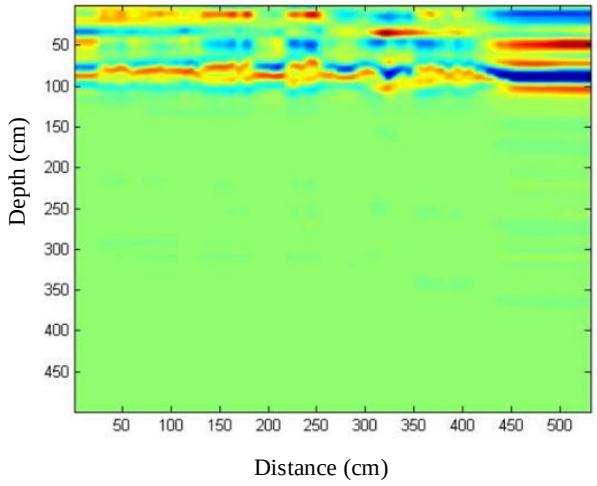

Fig. 9. Scanned image from SIR 2000 GPR system using the proposed VHF-UHF MCA.

IV. CONCLUSIONS

The proposed VHF-UHF MCA antenna was introduced for the GPR application. It was shown that the proposed antenna was easily assembled and disassembled. The antenna covered the bandwidth from 73 MHz to 500 MHz with its first cone. Good agreement was obtained between measured and simulated results. Also the antenna could cover the bandwidth from 130 to 1000 GHz when second cone is used. The antenna was tested using the SIR 2000 GPR model and the results was recorded and investigated.

REFERENCES

[1] R. J. Fontana, "Recent system applications of short-pulse ultra-wide band technology," *IEEE Trans. Microwave Theory Tech*., vol. 52, no. 9, pp. 80-87, Sep. 2004.

[2] J. Huang, Z. Hussein, and A. Petros, "A VHF microstrip antenna with wide-bandwidth and dual-polarization for sea ice thickness measurement," *IEEE Trans. Antennas and Propagat*., vol. 55, no. 10, pp. 2718-2722, Oct. 2007.

[3] A. Petros, J. Huang, and Z. Hussein, "A wide-band dual-polarized VHF microstrip antenna for global sensing of sea ice thickness," in *IEEE Antennas and Propagat. Society International Symposium*, Washington, DC, USA, pp. 684-687, July 3-8, 2005.

[4] R. J. Barton, P. Collins, P. Crittenden, M. Havrilla, and A. Terzuoli, "A compact passive broadband hexagonal spiral antenna array for VHF remote sensing," in *IEEE International Geoscience and Remote Sensing Symposium*, Barcelona, Spain, pp. 593-595, July 23-28, 2007.

[5] R. Anwar, N. Misran, M. Islam, and G. Gopir, "Compact multiband VHF antenna for transient radio telescope," in *International Conference on Space Science and Communication,* Negeri Sembilan, Malaysia, pp. 182-185, Oct. 26-27, 2009.

[6] T. Abouelnaga and E. Abdallah, "Two in one VHF-conical monopole antenna for GPR application," *IEEE Radar Conference*, Cincinnati, OH, USA, pp. 88-92, May 19-23, 2014.

[7] M. R. Abraham and S. O. Kundukulam, "Wide-band printed monopole VHF antenna," in *IEEE International Conference on Computing and Network Communications*, Trivandrum, India, pp. 833-837, Dec. 16-19, 2015.

[8] D. L. Zeppettella and M. Ali, "VHF antenna for airfoil structural integration," in *IEEE International Symposium on Antennas and Propagat. (APSURSI)*, Fajardo, Puerto Rico, pp. 1861-1862, June 26-July 1, 2016.

[9] Antenna catalog, SATIMO-ORBIT/FR, Dec. 2011.

[10] C. Balanis, *Antenna Theory Analysis and Design*. John Wiley and Sons Inc., New Jersey, USA, 2016.

[11] M. J. Ammann and Z. N. Chen, "Wideband monopole antennas for multi-band wireless systems," *IEEE Antennas and Propagat. Magazine*, vol. 45, no. 2, pp. 146-150, Apr. 2003.

[12] A. W. Rudge, K. Milne, A. D. Olver, and P. Knight, *The Handbook of Antenna Design*. Peter Peregrinus Ltd, London, UK, 1982.

[13] V. H. Rumsey, "Frequency-independent antennas," *IRE National Convention Record*, vol. 5, pp. 114-118, 1957.

[14] C. Balanis, *Modern Antenna Handbook*. John Wiley and Sons Inc., New York, USA, 2008.

[15] W. L. Stutzman, *Antenna Theory and Design*. John Wiley and Sons Inc., New York, USA, 1998.

[16] K. H. Kim, J. Kim, and S. O. Park, "An ultrawide-band double discone antenna with the tapered cylindrical wires," *IEEE Trans. on Antennas and Propagat*., vol. 53, no. 10, pp. 3403-3406, Oct. 2005.

[17] D. McNamara, D. Baker, and L. Botha, "Some design considerations for biconical antennas," in *Antennas and Propagat. Society International Symposium*, Boston, USA, pp. 173-176, June 25-29, 1984.

Tamer G. Abouelnaga was born in November 1976, he received his B.Sc. degree in Electronics Engineering from Menofiya University, Egypt, in May 1999, M.Sc. and Ph.D. degrees in Electrical Communication from Ain Shams University in July 2007 and June 2012, respectively. He worksas a Researcher in Microstrip Circuits Department, Electronic Research Institute, Cairo. He had published 30 papers, 19 papers in peer-refereed journals and 11 papers in international conferences in the area of RFID, TEM horn and DRA antennas design. His current research interests are in power dividers, RFID antennas and breast cancer detection. He participates in research projects in the area of GPR and digital beam forming circuits.

Esmat A. Abdallah graduated from the Faculty of Engineering and received the M.Sc. and Ph.D. degrees from Cairo University, Giza, Egypt, in 1968, 1972, and 1975, respectively. She was nominated as Assistant Professor, Associate Professor and Professor in 1975, 1980 and 1985, respectively. In 1989, she was appointed President of the Electronics Research Institute ERI, Cairo, Egypt, a position she held for about ten years. She became the

Head of the Microstrip Department, ERI, from 1999 to 2006. Currently, is at the Microstrip Department, Electronics Research Institute, Cairo, Egypt. She has focused her research on microwave circuit designs, planar antenna systems and nonreciprocal ferrite devices, and recently on EBG structures, UWB components and antenna and RFID systems. She acts as a single author and as a co-author on more than 127 research papers in highly cited international journals and in proceedings.

Transparent Circular Monopole Antenna for Automotive Communication

Sanjay Bandi [1], Deepak Kumar Nayak [2], B. T. P. Madhav [2], and Anilkumar Tirunagari [2]

[1] Research Scholar, Department of ECE, Koneru Lakshmaiah Education Foundation, Vaddeswaram, AP, India

[2] Antennas & Liquid Crystals Research Center, Department of ECE
Koneru Lakshmaiah Education Foundation, Vaddeswaram, AP, India
btpmadhav@kluniversity.in

Abstract ─ A novel fractal shaped antenna on transparent material is communicated in this article. The proposed antenna is flexible and conformal on the automotive surface to serve at vehicular communication applications. Polyvinyl chloride substrate material of ε_r=3 and loss tangent 0.02 is used in the antenna design with overall dimension of 55 x 40 x 3 mm. The virtual placement of the antenna on vehicular surface is simulated with the combination of ANSYS HFSS and Savant tools. Far-field radiation and the Electric-field distribution with respect to the antenna placement on vehicular structure is analyzed and presented in this work. The prototyped antenna measurements are in good agreement with the simulation.

Index Terms ─ Conformal antenna, flexible, Polyvinyl Chloride (PVC), vehicular communication.

I. INTRODUCTION

The advanced wireless modules with modern antenna elements are needed to access the condition of various parts of the automotive system and to timely report the data to a common control system in which the vehicle condition can be notified to the driver. Even a large family of antennas exists till date, but the compact and conformal antennas with good radiation performance and with attractive look is mostly preferred.

There are many antennas existing in the literature, and some are designed for different wireless and vehicular applications. The modelling of vehicular antenna at 100 MHz is discussed in [1]. A meta-resonator-based high impedance ground antenna is presented for vehicular applications in [2] and some interesting works on transparent glasses and materials like corning glass and IZTO/Ag/IZTO are reported in [3,4]. In vehicular technology WLAN, WiMAX and DSRC (dedicated short-range communication) applications-based antennas are discussed in [7-10].

In this letter, a novel fractal design is employed as the radiating structure, which is prototyped on conformal and transparent PVC substrate material. The radiation performance of the conformal antenna after placement on the vehicle is also discussed along with the effective electric-field distribution regions.

II. ANTENNA CONFIGURATION

Nowadays several modern vehicles are introduced with stylish body and with some of their metallic cabinets such as side view mirrors are being replaced with rigid and durable materials like plastic/fiber/polymer composites etc. Antennas which are designed on transparent substrates will make minimal presence on the vehicle rather than it appears as some beautiful design on the vehicle. Keeping view of this scenario, the transparent PVC material is considered for design of the antenna in an attractive manner. The proposed antenna structure on transparent PVC substrate is shown in Fig. 1. The radiating element of the proposed design is formed by taking the circular patch of radius 'R_1' then annular ring of width 'W' is formed by cutting a circle of radius 'R_2'. The effective permittivity 'ε_{eff}' is given by equation (1) as described in [5]:

$$\varepsilon_{eff} = 0.5(\varepsilon_r + 1) + 0.5(\varepsilon_r - 1)\sqrt{(1+10t/W)}, \quad (1)$$

where

$$W = (R_1 - R_2). \quad (2)$$

Later, circular slots are introduced in the radiating structure. These slots are iteratively made and merged together with the slots etched in previous iteration, and this process continued up to three levels and then terminated due to the limitation of fabrication of the antenna as shown in Fig. 1 (b). The scale factor '*sf*' is considered to compute the radii of next iteration slots. The scaling factor '*sf*' is determined through the parameters 'a_n', 'a_{n-1}' by equation (3):

$$sf = a_n / a_{n-1}, \quad (3)$$

where 'a_n', 'a_{n-1}' are n^{th} and $(n-1)^{th}$ circular cuts radii respectively. The scale factor is considered as 0.54. The overall shape of the patch obtained based on fractal concept, resembles like a wheel-shaped structure. The

Submitted On: September 8, 2018
Accepted On: December 25, 2018

coplanar waveguide feeding is used in the design with 50-ohm impedance at feed point. The feed line of width 'W_f' and two ground conductors on either side of the feed line with a gap 'g' are soldered to a 50-ohm SMA connector through which the antenna can be excited. The structural parameters are optimized to obtain the desired pass band performance under vehicular bands.

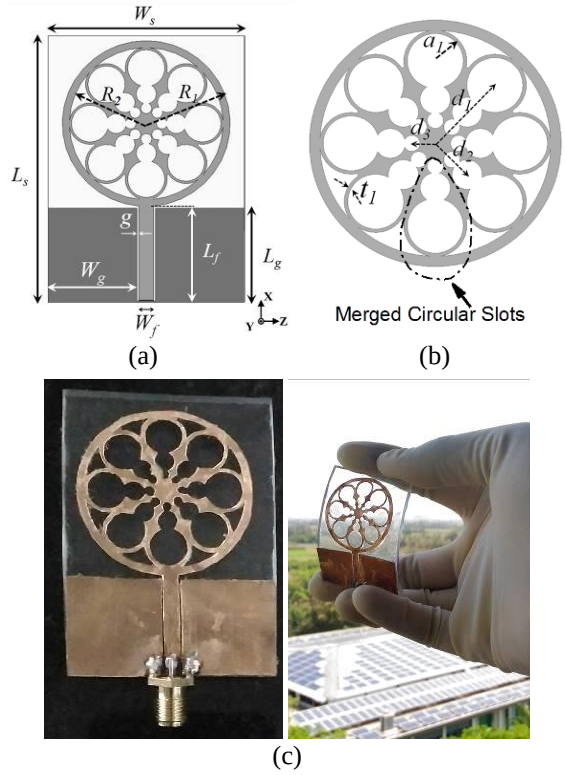

Fig. 1. Geometry of the proposed wheel-shaped fractal antenna: (a) front view, (b) structure of radiating element, and (c) prototype of the fabricated antenna with SMA connector. (L_s=55, W_s=40, L_g=19.4, W_g=18.155, L_f=19.87, W_f=3, g=0.345, R_1=17.1, R_2=15.72, a_1=4.35, d_1=11.44, d_2=6.82, d_3=4.46, t_1=0.475, h=3) (unit: millimeter).

III. SIMULATION AND MEASUREMENT CHARACTERISTICS

The proposed transparent antenna is simulated by bending the substrate at different bending angles mainly, 30^0, 45^0, 60^0, 90^0 and 120^0 respectively. The equation (4) is used to calculate the bending radius of the substrate:

$$\text{Bending radius,} \quad b_r = 0.5\left(L_s - f_b\right) \times (360 / \pi\theta), \quad (4)$$

where 'L_s' is length of the substrate, 'f_b' is the length of the feed line section on the flexible substrate and 'θ' is the bending angle which are indicated pictorially in Fig. 2 (a) for the conformal antenna configuration. The corresponding VSWR characteristics for the mentioned bending angles are presented in Fig. 2 (b). It witnesses the frequency shift towards the higher frequencies with the increase in bending angle.

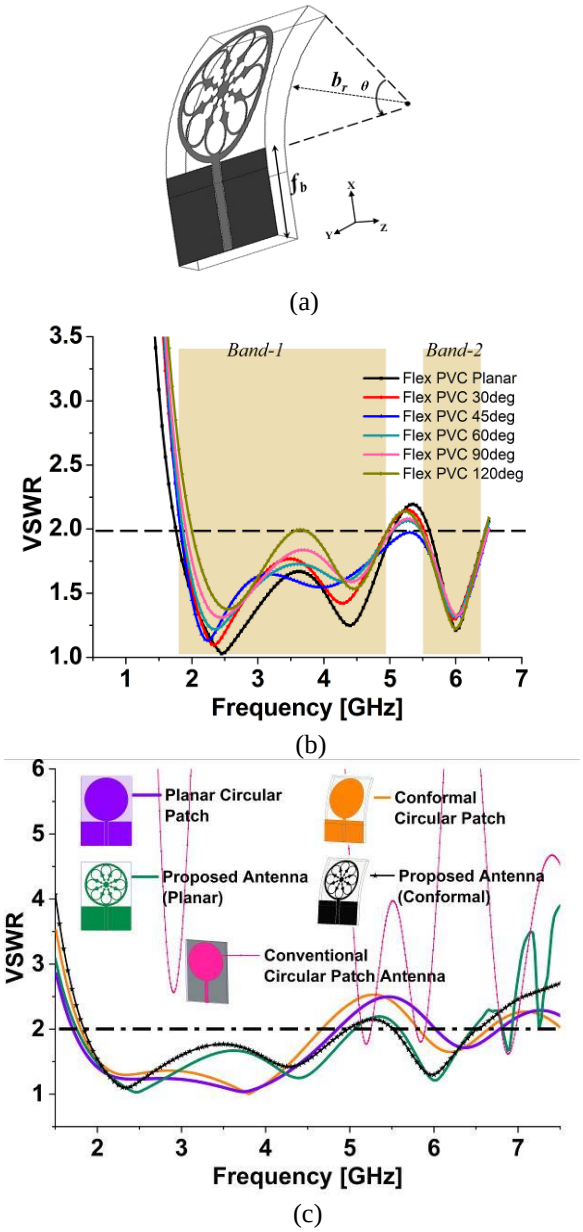

Fig. 2. Bending characteristics of the proposed antenna: (a) geometrical configuration, (b) simulated VSWR vs frequency characteristics of the antenna at different bending angles, and (c) VSWR comparison with respect to basic circular patch.

The proposed flexible fractal antenna on transparent material is compared with that of the circular monopole without any slots in planar and flexible versions. The level of transparency is increased because of the modified ground plane from the conventional patch to the proposed structure and also due to the etched

circular slots in the final structure. The variations in their operating bands are presented in terms of VSWR performance as shown in Fig. 2 (c) and characteristics are tabulated in Table 1. The proposed antenna geometry is fabricated on transparent PVC material and its VSWR is measured with MS2037C combinational analyzer, for both planar and conformal versions of the antenna. The simulated and measured VSWR characteristics of the planar antenna are presented in Fig. 3 (a) and the corresponding observations are tabulated in Table 1. The peak gain of the proposed antenna when mounted on side view mirror of the vehicle is measured by comparison method. The standard gain PowerLOG70180 series horn antennas are used as transmitting antennas and Keysight-EXG-X-Series Microwave Signal Generator is used as source to the antenna. The Friis transmission formula [5] is used to compute the peak gain of the antenna.

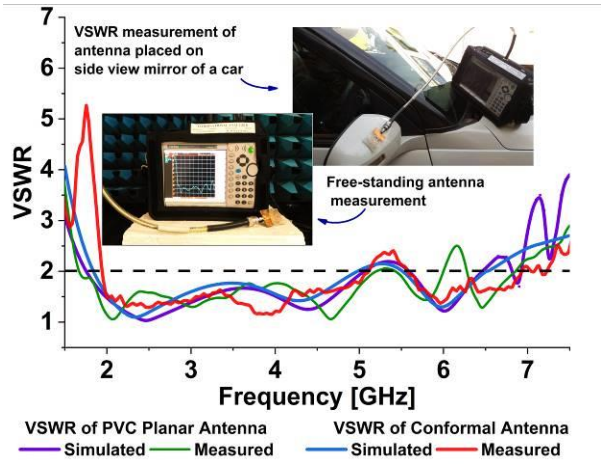

(a)

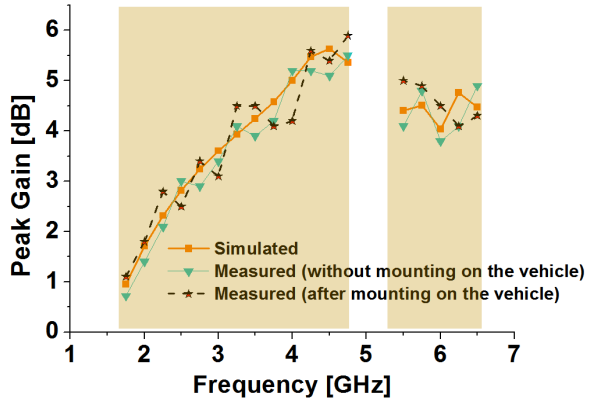

(b)

Fig. 3. Simulated and measured characteristics of the proposed transparent fractal antenna: (a) VSWR vs frequency characteristics, and (b) peak gain vs frequency characteristics.

In Fig. 3 (b), the variation of peak gain characteristics of the antenna is shown, and it has been observed that the antenna radiates with a maximum gain of 5.9 dB in its conformal mode of operation at a bending angle of 30^0.

Table 1: Operating band characteristics of proposed antenna

Antenna Type		Operating Bands [GHz]
Conventional Circular Patch Antenna	Planar	5.14-5.25/5.79-5.90/6.80-6.97
CPW fed Circular Patch Antenna	Planar	1.71-4.85/6.02-6.78
	Conformal	1.80-4.67/5.82-6.65
Proposed Fractal Antenna	Planar	1.75-5.1/5.55-6.5 (Simulated)
		1.66-5.1/5.43-6 (Measured)
	Conformal (30^0-bending angle)	1.85-5.0/5.5-6.54 (Simulated)
		1.95-5.1/5.55-6.9 (Measured)

IV. VEHICULAR MOUNTING CHARACTERISTICS OF THE ANTENNA

The features of vehicle-to-vehicle (V2V) safety communication usually operate by mutual exchange of vehicular-traffic information among the nearby vehicles. The antennas for these V2V systems can be mounted on various places on the body of the vehicle. Side view mirrors of most of the sport utility vehicles (SUV) and light trucks have the good scope of accommodating conformal antennas on or inside their shells. This kind of facility is useful in scenarios such as cross roads, intersections and blind-spots to detect other vehicles/ infrastructure for avoiding major fatalities. To study the radiation performance of the antenna, the proposed antenna is mounted on the shell of the side view mirror by bending the antenna with a bending angle of 30^0. This angle allows better conformal adherence on the side view mirror.

The far-field radiation characteristics of the proposed transparent antenna are shown in Fig. 4. The radiation patterns are observed at 2.4 GHz, 3.5 GHz and 5.9 GHz, where the applications of the vehicular communication are mainly concentrated.

The patterns are plotted according to the azimuth plane of the antenna mounted on vehicle with reference to the coordinate location of car body. The co-polarized radiation is better than cross-polarized radiation which is evident from Fig. 4, at a cost of ripple like behavior in the radiation performance. Antenna covers the all-around radiation, but some of its radiation is found to

be blocked in the side directions. Similar kind of nature is observed as frequency is increased. Some ripples are observed in the patterns which could be due to the increased scattering of the signal from the vehicular body. The computational aspects regarding the simulation using the shooting and bouncing rays (SBR) method employed by the simulation tool are presented in Table 2. It can be observed that the total number of rays launched are increased with frequency of excitation also, the total number of rays that contribute to the generation of far-field is in proportion with frequency. With increase in frequency, one can notice the blocked rays increased for a particular vehicular body.

Table 2: Computational statistics of SBR for calculating the far-field characteristics when antenna mounted on vehicular platform

Specification→ **Frequency** *(below)*	No. of Rays Launched	No. of Rays Blocked	No. of Rays Split	No. of Rays Exceed Max Bounce (A)	No. of Rays Escaped (B)	No. of Rays Contributed (A-B)	Total Simulation Time (CPU) in Seconds
2.4 GHz	10,363	3,19,294	52,822	44,726	36,104	80,830	7,276.0
3.5 GHz	12,581	4,44,479	54,214	46,652	38,476	85,128	10,459.0
5.9 GHz	18,388	8,04,833	57,498	51,164	44,687	95,851	10,600.0

Column-I	Column-II	Column-III	
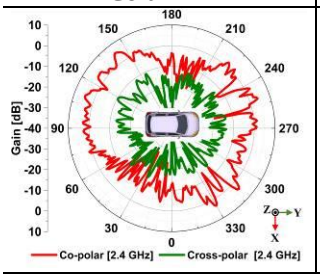	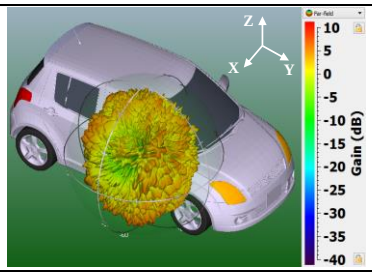	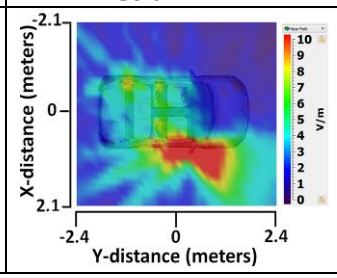	Maximum E-Field = 56.368 V/m at Location (in meters) X= 0.98m, Y= 0.48m
(a) At 2.4 GHz			
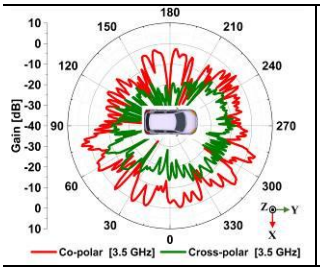	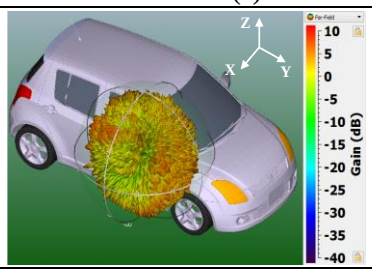	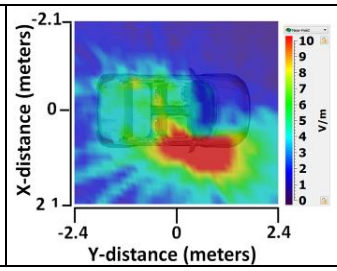	Maximum E-Field = 60.41 V/m at Location (in meters) X= 0.98m, Y= 0.48m
(b) At 3.5 GHz			
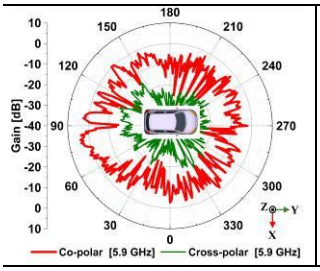	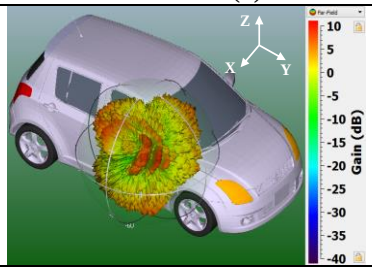	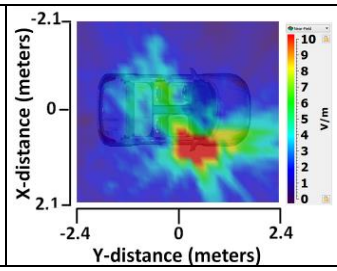	Maximum E-Field = 4.57 V/m at Location (in meters) X= 1.26m, Y= 1.32m
(c) At 5.9 GHz			

Fig. 4. Simulated field patterns of the proposed antenna when mounted on side view mirror of the vehicle: co-polar and cross-polarized patterns (*Column-1*), 3D far-field (*Column-II*), and Electric-field strength (V/m) near the vehicle (*Column-III*).

The electric-field strength within the vehicular surroundings is presented in Fig. 4 (*figures on the right)* for the frequencies at 2.4 GHz, 3.5 GHz and 5.9 GHz. The azimuth region of 4.8 meters in Y-direction (along the length of the car) and 4.2 meters (along the width of the car) is considered and shown graphically in Fig. 4. Here, the origin of the coordinate system is assumed to be co-located with the center of the footprint of the car.

Table 3: Performance comparison of proposed antenna with earlier literature

Ref.	Dimension of the Antenna (*L* x *W* x *h*)	Substrate Used	Operating Band (GHz)	Percentage Bandwidth (%)	Max Gain (dB)
This work	50 x 40 x 3 $0.45\lambda_g$ x $0.33\lambda_g$ x $0.025\lambda_g$	Transparent PVC	1.95-5.1/ 5.55-6.9	89.3/ 21.6	5.9
[2]	$0.51\lambda_g$ x $0.41\lambda_g$ x $0.05\lambda_g$	LTCC, Dupont	1.83/2.18	23	7
[3]	$1.98\lambda_g$ x $1.98\lambda_g$ x $0.0072\lambda_g$	1737 Corning glass	1.83-2.23	19.7	5
[4]	$0.199\lambda_g$ x $0.13\lambda_g$ x $0.0004\lambda_g$	IZTO/Ag/IZTO, FR4	1.1-1.65	40	1.84
[6]	$0.26\lambda_g$ x $0.24\lambda_g$ x $0.008\lambda_g$	FR4	2.57-3.29/3.95-4.73/ 6.55-12.31	22.52/17.9/61.0	~5.8
[7]	35 x 4 x 0.8 $0.29\lambda_g$ x $0.033\lambda_g$ x $0.006\lambda_g$	FR4	2.35-2.51/ 4.82-6.22	6/ 25	2.63/ 3.22
[8]	$0.5\lambda_g$ x $0.375\lambda_g$ x $0.0133\lambda_g$	FR4	2.17-2.5/ 4.98-6.31	14.13/ 23.56	3.65

VI. CONCLUSION

In this article, a transparent and conformal antenna is presented with wheel-shaped fractal structure for vehicular communication applications. The fabricated antenna is tested in planar and conformal mode with placement on the vehicle. The experimentally taken VSWR results of the conformal antenna after placing on the side-view mirror of the vehicle shows its operating band from 1.85-5 GHz and 5.55-6.5 GHz in simulation and 1.95-5.1 GHz, 5.55-6.9 GHz in measurements, which supports the WLAN, Bluetooth, WiMAX, DSRC, V2X vehicular applications. The measured radiation characteristics and the obtained gain of 5.9 dB makes the antenna as a good candidate for using in automotive applications.

ACKNOWLEDGMENT

We would like to thank DST for technical support through ECR/2016/000569 and EEQ/2016/000604.

REFERENCES

[1] L. Low, R. Langley, and J. Batchelor, "Modelling and performance of conformal automotive antennas," *IET Microwaves, Antennas & Propagat.*, vol. 1, no. 5, pp. 973-979, 2007.

[2] I. K. Kim, H. Wang, S. J. Weiss, and V. V. Varadan, "Embedded wideband metaresonator antenna on a high-impedance ground plane for vehicular applications," *IEEE Trans. Veh. Technol.*, vol. 61, no. 4, pp. 1665-1672, May 2012.

[3] J. Hautcoeur, F. Colombel, M. Himdi, X. Castel, and E. M. Cruz, "Large and optically transparent multilayer for broadband H-shaped slot antenna," *IEEE Antennas Wireless Propag. Lett*., vol. 12, pp. 933-936, 2013.

[4] Y. Kim, C. Lee, S. Hong, C. W. Jung, and Y. Kim, "Design of transparent multilayer film antenna for wireless communication," *Electronics Lett.*, vol. 51, no. 1, pp. 12-14, 2015.

[5] J. R. James, *Handbook of Microstrip Antennas*. IET, London, 1989.

[6] J. Liu, Z.-Y. Tang, and Y.-Z. Yin, "A differential CPW-fed ultra-wideband antenna with dual notched bands," *ACES Journal*, vol. 33, no. 6, pp. 610-615, 2018.

[7] C.-H. Ku, et al., "Compact planar dual-band folded dipole antenna for WLAN/WiMAX applications," *IEICE Electron. Express*, vol. 8, no. 2, pp. 64-69, 2011.

[8] L. C. Tsai, "A dual-band bow-tie-shaped CPW-fed slot antenna for WLAN applications," *Prog. Electromagn. Res. C.*, vol. 47, pp. 167-171, 2014.

[9] H. Honggang, et al., "Design of hexagon microstrip antenna for vehicle-to-vehicle communication," *The J. China Univ. Posts and Telecommun.*, vol. 23, no. 4, pp. 69-76, 2016.

[10] B. T. P. Madhav, T. Anilkumar, and S. K. Kotamraju, "Transparent and conformal wheel-shaped fractal antenna for vehicular communication applications," *AEU-Int. J. Electron. C.*, vol. 91, pp. 1-10, 2018.

Norm Constrained Noise-free Algorithm for Sparse Adaptive Array Beamforming

Wanlu Shi [1], Yingsong Li [1,2,*], Laijun Sun [3], Jingwei Yin [4], and Lei Zhao [5]

[1] College of Information and Communication Engineering, Harbin Engineering University, Harbin, 150001, China
*liyingsong@ieee.org

[2] Key Laboratory of Microwave Remote Sensing
National Space Science Center, Chinese Academy of Sciences, Beijing, 100190, China

[3] College of Electronic Engineering, Heilongjiang University, Harbin, 150080

[4] Acoustic Science and Technology Laboratory, Harbin Engineering University, Harbin, 150001, China

[5] Center for Computational Science and Engineering, School of Mathematics and Statistics
Jiangsu Normal University, Xuzhou, China

Abstract — In this paper, a reweighted l_1-norm constrained noise-free normalized least mean square (NLMS) (RL_1-CNFLMS) algorithm is proposed for dealing with sparse adaptive array beamforming. The proposed RL_1-CNFLMS algorithm integrates a reweighted l_1-norm penalty into the traditional objective function of constrained least mean square least mean square (LMS) (CLMS) algorithm to drive the weighted coefficient vector to sparsity. Besides, the Lagrange multiplier (LM) method and the gradient descent principle are employed during the derivation procedure for getting the update equation. Additionally, we utilize the l_1-l_2 optimization method to acquire the noise-free a posteriori error signal in normalizing process to achieve a quicker convergence speed, a better signal to interference plus noise ratio (SINR) performance as well as a higher array sparsity with an acceptable computational complexity. Simulation results turn out that by using the noise-free and norm constraint techniques, a fairly comparable beampattern is achieved by using only 38.4%, 39.4% and 69.4% antenna elements in contrast to the constrained NLMS (CNLMS), reweighted l_1-norm constrained LMS (RL_1-CLMS) and reweighted l_1-norm constrained normalized LMS (RL_1-CNLMS) algorithms, respectively.

Index Terms — Array beamforming, constrained LMS algorithm, l_1-norm constraint, noise-free normalizing, sparse adaptive beamforming.

I. INTRODUCTION

In the development of antenna array theory, adaptive beamforming algorithms have been recognized as a critical role in array signal processing. Based on the high capacity, adaptive beamforming algorithms have drawn significantly concern and widely applied to modern telecommunication systems, medical, radar, sonar and other areas [1].

Extensive studies have been reported that adaptive beamformers can create ideal beampatterns toward the direction of signal of interest (SOI) to keep a high gain and give nulls to prevent the influence of interferences [2-6]. Meanwhile, in this way the SINR is enhanced [2].

The existing researches suggest that adaptive beamforming algorithms can use the array weight vector to increase the gain of SOI and attenuate the interferences. The linearly constrained minimum variance (LCMV) algorithm was developed by Frost [2], and then, plenty of adaptive algorithms based on least mean square (LMS) principle have been devised for adaptive beamforming [3-6]. Many researches focus on the resolution, robustness and other properties rather than the sparsity of the antenna array [2, 3, 7]. To pursuit high performance, large arrays are always crucial in practice applications, especially in radar and satellite communication [4]. Thus, an antenna array utilizing less antenna elements to generate the beampattern without sacrificing performance is amazing technique.

Recently, a considerable method has grown up around the theme of sparse signal processing [8-21]. Inspired by sparse signal processing in system identification, channel estimation and other fields [8-19], the sparse adaptive beamforming algorithms have been proposed to exploit the sparsity of the corresponding antenna arrays [4-6]. However, new techniques are still needed to further improve these existing algorithms to achieve higher performance, e.g., low sidelobe level

Submitted On: November 27, 2018
Accepted On: February 9, 2019

(SLL) and fast convergence.

The specific objective of this study is to develop a normalizing approach for enhancing sparse adaptive beamforming algorithms to accelerate the convergence. In [22, 23], the l_1-l_2 minimization method is discussed, in which the noise-free error signal is obtained and then applied to other adaptive-filtering algorithms [24]. In this paper, we aim to develop a new variable convergence factor to promote the conventional constrained LMS (CLMS) algorithm for sparse adaptive beamforming by minimizing the noise-free a posteriori error signal. Simulation results indicate that a similar beampattern performance is obtained with less antenna elements, and a faster convergence speed as well as a better SINR are achieved for a circular antenna array beamforming.

II. MATHEMATICAL MODEL

As is shown in Fig. 1, a narrowband beamformer with N omnidirectional antennas is considered, and the output signal at time index k is formulated by:

$$y_k = \mathbf{w}^{\mathrm{H}}\mathbf{x}_k, \tag{1}$$

where $\mathbf{w}_k=[w_1,\ldots,w_N]^{\mathrm{T}}$ is the weighted coefficient vector, while $(\cdot)^{\mathrm{T}}$ and $(\cdot)^{\mathrm{H}}$ represent the transpose and Hermitian operators. The (M+1) input signal which composed of directed SOI (θ_s, φ_s), and interferences with direction of (θ_i, φ_i) (i=1,2,…M) is given by:

$$\mathbf{x}_k = \mathbf{A}_s\mathbf{E}_k + \mathbf{A}_i\mathbf{i}_k + \mathbf{n}_k, \tag{2}$$

where $\mathbf{A}_s$ and $\mathbf{A}_i$ are the steering matrices corresponding to the SOI and interferences, $\mathbf{E}_k$ as well as $\mathbf{i}_k$ are the complex SOI and interferences envelope vectors. $\mathbf{n}_k$ denotes the zero-mean white Gaussian noise vector.

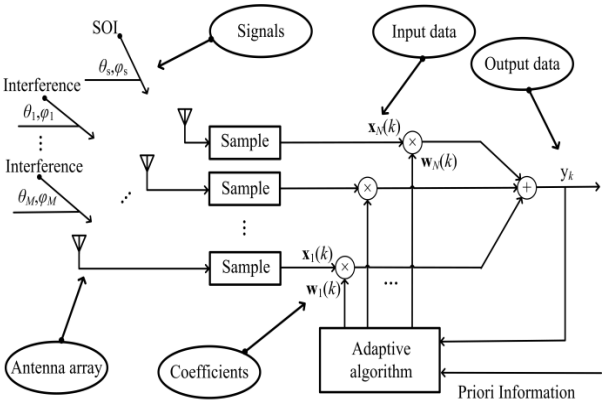

Fig. 1. The narrowband beamformer model.

Then, the beampattern for a given direction (θ, φ) is:

$$B(\theta,\phi) = \mathbf{w}^{\mathrm{H}}\exp\left\{\frac{-j2\pi\mathbf{Ap}}{\lambda}\right\}. \tag{3}$$

Herein, $\mathbf{A}$ is the steering matrix consists of $\mathbf{A}_s$ and $\mathbf{A}_i$, λ is the transmission wavelength, and $\mathbf{p}$ is the positions of antenna elements. The output SINR of a beamformer is expressed as [8]:

$$\mathrm{SINR} = \frac{\sigma_s^2|\mathbf{w}^{\mathrm{H}}\mathbf{A}_s|^2}{\mathbf{w}^{\mathrm{H}}\mathbf{R}_{\mathrm{n+i}}\mathbf{w}}, \tag{4}$$

where σ_s^2 is the SOI power, and $\mathbf{R}_{\mathrm{n+i}}$ is the covariance matrix of the interference-plus-noise which is depicted as:

$$\mathbf{R}_{\mathrm{n+i}} = E\left\{(\mathbf{i}_k+\mathbf{N}_k)(\mathbf{i}_k+\mathbf{N}_k)^{\mathrm{H}}\right\}, \tag{5}$$

where $E\{\cdot\}$ represents the expectation operator.

III. THE PROPOSED RL1-CNFLMS ALGORITHM

A. Review of the CLMS and CNLMS algorithms

The CLMS algorithm exerts a constraint condition on the cost function of LMS algorithm to solve the following problem [25]:

$$\min_{\mathbf{w}} E\left[|e_k|^2\right] \quad \text{subject to} \quad \mathbf{C}^{\mathbf{H}}\mathbf{w} = \mathbf{f}, \tag{6}$$

where $e_k=d_k-\mathbf{w}^{\mathrm{H}}\mathbf{x}_k$ represents the estimation error, and d_k is the desired output, while $\mathbf{C}$ and $\mathbf{f}$ are constrained matrix and vector which relates to the SOI and interferences.

The solution is then found out by using the LM method, and then, we obtain the following cost function:

$$L_{clms}(k) = E\left[|e_k|^2\right] + \boldsymbol{\lambda}_1^{\mathrm{H}}(\mathbf{C}^{\mathrm{H}}\mathbf{w}_k - \mathbf{f}). \tag{7}$$

In (7), $\boldsymbol{\lambda}_1$ is regarded as the LM vector. The gradient descent principle is also used for carrying out the solution of (6). In this case, the update equation is expressed as:

$$\mathbf{w}_{k+1} = \mathbf{w}_k - \mu\mathbf{g}_{\mathbf{w}}L_{clms}(k), \tag{8}$$

where μ acts as the convergence factor and $\mathbf{g}_{\mathbf{w}}L_{clms}(k)$ is gradient vector.

The instantaneous estimate is used to calculate the gradient vector $\mathbf{g}_{\mathbf{w}}L_{clms}(k)$, and we have:

$$\mathbf{g}_{\mathbf{w}}L_{clms}(k) = -2e_k^*\mathbf{x}_k + \mathbf{C}\boldsymbol{\lambda}_1. \tag{9}$$

Then, the final updating function is obtained and given by:

$$\mathbf{w}_{k+1} = \mathbf{P}\left[\mathbf{w}_k + \mu e_k^*\mathbf{x}_k\right] + \mathbf{f}_c, \tag{10}$$

with

$$\begin{cases}\mathbf{P} = \mathbf{I}_{N\times N} - \mathbf{C}(\mathbf{C}^{\mathbf{H}}\mathbf{C})^{-1}\mathbf{C}^{\mathbf{H}},\\ \mathbf{f}_c = \mathbf{C}(\mathbf{C}^{\mathbf{H}}\mathbf{C})^{-1}\mathbf{f}.\end{cases} \tag{11}$$

Then, the CNLMS algorithm is proposed to speed up the convergence process, which is the normalized version of CLMS algorithm [4, 25]. In the CLMS, the step size is fixed. If we use a variable step size μ_k that can minimize the instantaneous posteriori squared error, the convergence process will be greatly accelerated. That's to say, the CLMS algorithm can be normalized by letting the derivative in terms of μ be 0, which is to calculate [25]:

$$\frac{\partial[|e_{ap}(k)|^2]}{\partial\mu_k^*} = \frac{\partial\left[e_{ap}(k)e_{ap}^*(k)\right]}{\partial\mu_k^*} = 0, \tag{12}$$

where

$$e_{ap}(k) = e_k\left(1-\mu_k \mathbf{x}_k^{\mathrm{H}}\mathbf{P}\mathbf{x}_k\right). \tag{13}$$

Thus, we have:

$$\mu_k = \frac{\mu_0}{\mathbf{x}_k^{\mathrm{H}}\mathbf{P}\mathbf{x}_k + \xi_c}. \tag{14}$$

where ξ_c>0 is to avoid excessively large convergence factor, and μ_0 is the initial convergence factor.

Then, taking (14) into (10), we get the iteration equation for the CNLMS algorithm:

$$\mathbf{w}_{k+1} = \mathbf{P}[\mathbf{w}_k + \mu_0 \frac{e_k \mathbf{x}_k}{\mathbf{x}_k^{\mathrm{H}}\mathbf{P}\mathbf{x}_k + \xi_c}] + \mathbf{f}_c. \tag{15}$$

B. The proposed RL$_1$-CNFLMS algorithm

In this paper, a RL$_1$-CNFLMS algorithm for sparse adaptive beamforming is proposed, which uses the norm constraint technique to solve:

$$\min_{\mathbf{w}} E\left[\left|e_k\right|^2\right] \quad \text{subject to} \quad \begin{cases}\mathbf{C}^{\mathrm{H}}\mathbf{w}_k = \mathbf{f};\\ \|\mathbf{s}_k\mathbf{w}_k\|_1 = t,\end{cases} \tag{16}$$

where t is the sparseness constraint factor which is to force the small coefficients to zero, and $\mathbf{s}_k$ is presented as [8]:

$$[\mathbf{s}_k]_i = \frac{1}{\xi_{rl1} + |\mathbf{w}_{k-1}|_i}, i = 1,\ldots,N, \tag{17}$$

and ξ_{rl1}>0 is a constant analogous to ξ_c in (14).

The first step in finding out the solution is to utilize the LM method, and the corresponding cost function is:

$$\begin{aligned} L_{rl1}(k) = & E\left[\left|e_k\right|^2\right] + \boldsymbol{\lambda}_1^{\mathrm{H}}(\mathbf{C}^{\mathrm{H}}\mathbf{w}_k - \mathbf{f}) \\ & + \lambda_{rl1}[\|\mathbf{s}_k\mathbf{w}_k\|_1 - t], \end{aligned} \tag{18}$$

where $\boldsymbol{\lambda}_1$ and λ_{rl1} are the LMs.

Then, the instantaneous gradient estimation of (18) is given by:

$$\mathbf{g}_{\mathbf{w}} L_{rl1}(k) = -2e_k^*\mathbf{x}_k + \mathbf{C}\boldsymbol{\lambda}_1 + \lambda_{rl1}\mathbf{B}_{rl1}(k), \tag{19}$$

with

$$\mathbf{B}_{rl1}(k) = \frac{\mathrm{sgn}(\mathbf{w}_k)}{\xi_{rl1} + |\mathbf{w}_{k-1}|}, \tag{20}$$

where sgn(·) is the sign function which transforms each element in the vector as -1 for x<0, 0 for x=0 and 1 for x>0, respectively.

The gradient descent concept is used to address (16), resulting in the following update equation:

$$\mathbf{w}_{k+1} = \mathbf{w}_k - \mu\mathbf{g}_{\mathbf{w}} L_{rl1}(k). \tag{21}$$

The LMs $\boldsymbol{\lambda}_1$ and λ_{rl1} are assessable by using the constraints in (16). An approximating approach which considers the iteration process at the steady-state (i.e., $\mathbf{w}_{k+1}$=$\mathbf{w}_k$) is chosen to help to obtain the following equation [4, 6]:

$$\begin{cases}\mathbf{C}^{\mathrm{H}}\mathbf{w}_{k+1} = \mathbf{f},\\ \mathbf{B}_{rl1}(k)\mathbf{w}_{k+1} = t.\end{cases} \tag{22}$$

Based on (16), (19), (21) and (22), we finally acquire the equations below, for $\boldsymbol{\lambda}_1$ and λ_{rl1}, respectively:

$$\begin{cases}\boldsymbol{\lambda}_1 = \mathbf{D}(2e_k^*\mathbf{x}_k - \gamma_{rl1}\mathbf{B}_{rl1}(k)),\\ \lambda_{rl1} = (\frac{-2}{n\mu})(t - \mathbf{B}_{rl1}^{\mathrm{H}}(k)\mathbf{w}_k) + \frac{2e_k^*\mathbf{B}_{rl1}^{\mathrm{H}}(k)\mathbf{P}\mathbf{x}_k}{n},\end{cases} \tag{23}$$

with

$$\begin{cases}\mathbf{D} = (\mathbf{C}^{\mathrm{H}}\mathbf{C})^{-1}\mathbf{C}^{\mathrm{H}},\\ n = \|\mathbf{P}\mathbf{B}_{rl1}(k)\|_2^2.\end{cases} \tag{24}$$

Then, substituting $\boldsymbol{\lambda}_1$ and λ_{rl1} into (19) and (21), we can derive the updating equation:

$$\mathbf{w}_{k+1} = \mathbf{w}_k + \mu_0 e_k^*\mathbf{U} + \mathbf{f}_{rl1}(k), \tag{25}$$

where

$$\begin{cases} q = \mathbf{B}_{rl1}^{\mathrm{H}}(k)\mathbf{P}\mathbf{x}_k,\\ m = \mathbf{B}_{rl1}^{\mathrm{H}}(k)\mathbf{P}\mathbf{B}_{rl1}(k),\\ \mathbf{P} = \mathbf{I}_{N\times N} - \mathbf{C}(\mathbf{C}^{\mathrm{H}}\mathbf{C})^{-1}\mathbf{C}^{\mathrm{H}},\\ \mathbf{U} = \mathbf{P}(\mathbf{x}_k - \frac{q\mathbf{B}_{rl1}(k)}{m}),\\ \mathbf{f}_{rl1}(k) = (t - \mathbf{B}_{rl1}^{\mathrm{H}}(k)\mathbf{w}_k)(\frac{\mathbf{P}\mathbf{B}_{rl1}(k)}{m}). \end{cases} \tag{26}$$

To enable the algorithm to reach the steady-state more fleetly, the noise-free normalizing procedure is adopted in our proposed algorithm. The noise-free error signal obtained via the l_1-l_2 minimization method is introduced to many adaptive-filtering algorithms [24].

First, we rewrite the a priori error signal as:

$$e_k = e_{nf,k} + n(k), \tag{27}$$

where $n(k)$ is the noise-component and $e_{nf,k}$ is the expression of the a priori noise-free error signal, which is given by:

$$e_{nf,k} = d_k - \mathbf{x}_k\mathbf{w}_k. \tag{28}$$

Similarly, we use the a posteriori error signal:

$$\varepsilon_{nf,k} = d_k - \mathbf{x}_k\mathbf{w}_{k+1} = (1-\mu_k\mathbf{U}^{\mathrm{H}}\mathbf{x}_k)e_k - \mathbf{f}_{rl1}^{\mathrm{H}}\mathbf{x}_k, \tag{29}$$

Taking (27) into (29), and using straight-forward calculations, we have:

$$\varepsilon_{nf,k} = (1-\mu_k\mathbf{U}^{\mathrm{H}}\mathbf{x}_k)e_{nf,k} + n(k) - \mu_k\mathbf{U}^{\mathrm{H}}\mathbf{x}_k n(k) - \mathbf{f}_{rl1}^{\mathrm{H}}\mathbf{x}_k. \tag{30}$$

Then, take the expectation of the a posteriori squared error at time index k:

$$\begin{aligned} E[\varepsilon_{nf,k}^2] = & E[(1-\mu_k\mathbf{U}^{\mathrm{H}}\mathbf{x}_k)^2 e_{nf,k}^2] + E[n^2(k)] \\ & - E[(\mu_k\mathbf{U}^{\mathrm{H}}\mathbf{x}_k n^2(k))^2] \\ & - E[2(1-\mu_k\mathbf{U}^{\mathrm{H}}\mathbf{x}_k)e_{nf,k}\mathbf{f}_{rl1}^{\mathrm{H}}\mathbf{x}_k] \\ & + E[(\mathbf{f}_{rl1}^{\mathrm{H}}\mathbf{x}_k)^2]. \end{aligned} \tag{31}$$

In the formulations given above, $n(k)$ is a statistic independence and identically distributed white Gaussian signal, and $e_{nf,k}$ is very small when the algorithm converges so that its dependence is ignored. To keep the simplicity of the equation, as $\mathbf{U}^{\mathrm{H}}\mathbf{x}_k$ and $\mathbf{f}_{rl1}^{\mathrm{H}}\mathbf{x}_k$ are scalars, their instantaneous estimation is used in our derivation. With these assumptions, by minimizing $E[\varepsilon_{nf,k}^2]$ with respect to μ_k, yields:

$$\mu_k = \frac{\beta\left\{E[e_{nf,k}^2] - \mathbf{f}_{rl1}^{\mathrm{H}}\mathbf{x}_k E[e_{nf,k}]\right\}}{\mathbf{U}^{\mathrm{H}}\mathbf{x}_k\left\{E[e_{nf,k}^2] + E[n^2(k)]\right\}}, \quad (32)$$

where $0<\beta<1$ is a constant and $E[n^2(k)]=\sigma_n^2$ is the variance of noise.

Then, we will capture $E[e_{nf,k}]$ and $E[e_{nf,k}^2]$. The latter term $E[e_{nf,k}^2]$ can be approximated by the squared time average of $e_{nf,k}$ writing as:

$$E[e_{nf,k}^2] = \alpha E[e_{nf,k-1}^2]\mathrm{sign}[e_k] + (1-\alpha)e_{nf,k}^2. \quad (33)$$

The parameter α acts as the forgetting factor within (0, 1). In this case, the major task for us is to get the expression for $e_{nf,k}$ so as to address $E[e_{nf,k}]$ and $E[e_{nf,k}^2]$.

According to maximum a posteriori probability (MAP) [23], $e_{nf,k}$ can be recovered form e_k via the optimization problem:

$$f[e_{nf,k}] = 0.5|e_k - e_{nf,k}|^2 + \gamma|e_{nf,k}|, \quad (34)$$

where γ is a threshold parameter which balances the representation error and the sparsity. The optimal estimation of $e_{nf,k}$ is then calculated by minimizing $f[e_{nf,k}]$ with respect to $e_{nf,k}$, which is given by [23, 24]:

$$\hat{e}_{nf,k} = \mathrm{sign}[e_k]\max(|e_k| - \gamma, 0). \quad (35)$$

The threshold parameter γ is chosen as [22-24]:

$$\gamma = \sqrt{Q\sigma_n^2}, \quad (36)$$

with $1<Q<4$.

Until now, we have essentially studied all the expressions for μ_k which are summarized as follows:

$$\mu_k = \frac{\beta\left\{E[e_{nf,k}^2] - \mathbf{f}_{rl1}^{\mathrm{H}}\mathbf{x}_k E[e_{nf,k}]\right\}}{\mathbf{U}^{\mathrm{H}}\mathbf{x}_k\left\{E[e_{nf,k}^2] + E[n^2(k)]\right\}}, \quad (37)$$

where

$$\begin{cases} E[e_{nf,k}^2] = \alpha E[e_{nf,k-1}^2]\mathrm{sign}[e_k] + (1-\alpha)e_{nf,k}^2, \\ \hat{e}_{nf,k} = \mathrm{sign}[e_k]\max(|e_k| - \gamma, 0), \\ \gamma = \sqrt{Q\sigma_n^2}. \end{cases} \quad (38)$$

Finally, replacing μ_0 with μ_k in (25), we can acquire the updating equation for RL$_1$-CNFLMS algorithm which is omitted here for brief. It is found that the difference between the two algorithms, namely the RL$_1$-CNLMS in [6] and our proposed RL$_1$-CNFLMS is the calculation of step size, which requires a little computational complexity. That is to say, our proposed algorithm provides an acceptable computational complexity comparing to the existing algorithm.

IV. SIMULATIONS

In our experiments, a circular array is used to receive five QPSK narrowband signals. The signals, composing of an SOI and four interferences, come from the azimuths of 90°, 30°, 58°, 127°, 163°, respectively, with a uniform elevation of 45°. The interference to noise ratio is set to 30 dB. Other parameters are given in Table 1 in detail.

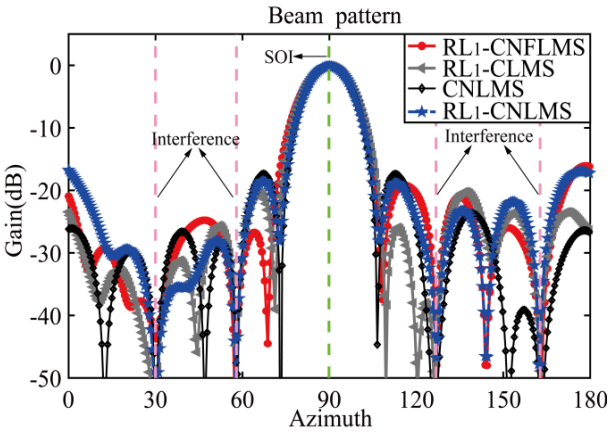

Fig. 2. Beam patterns of the proposed algorithm versus the CNLMS algorithm and the RL$_1$-CNLMS algorithm in [6].

Table 1: Parameters in simulations

Parameters	CNLMS	RL$_1$-CLMS	RL$_1$-CNLMS	RL$_1$-CNFLMS
Step-size (μ)	5×10^{-3}	5×10^{-9}	2×10^{-2}	-
Elements' interval	$2/\lambda$	$2/\lambda$	$2/\lambda$	$2/\lambda$
l_1-norm constraint	0.93	0.93	0.93	0.93
Signal frequencies	8GHz	8GHz	8GHz	8GHz
ε	5×10^{-3}	5×10^{-3}	5×10^{-3}	5×10^{-3}
α	-	-	-	0.52
δ	-	-	-	0.12
Q	-	-	-	1

The first set of experiment examined the impact of the developed RL$_1$-CNFLMS algorithm on beampatterns. The performance comparison of the proposed RL$_1$-CNFLMS, CNLMS, RL$_1$-CLMS and RL$_1$-CNLMS algorithms [6] are presented in Fig. 2. It can be seen that these algorithms are able to give resistant to the interferences by forming nulls and they can still remain high gain against the SOI around main lobe. As for our introduced algorithm, it has a quite similar main lobe with other algorithms as well as the same level of SLL.

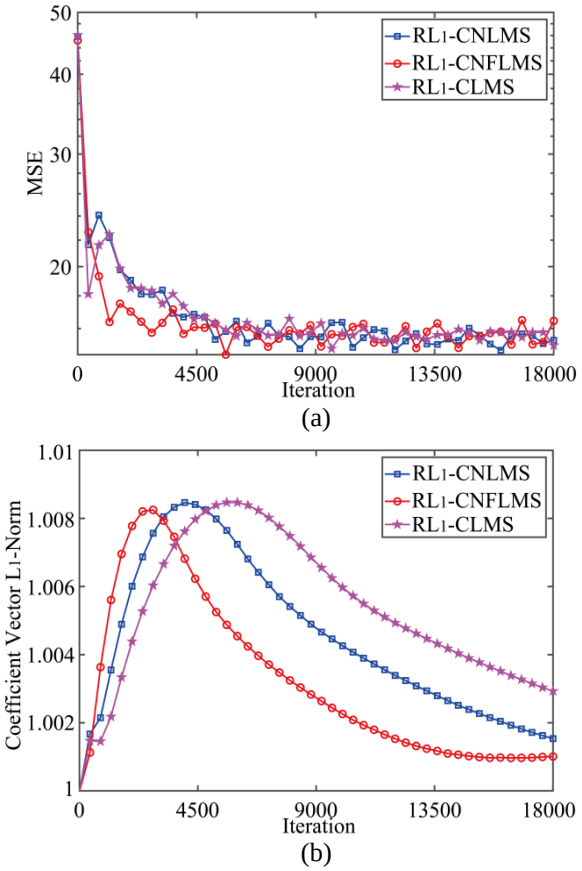

Fig. 3. The Mean square error (MSE) performance and the l_1-norm of coefficients for the proposed algorithm versus other related algorithms. (a) MSE performance, (b) l_1-norm.

Figure 3 shows the MSE performance and the coefficients' l_1-norm of the proposed RL$_1$-CNFLMS algorithm in contrast to other related beamforming algorithms. From Fig. 3, we can find that the proposed RL$_1$-CNFLMS have a superior convergence speed which validates the results in adaptive filtering and other fields, and verifies the effectiveness of our algorithm.

Figure 4 presents the beamformed antenna arrays. The sparse ratio, which is the proportion of the active antenna elements to the entire array, are set to be 65.2%, 55.4% and 38.4%, for RL$_1$-CLMS, RL$_1$-CNLMS and RL$_1$-CNFLMS algorithms. Considering Fig. 4 and referring to Fig. 2 and Fig. 3, it is obvious that our proposed algorithm has the ability to enhance the array sparsity and accelerate the convergence procedure with good beamforming properties.

In Fig. 5, the output SINR for different beamforming algorithms is discussed. We can see that the proposed RL$_1$-CNFLMS algorithm achieves better SINR for various SNRs in comparison with the related sparse adaptive beamformers.

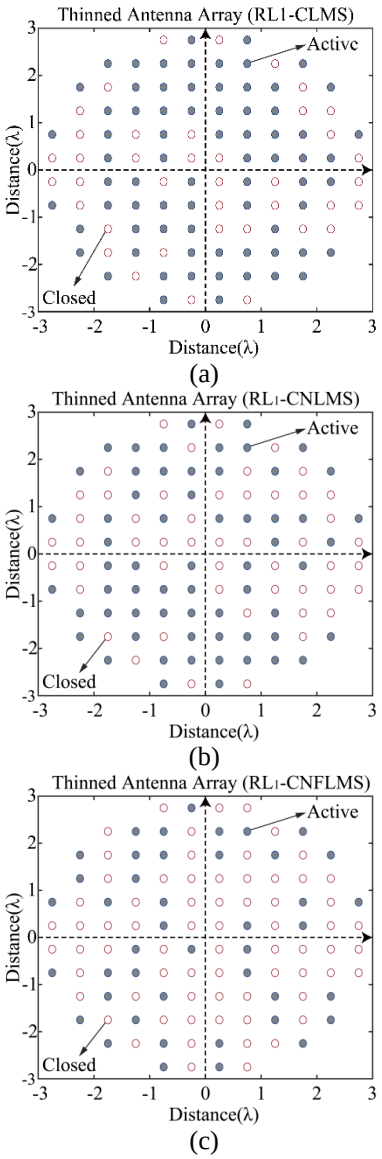

Fig. 4. Sparse arrays shrinked by RL$_1$-CNFLMS (proposed), RL$_1$-CLMS and RL$_1$-CNLMS [6].

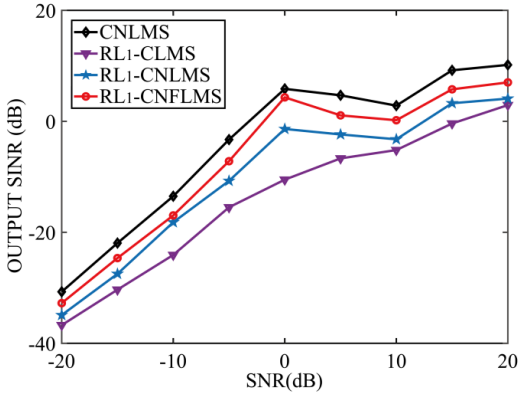

Fig. 5. Output SINR versus the input SNR.

From the discussions above, our developed RL_1-CNFLMS algorithm achieves a better capacity in sparsity, convergence process and output SINR with a comparable beampattern compared with other relevant sparse adaptive beamformers. As a consequence, the proposed RL_1-CNFLMS is worthwhile for practical applications.

V. CONCLUSION

In this paper, a RL_1-CNFLMS algorithm for sparse adaptive beamforming has been proposed and analyzed in detail. By means of the l_1-l_2 minimization method, the noise-free a posteriori error signal is obtained and adopted to normalize the sparse CLMS algorithm. The proposed RL_1-CNFLMS algorithm generates the desired beampattern while achieving a better performance in sparsity, convergence speed and output SINR along with an acceptable computational complexity. However, during the derivation procedure, as we use lots of approximations, the parameters maybe difficult to adjust. Also, the coupling in the array is neglected in our mathematical model, which may cause estimate error. All in all, we still have much more efforts to do in the future study.

In the future, we will consider the subarray method to construct the sparse blocked array beamforming using the technique in [26-28]. In addition, we will develop a platform to verify the proposed algorithms in a MIMO antenna array beamforming to analyze the effects of the mutual coupling in the array [29-31].

ACKNOWLEDGMENT

This work was partially supported by the National Key Research and Development Program of China (2016YFE111100), Key Research and Development Program of Heilongjiang (GX17A016), the Science and Technology innovative Talents Foundation of Harbin (2016RAXXJ044), the Natural Science Foundation of Beijing (4182077), China Postdoctoral Science Foundation (2017M620918), the Fundamental Research Funds for the Central University (HEUCFM180806, HEUCFG201829) and Opening Fund of Acoustics Science and Technology Laboratory (SSKF2016001).

REFERENCES

[1] H. L. Van Trees, *Detection, Estimation, and Modulation Theory, Part IV: Optimum Array Processing*, John Wiley & Sons, New York, NY, 2002.

[2] O. L. Frost, III, "An algorithm for linearly constrained adaptive array processing," *Proc. IEEE*, vol. 60, no. 8, pp. 926-935, Aug. 1972.

[3] J. A. Apolinário, Jr., S. Werner, P. S. R. Diniz, and T. I. Laakso, "Constrained normalized adaptive filtering for CDMA mobile communications," *IEEE Signal Processing Conference*, Rhodes, Greece, Sep. 1998.

[4] J. F. de Andrade, M. L. R. de Campos, and J. A. Apolinário, "L_1-Constrained normalized LMS algorithms for adaptive beamforming," *IEEE Transactions on Signal Processing*, vol. 63, no. 24, pp. 6524-6539, Dec. 2015. 10.1109/TSP.2015.2474302.

[5] W. Shi, Y. Li, and S. Luo, "Adaptive antenna array beamforming based on norm penalized NLMS algorithm," *2018 IEEE International Symposium on Antennas and Propagation and USNC-URSI Radio Science Meeting*, in press, Boston, America, July 2018.

[6] W. Shi, Y. Li, and J. Yin, "Improved constraint NLMS algorithm for sparse adaptive array beamforming control applications," *Applied Computational Electromagnetics Society Journal*, Accepted.

[7] S. A. Vorobyov, A. B. Gershman, and Z. Luo, "Robust adaptive beamforming using worst-case performance optimization: a solution to the signal mismatch problem," *IEEE Transactions on Signal Processing*, vol. 51, no. 2, pp. 313-324, Feb. 2003. 10.1109/tsp.2002.806865.

[8] O. Taheri and S. A. Vorobyov, *Reweighted l_1-Norm Penalized LMS for Sparse Channel Estimation and its Analysis*. Elsevier North-Holland, Inc. 2014.

[9] T. Jiang, X. Zhang, and Y. Li, "Bayesian compressive sensing using reweighted Laplace priors," *AEÜ - International Journal of Electronics and Communications*, vol. 97, pp. 178-184, 2018.

[10] Y. Chen, Y. Gu, and A. O. Hero, "Sparse LMS for system identification," *Proc. IEEE International Conference on Acoustic Speech and Signal Processing, (ICASSP'09)*, pp. 3125-3128, Taipei, Taiwan, Apr. 2009.

[11] O. Taheri and S. A. Vorobyov, "Sparse channel estimation with L_p-norm and reweighted L_1-norm penalized least mean squares," *IEEE International Conference on Acoustic Speech and Signal Processing (ICASSP'11)*, Prague, Czech Republic, pp. 2864-2867, May 2011.

[12] Y. Wang, Y. Li, and Z. Jin, "An improved reweighted zero-attracting NLMS algorithm for broadband sparse channel estimation," *IEEE International Conference on Electronic Information and Communication Technology*, Harbin, China, Aug. 2016.

[13] Y. Gu, J. Jin, and S. Mei, "l_0-norm constraint LMS algorithm for sparse system identification," *IEEE Signal Process. Lett.*, vol. 16, no. 9, pp. 774-777, Sept. 2009. 10.1109/LSP.2009.2024736.

[14] Y. Li, Y. Wang, R. Yang, et al., "A soft parameter function penalized normalized maximum correntropy criterion algorithm for sparse system identification," *Entropy*, vol. 19, no. 1, p. 45, Jan. 2017. 10.3390/e19010045.

[15] Z. Jin, Y. Li, and J. Liu, "An improved set-membership proportionate adaptive algorithm for

a block-sparse system," *Symmetry*, vol. 10, no. 3, p. 75, Mar. 2018. 10.3390/sym10030075.

[16] D. Angelosante, J. A. Bazerque, and G. B. Giannakis, "Online adaptive estimation of sparse signals: Where RLS meets the l_1-norm," *IEEE Transactions on Signal Processing*, vol. 58, no. 7, pp. 3436-3447, Mar. 2010. 10.1109/TSP.2010.2046897.

[17] O. Taheri and S. A. Vorobyov, "Reweighted l1-norm penalized LMS for sparse channel estimation and its analysis," *Elsevier Signal Processing*, vol. 104, pp. 70-79, May 2014.

[18] Y. Li, Y. Wang, and T. Jiang, "Sparse-aware set-membership NLMS algorithms and their application for sparse channel estimation and echo cancelation," *AEU - International Journal of Electronics and Communications*, vol. 70, no. 7, pp. 895-902, 2016.

[19] Y. Li, Y. Wang, and T. Jiang, "Norm-adaption penalized least mean square/fourth algorithm for sparse channel estimation," *Signal Processing*, vol. 128, pp. 243-251, 2016.

[20] R. Tibshirani, "Regression shrinkage and selection via the lasso," *J. R. Stat. Soc. Ser. B-Stat. Methodol*., vol. 58, no. 1, pp. 267-288, Jan. 1996.

[21] D. L. Donoho, "Compressed sensing," *IEEE Trans. Inf. Theory*, vol. 52, no. 4, pp. 1289-1306, Apr. 2006.

[22] I. Daubechies, M. Defrise, and C. De-Mol, "An iterative thresholding algorithm for linear inverse problems with a sparsity constraint," *Comm. Pure Appl. Math*., vol. 57, pp. 1413-1457, 2004.

[23] M. Zibulevsky and M. Elad, "l_1-l_2 optimization in signal and image processing," *IEEE Signal Process. Mag*., pp. 76-88, May 2010.

[24] M. Z. A. Bhotto and A. Antoniou, "A family of shrinkage adaptive filtering algorithms," *IEEE Trans. Signal Process*., vol. 61, no. 7, pp. 1689-1697, 2013.

[25] P. S. R. Diniz, *Adaptive Filtering: Algorithms and Practical Implementation*. New York, USA: Springer, 2010.

[26] Y. Li, Z. Jiang, W. Shi, X. Han, and B. D. Chen, "Blocked maximum correntropy criterion algorithm for cluster-sparse system identification," *IEEE Transactions on Circuits and Systems II: Express Briefs*, 10.1109/TCSII.2019.2891654.

[27] Y. Li, Z. Jiang, O. M. Omer-Osman, X. Han, and J. Yin, "Mixed norm constrained sparse APA algorithm for satellite and network channel estimation," *IEEE Access*, vol. 6, pp. 65901-65908, 2018.

[28] Y. Li, Z. Jiang, Z. Jin, X. Han, and J. Yin, "Cluster-sparse proportionate NLMS algorithm with the hybrid norm constraint," *IEEE Access*, vol. 6, pp. 47794-47803, 2018.

[29] K. Yu, Y. Li, and X. Liu, "Mutual coupling reduction of a MIMO antenna array using 3-D novel meta-material structures," *Applied Computational Electromagnetics Society Journal*, vol. 33, no. 7, pp. 758-763, 2018.

[30] L. Zhao, F. Liu, X. Shen, G. Jing, Y. Cai, and Y. Li, "A high-pass antenna interference cancellation chip for mutual coupling reduction of antennas in contiguous frequency bands," *IEEE Access*, vol. 6, pp. 38097-38105, 2018.

[31] T. Jiang, T. Jiao, Y. Li, and W. Yu, "A low mutual coupling MIMO antenna using periodic multi-layered electromagnetic band gap structures," *Applied Computational Electromagnetics Society Journal*, vol. 33, no. 3, pp. 305-311, 2018.

Different Array Synthesis Techniques for Planar Antenna Array

Tarek Sallam [1] and Ahmed M. Attiya [2]

[1] Faculty of Engineering at Shoubra
Benha University, Cairo, Egypt
tarek.sallam@feng.bu.edu.eg

[2] Microwave Engineering Dept.
Electronics Research Institute (ERI), Giza, Egypt
attiya@eri.sci.eg

Abstract ─ In this paper, a genetic algorithm (GA) is used to synthesize and optimize the excitation weights of a planar array for satellite communications based on ITU Radio Regulations 2016. The planar array is arranged into symmetric square lattices of subarrays. Each subarray is assumed to be consisting of 4×4 isotropic, uniform-spaced, and uniform-weighted elements. The proposed arrays are assumed to be consisting of 4×4 and 16×16 subarrays. A genetic algorithm is used to optimize the weights at the subarrays. Three different cases are studied in the paper. The first case is dealing with an amplitude-only weighting synthesis of the planar array. In this case the ratios of amplitude weights of subarrays are varied continuously from 0 to 1. In the second case, a phase-only synthesis of the planar array is discussed where the phases are varied in a continuous range between $-\pi/2$ and 0° while the amplitudes of all subarrays are the same. In the third case a complex weight synthesis is presented. In this case the ratios of the amplitudes are constrained between 0.7 and 1 whereas the phases are varied continuously from $-\pi/2$ to 0°. Moreover, the amplitude is varied with both continuous and discrete values. A comparison between the three methods is presented to develop the optimum technique for feeding an antenna array for satellite communication systems.

Index Terms ─ Antenna array, genetic algorithm, satellite antenna.

I. INTRODUCTION

Planar antenna arrays are good candidates for on-move earth segment of satellite communication systems [1–5]. From manufacturing point of view, it would be better to divide these planar arrays into smaller subarrays which are connected together through a common feeding network. The elements of these subarrays are usually fed with uniform distribution network. Due to the required constrains on the total radiation pattern of the complete antenna array according to the standards of the satellite communications, uniform distribution network would not be suitable for the feeding network between the subarrays. Thus, it would be required to synthesis the appropriate distribution for these subarrays to obtain the required specifications of the radiation pattern.

However, global synthesis of antenna arrays that generate a desired radiation pattern is a highly nonlinear optimization problem. Thus, analytical methods are not applicable any more. Several classical methodologies have been proposed to obtain suitable strategies for the optimal synthesis of antenna arrays [6]. Optimization algorithms differ in the complexity of computations and convergence rate. However, from the point of view of array synthesis, the result depends on the final convergence not on the method itself. It was shown in [7-11] that the evolutional optimization algorithms such as genetic algorithm (GA), bees algorithm, differential evolution algorithm, particle swarm optimization and colony selection algorithm are capable of performing better and more flexible solutions than the classical optimization algorithms and the conventional analytical approaches.

The GA is an excellent stochastic global optimization approach which is part of a larger field of evolutionary computations. This approach models genetics and natural selection in order to optimize a given cost function [12, 13]. Since its introduction, the GA has become a dominant numerical optimization algorithm in many disciplines. Details on implementing a GA can be found in [14], and a variety of applications to electromagnetics are reported in [15]. Some of the advantages of the GA include: (a) optimizing continuous or discrete variables, (b) avoiding calculation of derivatives, (c) handling a large number of variables, (d) suitability for parallel computing, (e) jumping out of a local minimum, (f) providing a list of optimum variables, not just a single solution, and (g) working with numerically generated data, experimental data, or analytical functions.

The GA implemented here is simple and flexible for

Submitted On: November 26, 2018
Accepted On: January 26, 2019

pattern synthesis of arbitrary arrays. This approach avoids binary coding and directly deals with real or complex weighting vectors. Using this approach, constraints on the phases and magnitudes of the complex weights are easily imposed for practical implementation of phase shifters and attenuators.

In this paper, we use the GA to synthesis the distribution network of the subarrays to obtain a complete radiation pattern which satisfies the required standards of satellite communications [14], [15]. Previous studies discussed briefly this distribution network by adjusting the amplitude of the feeding of each subarray [1-5].

On the other hand, the optimization techniques are dealing with the problem only form mathematical point of view. However, in practical application, the obtained distribution network may not be quite suitable for physical implementation. The simplest implementation of any arbitrary distribution network would be mainly composed of non-equal Wilkinson power dividers combined with lumped element resistors and transmission line sections [16]. For equal power division, the arms of the Wilkinson power divider would have equal characteristic impedance of $\sqrt{2}Z_0$ where Z_0 is the characteristic impedance of the feeding port. However, for large ratios of power divisions, the two arms of the characteristic impedance would have completely different values with very small and very large values. The large values of the characteristic impedance would correspond to very thin printed transmission line sections. On the other hand, the small values of characteristic impedance would correspond to very wide printed transmission line sections. This would introduce a quite complexity on the implementation of the non-equal power divider.

Thus, direct synthesis of the distribution network based on the amplitude only may not be quite suitable for implementation. This is the motivation in this paper to introduce the idea of using other distribution networks and compare between them. In addition to the conventional amplitude only distribution network, we introduce in this paper other three configurations, equal amplitude with non-equal phase distribution network, constrained non-equal amplitude with non-equal phase distribution network and discrete non-equal amplitude with non-equal phase distribution network. In constrained non-equal amplitude, the amplitude ratio is limited in continuous range from 0.7 to unity. However, in discrete constrained non-equal amplitude, the amplitude ratio is limited to four discrete values 0.7, 0.8, 0.9, and 1 only. This has an additional advantage in implementation where specific pre-designed power divider would be used directly as blocks in the complete distribution network. On the other hand, the non-equal phases can be simply implemented by adjusting the lengths of the transmission line sections after power division.

The present study is almost like other studies of beamforming such as null broadening beamforming [21], constrained normalized least-mean-square (CNLMS) beamforming [22], and linearly constrained minimum variance (LCMV) beamforming [23] as well as direction of arrival (DOA) techniques such as Cramér Rao bound (CRB) approach [24] which depend mainly on the array factor. The result of the present feeding distribution function would be the starting point for full wave analysis of the complete array configuration which includes mutual coupling [25] in this case.

II. FORMULATION OF THE PROBLEM

The complete antenna array is assumed to be composed of an array of subarrays as shown in Fig. 1. Each subarray is composed of $N_{ex} \times N_{ey}$ elements. The complete array is composed of $2N_{sx} \times 2N_{sy}$ subarrays. The array factor for this planar array can be presented as [17],

$$AF(\theta,\varphi) = 4\sum_{p=1}^{N_{sy}}\sum_{q=1}^{N_{sx}} b_{pq}\sum_{m=1}^{N_{ey}}\sum_{n=1}^{N_{ex}} a_{mn}\cos(X_{qn})\cos(Y_{pm}), \quad (1)$$

where,

$$X_{qn} = kd_x \sin\theta\cos\varphi\,[n-0.5+(q-1)N_{ex}], \quad (2\text{-a})$$

$$Y_{pm} = kd_y \sin\theta\sin\varphi\,[m-0.5+(p-1)N_{ey}], \quad (2\text{-b})$$

a_{mn} represents the complex weight of radiating element in the subarray, b_{pq} represents complex weight of the subarray $2N_{sx}$ is the number of subarrays in x direction, $2N_{sy}$ is the number of subarrays in y direction, N_{ex} is the number of elements in the subarray in x direction, N_{ey} is the number of elements in the subarray in y direction, d_x is the spacing between the radiating elements in the x direction, and d_y is the spacing between the radiating elements in the y direction. The distribution network of the total array is weighted only at the subarray level. Thus, the amplitudes of all elements inside each subarray are unity ($a_{mn} = 1$, for all m, n).

Since the planar array is symmetric about its both axes, the GA synthesizes only a quarter of the array. This quarter of the symmetric planar array is called a *unit* as shown in Fig. 2. In this case, the unit consists of $N_{sx}\times N_{sy}$ subarrays. In all following simulations, each subarray has 4×4 elements, and a square array is assumed. Thus, $N_{ex} = N_{ey} = 4$ elements, $N_{sx} = N_{sy} = N$, and $d_x = d_y = d$. Moreover, it is also shown that the unit itself is symmetric about its main diagonal.

The reason for choosing a subarray of 4×4 elements is that it would be quite complicated to design a feeding network on the same layer for a subarray of additional elements as it is shown in the proposed feeding network in [3].

The GA begins with a random set of array configurations called the *population* (rows of a matrix for linear array and matrices of a tensor in the case of planar array) consisting of variables such as element/subarray amplitude and phase. Each array configuration is evaluated by the cost function that returns a numerical value or score that characterizes how well the array

configuration performs. Array configurations with high costs are discarded, while array configurations with low costs form a mating pool. Two parents are randomly selected from the mating pool. Selection is inversely proportional to the cost. Offspring result from a combination of the parents. The offspring replace the discarded array configurations. Next, random array configurations in the population are randomly modified or mutated. Finally, the new array configurations are evaluated for their costs and the process repeats. The flowchart of the GA appears in Fig. 3.

In this paper, the array is planar, and hence each array configuration is a matrix (called *chromosome*) containing a number of columns equals the number of subarrays in *y* direction and a number of rows equals double the number of subarrays in *x* direction (the upper half for amplitude and lower half for phase). If the unit is only to be optimized, the chromosome will be $2N \times N$ matrix.

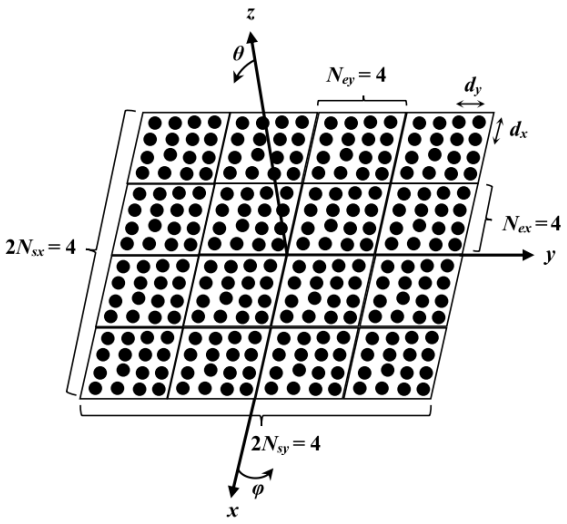

Fig. 1. Planar array with 4 × 4 subarrays each having 4 × 4 elements. In this case, the array is square with $N_{ex} = N_{ey} = 4$, $2N_{sx} = 2N_{sy} = 2N = 4$, and $d_x = d_y = d$.

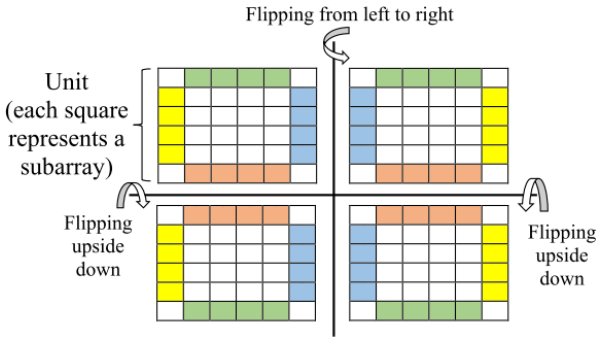

Fig. 2. A graphical representation of the whole symmetric planar array as composed from its building *unit*.

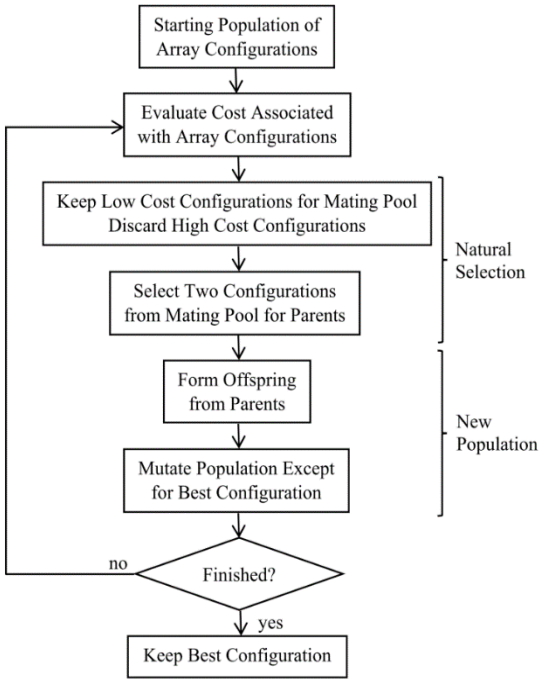

Fig. 3. Flowchart of the GA.

The cost function that is effective for the optimization of array weights for shaping the radiation pattern is defined as the error between the array factor and the required Mask and is normalized by the total number of points N_{tot} used to sample the AF and the Mask as follows:

$$\text{Cost} = \frac{1}{N_{tot}} \sum_{\text{i}} \frac{1+\text{sgn}(AF(\theta_i)_{dBi} - \text{Mask}(\theta_i)_{\text{dBi}})}{2} \left[AF(\theta_i)_{dBi} - \text{Mask}(\theta_i)_{\text{dBi}}\right]. \quad (3)$$

The cost function is expressed in dBi to allow for finer improvements as the optimizer converges.

It should be noted that, only the pattern points of AF those are greater than the Mask contribute to the total score of the cost function. For this reason, this cost function is often called the "don't exceed" square error criterion. This cost function is quite good for shaping sidelobe patterns since it does not penalize sidelobes below the mask. An optimal solution is defined as any solution which does not violate the mask, resulting in a score of zero.

It should be noted that this "don't exceed" sidelobe threshold is a nonlinear constraint which is not generally can be handled by analytical methods such as least squares [18, 19], which require the specification of an achievable far field pattern. The "don't exceed" sidelobe threshold case is of practical interest since usually one does not care how the sidelobes are arranged, only those are below the mask level. The main beam is excluded from the cost function. A far field pattern of $N_{tot} = 1000$

points evenly spaced in sine space is computed for each candidate array at each cost evaluation. Here sine space refers to the sine of the far field angle θ at a specific angle φ. Equally spacing pattern points in sine space rather than angle space provide a more uniform sampling of the sidelobe amplitudes. When the angle space is used, the outer sidelobes tend to be poorly represented. The lower the cost, the more fit the array distribution.

In this paper, the desired Mask function is the ITU Mask of the 2016 Edition of ITU Radio Regulations [20] which is formulated as follows:

a) In cases where the ratio between the antenna diameter (for the square planar array, which is our case, it is the array aperture length in either *x* or *y* direction) and wavelength is greater than 100, the Mask, for a given azimuth angle φ, is written as:

$$G(\theta) = G_{max} - 2.5 \times 10^{-3}(\frac{D}{\lambda}\theta)^2 \quad \text{for} \quad 0 \le \theta < \theta_m, \text{(4-a)}$$

$$G(\theta) = G_1 \quad \text{for} \quad \theta_m \le \theta < \theta_r, \text{(4-b)}$$

$$G(\theta) = 32 - 25\,log_{10}\,\theta \quad \text{for} \quad \theta_r \le \theta < 48°, \text{(4-c)}$$

$$G(\theta) = -10 \quad \text{for} \quad 48° \le \theta \le 90°, \text{(4-d)}$$

where θ is the elevation angle, $G(\theta)$ is the antenna gain in dB, G_{max} is the main beam antenna gain in dB, D is the antenna diameter, λ is the wavelength, and G_1 is the first sidelobe gain which is given by,

$$G_1 = 2 + 15 \log_{10} \frac{D}{\lambda}, \quad (5)$$

θ_m and θ_r are given by:

$$\theta_m = \frac{20\lambda}{D}\sqrt{G_{max} - G_1}, \quad (6)$$

$$\theta_r = 15.85(\frac{D}{\lambda})^{-0.6}. \quad (7)$$

b) In cases where the ratio between the antenna diameter and wavelength is less than or equal to 100, the Mask is given by,

$$G(\theta) = G_{max} - 2.5 \times 10^{-3}(\frac{D}{\lambda}\theta)^2 \quad \text{for} \quad 0 \le \theta < \theta_m, \text{(8-a)}$$

$$G(\theta) = G_1 \quad \text{for} \quad \theta_m \le \theta < \frac{100\lambda}{D}, \text{(8-b)}$$

$$G(\theta) = 52 - 10 \log_{10} \frac{D}{\lambda} - 25 \log_{10} \theta \quad \text{for} \quad \frac{100\lambda}{D} \le \theta < 48°, \text{(8-c)}$$

$$G(\theta) = 10 - 10 \log_{10} \frac{D}{\lambda} \quad \text{for} \quad 48° \le \theta \le 90°. \text{(8-d)}$$

In Fig. 4, the ITU Mask normalized with respect to G_{max} = 31 dBi of an array of 4×4 subarrays (16×16 isotropic elements) with inter-element spacing d of 0.65λ is plotted against its original uniform (non-optimized) AF at φ = 0°. Note that the Mask is symmetric about θ = 0°. The ultimate cost function value (UCFV) in this case is 12.96 dBi. Figure 5 shows the original uniform AF of 16×16-subarray array (64×64 elements) also plotted against its normalized ITU Mask, but this time with d = 0.7λ and G_{max} = 35 dBi. The UCFV now becomes 8.69 dBi.

In the following section, different schemes of weighting distribution functions are obtained by using genetic algorithm to satisfy the conditions of this Mask.

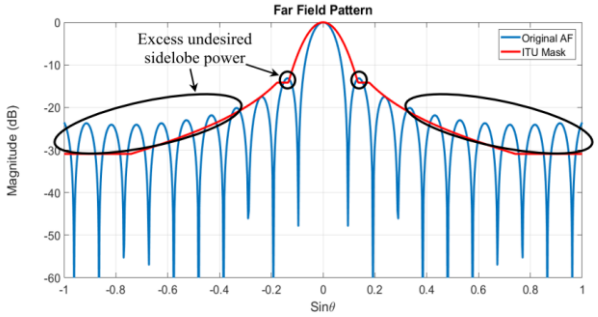

Fig. 4. The normalized ITU Mask of an array of 4 × 4 subarrays with d = 0.65λ and G_{max} = 31 dBi plotted against its original uniform AF at φ = 0°.

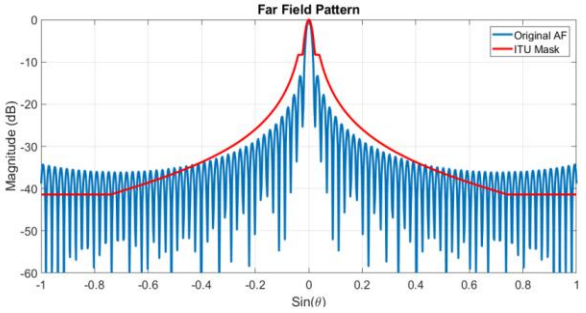

Fig. 5. The normalized ITU Mask of an array of 16 × 16 subarrays with d = 0.7λ and G_{max} = 35 dBi plotted against its original uniform AF at φ = 0°.

III. RESULTS AND DISCUSSIONS

The subarray excitation is represented as a complex valued weight b_{pq} with amplitude and phase. The proportions of amplitude, phase or both among subarrays can be altered to achieve the desired ITU response. In general, varying the amplitude and phase excitation offer more flexibility in the shaping of sidelobe power than aperiodic spacings between elements does. The strategy here is to implement the GA to design planar phased array antennas by controlling the weighted excitation applied to each subarray in the array while maintaining periodic element (or subarray) spacings. The GA is employed to perform amplitude-only, phase-only, and complex (both amplitude and phase) synthesis. In all simulations, an initial population of 10 random candidate array distributions is generated and evolved for 1,000 iterations (10,000 cost function evaluations).

A. Amplitude-only synthesis

First, we begin with the amplitude-only tapering of the planar array of 4×4 subarrays (the same array of Fig. 4). The subarray amplitude weights are allowed to vary continuously between 0 and 1 while all phases are kept at 0°. In this case, the unit is 2×2 subarrays (N = 2), thus

the total number of optimization variables is $N^2 = 4$. The array has a periodic element spacing $d = 0.65\lambda$ and a maximum gain $G_{max} = 31$ dBi. The optimized AF of this array at $\varphi = 0°$ is shown in the bottom of Fig. 6.

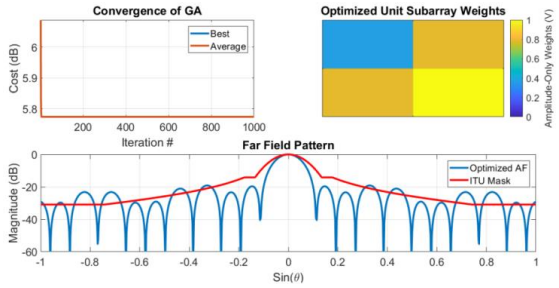

Fig. 6. The same array of Fig. 4 with amplitude-only synthesis of the array.

The convergence of the GA as a function of iteration is shown in the top left of the figure indicating that the UCFV is 5.77 dBi. The GA gives the optimized unit subarray amplitude weight values as shown in the top right of the figure. In comparison with the result in [1], the GA can give the same optimized unit subarray amplitude weight values of $\begin{pmatrix} 0.6 & 0.8 \\ 0.8 & 1 \end{pmatrix}$, but with a higher UCFV of 8.72 dBi. Thus, the result of the proposed approach, represented in Fig. 6, is better than that of [1].

Figure 7 shows the amplitude-only synthesis of the 16×16-subarray array of Fig. 5. The unit in this case is 8×8 subarrays with $N = 8$. Thus, there are $N^2 = 64$ total variables (subarray amplitude weights) for optimization. The amplitudes are varied continuously between 0 and 1. From the convergence curve of GA in Fig. 7, the UCFV is found to be 0.61 dBi.

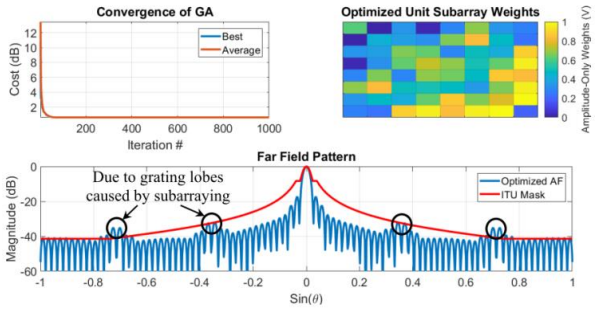

Fig. 7. The same array of Fig. 5 with amplitude-only synthesis of the array.

B. Phase-only synthesis

Amplitude-only synthesis of the weights of subarrays is simple linear optimization with fast convergence. However, the amplitude-only synthesis has a wide variation range in amplitude between 0 and 1. This wide range causes difficulties in the practical implementation of the feeding network. This is the motivation to study the possibility of synthesizing the array far field radiation pattern by varying the phases of the subarrays. This process of phase tapering is known as phase-only array synthesis. One of the main advantages of phase-tapered arrays is the relatively simple feed network that is required compared to amplitude tapered arrays.

The phase-only synthesis problem generally requires the application of nonlinear (the unknown phases appear in the complex exponent and are not easily found) optimization techniques for its solution.

Figure 8 shows the phase-only synthesis of the 4×4-subarray with the same parameters (N, d, and G_{max}) as of the amplitude-only weighted array in Fig. 6. With unity amplitude weighting, the unit has a total of $N^2 = 4$ subarray phase weights as the optimization variables with their values are allowed to vary continuously from $-\pi/2$ to 0°. It is clearly visible from Fig. 8 that the phase tapers have a modest ability to lower sidelobes and tend to be less efficient than amplitude tapers (the cost function cannot be fully satisfied and reaches to 9.21 dBi as an ultimate value).

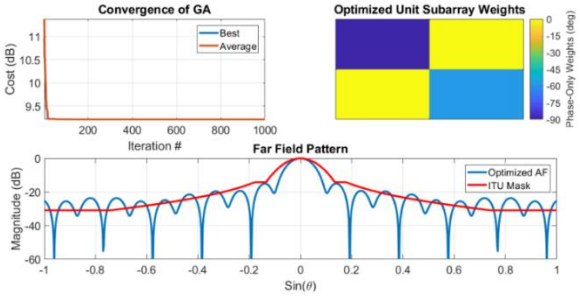

Fig. 8. As in Fig. 6, but with phase-only synthesis of the array.

Figure 9 shows the phase-only synthesis of the 16 × 16-subarray array with the same parameters as of the amplitude-only weighted array in Fig. 7. The unit has a total of $N^2 = 64$ subarray phase weights as the optimization variables with their values are also allowed to vary continuously from $-\pi/2$ to 0°. Again, as seen from Fig. 9, the cost function cannot be fully satisfied with the UCFV is just 1.91 dBi.

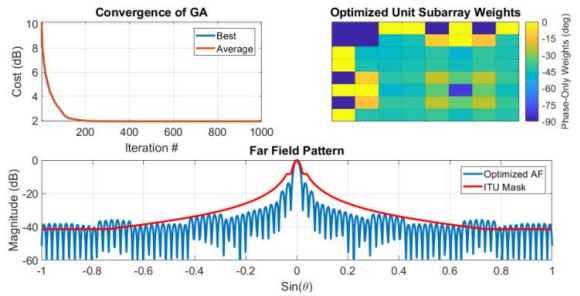

Fig. 9. As in Fig. 7, but with phase-only synthesis of the array.

C. Complex synthesis

In order to combine the advantage of amplitude-only synthesis from the point of view of easy linear optimization and fast convergence with the advantage of phase-only synthesis from the point of view of practical implementation, a complex (amplitude and phase) synthesis of the previous arrays is presented in this Section. However, in this case the amplitude is constrained between 0.7 and 1 to obtain a simpler feeding network. Two scenarios for varying the amplitudes are discussed, continuous variation, and discrete variation with four fixed values (0.7, 0.8, 0.9, and 1). The second scenario is more appropriate for implementation where pre-designed power divider would be used as blocks in the feeding network. In both cases, the phase is varied continuously from $-\pi/2$ to 0°. In this case, the total number of optimization variables (both subarray amplitude and phase weights of the unit) is $2N^2$.

Figure 10 shows the complex synthesis of the 4×4 array when the amplitude is varied in a continuous way. It can be noted that the cost function reaches 6.04 dBi as an ultimate value which is above the value of the amplitude-only synthesis by only 0.27 dBi and much better than the value of the phase-only synthesis. Figure 11 shows the complex synthesis of the same array but with the discrete variation of amplitude leading to the same optimized complex weights and also the same UCFV as of the continuous variation case but with a little different convergence.

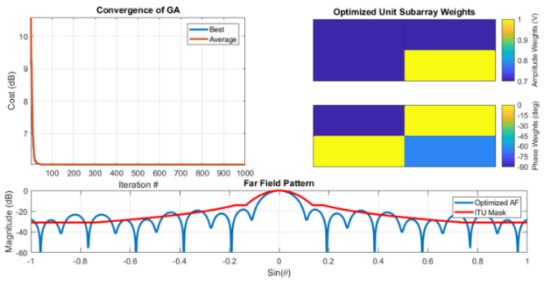

Fig. 10. As in Fig. 6, but with complex synthesis of the array. The amplitude is varied continuously in the range from 0.7 to 1.

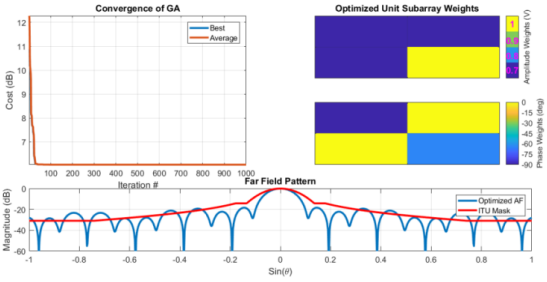

Fig. 11. As in Fig. 6, but with complex synthesis of the array. The amplitude is varied in discrete values 0.7, 0.8, 0.9 and 1.

Figure 12 shows the complex synthesis of the 16×16 array with the continuous variation of amplitude. The cost function reaches 0.65 dBi as an ultimate value which is nearly the same value of the amplitude-only synthesis and is also better than the value of the phase-only synthesis. Figure 13 shows the complex synthesis with the discrete variation of amplitude having a simpler feed network but at the price of a higher UCFV, it is now 0.90 dBi, than that of the continuous variation.

Of all the scenarios addressed in this work, this particular scenario was the most difficult to optimize and require more iterations to converge than the previous two scenarios and this can be clearly seen from the convergence curves of Figs. 10-13. Also, note that in all previous results, the unit is symmetric about its main diagonal. Table 1 summarizes the UCFV's of the two arrays for all types of synthesis discussed as well as the uniform case.

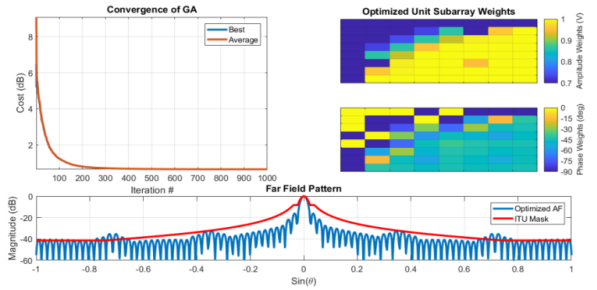

Fig. 12. As in Fig. 7, but with the complex synthesis of the array with continuous amplitude variation from 0.7 to 1.

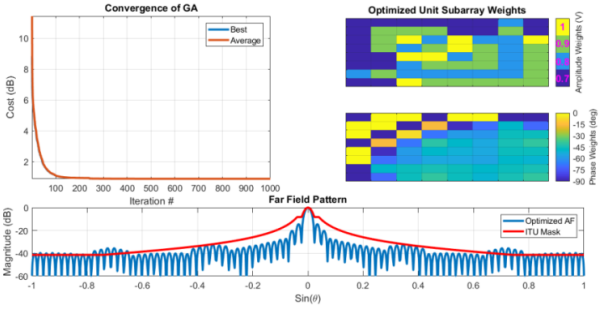

Fig. 13. As in Fig. 7, but with complex synthesis of the array. The amplitude is varied in discrete values 0.7, 0.8, 0.9, and 1.

Table 1: The summary of the UCFV's (in dBi) of the two arrays

Type of Synthesis	4 × 4	16 × 16
Uniform	12.96	8.69
Amplitude-only	5.77	0.61
Phase-only	9.21	1.91
Complex continuous	6.04	0.65
Complex discrete	6.04	0.90

IV. CONCLUSION

In this paper, four synthesis techniques are presented to optimize the radiation pattern of an antenna array to satisfy the requirements of ITU Mask for satellite communications. The techniques are, amplitude only distribution, phase only distribution, complex distribution with constrained amplitudes and complex amplitudes with discrete amplitudes. Based on the obtained results, the last two techniques are found to be the suitable ones for obtaining a good performance and practical implementation schemes.

ACKNOWLEDGMENT

This work was supported by Information Technology Industry Development Agency, ITIDA, Egypt, Information Technology Academia Collaboration (ITAC) program, Project No. PRP2018.R24.1.

REFERENCES

[1] A. García-Aguilar, J. M. Inclán-Alonso, L. Vigil-Herrero, J. M. Fernández-González, and M. Sierra-Pérez, "Printed antenna for satellite communications," *IEEE International Symposium on Phased Array Systems and Technology* (*ARRAY*), pp. 529-535, 2010.

[2] Y.-B. Jung, S.-Y. Eom, and S.-I. Jeon, "Experimental design of mobile satellite antenna system for commercial use," *IEEE Transactions on Consumer Electronics*, vol. 56, 2010.

[3] A. García-Aguilar, J. M. Inclán-Alonso, L. Vigil-Herrero, J. M. Fernández-González, and M. Sierra-Pérez, "Low-profile dual circularly polarized antenna array for satellite communications in the X band," *IEEE Transactions on Antennas and Propagation*, vol. 60, pp. 2276-2284, 2012.

[4] H. T. Zhang, W. Wang, M. P. Jin, and X. P. Lu, "A dual-polarized array antenna for on-the-move applications in Ku-band," *IEEE-APS Topical Conference on Antennas and Propagation in Wireless Communications* (*APWC*), pp. 5-8, 2016.

[5] J. M. Inclán-Alonso, A. García-Aguilar, L. Vigil-Herrero, J. M. Fernández-González, J. SanMartín-Jara, and M. Sierra-Perez, "Portable low profile antenna at X-band," *Proceedings of the 5th European Conference on Antennas and Propagation* (*EUCAP*), pp. 1923-1927, 2011.

[6] T. S. Angell and A. Kirsch, *Optimization Methods in Electromagnetic Radiation*. Springer Science & Business Media, 2004.

[7] G. K. Mahanti, A. Chakrabarty, and S. Das, "Phase-only and amplitude-phase synthesis of dual-pattern linear antenna arrays using floating-point genetic algorithms," *Progress In Electromagnetics Research*, vol. 68, pp. 247-259, 2007.

[8] K. Guney and M. Onay, "Amplitude-only pattern nulling of linear antenna arrays with the use of bees algorithm," *Progress In Electromagnetics Research*, vol. 70, pp. 21-36, 2007.

[9] S. Yang, Y. B. Gan, and A. Qing, "Antenna-array pattern nulling using a differential evolution algorithm," *Int. J. Microwave RF Computer-aided Engineering*, vol. 14, pp. 57-63, 2004.

[10] M. M. Khodier and C. G. Christodoulou, "Linear array geometry synthesis with minimum sidelobe level and null control using particle swarm optimization," *IEEE Trans. Antennas Propagat*., vol. 53, pp. 2674-2679, 2005.

[11] A. Akdagli and K. Guney, "A clonal selection algorithm for null synthesizing of linear antenna arrays by amplitude control," *Journal of Electromagnetic Waves and Applications*, vol. 20, pp. 1007-1020, 2006.

[12] J. H. Holland, "Genetic algorithms," *Scientific American*, pp. 66-72, July 1992.

[13] D. E. Goldberg, *Genetic Algorithms in Search, Optimization, and Machine Learning*. Reading, MA: Addison-Wesley, 1989.

[14] R. L. Haupt and S. E. Haupt, *Practical Genetic Algorithms*. 2nd edition, New York: John Wiley & Sons, 2004.

[15] R. L. Haupt and D. Werner, *Genetic Algorithms in Electromagnetics*. New York: John Wiley & Sons, 2007.

[16] D. M. Pozar, *Microwave Engineering*. 4th edition, John Wiley & Sons, 2012.

[17] R. Haupt, "Optimization of subarray amplitude tapers," *IEEE APS Symp*., pp. 1830-1833, June 1995.

[18] H. Hirasawa and B. J. Strait, "On a method for array design by matrix inversion," *IEEE Trans. Antennas Propagat*., vol. 19, pp. 446-447, May 1971.

[19] B. D. Carlson and D. Willner, "Antenna pattern synthesis using weighted least squares," *IEE Proc.-H*, vol. 139, no. 1, pp. 11-16, Feb. 1992.

[20] "Methods for the determination of the coordination area around an earth station in frequency bands between 100 MHz and 105 GHz," *2016 Edition of ITU Radio Regulations*, vol. 2, appendix 7, 2016.

[21] W. Li, Y. Zhao, Q. Ye, and B. Yang, "Adaptive antenna null broadening beamforming against array calibration error based on adaptive variable diagonal loading," *International Journal of Antennas and Propagation*, vol. 2017, Article ID 3265236, 2017.

[22] J. F. de Andrade, Jr., M. L. R. de Campos, and J. A. Apolinário, Jr., "L1-constrained normalized LMS algorithms for adaptive beamforming," *IEEE Trans. Signal Process*., vol. 63, no. 24, pp. 6524-6539, Dec. 2015.

[23] J. Xu, G. Liao, S. Zhu, and L. Huang, "Response vector constrained robust LCMV beamforming

based on semidefinite programming," *IEEE Trans. Signal Process*., vol. 63, no. 21, pp. 5720-5732, Nov. 2015.

[24] J. P. Delmas, M. N. El Korso, H. Gazzah, and M. Castella, "CRB analysis of planar antenna arrays for optimizing near-field source localization," *Signal Process*., vol. 127, pp. 117-134, 2016.

[25] K. Yu, Y. Li, and X. Liu, "Mutual coupling reduction of a MIMO antenna array using 3-D novel meta-material structures," *Applied Computational Electromagnetics Society Journal*, vol. 33, no. 7, pp.758-763, 2018.

Tarek Sallam was born in Cairo, Egypt, in 1982. He received the B.S. degree in Electronics and Telecommunications Engineering and the M.S. degree in Engineering Mathematics from Benha University, Cairo, Egypt, in 2004 and 2011, respectively, and the Ph.D. degree in Electronics and Communications Engineering from Egypt-Japan University of Science and Technology (E-JUST), Alexandria, Egypt, in 2015. He was a Researcher Assistant with the High Frequency Lab, National Institute of Standards (NIS), Giza, Egypt from 2005 to 2006. In 2006, he joined the Department of Engineering Mathematics and Physics, Faculty of Engineering at Shoubra, Benha University, where he is currently an Assistant Professor. He was a Visiting Researcher with the Electromagnetic Compatibility Lab, Department of Information and Communications Technology, Graduate School of Engineering, Osaka University, Osaka, Japan, from August 2014 to May 2015. His research interests include evolutionary optimization, artificial neural networks, phased array antennas with array signal processing and adaptive beamforming, and phased array radar with weather radar as a special case. His recent research has been on non-periodic and random antenna arrays.

Ahmed M. Attiya M.Sc. and Ph.D. Electronics and Electrical Communications, Faculty of Engineering, Cairo University at 1996 and 2001 respectively. He joined Electronics Research Institute as a Researcher Assistant in 1991. In the period from 2002 to 2004 he was a Postdoc in Bradley Department of Electrical and Computer Engineering at Virginia Tech. In the period from 2004 to 2005 he was a Visiting Scholar in Electrical Engineering Dept. in University of Mississippi. In the period from 2008 to 2012 he was a Visiting Teaching Member in King Saud University. He is currently Full Professor and the Head of Microwave Engineering Dept. in Electronics Research Institute. He is also the Founder of Nanotechnology Lab. in Electronics Research Institute.

Using MATLAB's Parallel Processing Toolbox for Multi-CPU and Multi-GPU Accelerated FDTD Simulations

Alec J. Weiss [1], Atef Z. Elsherbeni [1], Veysel Demir [2], and Mohammed F. Hadi [1]

[1] Department of Electrical Engineering
Colorado School of Mines, Golden, Colorado 80401, United States of America
aweiss@mines.edu, aelsherb@mines.edu, mhadi@mines.edu

[2] Department of Electrical Engineering
Northern Illinois University, DeKalb, Illinois 60115, United States of America
vdemir@niu.edu

Abstract — MATLAB is a good testbed for prototyping new FDTD techniques as it provides quick programming, debugging and visualization capabilities compared to lower level languages such as C or FORTRAN. However, the major disadvantage of using MATLAB is its slow execution. For faster simulations, one should use other programming languages like Fortran or C with CUDA when utilizing graphics processing units. Development of simulation codes using these other programming languages is not as easy as when using MATLAB. Thus the main objective of this paper is to investigate ways to increase the throughput of a fully functional finite difference time domain method coded in MATLAB to be able to simulate practical problems with visualization capabilities in reasonable time. We present simple ways to improve the efficiency of MATLAB simulations using the parallel toolbox along with the multi-core central processing units (CPUs) or the multiple graphics processing units (GPUs). Native and simple MATLAB constructs with no external dependencies or libraries and no expensive or complicated hardware acceleration units are used in the present development.

Index Terms — FDTD, MATLAB, multi-cores, multi-GPUs, parallel computing.

I. INTRODUCTION

The finite difference time domain (FDTD) method provides wide bandwidth simulations using time domain techniques to provide accurate, full wave electromagnetic simulations. The equations for the updating of field components can be solved through the use of finite difference approximations of Maxwell's equations. This method is inherently parallel as the update of field components of each cell within the simulation grid relies on field values all of which have been calculated at previous time and are within the vicinity of the cell. In their final form, the ease of parallelization becomes apparent. As an example, consider the updating equation for the x component the electric field:

$$\begin{aligned} E_x^{n+1} = {} & C_{exe}(i,j,k) \times E_x^n(i,j,k) \\ & + C_{exhz}(i,j,k) \times \left(H_z^{n+\frac{1}{2}}(i,j,k) - H_z^{n+\frac{1}{2}}(i,j-1,k) \right) \\ & + C_{exhy}(i,j,k) \times \left(H_y^{n+\frac{1}{2}}(i,j,k) - H_y^{n+\frac{1}{2}}(i,j,k-1) \right), \\ & + C_{exj}(i,j,k) \times J_{ix}^{n+\frac{1}{2}}(i,j,k), \end{aligned} \quad (1)$$

which is given from [1]. In this equation, we update e-fields using h-fields, currents, the previous value of the e-field, and a set of coefficients denoted with the letter 'C'. This equation demonstrates how each component is only updated based on previously calculated values, making it a prime candidate for relatively easy parallelization.

While most previous work focuses on parallelization of FDTD method in lower level programming languages using various software and hardware acceleration techniques such as in [2]–[6] (including extensive research on GPU acceleration), only a small number have researched parallelization using simpler languages such as MATLAB [7], [8]. This paper explores the use of MATLAB's parallel computing toolbox to extend the FDTD computation onto multiple cores of a central processing unit (CPU). The increased throughput of the simulation time observed on various systems using parallelization across multiple CPU cores is investigated. The research is then extended to look at the effectiveness of utilizing multiple graphics processing units (GPUs) for the same MATLAB based FDTD solver.

II. PARALLEL CPU COMPUTATION USING MATLAB

The MATLAB environment has two types of parallelization that can be utilized. These two types

Submitted On: April 29, 2019
Accepted On: May 31, 2019

are built-in parallelization, also known as implicit parallelization, and parallelism using MATLAB workers, also known as explicit parallelization [9], [10].

A. Implicit parallelization with MATLAB

Implicit parallelization in MATLAB takes place without any extra work required from the programmer. When performing operations such as elementwise multiplication, as done in many FDTD codes, MATLAB automatically will parallelize this to use multiple cores on a CPU. This will occur any time MATLAB finds a parallelizable operation of ample size that it thinks could be sped up by use of multiple cores. This provides speed increases for large and computationally dense problems. Unfortunately, this method gives the user no control over the parallelization of the code. It also is limited to a non-distributed machine and is unable to take advantage of capabilities of the GPU hardware. These locations where implicit parallelization is limited are places where explicit parallelization can be used better speed increases.

B. Explicit parallelization with MATLAB

Contrary to MATLAB's implicit parallelization, explicit parallelization does require extra work from the programmer to tell the system how to parallelize the code. This is done by first launching worker threads using the *parpool()* command. The number of workers to launch can be specified by putting a number as the first argument to this function. Once a parallel pool has been started in MATLAB, the single program multiple data (SPMD) keyword can be used to directly address each of the workers in the parallel pool. Once this keyword has been used, each of the workers can be individually addressed and communicate with one another using constructs similar to the message passing interface (MPI). We can access the index of each of the cores using the *labindex* variable and get the total number of cores in the pool with the *numlabs* variable.

III. EXPLICIT PARALLELIZATION OF MATLAB BASED FDTD SOLVER FOR CPUs

The code created and tested in this paper is an edited version of the code generated from [1]. Because of this, the FDTD solver is written purely in MATLAB and has many capabilities such as convolutional perfectly matched layer (CPML) boundary conditions, the ability to set material properties, and the capability to add lumped elements, sources, and test ports for full S-parameter simulations. Each of these capabilities is present in the final code providing a simulation environment that can be utilized for real world experiments. However at the current stage, it does not provide the near to far field capability.

Before parallelization could begin, some minor changes were required to be performed on the original code. This included changing all scripts (MATLAB m files) that will be called within the SPMD environment to be changed to functions. This is something that is required by MATLAB for transparency but also makes profiling and debugging in the SPMD environment easier and more informative. All functions used within the time marching loop along with some for data distribution and gathering fit into this scenario.

A. Distribution of domain

For the parallelization of the FDTD algorithm, the FDTD computational domain was split evenly amongst each of the cores. To minimize communication time and programming difficulty, the domain is only split along the z-axis. Distribution across only the z-axis is optimal because it reduces the number of block communications to a maximum of 2 whereas distribution in x-, y-, and z-axes would require up to 6 per core. The z-axis was chosen to decrease the data transfer time. Like all programming languages, MATLAB matrices are stored linearly in memory. In MATLAB arrays are accessed consecutively in memory first in x, then in y, and then in the z direction. This means that data in an xy plane is all accessed consecutively from memory therefore communicating data in an xy plane across the z direction is more efficient than communicating in other directions. A visualization of the subdomains can be seen in Fig. 1.

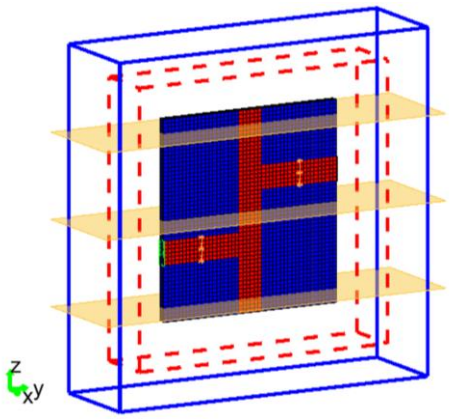

Fig. 1. Distribution of FDTD domain for a microstrip filter problem. The yellow planes represent the boundaries across which the domain is split.

The distribution of these subdomains in MATLAB is performed by first generating a list of z indices that each core must update. The problem domains are split up into subdomains evenly in the z direction. Each core will then calculate the E- and H-fields for one of these subdomains. These arrays of indices are then prepended or appended to provide memory for the transfer regions which will be discussed in a later section. Using these indices, the field components Ex, Ey, Ez, Hx, Hy, Hz and all of their updating coefficient arrays are distributed across multiple cores within our SPMD environment.

To ensure that the smallest amount of data is transferred across each of these boundaries, the original simulation space of this problem from [1] is rotated such that the largest dimension of the domain is along the z-axis. This rotation ensures that the boundaries along which the domain is split are the smallest possible. This is important because data must be communicated across these boundaries.

B. Distribution of sources, samples, and lumped elements

With the domain split across cores, the sources, sampling locations, and lumped elements in the simulation must also be distributed.

The lumped elements are simply contained as coefficients in the FDTD as formulated in [1]. This means that they are precalculated before the simulation time marching begins and are distributed with the rest of the domain. Because of this no further work is required to distribute them past the distribution of the domain coefficients as described in the previous section.

The sources and sampling locations are not precalculated as part of the updating coefficients. The sources are added as currents described in our updating equations (e.g., $J_{ix}^{n+\frac{1}{2}}$ for E_x^n). The sampled values are calculated from averages of our field components at given indices within the grid. Two steps must be taken to distribute the sources and samples. These steps are first to flag the core or cores on which the source or sample lies. This is done by comparing the z location of the source or sample to the z_{idx} values on each of the cores. If at least part of the source or sample resides on that core a flag is set. Each core which contains part of this source or sample then has the currents that it must update transferred to it. Once we have the required updating data on each of the cores containing parts of the sources or samples, each of the indices of these sources and samples are mapped to the local indices of the local matrices holding the field values on each core. This mapping allows these sources and samples to be updated in the same manner they typically are on a single core system.

Once the end of the time marching loop is reached, one final step must be taken to gather the sampled domain parameters back to the host CPU from which post-processing steps can be performed in the same way as a non-multicore implementation. For each sample, this is performed by looping through each core, checking if they have the flag set of containing that specific sample, and if they have copied the sampled data back to a single core. Once the data has been gathered from each core that contained part of the sample, the total sample can be reconstructed. After gathering and reconstruction, these samples can be postprocessed in the same way as data that was created from a single core implementation.

C. Transfer of domain boundaries

As previously mentioned, the domain is split evenly among cores along the z-axis. For continuity of the domain, field values must be transferred across these boundaries. For this implementation an approach like that implemented in [11] was taken. In this communication scheme a single xy-plane slice of the H-fields would be transferred up to the core containing the next section of the domain, and a single xy-plane of the E-fields would be transferred down providing full continuity across the boundary.

Because our domain is only split along the z-axis, the transfers are only required for our Ex, Ey, Hx, and Hy components. A figure of this transfer can be seen in Fig. 2. This highlights the H fields that must be transferred up and the E fields that must be transferred down. Taking a look specifically at one of the field updates we can see why this transfer is needed. In order to update the field Ex(i,j,k+1) we must first calculate the finite difference approximation from the fields Hz(i,j,k+1), Hz(i,j-1,k+1), Hy(i,j,k+1), and Hy(i,j,k). Looking at the figure, it can be seen that all of the required fields are available on core 2 except Hy(i,j,k) which must be transferred from core 1. This same concept applies when updating our Ey, Hx, and Hy fields.

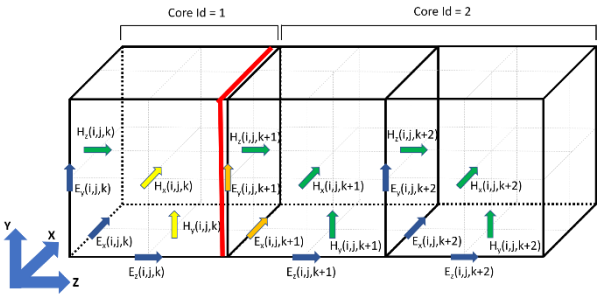

Fig. 2. Figure showing the transfer of E- and H-fields across a Z-axis split boundary. The red line denotes where the domain is split. H-field components that need to be transferred are in yellow and E-fields requiring transfer are in orange.

Each of these transfers in MATLAB can be performed using the labSend() and labReceive() commands. The syntax of these commands is very similar to mpiSend() and mpiRecv() commands when using MPI. Each of these transferred xy planes are held in memory buffers appended to the beginning and end of the e-field and h-field data on each core. It is also important to note that the field arrays were distributed such that the H-fields transferred up and E-fields transferred down were stored on the receiving core at the beginning and end of the field arrays respectively. This means that the original single core updating equations could be utilized with

only minor edits to work with the new multi-CPU code.

IV. EXTENSION TO MULTI-GPU

Up to this point, we have discussed running FDTD simulation on multiple CPUs. Luckily MATLAB provides a simple interface to extend this multi-CPU code to multiple GPUs.

A. Utilizing multiple GPUs in MATLAB

Running code on a single GPU in MATLAB simply requires declaring a variable (scalar value or matrix) within the *gpuArray()* command. Once that has been completed, all arithmetic operations and even most built-in MATLAB commands performed on the data will be done on the GPU. For example declaring two variables *a=gpuArray(magic(100));* and *b=gpuArray(magic(100));* and performing elementwise multiplication *c=a.*b* will accelerate the elementwise multiplication using the GPU. This same process can then be extended to multiple GPUs by declaring *gpuArray()* variables within an SPMD loop. When a parallel pool is created with *parpool()* MATLAB automatically maps each GPU device to a worker in the parallel pool (if there is enough hardware available). From here all GPU commands run within a SPMD loop from a parallel pool with labindex *n* will be run on the corresponding GPU *n*.

B. Extending FDTD simulation to multiple GPUs

Because the multi-CPU code was built to run on any number of cores *n*, the extension to using any given number of GPUs was simple. First a parallel pool is created with the number of workers equal to the number of GPUs we want to run on. If we were to say run on 4 GPUs, this would be *parpool(4)*. Once the parallel pool has started, each of the 4 parallel workers will automatically be mapped to a unique GPU device. This unique mapping gives us direct control over each of the GPUs. A figure to describe the mapping from the FDTD grid to the GPUs and then to the threads can be seen in Fig. 3.

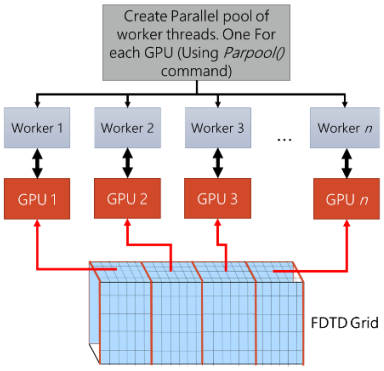

Fig. 3. Figure showing the mapping of our FDTD grid to *n* GPUs, and the mapping of those *n* GPUs to their corresponding parallel pool workers

With each of our workers mapped to a GPU, each of the field components and their updating coefficients, any arrays for updating sources, and any sampling arrays that typically reside on a CPU core are transferred to the GPU using a command such as *Hx=gpuArray(Hx);* because the typical CPU arrays are simply overwritten by our GPU arrays, no change in the code for updating or sampling is required. Once the simulation has finished, the code to gather the data also can stay the same. This is a result of the fact that MATLABs *gather()* command is overloaded to work both with distributed data on the CPU and on the GPU.

V. SIMULATION RESULTS

With the multicore code completed, correct operation was ensured by directly comparing voltage, current, and S-Parameter results of a microstrip filter problem seen in Fig. 1 (as first described on pages 171-177 in [1]) from the multi-CPU and multi-GPU codes to a verified single CPU code. This problem proved the simulation capability and correct operation of the new multi-CPU code. The comparison of the multi-GPU/CPU results can be seen in Fig. 4.

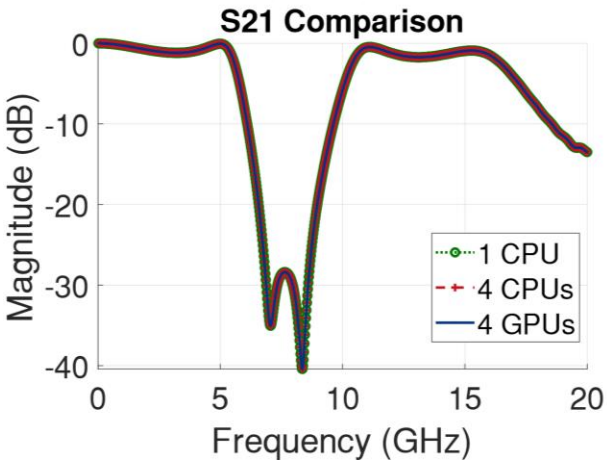

Fig. 4. Comparison of filter results obtained using a single CPU, a multi-CPU, and a multi-GPU FDTD implementation. This simulation was performed with about 1.4 million cells and 3000 time steps.

For the throughput testing of the codes, the air gap between the filter and the CPML region was incrementally increased evenly in all dimensions. This was done to prevent from impartially favoring grids with very large z dimensions, but with very small x and y dimensions. Increasing just the z dimension would provide the optimal throughput because it would provide the highest possible compute to data transfer ratio. Simulations with extremely large z dimensions are very uncommon and unrealistic for most simulation scenarios so they were avoided in the results shown here.

A. Multi-CPU results

The throughput of the multi-CPU code was timed on various computers with a varying number of cores. Tests were also performed to look at increases in throughput when moving from a single physical processor to 2 processors on the same motherboard, and when moving from physical cores to logical (hyperthreaded) cores. This timing was also performed using the non-multicore code and compared. The results from each of these computers can be seen in Figs. 5 through 7.

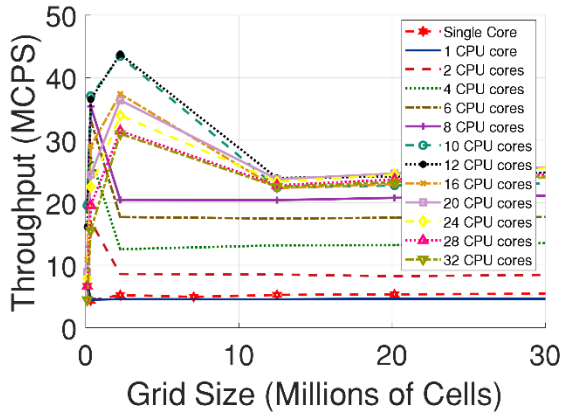

Fig. 5. Throughput in million cells per second (MCPS) vs grid size with various core counts when running an FDTD filter simulation. These simulations were performed on two Intel Xeon E5-2680 CPUs with 20MB of cache and 256GB of RAM. Each processor has 8 physical cores for a total of 16 physical cores and 32 virtual cores.

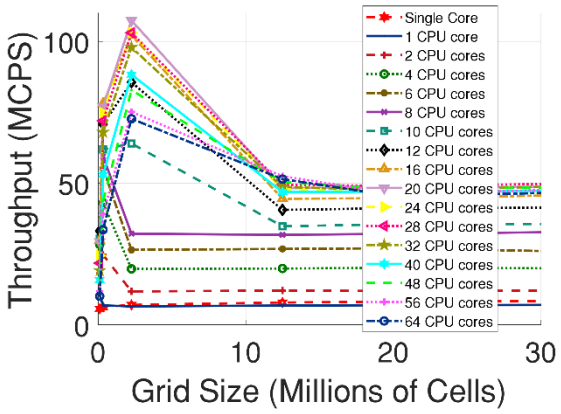

Fig. 6. Throughput in million cells per second (MCPS) vs grid size with various core counts when running an FDTD filter simulation. These simulations were performed on an Intel AMD Ryzen 2990WX and 128GB of RAM. This system has 32 physical cores on a single processor with hyperthreading for a total of 64 logical cores.

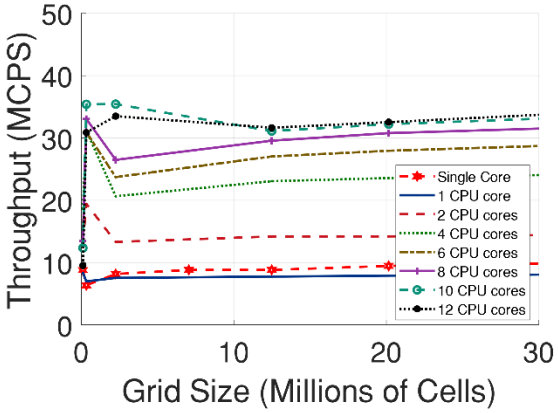

Fig. 7. Throughput in million cells per second (MCPS) vs grid size with various core counts when running an FDTD filter simulation. These simulations were performed on an Intel i7-5280 with 15MB of cache and 32GB of RAM. This system has 6 physical cores on a single processor with hyperthreading for a total of 12 logical cores.

When comparing the throughput of a single core without using SPMD (i.e., the original non-multicore code), it can be noticed that on every machine the non-multicore code outperformed the multicore code when using a single core. Again, this is due to the implicit parallelization MATLAB performs. Once the multicore code begins utilizing more than a single core, the benefits of explicit parallelization in MATLAB quickly surpass the throughput of implicit parallelization. The results of the speedup can be seen in Table 1 when the domain size is 20 million cells.

It should also be noticed that on each system there exists a region of higher throughputs when the grid size is sufficiently small. The size of the grid that this bump exists at is relative to the size of the system cache. This is shown clearly on the systems with multiple processors. The length of the bump can clearly be seen to extend when moving from utilizing a single processor to multiple processors (e.g., in Fig. 6 when moving from 8 cores to greater than 8 cores).

The final important trend to be observed is how the throughput is affected when a system moves from using only physical cores to using both physical and logical cores. Once the requested core count extends past the number of physical cores the system begins using logical hyperthreaded cores. Because this requires a lot of resource sharing within a core, in most cases we see little or no speedup by adding logical cores. The only case where this does not hold true is for the system used in Fig. 4 where substantial gains can be seen by utilizing both physical and logical cores.

Table 1: Speedups of a multicore implementation for various processors with SPMD over a standard single core MATLAB implementation

No. of Cores (Physical / Logical)	i7-5280 (6/12)	Xeon E5-2680 (16/32)	Ryzen 2990WX (32/64)
1	0.85	0.86	0.83
2	1.52	1.59	1.44
4	2.54	2.54	2.38
6	3.03	3.32	3.11
8	3.33	3.96	3.91
12	3.57	4.66	4.94
16	N/A	4.51	5.46
32	N/A	4.54	5.83
48	N/A	N/A	5.79
64	N/A	N/A	5.57

B. Multi-GPU results

The same code was then run on two computers with two different GPUs configurations. The first run was on a system with 2 discrete RTX 2080 GPUs and the second was on a system with 4 Titan-Z GPUs with each PCIe slot containing 2 GPUs. These results can be seen in Fig. 8 and Fig. 9.

As expected, GPU results are an order of magnitude faster than their CPU counterpart. The topic of single GPU acceleration of FDTD with MATLAB was described in depth in [7]. It can be seen from the current multi-GPU results that for low cell counts, the addition of multiple GPUs provides little to no speedup regardless of the system or how many GPUs are added. It is worth noting though that while it does not provide an increased throughput, it also does not seem to slow the simulation down. This similar throughput is caused by a low computation to data transfer time. It is worth noting also that compared to the CPU implementation, the data transfer between GPUs is very slow in MATLAB because data transfer between GPUs is done through the host. As we move to larger grid sizes, we can see that the larger number of GPUs provides a great increase in throughput over lower numbers of GPUs. Because of this, using multiple GPUs in almost all scenarios would be beneficial.

Each GPU throughput typically dropped a relatively drastic amount as grid sizes were increased. The exact cause of this while using MATLAB is unknown but it can be seen that this effect can be moved to much larger grid sizes by increasing the number of GPUs. This behavior was not observed while performing FDTD simulations using C/CUDA development [2]. When the FDTD formulation in [1] is programmed using C/CUDA for a single GPU, the performance on the RTX2080 GPU is on the order of 4 billion cells per second as demonstrated using the CEMS package [12].

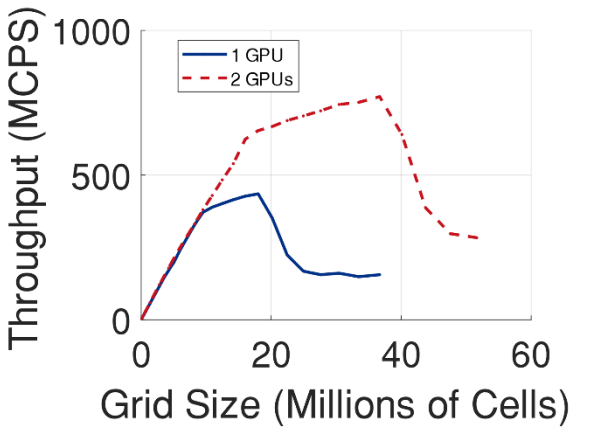

Fig. 8. Throughput in million cells per second (MCPS) vs. grid size for a FDTD filter problem on 2 RTX-2080 GPUs. Each of the 2 GPUs has 8GB of memory.

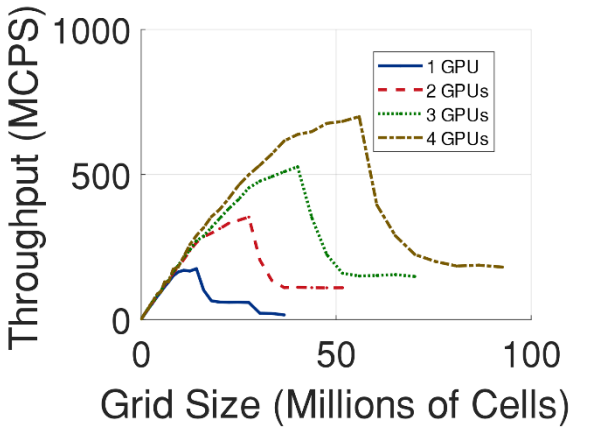

Fig. 9. Throughput in million cells per second (MCPS) vs. grid size for a FDTD filter problem on 4 Titan-Z GPUs. Each of the 4 GPUs has 6GB of memory.

VI. CONCLUSION

This paper described some of the methods used for developing a multi-CPU and multi-GPU FDTD simulation code using explicit MATLAB parallelization. After running on multiple computers, it was shown that utilizing explicit parallelization on CPUs always provided speed increases in the FDTD code over using MATLAB's built-in implicit parallelization. In some cases, speedups of 5x were attained by utilizing explicit parallelization. It was also shown that while parallelizing to physical cores on a system provided speed increases, extending this into hyperthreaded cores provided little to no benefit and in some cases can even decrease throughput. With the multi-GPU implementation we saw similar or increased performance of that on a single GPU.

It is expected that the implementation of a similar solver in a lower level language such as C or FORTRAN would drastically increase the throughput and efficiency

of moving to multiple devices. The use of exclusively MATLAB here though shows that relatively easy edits made to an FDTD solver in a higher level language can provide reasonable speedups over a single GPU or CPU implementation.

ACKNOWLEDGEMENT

This work was partially supported by a gift from Futurewei Technologies, Inc. to ARC Research Group at Colorado School of Mines.

REFERENCES

[1] A. Z. Elsherbeni and V. Demir, *The Finite-Difference Time-Domain Method for Electromagnetics with MATLAB® Simulations*. 2nd edition, Edison, NJ: Scitech Publishing, 2015.

[2] M. J. Inman, A. Z. Elsherbeni, J. G. Maloney, and B. N. Baker, "GPU based FDTD solver with CPML boundaries," in *2007 IEEE Antennas and Propagation Society International Symposium*, pp. 5255-5258, 2007.

[3] K. Hayakawa and R. Yamano, "Multi-core FPGA execution for electromagnetic simulation by FDTD," in *2015 2nd International Conference on Information Science and Control Engineering*, pp. 829-833, 2015.

[4] X.-M. Guo, Q.-X. Guo, W. Zhao, and W. Yu, "Parallel FDTD simulation using NUMA acceleration technique," *Progress In Electromagnetics Research Letters*, vol. 28, pp. 1-8, 2012.

[5] T. Nagaoka and S. Watanabe, "Multi-GPU accelerated three-dimensional FDTD method for electromagnetic simulation," in *2011 Annual International Conference of the IEEE Engineering in Medicine and Biology Society*, pp. 401-404, 2011.

[6] M. R. Zunoubi, J. Payne, and M. Knight, "FDTD multi-GPU implementation of Maxwell's equations in dispersive media," presented at the *Optical Interactions with Tissue and Cells XXII*, vol. 7897, p. 78971S, 2011.

[7] J. E. Diener and A. Z. Elsherbeni, "FDTD acceleration using MATLAB parallel computing toolbox and GPU," vol. 32, p. 6, 2017.

[8] W. Shao and W. McCollough, "Multiple-GPU-based frequency-dependent finite-difference time domain formulation using MATLAB parallel computing toolbox," *Progress In Electromagnetics Research M*, vol. 60, pp. 93-100, 2017.

[9] "MATLAB multicore," [Online]. Available: https://www.mathworks.com/discovery/matlab-multicore.html. [Accessed: 10-Jan-2019].

[10] "Parallel MATLAB: Multiple processors and multiple cores," [Online]. Available: https://www.mathworks.com/company/newsletters/articles/parallel-matlab-multiple-processors-and-multiple-cores.html. [Accessed: 10-Jan-2019].

[11] P. F. Baumeister, T. Hater, J. Kraus, D. Pleiter, and P. Wahl, "A performance model for GPU-accelerated FDTD applications," in *2015 IEEE 22nd International Conference on High Performance Computing (HiPC)*, pp. 185-193, 2015.

[12] V. Demir and A. Elsherbeni, *Computational Electromagnetics Simulator (CEMS) Software Package*. 2010.

Transient Analyses of Grounding Electrodes Considering Ionization and Dispersion Aspects of Soils Simultaneously: An Improved Multiconductor Transmission Line Model (Improved MTL)

Seyyed Sajjad Sajjadi, Vahid Aghajani, and Saeed Reza Ostadzadeh

Department of Engineering, Arak University, Arak, Iran
sajadi-elek@gmail.com, v-aghajani@msc.araku.ac.ir, s-ostadzadeh@araku.ac.ir

Abstract ─ This paper proposes an approximate model in the frequency domain for transient analysis of grounding electrodes buried in ionized and dispersive soils. The proposed method, called multi-conductor transmission line model (MTL), can easily treat the frequency dependence of electrical parameters of soil. It can also incorporate soil ionization by gradually changing the respective electrode radius. Extensive simulation results are presented to confirm the accuracy of the MTL.

Index Terms ─ Frequency dependence, ionization, multi-conductor transmission lines.

I. INTRODUCTION

The lightning performance of grounding systems plays a significant role in the safe and reliable operation of power networks [1, 2]. A grounding system, including buried horizontal electrodes, vertical rods and grounding grids, is designed to effectively dissipate large lightning surge currents into the soil, ensuring reduced grounding impedance. Such a provision prevents the generation of catastrophic overvoltage that could cause transmission line outages and equipment damages.

A proper design of a grounding system requires an efficient method for transient analysis of grounding electrodes buried in the ground, considering soil ionization and dispersion. The former arises when the lightning voltage on a rod exceeds the soil voltage breakdown, while the latter is due to the frequency dependence of electrical parameters of soil. A solution of the problem considering solely the nonlinear effect of soil ionization can be sought through the use of time-domain [3-5], frequency-domain [6-8], and hybrid time-frequency domain [9-13] methods. In the cases where soil dispersion is occurred, the frequency-domain techniques such as the method of moments (MoM) [14], the finite element method (FEM) [15], and the hybrid electromagnetic-method (HEM) [16] becomes more noticeable. For a comprehensive analysis of grounding systems, considering both the dispersion and ionization of soil, several hybrid time-frequency domain methods have been proposed. These include a combined FEM in the spatial domain with the finite difference time domain (FDTD) [9] and combined frequency-domain numerical techniques and circuit theory [10-13].

Despite the accuracy of the numerical methods mentioned above, they are generally less efficient than the so-called analytical solutions where the full wave analysis is approximated by using appropriate lumped circuit elements [17, 18] or assuming transverse electromagnetic (TEM) wave propagation along grounding conductors [19]. Although these methods are more appealing for their many features, including the generality of the solution in the form of closed mathematical relations and relatively fewer computation resources, these methods suffer from a number of drawbacks: a) soil ionization is included through a nonlinear conductance which is restricted to lengths less than 30m [20], and b) the couplings between conductors are ignored. Although improved transmission line model [21] and non-uniform transmission line model [22] were later proposed to consider mutual coupling between conductors in the grounding grid, they are combined with time-consuming numerical methods such as FEM and FDTD respectively.

In a recent work [23], these shortcomings have been resolved by considering each set of parallel conductors in the grounding grid as a multi-conductor transmission lines (MTL). A two-port network for each set of parallel conductors in the grid is then defined. Finally, the two-port networks are interconnected depending upon the pattern of connections in the grid and its representative equations then reduced. Through this approach, voltages and currents at any junction in the grid is easily extracted. Application of this modeling approach in analyzing grounding grids buried in soils with constant electrical parameters was investigated. Also, since it is in the frequency domain, it can be evidently used in soils with frequency-dependent electrical parameters. Hence in this paper it is improved to consider soil ionization by gradually changing the respective electrode radius. The simplicity and computation efficiency of the method

Submitted On: September 26, 2018
Accepted On: February 9, 2019

make it advantageous over the exact methods while being able to consider all practical characteristics such as ionization and dispersion of soils separately or simultaneously.

This paper is organized as follows. In Section II, the improved MTL approach is completely explained. In Section III, model evaluation and efficiency in transient analyses of grounding systems buried in dispersive and ionized soils separately and simultaneously is investigated. Finally concluding remarks are given in Section IV.

II. MODELING APPROACH

To extract MTL approach, at first assume single transmission line of length l as shown in Fig. 1 (a). The following set of equations describing the propagation phenomenon in this transmission line is as below:

$$-\frac{d^2}{dx^2}V = ZYV = PV, \tag{1}$$

$$-\frac{d^2}{dx^2}I = YZI = P_t V, \tag{2}$$

where Z and Y represent, respectively, the series impedance and parallel admittance per unit length, I and V are respectively, the phasor of current and voltage with respect to a point at infinite as shown in Fig. 1 (a). In addition, $P = ZY$, $P_t = YZ$ and x is the variable of length.

Applying a linear transformation in order to diagonalize P and P_t, solutions to (1) and (2) can be expressed as follows:

$$I_s = Y_0 \coth(\Psi l)V_s - Y_0 \operatorname{csch}(\Psi l)V_r, \tag{3}$$

$$I_r = -Y_0 \operatorname{csch}(\Psi l)V_s + Y_0 \coth(\Psi l)V_r. \tag{4}$$

Rewriting (3) and (4) in matrix form, we have:

$$\begin{bmatrix} I_s \\ I_r \end{bmatrix} = \begin{bmatrix} A & B \\ C & D \end{bmatrix}\begin{bmatrix} V_s \\ V_r \end{bmatrix}, \tag{5}$$

where $A = D = Y_0 \coth(\Psi l)$ and $B = C = -Y_0 \operatorname{csch}(\Psi l)$. V_s and I_s represent, respectively, the voltage and current at the sending end of the line, and V_r and I_r are, respectively, the voltage and current at the receiving end of the line. Also, ψ and l denote the propagation constant and length of transmission line respectively. Using (5), relation between sending and receiving currents and voltages for a conductor of length l can be represented as a two-port network as shown in Fig. 1 (b).

Now, consider a mesh 1×1 as shown in Fig. 2. In this figure, two pairs of parallel conductors are seen, i.e., (1-2) and (2-4) which are mutually coupled. As a result, the relation (5) is extended as (6) and (7) respectively for pairs (1-3) and (2-4),

$$\begin{bmatrix} I_{s1} \\ I_{s3} \\ I_{r1} \\ I_{r3} \end{bmatrix} = \begin{bmatrix} A_{11} & A_{12} & B_{11} & B_{12} \\ A_{21} & A_{22} & B_{21} & B_{22} \\ C_{11} & C_{12} & D_{11} & D_{12} \\ C_{21} & C_{22} & D_{21} & D_{22} \end{bmatrix}\begin{bmatrix} V_{s1} \\ V_{s3} \\ V_{r1} \\ V_{r3} \end{bmatrix}, \tag{6}$$

$$\begin{bmatrix} I_{s2} \\ I_{s4} \\ I_{r2} \\ I_{r4} \end{bmatrix} = \begin{bmatrix} A_{11} & A_{12} & B_{11} & B_{12} \\ A_{21} & A_{22} & B_{21} & B_{22} \\ C_{11} & C_{12} & D_{11} & D_{12} \\ C_{21} & C_{22} & D_{21} & D_{22} \end{bmatrix}\begin{bmatrix} V_{s2} \\ V_{s4} \\ V_{r2} \\ V_{r4} \end{bmatrix}. \tag{7}$$

According to (6) and (7), the two-port network in Fig. 1 (b) is generalized as shown in Fig. 3.

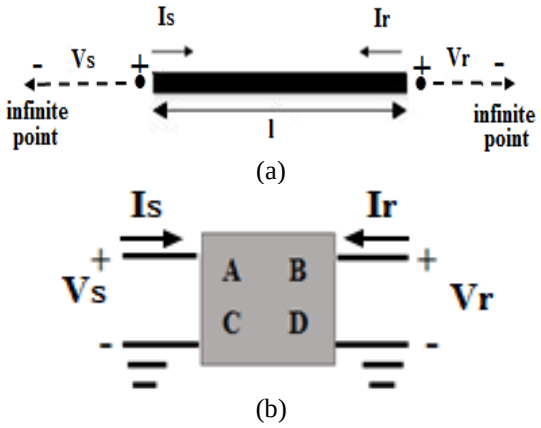

Fig. 1. (a) A conductor of length 1 with definition of voltage and current at sending and receiving points, and (b) representation of the conductor as a two-port network.

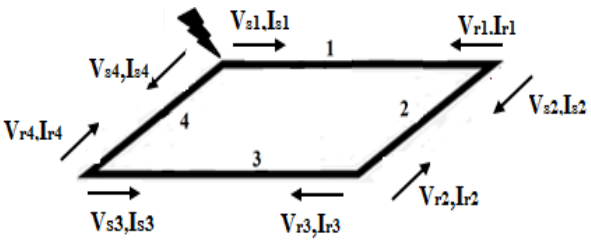

Fig. 2. Mesh 1×1 consisting of two pairs of parallel conductors.

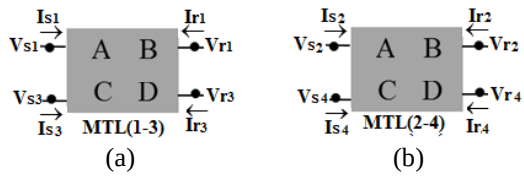

Fig. 3. Representation of two-port network for: (a) MTL (1-3), and (b) MTL (2-4) considering mutual coupling effect.

Due to mesh connections in Fig. 2, the two MTLs in Fig. 3 are connected as shown in Fig. 4. The relations (6) and (7) can be incorporated in a following matrix form:

$$\bar{I} = \overline{\overline{MTL}} \times \bar{V}, \quad (8)$$

where

$$\bar{I} = [I_{s1} \quad I_{s2} \quad I_{r1} \quad I_{r3} \quad I_{s2} \quad I_{s4} \quad I_{r2} \quad I_{r4}]^T, \quad (9)$$

$$\bar{V} = [V_{s1} \quad V_{s3} \quad V_{r1} \quad V_{r3} \quad V_{s2} \quad V_{s4} \quad V_{r2} \quad V_{r4}]^T, \quad (10)$$

$$\overline{\overline{MTL}} = \begin{bmatrix} A_{11} & A_{12} & B_{11} & B_{12} & & & & \\ A_{21} & A_{22} & B_{21} & B_{22} & & 0 & & \\ C_{11} & C_{12} & D_{11} & D_{12} & & & & \\ C_{21} & C_{22} & D_{21} & D_{22} & & & & \\ & & & & A_{11} & A_{12} & B_{11} & B_{12} \\ & 0 & & & A_{21} & A_{22} & B_{21} & B_{22} \\ & & & & C_{11} & C_{12} & D_{11} & D_{12} \\ & & & & C_{21} & C_{22} & D_{21} & D_{22} \end{bmatrix}. \quad (11)$$

It should be noted that in (11), mutual coupling between parallel conductors in the grid is completely included. In the cases of vertical rods, and horizontal electrodes, more elements of (11) are zero, because there is no parallel conductor.

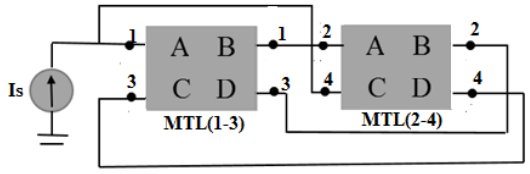

Fig. 4. Representation of two-port network for Fig. 2.

The above development is valid only for independent MTLs. However, for the two MTLs in Fig. 4, the following relations between currents and voltages can be established:

$$V_{s1} = V_{s4}, V_{r1} = V_{s2}, V_{r2} = V_{r3}, V_{s3} = V_{r4}, \quad (12)$$

$$I_s = I_{s1} + I_{s4}, I_{r1} = -I_{s2}, I_{r2} = -I_{r3}, I_{s3} = -I_{r4}. \quad (13)$$

By adding row 5 to 3, 7 to 4, 8 to 2 and 6 to 1 in (8), as well as applying (12) and (13), the following systems of equations is obtained:

$$\begin{bmatrix} V_{s1} \\ V_{s2} \\ V_{r3} \\ V_{r4} \end{bmatrix} = \begin{bmatrix} \bullet & \bullet & \bullet & \bullet \\ \bullet & \bullet & \bullet & \bullet \\ \bullet & \bullet & \bullet & \bullet \\ \bullet & \bullet & \bullet & \bullet \end{bmatrix}^{-1} \begin{bmatrix} I_s \\ 0 \\ 0 \\ 0 \end{bmatrix}. \quad (14)$$

Where "dots" in (14) indicate that these locations are filled with elements resulting from adding rows and columns. Also, the current source I_s in Fig. 4 represents the lightning current.

A. Improved MTL

The proposed MTL in the previous section is valid when ionization of soil is ignored. When, the electric field around the soil is greater than its critical value (E_c), ionization takes place. Such phenomenon is usually represented as gradually increasing radius of the electrode as shown in Fig. 5 (a). Hence, an improvement on the MTL is applied to a grounding electrode buried in an ionized soil as follows. Extension to grounding grids is straightforward.

Assume an electrode buried in a soil having conductivity of σ and dielectric constant of ε. Then divide it into N elemental conductors/segments which each one has radius of a_k and length of l_k. As shown in Fig. 5 (b), each segment can be represented as a two-port network.

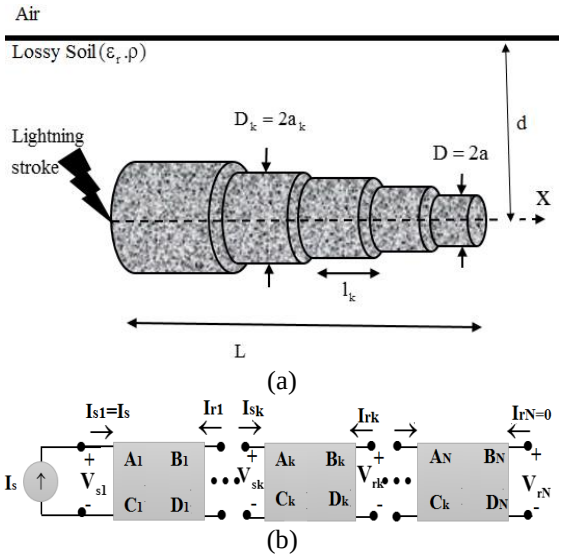

Fig. 5. (a) Ionization representation as gradually increasing radius, and (b) representation of each segment as a two-port network.

As known, the amount of current density draining to the surrounding soil from each segment in the frequency domain is given by:

$$J_k = (\sigma + j\omega\varepsilon)E_k. \quad (15)$$

On the surface of k-th segment, the relation between leakage current I_{Lk} and current density J_k is given as:

$$J_k = \frac{I_{Lk}/l_k}{2\pi a_k}, \quad (16)$$

where I_k is computed via subtracting currents at the sending and receiving points of the k-th segment, i.e.,

$$I_{Lk} = I_{sk} - I_{rk}. \quad (17)$$

Note that, once (14) is solved, via (8) sending and receiving currents at each conductor are easily computed. Finally, leakage current at each conductor is computed via (17). Now applying (16) on (15), the electric field on

the surface of k-th segment is easily computed, that is:

$$E_k = \frac{J_k}{\sigma + j\omega\varepsilon} = \frac{I_{Lk}/l_k}{2\pi(\sigma + j2\pi f\varepsilon)a_k}, \quad k = 1,2,..,N. \quad (18)$$

Then if the value of E_k is greater than the value of E_c, radius of each segment is increased as below:

$$a_{new,k} = a\frac{|E_k|}{E_c}, \quad k = 1,2...,N. \quad (19)$$

In (19), a is the original radius of the electrode. Then for the new value of radius, (14) is again solved. At the first stage of the iteration process for each segment, $a_k = a$. This process is continued up to $E_k < E_c$. When this condition is achieved, the sending voltage of each segment in time domain, $v_{sk}(t)$, is computed as follows,

$$v_{sk}(t) = \sum_{m=1}^{M} V_{sk,m}\cos(2\pi f_m t + \phi_{sk,m}), \quad (20)$$

where M denotes the total number of selected frequency components of lightning current waveform. Also, $V_{sk,m}, \phi_{sk,m}$ are respectively magnitude and phase of sending voltage of k-th segment. Further information about modeling process for grounding grids of arbitrary size can be found in [23].

III. MODEL EVALUATION AND SIMULATION RESULTS

To examine the performance (accuracy and computation efficiency) of the proposed method, various cases have been investigated. For brevity, we study different cases for which the results are available in the literature. These case studies include soil ionization and dispersion separately or simultaneously. We then perform a sensitivity analysis where the effects of soil dispersion and ionization on transient analysis of a buried electrode will be studied.

To take into account soil dispersion, the expression proposed in [16] is used for calculating the effective permittivity and conductivity, i.e.,

$$\sigma(f) = \sigma_0\left(1 + \left(1.2.10^{-6}.\sigma_0^{-0.73}\right)(f - 100)^{0.65}\right), \quad (21)$$

$$\varepsilon_r(f) = \begin{cases} 192.2 & f \le 10\text{kHz} \\ 1.3 + 7.6.10^3.f^{-0.4} & f \ge 10\text{kHz} \end{cases}, \quad (22)$$

where σ_0 is the low-frequency conductivity of soil.

A. Accuracy

In the first case study, validity of the proposed approach in considering dispersion of soil is investigated. Hence, a vertical rod having length of L=3m, radius of a=12.5mm is selected. This rod is injected by first stroke current with peak value of 30kA, zero-to-peak time of $8\mu s$ and maximum steepness of $40\text{kA}/\mu s$. Grounding potential rise (GPR) for the two values of soil conductivity of $\sigma_0 = 0.001, 0.0005$ S/m are shown in Fig. 6. The results are compared with those obtained using the finite element method (FEM) [15], as a reference solution. A comparison of the results in this figure confirms the accuracy of the proposed method.

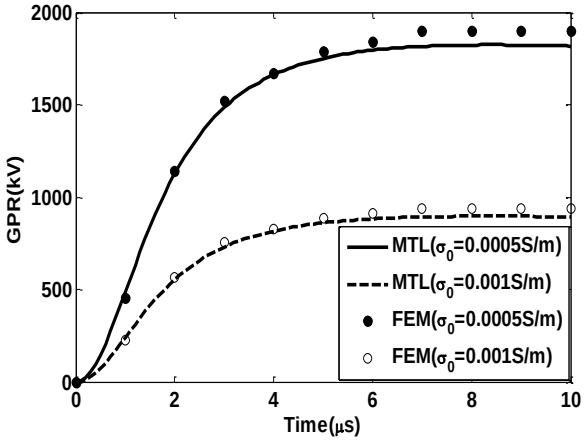

Fig. 6. Comparison of GPRs based on MTL and FEM [15] for validity in only-dispersive soils.

In the second example, capability of the MTL in only-ionized soils is investigated. To this aim, another case study carried out by measurement is selected from [24] and compared with the MTL. In this case, a horizontal electrode of length l=5m, radius a=4mm buried in depth of d=0.6m in soil with $\rho = 42\Omega.\text{m}$ and $\varepsilon_r = 10$ with $E_c = 350\,\text{kV/m}$ is considered. The GPRs computed by measurement and MTL are shown in Fig. 7 which are in good agreement with each other.

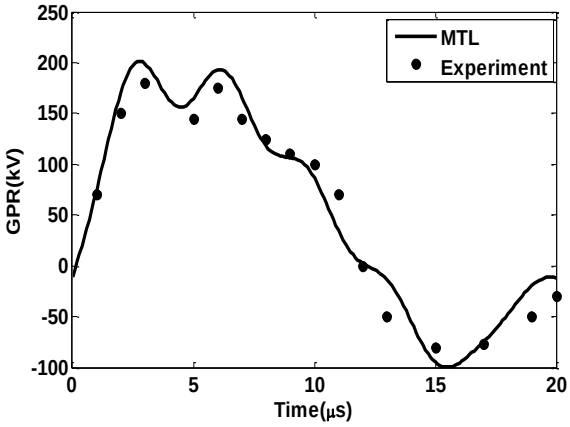

Fig. 7. Comparison of GPRs using MTL and measurement for validity in an only-ionized soil.

In another example to show capability of the MTL in considering ionization and dispersion simultaneously,

a horizontal electrode of length L=15m buried in a lossy soil with conductivity $\sigma_0 = 0.002\,\mathrm{S/m}$ is selected. The critical electric field of soil is assumed to be $E_c = 300\,\mathrm{kV/m}$, and the peak value of excitation pulse is 10kA. As shown in Fig. 8, once more excellent agreement with the results in [13] are depicted. Note that for clarity of Fig. 8, situations of only-ionization and only-dispersion are not included.

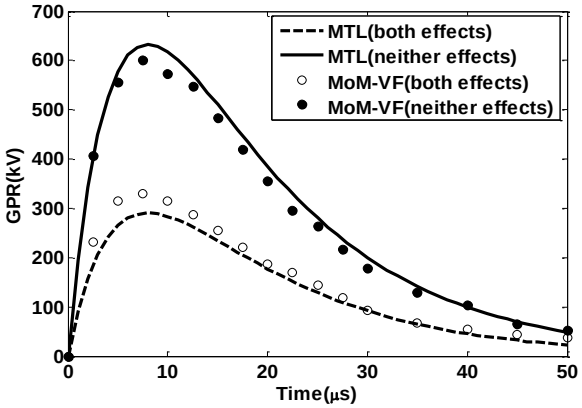

Fig. 8. Comparison of MTL-based GPRs with the MoM-VF results in [13] for validity.

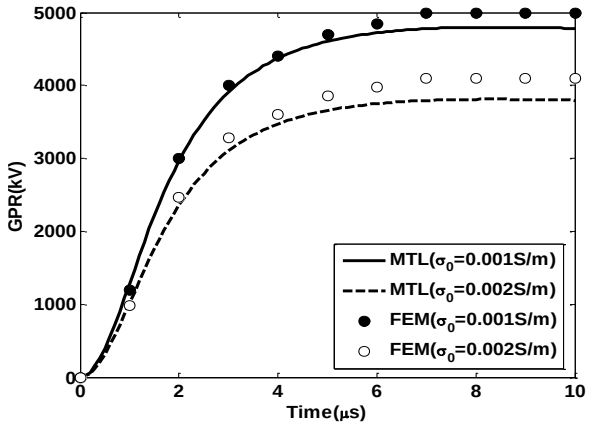

Fig. 9. Comparison of GPRs of the grounding grid by the MTL with FEM [15] for validity in an only-dispersive soil.

Finally, to show capability of the proposed model in considering mutual coupling between conductors, a grounding grid adopted from [15], is selected. The grid is an equally 2m×3m square and buried in depth of 0.5m inside a dispersive soil. The injection current is the same as the first example. The computed GPRs using FEM and MTL for $\sigma_0 = 0.001$, 0.002 S/m are computed and shown in Fig. 9. This figure shows that the results of the MTL are in good agreement with FEM [15].

B. Computational efficiency

In this section, to further show the accuracy of the MTL in comparison with the accurate models, a number of comparative data on the peak values of the GPRs and grounding resistances (R) in four situations, i.e., neither effects, only ionization, only dispersion and both effects, from the third example are listed in Table 1.

Table. 1: Comparison of peak values of GPRs and grounding resistances in different situations

Situation	**Neither Effects**		**Only Ionization**	
Method	MTL	[13]	MTL	[13]
GPR(kV)	615	605	300	310
R (Ω)	61.5	60.5	33	33.5
Situation	**Only Dispersion**		**Both Effects**	
Method	MTL	[13]	MTL	[13]
GPR(kV)	580	571	300	310
R (Ω)	58	57.1	30	31

The results in this table show good agreement with the ones in the published papers. The small differences in each situation in Table 1 undershoot might be due to the numerical errors introduced through the Fourier series that is used to obtain the time domain waveform of the lightning currents. Moreover, to show further efficiency of the MTL, the run-time of the MTL in computing GRRs for the different situations are listed in Table 2 which are very short in comparison with FEM and MoM. All computations were carried out on an Intel (R) Core (TM) i7-4702MQ CPU with 4GB of Ram.

Table 2: Approximate computation time of GPRs by different modeling approaches for the third example

Situation / **Method**	**Neither Effects**	**Only Ionization**
MTL	1 sec	1.4 sec
MoM	258 sec	Not applicable
FEM	27.5 min	Not applicable
Situation / **Method**	**Only Dispersion**	**Both Effects**
MTL	1.26 sec	1.5 sec
MoM	174 sec	Not applicable
FEM	19.3 min	Not applicable

IV. CONCLUSION

In this article, an efficient approach namely improved MTL was proposed in transient analysis of grounding electrodes considering ionization and dispersion of soil separately and simultaneously. This approach in despite of the approximate methods, can consider dispersion and ionization simultaneously, and coupling between parallel conductors is easily included as well. Moreover, its computational efficiency in contrast with numerical methods is considerably high. Extending the MTL for

multilayer soils [25] is in progress.

REFERENCES

[1] *IEEE Guide for Safety in AC Substation Grounding*, IEEE Std. 80, Jan. 2000.

[2] *IEEE Recommended Practice for Grounding of Industrial and Commercial Power Systems (IEEE Green Book)*, IEEE Std. 142, 1991.

[3] C. M. Portela, M. C. Tavaras, and P. Filho, "Accurate representation off soil behavior for transient studies," *IEEE Proceedings of Generation, Transmission and Distribution*, vol. 150, no. 6, Nov. 2003.

[4] O. Goni, E. Kaneko, and A. Ametani, "Finite difference time domain method for the analysis of transient grounding resistance of buried thin wires," *Applied Computational Electromagnetic Society Journal (ACES)*, vol. 22, no. 3, pp. 42-49, 2007.

[5] Z. Feng, X. Wen, X. Tong, H. Lu, L. Lan, and P. Xing, "Impulse characteristics of tower grounding devices considering soil ionization by the time-domain difference method," *IEEE Transactions on Power Delivery*, vol. 30, no. 4, pp. 1906-1913, Aug. 2015.

[6] A. Habjanic and M. Trlep, "The simulation of the soil ionization phenomenon around the grounding system by the finite element method," *IEEE Transactions Magnetics*, vol. 42, no. 4, pp. 867-870, Apr. 2006.

[7] L. Qi, X. Cui, Z. Zhao, and H. Li, "Grounding performance analysis of the substation grounding grids by finite element method in frequency domain," *IEEE Transactions Magnetics*, vol. 43, no. 4, pp. 1181-1184, Apr. 2007.

[8] K. Sheshyekani, S. H. H. Sadeghi, R. Moini, and F. Rachidi, "Frequency-domain analysis of ground electrodes buried in an ionized soil when subjected to surge currents: A MoM–AOM approach," *Electric Power System Research*, vol. 81, pp. 290-296, 2011.

[9] J. C. Salari and C. Portela, "Grounding systems modeling including soil ionization," *IEEE Transactions on Power Delivery*, vol. 23, no. 4, pp. 1939-1949, Oct. 2008.

[10] J. Cidrás, A. F. Otero, and C. Garrido, "Nodal frequency analysis of grounding systems considering the soil ionization effect," *IEEE Transactions on Power Delivery*, vol. 15, no. 1, pp. 103-107, Jan. 2000.

[11] B. Zhang, J. He, J. Lee, X. Cui, Z. Zhao, and J. Zou, "Numerical analysis of transient performance of grounding systems considering soil Ionization by coupling moment method with circuit theory," *IEEE Transactions on Magnetics*, vol. 41, no. 5, pp. 1440-1443, May 2005.

[12] B. Zhang, J. Wu, Jinliang He, and R. Zeng, "Analysis of transient performance of grounding system considering soil ionization by the time domain method," *IEEE Transactions on Magnetics*, vol. 49, no. 5, pp. 1837-1840, Feb. 2013.

[13] J. Wu, B. Zhang, J. He, and R. Zeng, "A comprehensive approach for transient performance of grounding system in the time domain," *IEEE Transactions on Electromagnetic Compatibility*, vol. 57, no. 2, pp. 250-256, Apr. 2015.

[14] D. Cavka, N. Mora, and F. Rachidi, "A comparison of frequency-dependence soil models: application to the analysis of grounding systems," *IEEE Transactions on Electromagnetic Compatibility*, vol. 56, no. 1, pp. 177-187, 2014.

[15] M. Akbari, K. Sheshyekani, and M. R. Alemi, "The effect of frequency dependence of soil electrical parameters on the lightning performance of grounding systems," *IEEE Transactions on Electromagnetic Compatibility*, vol. 55, no. 4, pp. 739-746, Apr. 2013.

[16] S. Visacro and Rafael Alipio, "Frequency dependence of soil parameters: Experimental results, predicting formula and influence on the lightning response of grounding electrodes," *IEEE Transactions on Electromagnetic Compatibility*, vol. 27, no. 2, pp. 927-935, 2012.

[17] L. Grcev, "On high-frequency circuit equivalents of a vertical ground rod," *IEEE Transactions on Power Delivery*, vol. 20, no. 2, pp. 1598-1603, May 2009.

[18] L. Grcev, "On HF circuit models of horizontal grounding electrodes," *IEEE Transactions on Electromagnetic Compatibility*, vol. 20, no. 2, pp. 67-70, Aug. 2009.

[19] D. S. Gazzana, A. S. Bretas, G. A. D. Dias, M. Tello, D. W. P. Thomas, and C. Christopoulos, "The transmission line modeling method to represent the soil ionization phenomenon in grounding systems," *IEEE Transactions on Magnetics*, vol. 50, no. 2, pp. 1163-1171, Feb. 2014.

[20] A. F. Imece, D. W. Durbak, H. Elahi, S. Kolluri, A. Lux, D. Mader, T. E. McDermott, A. Morched, A. M. Mousa, R. Natarajan, L. Rugeles, and E. Tarasiewicz, "Modeling guidelines for fast front transients," *IEEE Transactions on Power Delivery*, vol. 11, no. 1, pp. 493-506, Jan. 1996.

[21] Y. Liu, M. Zitnik, and R. Thottappilli, "An improved transmission line model of grounding system," *IEEE Transactions on Electromagnetic Compatibility*, vol. 43, no. 3, pp. 348-355, Aug. 2001.

[22] Y. Liu, N. Theethayi, and R. Thottappilli, "An engineering model for transient analysis of grounding system under lightning strikes: Nonuniform transmission-line approach," *IEEE Transactions on Power Delivery*, vol. 20, no. 2, pp. 722-730,

Apr. 2005.

[23] A. Jardines, J. L. Guardado, J. Torres, J. J. Chavez, and M. Hernandez, "A multiconductor transmission line model for grounding grid," *Electrical Power and Energy Systems*, vol. 60, pp. 24-33, Apr. 2014.

[24] A. Geri, "Behavior of grounding systems excited by high impulse currents: The model and its validation," *IEEE Transactions on Power Delivery*, vol. 14, no. 3, pp. 1008-1017, July 1999.

[25] Z. Li, G. Li, J. Fan, and Y. Yin, "Numerical simulation of substation grounding grids buried in vertical earth model based on the thin-wire approximation with linear basis functions," *Applied Computational Electromagnetic Society Journal (ACES)*, vol. 26, no. 4, pp. 32-39, 2011.

Robust Adaptive Beamforming Based on Fuzzy Cerebellar Model Articulation Controller Neural Network

Jiaqiang Yu, Pingqing Fan*, Cong Li, and Xiaotian Lu

Automotive Engineering College
Shanghai University of Engineering Science, Shanghai, 201620, China
a849710627@gmail.com, fanpingqing@163.com, licong@sues.edu.cn, ephgiw@163.com

Abstract **–** To solve the problem of degraded adaptive beamforming performance of smart antenna caused by array steering vector mismatch and array manifold errors, a robust beamforming algorithm based on Fuzzy Cerebellar Model Articulation Controller (FCMAC) neural network is proposed. The proposed algorithm is based on explicit modeling of uncertainties in the desired signal array response and a FCMAC neural network. The calculation of the optimal weight vector is viewed as a mapping problem, which can be solved using FCMAC neural network trained with input/output pairs. Our proposed approach provides excellent robustness against some types of mismatches and keeps the mean output array SINR consistently close to the optimal value. Moreover, the FCMAC neural network avoids complex matrix inversion operations and offers fast convergence rate. Simulation results show that the proposed algorithm can significantly enhance the robustness of the beamformer in the presence of array steering vector mismatch and array manifold errors, and the output performance is superior to the current methods.

Index Terms **–** Adaptive beamforming, FCMAC, neural network, robustness, steering vector mismatch.

I. INTRODUCTION

Adaptive beamforming is a technique used to receive desired signals and suppress interferences by adjusting the weight vectors of arrays adaptively. It is widely applied in various fields, including wireless communication, radar and sonar [1,2].

After the publication of the standard Capon beamformer [3], various robust adaptive beamformers have been developed based on different criterions, such as diagonal loading [4], Worst-Case performance optimal [5], Least Mean Squares(LMS) [6] and linear constraints [7]. To alleviate the performance degradation of the traditional adaptive beamformers caused by steering vector mismatch and array manifold errors, some robust adaptive beamforming based on steering vector estimation have been proposed in recent years [8-10]. To further increase the performance, several methods based on interference-plus-noise covariance matrix reconstruction were proposed after, including sparse reconstruction [11,12], spatial power spectrum sampling [13], annulus uncertainty set [14], subspace-based reconstruction [15]. Li et al. proposed a null broadening beamforming approach based on covariance matrix expansion to improve the performance of antenna array beamforming in the case of jammer motion [16].

Neural network is a nonlinear adaptive dynamical system and provides a new idea for adaptive beamforming algorithms [17-20]. Sallomi and Ahmed used artificial Feed Forward Neural Network (FFNN) for smart antenna adaptive beamforming [21]. Higuchi derive a frame-by-frame update rule for a mask-based minimum variance distortion-less response (MVDR) beamformer, which enables us to obtain enhanced signals without a long delay by combining it with unidirectional recurrent neural network-based mask estimation [22]. It is well known that the FCMAC is a special feed-forward neural network based on local approximation that can be adapted to solve the multidimensional nonlinear fitting problem [23-25]. Compared to global approximation methods such as BP neural network, CMAC has attractive features of special architecture, fast learning capability and a certain degree of generalization.

In this paper, we present an improved robust adaptive beamforming (RAB) algorithm based on FCMAC neural network. Firstly, we explicitly express the uncertainty of the expected signal array response based on the worst-case performance optimization, so the constrained optimization problem is transformed into a convex optimization problem. Secondly, the calculation of optimal weight is treated as a mapping problem by using the FCMAC neural network. The proposed RAB algorithm offers fast convergence rate and enhances the array system performance under non-ideal conditions. Lastly, several examples are presented to demonstrate the performances of the proposed robust beamforming algorithm.

II. SMART ANTENNA SYSTEM

The smart antenna system is an array of antennas that terminated into a smart signal processing unit to

Submitted On: April 20, 2018
Accepted On: December 29, 2018

make the transmission and reception of antenna system in an adaptive, spatially sensitive manner. Smart antennas are able to separate signals from multiple sources and enhance the performance of cellular communications systems. The adaptive algorithms that used by the digital signal processing (DSP) unit of antenna array system give the ability and the Intelligence of smart antenna systems. The block diagram of a smart antenna system with M elements is shown in Fig. 1.

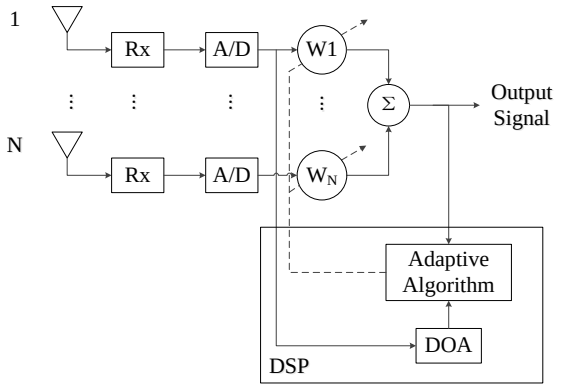

Fig. 1. Block diagram of a smart antenna system.

Where, A/D refer to the analog to digital convertor, w_1~w_M are the weights of an antenna array that obtained by the adaptive algorithm of DSP unit. DOA refer to the direction of arrival estimator that estimate the angle of arrival of the received signals.

III. SIGNAL MODEL

Adaptive Beamforming is an intelligence signal processing technique in which the received signals by each element of the antenna array are multiplied by complex weight vectors to adapt the magnitude and phase of the received signals in order to direct maximum radiation in the direction of desired users and nulling interferer sources. The signals received by different elements of an antenna array combined to form a single output. Classically, this is achieved by decreasing the mean square error (MSE) between the desired output and actual array output. Figure 2 shows the block diagram of adaptive beamformer.

In this part, we consider a uniform linear array consisting of *N* isotropic antenna elements spaced by the distance *d*. Assume that there are P far-field narrowband signals impinging on the array. At the time *t*, the array observation can be written as:

$$\mathbf{X}(t) = \boldsymbol{S}(t) + \boldsymbol{i}(t) + \boldsymbol{n}(t) = s(t)\boldsymbol{a} + \boldsymbol{i}(t) + \boldsymbol{n}(t), \quad (1)$$

where $\mathbf{X}(t) = [x_1(t), x_2(t), \ldots, x_N(t)]^T$, it is the complex vector of array observations, $\boldsymbol{S}(t)$, $\boldsymbol{i}(t)$, $\boldsymbol{n}(t)$ denote the statistically independent components of the desired signal, interference, and noise, respectively. $s(t)$ is waveform of the desired signal, $\boldsymbol{a}$ is desired signal steering vector. The output of a narrowband beamformer at time *t* is given by:

$$y(t) = \sum_{i=1}^{N} x_i(t) w_i = \mathbf{W}^{\mathbf{H}}\mathbf{X}(t), \quad (2)$$

where $\mathbf{W} = [w_1, w_2, \cdots, w_N]^{\mathrm{H}}$ represents complex weight vector. $(\cdot)^T$ and $(\cdot)^H$ denote the transpose and Hermitian transpose, respectively. The out signal-to-interference-plus-noise ratio (SINR) of the beamformer has the following form:

$$SINR = \frac{\sigma_s^2 |\mathbf{W}^{\mathbf{H}}\boldsymbol{a}|^2}{\mathbf{W}^{\mathbf{H}}\mathbf{R}_{i+n}\mathbf{W}}, \quad (3)$$

where σ_s^2 denotes the power of the desired signal, $\mathbf{R}_{i+n}$ denotes interference-plus-noise covariance matrix. According to the minimum variance distortionless response (MVDR) principles, the maximization of SINR (3) is equivalent to minimization interference plus noise power:

$$\min_{W} \mathbf{W}^{\mathbf{H}}\mathbf{R}_{i+n}\mathbf{W} \quad \text{subject to} \quad \mathbf{W}^{\mathbf{H}}\boldsymbol{a} = 1. \quad (4)$$

From (4), the well-known solution can be obtained by the following optimal weight vector:

$$\mathbf{W}_{opt} = \frac{\mathbf{R}_{i+n}^{-1}\boldsymbol{a}}{\boldsymbol{a}^H\mathbf{R}_{i+n}^{-1}\boldsymbol{a}}. \quad (5)$$

Inserting (5) into (3), the optimal SINR is given by:

$$SINR_{\mathrm{opt}} = \sigma_s^2 \mathbf{a}^{\mathbf{H}}\mathbf{R}_{i+n}^{-1}\boldsymbol{a}. \quad (6)$$

However, the exact $\mathbf{R}_{i+n}$ is unavailable in practical applications, it requires an infinite number of pure snapshots data without the desired signal. Therefore, it is usually replaced by sample covariance matrix $\hat{\mathbf{R}} = (1/K)\sum_{i=1}^{N}\mathbf{X}(i)\mathbf{X}^H(i)$, where *K* is the number of snapshots. The resultant beamforming algorithm is commonly referred to as the sample matrix inversion (SMI) algorithm:

$$\mathbf{W}_{\mathbf{SMI}} = \frac{\hat{\mathbf{R}}^{-1}\boldsymbol{a}}{\boldsymbol{a}^H\hat{\mathbf{R}}^{-1}\boldsymbol{a}}. \quad (7)$$

When the number of snapshots *K* is small, the large gap between the known $\hat{\mathbf{R}}$ and $\mathbf{R}_{i+n}$ can significantly affect the performance of the SMI algorithm, especially when there is a desired signal in the training samples. For this reason, this paper proposes a new robust adaptive beamforming algorithm.

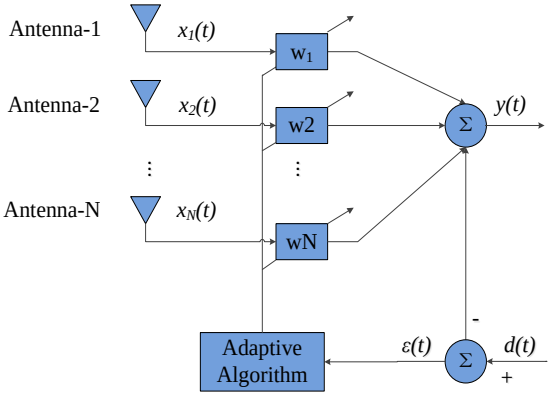

Fig. 2. Adaptive beamformer.

IV. ROBUST ADAPTIVE BEAMFORMING BASED ON FCMAC NEURAL NETWORK

A. Robust adaptive beamforming

In practical applications, we assume that the norm of the steering vector distortion Δ can be bounded by some known constant ε > 0:

$$\|\Delta\| \le \varepsilon. \tag{8}$$

According to [26], we can rewrite the optimization problem (4) as follows:

$$\min_{W} \mathbf{W^H R W} \quad \text{subject to} \quad \mathbf{W^H} \boldsymbol{a} = \varepsilon\|\mathbf{W}\| + 1, \tag{9}$$

where $\mathbf{R} = \mathrm{E}[\mathbf{X}(i)\mathbf{X}^H(i)]$ denotes theoretical covariance matrix of array out vector.

According to [27], considering the worst-case mismatch, a meaningful express of (9) can be written as:

$$\min_{\mathbf{W}} \max_{\Delta_1 \le \gamma} \mathbf{W^H}(\mathbf{R} + \Delta_1)\mathbf{W} \quad \text{subject to} \quad \mathbf{W^H} \boldsymbol{a} = \varepsilon\|\mathbf{W}\| + 1\,, \tag{10}$$

where the matrix Δ_1 takes all possible steering vector distortions into account, such as nonstationarity of the data, small training samples and quantization errors, etc. This situation is also referred to the worst-case optimization problem. To solve the (10), we can first solve the following optimization problem:

$$\max_{\Delta_1} \mathbf{W^H}(\mathbf{R} + \Delta_1)\mathbf{W} \quad \text{subject to} \quad \|\Delta_1\| \le \gamma. \tag{11}$$

Rewriting this problem as:

$$\min_{\Delta_1} -\mathbf{W^H}(\mathbf{R} + \Delta_1)\mathbf{W} \quad \text{subject to} \quad \|\Delta_1\| \le \gamma. \tag{12}$$

From the linearity of this objective function, the inequality constraint in (12) can be replaced by the equality constrain:

$$\|\Delta_1\| = \gamma. \tag{13}$$

We can use the Lagrange multiplier method to solve the (12) optimization problem:

$$\Psi(\Delta_1, \lambda) = -\mathbf{W^H}(\mathbf{R} + \Delta_1)\mathbf{W} + \lambda(\|\Delta_1\|^2 - \gamma^2). \tag{14}$$

Calculating the gradient of (14) and equating it to zero yields:

$$\Delta_1 = \frac{\mathbf{W W^H}}{2\lambda}. \tag{15}$$

Combining (15) and (13), we can obtain:

$$\lambda = \frac{\|\mathbf{W}\|^2}{2\gamma}, \tag{16}$$

$$\Delta_1 = \gamma \frac{\mathbf{W W^H}}{\|\mathbf{W}\|^2}. \tag{17}$$

Therefore, we can figure out the (11) by (17). Correspondingly, (10) can be written as:

$$\min_{\mathbf{W}} \mathbf{W^H}(\mathbf{R} + \gamma\mathbf{I})\mathbf{W} \quad \text{subject to} \quad \mathbf{W^H} \boldsymbol{a} = \varepsilon\|\mathbf{W}\| + \mathbf{1}. \tag{18}$$

In the same way, we construct Lagrange function:

$$\boldsymbol{L}(\mathbf{W}, \lambda) = \mathbf{W^H}(\mathbf{R} + \gamma\mathbf{I})\mathbf{W} + \lambda(\varepsilon^2\mathbf{W^H W} - \mathbf{1} - \mathbf{W^H a a^H W} + \mathbf{W^H a} + \mathbf{a^H W}). \tag{19}$$

Differentiating $\boldsymbol{L}(\mathbf{W}, \lambda)$ with respect to $\mathbf{W}$, λ and setting these partial derivatives to zero, we can obtain respectively:

$$(\mathbf{R}_{\mathrm{DL}} + \lambda\mathbf{G})\mathbf{W} = -\lambda\mathbf{a}, \tag{20}$$

$$\mathbf{W^H G W W^H a} + \mathbf{a^H W} = 1, \tag{21}$$

where matrices $\mathbf{R}_{\mathrm{DL}}$ and $\mathbf{G}$ are defined as:

$$\mathbf{R}_{\mathrm{DL}} = \mathbf{R} + \gamma\mathbf{I}, \tag{22}$$

$$\mathbf{G} = \varepsilon^2\mathbf{I} - \mathbf{a a^H}. \tag{23}$$

According to (20), we can obtain:

$$\mathbf{W_{RAB}} = -\lambda(\mathbf{R}_{\mathrm{DL}} + \lambda\mathbf{G})^{-1}\mathbf{a}. \tag{24}$$

Inserting this to (21) yields:

$$f(\lambda) = \lambda^2\mathbf{a^H}(\mathbf{R}_{\mathrm{DL}} + \lambda\mathbf{G})^{-1}\mathbf{G}(\mathbf{R}_{\mathrm{DL}} + \lambda\mathbf{G})^{-1}\mathbf{a} - 2\lambda\mathbf{a^H}(\mathbf{R}_{\mathrm{DL}} + \lambda\mathbf{G})^{-1}\mathbf{a} - 1 = 0. \tag{25}$$

To solve (25), we can use the method of matrix eigenvalue decomposition:

$$f(\lambda) = \lambda^2 \sum_{i=1}^{n} \frac{{g_i}^2 r_i}{(1+\lambda r_i)^2} - 2\lambda \sum_{i=1}^{n} \frac{{g_i}^2}{1+\lambda r_i} - 1, \tag{26}$$

where g_i and r_i denotes the generalized eigenvalue of matrices $\mathbf{G}$ and $\mathbf{R}_{\mathrm{DL}}$.

The above robust adaptive beamforming algorithm considers the problem of steering vector mismatch. Some methods are proposed that using the variable diagonal loading factor to calculate the weight of the beamformer [28]. In these papers, they make the diagonal loading factor equal to the standard deviation of the diagonal elements of the covariance matrix, which adapts to changes in the number of snapshots and does not require any prior information:

$$\gamma = std\big(diag(\mathbf{R})\big). \tag{27}$$

Since the above equation (24) involves matrix inversion, it is not practical for real-time implementation. Therefore, this paper uses the FCMAC neural network to calculate the optimal weight of a uniform linear antenna array. The trained FCMAC neural network model can convert the calculation of the optimal weight vector into a mapping problem. Furthermore, the FCMAC neural network with local approximation and good generalization performance can provide fast convergence rate.

B. The cerebellar model articulation controller neural network

The structure of CMAC neural network is shown in Fig. 3, which contains Input Space (X), Association Memory Space (A), Physical Space (W) and Output Space (Y). After being quantified, each vector in the Input Space is mapped to the Association Memory Space and activates $\mathrm{N_L}$ storage units, which is corresponding to $\mathrm{N_L}$ weights stored in the Physical Space. The output y_i of CMAC neural network equals to the sum of these $\mathrm{N_L}$ weights. For an input sample, the desired output value can always be achieved by adjusting the weight.

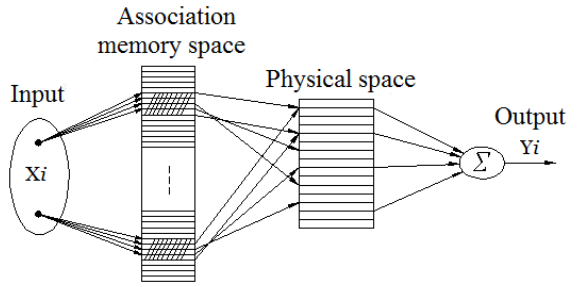

Fig. 3. The structure of CMAC neural network.

In the Association Memory Space, the input for each dimension is further divided into p layers and q blocks, and the number of equal-divided slices of each dimension is $[p(q-1)+1]$. The weight equals to the accumulation of the active blocks at each layer, so the number of possible weights is $(p \cdot q^n)$, where n is the input dimension. As shown in Fig. 4, assume that the two-dimensional input CMAC neural network is divided into 4 layers and 2 blocks, so the number of equal-divided slices of each dimension equals to 5, the number of possible weights equals to 16, but the number of weights N_L activated by each input variable X_i equals to 4, whose index are Bb, Dd, Ff and Gg. It can be seen that the CMAC neural network have similar outputs for similar inputs, which means that it possesses strong ability of local generation.

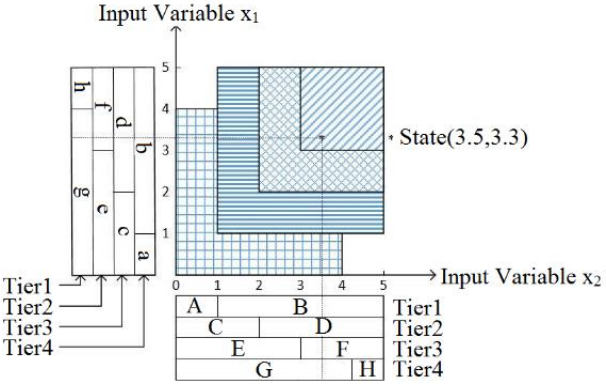

Fig. 4. The mapping principle of Association Memory Space.

The main working principle of CMAC neural network is divided into three mapping processes.

1) Conceptual mapping (X→A)

The input of CMAC can be regarded as a multi-dimension vector (X). It can be quantized first and then mapped to the corresponding activated units in Association Memory Space (A). The quantization algorithm is given by:

$$\overline{x_i} = \frac{x_i - x_{min}}{x_{max} - x_{min}} \cdot M, \qquad (28)$$

where $M = p(q-1)+1$. The quantized interval for each input variable overlaps in each quantization layer, and on any two units are exactly the same. There is a step Δq in every two quantization layers. When the input signal falls into a quantized interval, the corresponding memory cell is activated. The ceil() function and floor() function can be used to encode the address of the activated memory cell according to equation (31):

if $O_j > 0$

$$a_i = \begin{cases} 0 & \text{if } x_i < x_{min} + O_j \\ \text{ceil}\left(\dfrac{\overline{x_i} - x_{min} - O_j}{S_C}\right) & \text{otherwise} \end{cases}$$

else

$$a_i = \text{floor}((x_i - x_{min})/S_C), \qquad (29)$$

where $O_j = \Delta q \times N_j (N_j = 0,1,\ldots,N_L)$ represents the offset of each quantization layer, S_C is the size of memory cell. Therefore, the input vector X is mapped to a relevant binary address vector.

2) Address calculation (A→W)

The units in Physical Space (W) store the weight values and the address units in Association Memory Space (A) can be mapped to the corresponding weight units in W by Hash-coding.

3) Output mapping (W→Y)

This mapping relation is used to calculate the output of CMAC, which means that add all the weight values of the activated units in W and regard the result as the final output.

C. The fuzzy cerebellar model articulation controller neural network

As shown in Fig. 5, by introducing the fuzzy inference rules into a CMAC, this paper uses a more generalized network, called FCMAC. The Gaussian function is adopted here as the fuzzy membership function, which can be represented as:

$$G_j = \exp\left(-\frac{(\overline{x_j} - \mu_j)^2}{\delta_j^2}\right) \quad (j = 1,2,\cdots,N_L), \qquad (30)$$

where δ_j represents *j*th Gaussian function variance of memory cells, μ_j represents *j*th Gaussian function expectation of memory cells. The output of FCMAC can be expressed as:

$$y_i = \sum_{j=1}^{N_L} w_j G_j \quad i = 1,2,\cdots,N. \qquad (31)$$

The following algorithms are used to adjust the network weights

$$w_j(t) = w_j(t-1) + \frac{\alpha}{N_L} G_j\left(\overline{y_s} - \sum_{j=1}^{N_L} G_j\, w_j(t-1)\right), \quad j = 1,2,\cdots N_L, \qquad (32)$$

where α denotes the learning rate, $\overline{y_s}$ is the desired output and $\sum_{j=1}^{N_L} G_j\, w_j(t-1)$ is the actual output, only the activated weights are updated.

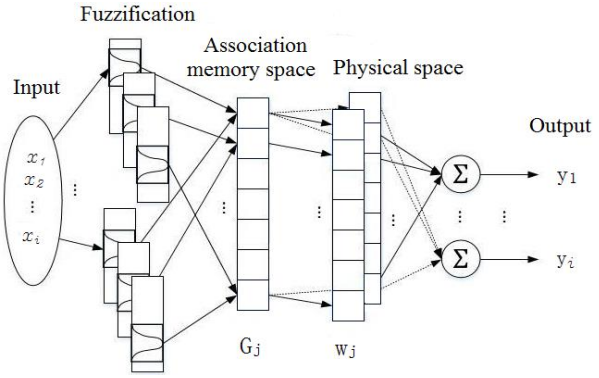

Fig. 5. The structure of FCMAC neural network.

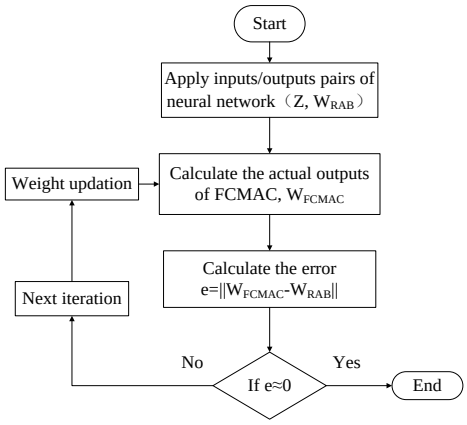

Fig. 6. Training process of FCMAC.

D. Training data generation and neural network learning

Firstly, the normalized samples are obtained according to the signal's different incidence angles θ and SNR parameters:

$$\mathrm{X_n} = X/\|X\|. \tag{33}$$

Then the correlation matrix of the incoming signals that received by *N* elements of antenna array system are generated as follows:

$$\mathbf{R} = \frac{1}{N}\sum_{n=1}^{N} X_n (X_n)^H = \begin{bmatrix} R_{11} & R_{12} & \dots & R_{1N} \\ R_{21} & R_{22} & \dots & R_{2N} \\ \dots & \dots & \dots & \dots \\ R_{N1} & R_{N2} & \dots & R_{NN} \end{bmatrix}, \tag{34}$$

where $(\cdot)^H$ refers to conjugate transpose of matrix. Then the first row of the correlation matrix $\mathbf{R}$ is used as the input of neural network since it contains adequate information of the received signal:

$$\boldsymbol{Z} = [R_{11} \;\; R_{12} \;\; \dots \;\; R_{1N}]. \tag{35}$$

Due to the fact that the neural network does not operate with complex number, the real and imaginary part of each element in $\mathbf{Z}$ vector is taken, which means the dimension of $\mathbf{Z}$ vector will be twice $(1 \times 2N)$. The antenna element optimal weight vector $\mathbf{W_{RAB}}$ calculated from equation (24) is used as the target output of the neural network, which can direct the main beam of radiation pattern toward desired signal and place nulls at interference directions in optimal form.

Assume that the angle θ of incoming signals range from -90°to 90° and the interval is 1°, then 181 sets of training sample data are generated to train the FCMAC network. The weights are iteratively corrected by using equation (32). The neural network training process is shown in Fig. 6.

As shown in Fig. 6, the FCMAC has established an approximation of the desired input-output mapping after the training is completed. In the performance phase, the FCMAC produces outputs to previously unseen inputs by interpolating between the inputs used in the training phase.

V. SIMULATION RESULTS

To examine the performance of the proposed algorithm, simulations were performed on a uniform linear array with *N*=10 sensors and inter-element spacing is half the wavelength of the desired signal. The parameters of the FCMAC network are p=4, q=3, and the learning constant α is 0.05. The presumed desired signal direction is set to 0°, interference directions are set to 40°, and the interference-to-noise-ratio (INR) equals to 35 dB. The additive noise is modeled as complex circularly symmetric Gaussian zero-mean spatially and temporally white process. The worst-performing optimal algorithm steering vector uncertainty set $\varepsilon = 3$. For each scenario, the average of 50 independent runs is used to plot each simulation point. The optimal SINR is also plotted for reference.

A. Example 1: Array beampatterns of the algorithms

In the example, the scenario with the signal look direction mismatch is considered and compared to the ideal case. We assume that both the presumed and actual signal spatial signatures are plane waves impinging from the DOAs 0° and 3° respectively. This corresponds to a 3° mismatch in the signal look direction. The input signal-noise-ratio (SNR) is set to 15dB and the number of snapshots *K* is set to 100. Figure 7 and Fig. 8 display the beampatterns of the different methods for the no-mismatch case and for a 3° mismatch respectively.

From Fig. 7, we can note that the FCMAC-RAB algorithm can direct the main beam of radiation pattern toward desired signal and place nulls at interference directions. Compared to the SMI, LSMI and LMS algorithm, the proposed beamformer have lower sidelobes and deeper null, which can prevent significant performance degradation in the case of unexpected interfering signals.

From Fig. 8, we note that the SMI and LMS algorithm does not have robustness to the steering vector mismatch, and may mistake the desired signal as interference. Although the LSMI algorithm has certain

stability to the steering vector mismatch, it is at the cost of decreasing the interference nulling-depth. The FCMAC-RAB algorithm can maintain a good beamforming capability and sufficient null-depth in the presence of interference. The corresponding amplitude distribution obtained by four different algorithms are given in Table 1. From Table 1, we can note that FCMAC-RAB algorithm is lower than LMS algorithm 8.7 dB in interference inhibition gain and 0.6 dB in sidelobe gain.

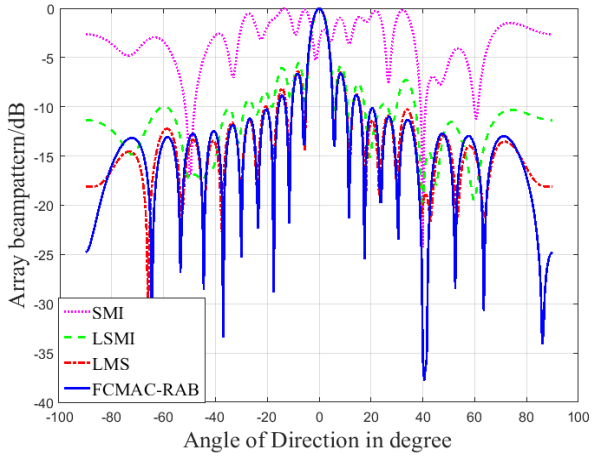

Fig. 7. Directional pattern of each beamforming algorithm (no mismatch).

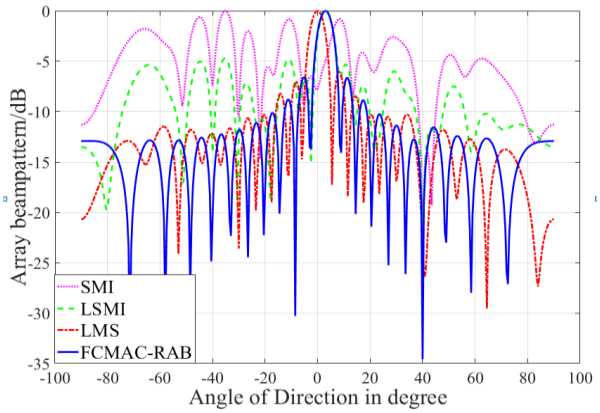

Fig. 8. Directional pattern of each beamforming algorithm (a 3° mismatch).

Table 1: Amplitude distribution obtained by different algorithms

Algorithm	SMI	LSMI	LMS	FCMAC
Sidelobe gain/dB	-4.7	-5.3	-6.1	-6.7
Interference gain/dB	-17.2	-17.7	-25.9	-34.6

B. Example 2: Robustness analysis of the algorithms

In this example, the output SINR of the beamformers versus input SNR and the number of snapshots K with the array pointing error are considered respectively.

Firstly, the number of snapshots K is set to 100 and the expected signal SNR varies from -10 to 30 dB. Comparing the output SINR of each algorithm with the expected signal SNR, the simulation results are shown in Fig. 9. Secondly, the expected signal SNR is set to 20 dB, the number of snapshots K is changed from 1 to 100. The relationship between the SINR of each algorithm and K is compared. The simulation results are shown in Fig. 10.

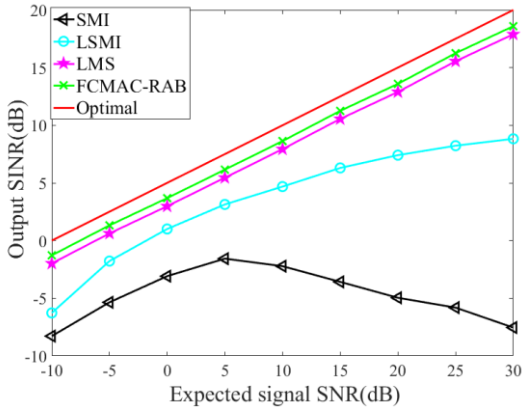

Fig. 9. The relationship between the system output SINR and input SNR for fixed K=100.

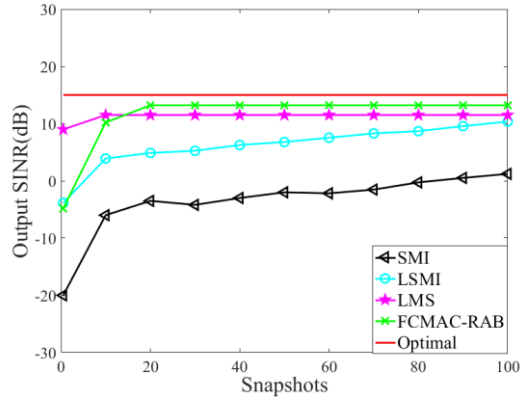

Fig. 10. The relationship between the system output SINR and the snapshots K for fixed SNR=20dB.

It can be observed from Fig. 9 and Fig. 10 that SMI algorithm is very sensitive even to slight mismatches and LSMI algorithm can improve the performance of the SMI algorithm. Obviously, the performance of the FCMAC-RAB algorithm is close to the optimal one at different SNR and K. Additionally, both the SMI and LSMI algorithms show a decrease in performance when the input SNR is high. This is because the algorithm

mistakes the desired signal as an interfering signal when the desired signal SNR is high. Compared with the LMS algorithm, the output performance of FCMAC-RAB algorithm is improved by 1dB. The result demonstrates that the proposed beamforming algorithm present quite bigger output SINR than all the other tested beamformers.

C. Example 3: Analysis of training performance under different neural networks

In this example, the performance of FCMAC network is compared with the Radial Basis Function (RBF) neural network. The number of trainings is set to 100 times. The other conditions are the same as example1. The simulation results are shown in Fig. 11.

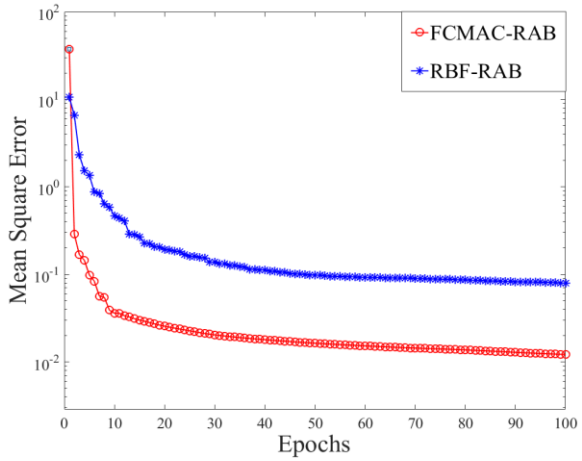

Fig. 11. Convergence of FCMAC and RBF neutral network.

As shown in Fig. 11, the best training performance of FCMAC neural network and RBF neural network are [0.0426] at epoch 20 and [0.118] at epoch 30, respectively. From the result, we can infer that FCMAC neural network provides faster convergence rate and smaller error than RBF neural network during training, which proves that FCMAC neural network has the characteristics of local approximation and fast learning speed.

VI. CONCLUSION

We have introduced a new robust adaptive beamforming algorithm based on FCMAC neural network to improve adaptive beamforming performance of smart antenna. The proposed algorithm is based on explicit modeling of uncertainties in the desired signal array response and a FCMAC neural network. Simulation results demonstrate that the RAB-FCMAC algorithm maintains a good beamforming capability and sufficient null-depth in the presence of interference. Compared to LMS algorithm, the FCMAC-RAB algorithm decreases 8.7 dB in interference inhibition gain and 0.6 dB in sidelobe gain. Furthermore, RAB-FCMAC algorithm keeps the mean output array SINR consistently close to the optimal value in a wide range of the SNR and the number of snapshots and offers faster convergence rate than RBF neural network.

ACKNOWLEDGMENT

The authors gratefully acknowledge that this work was partially supported by the Program of National Natural Science Foundation of China under Grant No. 51505275.

REFERENCES

[1] W. Li, X. Mao, Z. Zai, and Y. Li, "A low complexity high performance robust adaptive beamforming," *Applied Computational Electromagnetics Society*, vol. 32, no. 5, pp. 441-448, 2017.

[2] W. M. Jia, W. Jin, S. H. Zhou, and M. L. Yao, "Robust adaptive beamforming based on a new steering vector estimation algorithm," *Signal Processing*, vol. 93, no. 9, pp. 2539-2542, 2013.

[3] J. Capon, "High-resolution frequency-wave-number spectrum analysis," *Proc. IEEE*, vol. 57, no. 8, pp. 1408-1418, 1969.

[4] C. F. Liu and G. S. Liao, "Robust beamforming algorithm using worse-case performance optimization," *Journal of Xidian University (Natural Science)*, vol. 37, no. 1, pp. 1-7, 2010.

[5] Z. L. Yu, "Robust adaptive beamformers based on worst-case optimization and constraints on magnitude response," *IEEE Transactions on Signal Processing*, vol. 57, no. 7, pp. 2615-2628, 2009.

[6] J. A. Srar, K. S. Chung, and A. Mansour, "Adaptive array beamforming using a combined LMS-LMS algorithm," *IEEE Transactions on Antennas and Propagation*, vol. 58, no. 11, pp. 3545-3557, 2010.

[7] S. D. Somasundaram, "Linearly constrained robust Capon beamforming," *IEEE Transactions on Signal Processing*, vol. 60, no. 11, pp. 5845-5856, 2012.

[8] J. H. Qian, Z. S. He, and T. Liu, "Robust beamforming based on steering vector and covariance matrix estimation," *Circuits, Systems, and Signal Processing*, vol. 37, no. 10, pp. 4665-4682, 2018.

[9] Z. H. Li, Y. S. Zhang, and H. W. Liu, "A robust STAP method for airborne radar based on clutter covariance matrix reconstruction and steering vector estimation," *Digital Signal Processing*, vol. 78, no. 2, pp. 82-91, 2018.

[10] F. G. Yan, B. Cao, and J. J. Rong, "Spatial aliasing for efficient direction-of-arrival estimation based on steering vector reconstruction," *EURASIP Journal on Advances in Signal Processing*, vol. 1, p. 121, 2016.

[11] Y. J. Gu, N. A. Goodman, and S. H. Hong, "Robust adaptive beamforming based on interference

covariance matrix sparse reconstruction," *Signal Processing*, vol. 96, no. 5, pp. 375-381, 2014.
[12] C. W. Zhou, Y. J. Gu, S. He, and Z. Shi, "A robust and efficient algorithm for coprime array adaptive beamforming," *IEEE Transactions on Vehicular Technology*, vol. 67, no. 2, pp. 1099-1112, 2018.
[13] Z. Y. Zhang, W. Liu, W. Leng, A. G. Wang, and H. P. Shi, "Interference-plus-noise covariance matrix reconstruction via spatial power spectrum sampling for robust adaptive beamforming," *IEEE Signal Processing Letters*, vol. 23, no. 1, pp. 121-125, 2016.
[14] L. Huang, J. Zhang, X. Xu, and Z. F. Ye, "Robust adaptive beamforming with a novel interference-plus-noise covariance matrix reconstruction method," *IEEE Transactions on Signal Processing*, vol. 63, no. 7, pp. 1643-1650, 2015.
[15] X. Yuan and L. Gan, "Robust adaptive beamforming via a novel subspace method for interference covariance matrix reconstruction," *Signal Process*, vol. 130, pp. 233-242, 2017.
[16] W. X. Li, Z. Yu, Q. B. Ye, and S. Li, "An improved null broadening beamforming method based on covariance matrix reconstruction," *Applied Computational Electromagnetics Society*, vol. 32, no. 2, pp. 128-134, 2017.
[17] W. H. Orozco, P. M. Hector, and N. M. Mariko, "A new step-size searching algorithm based on fuzzy logic and neural networks for LMS adaptive beamforming systems," *Turkish Journal of Electrical Engineering and Computer Sciences*, vol. 24, no. 7, pp. 4322-4338, 2016.
[18] Z. D. Zaharis, C. Skeberis, and T. D. Xenos, "Design of a novel antenna array beamformer using neural networks trained by modified adaptive dispersion invasive weed optimization based data," *IEEE Transactions on Broadcasting*, vol. 59, no. 3, pp. 455-460, 2013.
[19] H. J. Che, C. Li, and X. He, "A recurrent neural network for adaptive beamforming and array correction," *Neural Networks*, vol. 80, no. C, pp. 110-117, 2016.
[20] R. Savitha, S. Vigneswaran, and S. Suresh, "Adaptive beamforming using complex-valued radial basis function neural networks," *TENCON 2009 - 2009 IEEE Region 10 Conference IEEE*, vol. 34, pp. 1-6, 2009.
[21] A. H. Sallomi and S. Ahmed, "Multi-layer feed forward neural network application in adaptive beamforming of smart antenna system," *Al-Sadeq International Conference on Multidisciplinary in It and Communication Science and Applications IEEE*, 2016.
[22] T. Higuchi, K. Kinoshita, and N. Ito, "Frame-by-frame closed-form update for mask-based adaptive MVDR beamforming," *IEEE International Conference on Acoustics, Speech and Signal Processing (ICASSP)*, 2018.
[23] J. S. Albus, "A new approach to manipulator control: The cerebellar model articulation controller (CMAC)," *Transactions of the Asme Journal of Dynamic Systems*, vol. 97, no. 3, pp. 220-227, 1975.
[24] C. C. Chung and C. M. Lin, "Fuzzy brain emotional cerebellar model articulation control system design for multi-input multi-output nonlinear," *Acta Polytechnica Hungarica*, vol. 12, no. 4, pp. 39-58, 2015.
[25] C. M. Lin and T. Y. Chen, "Self-organizing CMAC control for a class of MIMO uncertain nonlinear systems," *IEEE Transactions on Neural Networks*, vol. 20, no. 9, pp. 1377, 2009.
[26] S. A. Vorobyov, A. B. Gershman, and Z. Q. Luo, "Robust adaptive beamforming using worst-case performance optimization: a solution to the signal mismatch problem," *IEEE Trans. Signal Processing*, vol. 51, pp. 313-323, Feb. 2003.
[27] S. Shahbazpanahi, A. B. Gershman, and Z. Q. Luo, "Robust adaptive beamforming for general-rank signal models," *IEEE Trans. Signal Processing*, vol. 51, pp. 2257-2269, Sept. 2003.
[28] H. W. Yang, J. G. Huang, and C. Liu, "A modified diagonal loading adaptive beamforming method," *Computer Simulation*, vol. 27, no. 3, pp. 318-321, 2010.

Jiaqiang Yu, a Master candidate at the Shanghai University of Engineering Science, China. He has practiced in Shanghai Baolong Automotive Corporation for one year and he is mainly engaged in the study of automotive millimeter wave radar signal processing algorithm.

Pingqing Fan, an Associate Professor works at Shanghai University of Engineering Science, China. She is a Ph.D. candidate of Mechanical Engineering at Shanghai University, China. Her research interests include linear ultrasonic motor design and optimization, micro driver unit of robot and signal processing of millimeter wave radar.

Fast Solution of Low-Frequency Problems Using Efficient Form of MLACA with Loop-Tree Basis Functions

Zhaoneng Jiang [1], Xiaoyan Zhao [1], Ye Jiang [1*], Xuguang Qiao [1], and Quanquan Wang [2]

[1] Hefei University of Technology, Hefei 230009, jiangye@hfut.edu.cn

[2] Nanjing University of Posts and Telecommunications, Nanjing 210003, wangqq@njupt.edu.cn

Abstract ─ In this paper, an efficient scheme of numerical method is proposed to solve the low frequency (LF) problems, which combines the loop-tree basis functions with an efficient form of multilevel adaptive cross approximation (EFMLACA) algorithm. It utilizes the loop-tree basis functions to divide the vector part and scalar part of the impedance matrix. Meanwhile, the scalar part is frequency normalized. Through this operation, it can avoid the low frequency breakdown problem. In order to accelerate the matrix vector multiplication, the EFMLACA algorithm is applied. Meanwhile, the compressed block decomposition (CBD) preconditioner is applied to improve the condition number of poor convergence problems. The numerical results demonstrate that the memory requirement and computation time required for a matrix vector multiplication of EFMLACA algorithm is much less than that of MLACA and ACA-SVD. Moreover, the matrix vector multiplication of EFMLACA algorithm is also much more efficient than that of low-frequency multilevel fast multipole algorithm (LF-MLFMA).

Index Terms ─ **C**ompressed block decomposition (CBD), efficient form of multilevel adaptive cross approximation (EFMLACA) algorithm, low frequency.

I. INTRODUCTION

The numerical simulations of acoustics, microwave filter design, interconnect modeling, and electromagnetic scattering require the solution of Helmholtz equation. One of the popular approaches of numerical solution is to convert them into integral equations [1-3], which are then discretized using appropriate quadrature formulae. This usually leads to large-scale systems of linear algebraic equations, which are in turn solved via appropriately chosen iterative schemes (such as generalized minimal residual (GMRES) [4-5]. Most iterative schemes require the application of the matrix to a sequence of recursively generated vectors. Applying a dense matrix to a vector is an order N^2 procedure, where N is the number of nodes in the discretization of domain. As a result, the whole process is at least of order N^2, which is prohibitive for many large-scale problems.

A further reduction in operations count can be achieved by applying the fast numerical methods [6-10], thus significantly reducing the computational complexity and the memory requirement. The multilevel fast multipole algorithm (MLFMA) is one such method, which can reduces the computational complexity to $O(N\log N)$. It is very efficient for analyzing the models contain few sub-wavelength geometrical detail. When the electric field integral equation (EFIE) is used to analyze the low frequency (LF) problems (when the electrical size of objects is much less than wavelength), a phenomenon called the low frequency (LF) breakdown will be encountered. The origin of LF breakdown for EFIE is not the reason of mathematical, which is caused by the inevitable numerical round-off error on a finite-precision computer. When the frequency tends to zero, the vector part of impedance matrix is much smaller than that of scalar part, resulting in the vector part to be omitted.

In order to overcome this problem, loop-tree basis functions are applied. It separates the vector part and the scalar part of impedance matrix, and frequency normalization is utilized to enhance the role of vector part. In [11], a new method called the low-frequency multilevel fast multipole algorithm (LF-MLFMA) is introduced. However, the matrix vector multiplication of LF-MLFMA is very slow. The low-rank decomposition method is one of the most popular techniques, which has been widely applied to solve electromagnetic problems [12-18]. It is a technology for finding sparse representations of large scale matrix, and is a powerful way to find potentially useful information from the matrix. The multilevel adaptive cross approximation (MLACA) algorithm is one of the fast low-rank methods. In [16], the structure of the MLACA representation is given in a multilevel recursion manner. To improve the efficiency of ACA, some SVD techniques are introduced in [15,18] to recompress the matrices of ACA. In this paper, an efficient form of multilevel adaptive cross approximation (EFMLACA) algorithm is introduced. Moreover, the compressed block decomposition (CBD) [19] preconditioner is applied to further accelerate the

Submitted On: November 2, 2017
Accepted On: December 29, 2018

matrix vector multiplication.

The Section 2 contains the theory of loop-tree method of moments. In Section 3, we discuss the procedure of efficient form of multilevel adaptive cross approximation (EFMLACA) algorithm. The performance of EFMLACA algorithm is illustrated in Section 4 with numerical results. Finally, Section 5 gives very brief conclusions.

II. LOOP-TREE METHOD OF MOMENTS

The traditional method of moments (MoM) utilizes Rao–Wilton–Glisson (RWG) basis function to solve the electromagnetic problem. When the frequency trends to zero, electric field integral equation (EFIE) will encounters the LF breakdown problem. The form of EFIE is given in the following:

$$\vec{n}\times[-j\omega\mu_0 A(r)+\frac{1}{j\omega\varepsilon_0}\nabla\phi(r)]=\vec{n}\times E(r), \qquad (1)$$

where $A(r)$ denotes the magnetic vector potential, $\phi(r)$ denotes the scalar potential,

$$A(r)=\int_{S'} G(r,r')\cdot J(r')dS'$$
$$\phi(r)=\int_{S'} G(r,r')\nabla\cdot J(r')dS'$$

It can be observed from the formula (1) when the frequency tends to zero, the vector part $j\omega\mu_0 A(r)$ is much smaller than the scalar part $\nabla\phi(r)/j\omega\varepsilon_0$. Due to the inevitable numerical round-off error on a finite-precision computer, the information of vector potential will be omitted, and the rest of scalar potential is not accurate enough to describe the target surface current. Therefore, the solution is not stable. This problem can be improved by improving the accuracy of variables in the program, but if you want to solve this problem completely, the loop-tree basis function [20-21] is applied to modify the formula (1):

$$\begin{bmatrix} \omega Z_{LL} & \omega Z_{LC} \\ \omega Z_{CL} & \omega Z_{CC}+\omega^{-1}\tilde{Z}_{CC} \end{bmatrix}\begin{bmatrix} I_L \\ I_C \end{bmatrix}=\begin{bmatrix} V_L \\ V_C \end{bmatrix}, \qquad (2)$$

where,

$$Z_{LL}=T_L^t\cdot Z_A\cdot T_L, \quad Z_{LC}=T_L^t\cdot Z_A\cdot T_C$$
$$Z_{CL}=T_C^t\cdot Z_A\cdot T_L, \quad Z_{CC}=T_C^t\cdot Z_A\cdot T_C$$
$$\tilde{Z}_{CC}=T_C^t\cdot Z_\phi\cdot T_C, \quad V_L=T_L^t\cdot V, \quad V_C=T_C^t\cdot V$$

where T represents the transformation matrix obtained from RWG basis functions to Loop-Tree basis functions [20-21]. T_C denotes the transformation matrix from RWG basis functions to surface-tree basis functions. Meanwhile, T_L denotes the transformation matrix from RWG basis functions to surface-loop basis functions. Z_A denotes the vector part of impedance matrix Z, and Z_ϕ denotes the scalar part of Z. Due to the huge amount of calculation needed for analyzing the LF problems with large number of unknowns, an efficient form of multilevel adaptive cross approximation (EFMLACA) algorithm is proposed.

III. EFMLACA ALGORITHM

A. Multilevel adaptive cross approximation (MLACA)

Multilevel adaptive cross approximation (MLACA) algorithm [15-17] is based on tree structure to divide the object into many sub-domains shown in Fig. 1 (a), which is same as that of reference [15]. The impedance matrix Z can be expressed as:

$$[Z]=\sum_{l=3}^{L}[Z]_l,$$

where $[Z]_l$ denotes the matrix in level l. L denotes the total number of tree structure.

The MLACA algorithm decomposes the far-field matrix into relatively small sub-matrices multiplication. Only r rows and r columns (r denotes the rank of impedance matrix) of the matrix are required to fill, and the entire matrix is not required (shown in Fig. 1 (b)). Under the premise of ensuring the accuracy, as far as possible to extract the minimum rank value of each matrix, so as to effectively reduce memory consumption and computation time.

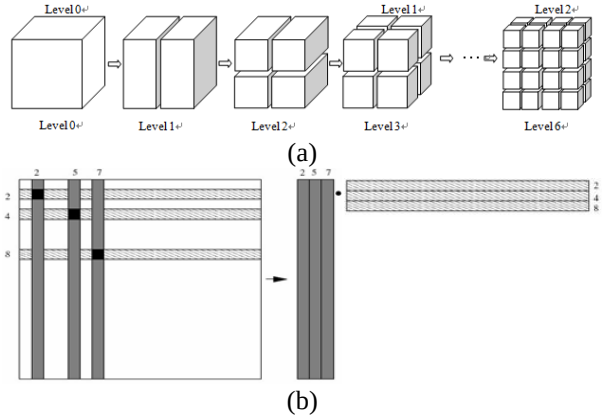

Fig. 1. (a) Subdivision of an object using tree structure in the MLACA algorithm, and (b) the scheme of selecting rows and columns in MLACA algorithm.

In the expression of ACA algorithm, the far-field matrix can be expressed in the following form:

$$[Z]^{m\times n}=[U]^{m\times r}[V]^{r\times n}, \qquad (3)$$

where $[Z]^{m\times n}$ denotes the far-field matrix, r denotes the rank of far field matrix ($r\ll\min(m,n)$). The dimensions of two sub-matrices are both very small. For the large-scale problems, the computation efficiency of matrix multiplication of ACA algorithm is relatively low.

B. Efficient form of MLACA (EFMLACA) algorithm

In this section, a sparse expression of ACA algorithm is applied to accelerate the matrix vector multiplication. It utilizes transform matrix to obtain a compressed representation of the original matrix. The transform matrix is a block diagonal unitary matrix, which is shown in Fig. 2.

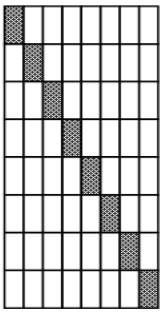

Fig. 2. The form of transform matrix.

The original matrix of equation (3) can be expressed as:

$$[Z]^{m\times n} = [W][\mathrm{Y}][W]^{\dagger}, \tag{4}$$

where $[W]$ is the transform matrix. $[W]^{\dagger}$ is the conjugate matrix of transform matrix $[W]$. The dimensions of $[Y]$ is very small, which requires little memory requirement.

The impedance matrix can be expressed as:

$$[Z]_{far} = \sum_{l=2}^{L}\sum_{i=1}^{M(l)}[W_{li}]\sum_{j=1}^{Far(l(i))}[Y_{lij}][W_{lj}]^{\dagger}, \tag{5}$$

where $M(l)$ is the number of nonempty groups at level l and, $Far(l(i))$ denotes the number of far interaction groups of the i-th nonempty group for each observer group $l(i)$ at level l. $[Z]_{far}$ denotes the far-field matrix. For each observation group, it needs to store the matrix $[W]$ only once. However, the $[U]$ and $[V]$ in equation (3) need to be stored many times for each observation group. The detailed solving process of transform matrix is given in the following.

(*i*) The filling process of matrix [*W*]

At the level l, extract the corresponding matrices $[V]_{ij}$ for each observation group j, which is formed by equation (3). Then concatenate all matrices $[V]_{ij}$ in a row and gain the transition matrix A, which is shown in Fig. 3.

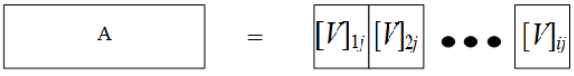

Fig. 3. The form of transition matrix A.

Then, the adaptive cross approximation-singular value decomposition (ACA-SVD) [18] is utilized to decompose the transition matrix A, which needs the whole information of matrix A:

$$[A]^{m\times n} \xrightarrow{ACA-SVD} [U']^{m\times k}[S']^{k\times k}\left\{[V']^{n\times k}\right\}^{*}, k \ll \min(m,n), \tag{6}$$

where n and m denotes dimensions of the matrix A. k denotes the rank of matrix A. $\left\{[V']^{n\times k}\right\}^{*}$ is the j-th diagonal block of $[W_l]$, which is a unitary matrix. Implement the procedure for all observation groups at level l as the above, can obtain $[W_l]$. Using the above procedures at all levels of octal tree structure, can gain the whole transform matrix of $[W]$.

(*ii*) The filling process of matrix [*Y*]

At the level l, the matrix $[W_l]$ is used to multiply the equation (3) on the both sides. The detail expression is given for a far-field sub-matrix in the following:

$$[Y_l] = [W]^{m\times r\,\dagger}[U']^{m\times r}[S']^{r\times r}\left\{[V']^{n\times r}\right\}^{*}[W_{lj}]^{n\times r}, \tag{7}$$

where r is much less than the dimensions of original matrix ($r \ll \min(m, n)$), so the dimension of matrix $[Y]$ is much smaller than that of original matrix. Using the equation (7) at all levels of tree structure, can obtain the whole matrix of $[Y]$.

The main idea of above procedure is to use transform matrix $[W]$ to recompress the far-field matrices of MLACA algorithm. The main memory requirement of EFMLACA algorithm is the storage of matrices $[W]$ and $[Y]$. The $[W]$ is a block diagonal matrix, which is very sparse. Meanwhile, the dimension of matrix $[Y]$ is very small. Therefore, the memory requirement of equation (4) is much less than that of equation (3).

C. Compressed block decomposition (CBD) preconditioner

In this paper, an efficient preconditioner is proposed to further accelerate the matrix vector multiplication. The amplitude difference of diagonal elements obtained by loop-tree basis functions is very large. Therefore, the impedance matrix should be diagonal normalized. In general, the inversion of whole impedance matrix are used as the preconditioner can get the best effect. However, computational complexity and memory consumption of its inverse process are too high, the good choice is to select an approximate matrix instead of the whole impedance matrix. The diagonal block matrices contain the strong interaction, which contain the main information of impedance matrix. Therefore, this paper applies the inversion of diagonal block matrices as the preconditioner to improve convergence problem. The compressed block decomposition (CBD) algorithm [19] is utilized to form the inversion of diagonal block matrices efficiently.

IV. NUMERICAL RESULTS

The low-frequency problems are analyzed in the

following, and the computational efficiency of EFMLACA algorithm is compared with traditional MLACA. The truncating tolerance of both EFMLACA and MLACA is 10^{-3}. The restart number of generalized minimal residual (GMRES) is 30 and the stop precision for restarted GMRES is set to be 10^{-4}.

The first low-frequency problem is a sphere, shown in Fig. 4. The radius is 0.5 meters and the frequency is 3MHz. The electrical size of the sphere is 0.01λ, which is a typical low-frequency problem. The number of tree structure is 3. The bistatic RCS of the structure is given in Fig. 5. It can be found that the results of EFMLACA algorithm are in agreement with that of Mie, which demonstrates the accuracy of EFMLACA algorithm. Figure 6 and Fig. 7 compare the efficiency of EFMLACA algorithm with that of MLACA and ACA-SVD [18]. The memory requirements and computation time required for a matrix vector multiplication (MVP) of EFMLACA and MLACA needed with the increase of the number of unknowns. It can be observed that the EFMLACA is much more efficient than that of traditional MLACA. The memory requirement and MVP time are only third of traditional MLACA. Through our simulation, it is found that the total number of layers affects the efficiency of the EFMLACA algorithm. Table 1 shows the best one of the total number of tree structure for EFMLACA algorithm varying with unknowns in this example. Table 2 also shows the computation time and steps needed for the iterative algorithm of CBD preconditioner and without preconditioner. It can be found that CBD preconditioner obviously improves the efficiency of matrix vector multiplication.

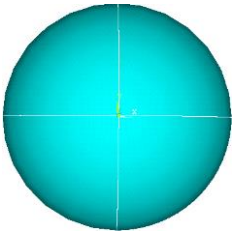

Fig. 4. The sphere model.

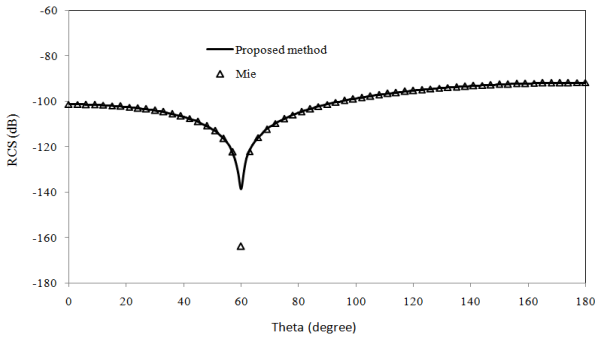

Fig. 5. The RCS results of the sphere structure.

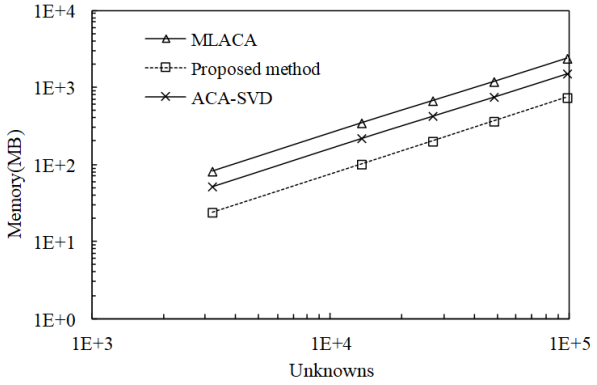

Fig. 6. The memory consumption of the far-field.

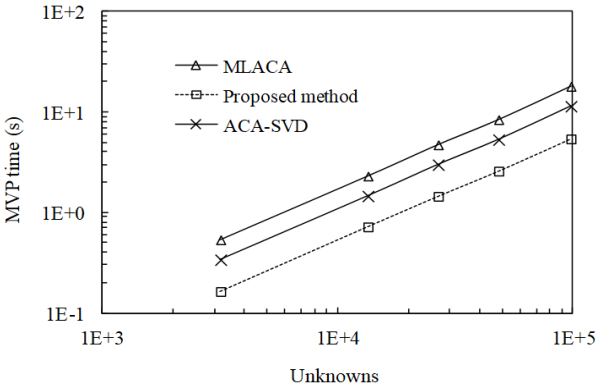

Fig. 7. The time needed of a matrix vector multiplication.

Table 1: The best one of the total number of tree structure for EFMLACA algorithm varying with unknowns in this example

Unknowns Number	The Best One
15000	1
30000	2
60000	3
80000	4
100000	5

Table 2: Computation time and steps needed for the iterative algorithm

Method	Step	Total Time (min)
Without Preconditioner	6741	167.1
CBD Preconditioner	103	2.57

The second low-frequency problem is a cylinder, shown in Fig. 8. The radius is 0.5 meters and the height is 1 meters. The frequency is 30MHz and the number of tree structure is 4. The electrical size of the cylinder is 0.1λ. Figure 9 shows the results of bistatic RCS. According to the figure, the results of EFMLACA is nearly same as that of LF-MLFMA. The efficiency of EFMLACA algorithm is also analyzed in Fig. 10 and

Fig. 11. It can be found that the EFMLACA algorithm is much faster than that of LF-MLFMA. Meanwhile, the memory requirements of the EFMLACA algorithm is nearly same as that of LF-MLFMA. Table 3 shows the best one of the total number of tree structure for EFMLACA algorithm varying with unknowns in this example. Table 4 shows the computation time and steps needed for the iterative algorithm. The computation time and steps of CBD preconditioner are much less that of without preconditioner. The total solving times of EFMLACA and LF-MLFMA are given in Fig. 12. The CBD preconditioner is applied in the two methods. It can be found that EFMLACA is much more efficient than LF-MLFMA.

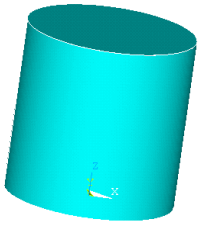

Fig. 8. The cylinder model.

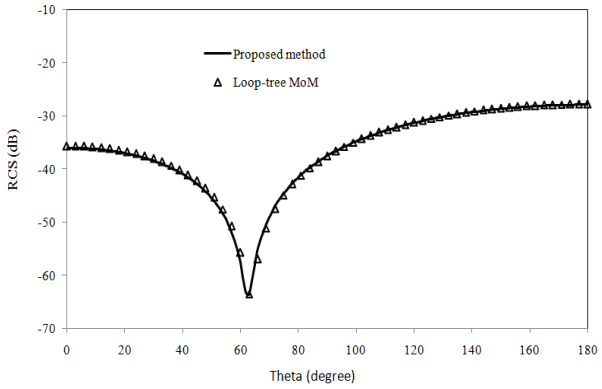

Fig. 9. The RCS results of the cylinder structure.

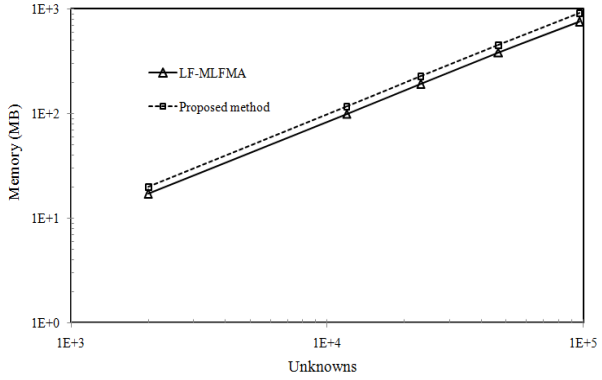

Fig. 10. The memory consumption of the far-field.

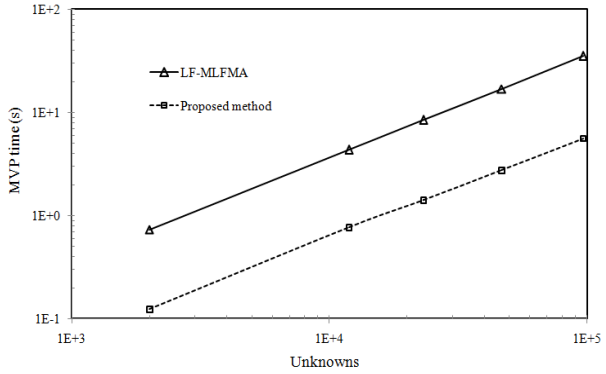

Fig. 11. The time needed of a matrix vector multiplication.

Table 3: The best one of the total number of tree structure for EFMLACA algorithm varying with unknowns in this example

Unknowns Number	The Best One
20000	1
40000	2
60000	3
80000	4
100000	5

Table 4: Computation time and steps needed for the iterative algorithm

Method	Step	Total Time (min)
Without Preconditioner	4987	117.2
CBD Preconditioner	86	2.01

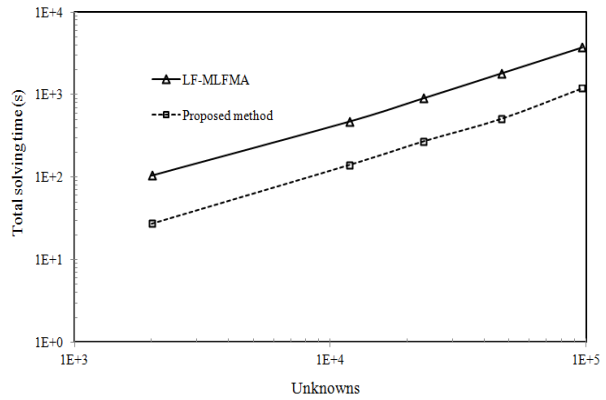

Fig. 12. The total solving times needed of EFMLACA and LF-MLFMA.

V. CONCLUSION

This paper introduces an efficient method to solve the electromagnetic scattering of low-frequency problem by using the EFMLACA algorithm combined with the CBD preconditioner. Numerical results show that EFMLACA algorithm can further improve the efficiency

and save the memory requirements. Meanwhile, the matrix vector multiplication of EFMLACA algorithm is also much more efficient than that of LF-MLFMA and ACA-SVD.

ACKNOWLEDGMENT

This work was supported in part by National Natural Science Foundation of China under Contract Number 61501159, 61501252, HeFei University of Technology Teacher Foundation of JZ2014HGBZ0372, Open Research Program of State Key Laboratory of Millimeter Waves of Southeast University under Contract Number K201602, Natural Science Foundation of Anhui Province (1608085MF124).

REFERENCES

[1] M. S. Al Salameh and A. M. Olaimat, "Method of moments modelling of cylindrical microwave integrated circuits interconnections," *International Journal of Numerical Modelling: Electronic Networks, Devices and Fields*, vol. 17, no. 2, pp. 119-133, 2004.

[2] P. De Doncker, "A volume/surface potential formulation of the method of moments applied to electromagnetic scattering," *Engineering Analysis with Boundary Elements*, vol. 27, no. 4, pp. 325-331, 2003.

[3] C. Essid, M. B. B. Salah, and A. Samet, "Hybrid spatial-spectral MoM analysis of microstrip structures," *International Journal of Numerical Modelling: Electronic Networks, Devices and Fields*, vol. 29, no. 4, pp. 763-772, 2016.

[4] H. De Sterck, "Steepest descent preconditioning for nonlinear GMRES optimization," *Numerical Linear Algebra with Applications*, vol. 20, no. 3, pp. 453-471, 2013.

[5] M. K. Kim and I. Yun, "An efficient implementation of the generalized minimum residual algorithm with a new preconditioner for the boundary element method," *Engineering Analysis with Boundary Elements*, vol. 35, no. 11, pp. 1214-1224, 2011.

[6] Ö. Ergül, "Fast and accurate solutions of electromagnetics problems involving lossy dielectric objects with the multilevel fast multipole algorithm," *Engineering Analysis with Boundary Elements*, vol. 36, no. 3, pp. 423-432, 2012.

[7] W. C. Chew, J. M. Jin, E. Michielssen, and J. Song, *Fast Efficient Algorithms in Computational Electromagnetics*, Boston, MA: Artech House, 2001.

[8] K. Zhang and J.-M. Jin, "Parallelized multilevel fast multipole algorithm for scattering by objects with anisotropic impedance surfaces," *International Journal of Numerical Modelling: Electronic Networks, Devices and Fields*, vol. 28, no. 1 pp. 107-119, 2015.

[9] J. P. De, S. R. Gago, D. W. Kelly, O. C. Zienkiewicz, and I. Babuska, "A posteriori error analysis and adaptive processes in the finite element method: Part II—Adaptive mesh refinement," *International Journal for Numerical Methods in Engineering*, vol. 19, no. 11, pp. 1621-1656, Nov. 1983.

[10] M. Zhang, L. W. Li, and A. Y. Ma, "Analysis of scattering by a large array of waveguide-fed wide-slot millimeter wave antennas using precorrected-FFT algorithm," *IEEE Microwave and Wireless Components Letters*, vol. 15, no. 11, pp. 772-774, Nov. 2005.

[11] J. Aronsson, M. Shafieipour, and V. Okhmatovski, "Solution of large multiscale EMC problems with method of moments accelerated via low-frequency MLFMA," *Electromagnetic Compatibility (EMC), 2011 IEEE International Symposium on*, pp. 260-263, 2011.

[12] M. Bebendorf, *Hierarchical Matrices: A Means to Efficiently Solve Elliptic Boundary Value Problems*, Lecture Notes in Computational Science and Engineering, vol. 63, pp. 49-98, 2008.

[13] J. M. Rius, J. Parron, A. Heldring, J. M. Tamayo, and E. Ubeda, "Fast iterative solution of integral equations with method of moments and matrix decomposition algorithm - singular value decomposition," *IEEE Trans. Antennas Propag.*, vol. 56, no. 8, pp.2314-2324, Aug. 2008.

[14] L. Grasedyck and W. Hackbusch, "Construction and arithmetics of H-matrices," *Computing*, vol. 70, no. 4, pp. 295-344, 2003.

[15] A. Heldring, J. M. Tamayo, C. Simon, E. Ubeda, and J. M. Rius, "Sparsified adaptive cross approximation algorithm for accelerated method of moments computations," *IEEE Trans. Antennas Propag.*, vol. 61, no. 1, pp.240-246, Jan. 2013.

[16] J. M. Tamayo, A. Heldring, and J. M. Rius, "Multilevel adaptive cross approximation (MLACA)," *IEEE Transactions on Antennas and Propagation*, vol. 59, no. 12, pp. 4600-4608, Dec. 2011.

[17] D. Ding, S. Shen, Z. Jiang, and R. Chen, "The modified multilevel compressed block decomposition algorithms for analyzing the scattering of objects in half space," *International Journal of Numerical Modelling: Electronic Networks, Devices and Fields*, vol. 27, no. 1, pp. 153-163, Jan. 2014.

[18] M. Bebendorf and S. Kunis, "Recompression techniques for adaptive cross approximation," *J. Integral Equations Appl.*, vol. 21, no. 3, pp. 331-357, 2009.

[19] T. Wan and Z. Jiang, "Multilevel compressed block decomposition-based finite element domain decomposition method for the fast analysis of finite periodic structures," *International Journal of Numerical Modelling: Electronic Networks, Devices and Fields*, doi: 10.1002/jnm.2194, Sep. 2016.

[20] J.-S. Zhao and W. C. Chew, "Integral equation solution of Maxwell's equations from zero frequency to microwave frequencies," *IEEE Trans. Antennas Propag.*, vol. 48, no. 10, pp.1635-1645, Oct. 2000.

[21] M.-M. Li, H. Chen, Z. Jiang, and R. Chen, "Three dimensional low-frequency fast multipole method for analysis of electromagnetic scattering," *Chinese Journal of Radio Science*, vol. 25, no. 1, pp. 127-131, Feb. 2010.

Analysis of RCS Signatures of Chipless RFID Tags Based on Arabic Alphabet Letters with Punctuation

Oussama Boularess [1,2], Lotfi Ladhar [3], Adnan Affandi [3], and Smail Tedjini [3]

[1] Sys'Com, ENIT, University of Tunis El Manar, BP 37, Belvédère 1002 Tunis, Tunisia

[2] Universty Grenoble-Alpes, LCIS, Valence, 26902, France

[3] King Abdulaziz University, Faculty of Engineering, Electrical and Computer Engineering Department
P.O. Box 80204, Jeddah 21589, Saudi Arabia
lladhar@kau.edu.sa

Abstract ─ In this paper, we investigate chipless RFID (Radio Frequency Identification) tags based on Arabic Alphabets with points, to be used as RF coding particles. First, the tags were designed by considering an Arial font to generate the metallic letters printed on flexible Kapton substrates. Next, the points were connected to form the main bodies of the letters to improve their Radar Cross Section (RCS) signatures when illuminated with incident electromagnetic waves within the frequency band of 2-8 GHz, for both horizontal and vertical polarizations. Good agreement between simulated and measured results has been obtained.

We have found that among all of the similar letters studied, those stripline connections provided us the best way to take into account of the presence of the points and then conveniently distinguish the RCS signals characterizing each letter with a unique RF response.

Finally, a lookup table for the identification of the 18 letters with punctuation that have been studied has been carried out.

Index Terms ─ Arabic letters, chipless, co/cross-polarization, RCS signature, RFID.

I. INTRODUCTION

Radio Frequency Identification (RFID) has been emerging in recent years as a robust technology for wireless data transmission [1]. The technology has several applications, such as asset identification [2], electronic toll collection, vehicle security [2,3], defense systems [4], and security services in the form of personal cards, paper money, access control at short distances [5], and information security [6,7]. Recently, the passive chipless RFID technology has received great research interest [8,9] owing to its lower fabrication cost and smaller size [2,10]. In the passive RFID systems at UHF frequencies, the reader unit and the tag communicate via backscattering of the electromagnetic waves [1]. In fact, the chipless tag can be manufactured by using materials such as plastic or conductive polymers [10,11]. These tags have been envisaged for various types of applications, such as automatic identification, where the natural resonance of the scattered tag is exploited as the identifier [12,13].

Chipless RFID systems are based on generating a unique radio-frequency signature from the tags, which in turn allows the use of cryptographic techniques [14,15] to prevent the counterfeiting of tags. However, such an identification technique highly depends on the geometry of the tag, and several tags based on surface acoustic waves [16], stub-loaded patches [17], stacked multilayer patches [18], and resonators [19] were developed to address the problem.

The tag resonators have attracted a particular interest since the RFID system based on these resonators only requires one antenna which plays the roles of emitter and receiver simultaneously. Many forms and shapes have been explored, such us spirals [19], shorted dipoles [20], Latin letters [21,22], Arab letters [23] to name a few. Recently, Latin letters with improved fonts were proposed for chipless RFID tags [24] and applied for the design of inkjet-printed ones [25].

In a recent work [23], Boularess et al. have investigated the use of Arab alphabet letters as coding chipless RFID particles. The main problem encountered in this approach was the high similarity between many Arab letters, which only differ by the presence (or absence) of one, two or three dots.

In this work, we carry out an in-depth study of the similarity between the Arab letters and investigate the proposed solution in [23] which consists of connecting the main body of the letter to the points with a thin stripline without affecting the visual appearance of the letter. We have also validated our simulations by experiments and have generated a lookup table for studied letters.

The paper is organized as follows: Section II

Submitted On: December 31, 2018
Accepted On: March 19, 2019

describes the working principle of the proposed technique to distinguish between similar letters by adding striplines. In Section III, the design procedure and simulated responses of excited tags under horizontal and vertical polarizations are given. Section IV is dedicated to the experimental validation of the proposed method and comparison between simulated and measured results. Finally, some conclusions are reported in Section V.

II. WORKING PRINCIPLE

In chipless RFID technology, a frequency spectrum is generated when the reader excites a tag based on Arab letters with a linear polarized wave. The above signal is decoded by the reader, which may assign a frequency signature to the tag. This unique RFID depends mainly on the geometry of the letter.

Since some Arabic letters differ from each other only by the presence of one, two, or three dots, the contribution of these points in the backscattered RCS signals is not detectable. For example, when we compare the RCS signals of two letters that are only different in shape by the presence or absence of these points, the retransmitted frequency has a very similar behavior. To address this problem, we connect the dots to the main body of the letter with a thin straight line, and this introduces a significant variation in the RCS as illustrated in Fig. 1. Several tags have been realized, and their signatures measured, to illustrate this phenomenon.

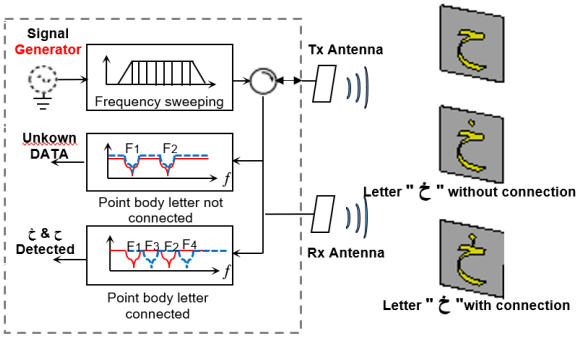

Fig. 1. System description for the modulation resonante frequency of the Arabic alphabet letter tags with and without the dot connections.

For proof-of-concept, we have considered an FSK code which is usually used in chipless RFID systems for coding tag-IDs, owing to its simplicity [12-13]. To apply FSK to the designed tag, when the RFID tag is illuminated with a spectrum of frequencies, a set of resonant frequencies is sent back to the reader. The modulated frequencies determine the EM signatures characterizing the tags based on Arabic letters.

III. SIMULATION METHOD AND ANALYSIS

By nature, the Arabic have complex geometries which can be created by using many fonts. First, we have selected the standard Arial as font for the generation of studied letters, because of its widespread use. Next, we have plotted the Arabic letters with AutoCAD 2016, and have imported them into the electromagnetic simulator CST (Computer Simulation Technology) for numerical analysis. The Arabic letters were illuminated with dual linearly horizontal and vertical polarized plane waves during the simulation process, and two probes were placed orthogonally, close to the tag, in order to record both the co- and the cross-polarized RCS values [6] produced by the tag. Finally, The RCS variation within the frequency band of 2-8 GHz was extracted in the far-field region. Simulations were carried for all the 18 letters of the Arabic alphabet that have similar shapes.

To illustrate the procedure, Fig. 2 presents the results related to selected tags based on letters, which only differ by the presence of a single dot. Figure 2 is dedicated to simulated co-polarized RCS values of chipless tags based on the letters "د" and "ذ". We observe that the RCS responses for letters "د" and "ذ" are quite similar, and the point effect is not significant. This is true for both co- and cross-polarizations. However, if we add a thin strip connecting the dot to the main body of the letter, we realize a noticeable change in value of the RCS, together with a frequency shift, for both co- and cross-polarizations.

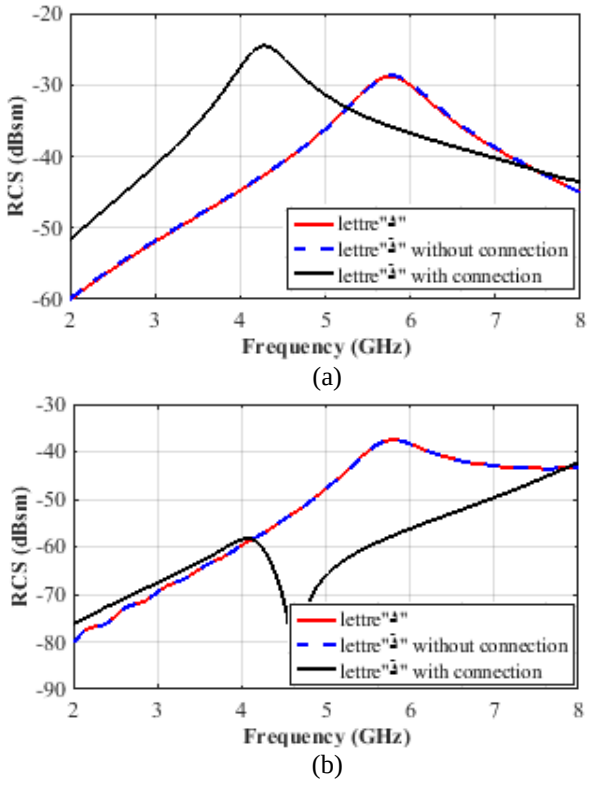

Fig. 2. Simultion of: (a) co- and (b) cross-polarized RCS of Arabic letters "د" and "ذ" with and without the strip connection.

Figure 2 (a) shows that the maximum peak values of the simulated co-polarized RCS signals for both the letters "ب" and "بْ" is -29 dBsm; however, by connecting the dot to the main body the RCS increases to -25 dBsm with a frequency shift of about 2 GHz. For cross-polarization results shown in Fig. 2 (b), we note also a clear difference in terms of the RCS level and the resonance frequency in the electromagnetic response of the studied letter due to the presence of the connecting metallic strip.

To better analyze the effect of the added connection, we have simulated the surface current distributions for the previous letter with and without the metallic strip, and we present the results in Fig. 3. We observe that the addition of the connecting strip improves the coupling between the dot with the main body of the letter and increases in the localized current induced on the dot, which may explain the increase in the RCS value of the "connected" letter, and the downward of the resonating frequency, because of an increase in the resonating current path.

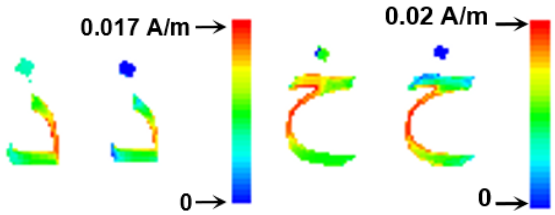

Fig. 3. Surface current distribution at the resonance frequencies of letters "بْ" and " and "خْ" with and without the connection.

IV. RESULTS AND DISCCUSION

A. Prototypes

The Arabic alphabetic shapes were realized by etching copper on a flexible Kapton substrate of thickness 0.1mm, relative permittivity 3.5 and a loss tangent of 0.004. The size of each chipless tag is 37×37mm^2. All the letters written with the standard Arial font, have a height of 24mm, and they generate resonating frequencies within the 2-8GHz band. We can classify Arabic letters into two groups: 10 letters with different shapes and 18 letters with similar shapes which may be regrouped into sub-groups of two or three letters, as shown in Fig. 4.

Fig. 4. Prototypes of the 18 similar letters which differ only by the presence or absence of dots.

As mentioned previously, similar letters that differ from each other only by the presence of the dots, have similar electromagnetic responses. To mitigate this problem, we need to connect the body of the letters with the dots using a 0.1mm width copper line as shown in Fig. 5.

Fig. 5. Photograph of the chipless tag based on the connected Arab letter "خْ".

B. Measurement setup

The measurement set-up is based on a bi-static radar approach, and is used to obtain the co- and cross-polarized RCS from the tags under test. As shown in Fig. 6, the experimental set-up includes an Agilent vector analyzer PNA-N5222A, which provides an incident power of 0 dBm within the frequency range 2 to 8 GHz, a dual-polarized wideband Vivaldi antenna with a maximum gain of 12 dBi covering the band 0.7-18 GHz, which acts both as a transmitter and a receiver, and a chipless tag (device under test) backed with absorbing materials and placed at 15 cm from the antenna to ensure that the tag is in the near-field region. The antenna detects the backscattered RCS signals from the tag when excited with both horizontally and vertically polarized incident electromagnetic waves. The far-field values are deduced from the near-field measurements by using an appropriate code.

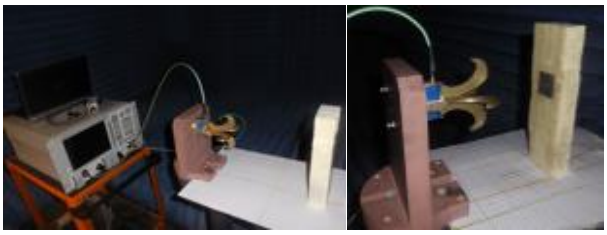

(a) (b)

Fig. 6. Photograph of the experimetal setup: (a) measurment setup, and (b) tag under test.

We have estimated the RCS value of the investigated tags by using the following equations [14]:

$$\sigma_{Co-Pol}^{tag} = \frac{R^4\,(4\pi)^3}{G_t\,G_r\,.\lambda}\left|S_{11/22}^{co\_tag} - S_{11/22}^{co\_no\ tag}\right|, \quad (1)$$

$$\sigma_{Cross-Pol}^{tag} = \frac{R^4\,(4\pi)^3}{G_t\,G_r\,.\lambda}\left|S_{11/22}^{cross\_tag} - S_{11/22}^{cross\_no\ tag}\right|, \quad (2)$$

where, R is the distance between the tag and the antenna, and λ the wavelength. G_t and G_r are the gain of the transmitting antenna and receiving antennas, respectively. $\sigma_{Cross-Pol}^{tag}$ and σ_{Co-Pol}^{tag} are the RCS values for co- and

cross-polarizations, obtained when the transmitting and the receiving antennas are positioned along the parallel (horizontal or vertical) and the perpendicular directions, respectively.

In (1) and (2), we have supposed that the RCS of tag can be directly extracted from the measured S-parameter. However, before measuring the letter's electromagnetic signature, a calibration procedure should be performed to remove the static environment effect [13]. During the calibration process, we first measure and record the received signal without the tag, take it as a reference, add the tag to be tested, and then perform the measurements of the backscattered signals.

C. Experimental results and discussion

We began by measuring the RCS of 4 tags corresponding to the letters "ش" and "غ" (co-pol.), and letters "ث" and "ج" (cross pol.) and compare the results to the simulations to validate the measurement procedure. The obtained results of this preliminary study are given in Fig. 7. The results presented in Fig. 7 show that we have good agreement between the simulation and the measurements. We add that the acceptable difference between the simulated and the measured RCS levels is due to losses which cannot totally be accounted in our simulations, such as losses during the calibration procedure and polarization losses due the misalignment of the antenna with the tag.

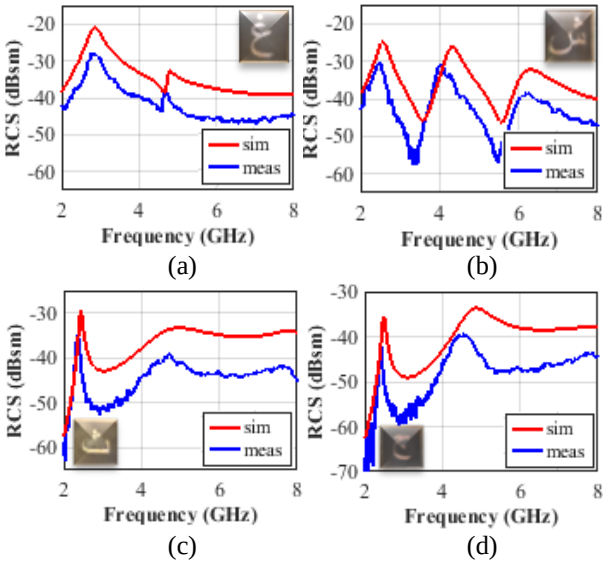

Fig. 7. Simulated and measured tags RCS versus frequency for: (a) letter " غ " letters (co-Pol. VV), (b) letter " ش " (co-Pol. HH), (c) letter " ج " (cross-Pol. HV), and (d) letter " ث " (cross-Pol. VH).

Having validated of our simulated (CST) results with the experiments, we will now focus on the measured results alone here on.

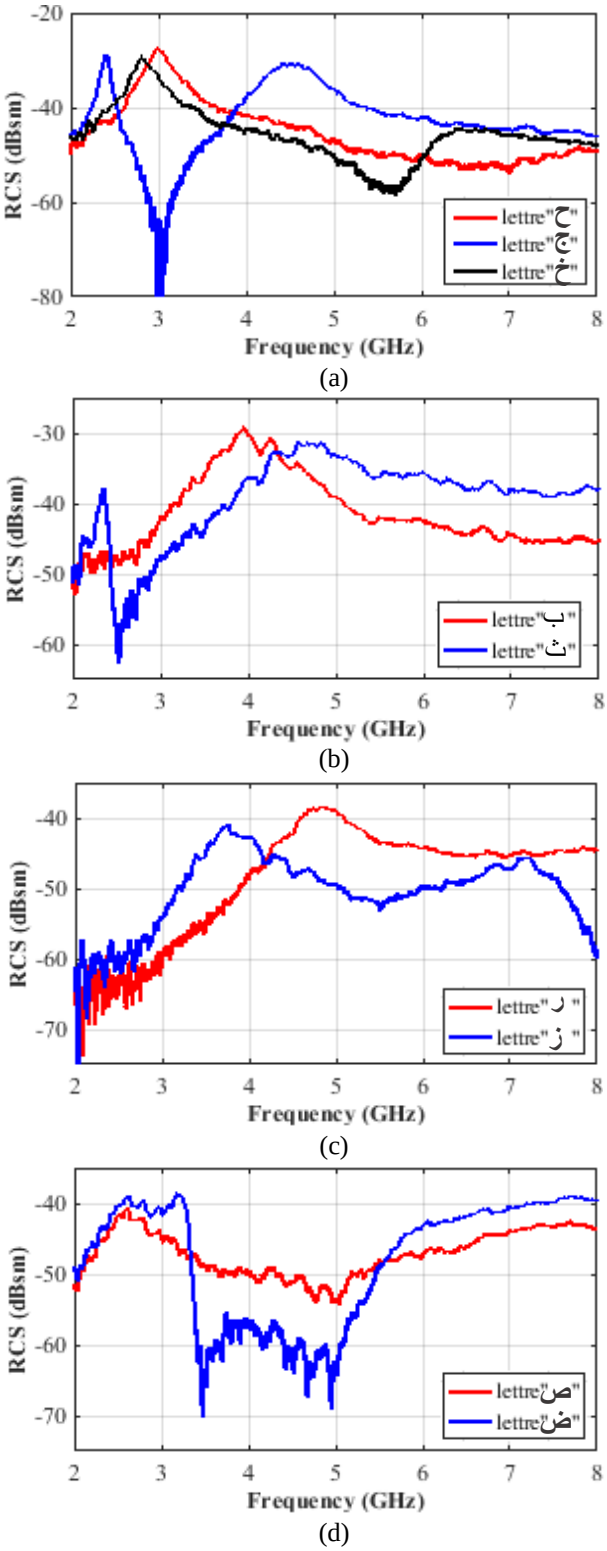

Fig. 8. Measured RCS versus frequency for tags tags based on: (a) letters "ح" ,"خ" and "ج" a (co-Pol. VV), (b) letters "ب" and ث" (co-Pol. HH), (c) letters "ر and ز" (cross-Pol. HV), and (d) letters " ص" and "ض" (cross-Pol. VH).

We have studied a few selected tags based on the letters that have a high level of shape-similarity to demonstrate that our proposed solution of connected dots to the main body of the letter is efficient. The results of this study are presented in Fig. 8.

First, we compare in Fig. 8 (a), the responses of the tags based on the letters "خ","ح" and "ج". We were able to distinguish between them where connecting the point of letters "خ" and "ج" permitted to allow the presence of only one point in their structure. Similarly, letters "**ب**" and "**ث**" (Fig. 8 (b)), letters "**ر**" and "**ز**" (Fig. 8 (b)) and letters "**ص**" and "**ض**" (Fig. 8 (c)) can be easily distinguished, after connecting the dots to the main bodies of the letters, by using the co- and/or cross-polarization measurements.

A thorough analysis of the RCS values for all the letters we have studied show that following the connection of the dots, all the letters are charcterized with unique electromagnetic signatures characterized by two unique resonance frequencies corresponding to both the horizontal and vertical polarizations. These results lead us to conclude that we can use similar arabic letters, that are only slightly different, by coding the particles in the RFID technology to generate the RF codes.

Table 1: Measured RCS lookup table for 24mm-height Arab letters with punctuation using both horizontal and vertical polarization excitations

Arabic Letters	Co-Polar		Cross-Polar	Arabic Letters	Co-Polar		Cross-Polar
	HH	VV	HV and VH		HH	VV	HV and VH
ر	4.85	4.83	4.84	د	5.62	5.65	5.68
ز	3.74 7.27	3.76	3.74 7.20	ذ	7.9	4.11	4.14 7.9
ب	3.95	7.81	3.95 7.88	ت	3.96	3.09	3.09
ث	4.84 2.35	2.35	2.35 4.71	ع	3.07 5.38	3.14 5.56	3.16 5.54
ش	2.49 4.03 6.26	2.52 4.01	2.50 4.00 6.26	غ	2.67 4.30 7.59	2.79 4.68	2.84 4.67 7.67
س	3.19 3.64	3.09 6.25	3.19 6.51	ظ	3.71 4.67	3.65 4.73	3.74 4.71
ج	2.40 4.27	2.40 4.53	2.41 4.56	ط	3.95	4.00 6.04	6.04 4.00
ح	7.84	2.99	2.99 7.80	ص	2.62 5.50	2.60 7.56	2.60 7.60
خ	6.18 774	2.80 6.42	2.89 6.45	ض	2.63 3.37	3.23 6.04	2.62 3.21

By the end of our study, we have generated a lookup table (see Table 1) for all the 18 similar letters, and have provided their resonant frequencies within the 2-8 GHz band, for both the horizontal and vertical polarizations of the incident electric field. The obtained results confirm that each of the tags based on an Arab letter can generate a unique electromagnetic signature.

Table 2: Main published works on chipless RFID tags based on alphabets

Ref.	Alphabet	Letter Font	Letter Police	Freq. Band (GHz)	Letter Height (mm)	Max. RCS (dBsm)
[22]	Latin	Arial	15	6-13	15	-22
[25]	Latin	Calibri with slots	48, 150, 275	0.1-20	33.65	-20
[23]	Arab	Arial	24	1-10	24	-
This work	Arab	Arial with connected dots	24	2-8 GHz	24	-20

In Table 2, we have regrouped the main published results related to chipless RFID tags based on alphabets. Only Latin and Arab letters were investigated until now, with few fonts such as Arial and Calibri. Usually, each alphabet has its own geometry, and then its own limitations when applied to design of chipless RFID tags. So, no unique solution can be proposed for all alphabets, e.g., with Latin tags [25]; thin slots were added within letters to increase their backscattered RCS, whereas in this work, we propose to connect the dots to the main body of the letter to better differentiate between similar ones.

V. CONCLUSION

In this paper, we have carried out both numerical and experimentally studies on the design of chipless RFID tags based on Arabic alphabet letters with dots. We have studied the RCS responses of these similar letters when illuminated with incident electromagnetic waves polarized both horizontally and vertically for better recognition. We have found that, for all the letters we have studied, connecting the dots to the main bodies of the letters with a thin metallic stripline enable us to endow each letter with a unique RF response that has a single resonance frequency; consequently, similar Arabic letters that are very similar each other can still be be coded in the context of chipless RFID technology, as though they are quite different.

ACKNOWLEDMENT

This project was funded by the King Abdulaziz City for Science and Technology (KACST), under Grant No. 32 – 36-ص م. The authors, therefore, acknowledge the technical and financial support of KACST.

REFERENCES

[1] N. C. Karmakar, *Handbook of Smart Antennas for RFID Systems*. Wiley-IEEE Press, 2010.

[2] K. Finkenzeller, *RFID Handbook: Radio-Frequency Identification Fundamentals and Applications*. 2nd ed., Wiley, 2004.

[3] R. Want, "An introduction to RFID technology," *IEEE Pervasive Computing*, vol. 5, no. 1, pp. 25-

33, Jan. 2006.

[4] Q. Xiao, C. Boulet, and T. Gibbons, "RFID security issues in military supply chains," in *2nd Int. Conf. Availability, Rel. and Security ARES*, Apr. 2007.

[5] R. Pateriya and S. Sharma, "The evolution of RFID security and privacy: A research survey," in *Int. Conf. Commun. Syst. and Network Technologies (CSNT)*, Katra, Jammu, June 2011.

[6] H. Rmili, D. Oueslati, L. Laadhar, and M. Sheikh, "Design of a chipless RFID tags based on natural fractal geometries for security applications," *Microwave and Optical Technology Letters*, vol. 58, no. 1, pp. 75-82, Jan. 2016.

[7] P. Kitsos and Y. Zhang, *RFID Security: Techniques, and Protocols*. New York: Springer Science, 2008.

[8] S. Tedjini, N. Karmakar, E. Perret, A. Vena, R. Koswatta, and R. E. Azim, "Hold the chips: Chipless technology, an alternative technique for RFID," *IEEE Microwave*, vol. 14, no. 5, pp. 56-65, July 2013.

[9] A. Fawky, M. Khaliel, A. El-Awamry, M. El-Hadidy, and T. Kaiser, "Novel pseudo-noise coded chipless RFID system for clutter removal and tag detection," in *IEEE Int. Conf. on RFID*, San Diego, CA, Apr. 2015.

[10] M. Oliveros, M. Carminati, A. Zanutta, T. Mattila, S. Jussila, and K. Nummila, "Photosensitive chipless radio-frequency tag for low-cost monitoring of light-sensitive goods," *Sensors and Actuators B, Chemical*, vol. 223, pp. 839-845, Feb. 2016.

[11] S. Preradovic, S. Roy, and N. Karmakar, "RFID system based on fully printable chipless tag for paper-/plastic-item tagging," *IEEE Antennas Propag. Mag*., vol. 53, no. 5, pp. 15-32, Oct. 2011.

[12] S. Preradovic, I. Balbin, N. Karmakar, and G. Swiegers, "A novel chipless RFID system based on planar multiresonators for barcode replacement," in *IEEE Int. Conf. on RFID*, Apr. 2008.

[13] R. Rezaiesarlak and M. Manteghi, "Complex-natural-resonance based design of chipless rfid tag for high-density data," *IEEE Trans. Antennas Propag*., vol. 62, no. 2, pp. 898-904, Feb. 2014.

[14] Y. Chen, Z. Chen, and L. Xu, "RFID system security using identity based cryptography," in *3rd Int. Symp. on Intell. Informa. Technology and Security Informatics (IITSI)*, Jinggangshan, Apr. 2010.

[15] D. Maimut and K. Ouafi, "Lightweight cryptography for RFID tags," *IEEE Security & Privacy*, vol. 10, no. 2, pp. 1584-1591, Dec. 1996.

[16] V. Plessky and L. Reindl, "Review on SAW RFID tags," *IEEE Trans. on Ultrasonics, Ferroelectrics and Freq. Control*, vol. 57, pp. 654-668, 2010.

[17] I. Balbin and N. C. Karmakar, "Phase-encoded chipless RFID transponder for large-scale low-cost applications," *IEEE Micro. and Wireless Comp. Lett*., vol. 19, pp. 509-511, 2009.

[18] S. Mukherjee and G. Chakraborty, "Chipless RFID using stacked multilayer patches," *App. Electr. Conf. (AEMC)*, pp. 1-4, Dec. 14-16, 2009.

[19] O. Necibi, S. Beldi, and A. Gharsallah, "Design of a chipless RFID tag using cascaded and parallel spiral resonators at 30 GHz," *2nd World Sym. on Web Applications and Net*., Sousse, Tunisia, Mar. 21-23, 2015.

[20] A. Ramos, E. Perret, O. Rance, S. Tedjini, A. Lázaro, and D. Girbau, "Temporal separation detection of chipless depolarizing frequency coded RFID," *IEEE T-MTT*, vol. 64, pp. 2326-2337, 2016.

[21] T. Singh, S. Tedjini, E. Perret, and A. Vena, "A frequency signature based method for the RF identification of letters," *IEEE RFID 2011*, Orlando, Florida, (USA), pp. 12-14, Apr. 2011.

[22] S. Tedjini, O. Boularess, T. Andriamiharivolamena, H. Rmili, and T. Aguili, "A novel design of chipless RFID tag based on alphabets," *Proc. IEEE International Microwave Symposium, IMS*, Honolulu, Hawaii, June 4-9, 2017.

[23] O. Boularess, H. Rmili, T. Aguili, and S. Tedjini, "Analysis of electromagnetic signature of arabic alphabet as RF elementary coding particles," *Wireless Power Transfer*, 2 (02), pp. 97-106, Sep. 2015.

[24] F. Mutlu, M. A. Demir, and O. Ergul, "Improved fonts for chipless radio-frequency-identification tags based on letters," *18th Mediterranean Microwave Symposium (MMS)*, pp. 247-250, Istanbul, Turkey, Oct. 31-Nov. 2, 2018.

[25] M. A. Demir, F. Mutlu, and O. Ergul, "Design of highly distinguishable letters for inkjet-printed chipless RFID tags," in *2018 IEEE-APS Topical Conference on Antennas and Propagation in Wireless Communications (APWC)*, pp. 783-786, 2018.

Oussama Boularess received the Master degree in Electrical and Electronics from the University of Tunis El Manar, Faculty of Sciences, in 2013. He is currently working toward the Ph.D. degree in System Communication at the National Engineering School of Tunis (ENIT), University of Tunis El Manar.

His areas of interests include chipless RFID design, ultra-wideband (UWB) antenna designs, UWB transceiver design for chipless RFID applications, Passive RFID.

Lotfi Ladhar received his engineering degree and his Ph.D. degrees in Telecommunications from High Institute of Communications of Moscow (RUSSIA) in 1985. From 1990 to 2001, he was Assistant Professor at the Air force Academy in Tunis – Tunisia. His research activities include patch antennas and propagation.

Adnan Affandi received his Master of Science (1978) in Electronic (Microwave Communications) and his Ph.D. in Electronics (1982) from Kent University, Canterbury, England. He is Full Professor with the Electrical and Computer Engineering Dept. in KAU. His research interests are Antenna Theory and Design, and microwave circuits.

Smail Tedjini, Doctor in Physics from Grenoble University in 1985. Assistant Professor Grenoble Institute of Technology (Grenoble-inp) 1981 to 1986, and Senior Researcher for the CNRS (Research French National Center) from 1986 to 1993. He became University Full Professor in 1993 and since 1996 he is Professor at the esisar, Embedded Systems Dpt. of Grenoble-inp. His main teaching topics concern Applied Electromagnetism, Radio Frequency, Wireless Systems and Optoelectronics. Now he has more than 30 years' experience in academic education, Research and management of university affairs. He is the Founder and past Director of the LCIS Lab. He is the Founder of ORSYS group and he leaded this group 2008-2014. He supervised more than 35 Ph.D.'s and he has more than 250 publications. He serves as Examiner/ Reviewer for ten Ph.D. degrees for universities in many countries (France, Germany, Finland, Spain, Ireland, Italy, Sweden, Vietnam, Australia, Singapore, India, Brazil, Egypt, Maghreb…). He is Member of several TPC and serves as expert/reviewer for national and international scientific committees and conferences including journals such as Piers, IEEE (MTT, AP, Sensors, MGWL), URSI, ISO, ANR, OSEO, FNQRT. Senior Member IEEE, President and Founder of the IEEE-CPMT French Chapter, Vice-President of IEEE Section France and elected as the Vice-Chair of URSI Commission D "Electronics & Photonics" in 2008. He was reelected as Vice-Chair of IEEE-France-section and he is serving as the Chair of URSI Commission "D" for the triennium 2011-2014, in particular the preparation on the General Assembly and Scientific Symposium which was held in Beijing August 2014.

Realization of Dielectric Sheets for Gain Improvement of Ultra-Wideband Horn Antennas Using 3D Printer Technology

Mehmet A. Belen [1] and Peyman Mahouti [2]

[1] Department of Electric and Electronic Engineering
University of Artvin Çoruh, Artvin, TURKEY
mehmetalibelen@artvin.edu.tr

[2] Department of Electronics and Communication Engineering
University of Yıldız Technical, Istanbul, TURKEY
pmahouti@yildiz.edu.tr

Abstract ─ In this work, 3D printing technology had been used to prototyped 10 dielectric sheets with relative dielectric constant of 2.5 for gain improvement of a TEM horn antenna. By loading the 3D printed dielectric sheets to the aperture of the horn antenna it is achieved to improve the radiation performance of the antenna over an ultra-wide operation band of 2-13 GHz. Here the Periodic dielectric sheets are designed to function similarly to a dielectric lens for focusing the incoming electromagnetic waves to increase directivity properties, while keeping their mismatching characteristics with less size and low manufacturing cost compared to its counterpart lens designs. The dielectric sheets had been prototyped via the use of 3D printing technology for experimental measurements. The measured performance of the proposed 3D printed dielectric loaded TEM horn antenna is compared with its counterpart ultra-wide band gain improvement methods for horn antennas in literature. From the measured results of the prototyped module, not only the proposed 3D printed dielectric sheets are smaller and have lower cost compared to their counterpart designs but also achieves to improve the gain characteristics of the antenna design over an ultra-wide band operation band without a distortion on antenna's S_{11} characteristics,

Index Terms ─ 3-D Printer, dielectric sheets, gain improvement, horn antenna.

I. INTRODUCTION

The gain performance of a horn antenna design is usually based on design size. For achieving a horn antenna design with high gain performance usually can be achieved with a heavy, bulky, and either impractically long or high cost designs, especially in case of application at low band [1-2]. One of the methods to reduce the size of a horn antenna is increasing the flare angle, however this would cause large quadratic phase error at the aperture, resulting in increase of radiation patterns beam width. In literature there are different studies on preventing the quadratic phase error by placing frequency selective surfaces, metamaterials or by dielectric lens structure to the aperture of the design [3-5].

Dielectric lenses are used in the microwave area as glass lenses are used in the optical field [6]. Dielectric lenses modifies the antennas radiation pattern thanks to their ability to focus the electromagnetic waves. For gain enhancements, dielectric lens structures converts the incoming quasi-spherical wave into near plane wave. In literature there are many types of microwave lens designs for antenna gain improvement where various types of shapes, material either 2-D or nonplanar 3-D structures had been used [7–13].

Due to their phase error, single mode horn antennas has the disadvantage of poor aperture efficiency. By adding a dielectric lens structure to the aperture of a horn antenna it is possible improve aperture efficiency of the design [14-16]. Also dielectric lenses can also be used to change the aperture phase for the reduction of side lobes [17]–[19].

Herein, design and realization of 3-D printed periodic Dielectric Sheets (DS) for ultra-wideband gain enhancement of horn antennas is studied. The main goal of work is to design and realize a low cost DS design that can be prototyped using 3-D printer technology in order to improve radiation performance of a horn antenna design over the operation band of 2-13 GHz without any distortion in S_{11} characteristics. For this purpose 10 layers of 3-D printed dielectric plates are placed in the aperture of a horn antenna.

In the next section the design, simulation and prototyping of the DS are presented. After that, the measurement results of the 3-D printed Dielectric Sheet Loaded Horn Antenna (DSLHA) are investigated, finally paper ends with conclusion section.

Submitted On: July 28, 2018
Accepted On: February 9, 2019

II. DESIGN AND FABRICATION OF DIELECTRIC SHEETS LOADED HORN ANTENNA

In this section, firstly an exponentially TEM horn antennas operates within the bandwidth of 2-13 GHz (Fig. 1) is taken for both simulation and measurement test of the 3-D printed dielectric lens'. The design parameters of the antenna are given in Table 1.

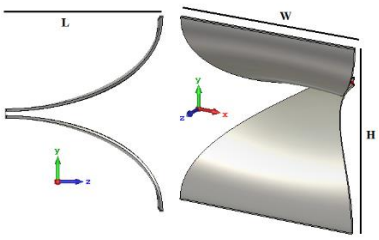

Fig. 1. Exponentially tapered TEM.

Table 1: Parameters of TEM horn antenna in (mm)

Aperture		Length
Width	**Height**	
74	73.5	60

The next element of the module is the DS element. As it mentioned before dielectric loaded horn antenna designs are based on integration of a dielectric material based lens structures and horn antennas for focusing the incoming electromagnetic waves. The proposed 3-D printable DS is shown in Fig. 2. The design consists of 10 parallel placed DS in front of the antenna. The dielectric constant of DS structures are ε_r = 2.5 with thickness value of *hs.* Also the DS units has an air gap distance of *d*. the optimal geometric parameters values for the proposed DS module are given in Table 2.

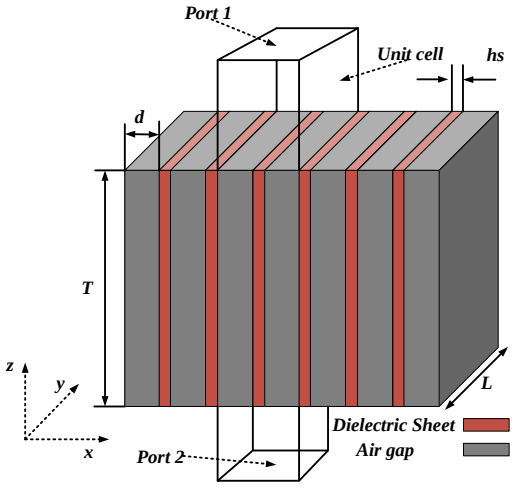

Fig. 2. Proposed DS model for DSLHA module design.

Table 2: Design parameters of dielectric sheet

T	25 (mm)	**h_s**	1.8 (mm)
L	73.5 (mm)	**Air gap (d)**	6.2 (mm)
Substrate	PLA 73%, ε_r = 2.5		

In Fig. 3 simulation setup of the DSLHA is presented. The simulated S_{11} ad gain of two antennas are shown in Fig. 4. As It can be seen from the simulation results both antennas have similar simulated bandwidths for $S_{11}<-6$ dB, thus using the 3-D printed DS for gain improvement has no distortive effect on S_{11} characteristics. As it can be seen from Fig. 4 (b), the proposed DSLHA module has a simulated gain values of almost 14 dB while the TEM horn antenna achieves almost 10 dB gain at 8 GHz frequency. In Fig. 5, the simulation results of far field gain of both antenna design are presented.

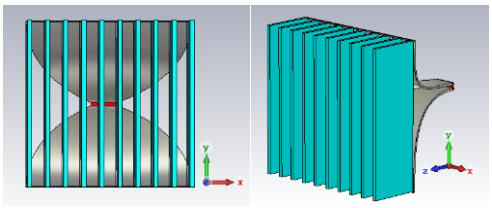

Fig. 3. Proposed module.

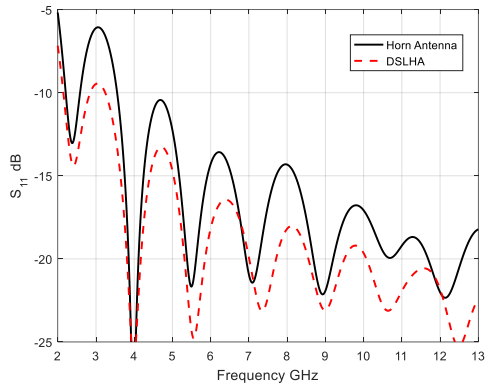

(a)

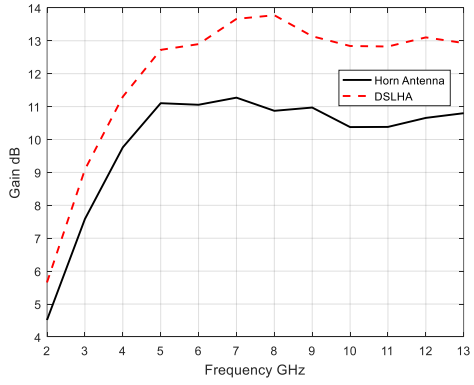

(b)

Fig. 4. Simulated (a) S_{11} and (b) gain.

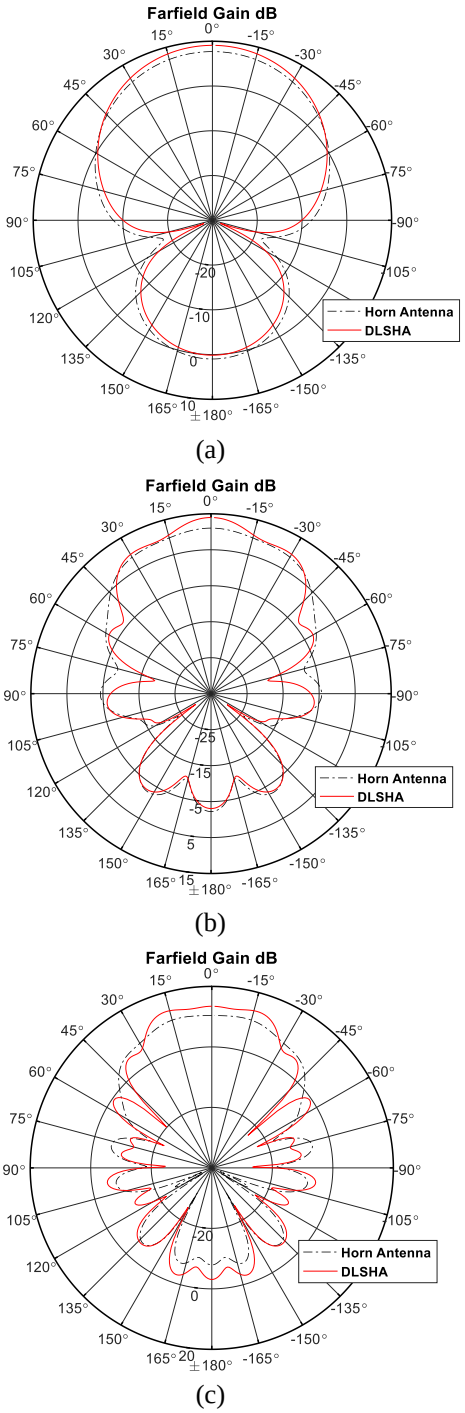

Fig. 5. Simulated far field Gain at: (a) 3, (b) 8, and (c) 12GHz.

III. MEASUREMENT

The measurement setup and results of the DSLHA are given in this section. Fig. 6 gives the prototyped TEM horn, 3-D printed Dielectric sheets, DSLHA and the measurement setup set-up in the laboratory environment.

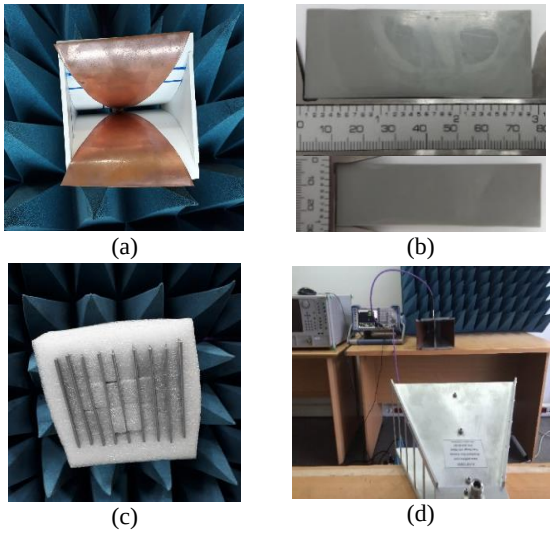

Fig. 6. (a) Prototyped TEM horn antenna, (b) 3D printed dielectric sheets, (c) prototyped DSLHA, and (d) measurement setup.

The S_{11} characteristics, and radiation patterns of the prototyped 3-D printed DSLHA are measured using 2 identical antenna in [20]. In Fig. 7 the measured S_{11} of the DSLHA and TEM horn antenna are given. From the Fig. 7 it can be concluded that implementation of DS elements to the horn antenna does not have any disruptive effect on the S_{11} characteristics over the operation band.

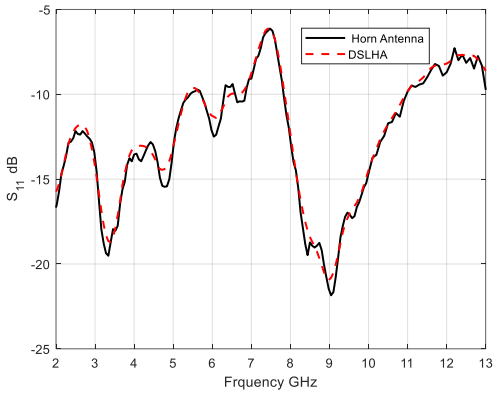

Fig. 7. Measured S_{11} characteristics.

The measured radiation patterns of the DSLHA and horn antenna are presented in Fig. 8, Tables 3-4. From the measurement results it can be concluded that the 3-D printed dielectric sheet designs can increase the directivity of the horn antennas over the operation band of 2-13 GHz. Especially the 3-D printed DS elements achieves to improve directivity of the TEM horn antenna @ 11-12 GHz by focusing the divided radiation towards the maximum direction.

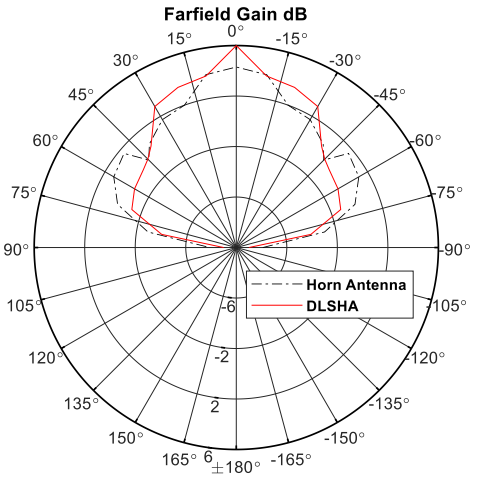

(a)

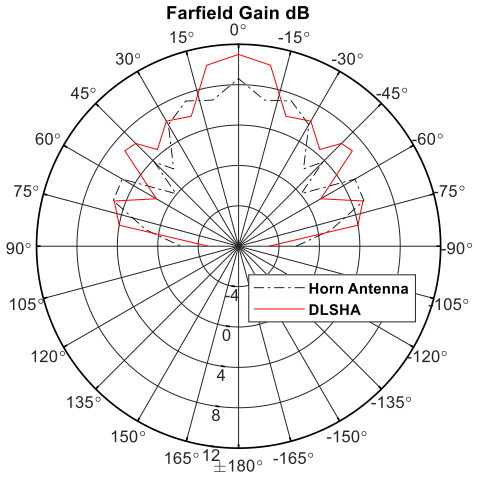

(b)

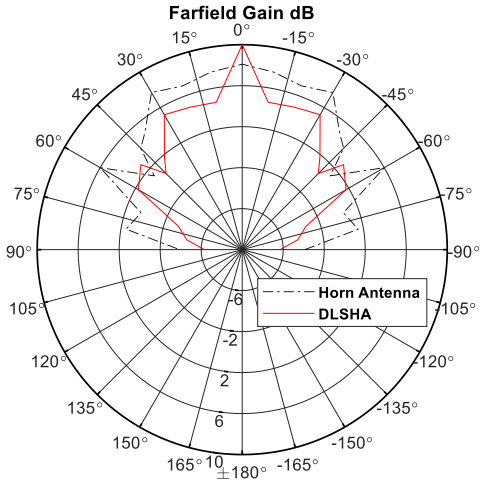

(c)

Fig. 8. Measured radiation patterns at: (a) 2, (b) 7, and (c) 12 GHz.

Table 3: Measured gain dB at ϕ=90º, θ=90º

f (GHz)	Model		Frequency (GHz)	Model	
	Horn	DSLHA		Horn	DSLHA
2	4	6	**8**	8.2	10.8
3	4	7	**9**	8	11
4	9	11	**10**	10	11.8
5	10	12	**11**	8	9.8
6	10	11	**12**	8	10
7	8.5	11	**13**	8.8	11

Table 4: Measured 3dB beam width in degree

Frequency (GHz)	Model		Frequency (GHz)	Model	
	Horn	DSLHA		Horn	DSLHA
2	60	60	**8**	100	35
3	100	60	**9**	60	80
4	60	60	**10**	60	35
5	60	30	**11**	100	50
6	50	30	**12**	80	30
7	70	30	**13**	70	60

Table 5: Comparison of gain enhancements of typical horn modules in the similar bandwidth

	Dielectric Size (mm)	Gain Enhancement (dB) Over Operation Band (GHz)					
		2	**5**	**7**	**9**	**11**	**13**
Here	25x73.5x1.6	2	2	2.5	3	1.8	2.2
[21]	---	---	2	0	0.5	0.2	1
[22]	100x100x30	---	4	3	5	0	0
[23]	100x100x30	---	4	5	5	4	4

Furthermore comparisons of the gain enhancements among the typical macro designed dielectric lens loaded horn modules [21-23] are given in table 5, respectively. From the table, one can concluded that the proposed DSLHA module achieves better performance with the relatively small volume within the requested operation band compared to its counterpart designs.

IV. CONCLUSION

Herein, a relatively small volume dielectric sheet design had been prototyped using 3-D printer technology to form a DSLHA module operates within the operation band of 2-13 which achieves an almost 2 dB gain improvement over the operation band of the implemented horn antenna. As it can be seen from both simulation and measurement results of gain and S_{11} characteristic, the proposed 3-D printed dielectric sheets does not have distortive effect on the S_{11} characteristics of design, while the dielectric sheets start to focus the radiation pattern of the horn antenna at higher operation frequency of 11-12 GHz to increase the maximum gain. Thus, it is expected that 3-D printer technology can be applied for fast, accurate and low cost prototyping of more complex dielectric lens designs.

REFERENCES

[1] W. L. Stutzman and G. A. Thiele, *Antenna Theory and Design*. 3rd ed., New York, NY, USA: Wiley, 2012.

[2] P. S. Kildal, K. Jakobsen, and K. S. Rao, "Meniscus lens corrected corrugated horn: A compact feed for a cassegrain antenna," *IEE Proc., Microw., Opt. Antennas*, vol. 131, no. 6, pp. 390-394, Dec. 1984.

[3] P. Mahouti, F. Güneş, M. A. Belen, Z. Sharipov, and S. Demirel, "TEM horn antennas with enhanced functionalities through the use of frequency selective surfaces," *The 3rd EMC Turkiye Conference*, Isik University, Maslak/Istanbul, 2-4 Sep. 2015.

[4] P. Mahouti, F. Güneş, M. A. Belen, A. Çalışkan, S. Demirel, and Z. Sharipov, "Horn antennas with enhanced functionalities through the use of frequency selective surfaces," *Int. J. RF Microwave Comp. Aid Eng.*, vol. 26, pp. 287-293, 2016. doi:10.1002/mmce.209.

[5] F. Güneş, Z. Sharipov, M. A. Belen, and P. Mahouti, "GSM filtering of horn antennas using modified double square frequency selective surface," *Int. J. RF Microwave Comp. Aid Eng*., vol. 27, 2017. DOI: 10.1002/mmce.2114.

[6] H. Zhu, S. W. Cheung, and T. I. Yuk, "Enhancing antenna boresight gain using a small metasurface lens: Reduction in half-power beamwidth," *IEEE Antennas Propag. Mag*., vol. 58, no. 1, pp. 35-44, Feb. 2016.

[7] J. R. Risser, *Microwave Antenna Theory and Design*. New York, NY, USA: McGraw-Hill, 1949.

[8] B. Chantraine-Bares, R. Sauleau, L. L. Coq, and K. Mahdjoubi, "A new accurate design method for millimeter-wave homogeneous dielectric substrate lens antennas of arbitrary shape," *IEEE Trans. Antennas Propag*., vol. 53, no. 3, pp. 1069-1082, Mar. 2005.

[9] W. E. Kock, "Metallic delay lens," *Bell System Tech. J*., vol. 27, pp. 58-82, Jan. 1948.

[10] W. E. Kock, "Metal lens antennas," *Proc. IRC*, vol. 34, no. 11, pp. 826-836, Nov. 1946.

[11] D. Ramaccia, F. Scattone, F. Bilotti, and A. Toscano, "Broadband compact horn antennas by using EPS-ENZ metamaterial lens," *IEEE Trans. Antennas Propag*., vol. 61, no. 6, pp. 2929-2937, June 2013.

[12] A. D. Olver and A. A. Saleeb, "Improved radiation characteristics of conical horns with plastics-foam lenses," *IEE Proc., Microw., Opt. Antennas*, vol. 130, no. 3, pp. 197-202, Apr. 1983.

[13] E. L. Holzman, "A highly compact 60-Ghz lens-corrected conical horn antenna," *IEEE Antennas Wireless Propag. Lett*., vol. 3, pp. 280-282, 2004.

[14] L. De Haro, A. G. Pino, J. L. Besada, A. M. Arias, and J. O. Rubinos, "Antennas feasibility study for a LMDS communication system," in *Proc. Antennas and Propag. Society Int. Symp*., vol. 3, pp. 2162-2165, July 11-16, 1999.

[15] R. Peritz, "A matched dielectric lens in a highly flared horn to produce focused feed patterns for a cassegrain antenna," in *Proc. Antennas and Propag. Society Int. Symp*., vol. 2, pp. 196-202, Sep. 1964.

[16] A. D. Olver and B. Philips, "Integrated lens with dielectric horn antenna," *Electron. Lett.*, vol. 29, no. 13, pp. 1150-1152, June 1993.

[17] R. O. dos Santos and C. L. S. S. Sobrinho, "FDTD method: Analysis of a one-dimensional array of H-plane sectoral horn antennas with dielectric lens," in *Proc. Microw. Optoelectron. Conf*., vol. 1, pp. 481-484, Aug. 6-10, 2001.

[18] A. Kezuka, Y. Yamada, and Y. Kazama, "Design of a feed horn for a FWA base station antenna through FDTD method," in *Proc. Joint Conf. 10th Asia-Pacific Conf. on Commun*., vol. 2, pp. 573-576, Sep. 1, 2004.

[19] L. Oh, S. Peng, and C. Lunden, "Effects of dielectrics on the radiation patterns of an electromagnetic horn," *IEEE Trans. Antennas Propag*., vol. 18, pp. 553-556, July 1970.

[20] LB8180, "0.8-18 GHz broadband horn antenna," (Aug. 14, 2017). Available at: http://www.ainfoinc.com/en/p_ant_h_brd.asp

[21] R. J. Bauerle, R. Schrimpf, E. Gyorko, and J. Henderson, "The use of a dielectric lens to improve the efficiency of a dual-polarized quad-ridge horn from 5 to 15 GHz," *IEEE Transactions on Antennas and Propagation*, vol. 57, no. 6, June 2009.

[22] A. S. Türk, A. K. Keskin, and M. D. Şentürk, "Dielectric loaded TEM horn-fed ridged horn antenna design for ultrawideband ground-penetrating impulse radar," *Turkish J. Elec. Eng. & Comp. Sci*., vol. 23, pp. 1479-1488, 2015.

[23] A. S. Türk and A. K. Keskin, "Partially dielectric-loaded ridged horn antenna design for ultrawideband gain and radiation performance enhancement," *IEEE Antennas and Wireless Propagation Letters*, vol. 11, 2012.

Design of Ultra-wideband and Transparent Absorber based on Resistive Films

Xinru Lu [1], Juan Chen [2], Youqi Huang [3], Zixian Wu [1], and Anxue Zhang [1]

[1] School of Electronic and Information Engineering
Xi'an Jiaotong University, Xi'an, 710000, China

[2] The Shenzhen Research School
Xi'an Jiaotong University, Shenzhen, 518000, China
chen.juan.0201@mail.xjtu.edu.cn

[3] China Building Materials Academy Co., Ltd
China Building Materials Academy Co., Ltd, Beijing, 100024, China

Abstract — Researching and developing of ultra-wideband capability and high light transmittance have been hot issues in the field of new artificial electromagnetic stealth material. In this paper, a novel transparent metamaterial absorber, made of resistive films and glass, has been presented. The simulation results show that, under the incidence of plane wave, the absorber realizes high absorption during frequency range from 3.5 GHz to 18.5 GHz while keeping insensitive to polarization. A prototype has been fabricated and tested, and the measurement results are in good consistent with simulation. Along with its high transmittance and superior absorption, we expect that the absorber has great potential applications in RCS (Radar Cross Section) reduction and electromagnetic shielding.

Index Terms — Absorber, broadband, RCS reduction, resistive film, transparent.

I. INTRODUCTION

Meta-material absorber, belonging to the category of artificial electromagnetic materials, has attracted much attention since Landy et al. [1] first proposed the "PMA" (perfect meta-material absorber) which achieved more than 88% absorption at 11.5 GHz in 2008. Changes of meta-material structure could affect its electrical parameters: effective permeability (μ_{eff}) and permittivity (ε_{eff}), in this way the impedance of meta-material is altered dependently. In transmission line theory, when the impedance of meta-material reaches to 377 Ω, meta-material realizes perfect impedance matching with free space. So, if an electromagnetic wave is incident on the meta-material, there would be no reflected energy. Especially when the meta-material contains metal backplane, the energy of incident wave is completely absorbed in it as there is no reflected or transmitted wave. Meta-material absorber offers a number of prominent technical advantages including thin thickness, lightweight, and strong flexibility, which surpasses traditional absorbing materials. With these advantages, meta-material absorber has immense potential in electromagnetic application, such as stealth, shielding, and electromagnetic compatibility (EMC) [2]. So far, researches on meta-material absorber have been reported. Great efforts have been devoted to improve the ability to work in wider domain of frequency, for example, in 3~20 GHz. This is because the regime from 3 GHz to 20 GHz covers most of communication bands for military radar. However, narrow bandwidth of absorption has always been the key difficulty in design [3].

In order to resolve the problem of narrow absorbing band, various methods including employing multi-resonant [4], [5], multi-layered structures [6] and new materials [7-10], have been brought up. Nevertheless, these absorbers have drawbacks of large thickness, limited bandwidth, and difficult fabrication. Apart from that, absorber loaded with resistance, causing circuit resonance, has obtained better result for broadening bandwidth.

In addition, traditional absorbing materials are often composed of magnetic metal powders, carbon materials and ferrite [11], and use metal plates as backplane in general. Their common feature is non-transparent, which means they cannot be used to in these situations which both need wave absorption and transparency, such as the display screen and window.

In this paper, we present a transparent, ultra-wideband and polarized-independent absorber. As the absorption is based on resistive loss from circuit resonance in structure, the working bandwidth is greatly broadened. The absorber is made of indium tin oxide (ITO) [12], polyvinyl butyral (PVB), and glass, so it has high optical transparency. It can achieve more than 70% absorption in the frequency range from 3.5 GHz to 18.5 GHz, and

Submitted On: December 3, 2018
Accepted On: March 3, 2019

the bandwidth is 136.3% of the central frequency. As shown in Table 1, this absorber exhibits larger bandwidth in contrast to recent papers on transparent and broadband meta-material absorber. Although some absorbers have higher absorptions, their bandwidth is not satisfied. A sample with 10×20 cells is fabricated and tested. The measured results show good agreements with simulation results.

II. DESIGN AND SIMULATION

In the field of meta-material absorber, it is most common, by using electromagnetic resonance, to actualize energy consumption in structure. When waves are incident on the surface, electrical resonance happens within the metal structure of each cell, and magnetic resonance happens between adjacent cells [16]. Energy vibrates intensively between dielectric and metal at resonant frequencies, and finally it is absorbed in dielectric because of dielectric loss. However, as electromagnetic resonance occurs merely at several frequency points, the absorption bandwidth is usually narrow. When resistance elements such as resistive film are introduced in the structure, circuit resonance which is more stable for frequency changes [17], occurs in RLC circuit formed by resistive film, dielectric medium, and metal backplane. Good impedance matching is achieved by proposed structure in wide frequency range, hence, the absorption bandwidth can be broadened significantly.

The schematic of the absorber structure is shown in Fig. 1. The absorber is composed of five layers (glass, resistive film, PVB, glass and resistive film, from top to bottom). The pattern of resistive film that is located in middle layer is given in Fig. 1 (c). We choose resistive film with low surface resistance as backplane to avoid transmitted wave. Both glass and PVB are lossless, and their relative permittivity are 6.2 and 3.1, respectively. The entire thickness of absorber is 5.38 mm, which is only 0.074 λ with regard to the lowest working frequency 3.5 GHz. R_{S1} and R_{s2} represent the resistances of resistive films located in the middle and bottom of structure, respectively. Related parameters are given below: R_{S1}= R_{s2}=20 Ohm/square, h1=3 mm, h2=0.38 mm, h3=2 mm, P=10.5 mm, L=9.5 mm, w=5 mm. Figure 2 shows a finite surface, which is obtained from arranging cells of absorber periodically along x-axis and y-axis. When electromagnetic waves are incident on the surface along –z axis direction, the large amount of wave energy is absorbed in the structure, leaving little reflected and transmitted energy.

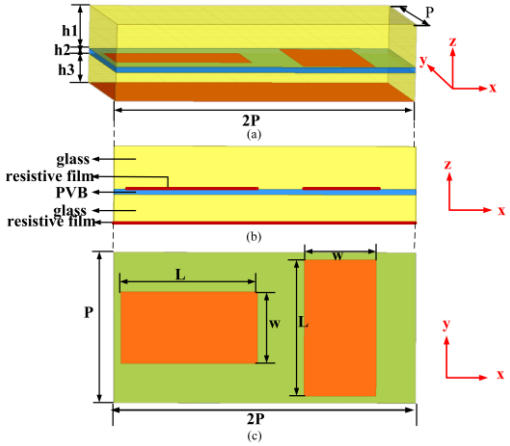

Fig. 1. Schematic of the absorber including: (a) structure of one unit cell, (b) sectional view, and (c) the pattern of resistive film.

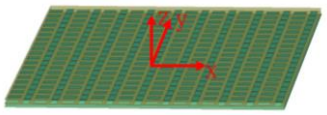

Fig. 2. A finite surface of absorber which is obtained from periodic arrangement of cells.

In order to give an accurate explanation to the mechanism of absorption, equivalent circuit model is presented according to the structure of absorber, shown in Fig. 3. Z_0, Z_1, and Z_2 are the impedances of free space, glass, and PVB material, where $Z_0 = 377\ \Omega$, $Z_1 = Z_0/\sqrt{\varepsilon_r(glass)}$, $Z_2 = Z_0/\sqrt{\varepsilon_r(PVB)}$. The impedance of the lossy FSS can be represented though a serial circuit formed by R_1, L_1 and C_1. $R_1 \approx R_{S1} \cdot D/A$ [18], where $D = 2 \cdot P^2$, $A = 2 \cdot w \cdot L$. $R_2 = R_{S2}$, which represents the impedance of resistive sheet. The lengths of equivalent transmission lines are also given in Fig. 3, corresponding to the thickness of dielectrics. Therefore, Zin is formed by series and parallel RLC resonance circuit and dependent on design parameters of structure. Ideally, when resonance happens, it makes Z_{in} equal to Z_0 and there are no reflected waves. Adjusting parameter of structure to generate multi-resonant frequency helps to form an ultra-wide absorption band.

Table1: Comparisons of proposed and some other absorbers

Ref.	Absorbing Ability	Principle	Transparency
[13]	More than 70% in 12.5 ~ 17G	Based on resistive films	Yes
[14]	More than 90% in 8.5 ~ 11G and 14.5 ~ 16.5G	Based on resistive films	Yes
[15]	More than 90% in 5.8 ~ 12.2G	Based on resistive films	Yes
This paper	More than 70% in 3.5 ~ 18.5G	Based on resistive films	Yes

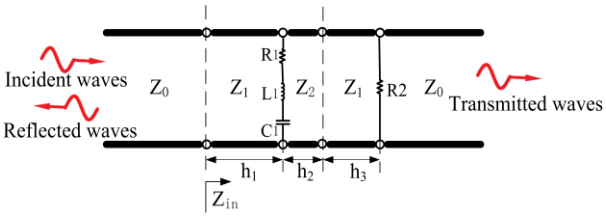

Fig. 3. Equivalent circuit model according to the structure of absorber.

Reflection (S11) and transmission (S21) coefficients from simulation are showed in Fig. 4. From Fig. 4 (a), it can be seen that S11 is lower than -5 dB in the region 3.5~18.5 GHz, which means the absorber can realize the function of stealth during an ultra-wide range of frequency band. From Fig. 4 (b), S21 is less than -15 dB in 1~21 GHz. It means the absorber has the ability of electromagnetic shielding, as the energy of transmission wave is weak enough to be ignored.

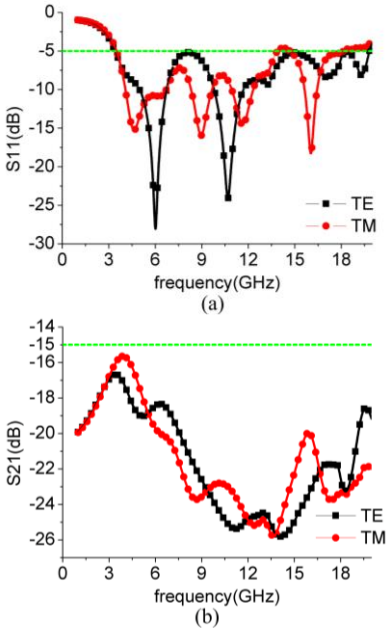

Fig. 4. (a) Reflection coefficients and (b) transmission coefficients from simulation, under the normal incidences of TE (transverse electric) and TM (transverse magnetic) waves.

The property of absorber can be quantitatively analyzed by the absorption rate. The absorption rate is calculated as follows:

$$A(\omega) = 1 - |S_{11}|^2 - |S_{21}|^2. \quad (1)$$

The calculated result of absorption rate is shown in Fig. 5. It can be seen from this figure that the absorption rate is more than 70% in the frequency range from 3.5 GHz to 18.5 GHz. Insensitivity is demonstrated in Fig. 5 simultaneously, since absorptions for TE and TM waves are roughly similar. Through simulation results, it proves that the absorber has ultra-wideband and insensitive absorption in band 3.5~18.5 GHz.

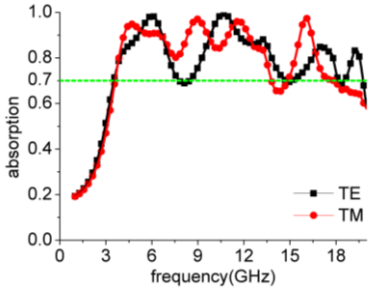

Fig. 5. Absorption rate from calculation, under the normal incidences of TE and TM waves.

In this section, we will analyze the effect of the parameters of R_{S1}, R_{s2} and h1 on the absorption rate. We only vary one parameter in the study while keeping others unchanged.

The influence of R_{S1} is investigated, as shown in Fig. 6 (a). When R_{S1} increases from 20 Ω to 140 Ω, two obvious resonate peaks, accompanying more efficient absorptions, appear at 6 GHz and 16.5 GHz. But the absorption rates in the transition band between these two peaks, are rapidly reduced. Taking into account the overall performance in 3~20 GHz, it is most suitable to set R_{S1} as 20 Ω. It can be observed that the absorption rates around two resonant peaks are not deteriorated excessively and those during the transition band remain at a relatively high level.

Figure 6 (b) shows the variation of absorbing with respect to R_{s2}. As the resistance of bottom resistive film rises, the performances in 3~20 GHz are gradually better whereas those in 1~3 GHz tend to be opposite.

The variation of absorption rate with respect to h1 is depicted in Fig. 6 (c). When h1=0, absorption rates are divided into two absorption peaks around 8.25 GHz and 15GHz, and those in the transition band are low. After adding glass above the absorber and setting thickness of glass as 3 mm, the absorption is improved in general and achieves wide-band absorption efficiency. However, when h1 increases to 6mm, the absorptions in 3.25~12 GHz become deteriorated. Therefore, we choose 3mm as the proper thickness of upper glass. It can be found that, by adding glass with proper thickness above the structure, the impedance of absorber gets adjusted [19], causing better impedance matching with air and wider absorption efficiency. Compared with absorber without upper glass, in particular, this impedance adjusting solves the problem that it is difficult to realize high absorption in low frequency band.

As we mentioned before, perfect impedance matching between absorber and air occurs when relative impedance of absorber is close to 1. In order to validate the impedance matching between absorber and air, the relative impedance of absorber is quantitively calculated according to [20]:

$$z(\omega) = \sqrt{\frac{(1+S_{11})^2 - S_{21}^2}{(1-S_{11})^2 - S_{21}^2}}, \quad (2)$$

where S11 and S21 are from simulation results, under incidence of TE waves. Module value of $z(\omega)$ is then obtained and displayed in Fig. 7. Module value of relative impedance mainly appears around 0.6 in 3.5~18.5 GHz. It is also observed from Fig. 7 and Fig. 5, when the module value of $z(\omega)$ is closer to 1, it helps improve the impedance matching; as a result, the absorber has better absorption efficiency.

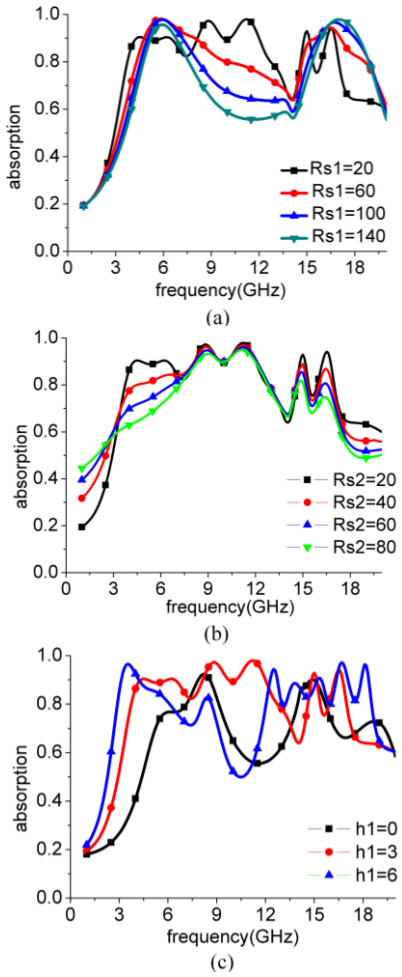

Fig. 6. Absorption rates when changing the values of parameters, and h1, shown in (a), (b), and (c), respectively.

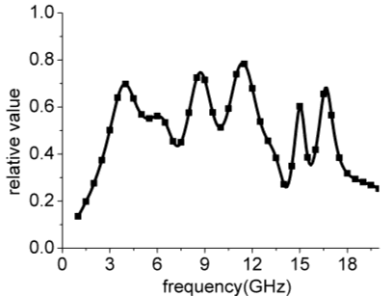

Fig. 7. Module value of relative impedance from calculation.

III. FABRICATION AND MEASUREMENT

To experimentally demonstrate the efficiency of absorber, a sample of absorber obtained by the periodic arrangement of 10×20 cells, whose model structure is shown in Fig. 2, has been fabricated and tested. The ITO films with 20 Ohm/square are deposited on two plates of glass with different thickness by magnetron sputtering method. The pattern shown in Fig. 1 (c) is then etched on the ITO using laser etching technique. The sample is finally obtained by assembling two plates of glass with PVB. Prototype under weak and strong light is shown in Fig.8 (a) and Fig. 8 (b), respectively, which validates the transparency of the absorber.

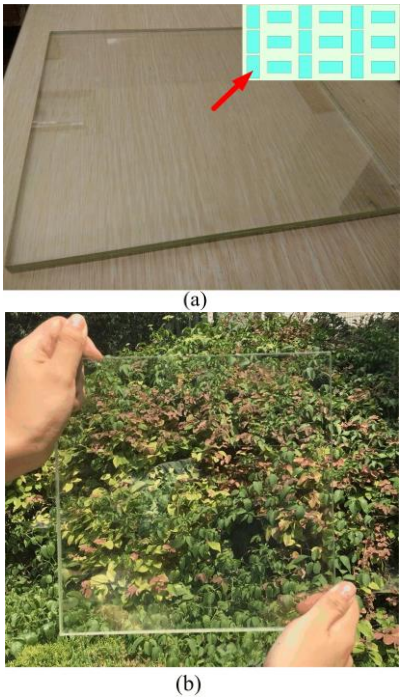

Fig. 8. (a) Photograph of sample under weak light, and (b) photograph of sample under strong light.

Figure 9 (a) shows the installation that measures the reflection coefficient of sample. Measurement is carried out in microwave anechoic chamber. Two horn antennas are placed at the ends of the revolving arms separately. One antenna serves as transmitter and the other is for reception. The sample is placed in the center of the revolving stage. The transmitter and receiver make up 20° towards the sample. The sample keeps enough distance with antennas to satisfy far-field condition. For testing of transmission coefficient, shown in Fig. 9 (b), transmitter is right in front of the sample, while receiver stands in the opposite.

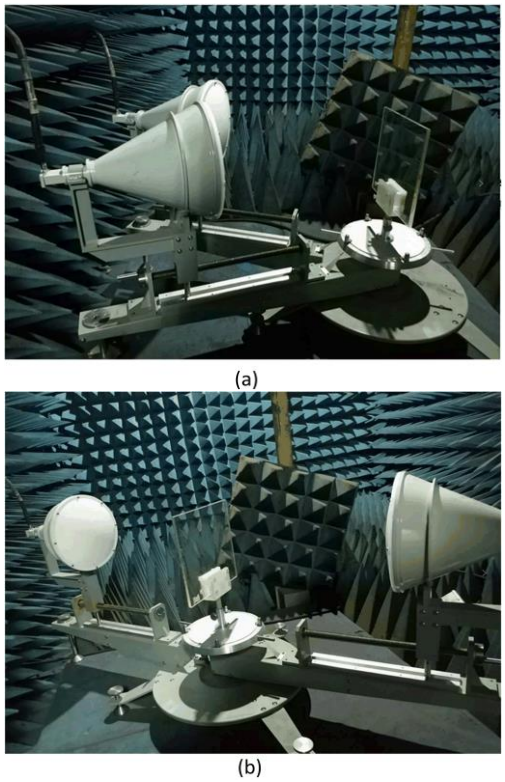

Fig. 9. (a) Photograph of experimental setup for reflection measurement, and (b) photograph of experimental setup for transmission measurement.

Measurement and simulation results are both shown in Fig. 10 to make a comparison. In this simulation, the absorber is 10×20 cells with same size as the sample, to reduce the effect of the size on the measured and simulated results. From Fig. 10, we can see that, under the incidence of plane wave, S11 from measurement achieves less than -5 dB in the range 3.5~18.5 GHz; S21 achieves less than -15dB during the whole working band. The measurement results are in good agreements with the simulation of finite absorber.

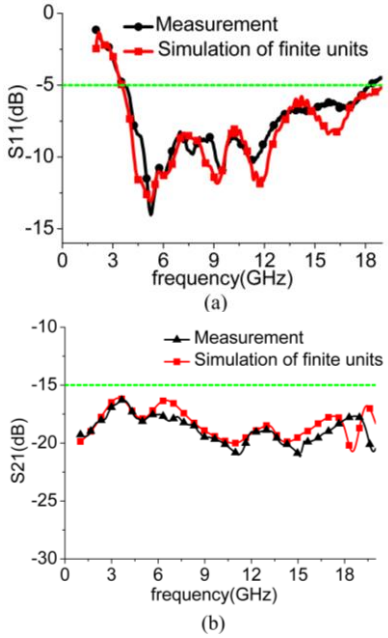

Fig. 10. The comparison between the measured result and simulated result: (a) for S11 and (b) for S21.

IV. CONCLUSION

In this paper, an ultra-wideband and transparent absorber is presented. The absorber is made of ITO, PVB, and glass, so it has the property of high light transmission. Lossy circuit resonance happens in the absorber structure under the incidence of plane wave, which helps broaden the absorption bandwidth. The novelty of structure attributes to the upper glass of absorber which adjusts impedance matching between the absorber and air. The absorber, validated by experiment and simulation, has over 70% absorption rates in the band 3.5~18.5 GHz. Owing to its excellent performance, simple structure, and convenient realization, the absorber has great application potential in the field of transparent stealth and electromagnetic shielding.

ACKNOWLEDGMENT

This work was supported by Technology Program of Shenzhen (Grant No. JCYJ20170816100722642), and also supported by the Natural Science Foundation of Guangdong Province (Grant No. 2018A030313429).

REFERENCES

[1] N. I. Landy, S. Sajuyigbe, J. Mock, D. R. Smith, and W. J. Padilla, "Perfect metamaterial absorber," *Physical Rev. Lett.*, vol. 100, no. 20, p. 207402, 2008.

[2] L. Yuan, X. Shen, S. Cui, and L. Fan, "Progress

and prospect of transparent and electromagnetic shielding material," *NA Mater. Science and Eng*., vol. 30, no. 2, pp. 82-84, 2007.

[3] Y. Peng, V. B. Lucas, H. Yongjun, and W. Jiang, "Broadband metamaterial absorbers," *Adv. Opt. Mater*., p. 1800995, 2018.

[4] M. B. Ghandehari, N. Feiz, and H. Bolandpour, "Design a multiband perfect metamaterial absorber based on hexagonal shapes," *ACES Conference*, 2015.

[5] Y. Ozturk and A. E. Yilmaz, "Multiband and perfect absorber with circular fishnet metamaterial and its variations," *ACES Journal*, vol. 31, no. 12, 2016.

[6] D. Wen, H. Yang, Q. Ye, and M. Lin, "Broadband metamaterial absorber based on a multi-layer structure," *Phys. Scr*., vol. 88, p. 015402, 2016.

[7] J. Chen, J. Li, and Q. Liu, "Designing graphene-based absorber by using HIE-FDTD method," *IEEE T. Antenna Propag*., vol. 65, no. 4, pp. 1896-1902, 2017.

[8] J. Chen, J. Li, and Q. Liu, "Analyzing graphene-based absorber by using WCS-FDTD method," *IEEE T. Micorw. Theory*, vol. 65, no. 10, pp. 3689-3696, 2017.

[9] N. Xu, J. Chen, J. Wang, X. Qin, and J. Shi, "Dispersion HIE-FDTD method for simulating graphene-based absorber," *IET Microw. Antenna P*., vol. 11, no. 1, pp. 92-97, 2017.

[10] N. Xu, J. Chen, J. Wang, and X. Qin, "A dispersive WCS-FDTD method for simulating graphene-based absorber," *J. Electromag. Wave*, vol. 31, no. 18, pp. 2005-2015, 2017.

[11] V. M. Petrov and V. V. Gagulin, "Microwave absorbing materials," *Inorg. Mater*., vol. 37, no. 2, pp. 93-98, 2001.

[12] Y. Qiu, Y. Chen, C. Zu, and Y. Jin, "Research progress of ITO thin films," *Advanced Ceramics*, vol. 37, pp. 304-324, 2016.

[13] Y. Da, X. Wei, and Y. Xu, "Experimental demonstration of transparent microwave absorber based on graphene," *Proceedings of 2016 IEEE MTT-S International Wireless Symposium (IWS)*, Shanghai, China, Mar. 2016.

[14] B. Zhou, D. Wang, W. Jia, and Y. Zhao, "Design and properties of optically transparent and dual band microwave absorbing metamaterial," *J. of Microwaves*, vol. 32, pp. 46-50, 2016.

[15] T. Jang, H. Youn, Y. Shin, and L. J. Guo, "Transparent and flexible polarization-independent microwave broadband absorber," *ACS Photonics*, vol. 1, pp. 279-284, 2014.

[16] X. Huang, Q. Fu, and F. Zhang, "Research advances of metasurface," *Aero Weapon*, vol. 1, pp. 28-34, 2016.

[17] Z. Zhou, D. Huang, X. Liu, W. Mou, and F. Kang, "Application developments of metamaterial in wideband microwave absorbing materials," *Material Engineering*, vol. 5, pp. 91-96, 2014.

[18] F. Costa and A. Monorchio, "Analysis and design of ultra-thin electromagnetic absorbers comprising resistively loaded high impedance surfaces," *IEEE T. Antenna Propag*., vol. 58, 2010.

[19] Y. Shen, Z. Pei, and S. Qu, "Design and fabrication of a wideband frequency selective surface absorber loaded with a high dielectric thin layer," *Journal of Functional Material*, vol. 19, no. 46, pp. 19075-19079, 2015.

[20] D. Smith, D. Vier, T. Koschny, and C. M. Soukoulis, "Electromagnetic parameter retrieval from inhomogeneous metamaterials," *Phys. Rev. Lett*., vol. 71, p. 036617, 2005.

Modeling of Via Interconnect through Pad in Printed Circuit Board

Avali Ghosh, Sisir Kumar Das, and Annapurna Das

Guru Nanak Institute of Technology
JIS Group, 157/F, Nilgunj Road, Sodepur, Kolkata-700114, India
avalighosh@gmail.com, dean_gnit@jisgroup.org, director_gnit@jisgroup.org

Abstract ─ In this paper the methods of finding inductance L of a cylindrical via and capacitance C due to via pad in printed circuit board (PCB) are described. Initially a thin cylindrical via of diameter d without pad is connected between a 50 ohm copper trace on the top of a dielectric substrate and a ground plane at the bottom. The line is terminated with matched load. The geometrical structure is simulated using Ansoft HFSS software tools to find the input reflection coefficient S_{11}. The value of inductance of the via is determined in terms of S_{11} using transmission line formulation. The theoretical and experimental results for L as a function of d, h, and d/h are compared with those obtained from empirical formulae developed by the other authors. The results are found in good agreement. Secondly a square via pad is added in the trace in absence of via. The equivalent capacitance C of the pad is calculated in the same way from S_{11} as it is done for L. Finally, the PCB model is configured with a cylindrical via connected between the pad in the trace and the ground plane. The complex load impedance values are obtained from the electrical equivalent circuit of the L-C combination. This impedance is also determined from the S_{11} parameter using HFSS.

Index Terms ─ Microstrip, PCB, reflection coefficient, via, via-pad.

I. INTRODUCTION

Vias are commonly used in PCB design to interconnect traces from one layer to another layer. In high frequency region, the traces behaves as transmission lines and the via presents inductance and/or capacitance in place of a short circuit connection between the traces. The resulting discontinuity at via position produces signal reflections and problems in the return current. An equivalent inductance and capacitance of the via are evaluated by many authors [1-12] to solve the issues related to signal integrity (SI).

An empirical formula for via inductance is given by Pucel [1] considering via image in terms of physical dimensions and electrical parameters of the substrate. Goldfarb and Pucel [2] have given an empirical formulae without considering the image for cylindrical via above a ground plane. They showed that their numerical and experimental results agree well with those obtained by Hoefer and Chattopadhayay [3]. Closed-form expressions of the resistance, capacitance, and inductance for interplane 3-D vias is described by Savidis and Friedman [4]. Wu and Fan [5] investigated crosstalk among signal vias considering various geometrical parameters. Some closed form expressions for the computation of the via capacitance is developed by Ndip et al. [6]. Ndip, et al. [7] introduced layer stack up scheme to solve electromagnetic reliability problem due to return current paths through via. A physics based via model is given by Zhang and Fan [8] at low frequency depending upon the via geometry. Hernandez-Sosa and Sanchez [9] described the method for calculating the equivalent self and mutual inductance of signal vias in parallel planes. For the performance assessment and optimization of signal integrity, the closed-form expressions for the via-pad capacitance and via- inductance is presented by Isidoro-Munoz et al. [10]. The coupling of signal from the center trace to the adjacent side traces due to radiated signal from the via is analytically described by Ghosh et al. [11-12].

This paper describes the methods of finding inductance L of a cylindrical via and capacitance C due to via pad in printed circuit board from the concepts of transmission line theory and using HFSS. Initially the model of via considered is a thin cylindrical post of diameter d connected between a 50 ohm copper trace on the top of a thin FR4 - epoxy dielectric substrate and a ground plane at the bottom without considering any presence of pad on the trace. The line is terminated with matched load. The structure is simulated using HFSS to find the input reflection coefficient S_{11}. The value of inductance is determined in terms of S_{11} using transmission line formulation. The theoretical and experimental values of L versus d, h, and d/h matched well with those obtained from empirical formulae developed by the other authors ([2],[4]). Subsequently, the PCB structure is taken where a square via pad is introduced in the trace without presence of via. Since no via is connected, the equivalent circuit of the via pad

Submitted On: August 24, 2018
Accepted On: December 9, 2018

is a capacitance C. This capacitance is calculated in the same way as it is done for L. Finally, the PCB model with a cylindrical via and a square pad is taken and the electrical equivalent impedance Z_L of the combination is determined from these L and C values. This impedance is also computed from the S_{11} parameter obtained using HFSS. The method described here introduces a good concept of finding via discontinuity impedance for academic interest.

II. TRANSMISSION LINE MODEL AND HFSS ANALYSIS

A. Inductance of via without viapad

The PCB structure considered here consists of a 50 ohm trace of length ℓ on the top of the FR4 dielectric substrate having $\varepsilon_r = 4.4$, $\tan\delta = 0.02$ and thickness h=1.6mm above a ground plane. The trace is terminated with matched loads. A cylindrical via is placed at the center of the length of the trace and connected to the ground as shown in Fig. 1. In this model it is assumed that the via diameter d<<effective wavelength λ_e inside the dielectric substrate and h<< λ_e. Since no via pad is considered, the equivalent circuit of the via is an inductance L as shown in Fig. 2. In the frequency range from 0.5GHz to 1.5GHz, the attenuation constant α due to copper and dielectric loss varies from 0.2 to 0.6nep/m and phase constant β varies from 19 to 57.4rad/m. Hence α << β and is neglected in the theory.

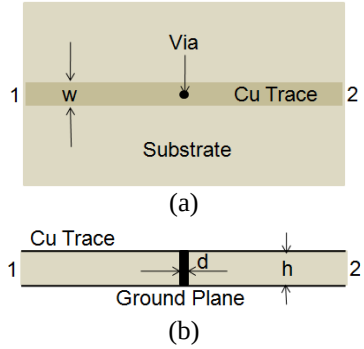

Fig. 1. Top and side view of PCB structure.

The input impedance at via position looking towards the load is given by:

$$Z_{in1} = Z_0 = 50 \text{ ohm.} \tag{1}$$

Therefore, the resultant load across via is:

$$Z_{L1} = \frac{50 \times j\omega L}{j\omega L + 50}, \tag{2}$$

which leads to:

$$L = \frac{50 Z_{L1}}{j\omega(50 - Z_{L1})}. \tag{3}$$

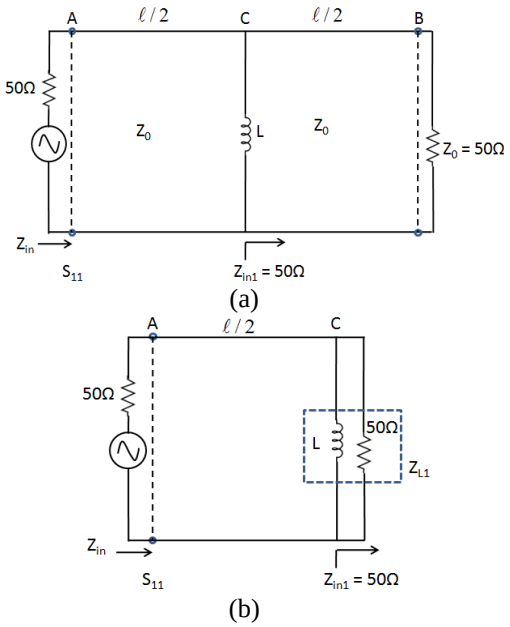

Fig. 2. Equivalent circuit.

Therefore, at the excitation port the input impedance is expressed by:

$$\frac{Z_{in}}{Z_0} = \frac{Z_{L1} + jZ_0 \tan(\beta\ell/2)}{Z_0 + jZ_{L1}\tan(\beta\ell/2)}. \tag{4}$$

Here $\beta = \frac{2\pi}{\lambda_e}$, $\lambda_e = \frac{\lambda_0}{\sqrt{\varepsilon_{eff}}}$, and is given by [13]:

$$\varepsilon_{eff} = \frac{\varepsilon_r + 1}{2} + \frac{\varepsilon_r - 1}{2}\left(1 + \frac{12h}{w}\right)^{-\frac{1}{2}} \text{ ; for } \frac{w}{h} \rangle\rangle 1.$$

From equation 4 the effective load at via can be obtained as:

$$Z_{L1} = \frac{Z_{in} - jZ_0 \tan(\beta\ell/2)}{1 - j\frac{Z_{in}}{Z_0}\tan(\beta\ell/2)}. \tag{5}$$

In terms of input reflection parameter S_{11}:

$$\frac{Z_{in}}{Z_0} = \frac{1 + S_{11}}{1 - S_{11}}. \tag{6}$$

Substituting equation (6) in equation (5), and using equation (3), the via inductance can be calculated. The complex value of S_{11} is determined using simulation with HFSS and for a given value of d/h ratio via inductance L is obtained from equations (3-6).

For the similar via model, [1] has given an empirical formula for inductance considering the image concepts:

$$L = \frac{\mu_0}{4\pi}\left[2h.\ln\left(\frac{2h + \sqrt{(d/2)^2 + (2h)^2}}{d/2}\right) + \left(d/2 - \sqrt{(d/2)^2 + (2h)^2}\right)\right]. \tag{7}$$

The results of the values of L versus d, h, and d/h are described in Section III.

B. Capacitance of via pad without via

The PCB structure considered here consists of same configuration as previously taken where a square via pad is placed at the center of the length of the trace without via as shown in Fig. 3. Since no via is present, the equivalent circuit of the via pad is a capacitance as shown in Fig. 4.

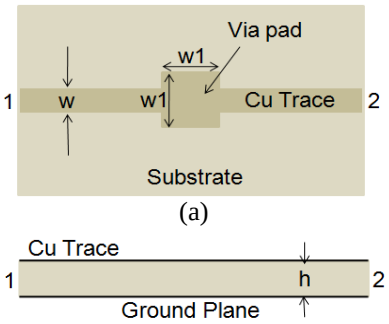

Fig. 3. Top and side view of PCB structure.

Similarly using equation (1), the resultant load across via from equivalent circuit as shown in Fig. 4 is:

$$Z_{L2} = \frac{50 \times \frac{1}{j\omega C}}{50 + \frac{1}{j\omega C}}, \tag{8}$$

which leads to:

$$C = \frac{1}{j\omega Z_{L2} 50}(50 - Z_{L2}). \tag{9}$$

The complex values of S_{11} for a different square via pad sizes (3.2, 4.2, 5.2, 6.2mm) are determined using simulation with HFSS. These values of S_{11} are used to determine Z_{L2} in the same manner as it was done for via inductance through equations (5) and (6). The capacitance C of via pad is then obtained from equation (9). The results of C versus normalized size of via pad with respect to trace width are described in Section III.

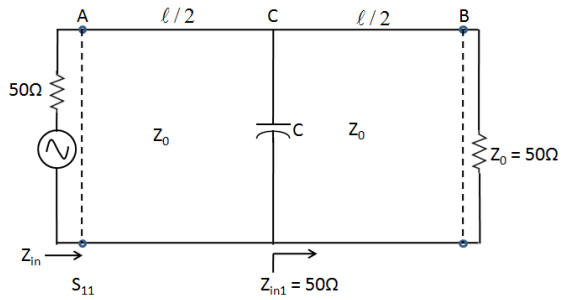

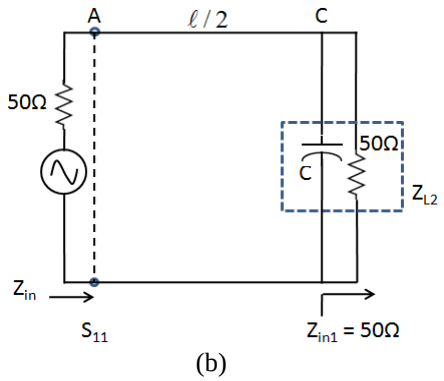

Fig. 4. Equivalent circuit.

C. Via with viapad

The PCB structure considered here consists of a cylindrical via connected to the trace through a viapad at the center of the length of the trace as shown in Fig. 5. Other end of via is connected to the ground.

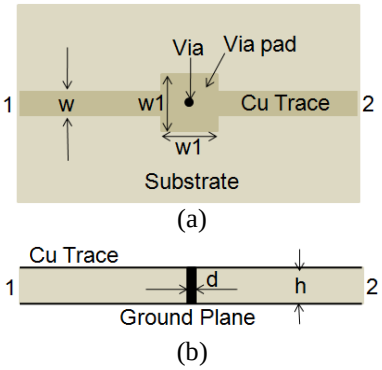

Fig. 5. Top and side view of PCB structure.

The equivalent circuit of this configuration is shown in Fig. 6. The resultant load at the via position is given by:

$$Z_{L3} = \frac{50 \times j\omega L}{50 + j\omega L - 50\omega^2 LC}. \tag{10}$$

The load impedance Z_{L3} is obtained from equation (10), by substituting the values of via inductance L (Eqn. 3) and via pad capacitance C (Eqn. 9).

In order to validate the values of L and C obtained above, the total load impedance (Fig. 6) is also computed using HFSS tool simulating the actual configuration of Fig. 5. This value is designated as Z_{Lhfss}. In the later method the complex value of S_{11} is determined to find the equivalent load impedance Z_{Lhfss} of via with via pad shunted by 50 ohm load in the similar way as it was done for via inductance through equations (5) and (6). Both the results of Z_{L3} and Z_{Lhfss} are agreed well as shown in Fig. 7 (a) and the effective impedance Z_L of the via with pad is determined from the average value

of Z_{L3} and Z_{Lhfss}.

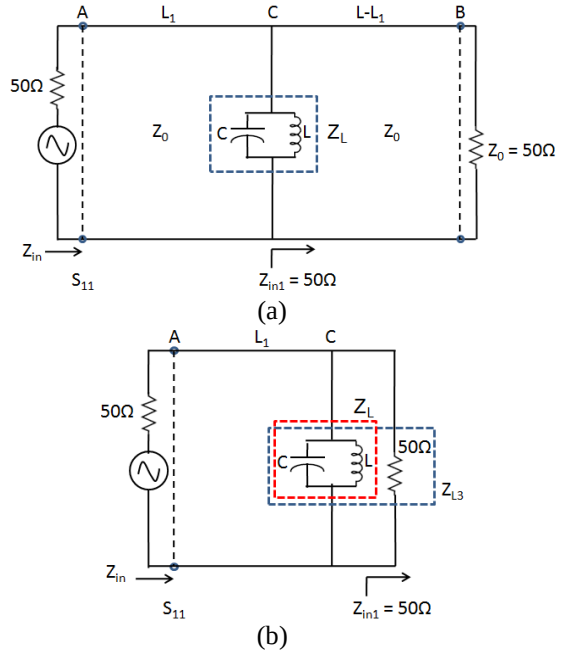

Fig. 6. Equivalent circuit.

III. RESULTS AND DISCUSSION

The geometric layout considered here consists of a 50 ohm trace of length ℓ on the top of the FR4 dielectric substrate is terminated with matched loads. The operating frequency range considered here is 0.5-1.5GHz. In the first model, since no via pad is considered, electrical equivalent parameter of via is an inductance. The inductance of cylindrical via is obtained from the concepts of transmission line theory and using HFSS. The inductance value is calculated from the input reflection coefficient. The results obtained by the present method are compared with those of [1] and experimental results as shown in Fig. 7 (b). It is found that the inductance value obtained by the present authors from equations (3-6) using transmission line theory and HFSS analysis, matched well with the results of [1] as well as of experimentation.

Analysis is further extended to find via inductance L versus d for given values of h and also L versus h for given values of d. The results are shown in Figs. 8 and 9. It is seen that the results of analytical method using transmission line theory and HFSS analysis of the present authors agree well with those of [1]. Because of limitations in fabrication facility and non-availability of substrates of different thicknesses, experimental results for very thin via and multiple thickness of substrate are not shown in Figs. 7, 8 and 9.

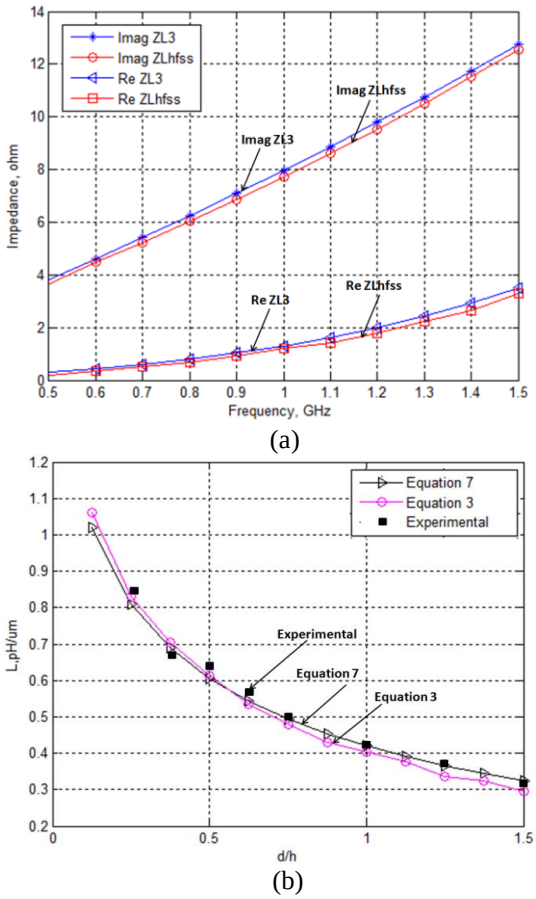

Fig. 7. (a) Input impedance versus frequency for loading with via along with pad. (b) Via inductance per unit length versus *d*/*h*.

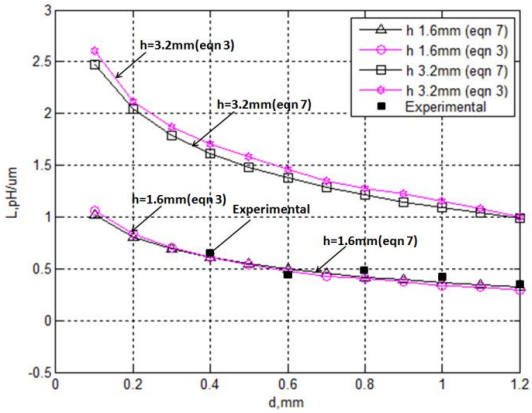

Fig. 8. Via inductance per unit length versus d for equations (9), (8), (7), and (9) with h as parameter.

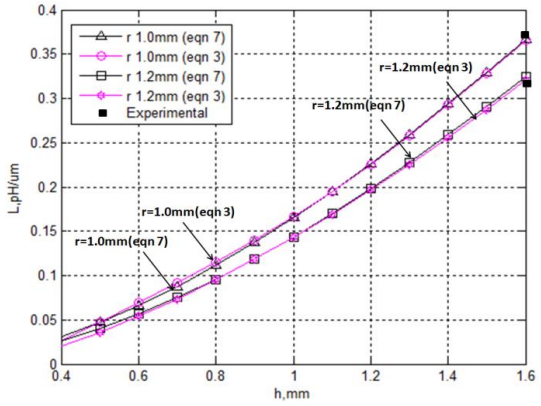

Fig. 9. Via inductance per unit length versus h for equations (9), (8), (7), and (9) with d as parameter.

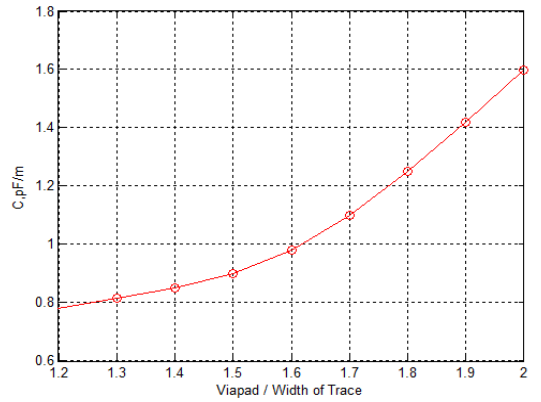

Fig. 10. Via pad capacitance per unit length versus via pad/width of trace.

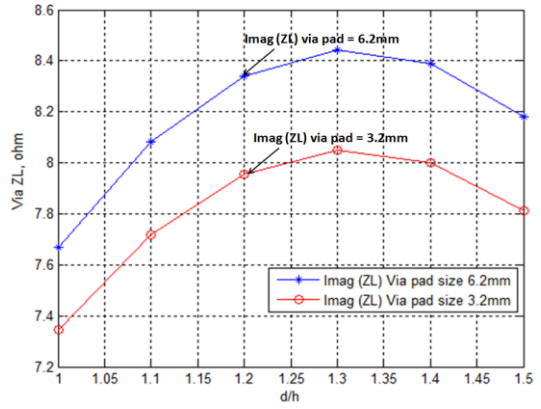

Fig. 11. Via $Z_L = R_L + jX_L$ versus *d*/*h* with via pad size as parameter.

In the second structure, electrical equivalent parameter of pad used for interfacing two layers through via is determined. The pad on a trace represents a capacitance. In this analysis this capacitance is obtained from the concepts of transmission line theory and using HFSS. The capacitance value is calculated from the input reflection coefficient. Capacitance of different sizes of the pad is determined as shown in Fig. 10. It is observed that the value of capacitance increases with increase in the size of via pad.

The Figs. 11-14 show the variation of complex impedance Z_{L3} represented by via along with pad versus d/h, pad size, and frequency.

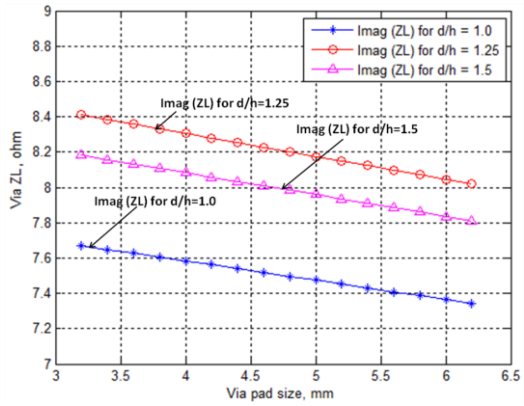

Fig. 12. Via $Z_L = R_L + jX_L$ versus via pad size with *d*/*h* as parameter.

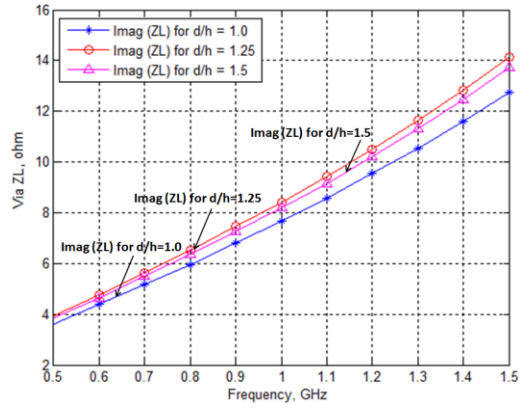

Fig. 13. Via $Z_L = R_L + jX_L$ versus frequency with *d*/*h* as parameter.

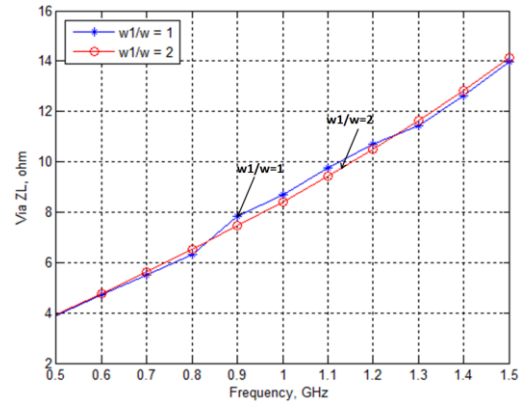

Fig. 14. Via Z_L versus frequency with normalized pad size *w*1/*w* as parameter.

IV. CONCLUSION

In this paper, the methods of finding via inductance L and capacitance C of via pad in the PCB are described using transmission line theory and HFSS analysis. The theoretical and experimental results are compared with those obtained from empirical formulae developed by the other authors and found good agreement. Different PCB configurations: (a) only via without pad, (b) only via pad in absence of via, and (c) via with pad, are simulated using HFSS to find the input reflection coefficient S_{11}. The values of inductance and capacitance are determined from the complex S_{11} parameter using transmission line formulation. These values L and C are used to determine the complex load impedance Z_{L3} at via location. The model with via and its pad is simulated with HFSS. S_{11} value of this combination is determined to find the complex load impedance Z_{Lhfss} at via location. Both the results Z_{L3} and Z_{Lhfss} are compared and found good agreement.

ACKNOWLEDGMENT

Authors acknowledge University Grant Commission (UGC-MRP), India for partial funding for this research work.

REFERENCES

[1] W. Hoefer and A. Chattopadhyay, "Evaluation of equivalent circuit parameters of microstrip discontinuities through perturbation of a resonant ring," *IEEE Trans. MTT*., vol. MTT-23, no. 12, pp 1067-1071, Dec. 1975.

[2] I. Savidis and E. G. Friedman, "Closed-form expressions of 3-D via esistance, inductance, and capacitance," *IEEE Transactions on Electron Devices*, vol. 56, no. 9, Sep. 2009.

[3] S. Wu and J. Fan, "Investigation of crosstalk among vias," *IEEE International Symposium on Electromagnetic Compatibility*, 2009.

[4] I. Ndip, F. Ohnimus, K. Lobbicke, C. Tschoban, M. Bierwirth, and S. Guttowski, "Equivalent circuit modeling of signal vias considering their return current paths," *2010 Asia Pacific International Symposium on Electromagnetic Compatibility*, Beijing, China, Apr. 12-16, 2010.

[5] I. Ndip, F. Ohnimus, S. Guttowski, and H. Reichl, "Modeling and analysis of return-current paths for microstrip-to-microstrip via transitions," *IEEE Electronic System-Integration Technology Conference(ESTC 2008)*, London, UK, Sep. 1-4, 2008.

[6] Y. Zhang and J. Fan, "Recent development of via models: Hybrid circuit and field analysis," *IEEE Electr. Design Adv. Package. Syst. Symp*., Dec 2010.

[7] G. Hernandez-Sosa and A. Sanchez, "Analytical calculation of the equivalent inductance for signal vias in parallel planes with arbitrary P/G via distribution," *8th International Caribbean Conference on Devices, Circuts and Systems (ICCDCS)*, 2012.

[8] A. Isidoro-Munoz, R. Torres-Torres, M. A. Tlaxcalteco-Matus, and G. Hernandez-Sosa, "Scalable models to represent the via-pad capacitance and via-traces inductance in multilayer PCB high speed interconnects," *International Conference on Devices, Circuits and Systems (ICCDCS)*, 2017.

[9] A. Ghosh, S. K. Das, and A. Das, "Analysis of radiation coupling from via in multilayer printed circuit board traces," *14th International Conference on Electromagnetic Interference & Compatibility (INCEMIC 2016)*, Bengaluru, India, Dec. 8-9, 2016.

[10] A. Ghosh, S. K. Das, and A. Das, "Analysis of crosstalk in high frequency printed circuit boards in presence of via," *International Conference on Electromagnetics in Advanced Applications IEEE-APS Topical Conference on Antennas and Propagation in Wireless Communications 2017*, Verona, Italy, Sep. 11-15, 2017.

[11] E. O. Hammerstad, "Equations for microstrip circuit design," *5th European Microwave Conference*, 268, 1975.

[12] Ansoft High Frequency Structure Simulation (HFSS), ver. 10, Ansoft Corporation, Pittsburgh, PA, 2005.

Small Size and Wide-Band Band Pass Filter with DGS/CRLH Structures

Ahmed A. Ibrahim[1*], Mahmoud A. Abdalla[2], and Wael A. E. Ali[3]

[1]Faculty of Engineering, Minia University, Minia, Egypt
*University Pierre and Marie Curie, Sorbonne University, Paris VI, France
ahmedabdel_monem@mu.edu.eg

[2]Electronic Engineering Department, Military Technical College (MTC), Cairo, Egypt
maaabdalla@ieee.org

[3]Department of Electronics and Communications Engineering, Arab Academy for Science, Technology & Maritime Transport (AASTMT), Alexandria, Egypt
wael.ali@aast.edu

Abstract ─ A small size and wide-band band pass filter with high performance for WiMAX applications is introduced. The filter is designed by utilizing one composite right left handed transmission line (CRLH-TL) metamaterial cell and two gap lumped capacitors. The filter has a center frequency of 5.3 GHz and a 3dB bandwidth from 4.2 GHz to 6.4 GHz. A lower than 0.5 dB insertion loss within pass-band is achieved. A single transmission zero at 6.52 GHz is achieved to increase the selectivity of the proposed filter. The rejection band is extended to be up to 10 GHz. A comparison between circuit simulation, EM simulation and measured results is introduced with good consistency between them. The filter has a small size (26.8×16.5 mm^2) which is smaller than recently reported wide band filters.

Index Terms ─ Band pass filter, CPW, CRLH-TL, DGS, gap capacitors.

I. INTRODUCTION

Band pass filters (BPFs) play a vital role in wireless communication systems. Special requirements must be achieved in microwave band pass filters such as compact size, low insertion loss, low cost, high selectivity and high attenuation in the rejection band [1]. In order to meet the high demand of increasing data rate in wide band communication systems, wide band microwave band pass filters are used. Many wideband BPFs with high performance, high selectivity and high attenuation in stop band have been reported such as using cross-coupled transmission line sections [2], ring resonators with open stubs [3], multimode resonators (MMRs) [4, 5], and cross-coupled MMRs [6]. The challenge in these design methods is always the design complexity and the filter performance.

Composite right/left handed transmission line (CRLH-TL) metamaterial has been utilized in microwave passive components. CRLH-TL metamaterial has anti-parallel phase and group velocities [7, 8]. Consequently, CRLH-TL has non-linear positive/negative zero phase shift. Because of these good characteristics, passive components such as power splitter [9] resonators [10, 11], filters [12-18], and couplers [19, 20] are designed. Also, great effort has been focused in its applications in the active circuits such as oscillator, switches and amplifier [21–23].

Defected ground structure (DGS) are achieved by etching a slot in metallic ground plane; this slot disturbs the current distribution in the ground plane. This disturbance affects the microstrip line features, such as the inductance and capacitance [24]. Such properties have been used to design compact microwave filters [25–28], wide band filter [29-31] and also high selective filters [32]. However, up to the authors' knowledge, few attempts have been suggested to make use of CRLH metamaterial and DGS together in filter design [33].

In this paper, a compact size and wideband BPF is introduced. The filter is based on CRLH-TL metamaterial with two coupled lumped capacitors. The filter has a center frequency of 5.3 GHz and bandwidth of 2.2 GHz which is suitable for wide band wireless applications. Furthermore, the filter has single transmission zero at 6.5 GHz to improve the filter selectivity. Also, the filter has good filtering capabilities with good pass-band selectivity and stop-band attenuation. The filter is designed, fabricated, and measured to verify the simulated results.

Submitted On: August 22, 2018
Accepted On: December 25, 2018

II. THEORY OF THE PROPOSED FILTER

A. Operating principle of CRLH capacitive-gap coupled resonator BPF

A conventional coupled gap resonator is realized using *N* series transmission line sections (approximately *λ/2*) with *N+1* capacitive gap between them, which can be realized as series capacitors. As shown in Fig. 1 (a), conventional capacitive coupled gap resonator band pass filter can be realized using one section of conventional transmission line coupled to filter output through two gap capacitors (C_1 and C_2). The electric length (θ_1) is a half wavelength.

The equivalent circuit of the CRLH capacitive-gap coupled resonator is shown in Fig. 1(b). It can be observed that the section of electrical length θ_1 is designed as a CRLH cell in T-configuration. Basically, the elements C_L and L_L are loading elements whereas C_R and L_R are usually parasitic elements. The main advantage of using this configuration is the utilization of the nonlinear behaviour of the progressive phase along the CRLH transmission line. As explained in [7], the design for one section filter can be expressed as:

$$\beta l = \pi. \tag{1}$$

The loading elements (series capacitance and shunt inductance) and parasitic elements are used to determine the negative left-handed and positive right-handed propagation constants, which can be expressed as [7]:

$$\beta_l = \left(\frac{-1}{\omega\sqrt{C_L L_L}}\right), \tag{2}$$

$$\beta_r = \left(\omega\sqrt{C_R L_R}\right). \tag{3}$$

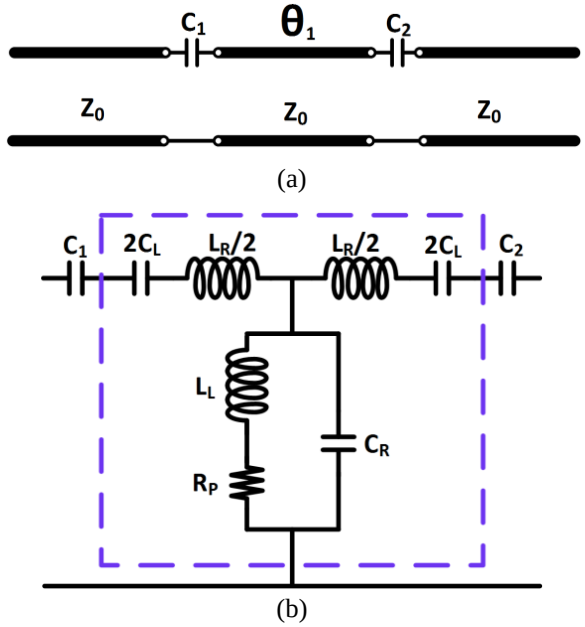

Fig. 1. (a) The schematic block diagram of the coupled resonator band pass filter, and (b) the CRLH version of the coupled gap resonator band pass filter.

B. Defected ground band stop filter for transmission zeros

The transmission zeros design was based on having a series defected ground structure that acts as a band stop filter. The equivalent circuit of the defected ground structure is the parallel *L-C* tank circuit. The values for pole lumped elements (L_P and C_P) are obtained in terms of the 3 dB cut off frequency (f_c) in GHz and pole frequency (f_p) in GHz as follows [24]:

$$C_P = \frac{5f_c}{\pi(f_P^2 - f_c^2)}\ pF, \tag{4}$$

$$L_P = \frac{250}{C_P(\pi f_P)^2}\ nH. \tag{5}$$

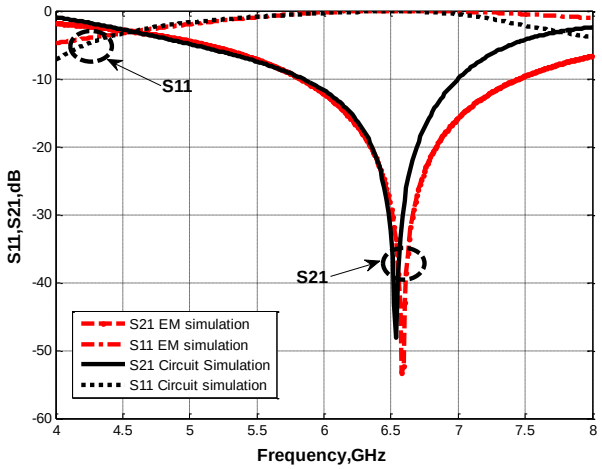

Fig. 2. The simulated S-parameters of DGS resonator filter (circuit model).

The DGS filter was designed to introduce a stop band centered at f_p= 6.5 GHz and a 3 dB cutoff frequency at f_c= 4.5 GHz. For testing purposes, a rectangular DGS resonator was etched in the ground plane and excited by a 50Ω coplanar waveguide transmission line. Consequently, the L_P and C_P extracted values are 1.851 nH, and 0.321 pF, respectively.

For verification purposes, the structure and circuit model were simulated using full wave simulations and circuit simulations, respectively. The simulated S-parameters are shown in Fig. 2. The two results in Fig. 2 demonstrate that there is a band stop filtering phenomenon. It can be noticed that the filter cut off frequency f_c = 4.5 GHz at which S_{21} magnitude is close to –3 dB. Also, the frequency f_P is 6.52 GHz at which the S_{21} magnitude is close to –50 dB.

III. CPW CRLH METAMATERIAL BAND PASS FILTER STRUCTURE

The geometry of the CPW CRLH band pass filter is shown in Fig. 3 (a) and Fig. 3 (b) with the detailed filter dimensions. The CPW CRLH filter is realized using one CRLH cell with T-configuration coupled to the two gap

capacitors. As it can be depicted from Fig. 3 (a) that the CRLH metamaterial unit cell is consisting of a series interdigital capacitor and shunt stub as an inductor. The filter is fed by 50 Ω transmission line and printed on RO4003 substrate (ε_r = 3.38, thickness = 0.813 mm and dielectric loss tangent = 0.0027). The equivalent circuit of the band pass filter is shown in Fig. 3(c). The circuit consists of CRLH unit cell coupled to output terminals by the two coupled capacitors. Due to this coupling, the roll off attenuation in the filter is increased. Based on the design equations (6) and (7), the values of the equivalent capacitance and inductance of the CRLH cell are specified.

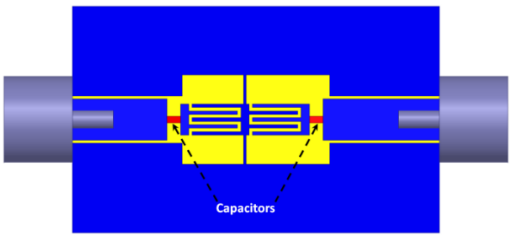

(a)

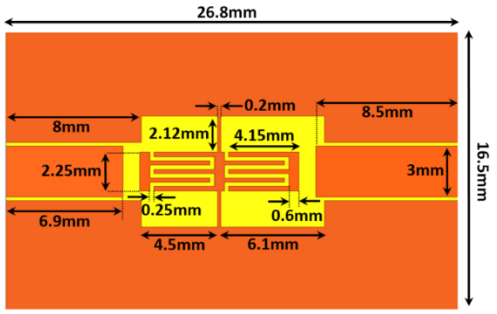

(b)

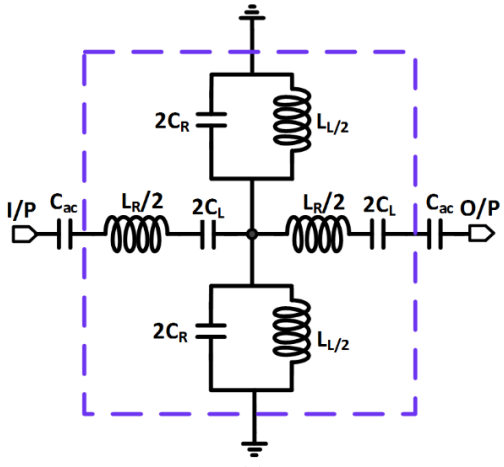

(c)

Fig. 3. The CPW composite right left handed band pass metamaterial filter: (a) 2-D layout, (b) filter dimensions and (c) the equivalent circuit model, C_{ac}=0.6 pF, C_L=0.6 pF, L_R=1 nH, C_R=0.5 pF, L_L=2.56 nH.

The interdigital capacitor and stub inductor dimensions were synthesized as [1]:

$$C_L = 3.937 \times 10^{-5} l_f (\varepsilon_r + 1)(0.11(n-3) + 0.252)\, pF, \quad (6)$$

where l_f is interdigital capacitor length in micrometer:

$$L_L = Z_o \tan(\beta l_s)/\omega, \quad (7)$$

where l_s is the stub length, Z_o and β are the characteristic impedance and the propagation constant, corresponding to the stub width, respectively.

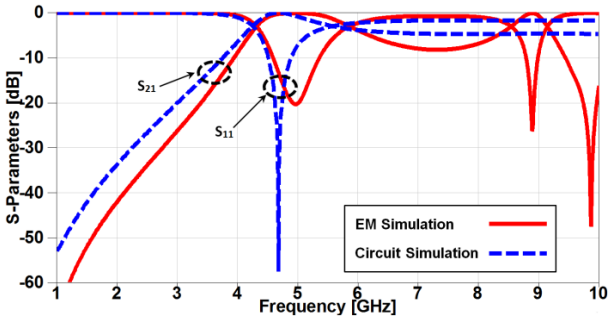

Fig. 4. The simulated scattering parameters magnitudes of the CPW CRLH filter.

The scattering parameters comparison between the circuit simulation and EM simulation of the CPW CRLH band pass filter is shown in Fig. 4. It can be noticed from the simulated EM results in Fig. 4 that the filter center frequency is 4.75 GHz and the 3 dB bandwidth is from 4.3 GHz to 5.5 GHz. The filter has good rejection band at lower frequency with more than –50 dB. However, it has lower rejection band at high frequency which reduces the filter selectivity at higher frequency band. Also, there is reasonable agreement between the achieved EM and circuit simulations.

IV. CPW CRLH METAMATERIAL FILTER WITH DGS

In order to enhance the filter performance and suppress the undesired peaks at the higher band of the CRLH metamaterial filter as shown in EM simulation of Fig. 4, two DGS-cells have been added to the filter structure. The idea is to utilize the DGS-resonators which have resonance frequency near the unwanted frequency band to achieve high rejection at high frequency band. The new filter is similar to the filter studied in the previous section with the difference of adding new structure consists of two DGS-units as illustrated in Fig. 5 (a). The two DGS resonators which are etched in the ground (top layer) have dimensions of 16 × 1 mm^2 as shown in Fig. 5 (b). The filter is printed on a Rogers RO4003 substrate with ε_r of 3.38 and a thickness h of 0.813 mm.

The simulated S-parameters of the BPF using EM and circuit simulations are illustrated in Fig. 6. It can be seen from the figure that the filter is operated at a center

frequency of 5.3 GHz with 3 dB bandwidth from 4.2 GHz to 6.4 GHz. The filter has insertion loss of lower than 0.5 dB and return loss higher than 12 dB over the achieved pass-band. Moreover, a transmission zero is achieved at frequency of 6.52 GHz to increase the filter selectivity. Also, a wide suppression level of approximately –10 dB is achieved in the higher frequency band from 7 GHz to 10 GHz.

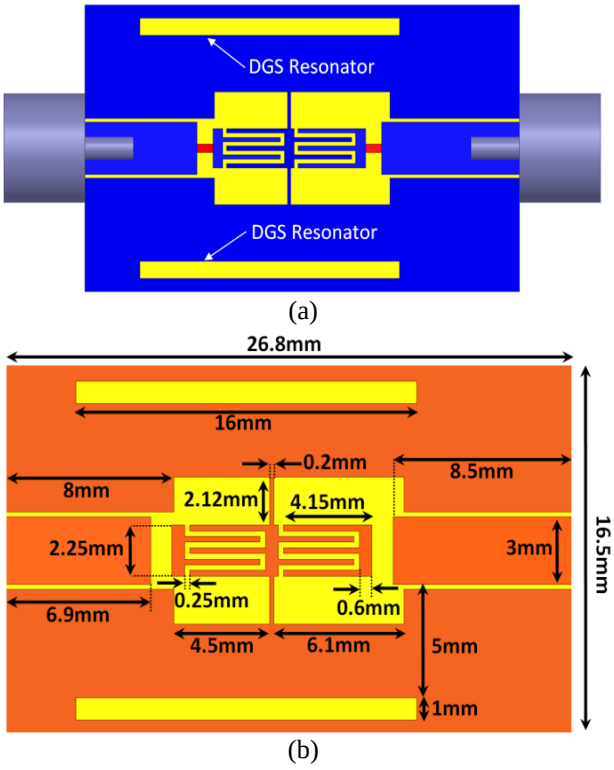

Fig. 5. The CPW CRLH filter with DGS: (a) 2-D layout and (b) filter dimensions.

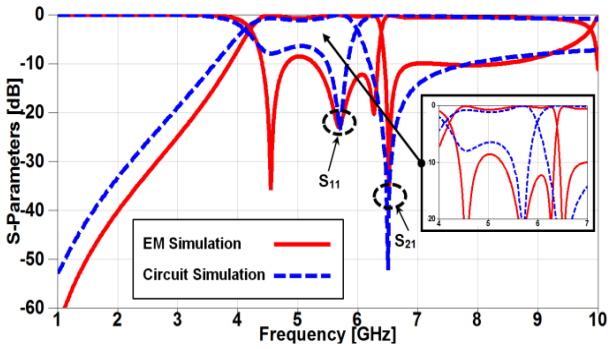

Fig. 6. The simulated scattering parameter of the CPW CRLH filter.

It is worth to comment from Fig. 4 and Fig. 6 that the DGS band stop has produced a transmission zero which eventually enhances the selectivity of the filter.

To study the effect of the values of the two lumped capacitors on the performance of the proposed filter, a parametric study is carried out. The simulated S-parameters of the proposed filter with different values of lumped capacitors are shown in Fig. 7. It is clear that the capacitance affects the matching of the proposed filter and the optimized value is chosen to be 0.6 pF.

V. EXPERIMENTAL RESULTS

Figure 8 shows the photograph of the fabricated CRLH band pass filter with DGS unit using a pair of 0.6 PF surface mounted capacitors. To confirm the simulation results from CST software, the proposed model of CPW CRLH filter is fabricated, tested and measured using ZVB-20 vector network analyzer (VNA).

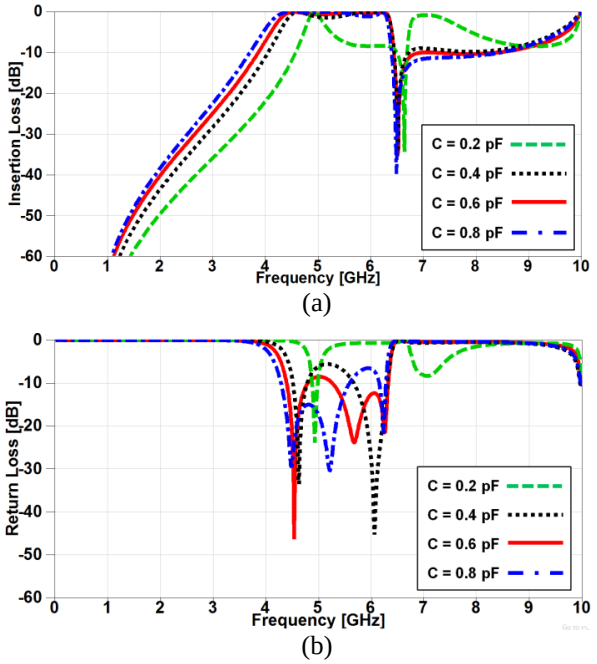

Fig. 7. The simulated scattering parameter of the proposed CPW CRLH filter: (a) insertion loss and (b) return loss.

The filter is printed on RO4003 substrate with thickness of 0.813 mm and dielectric constant of 3.38. Figure 9 shows a comparison between simulated and measured results of the proposed BPF. The measured results have insertion and return losses better than 0.5 dB and 12 dB, respectively. The stop band rejection is lower than –10 dB from 7 GHz up to 10 GHz. The filter has bandwidth from 4.5 GHz to 6.25 GHz with transmission zero at 6.3 GHz. It can be noticed from Fig. 9 that the simulated and measured results are in a good consistency. However, a frequency shift occurred due to the unpredictable fabrication tolerance and the soldering process of the SMA connectors and surface mounted capacitors. Table 1 summarizes the comparison of the proposed filter with other reported filters [2-6]. It is

obvious from table that the proposed filter has the minimum insertion loss ($|S_{21}|$) of 0.5 dB.

Furthermore, the proposed filter size has the smallest size of 16 × 6.49 mm^2. From bandwidth point of view, the proposed filter bandwidth is competitive. However, it is worth to comment that the proposed filter has the minimum number of zeros.

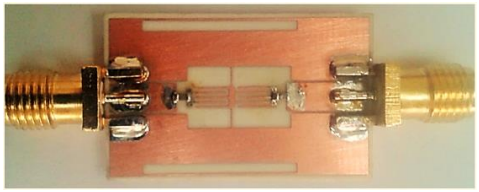

Fig. 8. The fabricated prototype photo of the CPW CRLH filter.

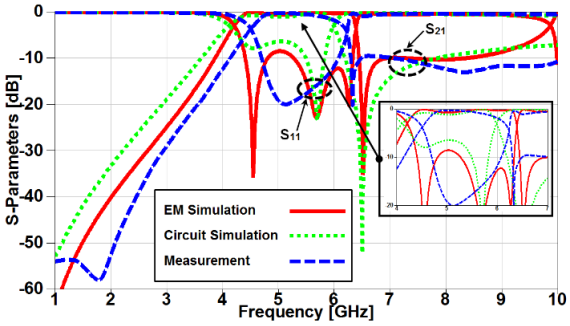

Fig. 9. The simulated and measured scattering parameter magnitudes of the CPW CRLH DGS filter.

Table 1: Comparison between the proposed filter with other reported wide band filters

Ref.	Freq. (GHz)	$\|S_{21}\|$ / $\|S_{11}\|$(dB)	ε_r / Thick (mm)	FBW (%)	T. Zeros	Size (mm^2)
[2]	3	1/12	3.2/0.762	48	3	65 × 37
[3]	6.92	0.81/12	3.38/0.762	78	6	18.1 × 10
[4]	3.2	2.2/12	2.65/1	20.6	6	56.3× 24.6
[5]	3	0.6/17	9.8/1.27	43.3	4	11 × 12
[6]	5.6	1.3/12	2.65/1	67.8	2	15.5 × 7.3
Prop. filter	5.3	0.5/12	3.38/0.813	41.5	2	16 × 6.49

VI. CONCLUSION

Compact size and high selective band pass filter for wireless applications has been presented. The CRLH-TL metamaterial is considered the main block of the filter with two gap capacitors. The proposed filter is suitable for wireless application(WiMAX). The filter has been operated at 5.3 GHz, bandwidth from 4.2 GHz to 6.4 GHz with insertion loss lower than 0.5 dB in the pass-band, return loss lower than –12 dB and with single transmission zero at 6.52 GHz in the stop band. The DGS has been used to enhance the rejection level. The simulation results agree with the measured results which confirm the suitability of the proposed BPF for modern wireless communications.

ACKNOWLEDGMENT

This work was supported by the French and Egyptian governments through a co-financed fellowship granted by the French embassy in Egypt (Institute français d'Egypte), and the scientific and technology development fund (STDF).

REFERENCES

[1] J. S. Hong, *Microstrip Filters for RF/Microwave Applications*. 2nd ed., Wiley Press, 2011.

[2] H. Shaman and J. S. Hong, "Input and output cross-coupled wideband bandpass filter," *IEEE Trans. Microw. Theory Techn.*, vol. 55, no. 12, pp. 2562-2568, Dec. 2007. DOI:10.1109/TMTT.2007.910066.

[3] J. G. Zhou, Y. C. Chiang, and W. Q. Che, "Wideband bandpass filter based on ring resonator with high selectivity and multiple transmission zeros," *Electron. Lett.*, vol. 50, no. 5, pp. 384-386, Feb. 2014. DOI: 10.1049/el.2013.2908.

[4] W. Feng, X. Gao, W. Che, and Q. Xue, "Bandpass filter loaded with open stubs using dual-mode ring resonator," *IEEE Microw. Wireless Comp. Lett.*, vol. 25, no. 5, pp. 295-297, May 2015. DOI:10.1109/ LMWC.2015.2410174-.

[5] J.-M. Huang, B. Zhang, and S. S. Li, "Novel compact quad-mode wideband bandpass filter with wide stopband using T-shaped resonator," *J. Electromagn. Waves Appl.*, vol. 28, no. 3, pp. 326-333, Feb. 2014. DOI.org/10.1080/09205071.2013. 870053.

[6] S. W. Ren, H. L. Peng, J. F. Mao, and A. M. Gao, "Compact quasielliptic wideband bandpass filter using cross-coupled multiple-mode resonator," *IEEE Microw. Wireless Compon. Lett.*, vol. 22, no. 8, pp. 397-399, Aug. 2012. DOI:10.1109/LMWC. 2012.2205230.

[7] C. Caloz and T. Itoh, *Electromagnetic Metamaterials Transmission Line Theory and Microwave Applications*. J. Wiley & Sons Press, 2006.

[8] G. V. Eleftheriades and K. G. Balmain, *Negative Refractive Metamaterials*. J. Wiley & Sons Press, 2005).

[9] P. Vélez, M. Durán-Sindreu, A. Fernández-Prieto, J. Bonache, F. Medina, and F. Martı, "Compact dual-band differential power splitter with common-mode suppression and filtering capability based on differential-mode composite right/left-handed transmission-line metamaterials," *IEEE Antennas and Wireless Propagation Letters*, vol. 13, pp. 536-539, 2014. DOI:10.1109/LAWP.2014.2311654.

[10] T. Yang, P.-L. Chi, and T. Itoh, "Compact quarter-wave resonator and its applications to miniaturized

diplexer and triplexer," *IEEE Transactions on Microwave Theory and Techniques*, vol. 59, no 2, pp. 260-269, 2011. DOI:10.1109/TMTT.2010.2095029.

[11] M. A. Abdalla and Z. Hu, "Compact metamaterial coplanar waveguide ferrite tunable resonator," *IET Microw, Antennas & Propagation*, vol. 10, no. 4, pp. 406-412, 2016. DOI:10.1049/iet-map.2015.0515.

[12] A. Ibrahim, A. Abdel-Rahman, and M. Abdalla, "Design of third order band pass filter using coupled meta-material resonators," *IEEE AP-S International Antenna and Propagation Symposium Digest*, Memphis, USA, pp. 1702-1703, July 6-11, 2014. DOI:10.1109/APS.2014.6905177.

[13] G. Shen, W. Che, W. Feng, and Q. Xue, "Analytical design of compact dual-band filters using dual composite right-/left-handed resonators," *IEEE Transactions on Microwave Theory and Techniques*, vol. 65, no. 3, pp. 804-814, 2017. DOI:10.1109/TMTT.2016.2631168.

[14] M. A. Fouad and M. A. Abdalla, "Ultra compact CPW dual band filter based on Π-generalized metamaterial NRI transmission line," *Journal of Electromagnetic Waves and Applications*, vol. 29, no. 8, pp. 1093-1103, May 2015. DOI:10.1080/09205071.2015.1044123.

[15] A. A. Ibrahim, M. A. Abdalla, and D. Budimir, "Coupled CRLH transmission lines for compact and high selective bandpass filters," *Microwave Optical Technology Letter*, vol. 59, no. 6, pp. 1248-1251, June 2017. https://doi.org/10.1002/mop.30518.

[16] A. K. Pandey, Y. Gaurav, and R. K. Chauhan, "Miniaturized band-pass filter based on composite right-/left-handed transmission-line unitcell," *Microwave and Optical Technology Letters*, vol. 57, no. 7, July 2015. DOI:10.1002/mop.29155.

[17] G. Jang and S. Kahng, "Design of a dual-band metamaterial bandpass filter using zeroth order resonance," *Prog. Electromagn. Res. C*, vol. 12, pp. 149-162, 2010. DOI:10.1109/APMC.2009.5384193.

[18] G. Jang and S. Kahng, "Compact composite right- and left-handed bandpass filter with interlocked gap coupling," *Microwave and Optical Technology Letter*, vol. 55, no. 2, pp. 403-405, 2013. DOI: 10.1002/ mop.27326.

[19] M. A. Abdalla and Z: Hu, "Tunable characteristics of ferrite composite right/left handed coplanar waveguide coupled line coupler – Measurement and experimental verification," *AEU-International Journal of Electronics and Communications*, vol. 96, pp. 113-121, Nov. 2018. DOI 10.1016/j.aeue.2018.09.022.

[20] M. A. Abdalla and Z. Hu, "Composite right/left-handed coplanar waveguide ferrite forward coupled-line coupler," *IET Microwaves, Antennas & Propagation*, vol. 9, no. 10, pp. 1104-1111, 2015. DOI:10.1049/iet-map.2014.0539.

[21] B.-T. Moon and N.-H. Myung, "Design of low phase-noise oscillator based on a hairpin-shaped resonator using composite right/left-handed transmission line," *IEEE Microwave and Wireless Components Letters*, vol. 24, no. 1, pp. 44-46, 2014. DOI:10.1109/LMWC.2013.2287234.

[22] D. H. Lee, J. Lee, and C. Nguyen, "Concurrent dual *K/Ka*-band T/R/calibration switch module with quasi-elliptic dual-bandpass frequency response implementing metamaterial transmission line and negative resistance," *IEEE Transactions on Microwave Theory and Techniques*, vol.64, no. 2, pp. 585-598, 2016. DOI:10.1109/TMTT.2015.2512578.

[23] R. Keshavarz, A. Mohammadi, and A. Abdipour, "A quad-band distributed amplifier with E-CRLH transmission line," *IEEE Transactions on Microwave Theory and Techniques*, vol. 61, no. 12, pp. 4188-4194 2013. DOI:10.1109/TMTT.2013.2288939.

[24] A. Boutejdar, N. E. Mohamed, A. A. Ibrahim, and M. A. Abdalla, "New compact dual band-pass filter using coupled double-ring resonators and DGS-technique," *Applied Computational Electromagnetics Society Journal*, vol. 31, no. 2, 2016.

[25] A. Boutejdar, M. Challal, A. Omar, E. Burte, R. Mikuta, and A. Azrar, "A novel band-stop filter using octagonal-shaped patterned ground structures along with interdigital and compensated capacitors," *Applied Computational Electromagnetics Society Journal*, vol. 26, no. 10, 2011.

[26] A. Boutejdar, A. A. Ibrahim,·and E. P. Burte, "DGS resonators form compact filters," *Microwaves & RF Journal*, vol. 54, no. 3, pp. 52-60, 2015.

[27] A. A. Ibrahim, H. Mohamed, and W. Ali, "Tunable dual/triple band-pass filter based on stub-loaded resonators for wireless applications," *Journal of Instrumentation*, vol. 12, no. 4, P04003, 2017. DOI:10.1088/1748-0221/12/04/P04003.

[28] A. Boutejdar, A. A. Ibrahim, and W. A. E. Ali, "Design of compact size and tunable band pass filter for WLAN applications," *Electronics Letters*, vol. 52, no. 24, pp. 1996-1997, 2016. DOI:10.1049/el.2016.3073.

[29] Z. Zeng, Y. Yao, and Y. Zhuang, "A wideband common-mode suppression filter with compact-defected ground structure pattern," *IEEE Transactions on Electromagnetic Compatibility*, vol. 57, no. 5, pp. 1277-1280, 2015. DOI: 10.1109/TEMC.2015.2440424.

[30] J. Lee and Y. Kim, "Ultra-wideband bandpass filter with improved upper stopband performance using defected ground structure," in *IEEE Microwave and Wireless Components Letters*, vol. 20, no. 6, pp. 316-318, June 2010.

[31] Y. Song, G. Yang, and W. Geyi, "Compact UWB bandpass filter with dual notched bands using defected ground structures," in *IEEE Microwave*

and Wireless Components Letters, vol. 24, no. 4, pp. 230-232, Apr. 2014.

[32] F.-C. Chen, H.-T. Hu, J.-M. Qiu, and Q.-X. Chu, "High-selectivity low-pass filters with ultrawide stopband based on defected ground structures," *IEEE Transactions on Components, Packaging and Manufacturing Technology*, vol. 5, no. 9. pp. 1313-1319, 2015. DOI:10.1109/TCPMT.2015.2461663.

[33] L. Chen and Y-L. Luo, "Compact filtering antenna using CRLH resonator and defected ground structure," *Electronics Letters*, vol. 50, no. 21, pp. 1496-1498, 2014. DOI:10.1049/el.2014.2703.

Ahmed A. Ibrahim was born in 1986. He received the B.Sc. degree, with grade of very good, in Electrical Engineering from the Electronic and Communication Engineering Department, Elminia University, Elminia, Egypt in 2007. He was awarded the M.Sc. degree in Electronic and Communication Engineering from Elminia University in 2011 and the Ph.D. degree from Electronic and Communication Engineering from Minia University in 2014. He is a Lecturer in Electronic and Communication Engineering Department. His research focused on the design and analysis of microstrip antennas, microstrip filters, and its application in wireless communications. Also metamaterial MIMO antenna and different metamaterial applications in microwave bands.

Mahmoud A. Abdalla was born in 1973. He received the B.Sc. and M.Sc. degrees in Electrical Engineering from the Electrical Engineering Department, Military Technical College, Cairo, Egypt in 1995 and 2000. He received the Ph.D. degree from School of Electrical Engineering, University of Manchester, UK, in 2009. He is now an Associated Professor and Head of Electromagnetic Eaves Group in Electronic Engineering Department, Military Technical College.

Abdalla was the recipient of the Egyptian Encouragement State Prize for Engineering Sciences in 2014. He published more than 180 peer-reviewed journal and conference papers. His research has focused on miniaturized, multiband and wideband microwave/ millimeter antennas. Components and absorbing materials with great attention is to employ metamaterial/EBG, structures. Abdalla is a Senior mMember of the IEEE and the European Microwave Association EuMA. He is currently a Reviewer in many high ranked electromagnetic journals.

Wael A. E. Ali was born in 1982. He received his B.Sc. and M.Sc. in Electronics and Communications Engineering from Arab Academy for Science, Technology and Maritime Transport (AASTMT), Alexandria, Egypt in 2004 & 2007, respectively. He obtained his Ph.D. in Electronics and Communications Engineering from Alexandria University, Alexandria, Egypt in 2012. He is currently an Associate Professor at Arab Academy for Science, Technology and Maritime Transport (AASTMT), Alexandria, Egypt. His research interests include smart antennas, microstrip antennas, microwave filters, metamaterials, and MIMO antennas and its applications in wireless communications.

An Equivalent Modeling Method for the Radiated Electromagnetic Interference of PCB Based on Near-field Scanning

Yin-Shuang Xiao [1], Dan Ren [2], Pei Xiao [1], and Ping-An Du [1*]

[1] School of Mechanical and Electrical Engineering
University of Electronic Science and Technology of China, Chengdu 611731, China
xiaoyinshuang@qq.com, xiaopei_uestc@sina.cn, dupingan@uestc.edu.cn*

[2] Institute of Electronic Engineering
China Academy of Engineering Physics, Mianyang 621900, China
rendan_uestc@163.com

Abstract ─ Since the structure complexity of a PCB makes its EMI modeling be very difficult or impossible, an equivalent modeling method to predict the electromagnetic radiation of a PCB is presented by means of a dipole array based on near-field scanning. Firstly, the equivalent modeling method is theoretically derived and its accuracy is validated by a commercial full-wave tool. Then, the equivalent model is applied to predict the electromagnetic coupling of different parts on a PCB and the electromagnetic leakage of a PCB in an enclosure with numerous small apertures. The results show that the proposed method has high efficiency and acceptable accuracy.

Index Terms ─ Dipole array, electromagnetic interference, equivalent modeling, printed circuit board (PCB), near-field scanning.

I. INTRODUCTION

The printed circuit board (PCB) is the most frequently-used component in electronic device. Since the PCB always radiates electromagnetic interference while working, it is necessary to model the PCB during the electromagnetic compatibility (EMC) analysis of an electronic device. However, the complexity of the structure of PCB makes its EMI modeling be very difficult and time-consuming, even impossible. Thus, investigation of the equivalent model with a simpler structure and similar EMI characteristics of the original PCB is of significance in applications [1-4].

In the EMC analysis area of PCB, Shi and Weng analyzed the electromagnetic emission information of PCB by near-field scanning, and the equivalent electric/ magnetic current source was applied to replace radiation characteristics of original source [5-6]. This method showed a good performance on far-field radiation characteristic prediction, but was not fit to represent near-field electromagnetic radiation and coupling characteristics. The optimizing work of equivalent model and dipole-dielectric-conducting plane (DDC) model which simultaneously considered the affection of dielectric slab and ground plane have been introduced by Tong [7-9]. Then Obiekezie proposed new equivalent dipole models, which predicted the EMI characteristic of 3D radiation source on the finite ground plane and characterized edge currents along a finite ground plane [10-11]. In [12], an equivalent modeling method without phase information was realized by using particle swarm optimization algorithm. The outer components, like heat sink structure and IC pins were considered in [13-15], and practical equivalent dipole models were established. A decomposition method was proposed to predict the coupling from a digital noise to the radio frequency (RF) antenna based on equivalent dipole modeling method and reciprocity theory in [16-18].

In this paper, an equivalent dipole modeling method of PCB is proposed, which can predict the near-field electromagnetic radiation characteristics of original PCB model, and validated by patch antenna with a commercial full-wave tool. Then, an improved analytical algorithm is established, and the efficiency of this algorithm is verified by calculating the coupling parameters of different parts of PCB and antenna array. Finally, the equivalent model is applied to predict the electromagnetic leakage of the PCB in an enclosure with numerous small apertures, and also shows very high accuracy.

II. EQUIVALENT MODELING METHOD

A. Basic theory

According to the basic theory of electromagnetic [19], the near field PCB radiated is quasi-static. It includes abundant radiation information of PCB. So it is

Submitted On: October 8, 2018
Accepted On: January 18, 2019

workable to make use of this critical information to establish the equivalent model of the PCB. On the other hand, the real radiating source on the PCB are onboard electric and magnetic current. They have similar radiating characteristics with electric and magnetic dipole. Therefore, electric and magnetic dipole are adaptable to be used to build the equivalent model we need.

In this paper, the magnetic near field is extracted by HFSS simulation, which includes three Cartesian components: H_x, H_y, and H_z. Correspondingly, the magnetic dipole is chosen to constitute the equivalent model of a PCB, which can be decomposed into three moment components: M_x, M_y, and M_z. As a result, the radiation characteristics of the equivalent model are mainly determined by the dipole and its image source of ground plane (GND). The dipole is located far away from the boundary of GND, so the edge diffraction is ignored. Besides, according to the image theory, the radiation of vertical magnetic moment can be ignored when the dipole is laid close to GND. So only tangential moment components M_x and M_y are considered.

When a dipole is located in (x_0, y_0, z_0), the magnetic field of point (x, y, z) in free space which is radiated by M_x, M_y and their image sources can be expressed as [18]:

$$\begin{aligned} H_x &= a_{H_x}^{M_x} M_x + a_{H_x}^{M_y} M_y \\ &= \frac{k_0^2 M_x}{4\pi}\Big[-\frac{(y-y_0)^2+(z-z_0)^2}{r_1^2} g_1(r_1) + g_2(r_1) \\ &\quad -\frac{(y-y_0)^2+(z-z_0+2h)^2}{r_2^2} g_1(r_2) + g_2(r_2)\Big] \\ &\quad + \frac{k_0^2 M_y}{4\pi}\Big[\frac{(x-x_0)(y-y_0)}{r_1^2} g_1(r_1) + \frac{(x-x_0)(y-y_0)}{r_2^2} g_1(r_2)\Big], \end{aligned} \tag{1a}$$

$$\begin{aligned} H_y &= a_{H_y}^{M_x} M_x + a_{H_y}^{M_y} M_y \\ &= \frac{k_0^2 M_x}{4\pi}\Big[\frac{(x-x_0)(y-y_0)}{r_1^2} g_1(r_1) + \frac{(x-x_0)(y-y_0)}{r_2^2} g_1(r_2)\Big] \\ &\quad + \frac{k_0^2 M_y}{4\pi}\Big[-\frac{(x-x_0)^2+(z-z_0)^2}{r_1^2} g_1(r_1) + g_2(r_1) \\ &\quad -\frac{(x-x_0)^2+(z-z_0+2h)^2}{r_2^2} g_1(r_2) + g_2(r_2)\Big], \end{aligned} \tag{1b}$$

$$\begin{aligned} H_z &= a_{H_z}^{M_x} M_x + a_{H_z}^{M_y} M_y \\ &= \frac{k_0^2 M_x}{4\pi}\Big[\frac{(x-x_0)(z-z_0)}{r_1^2} g_1(r_1) + \frac{(x-x_0)(z-z_0+2h)}{r_2^2} g_1(r_2)\Big] \\ &\quad \frac{k_0^2 M_y}{4\pi}\Big[\frac{(y-y_0)(z-z_0)}{r_1^2} g_1(r_1) + \frac{(y-y_0)(z-z_0+2h)}{r_2^2} g_1(r_2)\Big], \end{aligned} \tag{1c}$$

where h is the thickness of the PCB, r_1 r_2, $g_1(r)$, $g_2(r)$ are respectively defined as:

$$r_1 = \sqrt{(x-x_0)^2+(y-y_0)^2+(z-z_0)^2}, \tag{2a}$$

$$r_2 = \sqrt{(x-x_0)^2+(y-y_0)^2+(z-z_0+2h)^2}, \tag{2b}$$

$$g_1(r) = \frac{e^{-jk_0 r}}{r}\left[\frac{3}{(k_0 r)^2} + j\frac{3}{k_0 r} - 1\right], \tag{2c}$$

$$g_2(r) = \frac{e^{-jk_0 r}}{r}\left[\frac{2}{(k_0 r)^2} + j\frac{2}{k_0 r}\right]. \tag{2d}$$

The equation (1) can be written as the following matrix:

$$\begin{bmatrix} a_{H_x}^{M_x} & a_{H_x}^{M_y} \\ a_{H_y}^{M_x} & a_{H_y}^{M_y} \\ a_{H_z}^{M_x} & a_{H_z}^{M_y} \end{bmatrix} \begin{bmatrix} M_x \\ M_y \end{bmatrix} = \begin{bmatrix} H_x \\ H_y \\ H_z \end{bmatrix}. \tag{3}$$

Letting the number of scanning points be *m* and the number of dipoles be *n* ($m \geq n$ is required), (3) can be written as:

$$\begin{pmatrix} a_{H_{1x}}^{M_{1x}} & a_{H_{1x}}^{M_{1y}} & \cdots & a_{H_{1x}}^{M_{nx}} & a_{H_{1x}}^{M_{ny}} \\ a_{H_{1y}}^{M_{1x}} & a_{H_{1y}}^{M_{1y}} & \cdots & a_{H_{1y}}^{M_{nx}} & a_{H_{1y}}^{M_{ny}} \\ a_{H_{1z}}^{M_{1x}} & a_{H_{1z}}^{M_{1y}} & \cdots & a_{H_{1z}}^{M_{nx}} & a_{H_{1z}}^{M_{ny}} \\ \vdots & \vdots & \ddots & \vdots & \vdots \\ a_{H_{mx}}^{M_{1x}} & a_{H_{mx}}^{M_{1y}} & \cdots & a_{H_{mx}}^{M_{nx}} & a_{H_{mx}}^{M_{ny}} \\ a_{H_{my}}^{M_{1x}} & a_{H_{my}}^{M_{1y}} & \cdots & a_{H_{my}}^{M_{nx}} & a_{H_{my}}^{M_{ny}} \\ a_{H_{mz}}^{M_{1x}} & a_{H_{mz}}^{M_{1y}} & \cdots & a_{H_{mz}}^{M_{nx}} & a_{H_{mz}}^{M_{ny}} \end{pmatrix}_{3m\times 2n} \begin{pmatrix} M_{1x} \\ M_{1y} \\ \vdots \\ M_{nx} \\ M_{ny} \end{pmatrix}_{2n} = \begin{pmatrix} H_{1x} \\ H_{1y} \\ H_{1z} \\ \vdots \\ H_{mx} \\ H_{my} \\ H_{mz} \end{pmatrix}_{3m}. \tag{4}$$

The equation (4) can also be simplified as:

$$AM = H, \tag{5}$$

where the matrix *A* can be obtained by the defined near-field sampling grids and dipole locations. The Tikhonov regularization method addressed in [8] is applied to deal with the ill condition problem, and the regularization parameters are obtained by generalized cross validation (GCV) method, which is the value of $\min \mathrm{GCV}(\lambda)$.

B. Numerical validation

Figure 1 (a) gives a patch antenna model, its physical structure is a 60mm×60mm×1mm board (Rogers RT substrate) with a circle patch (radius is 23mm) on one face and a ground plane on the other face, and the excitation source is 1V voltage through a coaxial cable. The antenna model is calculated with HFSS at its working frequency 2.5GHz, and the magnetic field data on the plane 10mm off the antenna's top surface is extracted. The size of the scanning plane is 80mm×80mm, scanning resolution is 4mm, and the total number of sampling points is 441.

The constructed equivalent model is as shown in Fig. 1 (b), consists of an initial matrix of 9×9 dipoles within an area of 48mm×48mm. Each dipole can be represented by two tangential moment components M_x and M_y.

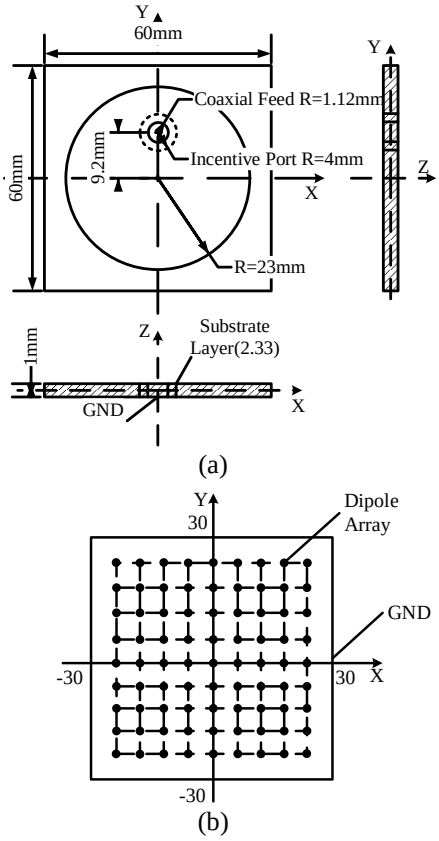

Fig. 1. (a) The physical structure of a patch antenna, and (b) the equivalent dipole array model of the antenna.

Importing the near-field data into MATLAB, the dipole moments are calculated by Tikhonov regularization method, Fig. 2 is the determination of regularization parameter (λ) by using GCV. Then equivalent model is obtained.

The magnetic fields on the plane 10mm above the upper surface of antenna from the original PCB and the equivalent model are compared in Fig. 3. It can be seen that the equivalent model can predict the radiating fields of the PCB quiet accurately, all the relative errors of each component calculated by (6), as summarized in Table 1, are smaller than 5%. It should be note that the relative error of H_x smaller than that of H_y and H_z is random. Actually, several attempts later we find that it will change with different near-field scanning and equivalent modeling parameters. Normally, we only need to consider that if the errors of H_x, H_y and H_z are smaller than 10%, then we think the equivalent model is available:

$$\sigma = \frac{\left|\sum_{m=1}^{M}\left|H_{im}^{means}\right| - \sum_{m=1}^{M}\sum_{n=1}^{N}\left|H_{im}^{model}\right|\right|}{\sum_{m=1}^{M}\left|H_{im}^{means}\right|} \quad i = x, y, z\,. \tag{6}$$

To extend the application of the equivalent modeling method, the following section will propose an improved analytical algorithm to enhance the efficiency of calculating board-level radio-frequency interference in [17].

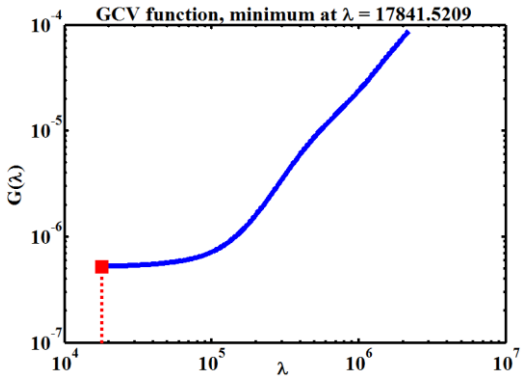

Fig. 2. Determination of regularization parameter by GCV.

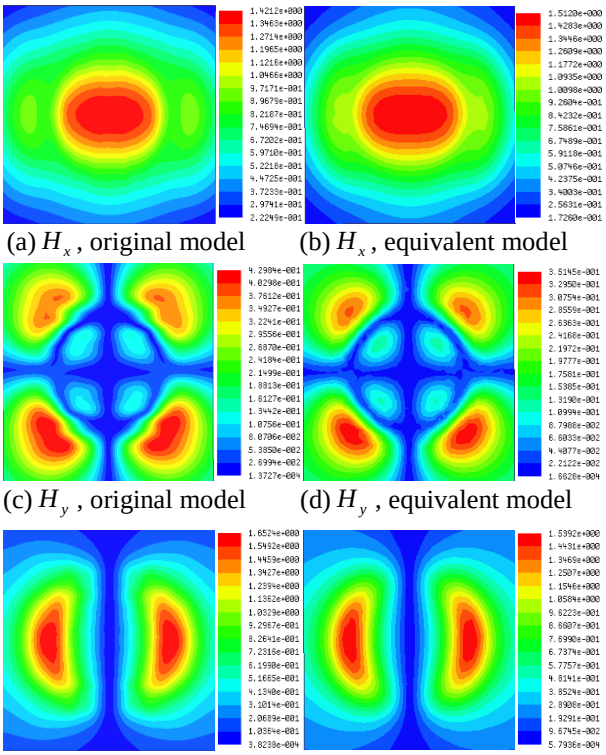

(a) H_x, original model (b) H_x, equivalent model

(c) H_y, original model (d) H_y, equivalent model

(e) H_z original model (f) H_z, equivalent model

Fig. 3. A comparison of magnetic field distribution between the original antenna model and the equivalent dipole model in free space by full-wave simulation.

Table 1: Relative errors of equivalent model

	H_x	H_y	H_z	H_{total}
10mm above the upper surface of PCB	0.58%	4.87%	4.49%	0.84%

III. RADIO-FREQUENCY INTERFERENCE ESTIMATION

A. Basic theory

According to [18], a decomposition method based on reciprocity theory is proposed to predict near-field coupling from a digital noise source to an RF antenna. This method consists of three main steps. Firstly, a Huygens' box is introduced to enclose the victim antenna, and the antenna is removed. Then, an equivalent dipole array model of working noise source is applied to calculate the tangential electromagnetic fields on the external surface of Huygens' box. This is a forward problem. Secondly, the victim antenna is excited, and the tangential electromagnetic fields on the internal surface of the same Huygens' box are recorded by using full-wave simulation. This is a reverse problem. Thirdly, the coupling parameter between noise source and victim antenna is calculated by the recorded tangential electromagnetic fields and reciprocity theory. Examples in [18] show that this method has achieved decent RFI estimation, but the calculation of the tangential electromagnetic fields is time-consuming in the second step. So the electromagnetic fields achieved by equivalent dipole model is proposed in this paper. This method can improve the calculating efficiency significantly with high accuracy, especially for antenna array where noise and victim sources share the same model. Then the original problem can be transformed into the equivalent problem as shown in Fig. 4, and the three main steps are described as follows.

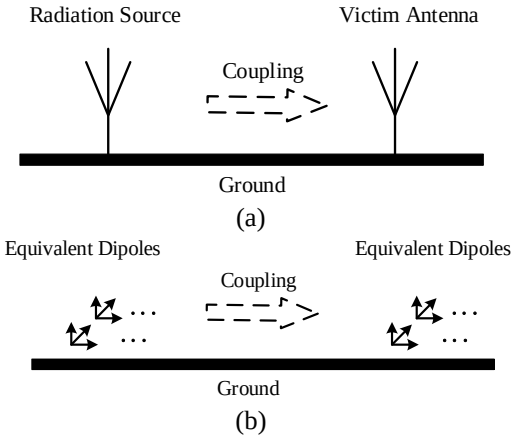

Fig. 4. (a) Original coupling problem, and (b) equivalent problem.

(1) Forward Problem: As shown in Fig. 5 (a), victim source is enclosed by Huygens' box, and then it is removed. Excite the noise source, and the induced electromagnetic fields on the port of noise source are named as E_a^{fwd}, H_a^{fwd}. Establish the equivalent dipole model of the noise source, and divide the surface of Huygens' box into small cells. Then the tangential electromagnetic field on each cell can be calculated by equivalent model, which named as E_c^{fwd}, H_c^{fwd}.

(*2) Reverse Problem*: Similar to step1, as illustrated in Fig. 5 (b), keep victim source being enclosed, remove the noise source, and excite the victim source instead. The excited electromagnetic fields are recorded as E_a^{rev}, H_a^{rev}. Then establish equivalent model of victim source, and calculate the tangential electromagnetic fields on the same cells, and they are named as E_c^{rev}, H_c^{rev}.

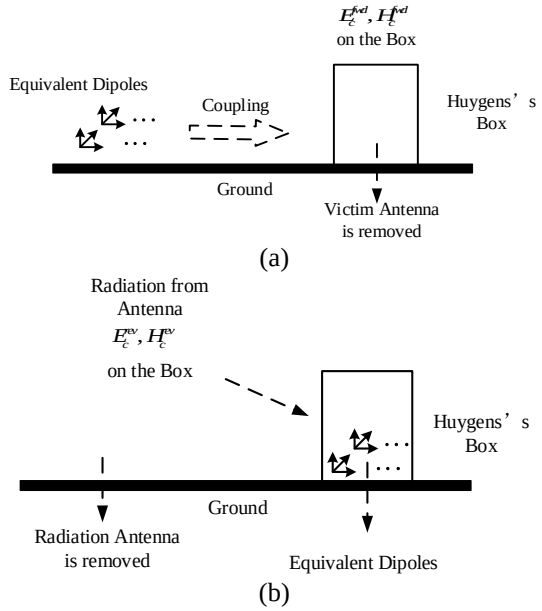

Fig. 5. (a) Forward problem, and (b) reverse problem.

(3) Interference Estimation: According to [18], based on the forward problem and reverse problem, the reciprocity theory can be expressed as:

$$\begin{aligned} &-\int_S \left(E^{rev}\times H^{fwd} - E^{fwd}\times H^{rev}\right)\cdot ds \\ &= \int_V \left(E^{rev}\times J^{fwd} + H^{fwd}\times M^{rev}\right) dv \\ &-\int_V \left(E^{fwd}\times J^{rev} + H^{rev}\times M^{fwd}\right) dv, \end{aligned} \tag{7}$$

where J and M represent the electric current and magnetic current source, respectively. "*fwd*" means the forward problem, and "*rev*" means the reverse problem. If equation (7) is integrated over the entire space, it can be simplified as:

$$\int_V \left(E_c^{rev}\cdot J_c^{fwd} - H_c^{rev}\cdot M_c^{fwd}\right)dv = \int_V \left(E_a^{fwd}\cdot J_a^{rev} - H_a^{fwd}\cdot M_a^{rev}\right)dv, \tag{8}$$

where subscript "*a*" means the antenna port, and "*c*" the electric/magnetic field and current on the Huygens' box. By dividing the Huygens' box into cells and replacing *J* and *M*: through electric field and magnetic field, the two terms on the left side of (8) are derived as:

$$\begin{aligned}\int_V \left(E_c^{rev}\cdot J_c^{fwd}\right)dv &= \int_{S_c}\left(E_c^{rev}\cdot J_c^{fwd}\right)ds \\ &= \sum_{cells} E_c^{rev}\cdot J_c^{fwd} S_{cell} \\ &= \sum_{cells} E_c^{rev}\cdot\left(\hat{n}\times H_c^{fwd}\right)S_{cell},\end{aligned} \tag{9}$$

$$\begin{aligned}\int_V \left(H_c^{rev}\cdot M_c^{fwd}\right)dv &= \int_{S_c}\left(H_c^{rev}\cdot M_c^{fwd}\right)ds \\ &= \sum_{cells} H_c^{rev}\cdot M_c^{fwd} S_{cell} \\ &= \sum_{cells} H_c^{rev}\cdot\left(E_c^{fwd}\times\hat{n}\right)S_{cell},\end{aligned} \tag{10}$$

where $\hat{n}$ is the normal vector of the cells, S_{cell} the area of a single cell. The right side of (8) can be written as [18]:

$$\int_V \left(E_a^{fwd}\cdot J_a^{rev}\right)dv = -\int_{S_a} E_a^{fwd}\cdot J_a^{rev} ds = -I_a^{rev}U_a^{fwd}, \tag{11}$$

$$\begin{aligned}\int_V \left(H_a^{fwd}\cdot M_a^{rev}\right)dv &= \int_V H_a^{fwd}\cdot\left(E_a^{rev}\times\hat{n}\right)dv \\ &= \int_V E_a^{rev}\cdot\left(\hat{n}\times H_a^{fwd}\right)dv \\ &= \int_V E_a^{rev}\cdot J_a^{fwd}dv \\ &= \int_{S_a} J_a^{fwd}E_a^{rev}ds = I_a^{fwd}U_a^{rev}.\end{aligned} \tag{12}$$

Substituting (9)-(12) into (8), we obtain:

$$\begin{aligned}&\sum_{cells}\hat{n}\times H_c^{fwd}\cdot E_c^{rev}S_{cell} + \sum_{cells}\hat{n}\times E_c^{fwd}\cdot H_c^{rev}S_{cell} \\ &= -I_a^{rev}U_a^{fwd} - I_a^{fwd}U_a^{rev} \\ &= -\frac{Z_{in}+Z_L}{Z_{in}Z_L}U_a^{fwd}U_a^{rev},\end{aligned} \tag{13}$$

where Z_{in} and Z_L are respectively the input impedance of the victim source and the load of the noise source, 50Ω in common. U_a^{rev} is the excitation voltage of the victim source, and here is 1V. Thus, the coupling voltage can be solved as:

$$\begin{aligned}U_a^{fwd} &= -\frac{Z_{in}Z_L}{U_a^{rev}(Z_{in}+Z_L)} \\ &\times\left(\sum_{cells}\hat{n}\times H_c^{fwd}\cdot E_c^{rev}S_{cell} + \sum_{cells}\hat{n}\times E_c^{fwd}\cdot H_c^{rev}S_{cell}\right).\end{aligned} \tag{14}$$

Assuming that U_{in} is the incident voltage of noise source, the scattering parameter can be calculated by (15):

$$\begin{aligned}S &= \frac{U_a^{fwd}}{U_{in}} \\ &= -\frac{Z_{in}Z_L}{U_a^{rev}U_{in}(Z_{in}+Z_L)} \\ &\times\left(\sum_{cells}\hat{n}\times H_c^{fwd}\cdot E_c^{rev}S_{cell} + \sum_{cells}\hat{n}\times E_c^{fwd}\cdot H_c^{rev}S_{cell}\right).\end{aligned} \tag{15}$$

B. Numerical validation

As illustrated in Fig. 6, a patch antenna array model is constructed with four antenna elements which are the same as that in Section II. Assuming that Part 1 is the noise source, Part 2, 3, 4 are the victim sources. A 60mm×60mm×60mm Huygens' box is applied to enclose the victim sources, then its surface is divided into small cells with a size of 1mm×1mm. Based on the equivalent dipole model of the single patch antenna in Section II, both the tangential electromagnetic fields on the Huygens' box in the forward problem (E_a^{fwd} , H_a^{fwd}) and reverse problem (E_c^{rev} , H_c^{rev}) can be calculated from the dipoles.

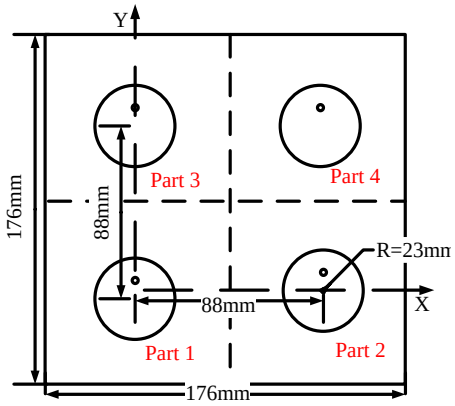

Fig. 6. Patch antenna array structure.

Substituting all the data into (14) and (15), the scattering parameters are calculated. Figure 7 shows the comparison of the scattering parameters between the proposed method and HFSS simulation. Note that part 2 and part 3 share the same scattering parameter because of their symmetry. It can be seen that the proposed method can predict the scattering parameters well. Thus, the worst coupling frequency (2.5 GHz, it is both the frequency point corresponding to the peak of scattering parameters and the working frequency of patch antenna) could be identified with high efficiency, and the precision of equivalent dipole model is further validated.

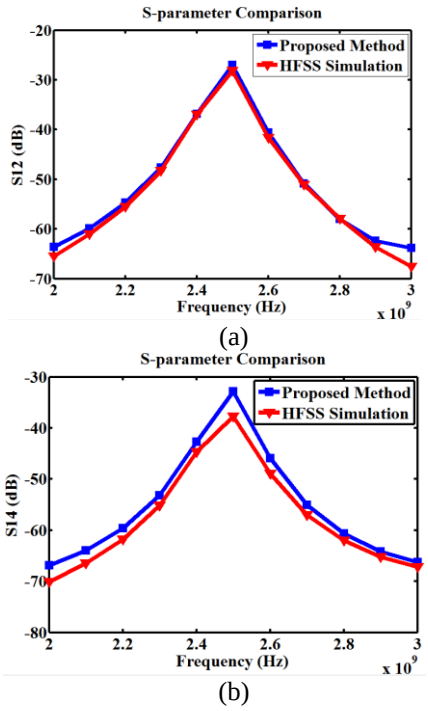

Fig. 7. Comparison of scattering parameters: (a) S_{12} and (b) S_{14} .

IV. ELECTROMAGNETIC LEAKAGE ESTIMATION

This section will verify the estimation accuracy of electromagnetic leakage with our equivalent dipole model. Figure 8 (a) shows an M micro-strip line which is a common trace structure on a PCB. Applying the method described in Section II, its equivalent dipole model is established as illustrated in Fig. 8 (b).

Place respectively the original micro-strip line model and its equivalent model into a shielding cavity with aperture arrays, and calculate these two models by HFSS at 1GHz. The cavity's size is 240mm×60mm×200mm, and 12 apertures are uniformly distributed on one face of the cavity, and other details of the cavity and aperture arrays are shown in Fig. 9.

Figure 10 demonstrates the HFSS simulation results of the magnetic field at 1GHz on the plane 3mm above the aperture face (outside of the cavity) from these two models, and the relative errors are summarized in Table 2. It can be seen that the equivalent dipole model can predict the electromagnetic leakage with acceptable errors (smaller than 10%), which depicts that the equivalent model is applicable to describe the interaction between the original PCB model and the enclosure. On the other hand, the results in a half-closed environment are slightly worse than in free place, because multiple reflection of electromagnetic fields in cavity may change real current distribution on PCB, and make the error of equivalent model bigger.

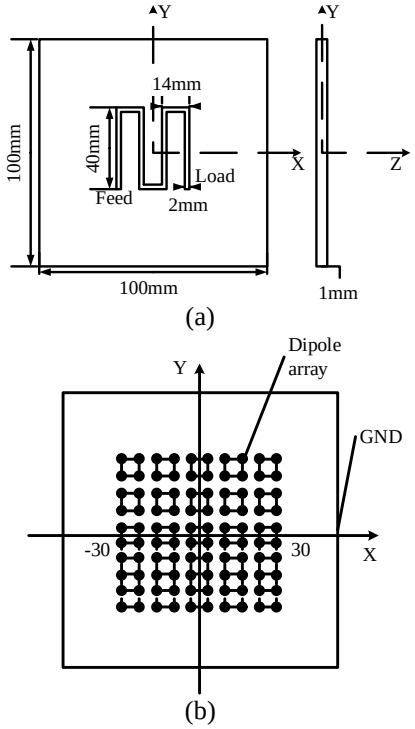

Fig. 8. (a) Physical structure of M micro-strip line, and (b) equivalent dipole array model of micro-strip line

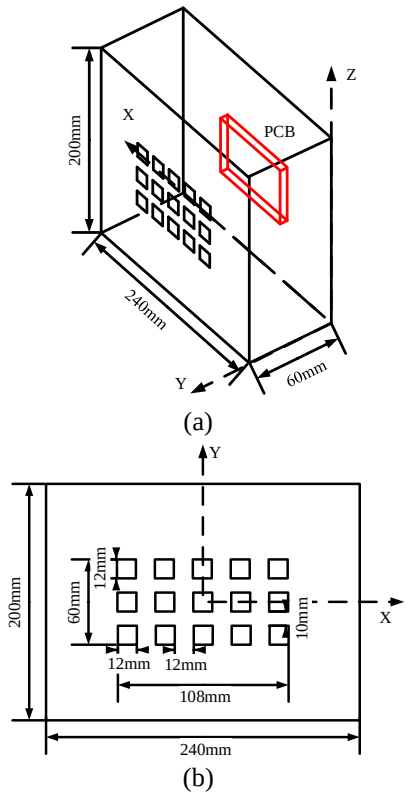

Fig. 9. (a) Structure of shielding cavity, and (b) structure of aperture face.

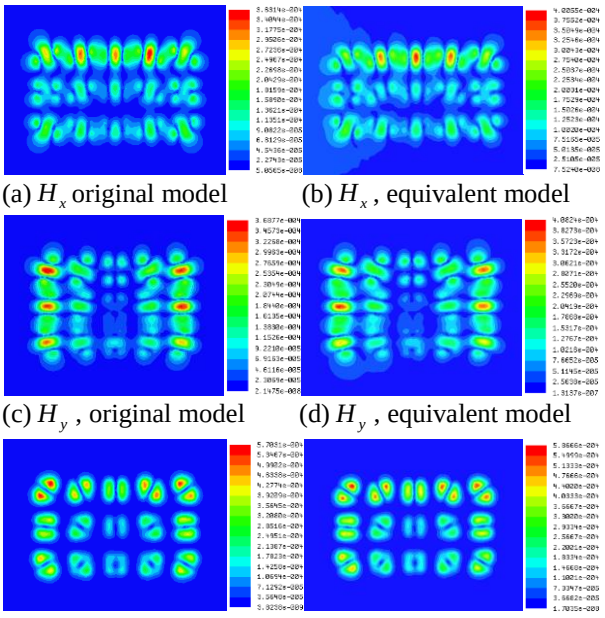

(a) H_x original model (b) H_x, equivalent model

(c) H_y, original model (d) H_y, equivalent model

(e) H_z, original model (f) H_z, equivalent model

Fig. 10. Magnetic field distribution comparison between original antenna model and equivalent dipole model in aperture array cavity by full-wave simulation.

Table 2: Relative errors of equivalent model

	H_x	H_y	H_z	H_{total}
3mm above the aperture face (outside) of PCB	9.33%	3.94%	6.57%	5.07%

V. CONCLUSION

This paper proposes an equivalent dipole modeling method of a PCB. This method can model original PCB emission characteristics when its physical structure and circuit structure are uncertain or complicated, and can be applied in some common structures like board-level patch antenna, micro-strip line, and other complicated IC structures. An improved analytical algorithm of board-level electromagnetic coupling estimation is also proposed using the equivalent dipole modeling method and reciprocity theory. Compared with full-wave simulation, the proposed method can predict the electromagnetic coupling parameters and the worst coupling frequency fast, especially when the structure of noise source is the same as that of victim source like the patch antenna array. Then, the application of equivalent dipole model is extended to predict the electromagnetic leakage of a PCB in an enclosure with numerous small apertures, and the calculation precision is validated by a common micro-strip line model. Finally, the limitation of the proposed equivalent method is that it only applies to relative lower frequency (smaller than 4GHz). Because with an increase of the frequency, the number of the equivalent dipole increases and the relative errors also become greater. However, with emergence of higher frequency electronic equipment, further work can be done to explore the equivalent model of PCB in these kind of devices. Besides, method to decrease the relative errors of equivalent model in half enclosed cavity also can be further taken into consideration.

ACKNOWLEDGMENT

This work is supported by the National Natural Science Foundation of China (Grant No. 51675086).

REFERENCES

[1] S. Deng, T. H. Hubing, and D. G. Beetner, "Using TEM cell measurements to estimate the maximum radiation from PCBs with cables due to magnetic field coupling," [J]. *IEEE Transactions on Electromagnetic Compatibility*, vol. 50, no. 2, pp. 419-423, 2008.

[2] B. L. Nie, P. A. Du, Y. T. Yu, et al., "Study of the shielding properties of enclosures with apertures at higher frequencies using the transmission-line modeling method," [J]. *IEEE Transactions on Electromagnetic Compatibility*, vol. 53, no. 1, pp. 73-81, 2011.

[3] P. Xiao, P. A. Du, D. Ren, et al., "A hybrid method for calculating the coupling to PCB inside a nested shielding enclosure based on electromagnetic topology," [J]. *IEEE Transactions on Electromagnetic Compatibility*, vol. 58, no. 6, pp. 1701-1709, 2016.

[4] P. Xiao, P. A. Du, B. L. Nie, et al., "Reduced technique for modeling electromagnetic immunity on braid shielding cable bundles," [J]. *Chinese Physics B*, vol. 26, no. 9, pp. 175-183, 2017.

[5] J. Shi, M. A. Cracraft, J. Zhang, et al., "Using near-field scanning to predict radiated fields," [C]. *International Symposium on Electromagnetic Compatibility, IEEE*, vol. 1, pp. 14-18, 2004.

[6] H. Weng, D. G. Beetner, and R. E. Dubroff, "Prediction of radiated emissions using near-field measurements," [J]. *IEEE Transactions on Electromagnetic Compatibility*, vol. 53, no. 4, pp. 891-899, 2011.

[7] X. Tong, D. W. P. Thomas, et al., "Reduction of sensitivity to measurement errors in the derivation of equivalent models of emission in numerical computation," [J]. *Applied Mathematics & Computation*, vol. 26, no. 7, pp. 603-610, 2011.

[8] X. Tong, *Ph.D. dissertation*, United Kingdom: the University of Nottingham, 2010.

[9] X. Tong, D. W. P. Thomas, A. Nothofer, et al., "Modeling electromagnetic emissions from printed circuit boards in closed environments using equivalent dipoles," [J]. *IEEE Transactions on Electro-*

magnetic Compatibility, vol. 52, no. 2, pp. 462-470, 2010.

[10] C. Obiekezie, D. W. P. Thomas, A. Nothofer, et al., "Prediction of emission from a source placed inside a metallic enclosure over a finite ground plane," [C]. *International Symposium on Electromagnetic Compatibility, IEEE*, pp. 1-5, 2012.

[11] C. Obiekezie, D. W. Thomas, A. Nothofer, et al., "Extended scheme using equivalent dipoles for characterizing edge currents along a finite ground plane," [J]. *Applied Mathematics & Computation*, vol. 28, no. 11, pp. 1111-1121, 2013.

[12] F. P. Xiang, E. P. Li, X. C. Wei, et al., "A particle swarm optimization-based approach for predicting maximum radiated emission from PCBs with dominant radiators," [J]. *IEEE Transactions on Electromagnetic Compatibility*, vol. 57, no. 5, pp. 1197-1205, 2015.

[13] Z. Yu, J. A. Mix, S. Sajuyigbe, et al., "An improved dipole-moment model based on near-field scanning for characterizing near-field coupling and far-field radiation from an IC," [J]. *IEEE Transactions on Electromagnetic Compatibility*, vol. 55, no. 1, pp. 97-108, 2013.

[14] Z. Yu, J. A. Mix, S. Sajuyigbe, et al., "Heat-sink modeling and design with dipole moments representing IC excitation," [J]. *IEEE Transactions on Electromagnetic Compatibility*, vol. 55, no. 1, pp. 168-174, 2013.

[15] J. Zhang, D. Pommerenke, and J. Fan, "Determining equivalent dipoles using a hybrid source-reconstruction method for characterizing emissions from integrated circuits," [J]. *IEEE Transactions on Electromagnetic Compatibility*, vol. 59, no. 2, pp. 567-575, 2017.

[16] J. Pan, L. Li, X. Gao, et al., "Application of dipole-moment model in EMI estimation," [C]. *IEEE International Symposium on Electromagnetic Compatibility, IEEE*, pp. 350-354, 2015.

[17] H. Wang, V. Khilkevich, Y. J. Zhang, et al., "Estimating radio-frequency interference to an antenna due to near-field coupling using decomposition method based on reciprocity," [J]. *IEEE Transactions on Electromagnetic Compatibility*, vol. 55, no. 6, pp. 1125-1131, 2013.

[18] J. Pan, H. Wang, X. Gao, et al., "Radio-frequency interference estimation using equivalent dipole-moment models and decomposition method based on reciprocity," [J]. *IEEE Transactions on Electromagnetic Compatibility*, vol. 58, no. 1, pp. 75-84, 2016.

[19] J. D. Jackson, *Classical Electrodynamics*. [M]. J. Wiley, 1998.

Yin-Shuang Xiao was born in Chongqing, China, in 1991. She received the Bachelor of Industrial Engineering degree from UESTC, Chengdu, China, in 2014. She is currently a Master student at UESTC. Her research interests are electromagnetic compatibility (EMC), computational electromagnetic (CEM), multi-conductor transmission line (MTL), etc.

Dan Ren was born in Huainan, Anhui Province, China, in 1986. He received the doctoral degree of Mechanical Engineering from UESTC, Chengdu, China, in 2017. He is currently a Research Assistant at Institute of Electronic Engineering, China Academy of Engineering Physics. His research interests include numerical computation, electromagnetic measurement, electromagnetic simulation and High Power Microwave.

Pei Xiao was born in Shaoyang, Hunan Province, China, in 1989. He received the Bachelor of Industrial Engineering degree from UESTC, Chengdu, China, in 2013. He is currently a Ph.D. student at UESTC. His research interests are numerical computation, theoretical electromagnetic analysis including the EMT method, and EMC/EMI in Multi-conductor transmission line (MTL).

Ping-An Du received the M.S. and Ph.D degrees in Mechanical Engineering from Chongqing University, Chongqing, China, in 1989 and 1992, respectively. He is currently a Full Professor of Mechanical Engineering at the University of Electronic Science and Technology of China, Chengdu, China. His research interests include numerical simulation in EMI, vibration, temperature, and so on.

Plane Wave Scattering by a Dielectric Circular Cylinder in the Vicinity of a Conducting Strip (TM Case)

Hassan A. Ragheb

Department of Electrical Engineering
The British University in Egypt, El Sherouk City, Misr-Ismaillia Road, Egypt
Hassan.Ragheb@bue.edu.eg

Abstract ─ Scattering of plane electromagnetic waves by a dielectric circular cylinder in the vicinity of a conducting strip is presented. Two methods of solution are introduced. The first is an exact solution in which the scattered field from conducting strip is expressed in terms of Fourier series of radial and angular Mathieu function of unknown coefficient. Meanwhile the scattered field from the circular cylinder is expressed in terms of Fourier series of Bessel functions of unknown coefficient. The unknown coefficient can be obtained by enforcing the boundary conditions. The application of the boundary condition requires the use of the addition theorem of Mathieu to Bessel functions and vice versa. The second method is based in an asymptotic technique introduced by Karp and Russek for solving scattering by wide slit. The technique assumes the total scattered field from the strip and the dielectric cylinder as the sum of the scattered fields from the individual element due to a plane incident wave plus scattered fields from factious line sources of unknown intensity located at the center of every element. The line sources account for the multiple scattering effect. By enforcing the boundary conditions, the intensity of the line sources can be calculated. Numerical examples are calculated using both methods showing excellent agreement in all cases.

Index Terms ─ Dielectric cylinder and conducting strip, multiple-scattering, scattering cross section.

I. INTRODUCTION

The scattering of a plane electromagnetic waves by a perfectly conducting strip grating was the subject of many investigations [1] and [2]. Different methods have been used for solving such a problem, among them is the self-consistent method [3]. This method is based on the previous knowledge of the responses of the isolated objects in the multi-object scattering problem. In an approximate treatment the self-consistent method was used by Karp and Russek [4]. The solution is restricted to the case where the spacing between the objects is much greater than the maximum dimension of any one object. This technique has been extended to the case of scattering of plane waves by wide double wedges (Elsherbeni and Hamid [5]). Hansen [6] used the integral equation approach in order to calculate the diffracted field of a plane acoustic wave through two or more parallel slits in a plane screen.

Scattering by dielectric cylinders has also been widely investigated. Yousif and Kohler [7], presented Mueller scattering matrix elements and the cross sections for the scattering of an electromagnetic plane wave from two infinitely long, parallel, circular dielectric cylinders at oblique incidence. Dunster [8], studied the case of two parallel infinite dielectric cylinders, of equal diameter and dielectric constant, illuminated by a plane electromagnetic wave. Henin et al. [9], presented a rigorous semi-analytical solution for scattering from an array of circular dielectric cylinders due to an obliquely incident plane wave.

Recently, the scattering by two dielectric coated elliptic cylinders [10] and by metamaterial coated elliptic cylinders [11] has been addressed. In addition, pattern equation method has been developed for solving problems of scattered electromagnetic waves by dielectric coated conducting bodies [12] and [13]. Also scattering of electromagnetic waves by inhomogeneous dielectric gratings loaded with conducting strips were investigated by Yamasaki [14].

The TM and TE scattering by a conducting strip loaded by a circular dielectric cylinder was presented by Karunaratne et al. [15] and [16]. They restrict their solution to the case of radial orientation of the strip with respect to the dielectric cylinder center. They employed the integral equation formulation along with the moment method in solving this problem.

Two major objectives are addressed in the present paper. The first is to show the application of the addition theorem of Mathieu to Bessel function and vice versa. The second is to solve a mixed objects problem such as a dielectric cylinder and perfectly conducting strip as multiple scattering problem. The restriction in [15] has been released in our work and the conducting strip can take any orientation. An exact analytical solution based on boundary value method along with an approximate

Submitted On: August 14, 2018
Accepted On: February 13, 2019

solution based on the technique in [4] of a plane electromagnetic wave incident a dielectric circular cylinder near a conducting strip are considered.

II. FORMULATION OF THE PROBLEM

Figure 1 shows the cross sections of an infinitely long dielectric circular cylinder near a conducting strip of infinite length with their axes parallel to the *z*-axis. The conducting strip has a width $2d$ and the dielectric cylinder has radius a and permittivity ε. The center of the of dielectric circular cylinder is located at the origin of the global coordinates $(\rho,\ \phi, z)$. In addition to the global coordinate system, a local coordinates (u, v, z) is defined at the center of the conducting strip which is located at $(\rho = b,\ \phi = 0)$.

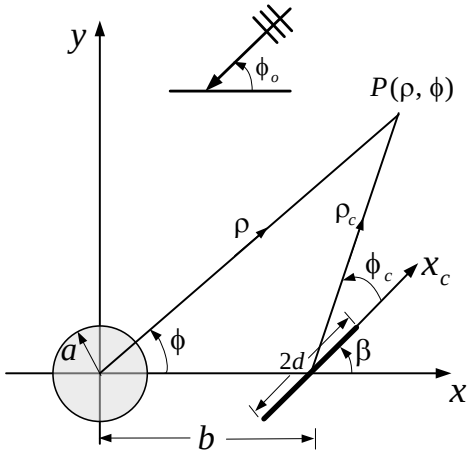

Fig. 1. Geometry of the problem.

A plane wave, with $e^{j\omega t}$ time dependence, is incident with an angle ϕ_o with respect to the *x*-axis of the global coordinate system and polarized in *z*-direction:

$$E_z^i = e^{-jk_o\rho\cos(\phi-\phi_o)}, \tag{1}$$

where k_o is the wave number of free space. The incident wave can be expressed in terms elliptic wave function of the local coordinates at the center of the conducting strip:

$$E_z^{inc} = \sqrt{8\pi}\, e^{-jk_o b\cos\phi_o} \sum_{n=0}^{\infty} j^{-n} \left[\frac{Je_n(h,\zeta_c)\ \ Se_n(h,\eta_c)\, Se_n(h,\cos\phi_{01})}{N_n^{(e)}(h)} + \frac{Jo_n(h,\zeta_c)\, So_n(h,\eta_c) So_n(h,\cos\phi_{01})}{N_n^{(o)}(h)}\right], \tag{2}$$

where

$$\phi_{01} = \phi_o - \beta.$$

$Je_n(h,\zeta_c)$ and $Jo_n(h,\zeta_c)$ are respectively the even and the odd modified Mathieu functions of the first kind and order *n*. Also, $Se_n(h,\eta_c)$ and $So_n(h,\eta_c)$ are respectively the even and the odd angular Mathieu functions of order *n*. $N_n^{(e)}(h)$ and $N_n^{(o)}(h)$ are normalized functions. The arguments of the Mathieu functions are $h = k_o d$, and $\eta = \cos v$, where u and v are elliptical cylindrical coordinates defined by:

$$x = d\ \cosh u \cos v, \quad y = d\ \cosh u \sin v. \tag{3}$$

The incident wave is also expanded in terms of Bessel functions of the circular cylindrical coordinates:

$$E_z^{inc} = \sum_{n=0}^{\infty} 2\kappa_n j^{-n} J_n(k_o\rho)\cos n(\phi-\phi_o), \qquad \kappa_n = \begin{cases} 0.5 & n=0 \\ 1 & n>0 \end{cases}. \tag{4}$$

The scattered field from the conducting strips can be expressed in terms of local coordinates as:

$$E_z^{ss} = \sqrt{8\pi}\sum_{n=0}^{\infty} A_n\, He_n^{(1)}(h,\zeta_c)\, Se_n(h,\eta_c). \tag{5}$$

While, the scattered field inside the dielectric circular cylinder is given by:

$$E_z^{sci} = \sum_{n=0}^{\infty} B_n\ J_n(k\rho)\ \cos n(\phi-\phi_o), \tag{6}$$

and the scattered field outside the dielectric cylinder is given by:

$$E_z^{sco} = \sum_{n=0}^{\infty} C_n\ H_n^{(1)}(k_o\rho)\ \cos n(\phi-\phi_o). \tag{7}$$

The total field outside the dielectric cylinder is:

$$E_z^{tot} = E_z^{inc} + E_z^{ss} + E_z^{sco}, \tag{8}$$

This total field must satisfy the boundary conditions:

$$E_z^{tot} = 0, \text{ on the surface of the conducting strip,} \tag{9}$$

$$E_z^{tot} = E_z^{sci}, \text{ on the surface of dielectric cylinder,} \tag{10}$$

$$H_\phi^{tot} = H_\phi^{sci}, \text{ on the surface of dielectric cylinder.} \tag{11}$$

To apply these boundary condition E_z and E_ϕ must be expressed in terms of circular cylindrical coordinate system $(\rho,\ \phi, z)$ when applying the boundary conditions on the cylinder surface, while they must be expressed in terms of elliptical coordinates when applying boundary conditions on the strip surface. This is done using the addition theorem of Mathieu function, from elliptical to circular cylindrical coordinates is:

$$He_p^{(1)}(h,\zeta)\, Se_p(h,\eta) = \sqrt{\frac{\pi}{2}}\sum_{m=0}^{\infty}\sum_{s=0}^{\infty} \kappa_s\ (j)^{m-p}\ De_m^p(a)\, J_s(k_o\rho)\ \ R_{s,m}, \tag{12}$$

$$R_{s,m} = \left[H_{s-m}^{(1)}(k_o b)\cos(s\phi - m\beta) + (-1)^m\, H_{s+m}^{(1)}(k_o b)\cos(s\phi + m\beta)\right],$$

and from circular cylindrical to elliptical coordinates is:

$$H_n^{(1)}(k_o\rho)\, cosn(\phi-\phi_0) = \sum_{\ell=0}^{\infty} W_{\ell,n}\, Je_\ell(h,\zeta_c)\, Se_\ell(h,\eta_c) + \sum_{\ell=1}^{\infty} X_{\ell,n}\ Jo_\ell(h,\zeta_c)\, So_\ell(h,\eta_c) \tag{13}$$

$$W_{\ell,n} = \frac{\sqrt{2\pi}}{N_\ell^{(e)}(a_1)}\ \sum_{s=0}^{\infty} (j)^{(\ell-s)}\, De_s^\ell(a_1)\, N_{n,s}\ ,$$

$$N_{n,s} = H_{n+s}^{(i)}(kb)\cos(s\beta + n\phi_0) + (-1)^s H_{n-s}^{(i)}(kb)\cos(s\beta - n\phi_0),$$

$$X_{\ell,n} = \frac{\sqrt{2\pi}}{N_\ell^{(o)}(a_1)}\sum_{s=1}^{\infty} (j)^{(\ell-s)}\, Do_s^\ell(a_1)$$

$$\{H_{n-s}^{(i)}(kb)\sin(s\beta - n\phi_0) + (-1)^s H_{n+s}^{(i)}(kb)\sin(s\beta + n\phi_0)\}.$$

Employing equation (13) into (7) and applying boundary condition (9), at $\zeta_c = 1$, then multiplying both sides of the resulting equation by $Se_m(h,\eta_c)$ and integrate

over v from 0 to 2π, we obtain:

$$A_n = -\frac{Je_n(h,1)}{He_n^{(1)}(h,1)}\left(\frac{j^{-n}\ e^{-jkbcos\phi_o}}{N_n^{(e)}(h)}\right.$$
$$\left. Se_n(h,cos\phi_{01}) + \frac{1}{\sqrt{8\pi}}\sum_{p=0}^{\infty} C_p W_{n,p}\right). \quad (14)$$

Employing (12) into (5), and applying Boundary condition (10), then multiplying both sides of the resulting equation by $cosm\phi$ and integrating over ϕ from 0 to 2π, we obtain:

$$2j^{-m}\, J_m(k_o a)\cos(m\phi_o) + 2\pi J_m(k_o a)$$
$$\sum_{n=0}^{\infty} A_n \sum_{p=0}^{\infty} (j)^{p-n} De_p^n(h)\ M_{m,p} + C_m\, \chi_m\, H_m^{(1)}(k_o a)$$
$$\cos(m\phi_o) = \chi_m\, B_m\ \cos(m\phi_o)\, J_m(ka),$$
$$\chi_m = \begin{cases} 2 & m = 0 \\ 1 & m > 0 \end{cases}, \quad (15)$$
$$M_{m,p} = \left[H_{m-p}^{(1)}(k_o b) + (-1)^p\, H_{m+p}^{(1)}(k_o b)\right]\cos(p\beta).$$

To apply the boundary condition $H_\phi^{tot} = H_\phi^{sci}$ on the surface of the dielectric cylinder, one must obtain H_ϕ^{inc}, H_ϕ^{ss}, and H_ϕ^{sci}, using, $H_\phi = \frac{-j\omega\varepsilon}{k^2}\frac{\partial E_z}{\partial \rho}$.

Applying boundary condition (11), we obtain:

$$2j^{-m}\, J_m'(k_o a)\ \cos(m\phi_o) + 2\pi\, J_m'(k_o a)$$
$$\sum_{n=0}^{\infty} A_n \sum_{p=0}^{\infty} (j)^{(p-n)} De_p^n$$
$$+C_m \chi_m\ H_n^{(1)'}(k_o a)\cos(m\phi_o)$$
$$= \sqrt{\varepsilon_r}\ B_m\ \cos(m\phi_o)\,\chi_m\ J_m'(ka). \quad (16)$$

From equations (14), (15) and (16), one can get:

$$[Z][C] = [G], \quad (17)$$
$$z_{i,j} = \sqrt{\frac{\pi}{2}}\frac{JJ_i(\varepsilon_r,a)}{JH_i(\varepsilon_r,a)}\sum_{n=0}^{\infty}\frac{Je_n(h,1)}{He_n^{(1)}(h,1)} W_{n,j}$$
$$\sum_{s=0}^{\infty} (j)^{(s-n)}\ De_s^n(h) M_{i,s}, \quad (18)$$
$$z_{i,i} = \chi_i\ \cos(i\phi_o)$$
$$+\sqrt{\frac{\pi}{2}}\frac{JJ_i(\varepsilon_r,a)}{JH_i(\varepsilon_r,a)}\sum_{n=0}^{\infty}\frac{Je_n(h,1)}{He_n^{(1)}(h,1)}$$
$$W_{n,i}\sum_{\ell s=0}^{\infty} (j)^{(s-n)}\ De_s^n(h) M_{i,s}, \quad (19)$$
$$g_m = 2j^{-m}\ \cos(m\phi_o)\frac{JJ_m(\varepsilon_r,a)}{JH_m(\varepsilon_r,a)}$$
$$-2\pi\frac{JJ_m(\varepsilon_r,a)}{JH_m(\varepsilon_r,a)}\sum_{n=0}^{\infty}\frac{Je_n(h,1)}{He_n^{(1)}(h,1)}\frac{e^{-jkbcos\phi_o}\ j^{-n}}{N_n^{(e)}(h)}$$
$$Se_n(h,cos\phi_{01})\sum_{s=0}^{\infty} (j)^{(s-n)}\ De_s^n(h) M_{m,s}, \quad (20)$$
$$JJ_m(\varepsilon_r,a) = J_m(ka)\, J_m'(k_o a) - \sqrt{\varepsilon_r}\, J_m(k_o a)\, J_m'(ka), \quad (21)$$
$$JH_m(\varepsilon_r,a) = \sqrt{\varepsilon_r}\, H_m^{(1)}(k_o a)\, J_m'(ka) - H_m^{(1)'}(k_o a)\, J_m(ka), \quad (22)$$

The scattered electric field in the outer region can be obtain from (7), by employing asymptotic Hankel function expression $H_m^{(1)}(k_o\rho) = \frac{1}{\sqrt{k_o\rho}}\, e^{j(k_o\rho - (\frac{(2m+1)}{4})\pi)}$, as:

$$E_z^{totsc} = \sqrt{\frac{2}{\pi}}\frac{e^{jk_o\rho}}{\sqrt{k_o\rho}}\, e^{-j\pi/4)}\, P(\phi) = c(k_o\rho)P(\phi), \quad (23)$$
$$P(\phi) = 2\pi e^{-jk_o b\, cos\phi}\sum_{n=0}^{\infty} A_n(-j)^n\, Se_n(h,\cos(\phi-\beta))$$
$$+\sqrt{\frac{\pi}{2}}\sum_{n=0}^{\infty} C_n(-j)^n\cos n(\phi-\phi_o), \quad (24)$$

III. APROXIMATE SOLUTION

The approximate solution follows the technique that was established by Karp and Russek [4]. To apply this technique one needs to obtain the far scattered field from conducting strip and the dielectric cylinder due to both plane wave and line source excitations. Although this solution is approximate, it produces accurate results and it is much easier to compute compared to the exact solution. This is because it doesn't have matrix equation to form and solve like the exact solution.

A. Plane wave excitation of the conducting strip

Consider the plane wave of equation (2), is incident on the conducting strip. The scattered field from the conducting strip is expressed in equation (5).

Applying the boundary conditions on the conducting strip surface and multiplying both sides of the resulting equation by $Se_n(h,\eta_c)$ and integrating over ν_i from 0 to 2π, one obtains:

$$A_m = -j^{-m}\, e^{-jk_o b\, cos\phi_o}\frac{Je_m(h,1)\, Se_m(h,cos\phi_{01})}{He_m^{(1)}(h,1)N_m^{(e)}(h)}. \quad (25)$$

Once the coefficients are calculated the scattered electric field in the outer region is given by Equation (7). Since $He_m^{(1)}(h,\zeta) = \frac{1}{\sqrt{h\zeta}}\, e^{j(h\zeta - (\frac{2m+1}{4})\pi)}$ and for large $h\zeta$ it can be represented in terms of circular cylindrical coordinates ($h\zeta = k_o\rho_c$). In this case the total scattered field is given by:

$$E_z^{(s)} = c(k_o\rho_c)\, f_s(h,b,\phi_c,\phi_o), \quad (26)$$
$$f_s(h,b,\phi_c,\phi_o) = 2\pi\sum_{n=0}^{\infty}(-j)^n\ A_n Se_n(h,cos\phi_c). \quad (27)$$

B. Line source excitation of the conducting strip

Consider a line source of unit intensity placed at (x_0, y_0) with respect to the coordinates at the center of the conducting strip, then the z-component of the electric field due to such a line source can be expressed as:

$$E_z^{inc} = 4\left[\sum_{m=0}^{\infty}\frac{Se_m(h,\eta_0)}{N_m^{(e)}(h)} Se_m(h,\eta)\right.$$
$$\left\{\begin{matrix} Je_m(h,\zeta_0)\, He_m^{(1)}(h,\zeta) \\ Je_m(h,\zeta) He_m^{(1)}(h,\zeta_0)\end{matrix}\right. + \frac{So_m(h,\eta_0)}{N_m^{(o)}(h)} So_n(h,\eta)$$
$$\left.\left\{\begin{matrix} Jo_m(h,\zeta_0)\, Ho_m^{(1)}(h,\zeta) & u > u_0 \\ Jo_m(h,\zeta)\, Ho_m^{(1)}(h,\zeta_0) & u < u_0\end{matrix}\right.\right], \quad (28)$$
$$\zeta_0 = \left[\frac{1}{2}\left(\frac{s_0^2}{d^2}+1\right) + \left(\frac{1}{4}\left(\frac{s_0^2}{d^2}+1\right)^2 - \frac{x_0^2}{d^2}\right)^{1/2}\right]^{1/2}, \quad (29)$$
$$\eta_0 = \frac{x_0}{\zeta_0 d}, \quad \psi_0 = tan^{-1}\left[\frac{y_0}{x_0}\right], \quad (30)$$
$$s_0 = ((x_0)^2 + (x_0)^2)^{1/2}. \quad (31)$$

The scattered field from the strip can be written as:

$$E_z^{(s)} = 4\sum_{n=0}^{\infty} D_n\, He_n^{(1)}(h,\zeta)\, Se_n(h,\eta). \quad (32)$$

Matching the boundary condition corresponding to

E_z and multiply both sides of the resulting equation by $Se_m(h,\eta)$ and integrating over v_i from 0 to 2π, we get:

$$D_n = -\frac{He_n^{(1)}(h,\zeta_0)\,Je_n(h,1)\,Se_n(h,\eta_0)}{He_n^{(1)}(h,1)\;N_n^{(e)}(h)}. \quad (33)$$

Once the coefficients are calculated the scattered electric field in the outer region is:

$$E_z^{(z)} = c(k_o\rho_c)\,g_s(h,\phi_c,\zeta_0,\eta_0), \quad (34)$$

where

$$g_s(h,\phi_c,\zeta_0,\eta_0) = \sqrt{8\pi}\sum_{n=0}^{\infty} j^{-n}\,D_n\,Se_n(h,cos\phi_c). \quad (35)$$

C. Plane wave excitation of the dielectric cylinder

The plane wave of equation (1) is considered incident on the dielectric cylinder, which can be expanded as in equation (4). The scattered field inside the dielectric circular cylinder is given by equation (6) while the scattered field outside the dielectric cylinder is given by equation (7). The total field outside the dielectric cylinder is:

$$E_z^{tot} = E_z^{inc} + E_z^{sco}. \quad (36)$$

This total field must satisfy the boundary conditions: $E_z^{tot} = E_z^{sci}$ and $H_\phi^{tot} = H_\phi^{sci}$, on the surface of the dielectric cylinder. Applying these boundary condition:

$$j^{-n}J_n(k_oa) + \chi_m\,C_n\,H_n^{(1)}(k_oa) = \chi_m B_n\,J_n(ka), \quad (37)$$

$$j^{-n}J'_n(k_oa) + \chi_m\,C_n\,H_n^{(1)\prime}(k_oa) = \chi_m B_n\,\sqrt{\varepsilon_r}\,J'_n(ka). \quad (38)$$

Solving (37) and (38), we obtain:

$$C_n = \frac{j^{-n}\left(\sqrt{\varepsilon_r}\,J_n(k_oa)\,J'_n(ka) - J'_n(k_oa)J_n(ka)\right)}{\chi_m\left(J_n(ka)\,H_n^{(1)\prime}(k_oa) - \sqrt{\varepsilon_r}\,J'_n(ka)\,H_n^{(1)}(k_oa)\right)}. \quad (39)$$

Once the coefficients are calculated the scattered electric field in the outer region is:

$$E_z^{(s)} = c(k_o\rho)\,f_c(a,\varepsilon_r,\phi,\phi_o), \quad (40)$$

$$f_c(a,\varepsilon_r,\phi,\phi_o) = \sqrt{\frac{\pi}{2}}\sum_{n=0}^{\infty}(-j)^n C_n\,cosn(\phi-\phi_o). \quad (41)$$

D. Line source excitation of the dielectric cylinder

Consider a line source of unit intensity placed at (ρ_0,ϕ_0) with respect to the coordinates at the center of the conducting strip, the z-component of the electric field due to such a line source can be expressed as:

$$E_z^{inc} = \begin{cases}\sum_{n=0}^{\infty} 2\kappa_n\,H_n^{(1)}(k_o\rho_o)\,J_n(k_o\rho)cosn(\phi-\phi_o) & ,\rho<\rho_o\\ \sum_{n=0}^{\infty} 2\kappa_n\,H_n^{(1)}(k_o\rho)\,J_n(k_o\rho_o)cosn(\phi-\phi_o) & ,\rho>\rho_o\end{cases}. \quad (42)$$

The scattered field inside the dielectric circular cylinder is given equation (6), while the scattered field outside the dielectric cylinder is given by:

$$E_z^{sco} = \sum_{n=0}^{\infty} F_n\,H_n^{(1)}(k_o\rho)\,cosn(\phi-\phi_o). \quad (43)$$

Applying boundary conditions (37), and (38), gives:

$$F_n = \frac{\left(\sqrt{\varepsilon_r}\,J_n(k_oa)\,J'_n(ka) - J'_n(k_oa)J_n(ka)\right)}{\chi_m\left(J_n(ka)\,H_n^{(1)\prime}(k_oa) - \sqrt{\varepsilon_r}\,J'_n(ka)\,H_n^{(1)}(k_oa)\right)}\,H_n^{(1)}(k_o\rho_o). \quad (44)$$

Once the coefficients are calculated the scattered electric field in the outer region is:

$$E_z^{(s)} = c(k_o\rho)\,g_c(a,\varepsilon_r,\phi,\rho_o,\phi_o), \quad (45)$$

$$g_c(a,\varepsilon_r,\phi,\rho_o,\phi_o) = \sqrt{\frac{\pi}{2}}\sum_{n=0}^{\infty}(-j)^n\,F_n\,cosn(\phi-\phi_o). \quad (46)$$

Now consider the problem of the dielectric cylinder and the conducting strip shown in Fig. 1. Assuming a fictitious line source C_2 at the center of the conducting strip, the far scattered field from the dielectric cylinder is:

$$E^{sc} = c(k_o\rho)\,[f_c(a,\varepsilon_r,\phi,\phi_o) + C_2 g_c(a,\varepsilon_r,\phi,b,0)]. \quad (47)$$

The partial scattered field from the conducting strip can be determined in two ways. The first at $\phi = 0$, the value of $E^{sc}[c(k_o\rho)]^{-1}$ can be considered as the intensity of a line source times the response (43), i.e.,

$$E^{sc} = c(k_o\rho)\,[f_c(a,\varepsilon_r,\phi,\phi_o) + C_2 g_c(a,\varepsilon_r,\phi,b,0)]\;g_s(h,\phi_c,\zeta_0,\eta_0). \quad (47)$$

Second, this partial scattered field is given by:

$$E^{pss} = c(k_o\rho_c)\;C_1\,g_s(h,\phi_c,\zeta_0,\eta_0). \quad (48)$$

From (43) and (44):

$$C_1 = f_c(a,\varepsilon_r,0,\phi_o) + C_2 g_c(a,\varepsilon_r,0,b,0). \quad (49)$$

Similarly, the far scattered field from the conducting strip due to the fictitious line source C_1 and incident plane wave is given by:

$$E^{ss} = c(k_o\rho_c)\,[f_s(a,b,\phi_c,\phi_{01}) + C_1 g_s(h,\phi_c,\zeta_{0c},\eta_{0c}). \quad (50)$$

The partial scattered field from the dielectric cylinder can be determined in two ways. The first at $\phi_c = \pi - \beta$, the value of $E^{ss}[c(k_o\rho_c)]^{-1}$ can be considered as the intensity of a line source times the response (46), i.e.,

$$E^{psc} = c(k_o\rho)\,[f_s(h,b,(\pi-\beta),\phi_{01}) + C_1 g_s(h,(\pi-\beta),\zeta_{0c},\eta_{0c})]\;g_c(a,\varepsilon_r,\phi,\rho_0,\phi_0). \quad (51)$$

Second, this partial scattered field is given by:

$$E^{psc} = c(k_o\rho)\;C_2\;g_c(a,\varepsilon_r,\phi,\rho_0,\phi_0). \quad (52)$$

From (70) and (71), one can obtain:

$$C_2 = f_s\big((h,b,(\pi-\beta),\phi_{01})\big) + C_1\,g_c(h,(\pi-\beta),\zeta_{0c},\eta_{0c}). \quad (53)$$

From (49) into (53):

$$C_1 = \frac{f_c(a,\varepsilon_r,0,\phi_0) + f_s(h,b,(\pi-\beta),\phi_{01})g_c(a,\varepsilon_r,0,b,0)}{1-g_s(h,(\pi-\beta),\zeta_{0c},\eta_{0c})g_c(a,\varepsilon_r,0,b,0)}.$$

Once C_1 and C_2 are obtained, one can determine the z-component of the total scattered field from the present system as:

$$E_z^s = c(k_o\rho)P(\phi), \quad (54)$$

$$P(\phi) = f_c(a,\varepsilon_r,\phi,\phi_0) + C_2 g_c(a,\varepsilon_r,\phi,b,0) + e^{-jk_ob\,cos\phi}\,[\,f_s(h,b,(\phi-\beta),\phi_{01}) + C_1 g_s(h,(\phi-\beta),\zeta_{0c},\eta_{0c}\,)]. \quad (55)$$

The plane wave scattering properties of a two-dimensional body of infinite length are conveniently described in terms of the echo width, i.e.,

$$W(\phi) = \frac{4}{k}|P(\phi)|^2. \quad (56)$$

IV. RESULTS AND DISCUSSION

In order to check our computational accuracy our results for both exact and approximate solution are compared with the published data b Karunaratne et al. [15]. In this example, $a = 0.5\ \lambda$, $d = 0.25\ \lambda$, $b = 0.75\ \lambda$, $\beta = 0^o$, $\varepsilon_r = 4.0$, and $\phi_o = 90^o$. Results shown in Fig. 2 corresponding to this case are in excellent agreement compared with those of the same case published in [15].

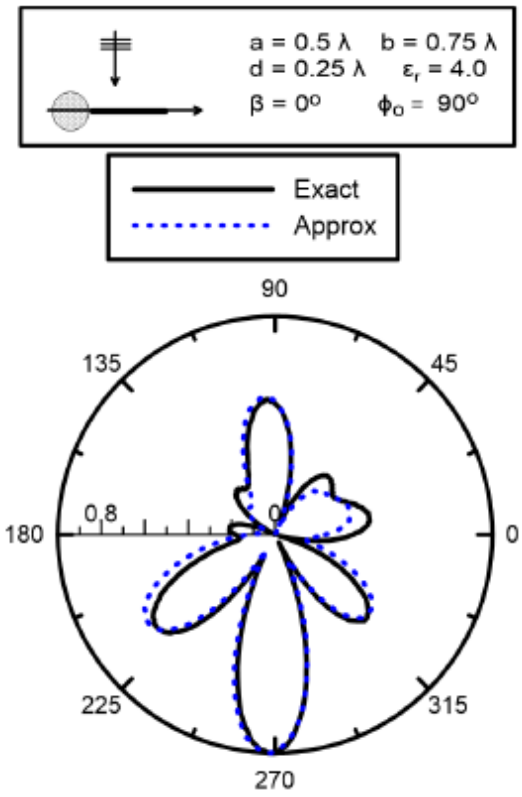

Fig. 2. Normalized far field pattern of a plane wave scattered by dielectric cylinder touching a conducting strip.

The results presented next are for some cases of different directions of the incident wave and different orientation of the conducting strip. Both methods presented earlier are used in our calculations of the normalized far field pattern for each case. In general excellent agreement for both methods is noticed. The first case is of a plane wave normally incident on a dielectric cylinder and conducting strip with $\beta = 0^o$. As can be seen from Fig. 3 the forward and backscattering echo widths are similar. Results of both methods agrees very well here at all angles. As the conducting strip orientation changes to $\beta = 20^o$ keeping the same direction of the incident wave at $\phi_o = 90^o$, the scattering field in the forward direction is changed as shown in Fig. 4. All other parameters in first and second case are kept the same as illustrated in Figs. 3 and 4.

The scattering field was calculated again for different conducting strip orientation in order to show the effect of the orientation on the forward and backscattering fields. Figure 5 illustrates three cases of the echo width scattering pattern at $\beta = 0^o$, $\beta = 45^o$, and $\beta = 90^o$, respectively. As one can see from Fig. 5, the forward scattered field is forming more lobes as β increases while the backscattered field is decreasing. That shows there is a substantial change in the forward and backscattering fields with the change of the conducting strip orientation.

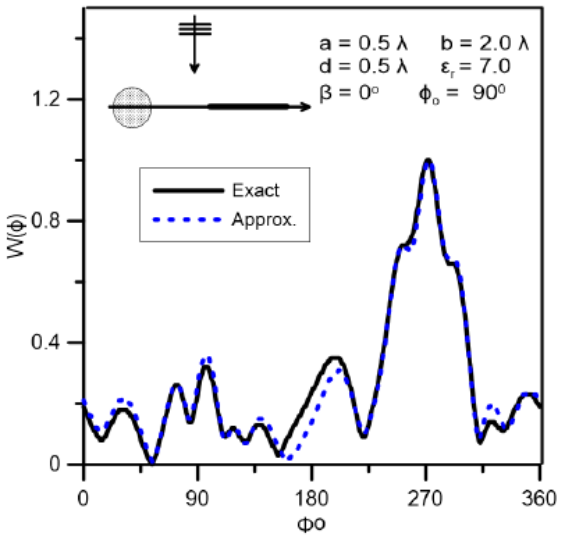

Fig. 3. Normalized far field pattern of a plane wave scattered by dielectric cylinder near a horizontal conducting strip.

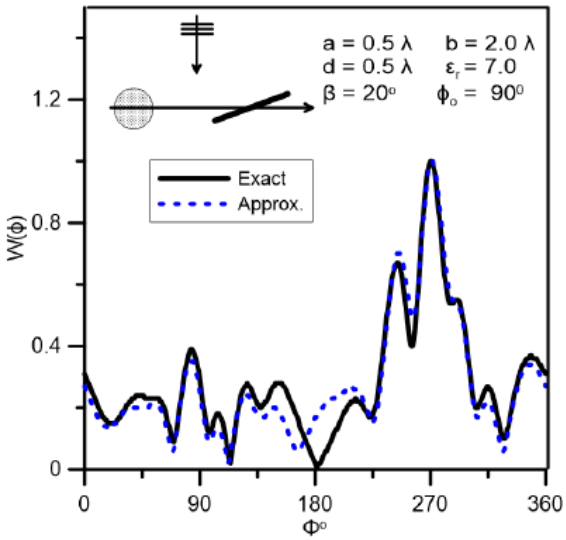

Fig. 4. Normalized far field pattern of a plane wave scattered by dielectric cylinder near a tilted conducting strip.

The direction of the incident wave is changes in the following two cases. Firstly, we are taking $\phi_o = 0^o$, and considering $\beta = 90^o$ in which the conducting strip is facing the incident plane wave followed by the dielectric cylinder. As shown in Fig. 6, the pattern shows a maximum forward scattered field while the backscattered field is minimal.

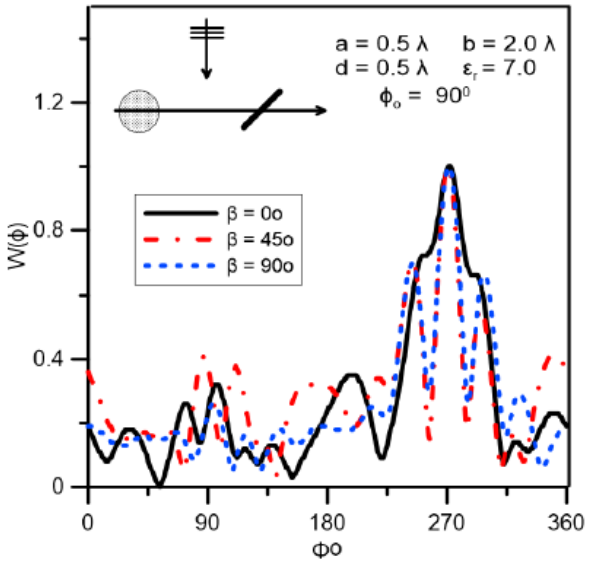

Fig. 5. Normalized far field pattern of a plane wave scattered by dielectric cylinder near a tilted conducting strip at different tilt angles.

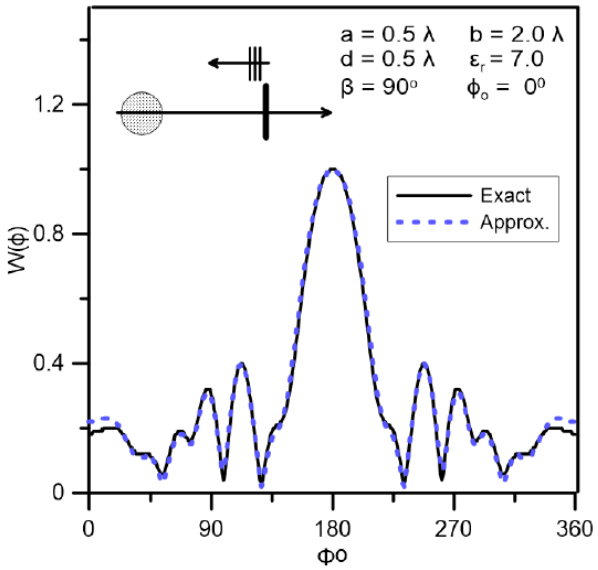

Fig. 6. Normalized far field pattern of a plane wave scattered by dielectric cylinder near a vertical conducting strip.

Secondly we are taking $\phi_o = 180^o$, and considering $\beta = 90^o$ in which the dielectric cylinder is facing the incident plane wave followed by conducting strip. As shown in Fig. 7, the pattern shows a maximum forward scattering echo width while the backscattering echo width is relatively higher than the previous case.

V. CONCLUSION

Scattering of an electromagnetic wave by a dielectric cylinder in the vicinity of a conducing strips is achieved. The far field pattern of this system is illustrated for different cases of strip orientation and different directions of the incident plane wave. It is found that back scattering echo width can be minimized by placing the conducting strip facing the incident plane wave followed by the dielectric cylinder.

ACKNOWLEDGMENT

The author wishes to thank T*he British University in Egypt* for providing all the facilities required to perform this research.

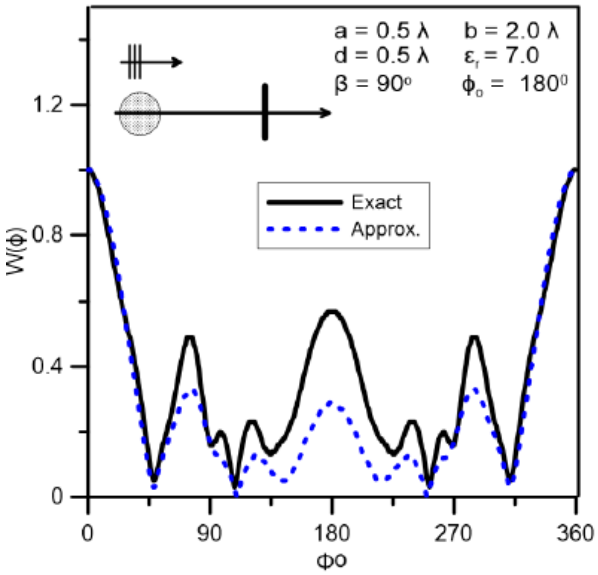

Fig. 7. Normalized far field pattern of a plane wave scattered by dielectric cylinder near a vertical conducting strip.

REFERENCES

[1] R. I. Primich, "Some electromagnetic transmission and reflection properties of a strip grating," *I. R. E. Trans. on Antennas and Propagation*, vol. 5, pp. 176-182, 1957.

[2] M. D. Arnold, "An efficient solution for scattering by perfectly conducting strip grating," *Journal of Electromagnetic Waves and Applications*, vol. 20,

no. 7, pp. 891-900, 2006.

[3] J. W. Young and J. C. Bertrand, "Multiple scattering by two cylinders," *Journal of Acoustic Society of America*, vol. 58, pp. 1190-1195, 1975.

[4] S. N. Karp and A. Russek, "Diffraction of waves by a wide slit," *Journal of Applied Phys*., vol. 27, pp. 353-361, 1956.

[5] A. Elsherbeni and M. Hamid, "Diffraction by a wide double wedge," *IEEE Trans. on Antennas and Propag*., vol. 32, pp. 1262-1264, 1984.

[6] E. B. Hansen, "The diffraction of a plane wave through two or more slits in a plane screen," *Applied Science Research*, vol. B8, pp. 73-83, 1959.

[7] H. A. Yousif and S. Kohler, "Scattering by two penetrable cylinders at oblique incidence. I. The analytical solution," *J. Opt. Soc. Am*., vol. 5, no. 7, July 1988.

[8] M. Dunster, "Electromagnetic wave scattering by two parallel infinite dielectric cylinders," *Studies in Applied Mathematics*, vol. 131, pp. 302-316, 2013.

[9] B. H. Henin, A. Z. Elsherbeni, and M. Al Sharkawy, "Oblique incidence plane wave scattering from an array of circular dielectric cylinders," *Progress In Electromagnetics Research, PIER*, 68, pp. 261-279, 2007.

[10] H. Ragheb and E. Hassan, "Multiple scattering of plane electromagnetic waves by two dielectric coated conducting strips," *2005 IEEE/ACES International Conference on Wireless Comm. and Applied Computational Electromagnetics*, Honolulu, Hawaii, USA, Apr. 3-7, 2005.

[11] B. N. Khatir and A. Sebak, "Transverse electric wave scattering by parallel metamaterial coated elliptic cylinders," *EMTS 2007 - International URSI Commission B - Electromagnetic Theory Symposium*, Ottawa, Canada, July 26-28, 2007.

[12] A. G. Kyurkchan, D. B. Demin, and N. I. Orlova, "Solution based on the pattern equation method for scattering of electromagnetic waves by objects coated with dielectric materials," *Journal of Quantitative Spectroscopy and Radiative Transfer*, vol. 106, pp. 192-202, 2007.

[13] A. G. Kyurkchan and E. A. Skorodumova, "Solving of problems of electromagnetic waves scattering by complex-shaped dielectric bodies via the pattern equations method," *Journal of Quantitative Spectroscopy and Radiative Transfer*, vol. 110, pp. 1335-1344, 2009.

[14] T. Yamasaki, "Scattering of electromagnetic waves by inhomogeneous dielectric gratings loaded with conducting strips-matrix formulation of point matching method," *2016 international Conference on Mathematical Methods in Electromagnetic Theory*, 2016.

[15] M. G. Karunaratne, K. A. Michalski, and C. M. Butler, "TM scattering from a conducting strip loaded by a dielectric cylinder", *IEE Proceedings*, vol. 132, pt. H, no. 2, pp. 115-122, Apr. 1985.

[16] M. G. Karunaratne, K. A. Michalski, and C. M. Butler, "TE scattering from a conducting strip loaded by a dielectric cylinder," *IEE Proceedings*, vol. 132, pt. H, no. 6, pp. 375-383, Oct. 1985.

Hassan Ragheb was born in Port-Said, Egypt, in 1953. He received the B.Sc. degree in Electrical Engineering from Cairo University, Egypt, in 1977 and the M.Sc. and Ph.D. degrees in Electrical Engineering from the University of Manitoba, Winnipeg, Canada, in 1984 and 1987, respectively. From 1987 to 1989, he was a Research Assistant in the Department of Electrical Engineering, University of Manitoba. From 1989 to 2016 he was with the Department of Electrical Engineering at the King Fahd University of Petroleum and Minerals, Saudi Arabia, where he was a Professor of Electrical Engineering. In January 2018 he joined the Electrical Engineering Department at the British University in Egypt where he is currently a Professor of Electrical Engineering. His research interests include electromagnetic scattering by multiple and coated objects, microstrip antennas, phased arrays, slot and open ended waveguide antennas.

Metamaterial Sensor for Transformer Oil, and Microfluidics

Mehmet Bakır [1], Muharrem Karaaslan [2], Faruk Karadag [3], Sekip Dalgac [2], Emin Ünal [2], and Oğuzhan Akgöl [2]

[1] Department of Computer Engineering
Bozok University, Yozgat, 66200, Turkey
mehmet.bakir@bozok.edu.tr

[2] Iskenderun Technical University
Department of Electrical and Electronics Engineering, Hatay, 31200, Turkey
Muharrem.karaaslan@iste.edu.tr, emin.unal@iste.edu.tr, oguzhan.akgol@iste.edu.tr

[3] Department of Physics
Cukurova University, Adana, 01030, Turkey
fkaradag.cu.edu.tr

Abstract ─ Metamaterial sensor which is composed of split square rings to operate in X band for liquid and microfluidics has been proposed in this study. For measurement and simulation, we have designed and manufactured a sample holder for easy injection and measurement of fluids. Dielectric properties of the fluid samples have been changed according to the usage time, humidity etc. Proposed structure reacts to the dielectric constants of the transformer oil or the other microfluidics by resonance frequency which is also validated by simulation and testing. While 70MHz bandwidth change in the resonance frequency for transformer oil has been observed, it dramatically increases to 210MHz and decreases to 40MHz for methanol and olive oil adulteration. Reflection coefficient measurements for clear (unused) transformer oil, methanol and olive oil along with corn oil have been performed. Tested results are generally compatible with the simulated ones. Proposed structure, can be effectively used for liquids whose dielectric constant varying from 2 to 24. Simulation study shows us that the proposed structure gives 560MHz bandwidth when clear transformer oil is replaced with acetone. Implementation of transformer oil as well as microfluidics with high quality factor is the novel side of proposed sensor study.

Index Terms ─ Industrial oil, olive oil, metamaterials, microfluidics, sensor.

I. INTRODUCTION

Permittivity of a material gives us lots of information about purity, temperature and humidity since it changes according to these environmental factors and purity. This information can easily be used for developing sensors in microwave frequencies [1-5]. For this purpose, different techniques such as resonance cavity [6], resonant/reflection or transmission [7-8] can be employed. Metamaterials which are manmade structures showing exotic properties like negative refractive index have effectively been used in antennas, cloaking, microwave absorbers, energy harvesting and sensor applications [9-15].

Sensor applications of metamaterials can be realized by taking split ring resonators (SRR) as the basis for concentrating the electromagnetic field and sensing related parameters according to the materials' complex permittivity changes. There are some studies in the literature investigating the use of metamaterials as liquid sensors. In [16], spiral shaped MTM coupled with microfluidic channel is experimentally realized and the corresponding resonance frequency shifts 150MHz according to dielectric constant changes from 25 to 75. In [17], a microwave microfluidic sensor is proposed to determine the dielectric properties of alcohol derivatives including methanol, ethanol and hexane and a maximum of 61.5MHz bandwidth is observed. In [18], a microfluidic sensor is implemented from a single SRR for purity sensing of methanol and ethanol mixtures with water. Experimental study results showed 90MHz bandwidth with a Q factor of 28. In [19], a complementary SRR type MTM is proposed and 300MHz bandwidth is obtained with considerably small Q factors. In [20], three different types of sensor applications demonstrated experimentally and numerically by utilization of microfluidic channel. In that study 200MHz bandwidth with high Q factor has been obtained.

Most MTM sensors employ the changes in resonance frequency which shifts according to the parameter which

Submitted On: July 19, 2018
Accepted On: December 25, 2018

is being sensed [21-22]. In addition to the microfluidic sensor applications, fuel adulteration and transformer oil aging sensor are another type of usage area for MTM sensors. Fuel adulteration is such a global problem especially in Asian countries where the governments applies strict polies to prevent oil adulterations which sometimes reach up to 30% [23]. Density, emission test and filter paper test methods have been implemented in sensing the fuel adulteration. These methods are laboratory based and the prices of the equipment used in these methods are high [24-25].

Measuring the dielectric properties of transformer oils used in power systems is commonly conducted. Measuring with transmission/reflection method has done for transformer oil before and after process in [26]. Transformer oil is basically the refined mineral oil which is extracted from crude oil by distillation. This oil is used as an insulator, therefore, its insulation and cooling properties are high. Having high purity and long life are also expected from transformer oils. In order to examine the characteristics of oil, complex and expensive chemical methods can be applied. Antennas designed by using microstrip structures can also be applied for transformer oil as in [27]. By varying the height of the transformer oil layer, the volume ratio between air and liquid can be changed as a function of this height. Due to the production and testing needs, this technique may not always applicable to sensor studies and it must be reconfigured when the material under test has been changed. Our method used in this study is similar to the method used in [27, 28]. Single side metamaterial is designed, simulated and tested for transformer oil. The base of these studies depends on adding particles by changing the resonance frequency.

This study has been conducted to reveal an alternative method for adulteration and transformer oil aging sensor with minimum disadvantages. In this study, we have developed a chiral MTM sensor based on square ring resonators which are placed on low loss Arlon DiClad 527 material which will be explained in the next section with details. Since waveguide boundaries present sensitive measurement with limited options, we have also developed a sensor layer which is based on a method initially used for measuring dielectric constant of materials in 2003 [28]. Variation in sensor layer's dielectric characteristics results in a resonance shift in reflectance of the proposed chiral metamaterial. Therefore, frequency shifts measured from reflectance pattern can be used for sensing physical and biological parameters of the samples placed in the sensor layer. By utilization of this sensor layer, we have succeeded practical, sensitive and fast measurements for transformer oil aging and fuel adulterations. Our study differs from the mentioned studies with the fact that it has a greater quality factor and shows wider application areas as microfluidic sensing of methanol, acetone and olive oil.

Organization of the study is as follows, design and materials along with the sensor layer is introduced in Section 2. In Section 3, numerical and experimental findings have been presented. The obtained results are discussed in Section 4.

II. THEORY, DESIGN AND NUMERICAL SETUP

In microwave characterization of the metamaterial based sensor applications, resonance cavity [29], proximity [30] and waveguide [31] methods are frequently used. When a material with known dielectric constant is placed into the sensor layer for characterization, the capacitance decreases or increases. In all three methods, when a material with given permittivity is placed into the sensor for characterization, a capacitor effect is created [20] which is directly related to the size of the sample holder. Due to the capacitive effects of a material placed in a sample holder, resonance frequency shifts to the upper or lower frequencies according to the material' complex permittivity values. Our proposal in this study is waveguide based since developed sample holder is complying with X band WR90 waveguide. When we compare the proposed structure with similar waveguide based studies as in [27,28], our proposed structure has a wider bandwidth and a greater quality factor which are important parameters for sensor applications since similar structures are compatible for only dielectric constant values varying between 1-3. When different materials such as methanol, acetone, petrol, diesel or transformer oil are considered, the resonance frequency is expected to shift lower or higher frequencies according to the material's complex permittivity values. In order to explain sensor usage of the proposed structure, we have initially measured the complex permittivity values of materials by using 85070E dielectric probe kit which is employed with the vector network analyzer. The samples were then placed into the sample holder and the reflection coefficients of the samples were measured. After having both reflection coefficient and complex permittivity values, we entered the obtained information about the materials and microfluidics into the electromagnetic simulation software to design the sensor structure. Fluid materials inside the sample holder are sensitive to the frequency due to its complex permittivity values. As the frequency increases, the effects of the material become more visible compared to the lower frequencies. For this reason, we have decided to work in X band which is between 8GHz and 12 GHz where the mentioned effects are more visible.

In this study, chiral shaped metamaterial that has nested split square resonators is placed on low loss Arlon DiClad 527 material having a dielectric constant of 2.5 and loss tangent of 0.0022. Nested square split rings have 135° angle difference in order to increase the mutual

capacitance and inductance effects. As shown in Fig. 1 (b), back side resonators have different angles from the front side resonators. This design is especially chosen by simulation studies for maximum sensitivity. Resonators on back and front side are composed of copper that has a thickness of 0.035mm and conductivity of 5.8 x 10^6 S/m. Dimensions of the proposed structure is given in Fig. 1 (c). As briefly shown in Fig. 1 (d), the front and back side of the waveguide sample holder was closed with 25µm kapton film which was also added to simulation to simulate accurately as in experimental conditions.

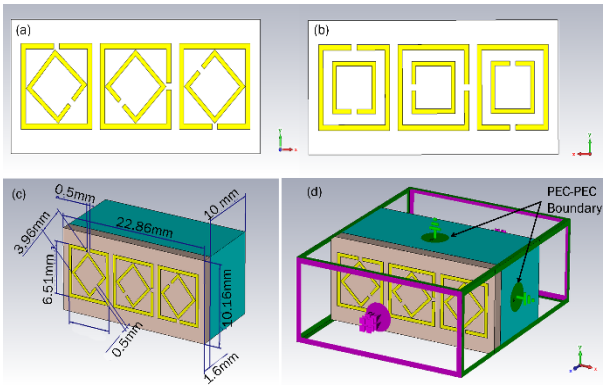

Fig. 1. Proposed structure: (a) front view, (b) back view, (c) dimensions of the structure, and (d) PEC-PEC boundary conditions.

Transformer oil and alcohol derivatives were placed in the sensor layer and outputs were read by a vector network analyzer. For this reason, all measurement system can be accepted as non-destructive and real time. Metamaterial sensor outputs are directly affected from the material's dielectric constant which is placed inside the sensor layer. For best sensitivity, sensor dimensions are optimized for X band operation. After the design phase, we manufactured the proposed structure by using LPKF Laser & Electronic AG, Promat E33 model Computerized Numerical Control (CNC) and printed circuit board (PCB) machine as presented in Fig. 2 (a). For sample placement and measurements, sample holder was produced by the same materials with WR90 waveguides in order to decrease physical effects during measurements. Manufactured sample holder seen in Fig. 2 (b) has a thickness of 10 mm and is placed between a WR90 waveguide and a corresponding adaptor as shown in Fig. 2 (d). Complex permittivity measurements in this study has been performed by employing 85070E dielectric probe kit as shown in Fig. 2 (c) after a complete calibration using pure water, air and a calibration kit associated with the probe. The complete measurement setup is given in Fig. 2 (d).

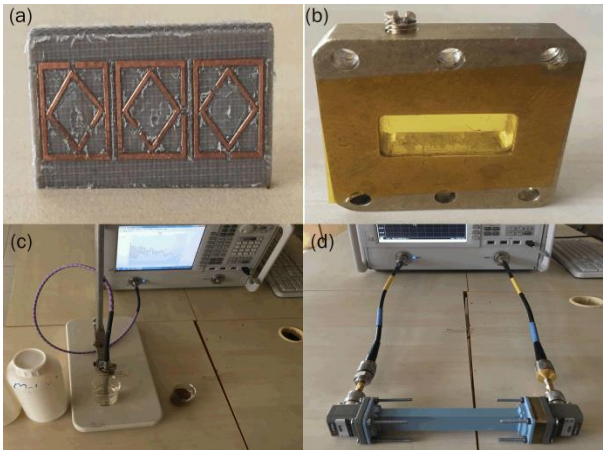

Fig. 2. (a) Manufactured CMS structure by using LPKF E-33 CNC machine (front side), (b) sample holder and kapton film which is used to prevent leakage from sample holder, (c) measurement of dielectric constant of new (left side) and used (right) side by using 85070E dielectric measurement kit, and (d) S11 reflection coefficient measurement picture.

The complex permittivity can have real and imaginary components, such that $\varepsilon=\varepsilon'-j\varepsilon''$. Thus, the loss tangent is defined as the ratio of the imaginary to real part of the complex permittivity ($\delta=\varepsilon''/\varepsilon'$). In this study, permittivity and loss tangent of the samples which are going to be tested in X- band, obtained from Agilent 85070E Dielectric probe kit. In order to prevent calibration and test errors, calibration process has been performed according the current state of art in X band.

Open-ended coaxial probe (OCP) method is currently one of the most popular techniques for measuring the complex dielectric permittivity of many materials. Non-destructive, broadband (RF and microwave ranges), and high-temperature measurements can be performed with this method using commercially available dielectric probe kits. Its well-developed theory makes it possible to obtain sufficiently accurate results for both medium-loss and high-loss media

S-parameters describe the relationship between the input and output ports and they can be used in the sensor applications of metamaterials [27-28]. In this study, we used S11 parameter also known as the return loss which refers to the reflection coefficient parameter (port 1 to port 1) with time gating experimentally measured by a Vector network analyzer (VNA). S_{11} parameter was utilized for validation of transformer oil fuel status and fuel adulteration sensing by using TE polarization mode which is the propagation mode where the electric field is normal (transverse) to the incident wave.

Our sensor is based on a waveguide design and it is

suitable for materials with low dielectric constants about 1.8 to 2.6 in our case. The experimental studies were conducted by placing different materials with different dielectric constants according to its physical properties such as purity. Resonance frequency is measured by VNA and it was observed that this frequency shifts in terms of the dielectric constant of the material when it is placed into the sensing layer. After having a shift in the resonance frequency, we can comment about the purity or other physical properties of the sample under test. This procedures was performed for used and unused transformer oils, as well as in the gasoline and methanol purity measurements.

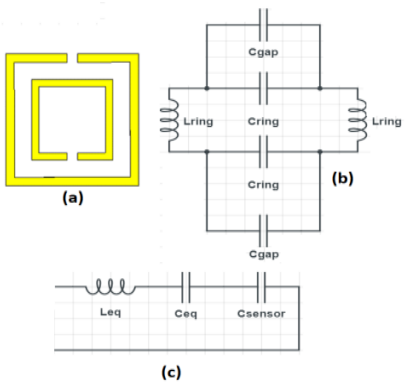

Fig. 3. Equivalent circuit diagram of the SRR.

The equivalent circuit model of the proposed sensor structure is drawn which can be seen in Fig. 3. The structure includes different passive elements labeled as Lring, Cring and Cgap. Lring represents the inductive effects of the resonator, Cring also known as capacitive effect occurs between two resonator layers and finally Cgap equals to the capacitive effect between the gaps. This equivalent circuit model is obtained based on SRR types of metamaterials [32]. In addition, the sensor layer which is placed at the back side of the structure creates capacitive effect on the structure. The final equivalent circuit diagram contains serially connected passive elements called as Leq, Ceq and Csensor and the final diagram is given in Fig. 3 (c):

$$\boldsymbol{C_{tot}}:\boldsymbol{C_0}+\boldsymbol{C_{eq}}+\boldsymbol{\varepsilon_{samp}}\boldsymbol{c_{sens}}. \quad (1)$$

$\boldsymbol{C_0}$ is the environmental capacitive effect which is formed due to the air and dielectric layer. In addition, Ceq is the total capacitive value of the resonator layer. Furthermore, $\boldsymbol{\varepsilon_{samp}}\boldsymbol{C_{sens}}$ is the capacitice effect of the sensor layer placed at the back side of the structure. That capacitive effect will change with the help of inserting different types of dielectric values ($\boldsymbol{\varepsilon' + \varepsilon''}$) of material. Therefore, the total capacitive effect will change leading to different resonant frequency values for the sensor layer. The corresponding resonant frequency can be expressed by:

$$f_0=1/(2\pi\sqrt{L_{tot}C_{tot}}). \quad (2)$$

III. RESULTS AND DISCUSSION

A. Transformer oil sensing application

As shown in Fig. 1, sample holder is just behind the proposed structure and the material under test which is affecting the reflection coefficient of the system. First of all, the validation is realized with clear and dark transformer oil. In this work, all simulations and experimental tests have been performed in X-band between 8GHz and 12GHz which is compatible with WR-90 standard waveguide. As shown in Fig. 4, complex permittivity of the clear oil is higher than the dark transformer oil between 8-GHz and 12GHz. The results in the Fig. 3 show that, increasing the ratio of nanoparticles decreases the complex permittivity because of the oil saturation [27].

After obtaining the complex permittivity values of the industrial oil, these data were used in the simulation software to identify the mentioned oils in the computer environment. The simulation study was then performed and the obtained results were presented in Fig. 5 with the experimental results for comparison. When clear oil was placed in the setup, the resonance frequency is observed at 8.78 GHz. After determining the resonance point for the clear oil (unused), the sample was replaced with dark transformer oil (used). In this case, the resonance frequency decreased down to 8.71GHz dramatically as expected from the simulation results. This shift is directly related with the complex permittivity values of the samples placed in sample holder. Complex permittivity is directly proportional with capacitance which is inversely proportional with resonance frequency for this setup.

Reflection coefficients of these two oil samples have been simulated and tested by CST Microwave studio and Agilent PNA series network analyzer, respectively. 70MHz difference is observed during the simulation while testing the dark (used) and clear (unused) transformer oils. Measured and simulated results of the reflection coefficient are compatible with each other and the minimum calculated quality factor is greater than 290. This value is higher than that in similar metamaterial sensor studies in literature [33-35]. Although 70MHz for dark and clear transformer oil may look small, it still provides a significant margin to distinguish the samples easily when the vector network analyzer is employed. Bandwidth is important for sensitivity of the structure and this small bandwidth is also expected from the small differences observed in complex permittivity values of clear and dark transformer oils. As seen in Fig. 4, the dielectric constant values are 2.8 and 2.7, respectively while tangent loss values remain the same. Small mismatches between simulation and tests can be seen in Fig. 4, which were caused by the calibration and test

errors of the system.

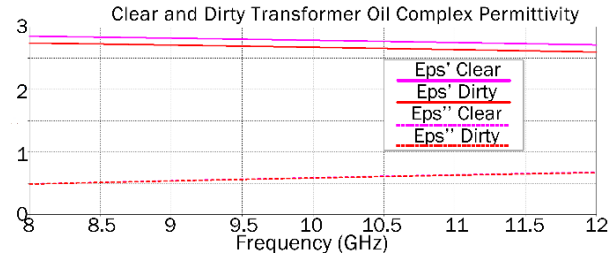

Fig. 4. Complex permittivity values of dark and clear transformer oil between 8 GHz – 12 GHz which is measured by open ended probe and 85070E dielectric measurement kit.

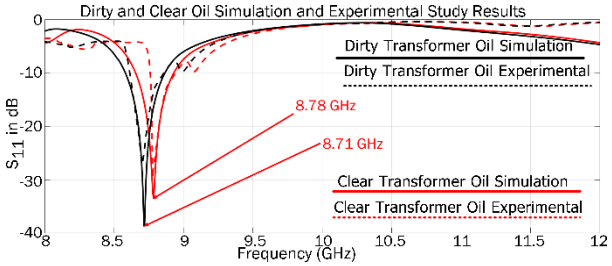

Fig. 5. Simulated and measured reflection coefficients of clear and dark transformer oil between 8GHz – 12 GHz.

In order to explain the operation principle of the proposed chiral metamaterial sensor, surface current distribution at the resonance frequency of 8.71 GHz which is belong to the used transformer oil was simulated and surface current distribution is plotted below. It is clearly understood from the Fig. 6 that the surface current generally concentrated on the resonators due to the strong magnetic fields. In addition, we can observe that parallel and anti-parallel surface current distributions take place on the resonator layers. While parallel current takes place due to the electric field, anti-parallel current occur because of the magnetic fields. This figure also explains the importance and behavior of the resonators at the resonant frequency.

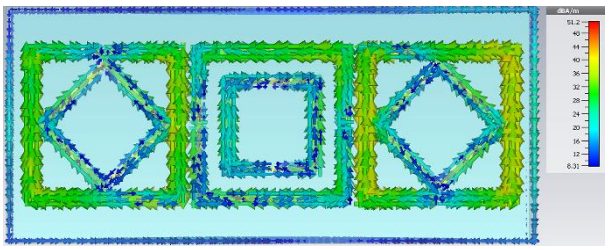

Fig. 6. Simulated surface current distribution at the resonance frequency of 8.71 GHz for used transformer oil.

B. Alcohol (microfluidic) sensing application

Another type of validation which was performed here is related with alcohols. Alcohols are particularly chosen since they are commonly used in chemical industry and to represent other microfluidics' validation. For this purpose, three different volume fractions of methanol – distilled water mixtures had been prepared. These are, pure methanol, 20% water with 80% methanol and 80% water with 20% methanol, respectively. For this setup, we have replaced the used and unused transformer oils with methanol – water mixtures to show the resonance frequency shifts. As previously performed, complex permittivity values of these samples have been measured by using 85070E dielectric measurement kit and network analyzer. Measurement results between 8GHz and 12GHz are presented in Fig. 7. Figure 7 shows a good example of Debye dielectric relaxation for methanol at 23°C with single relaxation time measured with an open-ended coaxial probe connected to a vector network analyzer. At lower frequencies, in a static region where the dipoles have time to follow the variations of the applied field, the dielectric constant of methanol mixtures which is prepared by using three different volume fractions of water and methanol reaches to maximum values. Similarly, dielectric constant values decrease in accordance with the formulas given in [36].

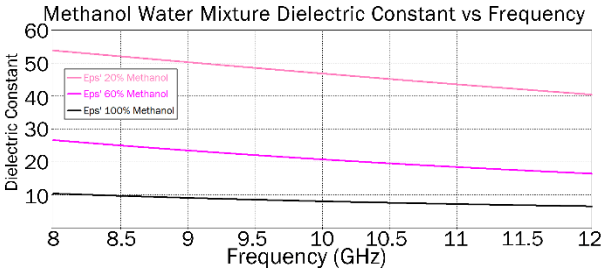

Fig. 7. Methanol & water mixture dielectric constant measurement results between 8 GHz – 12 GHz.

As seen clearly from the figure, while dielectric constant of pure methanol starts from 10, the others start from 27 and 55, respectively. Their values decrease as the frequency increases. After having complex permittivity values, the overall structure has been simulated by entering the experimentally obtained dielectric constant values to the sample holder in the computer environment. In order to validate the simulation results, we have also prepared samples for methanol and measured their reflection coefficients. The simulated and tested reflection coefficient parameters are presented in Fig. 8. As it is seen from the figure, 210MHz bandwidth is observed between pure methanol and 20% methanol. Resonance frequency for 100% methanol was obtained at 9.17 GHz, this value increased to 9.26 GHz when 20% percent distilled water added into

the methanol solution. When volume fraction of water increased to 80%, resonance frequency increased to 9.38 GHz. One of the important features of sensors is linearity and it is clearly seen from the figure that the results are linear both in simulation and the experimental testing.

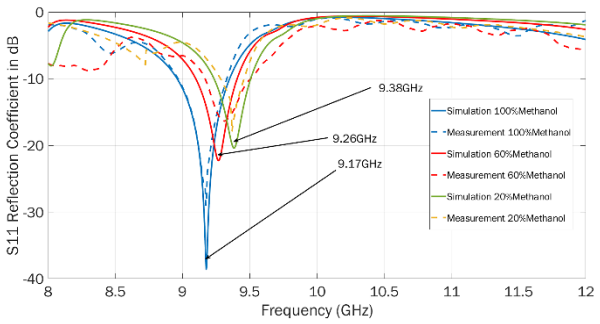

Fig. 8. S_{11} reflection coefficient measurement and simulation comparison between 8 GHz – 12 GHz for 100% volume fraction of Methanol, 60% volume fraction of methanol and 20% volume fraction of methanol with water mixture.

C. Olive oil adulteration example

Another example for the usage of the proposed metamaterial sensor is olive oil adulteration. Since the production of olive oil decreases and controversially the demand on it increases, some manufacturers mix olive oil with corn, palm, sunflower seed or other oils. In this part, we have prepared two samples; which are olive oil and corn oil. As the first step which is similar to the procedure mentioned before, we performed a complex permittivity measurement of these samples, after that we simulated and tested the reflection coefficient by using our proposed structure. As it is seen from Fig. 9, complex permittivity values of the olive oil and corn oil are very similar between 8GHz and 12GHz which is measured by calibrated 85070E dielectric probe kit. As it is seen from Fig. 7, Reel part of the complex permittivity of 100% olive oil' dielectric constant starts from 2.78 while corn oil starts from 2.6. After the experimental measurement of dielectric constant, a set of simulation and test results related to different oil samples are plotted in Fig. 10. Simulated S_{11} parameter when sample holder is filled with corn oil has the resonance frequency at 8.61 GHz while olive oil resonance frequency is observed at 8.56 GHz. Tested resonance frequencies for olive and corn oil samples are similar to the simulated ones. Small errors were observed during testing because of the laboratory environment, testing cable losses and calibration errors of the network analyzer. Compatible results with alcohol and transformer oil validations have also been observed. Losses in the simulation and testing are caused from loss tangent of the oils. Although 50MHz difference may seem to be small value for sensors, it can be sensed easily by a calibrated vector network analyzer.

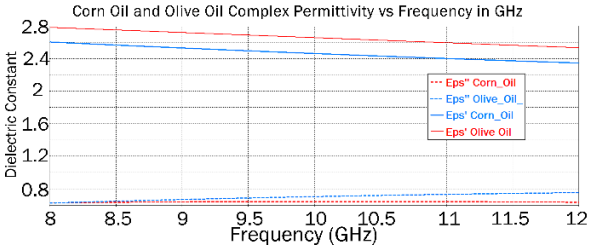

Fig. 9. Corn oil and olive oil complex permittivity measurements between 8GHz – 12 GHz by using calibrated 85070E dielectric probe kit.

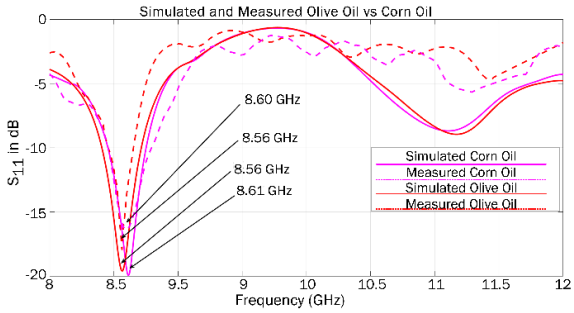

Fig. 10. S_{11} reflection coefficient measurement and simulation comparison of pure corn oil and olive oil between 8GHz – 12 GHz.

D. Simulation of reflection coefficient for multipurpose sensing

In this section, we have simulated the reflection coefficient parameters of the proposed metamaterial sensor for different fluid sensing applications. In order to show application examples of the proposed structure, we have measured the complex permittivity values of acetone, clear oil (unused transformer oil), dark oil (used transformer oil) and methanol. Obtained values are given in Table 1. In order to show the wide range of sensor application of the proposed structure, we have simulated the reflection coefficient when the sample holder was filled with these materials. Simulated reflection coefficient plot is presented in Fig. 11. According to the figure, when dielectric constant increased from 2.73 to 24, resonance frequencies of the reflection coefficients are increased from 8.71 GHz to 9.27 GHz which means that total bandwidth is 560MHz which corresponds to the dielectric constant changes.

Table 1: Dielectric constant values of some of the fluid measured between 8 GHz – 12 GHz by using 85070E dielectric probe kit

Material	Dielectric Constant
Acetone	24
Clear Oil	2.85
Dark Oil	2.73
Methanol	10.40

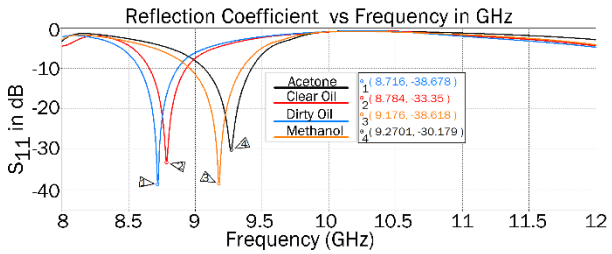

Fig. 11. Simulated reflection coefficient S_{11} parameter of the proposed structure when sample holder is filled with acetone, clear oil, dark oil and methanol between 8 GHz–12 GHz.

IV. CONCLUSION

A novel shaped metamaterial based sensor composed of traditional split square rings have been proposed to operate in X-band for sensing transformer oils and other fluid materials as methanol purity and olive oil adulteration. One of the important part of the proposed study is to have compatible operation for materials whose dielectric constants varying from 2 to 24 with high quality factor when it is compared with similar studies. Simulation studies have been validated with experimental ones. Generally, compatible results have been observed between them. Dielectric constant values are directly affecting the resonance frequency as well as the quality factor. If dielectric constants of the materials under test are close to each other, the resonance frequency difference between them would also be close to each other which can be counted as a weak part of this study. Due to the wide range of dielectric constant response, we believe that the proposed structure can be adapted to other microfluidic sensor applications.

ACKNOWLEDGMENT

We would like to thank the Scientific and Technological Research Council of Turkey (117M855) for the financial support.

REFERENCES

[1] M. Karaaslan and M. Bakir, "Chiral metamaterial based multifunctional sensor applications," *Progress In Electromagnetics Research*, vol. 149, pp. 55-67, 2014.

[2] L. Changjun and T. Fan, "An SIW resonator sensor for liquid permittivity measurements at C band," *IEEE Microwave Wirel. Compon. Lett.*, vol. 25, no. 11, pp. 751-753, 2015.

[3] M. Bakir, M. Karaaslan, F. Dincer, O. Akgol, and C. Sabah, "Electromagnetic energy harvesting and density sensor application based on perfect metamaterial absorber," *International Journal of Modern Physics B*, vol. 30, no. 20, p. 1650133, 2016.

[4] A. Ebrahimi, W. Withayachumnankul, S. Al-Sarawi, and D. Abbott, "High-sensitivity metamaterial-inspired sensor for microfluidic dielectric characterization," *IEEE Sensors J.*, vol. 14, no. 5, pp. 1345-1351, 2014.

[5] A. Salim, S. H. Kim, J. Y. Park, and S. Lim, "Microfluidic biosensor based on microwave substrate-integrated waveguide cavity resonator," *Journal of Sensors*, 1324145, pp. 1-13, 2018.

[6] J. F. Sadat, K. Fatemeh, and A. S. Javad, "Nondestructive aging of transformer oil using electromagnetic waves," *Elect. Power Distribut. Net. Conf. (EPDC), 2015 20th Conf. IEEE*, pp. 277-9, 2015.

[7] S. Guenneau, C. Amra, and D. Veynante, "Transformation thermodynamics: Cloaking and concentrating heat flux," *Optics Express*, vol. 20, no. 7, pp. 8207-8218, 2012.

[8] D. Shrekenhamer, W. Chen, and W. J. Padilla, "Liquid crystal tunable metamaterial absorber," *Phys. Rev. Lett.*, vol 110, 177403, 2013.

[9] M. Mrnka, P. Vasina, M. Kufa, V. Hebelka, and Z. Raida, "The RF energy harvesting antennas operating in commercially deployed frequency bands: A comparative study," *International Journal of Antennas and Propagation*, vol. 2016, Article ID 7379624, 11 pages, 2016. doi:10.1155/2016/7379624.

[10] T. Almoneef and O. M. Ramahi, "A 3-dimensional stacked metamaterial arrays for electromagnetic energy harvesting," *Progress In Electromagnetics Research*, vol. 146, pp. 109-115, 2014.

[11] M. Schueler, C. Mandel, M. Puentes, and R. Jakoby, "Metamaterial inspired microwave sensors," *IEEE Microwave Magazine*, vol. 13, no. 2, pp. 57-68, 2012.

[12] A. Vora, J. Gwamuri, N. Pala, A. Kulkarni, J. M. Pearce, and Ö. D. Güney, "Exchanging ohmic losses in metamaterial absorbers with useful optical absorption for photovoltaics," *Sci. Rep.*, vol 4, p. 4901 2014.

[13] M. Bakır, M. Karaaslan, F. Dincer, K. Delihacioglu, and C. Sabah, "Tunable perfect metamaterial absorber and sensor applications," *J. Mater. Sci. Mater. Electron.*, vol. 27, pp. 12091-12099, 2016.

[14] M. Bakır, M. Karaaslan, O. Altıntaş, M. Bagmancı, V. Akdogan, and F. Temurtaş, "Tunable energy harvesting on UHF bands especially for GSM frequencies," *International Journal of Microwave and Wireless Technologies*, vol. 10, pp. 67-76, 2018.

[15] G. Galindo-Romera, F. J. Herraiz-Martínez, M. Gil, J. J. Martínez-Martínez, and D. Segovia-Vargas, "Submersible printed split-ring resonator-based sensor for thin-film detection and permittivity characterization," *IEEE Sens. J.*, vol. 16, pp. 3587-3596, 2016.

[16] N. Wiwatcharagoses, K. Y. Park, J. Hejase, L. Williamson, and P. Chahal, "Microwave artificially

structured periodic media microfluidic sensor," *in Proc. IEEE 61st Electronic Components and Technology Conference (ECTC)*, pp. 1889-1893, 2011.

[17] A. A. Abduljabar, D. J. Rowe, A. Porch, and D. A. Barrow, "Novel microwave microfluidic sensor using a microstrip split-ring resonator," *TMTT*, pp. 679-688, 2014.

[18] W. Withayachumnankul, K. Jaruwongrungsee, A. Tuantranont, C. Fumeaux, and D. Abbott, "Metamaterial-based microfluidic sensor for dielectric characterization," *Sensors and Actuators A: Physical*, vol. 189, pp. 233-237, 2013.

[19] M. Bakır, "Electromagnetic-based microfluidic sensor applications," *J. Electrochem. Soc*., vol. 164, no. 9, pp. B488-B494, 2017.

[20] A. Ebrahimi, W. Withayachumnankul, S. Al-Sarawi, and D. Abbott, "High-sensitivity metamaterial-inspired sensor for microfluidic dielectric characterization," *IEEE Sensors J*., vol. 14, no. 5, pp. 1345-1351, 2014.

[21] M. Yoo, H. K. Kim, and S. Lim, "Electromagnetic-based ethanol chemical sensor using metamaterial absorber," *Sensors and Actuators B: Chemical*, vol. 222, pp. 173-180, 2016.

[22] C. A. Agostini, "Differential fuel taxes and their effects on automobile demand," *Cepal Rev*., vol. 102, pp. 101-111, 2010.

[23] V. J. Felix, P. A. Udaykiran, and K. Ganesan, "Fuel adulteration detection system," *Indian J. Sci. Technol*., vol. 8, no. S2, pp. 90-95, 2015.

[24] S. Kher, S. Chaubey, J. Kishore, and S. M. Oak, "Detection of fuel adulteration with high sensitivity using turnaround point long period fiber gratings in b/ge doped fibers," *IEEE Sensors J*., vol. 13, no. 11, pp. 4482-4486, 2013.

[25] S. Wang, L. Zhu, and W. Wu, "A novel frequency-reconfigurable patch antenna using low-loss transformer oil," in *IEEE Transactions on Antennas and Propagation*, vol. 65, no. 12, pp. 7316-7321, 2017.

[26] F. S. Jafari, F. Kazemi, and A. S. Javad, "Non-destructive aging of transformer oil using electromagnetic waves," *2015 20th Conference on Electrical Power Distribution Networks Conference (EPDC)*, Zahedan, pp. 277-279, 2015.

[27] F. S. Jafari and A. S. Javad, "Frequency-selective surface to determine permittivity of industrial oil and effect of nanoparticle addition in X-band," *J. Electron. Mater*., vol. 47, pp. 1397-1404, 2018.

[28] Y. Wang and M. N. Afsar, "Measurement of complex permittivity of liquids using waveguide techniques," *Progr. Elect. Res*., vol. 42, pp. 131-142, 2003.

[29] K. Bhattarai, S. Silva, K. Song, A. Urbas, S. Lee, Z. Ku, and J. Zhou, "Metamaterial perfect absorber analyzed by a meta-cavity model consisting of multilayer metasurfaces," *Scientific Reports*, vol. 7, pp. 10569, 2017.

[30] S. Qiu, Y. Huang, X. He, Z. Sun, P. Liu, and C. A. Liu, "Dual-mode proximity sensor with integrated capacitive and temperature sensing units," *Measurement Science and Technology*, vol. 26, pp. 105101, 2015.

[31] F. S. Jafari and A. S. Javad, "Reconfigurable microwave SIW sensor based on PBG structure for high accuracy permittivity characterization of industrial liquids," *Sensors and Actuators A: Physical*, vol. 283, pp. 386-395, 2018.

[32] S. Naoui, L. Latrach, and A. Gharsallah, "Equivalent circuit model of double split ring resonators," *International Journal of Microwave and Optical Technology*, vol. 11, no. 1, pp. 1-6, 2016.

[33] M. Bakır, M. Karaaslan, E. Unal, O. Akgol, and C. Sabah, "Microwave metamaterial absorber for sensing applications," *Opto-Electronics Review*, vol. 25, p. 318, 2017.

[34] O. Altıntaş, M. Aksoy, O. Akgol, E. Unal, M. Karaaslan, and C. Sabah, "Fluid, strain and rotation sensing applications by using metamaterial based sensor," *J. Electrochem. Soc*., vol. 164, no. 1), pp. B567-B573, 2017.

[35] A. Salim and S. Lim, "Review of recent metamaterial microfluidic sensors," *Sensors*, vol. 18, pp. 232, 2018.

[36] P. M. Meaney, A. P. Gregory, J. Seppälä, and T. Lahtinen, "Open-ended coaxial dielectric probe effective penetration depth determination," in *IEEE Transactions on Microwave Theory and Techniques*, vol. 64, no. 3, pp. 915-923, 2016.

A Novel Zigzag Line-based EBG Structure for the Simultaneous Switching Noise Suppression

Qiannan Xue [1,2*], Ziyuan Wang [2], Yi Tian [2], and Peng Wang [2]

[1] State Key Laboratory of Precision Measuring Technology & Instruments
College of Precision Instrument and Opto-electronics Engineering, Tianjin University, Tianjin, China

[2] Tianjin Key Laboratory for Civil Aircraft Airworthiness and Maintenance
Civil Aviation University of China, Tianjin 300300, China
*qiannanxue@163.com

Abstract ─ Simultaneous switching noise (SSN) generated between the power supply and the ground plane of a high-speed digital circuit is considered to be one of the most important factors affecting the signal integrity of a circuit system. In order to suppress the simultaneous switching noise, a new coplanar electromagnetic band-gap structure is proposed in this paper. Based on the zigzag line and square patch bridge, the inductance between the neighboring units can be enhanced. The results showed that the bandwidth of the band-gap is 0.1 ~ 12.6GHz when the depth of the new electromagnetic band-gap (EBG) structure is -30 db. Compared to the same parameter of the L-bridge structure, the relative bandwidth is about 48.7% and the cut-off frequency of the stop-band lower limit is reduced by 600MHz. The simultaneous switching noise on the power supply plane can be suppressed in all directions, and the signal integrity is less affected when the signal is transmitted by the differential line.

Index Terms ─ Coplanar electromagnetic band-gap, electromagnetic band-gap structure, high-speed digital circuits, simultaneous switching noise.

I. INTRODUCTION

With the rapid development of modern high-speed digital circuits [1], the operating frequency of the system clock is getting higher and higher. And according to the requirements of high power and low supply voltage, how to provide a clean power for the circuit system has become a major challenge in high-speed digital circuit system design [2]. On the interconnection, the high-speed signal transmission will be unstable caused by some noise, affecting the signal integrity (SI) [3, 4] and resulting in electromagnetic interference (EMI) [5]. Simultaneous switching noise (SSN) [6] problem not only reduces the noise tolerance of digital circuits, but also reduces the performance of analog circuits in mixed-signal systems. Conventional methods commonly used in the suppression of SSN circuit were that increasing the decoupling capacitors, power supply segmentation or designing through-hole location. Because of limited scope of application or the method too complex, these methods have not been widely used. In recent years, people gradually pay attention to use Electromagnetic band-gap structure (EBG) [7, 8] or SSN suppression.

EBG structure is a periodic structure that can control the propagation of electromagnetic waves. By correctly selecting the size, material and shape of the scattering medium, electromagnetic waves can be propagated in some frequency bands. The structure was first proposed to be used in the antenna to suppress the surface wave. The EBG structure could better inhibit the spread of electromagnetic waves in a certain frequency range. So it has been used in high-speed printed circuit board (PCB) [9] for SSN suppression. Several structures of the electromagnetic band-gap were designed, such as mushroom-liked electromagnetic band-gap structure [10], Fork-like EBG [11], FTS-EBG and so on. The structure of the mushroom-liked electromagnetic band-gap has prominent advantages in suppressing simultaneous switching noise. However, complex fabrication procedure, increasing cost and reliability associated with the printed circuit board and the narrow frequency of suppressing synchronous switching limit the application in high-speed digital circuits. Therefore, there are more and more researches focused on coplanar electromagnetic band-gap structures. This paper reported a new coplanar EBG structure which is based on the L-bridge EBG [12] structure. The zigzag line and the square patch bridge are used to construct the unit lattice to realize the new electromagnetic band-gap structure, which make the inductance between the neighboring units lattices enhanced. It could be expected to achieve better suppression characteristics for simultaneous switching noise in a high-speed digital circuit.

Submitted On: June 22, 2017
Accepted On: March 26, 2018

II. STRUCTURE DESIGN OF NEW COPLANAR EBG POWER

The planar electromagnetic band-gap structure proposed in this paper is designed based on local resonance principle. Local resonant electromagnetic band-gap structure of the principle, mainly through the electromagnetic band-gap itself to form a periodic structure of local resonance band-gap, inhibit the propagation of electromagnetic waves nearby, which can inhibit the simultaneous switching noise. The new coplanar EBG structure (marked as NW-EBG) mainly increases the equivalent inductance L by increasing the bridge wire on the EBG structure, which could reduce the stop-band center frequency of the EBG structure, increase the stop-band width of the EBG structure and finally improve the suppression effect of the EBG structure on the SSN.

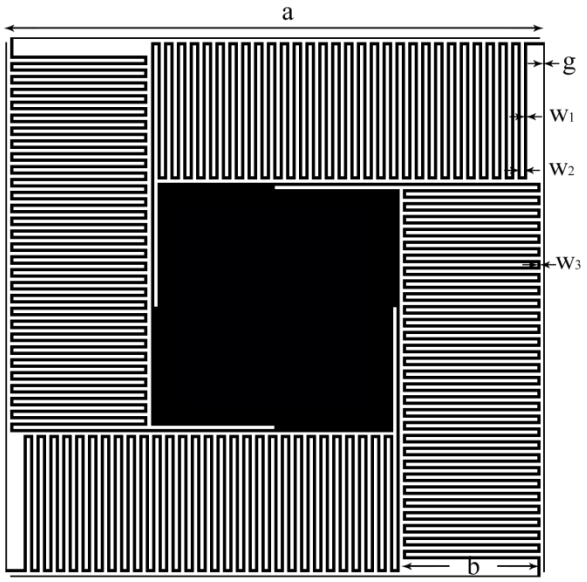

Fig. 1. The new structure design.

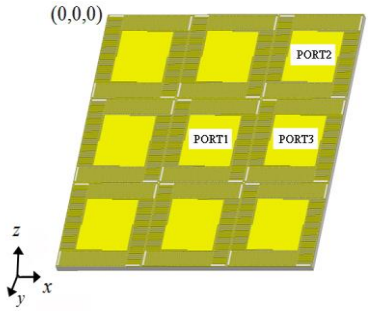

Fig. 2. The 3D view of simulation model.

The new structure consists of the center square and four side outwardly extending conductor lines. Four conductor lines are extended outwardly from the midpoint of the four corners of the center square, and the four conductor lines are bent around the center square with zigzag structures.

NW-EBG structure design size shown in Fig. 1, where a = 30mm, b = 5.2mm, w1=w2=w3=0.2mm, g = 0.1mm, line spacing are 0.2mm.

The circuit was fabricated by printed circuit board process. A double-layer PCB with 3 × 3 cell array was designed, and the EBG structure was embedded in the plane of the power plane. The total area of the new power layer structure designed in this paper is 81 cm^2, which is designed in the form of 3 × 3, each cell 9cm^2. The new coplanar EBG structure was simulated by the Ansoft HFSS, and three lumped ports were set up as shown in the Fig. 2. Port 2 and port 3 were set as output ports and port 1 was set as the input port.

III. DATA ANALYSIS AND SIMULATION VERIFICATION

A. Comparison with typical L-bridge type EBG structure characteristics

The L-bridge EBG structure is a typical electromagnetic band-gap structure. Draw a dashed line parallel to the horizontal axis at the position where the depth (longitudinal axis) is -30db. There are multiple intersections between dashed lines and curves. The adjacent intersection points with the largest difference in abscissa will be selected. The intersection point with small abscissa value is the lower limit. The intersection point with large abscissa value is the upper limit. As can be seen from the Table 1 and Fig. 3, L-bridged –EBG of low limit frequency is 0.7GHz, upper limit frequency is 4.7GHz, middle frequency is 2.7GHz, stop-band bandwidth is 4GHz, and relative band-stop bandwidth is 148.1%. The NW-EBG of low limit frequency is 0.1GHz, upper limit frequency is 12.6GHz, middle frequency is 6.35 GHz, stop-band bandwidth is 12.5 GHz, and relative band-stop bandwidth is 196.9%. Figure 4 shows the histogram of the middle frequency of the two EBG structures.

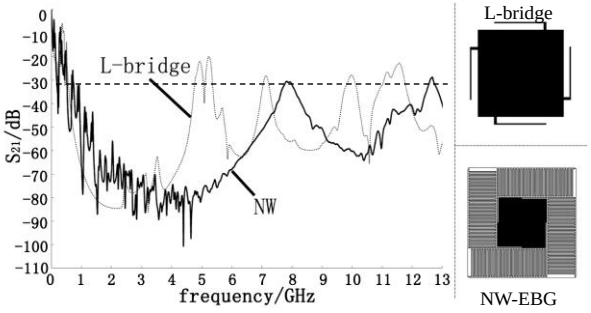

Fig. 3. Comparison of characteristic curve.

Table 1: Comparison of high frequency characteristics

EBG Type	L-Bridged-EBG	NW-EBG
Low limit frequency (GHz)	0.7	0.1
Upper limit frequency (GHz)	4.7	12.6
Middle frequency (GHz)	2.7	6.35
Stop-band bandwidth (GHz)	4	12.5
Relative band-stop bandwidth	148.1%	196.9%

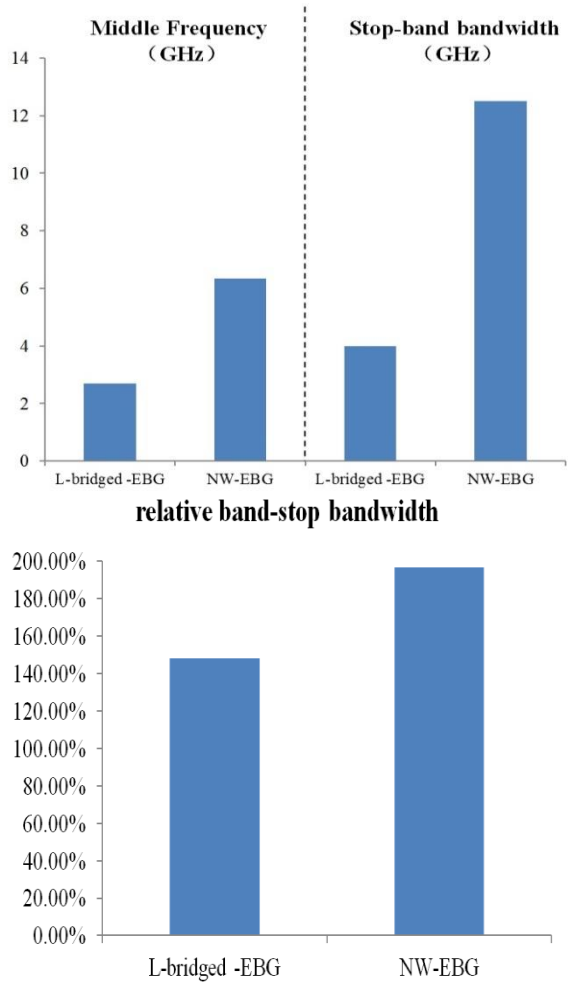

Fig. 4. Middle frequency, stop-band bandwidth and relative band-stop bandwidth of the two EBG structures.

We have compared the band-gap characteristics of NW-EBG and L-bridge-EBG. The suppression frequency of NW-EBG is 0.1-12.6GHz, the band-stop bandwidth is 12.5GHz and the relative band-stop bandwidth is 196.9% when the suppression depth is -30dB. Compared with L-bridge-EBG, the lower cut-off frequency of NW-EBG structure decreases from 700MHz to 100MHz, and the relative stop-band bandwidth increases from 148.1% to 196.9%, and the bandwidth is 48.8% of the 4GHz expanded to 12.5GHz. It can be seen that the NW-EBG structure can suppress the SSN at a lower operating frequency, and the inhibition range is wider than the L-bridge-EBG.

Figure 4 shows the histogram of stop-band bandwidth and relative band-stop bandwidth of the two EBG structures.

B. Omnidirectional suppression performance of a new planar EBG structure

By comparing the basic trend of the S21 and S31 characteristic curves, it is proved that the electromagnetic band-gap structure can suppress the simultaneous switching noise (SSN) between the power supply layer and the ground. Figure 5 shows the loss characteristics of port 2 and port 3 in the NW-EBG structure under different port outputs. It can be seen that the curves of S21 and S31 are basically consistent when the suppression depth is -30dB, which indicates that the NW-EBG structure can suppress the SSN in all directions.

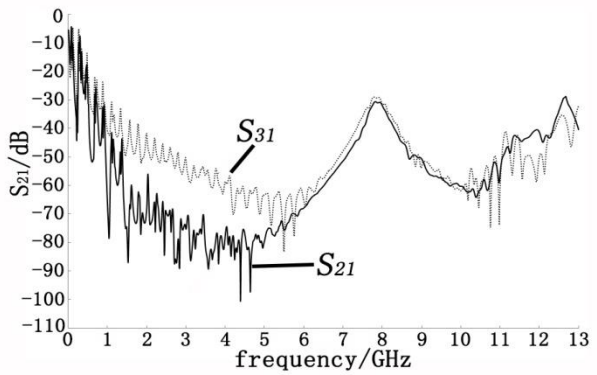

Fig.5. Comparison of S21 and S31 characteristic curve of NW-EBG.

C. Comparison of suppression characteristics of test and simulation

It can be seen from Table 2 that the difference between the test curve and the simulation characteristic parameters of the simulation curve is very small. It is further explained that the coplanar EBG power supply layer with a metal connection width of 0.2mm can fully detect the simultaneous switching noise of the high-speed printed circuit board. To the suppression, the most suitable for high-speed printed circuit board design and production.

Table 2: Comparison of suppression characteristics parameters of test and simulation

EBG Type	Test	Simulation	Recovery
Middle Frequency (GHz)	7.12±0.06	6.35	89.19%
Stop-band bandwidth (GHz)	12.88±0.07	12.5	97.05%
Relative band-stop bandwidth	189.97%±0.85%	196.9%	109.41%

IV. CONCLUSION

In this paper, a novel coplanar EBG structure is proposed, which is applied to the plane of PCB power supply. The unit cell is composed of a combination of zigzag line and square patch, which could enhance the inductance between the neighboring units. Compared with the traditional L-bridge structure, the band-stop bandwidth is increased by 48.7% as shown from the simulation results. The novel coplanar EBG power supply layer structure has a lower suppression frequency, a wider suppression bandwidth, and can effectively suppress simultaneous switching noise on the high-speed circuit all-directionally.

ACKNOWLEDGMENT

This work is supported by the National Natural Science Foundation of China (No. 61601469).

REFERENCES

[1] G. H. Shiue, J. H. Shiu, Y. C. Tsai, et al., "Analysis of common-mode noise for weakly coupled differential serpentine delay microstrip line in high-speed digital circuits," *IEEE T. Electromagn. C*, vol. 54, pp. 655-666, June 2012.

[2] N. A. Azmi, R. C. Ismail, S. S. Jamuar, et al., "Design of DC high voltage and low current power supply using Cockroft-Walton (C-W) voltage multi-plier," *2016 3rd International Conference on Electronic Design (ICED)*, Phuket, Thailand, Aug. 11-12, 2016.

[3] M. S. Zhang, H. Z. Tan, and J. F. Mao, "Signal-integrity optimization for complicated multiple-input multiple-output networks based on data mining of S-parameters," *IEEE T. on Components, Packaging and Manufacturing Technology C*, vol. 4 , pp. 1184-1192, Mar. 2014.

[4] B. Ravelo, A. Thakur, A. Saini, and P. Thakur, "Microstrip dielectric substrate material characterization with temperature effect," *Applied Computational Electromagnetics Society Journal*, vol. 30, pp. 1322-1328, Dec. 2015.

[5] D. Atanu and S. A Simon, "Electromagnetic interference simulations for wide-bandgap power electronic modules," *IEEE Journal of Emerging and Selected Topics in Power Electronics C*, vol. 4, pp. 757-766, May 2016.

[6] M. M. Bait-Suailam and O. M. Ramahi, "Ultra-wideband mitigation of simultaneous switching noise and EMI reduction in high-speed PCBs using complementary split-ring resonators," *IEEE T. Electromagn. C.*, vol. 54, pp. 389-396, Apr. 2012.

[7] M. A. Alshargabi, Z. Z. Abidin, and M. Z. M. Jenu, "High speed PCB & spiral with patch EBG planar integration for EMI reduction," *2015 International Conference on Computer, Communications, and Control Technology (I4CT)*, Kuching, Malaysia, Apr. 21-23, 2015.

[8] S. Manshari, F. Hodjat Kashani, and Gh. Moradi, "Mutual coupling reduction in CBS antenna arrays by utilizing tuned EM-EBG and non-planar ground plane," *Applied Computational Electromagnetics Society Journal*, vol. 31, pp. 750-755, July 2016.

[9] X. M Wang, Y. Q Zhou, H. H, Peng, et al., "One-key test system for relay protection equipment of intelligent substation," *Electric Power Automation Equipment C*, vol. 33, pp. 155-159, Mar. 2013.

[10] M. Zhang, J. Mao, and Y. Long, "Power noise suppression using power-and-ground via pairs in multilayered printed circuit boards," *IEEE T. Adv. Packaging C*, vol. 1, pp. 374-385, Mar. 2011.

[11] S. K. Mahto, A. Choubey, and R. Kumar, "A novel compact multi-band double Y-slot microstrip antenna using EBG structure," *2015 International Conference on Microwave and Photonics (ICMAP)*, Dhanbad, India, Dec. 11-13, 2015.

[12] L. F Shi, G. Zhang, M. M. Jin, et al., "Novel subregional embedded electromagnetic bandgap structure for SSN suppression," *IEEE Transactions on Advanced Packaging and Manufacturing Technology C*, vol. 6, pp. 613-621, Mar. 2016.

Modified Combined Tangential Formulation for Stable and Accurate Analysis of Plasmonic Structures

Barışcan Karaosmanoğlu and Özgür Ergül

Department of Electrical and Electronics Engineering
Middle East Technical University, Ankara, Turkey
{bariscan,ozergul}@metu.edu.tr

Abstract ─ We consider a modified combined tangential formulation (MCTF) for stable and accurate analysis of plasmonic problems involving metallic objects modeled as penetrable bodies. For a wide range of negative real permittivity values, corresponding to varying characteristics of metals at THz, infrared, and visible frequencies, MCTF provides accurate solutions in comparison to the conventional formulations for penetrable objects. We further show that, for structures with subwavelength dimensions, penetrable models formulated with MCTF can be essential for accurate analysis, rather than the perfectly conducting formulations, even at the lower THz frequencies.

Index Terms ─ Plasmonic problems, scattering, surface integral equations.

I. INTRODUCTION

Most metals at optical frequencies are known to possess plasmonic properties, which can be employed in diverse applications, such as sensing, energy harvesting, optical links, and super-resolution. In parallel with this, for numerical modeling of plasmonic structures involving arbitrary geometries, traditional solvers have been modified to handle negative permittivity values that can be used to represent metals at optical frequencies [1]. While volume formulations are mostly used in this area, plasmonic problems with increasing complexity and sizes often need more efficient solvers that are based on surface formulations [2]–[5]. In fact, if the structures can be represented as homogeneous or piecewise homogeneous objects, surface integral equations can provide the desired efficiency without sacrificing the accuracy. On the other hand, since most of the formulations have been developed for ordinary dielectric and magnetic objects [6], new numerical problems arise when the traditional solvers are employed to analyze plasmonic structures.

As a background of this study, we refer to [7] and [8], where we showed that the conventional formulations may require very dense discretizations with respect to wavelength in order to obtain sufficient accuracy for plasmonic objects, while some formulations even break down as the negative permittivity increases. Therefore, we need more accurate and stable formulations that can be used in wide ranges of permittivity values, especially for increasingly large negative permittivities to close the gap towards perfect electric conductor (PEC) models. We recently introduced a modified combined tangential formulation (MCTF) that falls into this category and we showed the advantages of MCTF over other penetrable formulations for plasmonic structures of several wavelengths [10]. Specifically, MCTF provides accurate and stable solutions for large permittivity values that are typical at the infrared and higher THz frequencies. In this contribution, we further show the advantages of MCTF at much lower frequencies. When the frequency drops to lower THz ranges, PEC models are assumed to be valid, while this is not true if the dimensions of the structures are very small with respect to wavelength. Therefore, penetrable formulations may still be needed, even when the frequency is low. As shown in this letter, MCTF can also provide accurate analysis of such subwavelength metallic objects, in comparison to the conventional PEC models and their typical formulations with the electric-field integral equation (EFIE).

II. MCTF FOR DIFFERENT REGIMES

MCTF is a tangential formulation, similar to the combined tangential formulation (CTF) and the variants of the Poggio-Miller-Chang-Harrington-Wu-Tsai (PMCHWT) formulation. Hence, with the low-order discretizations employing the Rao-Wilton-Glisson functions and Galerkin scheme, it naturally provides more accurate solutions than the normal and mixed formulations [9], such as the electric and magnetic current combined-field integral equation (JMCFIE). For plasmonic problems involving structures comparable to wavelength, the advantages of MCTF are its higher efficiency in comparison to PMCHWTs, its better stability in comparison to CTF, and its better accuracy in comparison to JMCFIE and similar normal/mixed formulations [10].

In the frequency domain, matrix equations derived

Submitted On: June 26, 2017
Accepted On: February 17, 2018

from MCTF can be written as [10]:

$$\bar{\boldsymbol{Z}} = \begin{bmatrix} \eta_o \bar{\boldsymbol{T}}_o + \eta_p \bar{\boldsymbol{T}}_p & \left(-\bar{\boldsymbol{K}}_o - \bar{\boldsymbol{K}}_p\right) \\ \eta_o \eta_p \left(-\bar{\boldsymbol{K}}_o - \bar{\boldsymbol{K}}_p\right) & \eta_p \bar{\boldsymbol{T}}_o + \eta_o \bar{\boldsymbol{T}}_p \end{bmatrix}, \tag{1}$$

where $\bar{\boldsymbol{T}}_{o,p}$ and $\bar{\boldsymbol{K}}_{o,p}$ are the electric-field integral operator and the magnetic-field integral operator, respectively, which are tested tangentially $(\hat{\boldsymbol{a}}_n \times \hat{\boldsymbol{a}}_n \times)$, i.e.,

$$\begin{aligned} \bar{\boldsymbol{T}}_u[m,n] &= ik_u \left\langle \boldsymbol{t}_m(\boldsymbol{r}),\, g_u(\boldsymbol{r},\boldsymbol{r}')\boldsymbol{b}_n(\boldsymbol{r}') \right\rangle \\ &\quad - \frac{i}{k_u} \left\langle \boldsymbol{t}_m(\boldsymbol{r}),\, \nabla' \cdot \boldsymbol{b}_n(\boldsymbol{r}') \nabla' g_u(\boldsymbol{r},\boldsymbol{r}') \right\rangle, \end{aligned} \tag{2}$$

$$\bar{\boldsymbol{K}}_u[m,n] = \left\langle \boldsymbol{t}_m(\boldsymbol{r}),\, \boldsymbol{b}_n(\boldsymbol{r}') \times \nabla' g_u(\boldsymbol{r},\boldsymbol{r}') \right\rangle, \tag{3}$$

for $u = o$ (outer/vacuum) and $u = p$ (inner/plasmonic). In the above, $\eta_u = \sqrt{\mu_u}/\sqrt{\varepsilon_u}$ represents the intrinsic impedance, $k_u = \omega\sqrt{\mu_u}\sqrt{\varepsilon_u} = 2\pi/\lambda_u$ represents the wavenumber, and $g_u(\boldsymbol{r},\boldsymbol{r}') = \exp(ik_u|\boldsymbol{r}-\boldsymbol{r}'|)/4\pi|\boldsymbol{r}-\boldsymbol{r}'|$ is the homogeneous-space Green's function. In addition, $\boldsymbol{t}_m$ and $\boldsymbol{b}_n$ represent testing and basis functions (the same set of the RWG functions). The limit term in the MFIE operator is extracted, as usual.

A. Fixed electrical size

Considering a metallic object with a fixed electrical size, i.e., *kD*=constant, increasing negative permittivity $(\varepsilon_R \to -\infty)$ leads to $(\eta_p \to 0)$, $(k_p \to i\infty)$, and,

$$\lim_{\varepsilon_R \to -\infty} \bar{\boldsymbol{T}}_p = -\bar{\boldsymbol{I}}/2, \qquad \lim_{\varepsilon_R \to -\infty} \bar{\boldsymbol{K}}_p = 0, \tag{4}$$

where $\bar{\boldsymbol{I}} = \left\langle \boldsymbol{t}_m(\boldsymbol{r}), \boldsymbol{b}_n(\boldsymbol{r}') \right\rangle$. Then, MCTF turns into EFIE as:

$$\lim_{\varepsilon_R \to -\infty} \bar{\boldsymbol{Z}} = \eta_o \begin{bmatrix} \bar{\boldsymbol{T}}_o & -\bar{\boldsymbol{K}}_o \\ 0 & -\bar{\boldsymbol{I}}/2 \end{bmatrix}, \tag{5}$$

where the second row makes the magnetic current zero (due to vanishing small right-hand side of this row). With a well balance of the matrix blocks [10], convergence to EFIE is achieved via a vanishing $\eta_p \bar{\boldsymbol{T}}_p$, hence without a numerical problem. We note that all penetrable formulations should reduce into an appropriate PEC form; however, this can be numerically difficult for many conventional formulations. The limiting process is useful to show the stability of MCTF as the frequency goes down for a fixed electrical size and the object becomes PEC.

B. Fixed metric size

For an object with a fixed metric size, decreasing frequency has a different effect, since the material tends to become perfectly conducting, but at the same time, the object becomes electrically small. In fact, there is a balance between material and size, i.e., $\omega \to 0$, $\varepsilon_R \to -\infty$, $\eta_p \to 0$, $k_p \sim$ constant, and,

$$\eta_p \bar{\boldsymbol{T}}_p \sim c \left\langle \boldsymbol{t}_m(\boldsymbol{r}),\, \nabla' \cdot \boldsymbol{b}_n(\boldsymbol{r}') \nabla' g_u(\boldsymbol{r},\boldsymbol{r}') \right\rangle, \tag{6}$$

The constant c in (6) depends on the type of the metal and the model used (Drude, Lorentz-Drude, etc.). But, the bottomline is that MCTF in (5) does not converge into a PEC formulation. In fact, localization of the inner interactions as the negative permittivity increases is balanced with the decreasing electrical size of the object. Therefore, MCTF provides more correct interpretation of the physical problem, while using a PEC model and a related integral equation may lead to deviating results, as shown below.

III. NUMERICAL RESULTS

First, we consider the stability and accuracy of MCTF for a fixed electrical size. Fig. 1 presents the results of scattering problems involving plasmonic spheres of diameter $1.04\lambda_o$. For the relative permittivity, we consider different values $\varepsilon_r = (\varepsilon_R + i)$, where ε_R changes from –512 to 32. The spheres are illuminated by plane waves. For numerical solutions, the problems are discretized with $\lambda_o/10$ triangles, leading to matrix equations involving 2166 unknowns. In addition to different formulations, the problems are solved via Mie series to obtain reference values. In Fig. 1, the relative error in the far-zone electric field and the number of GMRES iterations (for 10^{-4} residual error, without preconditioning and restart) are plotted with respect to ε_R. For positive values of ε_R, it can be observed that the accuracy deteriorates as the contrast increases, as a result of increasing geometric deviation, integration problems, formulation issues (unbalanced blocks, ill conditioning, etc.), or the combination of these problems. Focusing on the negative values, we observe that JMCFIE results have very large errors that become relatively smaller, but still significant, as the contrast increases. In the same direction (increasing contrast), the error of CTF increases dramatically up to around 20% when $\varepsilon_R = -512$. Interestingly, the number of iterations for CTF drops, showing that the increasing error is not related to conditioning. MCTF has the same accuracy as PMCHWT and its scaled (balanced) version PMCHWT-S. All these these formulations provide quite stable results in terms of the accuracy for all negative values of ε_R. On the other hand, MCTF requires less iterations than PMCHWT (especially for small values of negative ε_R) and PMCHWT-S (especially for large values of negative ε_R). Hence, in terms of the efficiency, MCTF is more reliable than PMCWHTs for plasmonic simulations.

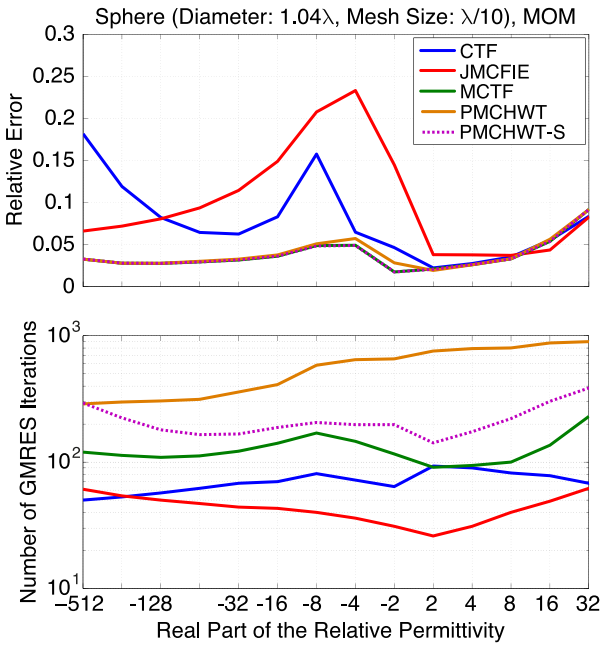

Fig. 1. Solutions of scattering problems involving spheres of diameter $1.04\lambda_o$. Far-zone relative errors and iteration counts are investigated with respect to the relative real permittivity values.

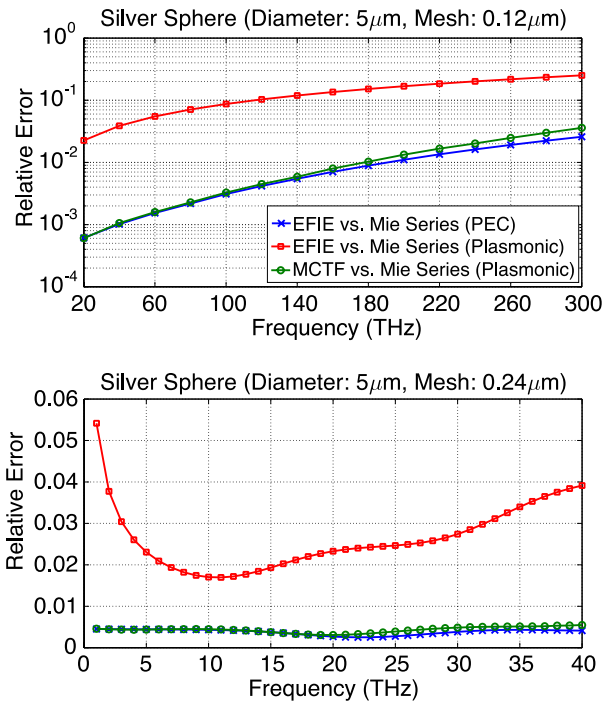

Fig. 2. Solutions of scattering problems involving a silver sphere of diameter $5\ \mu m$. Far-zone relative errors in numerical solutions are investigated with respect to the frequency. Reference solutions are obtained by using Mie-series for plasmonic (silver) and PEC cases.

Next, we consider the stability and accuracy of MCTF for a fixed metric size. Figure 2 presents the results of scattering problems involving a silver sphere of diameter $5\ \mu m$ illuminated by plane waves. The Lorentz-Drude model is used for the relative permittivity of the silver. In Fig. 2, the relative errors (in the far-zone electric field) in the numerical solutions of MCTF and EFIE (PEC model) in comparison to the plasmonic Mie-series solutions are plotted. In the 20–300 THz range (discretization size $0.12\ \mu m$), where the sphere size is approximately $0.33-5\lambda_o$, the error in the EFIE solutions decreases down to 2% as the frequency drops. However, as shown in the plot for the 0–40 THz range, the EFIE error increases back to 5% when the frequency further drops. The error in MCTF with respect to plasmonic Mie-series solutions is mostly below 1% (larger errors occurs above 180 THz since the discretization size with respect to wavelength is large), while it is completely stable in the 0–40 THz range. Finally, as also shown in Fig. 2, EFIE is consistent with the PEC Mie-series solutions, indicating that the perfectly conducting model itself deviates from the physical (silver) model, despite the frequency drops down to several THz.

IV. CONCLUSION

We present the accuracy and stability of MCTF for plasmonic problems involving metallic objects with negative permittivity values. Considering objects comparable to the wavelength, MCTF provides accurate solutions for different permittivity values, leading to stable plasmonic-to-PEC transition as the negative permittivity gets larger. We further show that, small objects with respect to wavelength may also require penetrable models (hence, MCTF) despite the frequency can be only in the order of several THz. These results on canonical objects make MCTF attractive for the analysis of metallic structures with different sizes at THz, infrared, and higher optical frequencies.

ACKNOWLEDGMENT

This work was supported by the Scientific and Technical Research Council of Turkey (TUBITAK) under the Research Grants 113E129 and 114E498, and by the Turkish Academy of Sciences (TUBA).

REFERENCES

[1] P. B. Johnson and R. W. Christy, "Optical constants of the noble metals," *Phys. Rev. B*, vol. 6, no. 12, pp. 4370-4379, Dec. 1972.

[2] M. G. Araujo, et al., "Comparison of surface integral equation formulations for electromagnetic analysis of plasmonic nanoscatterers," *Opt. Exp.*, vol. 20, no. 8, pp. 9161-9171, Apr. 2012.

[3] Ö. Ergül, "Analysis of composite nanoparticles with surface integral equations and the multilevel

fast multipole algorithm," *J. Opt.*, vol. 14, no. 6, pp. 062701-1-4, June 2012.

[4] D. M. Solis, J. M. Taboada, and F. Obelleiro, "Surface integral equation method of moments with multiregion basis functions applied to plasmonics," *IEEE Trans. Antennas Propag.*, vol. 63, no. 5, pp. 2141-2152, May 2015.

[5] H. Gomez-Sousa, O. Rubinos-Lopez, and J. A. Martinez-Lorenzo, "Comparison of iterative solvers for electromagnetic analysis of plasmonic nanostructures using multiple surface integral equation formulations," *J. Electromagn. Waves Appl.*, vol. 30, no. 4, Feb. 2016.

[6] P. Ylä-Oijala, M. Taskinen, and S. Järvenpää, "Surface integral equation formulations for solving electromagnetic scattering problems with iterative methods," *Radio Sci.*, vol. 40, no. 6002, Dec. 2005.

[7] B. Karaosmanoğlu, A. Yılmaz, and Ö. Ergül, "On the accuracy and efficiency of surface formulations in fast analysis of plasmonic structures via MLFMA," in *Proc. Progress in Electromagnetics Research Symp. (PIERS)*, pp. 2629-2633, 2016.

[8] B. Karaosmanoğlu and Ö. Ergül, "Accuracy of the surface integral-equation formulations for large negative permittivity values," in *Proc. Progress in Electromagnetics Research Symp. (PIERS)*, 2017.

[9] Ö. Ergül and L. Gürel, "Comparison of integral-equation formulations for the fast and accurate solution of scattering problems involving dielectric objects with the multi-level fast multipole algorithm," *IEEE Trans. Antennas Propag.*, vol. 57, no. 1, pp. 176-187, Jan. 2009.

[10] B. Karaosmanoğlu, A. Yılmaz, and Ö. Ergül, "Accurate and efficient analysis of plasmonic structures using surface integral equations," *IEEE Trans. Antennas Propag.*, vol. 65, no. 6, pp. 3049-3057, June 2017.

Barışcan Karaosmanoğlu received the B.Sc. degree in Electronics and Communication Engineering from Doğuş University, Istanbul, Turkey, in 2011, and the M.S. degree in Electrical and Electronics Engineering from Bilkent University, Ankara, Turkey, in 2013. He is currently pursuing the Ph.D. degree with the CEMMETU Research Group, Middle East Technical University, Ankara. His current research interests include fast and accurate algorithms, parallel programming, broadband algorithms, integral equations, optimizations, optical metamaterials, and plasmonic materials. Karaosmanoğlu was a recipient of the 2015 IEEE AP-S Student Paper Competition Honorable Mention, the 2015 Leopold B. Felsen Award for Excellence in Electrodynamics, and the 2016 URSI-TR Best Student Paper Award.

Özgür Ergül is an Associate Professor in the Department of Electrical and Electronics Engineering at Middle East Technical University (METU), Ankara, Turkey. He is the Principal Investigator of the CEMMETU research group (http://cem.eee.metu.edu.tr). His research interests include fast and accurate algorithms for the solution of electromagnetics problems involving large and complicated structures, integral equations, iterative methods, parallel programming, and high-performance computing. He is a recipient of the 2007 IEEE Antennas and Propagation Society Graduate Fellowship, 2007 Leopold B. Felsen Award for Excellence in Electrodynamics, 2010 Serhat Ozyar Young Scientist of the Year Award, 2011 URSI Young Scientists Award, 2013 Science Academy Young Scientists Award, the first ever (2013) ACES Early Career Award, 2013 Parlar Foundation Research Incentive Award, 2014 Parlar Foundation Instructor of the Year Award, 2014 METU Young Scientist Award, 2014 TUBITAK Incentive Award, 2015 Turkish Academy (TUBA) Young Scientist Award, and 2017 IEEE Turkey Section Research Incentive Award. He is the author of the undergraduate textbooks "Guide to Programming and Algorithms Using R" (Springer) and "Introduction to Electrical Circuit Analysis (Wiley)", co-author of the graduate textbook "The Multilevel Fast Multipole Algorithm (MLFMA) for Solving Large-Scale Computational Electromagnetics Problems" (Wiley-IEEE), and coauthor of 300 journal and conference papers. He is also serving as an Associate Editor of IEEE Antennas and Propagation Magazine (Open Problems in CEM Column), a Column Editor of the URSI Bulletin (Solution Box), and an Editorial Board Member of the Scientific Reports (Nature Publishing Group). Ergül is the Chair of the IEEE AP/MTT/EMC/ED Turkey chapter and the Editor-in-Chief of Turkish Journal of Electrical Engineering and Computer Sciences (a multidisciplinary SCI-E journal).

Genetic Algorithm Optimization of a Dual Polarized Concentric Ring Array

Pedro Mendes Ruiz [1], Israel D. Hinostroza Sáenz [1], Régis Guinvarc'h [1], and Randy Haupt [2]

[1] SONDRA
CentraleSupélec, Gif-sur-Yvette, 91190, France
{pedro.mendesruiz, israel.hinostroza, regis.guinvarch}@centralesupelec.fr

[2] Electrical Engineering and Computer Science
Colorado School of Mines, Golden, CO 80401, USA
rhaupt@mines.edu

Abstract **—** We use a genetic algorithm to minimize the relative sidelobe level (RSLL) of a dual polarized concentric ring array. The optimization variables are the placement of uniformly weight spiral antennas in an aperture with a small area. We optimized a cost function with isotropic sources instated of spiral elements to make the cost function reasonable to evaluate. We developed approaches to calculate a faster cost function and reduce the number of function calls in the optimization. We then calculated the array with an approximation of the element pattern to evaluate its performances.

Index Terms **—** Concentric ring array, genetic algorithms, optimization, phased array, planar array, spiral antenna, wideband array.

I. INTRODUCTION

Dual circularly polarized wideband arrays find use in several applications, including weather radar [1] and synthetic aperture radar [2]. As in [3], the array design in this paper has a bandwidth from 1 to 2 GHz with a maximum scan angle of 30°. The bandwidth is defined by a reflection coefficient smaller than -10 dB, dual circular polarization with an axial ratio smaller than 3 dB, and a relative sidelobe level smaller than -10 dB. Two-arm center-fed spiral antennas [4] are excellent elements for this application, because they are very wideband, conformal and circularly polarized. Dual polarization is possible by interleaving spirals of opposite polarization [5], [6]. A dual polarized concentric ring array was developed using two-arm center-fed Archimedean spirals as the radiating element with each ring of spirals backed by a cavity. To ensure a good axial ratio, we use the sequential rotation technique [7]. Non-uniformly spaced concentric rings mitigate the sidelobes [6]. In [3] we added a size constraint to the optimization to reduce the size of the array. This work expands on the paper presented at the ACES 2017 conference in Florence [8]. The goal of the genetic algorithm optimization [9] described in this work is to find a smaller array than in [6] with a similar bandwidth by optimizing the rings positions using the size constraint in [3].

II. CONCENTRIC RING ARRARY

A diagram of the concentric ring array, which has $N_r = 4$ rings, appears in Fig. 1. Variables in the i-th ring design ($i = 0, \dots, N_r - 1$) include the ring spacing Δ_i and the ring rotation Φ_i. The array consists of Archimedean spirals with a diameter of $D_{spi} = 10.5$ cm and a lower cut-frequency of 1 GHz [6]. The spacing between elements of the same polarization within a ring has an approximate value of $d_{elem} = 24.34$ cm [6]. Every other element in a ring is RH (right hand) polarized, while the others are LH (left hand) polarized. The array is modeled using isotropic point sources for the optimization.

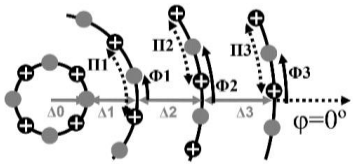

Fig. 1. Concentric ring array: filled and cross circles represent RH and LH polarized spirals, respectively.

The number of spirals of the same polarization (N_i) in a ring of radius r_i is determined by:

$$N_i = \left\lfloor \frac{2\,\pi\, r_i}{d_{elem}} \right\rfloor, \tag{1}$$

where $\lfloor x \rfloor$ is the floor function. We can then calculate the angular distance between two elements of the same polarization as follows:

$$\Pi_i = \frac{2\,\pi}{N_i}. \tag{2}$$

For the optimization, the values of the ring rotations are restricted to $0 \le \Phi_i \le \Pi_i$ and the array radius is limited by a maximal value R_{max} = 1.3m [3]. This optimization results in an array with a radius close to the maximum allowed. The surface area obtained in that case is equivalent to 42% of that in [6], similar to [3].

Submitted On: June 29, 2017
Accepted On: February 17, 2018

III. ONE RING ARRAY

As our final goal is to minimize the RSLL of the concentric ring array at all frequencies, we first look at the array factor (AF) at the highest frequency in the bandwidth, 2 GHz. In order to consider all steering directions up to θ_s, we will look at the u-v space in the region:

$$u^2 + v^2 \leq (1 + \sin\theta_s)^2. \quad (3)$$

In Fig. 2 we show the AF of a one ring array calculated at 2 GHz inside the region defined by $u^2 + v^2 \leq 1.5^2$, which contains all the sidelobes that can appear in the visible zone at 2 GHz for a maximal steering of $\theta_s = 30^o$. By looking at the AF with the u-v axes normalized by d_{elem}/λ, we observe high sidelobes in the rings with an integer radius, corresponding to the grating lobe regions. In the concentric ring array we should expect to have the larger sidelobes appearing in those regions.

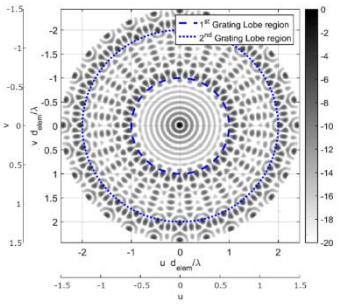

Fig. 2. Array Factor of a one ring array with a radius of 1.085 m and 28 elements uniformly spaced, showing all sidelobes that appear in the visible zone at 2 GHz for a maximal steering of $\theta_s = 30^o$. The u-v axes are shown for the AF at 2 GHz, as well as the axis normalized by d_{elem}/λ. The 1st (dashed) and 2nd (dotted) Grating Lobe (GL) regions are highlighted in the Array Factor.

IV. ARRARY BANDWIDTH

The isolated spirals used in this array have a reflection coefficient h[i]gher than -10 dB for frequencies below 1 GHz, so this is used as the lower limit of the bandwidth. In order to calculate the higher limit of the bandwidth of the array, we used a mean radiated element model to find the total radiated field, and then find the RSLL, that should be smaller than -10 dB [6].

To obtain an approximation of the embedded element pattern, which we will call $\boldsymbol{E}_{model}$, we simulated a small one ring array in FEKO. The array had 8 spiral elements (4 per polarization) backed by a cavity [6], and we simulated it with one of the spirals being excited with a voltage source and the other 7 spirals were adapted with 220 Ω loads. In order to calculate the array pattern with the spiral elements and using the sequential rotation technique, we first calculated the radiated field of each of the rotated elements:

$$\boldsymbol{E}_{\boldsymbol{el}_{j\,i}} = rotation\left(\boldsymbol{E}_{model}, \alpha_{rot_{j\,i}}\right),\ \alpha_{rot_{j\,i}} = \pm\gamma_{j\,i}, \quad (4)$$

where $\gamma_{j\,i}$ is the angular position of the j-th element in the i-th ring of the array, having a positive value for the LH polarized elements and a negative value for the RH polarized elements. Then, we summed the radiated fields, multiplying each of them by the corresponding sequential rotation phase $\alpha_{rot_{j\,i}}$ as well as the steering phase and the positioning phase, $\delta_{pos_{j\,i}}$:

$$\boldsymbol{E}(\varphi,\theta) = \sum_{i=0}^{N_r-1}\sum_{j=1}^{N_i} e^{-j\delta_{pos_{j\,i}}}\, e^{-j\alpha_{rot_{j\,i}}}\, \boldsymbol{E}_{\boldsymbol{el}_{j\,i}}(\varphi,\theta), \quad (5)$$

$$\delta_{pos_{j\,i}} = \frac{2\pi}{\lambda}\left(x_{ji}\,(u-u_s) + y_{ji}\,(v-v_s)\right), \quad (6)$$

with N_i being the number of elements in the i-th ring. x_{ji} and y_{ji} are the positions of the j-th element in the i-th ring. u and v are the observation direction in the u-v space. u_s and $v_s$are the steering directions in the u-v space.

V. GENETIC ALGORITHM OPTIMIZATION

A. First optimization: Optimizing all sidelobes

The goal of the optimization is to minimize the RSLL in the desired bandwidth (1-2 GHz), considering a maximum steering of θ_s=30°. In order to find the maximum sidelobe level, the array pattern was calculated, at 2 GHz, in the region defined by $u^2 + v^2 \leq 1.5^2$ (equation 3). The cost function analyzes that region and returns the highest RSLL in dB.

Table 1: Optimization optimal values

	Δ0 (cm)	Δ1 (cm)	Δ2 (cm)	Δ3 (cm)	Φ1 (rad)	Φ2 (rad)	Φ3 (rad)
1st Opt.	46.81	28.92	27.86	27.77	0.0467	0.0784	0.1399
2nd Opt.	46.53	27.07	28.25	29.84	0.1319	0.0895	0.0562
3rd Opt.	47.00	26.62	30.05	27.96	0.0871	0.2416	0.1452

The genetic algorithm had a population size of 200 and ran for a maximum of 200 generations. A single function call for a concentric ring array of isotropic point sources took between 3.8 and 6.3 s. The whole optimization took 38 hours to finish using 4 cores, with a mean of 55 generations before reaching the stop criterion for each of the eight genetic algorithm iterations and a total of 88985 evaluations of the cost function. The optimization results can be seen in Table. 1. Figure 3 shows the optimized array pattern in u-v space at 2 GHz. Figure 4 is the u-cut of the Array Factor that has the highest sidelobes. We note that the RSLL stays bellow -11dB for scanning up to 30° and a frequency up to 2 GHz with a maximum radius of 1.3m. We also note that there are two groups of high sidelobes in the regions corresponding to the grating lobe regions, as we expected from the results in Section III. In Fig. 5 we plot the RSLL of the optimized array using the method presented in Section IV, which resulted in a bandwidth from 1-1.3 GHz (27% of [6]). To better explain

what is happening in the array pattern, we will look at the radiated field of the steered array at 2 GHz (Fig. 6). We observe that the 1st ring of grating lobes is getting larger while the 2nd ring of grating lobes is being attenuated.

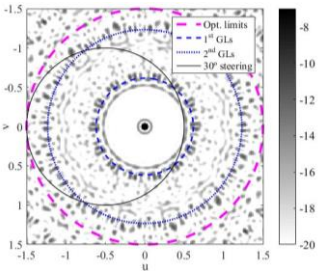

Fig. 3. Array factor of the array obtained from the 1st optimization at 2 GHz. In thick dashed pink we have the limits of the sidelobe search for the optimization cost function. In thin dashed blue and dottted blue, we have the 1st and 2nd grating lobe regions, respectively. In black we have the visible zone once steered to $[\theta_s, \phi_s] = [30°, 0°]$.

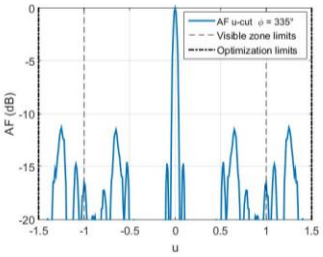

Fig. 4. Array factor representative u-cut ($\phi = 335°$) for the concentric ring array optimized at the $\theta_s < 30°$ zone, at 2 GHz (1st optimization).

B. Second optimization: Avoiding 2nd GLs

By taking into account this reduction in the 2nd grating lobes, we decided to re-optimize the array, changing the optimized region in the AF to exclude those sidelobes, so the 1st grating lobes are prioritized and thus further reduced, which compensates the increase they get when we steer the array.

Now, the optimized region of the sidelobes in the AF at 2 GHz is defined by $u^2 + v^2 \leq 1.15^2$, which corresponds to $(u\, d_{elem}/\lambda)^2 + (v\ d_{elem}/\lambda)^2 \leq 1.866^2$ by normalizing as in section III and includes all sidelobes until just before the 2nd grating lobe region. By using the same optimization procedure as in section V-A, we got the results presented in Table 1. A single cost function call took between 2.2 and 3.7 s, 59% of the time required by the cost function in section V-A, which happens because less points are being computed in the u-v space.

The whole optimization took 21 hours to finish using 4 cores, with a mean of 48 generations before reaching the stop criterion for each of the eight genetic algorithm iterations and a total of 77988 evaluations of the cost function. In Fig. 7 we show the AF of the optimized array and, in Fig. 8, two u-cuts of that AF representative of the sidelobe level. We can see from the figures that the new optimization was able to further reduce the prioritized sidelobes by relaxing the constraints on the sidelobes appearing in the 2nd GL region. In Fig. 5 we show the RSLL calculated via the method in section IV, and we observe that the bandwidth was successfully increased to 1-2 GHz (95% of [6]).

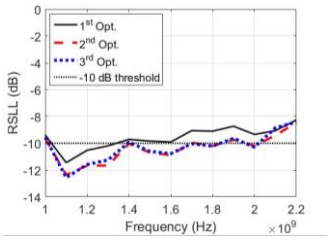

Fig. 5. RSLL in function of frequency of the 1st (continuous black), 2nd (dashed red) and 3rd (dotted blue) optimized array using the method described in Section IV.

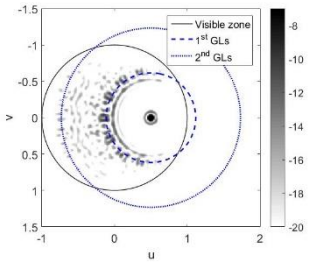

Fig. 6. Electric field of the array obtained from the 1st optimization with a steering of $[\theta_s, \phi_s] = [30°, 0°]$, calculated using the method from section IV, in the u-v space. In continuous black we have the visible zone. In dashed blue and dottted blue, we have the 1st and 2nd grating lobe regions, respectively.

C. Third optimization: using only half of the AF

Finally, we noticed that by optimizing the sidelobes in half of the u-v space, we got very similar results while significantly reducing the computation time. The optimization was repeated with the new cost function with the results presented in Table 2. The cost function evaluation time reduced to 1.1-1.9 s, 30% of the time required in section V-A. The whole optimization took 8 hours to finish using 4 cores, with a mean of 36 generations before reaching the stop criterion for each of the eight genetic algorithm iterations and a total of 59387 evaluations of the cost function. The resulting AF is similar to that obtained in the 2nd optimization (Fig. 7). In Fig. 5 we show the RSLL calculated via the method from Section IV. The resulting RSLL is so similar to that from the array of the 2nd optimization that their curves are almost superposed, showing that limiting the optimized zone to half of the u-v space is a good approach to reduce the computation time. Further reducing the optimized zone created an imbalance in the sidelobes of the

optimized array, resulting in larger sidelobes for the worst case scenario.

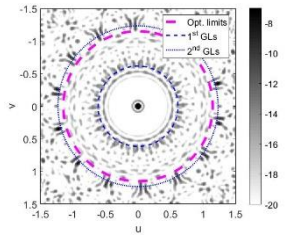

Fig. 7. Array factor of the array obtained from the 2nd optimization at 2 GHz. In thick dashed pink we have the limits of the sidelobe search for the optimization cost function. In thin dashed blue and dottted blue, we have the 1st and 2nd grating lobe regions, respectively.

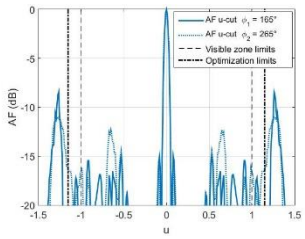

Fig. 8. Array factor representative u-cuts ($\phi_1 = 165°$and $\phi_2 = 265°$) for the concentric ring array optimized at the $(u\, d_{elem}/\lambda)^2 + (v\, d_{elem}/\lambda)^2 \leq 1.866^2$ zone, at 2 GHz (2nd optimization).

VI. RESULTS DISCUSSION

By using three criteria for defining the array bandwidth, we have shown that limiting the optimized zone of the AF to exclude the 2nd GL zone is a good strategy for reducing the optimization time. The sidelobes in the 2nd GL zone are attenuated once the radiating pattern of the array's elements are taken into account. Prioritizing the sidelobes in the 1st GL zone when optimizing the array's AF compensates their rise once the radiating pattern is considered. By optimizing only half of the u-v space there was no bandwidth reduction, proving it to be a great way to reduce the computation time of the cost function. Further reduction of the optimized region consistently caused a reduction in the bandwidth, so it was not considered in this paper. As for the time reduction, there are two main factors. First, by limiting the optimized zone in the AF, there are less points to be computed in the u-v space, which results in a faster cost function. This is true for both the 2nd and 3rd optimizations. Second, in the 2nd and 3rd optimizations the genetic algorithms converged faster. We cannot draw any special conclusions from this faster convergence as we would need to validate that fact by re-optimizing the array enough times to have statistically meaningful results, which was time prohibitive in our case.By comparing the first and last optimizations, the latter spent 22.3% of the time needed for the first one while enhancing the bandwidth from 27% to 95% (1-2 GHz) of [6].

Table 2: Comparison of results

Optimized zone	$\theta_s < 30°$ at 2 GHz	Avoid 2nd GL	Avoid 2nd GL, $u > 0$
Bandwidth (GHz)	1-1.3 (27%)	1-2 (95%)	1-2 (95%)
Cost function call time (s)	3.8-6.3 (100%)	2.2-3.7 (59%)	1.1-1.9 (30%)
Cost function calls	88985 (100%)	77988 (88%)	59387 (67%)
Opt. time (h)	38 (100%)	21 (55%)	8 (22%)

VII. CONCLUSIONS

By analyzing the concentric ring array topology with a size constraint [3] and redesigning its cost function, it was possible to find an array with 95% of the bandwidth in [6] and 42% of its surface, as well as an optimization 4.5 times faster than in [3]. For the bandwidth, the key factor was to identify the sidelobes to be optimized when considering the embedded element model. As for the time reduction, by reducing the optimized area, we got a cost function that is 3.4 times faster.

REFERENCES

[1] C. Fulton, J. Herd, S. Karimkashi, G. Zhang, and D. Zrnic, "Dual-polarization challenges in weather radar requirements for multifunction phased array radar," *2013 IEEE Int. Symp. on Pha. Array Syst. and Tech*., Waltham, MA, pp. 494-501, 2013.

[2] E. Pottier and L. Ferro-Famil, "Advances in sar polarimetry applications exploiting polarimetric spaceborne sensors," in *Proc. IEEE Radar Conference, RADAR '08*, 2008.

[3] P. Mendes Ruiz, I. Hinostroza, R. Guinvarc'h, and R. L. Haupt, "Size constraint in design of concentric ring array," in *IEEE Int. Symp. on Ant. & Prop. (APSURSI)*, 2015.

[4] J. A. Kaiser, "The archimedean two-wire spiral antenna," *IRE Trans. on Ant. & Prop*., 8 (3), 312-323, 1960.

[5] R. Guinvarc'h and R. L. Haupt, "Dual polarization interleaved spiral antenna phased array with an octave bandwidth," *IEEE Trans. on Ant. & Prop*., vol. 58, no. 2, pp. 397-403, 2010.

[6] I. D. Hinostroza Saenz, R. Guinvarc'h, R. L. Haupt, and K. Louertani, "A dual-polarized wideband planar phased array with spiral antennas," *IEEE Trans. on Ant. & Prop*., vol. 62, no. 9, pp. 4547-4553, 2014.

[7] J. Huang, "A technique for an array to generate circular polarization with linearly polarized elements," *IEEE Trans. Ant. Prop*., 34(9), 1113-1124, 1986.

[8] P. Mendes Ruiz, I. Hinostroza, R. Guinvarc'h, and R. L. Haupt, "Genetic algorithm optimization of a dual polarized concentric ring array," *2017 Int. Ap. Comp. Elec. Soc. Symp. Italy (ACES)*, Florence, pp. 1-2, 2017.

[9] R. L. Haupt, *Genetic Algorithms in Electromagnetics*. John Wiley & Sons, New Jersey, USA, 2007.

Design of Double Layers Miniaturized Trimmed Semi-Rectangular Monopole with Partial Ground Plane for Short Ranges Wireless Systems

Haitham Alsaif

Department of Electrical Engineering
University of Hail, Hail City, KSA
hal-saif@hotmail.com

Abstract ─ This paper presents a new miniaturized design of antenna with extremely wide bandwidth. The design consists of trimmed half rectangular patch printed on a 10x13 mm^2 substrate of Rogers Duroid RT5880Lz with relative permittivity of ϵr=1.96 and loss tangent of 0.0009. The monopole has a partial modified ground plane structure to enhance the impedance matching and to provide wider bandwidth from 2.6 GHz to 15.7 GHz with reflection coefficient less than -10 dB. The proposed design has been tested, optimized, and experimentally measured for verifications; simulated and measured results have achieved high concord. The presented monopole is suitable for short range wireless systems as well as lower 5G bands applications.

Index Terms ─ Lower 5G, patch, short range systems, UWB antenna.

I. INTRODUCTION

Recently, miniaturized antennas with wide operating frequencies have gained more attention in the modern wireless communication systems [1-3]. This is due to the significant features of such antennas in extremely reduced structure size, high speed data rates, simplicity, and power consumption results for in longer battery life. Hence, varies of ultra wide band antennas have been introduced and published recently to satisfy the dramatic increment in the demand of wireless systems [4-12]. These antennas have different geometric designs, structure sizes, and performance as well; it has been observed that the majority of them have large structure size as ultra wideband designs in [13-15]. Their sizes are 36x35, 39x38, and 53x49 mm2, respectively. Thus, the size can be an obstacle to implement the monopole in compact wireless systems. In addition, some proposed antennas do not cover the entire UWB allocated for short communication system by FCC from 3.1 GHz to 10.6 GHz [16] for instance the design in [14]. Moreover, several UWB antennas have low power gain which is a critical factor for wireless system and plays a vital role in saving the battery life [17-19]. Based on that, the proposed monopole antenna in this paper has overcome these shortages without scarifying in the main performance parameters. This design is characterized by miniaturized structure size, high impedance matching, and high power gain. Also, the antenna has an omni directional radiation pattern in total. Thus, the design can be placed in any position within the gadget or device and has wider radiation. The patch is suitable for short ranges wireless applications, lower fifth generation systems, and many ultra wide band applications [20].

II. PROPOSED MONOPOLE DESIGN

Two dimensional design and fabricated model of the suggested miniaturized 13x10 mm^2 antenna are shown in Figs. 1 (a, b, and c) labeled with parameters revealed in Table 1. As demonstrated in the former figure, the antenna has a partial ground plane at which I-shape slots placed to enhance impedance matching leading to wider bandwidth as presented in details in the following section. The proposed design consists of a trimmed half rectangle made on a substrate of Rogers RT 5880LZ material with relative permittivity of ϵr=1.96 and loss tangent of 0.0009. The monopole is fed by a 6.5 mm long and 1.8 mm wide microstrip feeding line with a characteristic impedance of 50 ohm. The patch has been designed using an industrial standards modeling software and fabricated for more verifications.

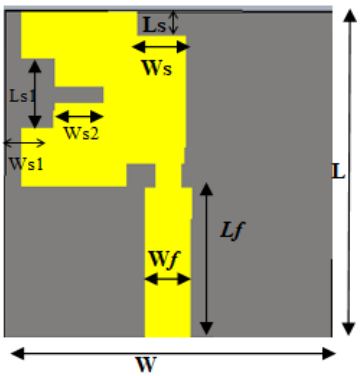

(a)

Submitted On: November 8, 2017
Accepted On: March 5, 2019

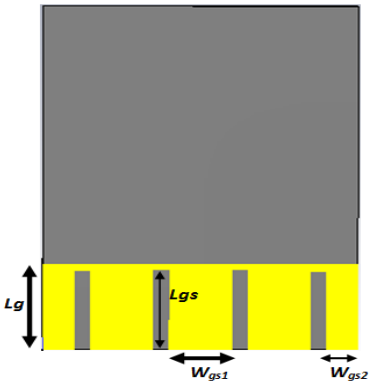

(b)

(c)

Fig. 1. (a) Geometry of the proposed antenna top layer, (b) bottom layer, and (c) image of fabricated design.

Table 1: The presented half rectangular antenna parameters in mm

Parameter	Value in mm	Parameter	Value in mm
L	13	Lg	3.5
W	10	Lgs	3.25
H	0.9	Wgs1	2
Wf	1.8	Wgs2	1
Lf	6.5	Ls	1
Ls1	2.5	Ls2	2

III. MODELING RESULTS AND EXPERIMENTAL MEASUREMENTS

In general, narrow band antenna contains single resonant frequency while ultra wide band antenna has multiple resonant frequencies together creating the ultra-wideband width [21]. According this concept, the presented antenna contains two main resonant frequencies at 5.8 GHz and 10.6 GHz creating a wide bandwidth starting from 2.6 to 15.7 GHz as shown in Fig. 2. Measured and simulated reflection coefficients have an acceptable alignment with minor deviations due to popular causes for instance measuring and fabrication equipment tolerance, soldering effects etc.

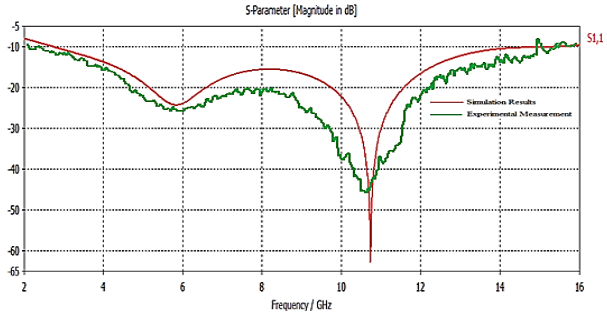

Fig. 2 reflection coefficient (S11) in dB versus operating frequency in GHz

As part of the optimization and analysis process, the proposed monopole parameters and several substrate materials have been examined for improving performance in terms of bandwidth and radiation pattern while maintaining minimized structure size. Numerous popular dielectric materials, which are Polyimide, FR-4, and Rogers RT 5880LZ with relative permittivity of 3.5, 4.3, and 1.96 respectively, have been studied. Figure 3 displays reflection coefficient parameter for the previous materials versus operating frequency. Obviously, using Rogers RT 5880LZ (εr =1.96) bandwidth is the widest with extremely diminished power loss and S11 reaches below -60 dB. Thus, at this resonant frequency, the accepted power by the radiator is more than 99.9% of input power [2]. Figure 4 illustrates the antenna reflection coefficient (S11) with and without I-shape slots. It is clearly overserved that the significant effects of this modification on the impedance matching and bandwidth. Besides, the microstrip feeding line width plays key role in the optimization process. Since the feeding line is transferring the input power into radiator structure where both have to be at high matching. Figure 5 displays multiple values of wf in mm where the optimum S11 is obtained at 1.8 mm.

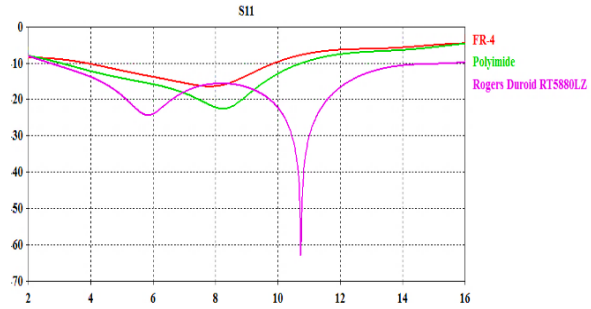

Fig. 3. Reflection coefficient in dB vs frequency in GHz using several popular substrate materials (Polyamide, FR4, and Rogers Duroid RT5880 LZ).

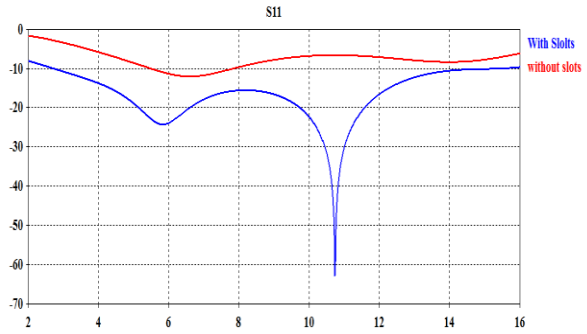

Fig. 4. The S11 parameter in dB for the proposed antenna showing the effect of the partial ground plane structure (DGS).

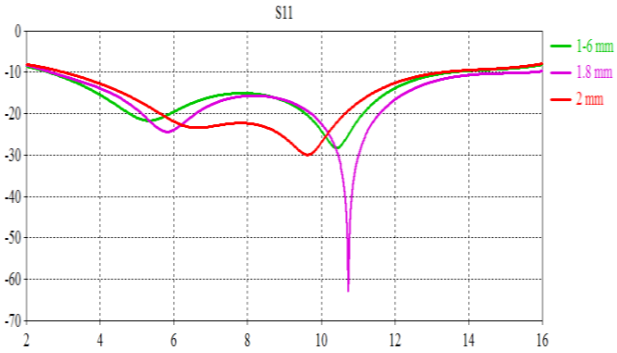

Fig. 5. Studying the width parameter of the feeding line (wf) for the presented design.

Figure 6 shows the presented antenna normalized radiation pattern at the two orthogonal planes elevation (E) and azimuth (H) at 5.8 GHz, and 10.6 GHz. the radiation patterns are revealed at the two orthogonal planes, E plane or elevation plane and H plane or azimuth plane in polar forms. Throughout the entire bandwidth, the radiation pattern at the azimuth plane has an omni-directional pattern. Besides, elevation plane has approximately bi-directional form with minor distortion. Hence, the presented patch is independent of placement position during the broad bandwidth. Also, the measured power gain of the proposed monopole has been plotted over the wide bandwidth in Fig. 7. It can be noticed that the design has high gain with a maximum of 6 dB.

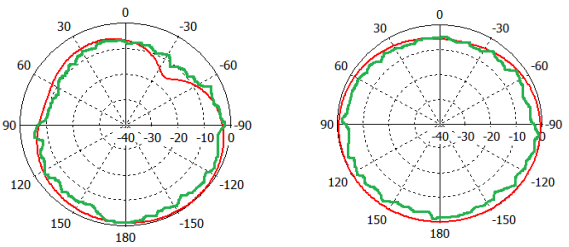

(a)

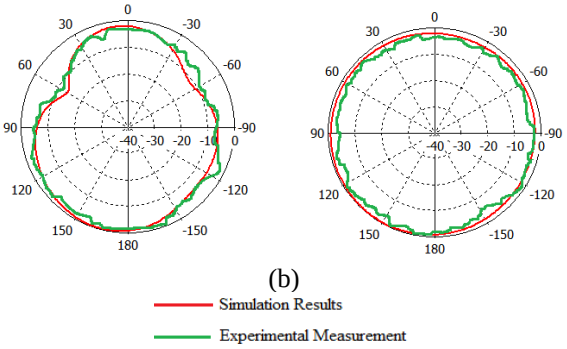

(b)

Simulation Results

Experimental Measurement

Fig. 6. The normalized radiation pattern for E and H planes in polar form at the two resonant frequencies.

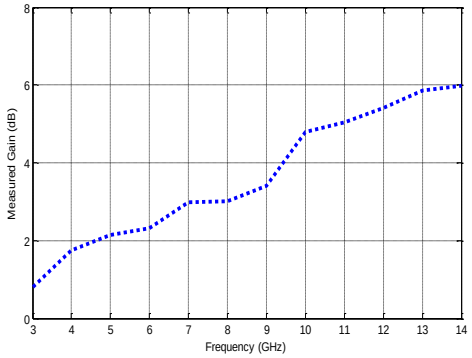

Fig. 7. Measured power gain in dB vs the operating frequency.

IV. CONCLUSION

A novel miniaturized antenna design is proposed for ultra wideband systems. The monopole is minimized with a total size of (13 x 10x 0.9 mm^3), while retaining high features performance. The presented monopole has an extreme wide bandwidth ranging from 2.62 GHz to 15.7 GHz with a bandwidth of more than 13GHz which covers the band set by FCC [16]. The antenna is characterized is by an omni-directional pattern through the operating frequency. Lastly, the trimmed design has competing performance in comparison with several other larger structure designs which makes it exceedingly appropriate for extremely compact wireless applications.

ACKNOWLEDGMENT

This work has been supported by the Deanship of Scientific Research (DSR) at the University of Hail, KSA with a project number is (BA-1512).

REFERENCES

[1] R. J. Fontana, "Recent system applications of short-pulse ultra-wideband (UWB) technology," *IEEE Trans. MTT*, vol. 52, pp. 2087-2104, 2004.

[2] H. Schantz, *The Art and Science of Ultra Wideband*

Antennas. Norwood, MA: Artech House, 2005. W.-K. Chen, Linear Networks and Systems (Book style). Belmont, CA: Wadsworth, pp. 123-135, 1993.

[3] S. Ashok Kumar and T. Shanmuganantham, "Design and analysis of implantable CPW fed X-monopole antenna for ISM band applications," *Telemed. e-Health*, vol. 20, no. 3, pp. 246-252, Mary Ann Liebert Inc, USA, 2014.

[4] M.-C. Tang, T. Shi, R. W. Ziolkowski, "Planar ultrawideband antennas with improved realized gain performance," *EEE Trans. Anten. Propag*., vol. 64, pp. 61-9, 2016. http://dx.doi.org/10.1109/TAP.2015.2503732

[5] Y. J. Ren and K. Chang, "Ultra-wideband planar elliptical ring antenna," *Electronics Lett*., vol. 42, no. 8, pp. 447-449, Apr. 2006.

[6] M. G. N. Alsath and M. Kanagasabai, "Compact UWB monopole antenna for automotive communications," *IEEE Trans. Antennas Propag*., vol. 63, no. 9, pp. 4204-8, 2015.

[7] S. Kharche, G. S. Reddy, B. Mukherjee, R. Gupta, and J. Mukherjee, "MIMO antenna for bluetooth, Wi-Fi, Wi-MAX and UWB applications," *Prog. Electromag. Res. C*, vol. 52, pp. 53-62, 2014.

[8] N. M. Awad and M. K. Abdelazeez, "Multislot microstrip antenna for ultra-wide band applications," *Journal of King Saud University Engineering Sciences*, 2016, http://dx.doi.org/10.1016/j.jksues.2015.12.003

[9] H. A. Atallah, A. B. Abdel-Rahman, K. Yoshitomi, and R. K. Pokharel, "Design of dual bandnotched CPW-fed UWB planar monopole antenna using microstrip resonators," *Prog. Electromagn. Res. Lett*., vol. 59, pp. 51-6, 2016.

[10] M. N. Moghadasi, H. Rousta, and B. S. Virdee, "Compact UWB planar monopole antenna," *IEEE Antennas Wireless Propag. Lett*., vol. 8, no. 22, pp. 1382-1385, 2009.

[11] O. M. H. Ahmed, A. R. Sebak, and T. Denidni, "Compact UWB printed monopole loaded with dielectric resonator antenna," *Electronics Letters*, vol. 47, no. 1, pp. 7-8, 2011.

[12] S. Kharche, G. S. Reddy, B. Mukherjee, R. Gupta, and J. Mukherjee, "MIMO antenna for bluetooth, Wi-Fi, Wi-MAX and UWB applications," *Prog. Electromag. Res. C*, vol. 52, pp. 53-62, 2014.

[13] F. Zhu, S. Gao, A. T. S. Ho, C. H. See, R. A. Abd-Alhameed, J. Li, and J. Xu, "Compact-size linearly tapered slot antenna for portable ultra-wideband imaging systems," *International Journal of RF and Microwave Computer-Aided Engineering*, vol. 23, no. 3, 2013.

[14] F. Zhu, S. Gao, A. T. S. Ho, R. A. Abd-Alhameed, C. H. See, J. Z. Li, and J. D. Xu, "Miniaturized tapered slot antenna with signal rejection in 5–6 GHz band using a balun," *IEEE Antennas Wireless Propag. Lett*., vol. 11, pp. 507-510, 2012.

[15] K. Shambavi and Z. C. Alex, "Design of printed dipole antenna for ultra wideband applications," *Microwave and Optical Technology Letters*, vol. 54, no. 3, 2012.

[16] Federal Communication Commission, First Report and Order, Revision of Part15 of the Commission's Rules Regarding Ultra-Wideband Transmission System, FCC 02 48, 2002

[17] R. Azim, A. T. Mobashsher, and M. T. Islam, "Ultra-wideband slot antenna with notched band for world interoperability for microwave access," *International Journal of Communication Science and Engineering*, vol. 7, no. 7, 2013.

[18] F. Zhu, S. Gao, A. T. S. Ho, C. H. See, R. A. Abd-Alhameed, J. Li, and J. Xu, "Design and analysis of planar ultra-wideband antenna with dual band-notched function," *Prog. Electromagn. Res*., vol. 127, pp. 523-536, 2012.

[19] M. N. Srifi, S. K. Podilchak, M. Essaaidi, and Y. M. M. Antar, "Compact disc monopole antennas for current and future ultrawideband (UWB) applications," *IEEE Transactions on Antennas and Propagation*, vol. 59, no. 12, 2011.

[20] GSMA Spectrum, 5G Spectrum, Public Policy Position, Nov. 2016. Available at: https://www.gsma.com/spectrum/wp-content/uploads/2016/06/GSMA-5G-Spectrum-PPP.pdf

[21] A. Gautam, S. Yadav, and B. Kanaujia, "A CPW fed compact UWB microstrip antenna," *IEEE Antennas and Wireless Propagation Letters*, vol. 12, pp. 151-154, 2013.

Gain Enhancement of Microstrip Patch Antenna Using Metamaterial Superstrate

H. R. Vani [1], M. A. Goutham [1], and Paramesha [2]

[1] Department of Electronics and Communication Engineering
Adichunchanagiri Institute of Technology (AIT), Chikkamagaluru, Karnataka
Vani4ait@gmail.com

[2] Department of Electronics and Communication Engineering
Government Engineering College, Hassan, Karnataka

Abstract ─ In this work, a gain enhancement of conventional microstrip patch antenna has been treated for WLAN applications. About 1.3dB gain enhancement, compared to a conventional patch, has been achieved by loading the microstrip patch with a metamaterial superstrate composed of 2x3 array of Square Split Ring Resonator. Simulations have been carried out using Ansys HFSS. Measured results have been taken to validate the simulation result.

Index Terms ─ Metamaterials, microstrip patch antenna.

I. INTRODUCTION

Modern wireless communication system requires high data rate that depends on the gain of the antenna. Towards this, metamaterial starts playing a very important role in the design of an antenna [1]-[3]. In [4], gain enhancement of microstrip patch antenna (MPA) is achieved by using graded index dielectric superstrate. In [5], a planar two-layer superstrate over a printed patch antenna to enhance the broadside gain is considered. The problem of enhancing the directivity of an aperture coupled microstrip patch antenna using one dimensional electromagnetic bandgap (EBG) structure is treated in [6]. It was found that the directivity level, beamwidth as well as reflection coefficient and gain could be enhanced by using superstrate with two layers. In [7], study of performance parameters of patch antennas with different feeding methods is presented and compared with that of patch antennas without dielectric superstrate. It was found that the directivity level, beam width as well as reflection coefficient and VSWR could be further enhanced by using superstrate with two layers rather than one, regardless of the feeding method. In [8], a meandered line-double split ring resonator (DSRR) superstrate loaded high gain circular patch antenna is presented for X-band and showed that the superstrate loading has minor effect on the return loss characteristics but a major effect on the gain characteristics of the circular patch. Scope for miniaturization and compactness of an antenna leads to the design of novel antenna structure loaded with metamaterial. Hence, in the proposed work, a metamaterial superstrate loaded microstrip patch antenna is designed on low cost, FR4 epoxy substrate for WLAN application.

II. ANTENNA DESIGN

A. Microstrip patch antenna without superstrate

The microstrip patch antenna with co-axial feeding is designed using ANSYS HFSS on a less expensive, widely available FR4 epoxy substrate with relative permittivity of 4.4 and dielectric loss tangent of 0.02 for 5.5 GHz WLAN application. Figure 1 shows simulated top view of MPA. The dimension of the patch and the substrate is 12mm x 16mm x 0.1mm and 26mm x 30mm x 1.6mm respectively. The equations to calculate the dimension of patch antenna are given in [9].

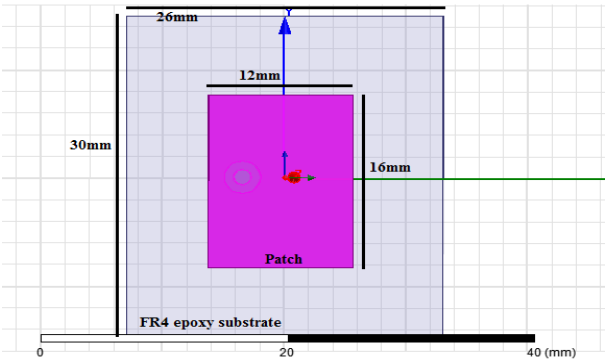

Fig. 1. Simulated top view of rectangular MPA.

Submitted On: August 6, 2018
Accepted On: March 18, 2019

B. Proposed MPA with metamaterial superstrate

The proposed design consists of metamaterial superstrate loaded microstrip patch antenna. Figure 2 (a) shows the geometry of square split ring resonator metamaterial. The dimension of the ring is 6mm x 6mm. The gap width is 1.5mm. Figure 2 (b) shows the simulated metamaterial superstrate loaded microstrip patch antenna. The metamaterial superstrate is composed of 2x3 array of Square Split Ring Resonator on a FR4 epoxy material. The superstrate dimension is 26mm x 30mm x 1.6mm and is placed at a height of 5mm from the substrate. The fabricated metamaterial superstrate loaded MPA prototype is shown in Fig. 2 (c).

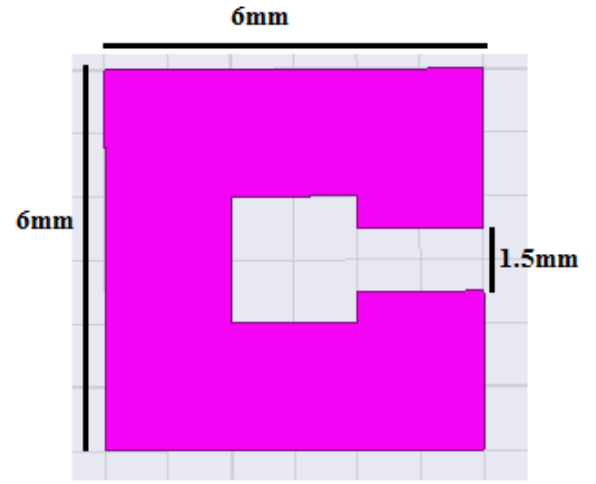

(a)

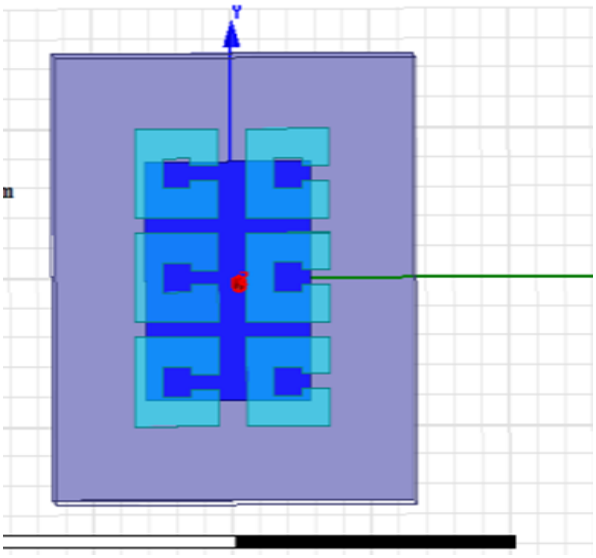

(b)

(c)

Fig. 2. (a) Metamaterial unit cell, (b) simulated metamaterial superstrate loaded MPA, and (c) fabricated metamaterial superstrate loaded MPA.

III. SIMULATED AND MEASURED RESULTS

The S-parameters for metamaterial unit cell is shown in Fig. 3 (a). S11 and S21 parameters crosses at 4.8GHz and 6.1 GHz. Hence, the unit cell structure reflects the electromagnetic waves in this band [10]. The measurements are taken on Vector Network Analyzer (Rohde and Schwarz, German make ZVK Model No. 1127.8651). The simulated and measured return loss of microstrip patch antenna with and without superstrate loading is shown in Fig. 3 (b). The summary of simulation and tested results is shown in Table 1.

From Fig. 4 it is clearly seen from simulation that the antenna gain is increased by 1.2dB when metamaterial superstrate is included in the system.

The experimental setup for the gain measurement is shown in Fig. 5. Two steps were used for the estimation of antenna gain. In the first step estimation of gain without metamaterial superstrate is made followed by estimation of gain with metamaterial superstrate. For gain calculation equation in [7] is used:

$$G(dB) = 10\log\left(\frac{P_r}{P_t}\right) - G_t(dB) - 20\log\left(\frac{\lambda_0}{4\pi R}\right)(dB). \quad (1)$$

Where P_t and P_r are transmitted and received powers respectively. G_t is the gain of the pyramidal horn antenna

equal to 17dB. *R* is the distance between transmitting antenna and antenna under test. The gains obtained from measurements are 3.7dB and 5dB for patch antenna without and with metamaterial superstrate loading respectively. The enhancement in gain is better with less number of rings on the FR4 epoxy superstrate than that obtained in [10].

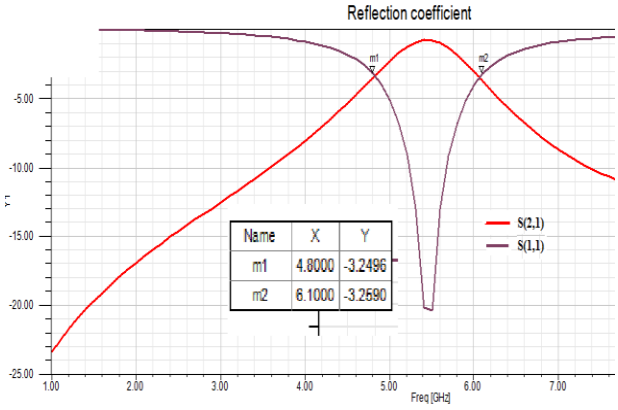

(a)

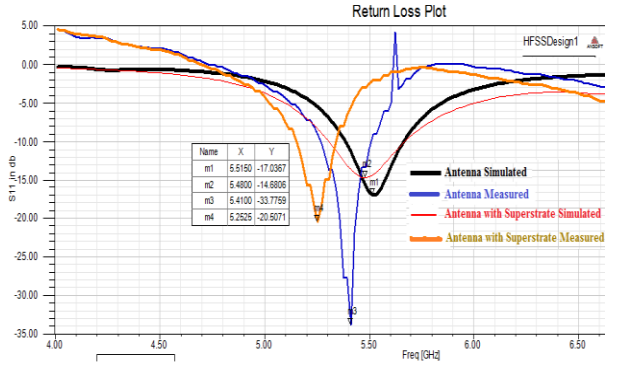

(b)

Fig. 3. (a) S-parameters for the metamaterial unit cell. (b) Simulated and measured |S11| responses of the microstrip patch antenna with and without superstrate loading.

Table 1: Summary of simulation and tested results

Parameters	**MPA without Superstrate**		**MPA with Superstrate**	
	Simulated	**Fabricated**	**Simulated**	**Fabricated**
Resonant Frequency (in GHz)	5.51	5.41	5.48	5.25
Return Loss (in dB)	–17.03	–33.77	-14	-20

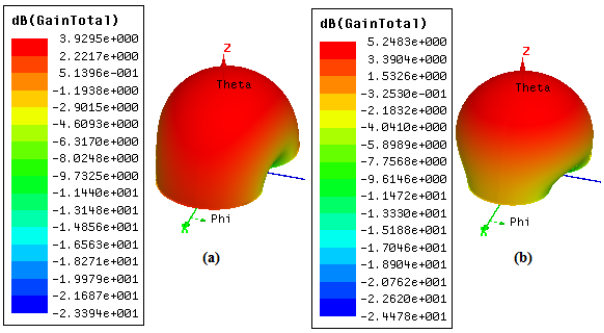

Fig. 4. (a) and (b) simulated 3D gain plot for microstrip patch antenna without and with superstrate loading.

Fig. 5. Experimental setup for the estimation of antenna gain.

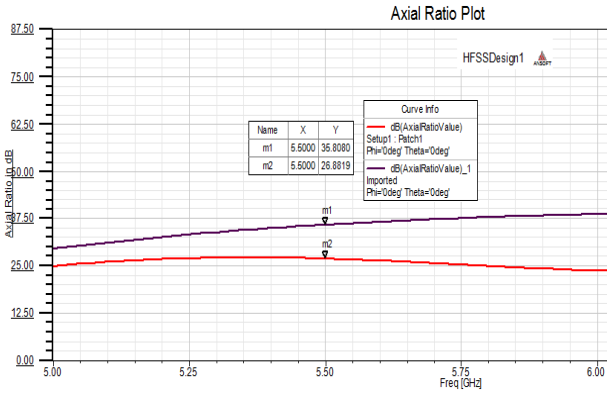

Fig. 6. Variation of axial ratio with frequency.

HFSS simulation of variation of axial ratio with frequency is shown in Fig. 6. At 5.5GHz, the axial ratio is 26.8dB and 35dB for MPA with and without

superstrate respectively. This indicates that the antennas are linearly polarized.

IV. CONCLUSION

A Square Split Ring Resonator metamaterial superstrate loaded microstrip patch antenna for gain enhancement has been presented in this paper for WLAN applications. A comparison of the characteristics of the proposed antenna with a conventional patch antenna shows that the superstrate loading has minor effect on the return loss characteristics but a major effect on the gain characteristics of the patch. The superstrate loading has enhanced the gain by about 1.3 dB as compared to a conventional patch.

ACKNOWLEDGMENT

The author would like to thank the Department of Applied Science, Gulburga University, Karnataka for testing the antennas.

REFERENCES

[1] M. Gil, F. Aznar, A. Velez, et al., "Electrically small resonators for metamaterial and microwave circuit design," in *Passive Microwave Components and Antennas, V. Zhurbenko*, Ed., InTech, 2010.

[2] J. D. Baena, R. Marque's, and F. Medina, "Artificial magnetic metamaterial design by using spiral resonators," *Physical Review B*, 69, 014402, 2004.

[3] S. A. Tretyakov, C. R. Simovski, and M. Hudlicka, "Bianisotropic route to the realization and matching of backward-wave metamaterial slabs," *Physical Review B*, 75, 153104, 2007.

[4] Y. Li, K. Yoo, R. Mittra, G. Lu, D. Zeng, and Y. Guan, "Directivity enhancement of microstrip antennas using dielectric superstrates," *2010 International Conference on Applications of Electromagnetism and Student Innovation Competition Awards (AEM2C)*, Taipei, pp. 206-209, 2010.

[5] H. Errifi, A. Baghdad, A. Badri, and A. Sahel, "Directivity enhancement of aperture coupled microstrip patch antenna using two layers dielectric superstrate," *Proceedings of 2014 Mediterranean Microwave Symposium (MMS2014)*, Marrakech, pp. 1-4, 2014.

[6] J. C. Iriarte, *et al*., "EBG superstrate for gain enhancement of a circularly polarized patch antenna," *2006 IEEE Antennas and Propagation Society International Symposium*, Albuquerque, NM, pp. 2993-2996, 2006.

[7] H. Errifi, A. Baghdad, A. Badri, and A. Sahel, "Optimization and performance analysis of probe-edge-inset and aperture feed patch antenna covered by dielectric superstrate," *2015 International Conference on Wireless Networks and Mobile Communications (WINCOM)*, Marrakech, pp. 1-8, 2015.

[8] D. Gangwar, S. Das, and R. L. Yadava, "A meander line-DSRR double superstrate loaded high gain circular patch antenna," *2017 IEEE Applied Electromagnetics Conference (AEMC)*, Aurangabad, pp. 1-2, 2017.

[9] C. A. Balanis, *Antenna Theory: Analysis and Design*. Wiley-Interscience, New York, NY, USA, 2005.

[10] M. Saravanan, G. V. Beslin, and S. M. Umarani, "Gain enhancement of patch antenna integrated with metamaterial inspired superstrate," *Journal of Electrical Systems and Information Technology*, 2018.

Vani H. R. did her B.E. in Instrumentation Technology in 1991 from Mysore University, M.Tech in Industrial Electronics from NITK, Surathkal in 2003. She is working as Associate Professor in ECE at Adichunchanagiri Institute of Technology (AIT), Chikkamagaluru Karnataka. She is a Life Member of ISTE, New Delhi.

Goutham M. A., did his B.E. in Electronics and Communication. Engineering in 2001 from Kuvempu University, M.Tech in (Digital Electronics and Communication Systems) from Visveswaraiah Technological University (VTU) Belagavi, in 2005 and Ph.D. from Jadhavpur University, West Bengal, India in 2010. He is Professor in Electronics and Communication. Engineering Dept. with an experience of 15 years at Adichunchanagiri Institute of Technology (AIT), Chikkamagaluru, Karnataka. His current research interest includes MEMS, Wireless and Ad-hoc networks. He is a Life Member of ISTE, New Delhi.

Paramesha did his B.E. in Electronics and Communication. Engineering in 1989, M.Tech in Microwave Engineering from Banaras Hindu University, Varanasi, India in 1997 and Ph.D. from Indian Institute of Technology (IIT), Kharagpur, West Bengal, India in 2007. He is Professor and Head in Electronics and Communication Engineering Department at GEC, Hassan, Karnataka. His current research interest includes antennas for Satellite Communication, Microwave Antennas, and Millimeter systems. He is a Life Member of ISTE, New Delhi.